ICCEE2023 Proceedings

Abdelsalam Zidan, Mahmoud Nasr, Manabu Fujii, and Mona G. Ibrahim
Influence of variable hydraulic retention time (HRT) on the treatment of synthetic domestic wastewater using a down-flow hanging sponge (DHS) reactor

Ibrahim Moukhtar , Marwa Mahmoud Hamed, Loai S Nasrat, Adel Z. El-Dein, Esam H. Abdelhameed[1], A. El-Tayeb [1],
Nanotechnology-Based Single Phase Liquid Immersion Cooling Strategy for Thermal Performance Enhancement of Lithium-Ion Battery Pack

Ahmad Abo El Ezz École de technologie supérieure, Université du Québec, Montréal, Canada
Seismic risk assessment of hazardous materials storage tanks in energy facilities

A. A. Mohamed, A. S. Fathalla, E.-S. Z. El-Ashtoukhy, G.H. Sedahmed1 and M. A. EL-Naggar
Intensification of the rate of mass transfer in tubular reactors using longitudinal baffles sheets

Ahmed Gamal Mohamed Zaki, Mohamed Morsy Elgohary and Ibrahim S. Seddiek
The future of new Alternative marine fuel for passenger ships

Ahmed G. Mohamed , Aya A. Elbauomy Arab Academy for Science, Technology and Maritime Transport, Egypt Green Hydrogen Toward Sustainable Marine Fuel

Ahmed Wahba Gabr, Abbas Anwar Ezzat, A.H. EL-Shazly, Wael Bakr, Mohammed Shamakh and N.S. Yousef [2] Khalda Petroleum Co., Modelling and Simulation of CO2 Removal from Natural Gas by Membranes

Alaa Dandash[1, a,] Shaban Nosier[2] , Heba Abdallah[3,b], Samah A. Hawash[4- 5,c] and Usama Eldemerdash[6,d] Removal of Phenol from Wastewater by Different Polymeric Membranes Using Pervaporation Technique

Nagat A. Mostafa[1] and Aliaa M. Monazie[†2] Comparative and optimization study of utilizing alginate and agar flocculants for water treatment

Aya A. Elbauomy[1, a], Mohamed R. Shouman[2, b] and Mohamed M. Elgohary [3,] comparative assessment of hydrogen and ammonia fuel for reducing ship emissions

D.N. Shaaban[†1], M.A. El-Naggar[1], S.A. Nosier1, G.H. Sedahmed[1] and A.S. Fathalla Reduction of hexavalent chromium to trivalent chromium by using a fixed bed of iron solid cylinders

A. El-Tayeb*,1, Jackleen S. Same*,1, Esam H. Abdelhameed1, Adel Z. El-Dein1,2, Ibrahim Moukhtar1, Simulation Study to investigate the effect of Anode Material and Thickness on the Thermal Properties of Lithium-Ion Batteries

Hani Ezz[1,a], Mona G. Ibrahim[1,2,b], Mahmoud Nasr[1,3,c] ,Algae-bacterial granular sludge for domestic wastewater treatment: A sustainable development approach

A. El-Tayeb*,1, Asmaa A. Mohamed1,*, Esam H. Abdelhameed1, Adel Z. El-Dein1,2, Ibrahim Moukhtar1, Advanced Nanotechnology-based Techniques for LIB Performance Improvement

Khadiga M. Mekky[1], Mahmoud Nasr[1,2], Kamal Sharobim[3], Manabu Fujii[4], and Mona G. Ibrahim[1,5] A Life Cycle Assessment for Environmental Evaluation of Concrete Mixes with Water Treatment Sludge

Kareem Wagdy[1, a], Osama A. Elsamni[1,b] , Mohamed Shawky[1,c] , Sami Elsherbiny[1,d] Enhancing the heat transfer of gases in PTC absorber tubes using porous twisted tape inserts

Lamiaa Abdallah[1, a] and Tarek El-Shennawy[2,b] Evaluating the Carbon Footprint (CFP) of a Refinery and Suggested Decarbonization Measures

Lengu Peter Tuok 1, a , Marwa Elkady 2,c , Abdelrahman Zkria 2,3 , Tsuyoshi Yoshitake 2,c , Usama Nour Eldemerdash 5,b Synthesis and characterization of ZnO nanoparticles and how temperature variation affects their morphological structure

Mahmoud A. Farouk [1.2] , Mohamed M. Elgohary[1] , Ashraf A. Zahran [3] , Mohamed R. Shouman [2] Experimental research for reducing emissions in maritime industry

Manal Wael[1, a], Sally Hosny[1], Ehab Lotfy[1] and Erfan Abd El Latif[1] Sustainable techniques of retrofitting non-ductile reinforced concrete beam-to-column joints subjected to cyclic loading

Marwa Nabil[1, a] Bio-active glass (S45P0) for waste water treatment

Marwan Magdy Abdelfattah1, a, Mohamed Morsy Elgohary2, a,b and Ibrahim S. Seddiek3, c. New Alternative Marine Fuels

Medhat Aboelkheir[1, a], Mohamed.M.El Gohary[1,b] ,Ibrahem Sadek[2,c] . Performance analysis of combined waste heat recovery cycle for improving the energy efficiency

Mohab I. Mefreh[*], Mohamed A. Alnakeeb , Mohamed A. Hassab, Wael M. El-Maghlany Effect of Changing the Amplitude of a Sinusoidal Corrugated Absorber Plate of a Two-Pass Solar Air Heater

Mohamed T. Eltantawy [1,a], Mohamed R. Shouman [2] and Mohamed M. Elgohary [1,b] Numerical investigation of photovoltaic solar system performance for a high-speed ship

M. H. Abdel-Moniem†, E. R. Lotfy, Design and Simulation of a Thermally Controlled Wind Tunnel M.K. El- Saadawy[1, a], H.M.Khalil[2,b] , Y.Abuouf[3,c] and I.G.Adam[4,d] Sensitivity analysis for slug liquid holdup correlations

Mohamed Lotfy [1, a], Radwan M. El-Zoheiry [2,b], Hesham M. El-Batsh [3,c] and Ahmed I. EL-Seesy [4,d] Castor Biodiesel Production and its Combustion Characteristics in Diesel Engine Working With Diesel Fuel and Different Additives: A Critical Review

Mohamed Tamer Mansour[1, a,] Amgad El-Deib[1,b] Tamer M. Mansour [2,c] Utilizing Green Hydrogen as Clean Economical Thermal Energy Substitute to Conventional Fossil Fuel Combustion Boilers

N. Roushdy[1]†, Mohamed S. Elnouby[2], A. A. M. Farag[3], O. El-Shazly[4], E. F. El-Wahidy[4] Metal sulfide investigations for energy conversion and production

NOHA SHAABAN[a], WALID I. ZIDAN[b] Simulation of Fluid Flow and Heat Transfer for Disposal of Radioactive Waste from Fission-based Molybdenum-99 Production

Ahmed. A. Abdel-Naby, Omina. M. Nawar*, Eslam. R. Lotfy Numerical investigations of Darrieus turbine for tidal power applications

R.E. Mohamed[1,a], and M.M. Abd-El-Mooty[2,b] Sustainable environmental Coastal development of the surf zone of Alexandria

S. A. Attia[†1], M. A. El-Naggar[1], A. A. Zatout[1], E.-S. Z. El-Ashtoukhy[1] G. H. Sedahmed[1] and A. S. Fathalla[1], Removal of sulfides from industrial wastewater solutions by electrocoagulation

S.E. Tantawy[1], R.I. Saman[1], A.M. Soultan[1], A.N. Soliman[1], A.A. Shahien[1], D.M. Moustafa[1], M.F. ElKady[1,2] ZIF 8@graphene hybrid preparation and characterization nano-hybrid material

T.M. Ahmed , A.M. Abdelrahman , Y.M. Ahmed and A.A. Banawan Numerical investigation of the effect of different configurations on the resistance of twin-hull ships

Wisdom Kwame Kewu, Ahmed Hassan Elshazly, Abdelrahman Zkria, Hiroshi Naragino, And Usama Nour Eldemerdash Synthesis and characterization of NiO nanoparticles for potential application in enhanced oil recovery

Yasmen Heiba, Mahmoud Nasr, Manabu Fujii, Abdallah E. Mohamed and Mona G. Ibrahim Evaluation of tomato irrigation treatments sustainability: a principal component analysis

A. El-Tayeb, Jackleen S. Same, Esam H. Abdelhameed, Adel Z. El-Dein, Ibrahim Moukhtar, Simulation Study to investigate the effect of Anode Material and Thickness on the Thermal Properties of Lithium-Ion Batteries

Influence of variable hydraulic retention time (HRT) on the treatment of synthetic domestic wastewater using a down-flow hanging sponge (DHS) reactor

Abdelsalam Zidan[1,2], Mahmoud Nasr[1,3], Manabu Fujii[4], and Mona G. Ibrahim[1,5] *

[1]*Department of Environmental Engineering, Egypt-Japan University of Science and Technology (E-JUST), Alexandria 21934, Egypt; abdelsalam.zidan@ejust.edu.eg (A.Z.)*

[2]*Department of Civil Engineering, Faculty of Engineering, Menoufia University, Menoufia 32511, Egypt*

[3]*Department of Sanitary Engineering, Faculty of Engineering, Alexandria University, Alexandria 21544, Egypt*

[4]*Department of Civil and Environmental Engineering, School of Environment and Society, Tokyo Institute of Technology, Tokyo 152-8550, Japan*

[5]*Department of Environmental Health, High Institute of Public Health, Alexandria University, Alexandria 21544, Egypt*

[†]*E-mail: mahmoud.nasr@ejust.edu.eg; Tel.: +20-01006390400*

Keywords: synthetic domestic wastewater; microbial biomass; down-flow hanging sponge; nitrification; natural aeration

Abstract. In this study, a down-flow hanging sponge (DHS) system was investigated for synthetic domestic wastewater (SDW) treatment for more than 120 days with regular feeding. The DHS unit was run at varying hydraulic retention times (HRTs = 6.0-2.0 h) and a fixed COD concentration (COD = 531.62±93.6 mg/L) to investigate the influence of these parameters on the elimination of COD, NH_3, and TSS from SDW. The findings demonstrated that COD, NH_3, and TSS removal efficiencies achieved 94.12±5.21, 93.18±3.19, and 88.07±4.72% at HRT of 6.0 h, respectively. Reducing the HRT to 2.0 h significantly decreased COD, NH_3, and TSS removals to 75.34±3.64, 79.46±2.81, and 72.4±4.17%, respectively. The sponge media supplied a high HRT while retaining a high biomass content, increasing the retention time of the solids. Therefore, this study proposes a suitable and cost-effective method for SDW treatment, achieving acceptable discharge standards, without the need for external artificial aeration or further sludge treatment processes.

Introduction

Domestic wastewater (DWW) is widely produced by daily tasks including bathing, cleaning one's hands, house, and car, washing clothes and kitchenware, and defecating and micturition. DWW has a small number of different organisms and millions of intestinal bacteria, which provide additional risks to the population. Hence, DWW cleansing is essential for ensuring the longevity of water bodies and aquatic life. [1].

The DHS unit is based on the concept of a traditional trickling filter, but instead of using pebbles, gravels, or plastic bits, it employs high-porosity sponge holders. A series of polyurethane sponges are used by DHS units as a medium to hold microorganisms [2]. Without the need for artificial aeration, oxygen is spontaneously absorbed into the residential wastewater flowing through the reactor as the sponge medium of the DHS unit is exposed to the atmosphere through natural ventilation gaps.

The amount of time needed for wastewater to pass through the DHS reactor is known as the HRT. Wastewater is essential to remain in the reactor to interact with the bacteria that adhere to the sponge medium. The DHS reactor's volume, the porosity of the sponge medium, and the wastewater flow rate all affect the HRT. The outcomes demonstrated that the DHS reactor's COD removal efficiency was 89, 80, and 56% for HRT of 6, 4, and 2 hours, respectively [3]. Other parameters, such as ammonia and phosphorus, have similar results [4].

The major goal of this paper is to assess how well the DHS reactor performs when operating at various HRTs between 6.0 and 2.0 h at a constant COD concentration of 531.6293.6 mg/L. The removal effectiveness of COD, ammonia, and TSS are highlighted.

MATERIALS AND METHODS

Characteristics of influent wastewater

The SDW was made by a slight modification from a previous study [5] SDW used during the experiments was consisted of $MgCl{\cdot}6H_2O$ (18 mg/L), 70 mg/L NH_4Cl to be nitrogen source, KH_2PO_4 (11 mg/L), and 200 mg/L $C_2H_3NaO_2{\cdot}3H_2O$. 300 mg/L of Glucose was utilized to produce carbon in the process. Trace elements were consisted of 50 mg/L $MgSO_4{\cdot}7H_2O$, 120 mg/L $ZnSO_4{\cdot}7H_2O$, 40 mg/L $MnSO_4{\cdot}2H_2O$, 10 mg/L $FeSO_4{\cdot}7H_2O$, 150 mg/ L H_3BO_3, 25 g/L $NiCl_2{\cdot}6H_2O$, and 80 mg/L NaCl.

Table 1. Wastewater characteristics.

Parameter	TSS	COD	NH_3	Conductivity	pH
Unit	mg/L	mg/L	mg/L	(µS)	
Value	102.26±13.12	531.62±93.6	66.22±3.47	1316.18±40	7.12±0.82

Configuration of DHS reactor

Fig. 1 demonstrates the graphical layout of the pilot-scale DHS system. The cylindrical polymethyl methacrylate reactor has a height and diameter of 1.5 m and 0.15 m. According to the number and size of sponges inside the reactor, its actual volume was 5.1 L. The sponge media were divided into three parts of the same size (0.4 m high), each containing 1.7 L of sponge scattered at random. The air was naturally spread by openings situated at various elevations of the DHS unit. The sponge items are made of polyurethane and are 3.20 cm in height by 1.60 cm in radius. The DHS was built with a polyurethane sponge that has 0.63 mm-wide pores. It has a specific surface area of 250 m^2/m3, a density of 30 kg/m^3, and a porosity of 90%. About 250 sponges were placed into each section added up to 0.4 m in height, dispersed randomly, and surrounded by a cylindrical net composed of durable plastic.

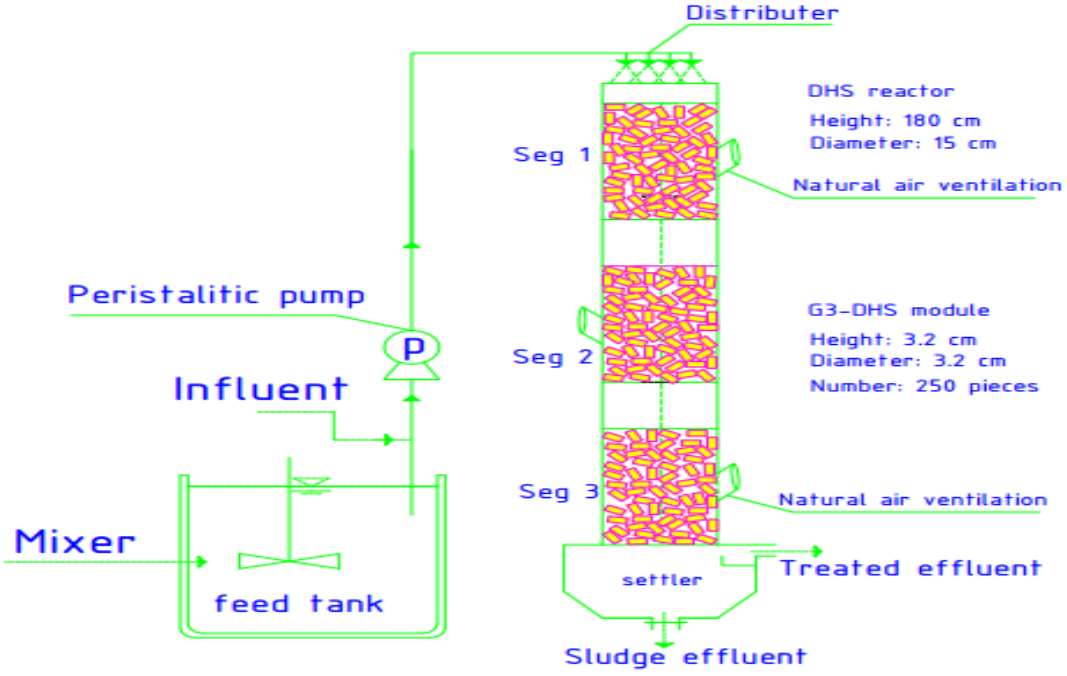

Fig. 1, Configuration of the DHS unit utilized to treat SDW.

Reactor operation

The DHS reactor initially became operational after one month adaptation period to synthetic domestic wastewater. SDW was fed into the upper part of the reactor during the experiment, moved through a distributor, and then gravitationally flowed into the sponge medium, where it was collected in the settling tank. Before beginning to operate in each stage to achieve stable conditions, the system was operated for half a month, which was shown by stable effluent COD and effluent NH_3 concentrations within 6% change for three sequential readings. The DHS model was fed using a peristaltic pump (Master Flex 07522-30, Master Flex, UK) with a changeable flow rate. The flow rate increased from 20.4 to 61.2 L/d, and this corresponded to a decrease in HRT from 6.0 to 2.0 h as shown in Table 2. The DHS unit was operated at a temperature of 23–30 ° C.

Table 2. Operational conditions.

Parameters	[Unit]	Step 1	Step 2	Step 3	Step 4	Step 5
HLR	[$m^3/m^2/d$]	1.15	1.39	1.73	2.31	3.46
SRT	[d]	151.96	86.74	70.33	60.91	52.03
HRT	[h]	6.0	5.0	4.0	3.0	2.0
temperature	[º C]	23-30				
Flow rate (Q)	[L/d]	20.4	24.5	30.6	40.8	61.2
F/M ratio	[Kg COD/kg VS/d]	0.12	0.14	0.15	0.20	0.28

Analytical methods

Analyses were performed based on ‘‘Standard Method for Examination of Water and Wastewater’’ by APHA [6]. COD, TSS, and NH_3 were analyzed from the effluent and the influent per unit three times per week to assess the reactors’ performance. Other parameters including conductivity and pH were measured by a Multi-Parameter Water Quality Meter, WQC-22A (Japan) [7]. A glass fiber filter (0.45 µm) was utilized to calculate volatile solids (VS) and TSS. The sludge concentration of the DHS unit was assessed after the termination of each phase. TSS and VS were calculated as defined by the “Standard Method for Examination of Water and Wastewater” APHA [6].

RESULTS AND DISCUSSION

DHS performance for the removal of COD

Fig. 2a shows how HRT affects effluent COD content and COD removal effectiveness. According to the presented results, the DHS reactor performance was negatively impacted by reducing the HRT. Due to the HRT being reduced from 6.0 to 2.0 h, the COD content in the treated wastewater increased from 30.84±9.8 to 136.56±38.6 mg/L. The sponge media inside the reactor was filled by a big number of microbial biomass, consuming the readily biodegradable fraction of COD. But, under lower HRTs, the adherent biomass does not have enough time to convert most organic compounds into CO_2, H_2O, NH_3, energy, or other end products [8]. Nonetheless, the DHS reactor produced effluent quality conforming to discharge standards (COD <80 mg/L) for reuse in controlled irrigation uses when running at an HRT of 4 h and produced effluent with a concentration of 75.72±14.35 mg/L. In related research, Tawfik et al. [9] revealed that the remaining COD concentration in the treated wastewater raised from 38.0 to 63.0 mg/L due to decreasing the HRT from 4.0 to 2.0 h, respectively. The DHS reactor attained an effluent quality of 30.84±9.8 mg/L for COD at HRT of 6.0 h which is better than those achieved in other studies by using different systems [10]. This significant COD elimination in the DHS reactor could be primarily attributed to entrapment and/or adsorption within the sponge. Due to a drop in HRT, there is less time available to decompose the organic components that are present in wastewater, which results in a decline in COD removal efficiency [11]. By decreasing HRTs from 6.0 to 2.0 h and consequently increasing the hydraulic loading rate from 1.15 to 3.46 L/d, SRT for synthetic domestic wastewater removal decreased from 151.96 to 52.03 d. The decrease in SRT is an important factor in reducing COD removal efficiency because SRT gives heterotrophs a great opportunity to oxidize biodegradable organic matter [9].

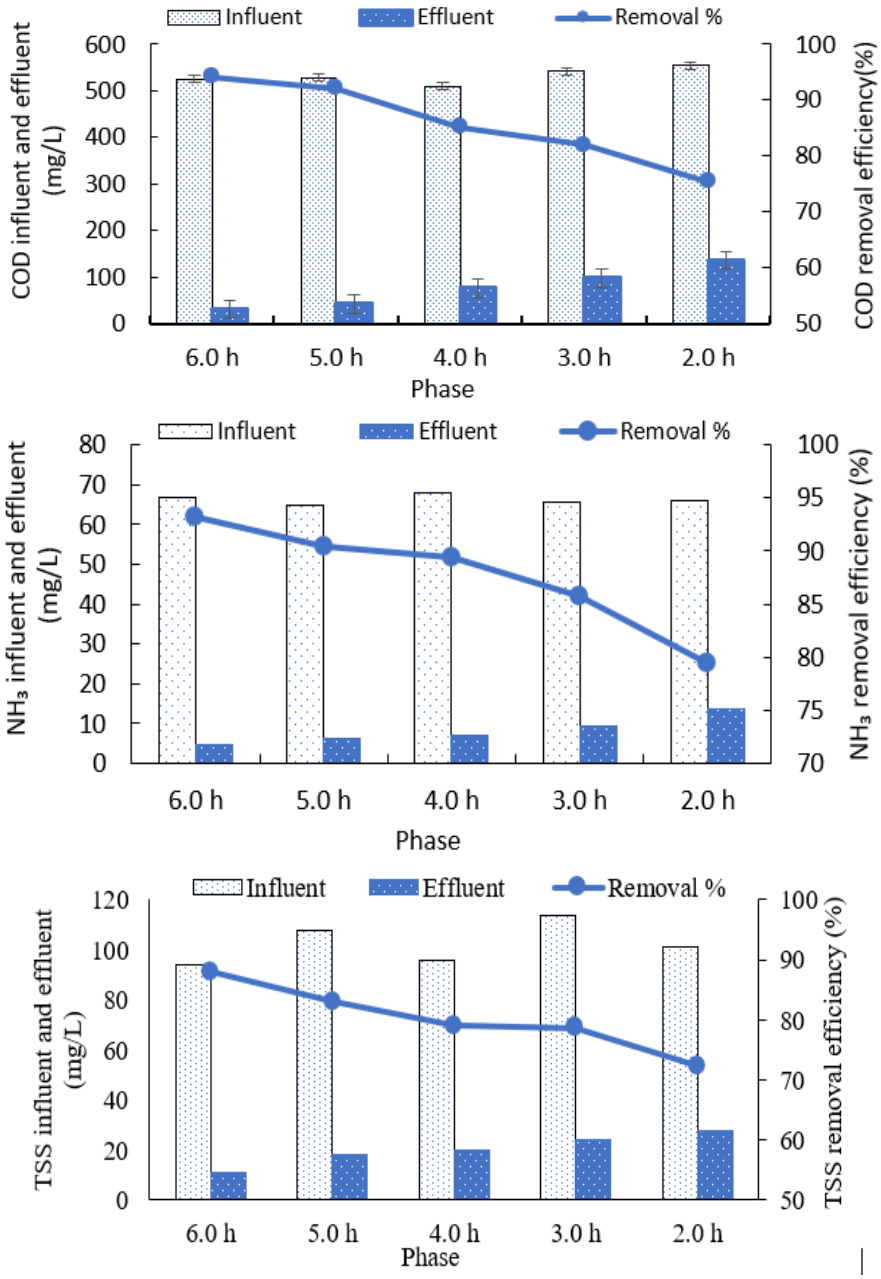

Fig. 2, Effect of changing HRT on DHS performance for (a) COD removal (b) NH_3 removal; (c) TSS removal.

DHS performance for the removal of NH_3

The impact of HRT on the nitrification efficacy in the DHS unit is presented in Fig. 2b. The findings demonstrated that reducing the HRT from 6.0 to 2.0 h considerably decreased the ammonia removal, primarily due to a shorter sludge residence period (SRT). Under HRT of 6.0 h, the DHS reactor removed 93.18±3.19% of NH_3 which is considerably higher than that at an HRT of 2.0 h (79.46±2.81%). According to Onodera et al. [12], and Tawfik et al. [4] [9], the effectiveness of ammonium oxidizing microorganisms and consequently NH_3 removal efficacy was lowered by about 13.72% at reducing the HRT from 6.0 to 2.0 h., because of an elevating imposed F/M ratio from 0.12 to 0.28 (kg COD/kg VS d), causing the heterotrophs to be diluted. These findings are similar to Mahmoud et al. [13], who reported that doubling the HRT of the DHS reactor from 2.0 to 4.0 h resulted in an increase in the removal efficacy of ammonia from 83 ± 9% to 89 ± 9%. This indicates that the HRT is having an impact on the oxidation of ammonia because of its controlling for nitrifiers growth, especially nitrite, and ammonium oxidizing microorganisms. This observation was made as a result of the growth of nitrite-oxidizing bacteria (NOB) in the sponge media throughout the 6.0 h HRT experiment. It is believed that the rise in flow rate from 20.4 to 61.2 L/d when HRT was dropped to 2.0 h caused NOB to be washed out of the sponge medium [13].

DHS performance for the removal of TSS

Fig. 2c demonstrates the effect of changing HRT on DHS performance for TSS removal. The TSS removal efficiency of the DHS system achieved 88.07±4.72% at an HRT of 6.0 h. The corresponding remaining concentration of TSS in the treated effluent was 11.18±0.92 mg/L. Lowering the HRT to 2.0 h increased the final effluent concentration to 27.87±1.62 mg/L. This can be attributed to the amplification of the shear force of the water flow with increasing hydraulic loading. This could cause the trapped sludge inside the DHS sponge to be disturbed, increasing the amount of TSS in the effluent. In addition, the high imposed flow rate led to washing an amount of biomass out. The DHS unit maintained a low sludge content in the sponge medium at the start of the experimental period, leaving space for suspended particles in the wastewater to accumulate. Adhesion of the organic matter within the sponge medium and subsequent decomposition by the DHS reactor could be the mechanism for removing the TSS. The effluent TSS in the DHS unit was kept at a low level despite the high COD concentration. This could have occurred as a result of sludge decomposition (i.e., bacterial autolysis and predation by protozoans and metazoans) due to the low F/M resulting from the high sludge concentration within the DHS unit [14]. These findings are comparable to those that were attained when two DHS reactors connected in series were used to treat low-strength sewage [12] and better than those attained by alternative treatment technologies, such as vertical flow reactors [15]. The value of TSS in the final effluent from the DHS reactor was less than 40 mg/L, therefore, the DHS system achieved the Egyptian wastewater discharge standards as per EGYPT LAW 48 of 1982.

Conclusion

The findings of this work demonstrate that SDW can be effectively treated by a DHS system at various HRTs ranging from 6.0 to 2.0 h. COD, NH_3, and TSS removal efficiencies decreased from 94.12±5.21 to 75.34±3.64, 93.18±3.19 to 79.46±2.81, and 88.07±4.72 to 72.4±4.17% with decreasing HRT from 6.0 to 2.0 h. This show that the DHS system was able to produce effluent compliant with the Egyptian wastewater discharge standards (COD < 80, andNH_3< 4 mg/L) at HRTs ≥4 compared to 2.0 h for TSS effluent (TSS < 40).

References

[1] A. Oghenerobor, O. David, O. Tomilola and A. Jadesola, "POLLUTANTS IN WASTEWATER EFFLUENTS: IMPACTS AND REMEDIATION PROCESSES," *international journal of environmental research and earth science*, vol. 3, pp. 50-59, 2014.

[2] S. Uemura, S. Suzuki, K. Abe, K. Kubota, T. Yamaguchi, A. Ohashi, Y. Takemura and H. Harada, "Removal of organic substances and oxidation of ammonium nitrogen by a down-flow hanging sponge (DHS) reactor under high salinity conditions.," *Bioresource technology*, vol. 101, no. 14, p. 5180–5185, 2010.

[3] M. Mahmoud, A. Tawfik and F. El-Gohary, "Simultaneous Organic and Nutrient Removal in a Naturally Ventilated Biotower Treating Presettled Municipal Wastewater," *Journal of Environmental Engineering*, vol. 136, pp. 301-307, 2010.

[4] A. Tawfik, F. El-Gohary, A. Ohashi and H. Harada, "Optimization of the performance of an integrated anaerobic-aerobic system for domestic wastewater treatment," *Water science and technology*, vol. 58, no. 1, p. 185–194, 2008.

[5] I. K. Kapdan and B. Erten, "Anaerobic treatment of saline wastewater by Halanaerobium lacusrosei," *Process Biochemistry*, vol. 42, no. 3, pp. 449-453, 2007.

[6] 2. e. A. P. H. A. W. D. APHA (American Public Health Association), "Standard Methods for the Examination of Water and Wastewater,," 2005.

[7] T. Nguyen, H. Le, N. Dinh and T. Dinh, "A research on the performance of down-flow hanging sponge (DHS) reactor treating domestic wastewater," *Vietnam Journal of Science and Technology*, p. 56, 2018.

[8] A. Zidan, M. Nasr, M. Fujii and M. Ibrahim, "Environmental and Economic Evaluation of Downflow Hanging Sponge Reactors for Treating High-Strength Organic Wastewater.," *Sustainability*, vol. 15, p. 6038, 2023.

[9] A. Tawfik, F. El-Gohary, A. Ohashi and H. Harada, "Optimization of the performance of an integrated anaerobic-aerobic system for domestic wastewater treatment," *Water science and technology*, vol. 58, no. 1, p. 185–194, 2008b.

[10] I. Machdar, Y. Sekiguchi, H. Sumino, A. Ohashi and H. Harada, "Combination of a UASB reactor and a curtain type DHS (downflow hanging sponge) reactor as a cost-effective sewage treatment system for developing countries," *Water Sci Techno*, vol. 42, no. 3-4, p. 83–88, 2000.

[11] M. Musa and S. Idrus, "Effect of Hydraulic Retention Time on the Treatment of Real Cattle Slaughterhouse Wastewater and Biogas Production from HUASB Reactor," *Water*, vol. 12, p. 490, 2020.

[12] T. Onodera, W. Yoochatchaval, H. Sumino, M. Mizuochi, T. Okadera, T. Fujita, P. Banjongproo and K. Syutsubo, "Pilot-scale experiment of down-flow hanging sponge for direct treatment of low-strength municipal wastewater in Bangkok, Thailand," *Bioprocess and biosystems engineering*, vol. 37, no. 11, p. 2281–2287, 2014.

[13] M. Matsubayashi, H. Harada, T. Okubo and S. Uemura, "Recovery of partial nitrification in a down-flow hanging sponge reactor by salt shock loading. Journal of environmental science and health. Part A, Toxic/hazardous substances," *environmental engineering*, vol. 51, pp. 1-5, 2015.

[14] T. Onodera, K. Matsunaga, K. Kubota, R. Taniguchi, H. Harada, K. Syutsubo, T. Okubo, S. Uemura, N. Araki, M. Yamada, M. Yamauchi and T. Yamaguchi, "Characterization of the retained sludge in a down-flow hanging sponge (DHS) reactor with emphasis on its low excess sludge production,," *Bioresource Technology*, vol. 136, pp. 169-175, 2013.

[15] A. Gross, D. Kaplan and K. Baker, "Removal of chemical and microbiological contaminants from domestic greywater using a recycled vertical flow bioreactor (RVFB),," *Ecological Engineering*, vol. 31, no. 2, pp. 107-114, 2007.

Nanotechnology-Based Single Phase Liquid Immersion Cooling Strategy for Thermal Performance Enhancement of Lithium-Ion Battery Pack

Ibrahim Moukhtar [1], Marwa Mahmoud Hamed[1, b], Loai S Nasrat[2], Adel Z. El-Dein[1,3], Esam H. Abdelhameed[1], A. El-Tayeb [1,a]

[1] Electric Engineering Department, Faculty of Energy Engineering, Aswan University, Aswan, Egypt.

[2] Electric Engineering Department, Faculty of Engineering, Aswan University, Aswan, Egypt.

[3] Faculty of Technological Industry and Energy, Thebes Technological University, Thebes, 85863, Luxor, Egypt.

[a]*E-mail: Ahmed_al_tayeb@aswu.edu.eg,* [b]*E-mail: oldmemories.1991@gmail.com*

Keywords: Nanotechnology, Liquid Immersion Cooling, Thermal Performance, Battery energy storage systems, Lithium-Ion Battery.

Abstract. Battery energy storage systems are key technologies that enable for renewable and hybrid energy systems, whereas the cooling technology is an arguable and essential part in those systems. This paper proposes a thermal management system for a Lithium-ion-based BESS employing an immersing cooling strategy. Thermal conductivity, density, and heat capacity of the coolant material are factors that have significant influence on the maximum temperature and temperature uniformity of the battery system. Nanotechnology has been introduced in this study to improve the thermal physical properties of the coolant material (pure mineral oil) through utilizing Aluminum oxide as dielectric nanoparticles with volume fraction of 30% to generate a new nanofluid coolant for Lithium-ion battery pack. The proposed cooling strategy has been studied at various conditions of flow speed i.e.0.001m/s, 0.003m/s, and 0.005m/s, the results are compared with the pure mineral oil based immersion cooling. The thermal conductivity of the proposed nanofluid coolant increases with the increase of nanoparticles concentration; as a result, the battery temperature is minimized which leads to increase the battery lifespan. A 3D lithium-ion battery model has been implemented using Finite Element Method based simulating programs. The results demonstrate the effectiveness of the proposed strategies. The proposed nanofluid-based cooling system reduces the maximum temperature of the battery pack comparing with that uses pure mineral oil even in case of static or forced flow methodologies.

Introduction

Battery energy storage system is one of sustainable and renewable energy systems essential demands. Recently, Lithium-ion battery-based energy storage systems occupy a significant role in those applications, due to their features such as high energy density, high rated voltage, and low self-discharge rate properties [1]. However, high temperature acts as a critical problem that negatively affects the performance of lithium-ion (Li-ion) batteries. Therefore, it's necessary to keep the Li-ion battery temperature at an optimum temperature range of 15° to 35° C [2]. Accordingly, many studies present various developed techniques of battery thermal management systems (BTMSs) [3]. Three main techniques of BTMSs are widely used in the industrial applications e.g. Air, liquid, and phase change material cooling strategies [4, 5, 6]. Authors investigated the enhancement of li-ion battery performance utilizing either individual cooling technologies or combined cooling strategies upon two or more cooling techniques [4]. Liquid coolant has a high heat transfer coefficient and thermal conductivity, therefore, it has more significant cooling effective comparing to others. Owing to safety, reliability, simplicity and efficient BTMS, this paper introduces a direct contact liquid cooling (liquid immersion cooling) strategy utilizing dielectric oil.

In order to transfer the generated heat of the Li-ion batteries through direct contact, Li-ion batteries can be immersed in a dielectric, nontoxic, nonflammable fluid, such as mineral oil, silicon oil, ester oils, or fluorinated hydrocarbons oils. This approach is known as liquid immersion cooling technique [7].

According to the used coolant properties, immersing cooling systems can be classified into two categories: single-phase and two-phase immersion systems [8]. Single-phase immersion cooling is the situation in which the phase of the coolant remains constant throughout the cooling operation. On the other hand, the two-phase immersion cooling system is referred to when the coolant material converts from one phase state to another while heat is being transferred. Typically, this happens because the coolant has a lower freezing or boiling point. Mineral oils and silicon oils are regarded as single-phase cooling fluids with boiling points of 107°C and 140°C, respectively, whereas Novec7000 has a boiling point of just 34°C thus it is considered a two-phase immersion cooling fluid. Because of their minimal maintenance needs and inexpensive cost, single-phase cooling systems are more applicable than the latter [9].

Thermo-physical characteristics of the coolants used in liquid cooling strategies are intangible factors that can have an impact on thermal performance whether it is direct or indirect. Nanofluid has garnered a lot of interest in recent years for their improved performance in battery pack cooling applications [5]. Nanoparticles additives e.g. Al, Cu, Ni, Ag, Al_2O_3, CuO, Fe_3O_4, TiO_2 can significantly increase the thermal conductivity of the fluid, accordingly improve the heat transfer between the battery surface and the coolant fluid [3, 5]. Authors in [9] studied the performance analysis of immersion cylindrical Li-ion cell in a thin cylindrical tank containing water-Al_2O_3 nanofluid. Authors of [3] investigated indirect cooling system based on suspending different concentration of TiO_2 nanoparticles in water. Optimal nanofluids including mixing of various concentration for different nanoparticles have been introduced in [11] for industrial applications.

This manuscript aims to improve the thermal performance of Li-ion batteries via utilizing nanofluid as an immersion cooling fluid rather than mineral oil. The suggested nanofluid coolant incorporates the Aluminum oxide (Al_2O_3) as dielectric nanoparticles with 30% volume fraction in the pure mineral oil to generate improved thermophysical properties [12]. These improved coolant properties are able to reduce Li-ion battery temperature. The following part contains information on the employed Li-ion battery characteristics, and geometry modeling. Following is the thermophysical parameter of the proposed coolant that has been introduced. Finally, simulation results of various case studies that have been carried out.

Lithium-ion Battery Model

Software based on the finite element method has been used to simulate the 18650 cylindrical Li-ion battery cells through setting up a one-dimensional thermal-electrochemical model for expressing the physics and chemistry of the battery materials. The cell model is setup of three domains: separator, positive porous electrode (LiyMn2O4), and negative electrode (LixC6 MCMB). This model demonstrates the Li-ion Battery interface for studying the discharge and charge of a Li-ion battery for a given set of material properties. The model can be utilized to investigate the influence of various thermal design parameters, e.g. thermal conductivity, heat capacity, dynamic viscosity, and thermal energy density, under different operating conditions. For study the thermal performance of the battery, a 3D thermal and electrochemical coupled model is developed using the heat transfer in solids and fluids interface. The 3D model has ability to estimate the cell internal temperature distribution as well as the average cell temperature. The flow of the cooling fluid around the battery in a flow chamber is additionally included in the thermal model. The rate of heat transmission is permitted to be influenced by fluid flow. This approach is accomplished by a no-isothermal flow multi-physics node where 1D and 3D dimension models are coupled. Moreover, lumped battery interface is established to present the ohmic, activation, and concentration overpotential contributions. The electrochemical heating multi-physics coupling node is used to couple the temperature and the generated heat source between the lumped battery and heat transfer interfaces. Model 18650 cylindrical Li-ion battery geometry parameters have been taken as follows: battery radius, battery height, mandrel radius, connector radius, connector height are 9.0 mm, 65.0 mm, 2.0 mm, 3.0 mm, and 3.0 mm, respectively, whereas its physical parameters are indicated in Table 1. Nine cells are arranged in a square arrangement for the battery pack in this investigation. The size and direction of the coolant chamber, as well as the battery pack, are shown in Fig. 1. Static cooling technique with ignored flow is depicted in Fig.1(a), whereas Fig.2(b)

depicts a dynamic cooling technique where the flow is laminar. On the top of battery pack, a heat flux boundary condition is specified using a heat transfer coefficient of h = 20 W/(m^2·K) and an ambient temperature of 298.15 ^{o}K, which typically corresponds to natural air cooling by low velocity forced convection.

Table 1: Physical parameters of 18650 cylindrical lithium-ion battery model.

	Positive	**Separator**	**Negative**
Electrode particle radius [m]	1.70e-6		2.50e-6
Volume fraction of active substances	0.170		0.444
Length of electrode [m]	55e-6	30e-6	55e-6
Electrode thermal conductivity [W/(m·K)]	1.58	0.344	1.04
Current collector thermal conductivity [W/(m·K)]	170		398
electrode density [kg/m^3]	2328.5	1008.98	1347.33
current collector density [kg/m^3]	2770		8933
electrode heat capacity [J/(kg·K)]	1269.21	1978.16	1437.4
current collector heat capacity [J/(kg·K)]	875		385
Initial lithium-ion concentration [mol/m^3]	20925		2205

Coolant Thermophysical Properties

The liquid immersing cooling strategy proposed in this study aims to reduce the maximum temperature via direct contact between cell surface and fluid. Thermal conductivity, viscosity, density, and flow rate of the coolant are the key factors that affect the rate of heat transferring between the coolant and the battery [5]. Incorporation of solid nanoparticles into conventional liquids to enhance their effective thermophysical properties is a common approach [13]. As a result of the addition of suitable nanoparticles, the fluid's convective heat transfer coefficient can be increased, making it suitable for a variety of cooling systems [14]. Numerous nanoparticles can enhance the liquid's thermophysical features, but for the cooling technique described in this research, the nanoparticles must be electrical insulators, such as Al_2O_3, BN, or SiO_2, to prevent battery shorting i.e. the flow of electric current between the battery cells [15].

Mineral oil is widely used as a dielectric coolant medium for BTMS based direct cooling strategy [17]. Thermal conductivity, heat capacity, density, and viscosity of pure mineral oil and Alumina nanoparticles are all presents in Table 2. On the other hand, the Aluminum oxide, also referred to as alumina (Al_2O_3) nanoparticles, have a number of advantageous characteristics, including high thermal conductivity, thermal stability, oxidation, high strength and stiffness, mechanical strength, high adsorption capacity, and electrical insulation. Furthermore, it is an inexpensive and non-toxic nanoparticle [16]. Therefore, Al_2O_3 is introduced in this study as additive dielectric nanoparticles with 30% volume fraction to a pure mineral oil (conventional cooling fluid). The mathematical equations of effective thermal conductivity, heat capacity, density, and dynamic viscosity of nanofluids according to Maxwell nanofluid have been used to establish the thermophysical features of nanofluids [3,16]. Nanofluid's Thermal conductivity is defined as:

$$\frac{Knf}{Kf} = \frac{(Kf+2Knp)+2\phi(Knp-2Kf)}{(Kf+2Knp)-\phi(Knp-2Kf)} \quad (1)$$

where Knf , Kf, and Knp refer to thermal conductivity of nanofluid, basic fluid, and nanoparticles, respectively. While ϕ refers to a volume fraction concentration that undoubtedly has an impact on enhancing coolant performance. In addition to density, heat capacity, and viscosity are effective features of the proposed nanofluid which can be defined by Eq.2, Eq.3, and Eq.4, respectively. Subscripts of f, and np are referred to fluid and nanoparticles, respectively [3,16].

$$\rho_{nf} = (1-\phi)\rho_f + \phi\,\rho_{np} \quad (2)$$

$$(\rho C_p)_{nf} = (1-\phi)(\rho C_p)_{np} + \phi\,(\rho C_p)_f \quad (3)$$

$$\mu_{nf} = \mu_f(1-\phi)^{-2.5} \quad (4)$$

Table 2: Thermophysical properties of the Coolants [17, 6, and 5]

	Pure Mineral Oil	Aluminum Oxide	Nanofluid
Thermal Conductivity (W/(m·K)	0.13	42.3	0.295
Heat Capacity (J/(kg·K)	1900	729	1147.299
Density (kg/m$^{3)}$	924.1	3880	1810.87
Viscosity (m^2/s)	0.56×10^{-4}	-	1.37×10^{-4}

Simulation Results and Discussion

This section introduces the results of the proposed cooling technique for 18650 li-ion battery that has been modeled using a finite element method based simulating program. An alternating charge current with a 5 C-rate and a 720 second charge duration has been set using a square wave function. The cell was initially set to a 20% charge. The battery's initial temperature and the ambient temperature were both 298.15 K. The conducted simulations can be classified into four scenarios; the first scenario investigates the impact of adding 30% volume fraction of alumina nanoparticle to mineral oil on a single Li-ion cell's thermal performance with static cooling (without laminar flow). According to Fig. 2, employing nanofluid significantly enhances thermal performance by decreasing the cell's maximum temperature by 4.83^{o}K (1.5 %) compared with pure mineral oil. The effect of various flow velocities e.g. 0.001, 0.003, and 0.005 m/s has been implemented on a single lithium-ion cell by utilizing both pure mineral oil and the proposed nanofluid as a coolant in the second scenario. A chart of the maximum cell temperature using both coolants at various flow rates has been indicated in Fig 3. According to the obtained results of this scenario, the maximum cell temperature significantly decreases at 0.003 m/s whereas it is slightly decreased at 0.005 m/s. The third and fourth cooling scenarios have been conducted to evaluate the impact of implementing static and dynamic cooling strategies, respectively, on a 9 cells battery pack utilizing the original and the proposed nanofluid coolants. For the static cooling strategy, the maximum temperature of the battery back using mineral oil and the proposed nanofluid is illustrated in Fig 4. It can be seen that, due to the heat transmission capacity of the nanofluid is greater than that of the basic fluid, the maximum temperature of the battery surface when using nanofluids as a coolant is lower than that using pure mineral oil. As it was expected, the distribution of temperature within the battery pack is affected due to the Brownian motion of nanoparticles (AL2O3) in the base fluid (mineral oil). Figure 5 depicts the results of the 4th cooling scenario i.e. the temperature distribution for the proposed dynamic immersion cooling strategy at 0.003 m/s flow of both coolants (the mineral oil and the proposed nanofluid). When using mineral oil, the maximum temperature of the battery pack reaches 309.67^{o}K, whereas, it reduced to 307.36^{o}K when using the nanofluid.

Conclusion

A new direct cooling method i.e. single phase liquid immersion cooling strategy utilizing a nanofluid coolant has been proposed for an 18650 cylindrical battery pack. The thermal-electrochemical model has been developed and implemented using simulating software that is based on the finite element method programming. This study focuses on dispersing Al_2O_3 nanoparticles in pure mineral oil to produce nanofluid for Li-ion battery back immersion cooling, so that four different scenarios have been done. In the first scenario, the original and proposed coolants have been used to cool a single battery cell using static cooling strategy. In the second scenario, a dynamic cooling strategy has been conducted i.e. immersion cooling performed through changing the coolant flow rate at 0.001, 0003, and 0.005 m/s. In the third scenario, the effectiveness of nanotechnology-based static immersion cooling has been

tested. In the final scenario dynamic cooling of at appropriate coolant flow rate (i.e. 0003 m/s) has been evaluated. It can be concluded that the use of nanofluid in a dynamic cooling to transfer heat from Li-ion batteries is substantially efficient; however, the optimal coolant flow rate should be selected to get high thermal performance of cooling system with minimum cost.

Acknowledgements

The authors appreciatively recognize the Egyptian Science and Technology Development Fund (STDF) for subsidizing this work among the STDF project with ID no. 43247.

References

1. Zhang, F., Lin, A., Wang, P., & Liu, P. (2021). *Optimization design of a parallel air-cooled battery thermal management system with spoilers*. Applied thermal engineering, 182, 116062/ https://doi.org/10.1016/j.applthermaleng.2020.116062.
2. Chen, D., Jiang, J., Kim, G. H., Yang, C., & Pesaran, A. (2016). *Comparison of different cooling methods for lithium ion battery cells*. *Applied Thermal Engineering*, *94*, 846-854/https://doi.org/10.1016/j.applthermaleng.2015.10.015.
3. Wiriyasart, S., Hommalee, C., Sirikasemsuk, S., Prurapark, R., & Naphon, P. (2020). *Thermal management system with nanofluids for electric vehicle battery cooling modules*. Case Studies in Thermal Engineering, 18, 100583/ https://doi.org/10.1016/j.csite.2020.100583.
4. Hamed, M. M., El-Tayeb, A., Moukhtar, I., El Dein, A. Z., & Abdelhameed, E. H. (2022). *A review on recent key technologies of lithium-ion battery thermal management: External cooling systems*. Results in Engineering, 100703/ https://doi.org/10.1016/j.rineng.2022.100703.
5. Deng, Y., Feng, C., Jiaqiang, E., Zhu, H., Chen, J., Wen, M., & Yin, H. (2018). *Effects of different coolants and cooling strategies on the cooling performance of the power lithium ion battery system: A review*. Applied Thermal Engineering, 142, 10-29/ https://doi.org/10.1016/j.applthermaleng.2018.06.043.
6. Jackleen S. Same, A. El-Tayeb, I. Moukhtar, Esam H. Abdelhameed, and Adel Z. El-Dein: "*Effect of thermal parameters on Behaviour of a Lithium-Ion Battery: Simulation Study*", International Journal of Electrochemical Science, Vol. 17, Issue 9, Article Number:, 2022, DOI: 10.20964/2022.09.65.
7. Roe, C., Feng, X., White, G., Li, R., Wang, H., Rui, X., ... & Wu, B. (2022). *Immersion cooling for lithium-ion batteries–A review*. Journal of Power Sources, 525, 231094/ https://doi.org/10.1016/j.jpowsour.2022.231094.
8. Cheng, C. C., Chang, P. C., Li, H. C., & Hsu, F. I. (2020). *Design of a single-phase immersion cooling system through experimental and numerical analysis*. International Journal of Heat and Mass Transfer, 160, 120203/ https://doi.org/10.1016/j.ijheatmasstransfer.2020.120203.
9. Information on https://submer.com/blog/single-phase-vs-two-phase-immersion-cooling/.
10. Sefidan, A. M., Sojoudi, A., & Saha, S. C. (2017). *Nanofluid-based cooling of cylindrical lithium-ion battery packs employing forced air flow*. International Journal of Thermal Sciences, 117, 44-58/ https://doi.org/10.1016/j.ijthermalsci.2017.03.006.
11. Esfe, M. H., Alidoust, S., & Toghraie, D. (2023). *Comparison of thermal conductivity of water-based nanofluids with various combinations of MWCNT, CuO, and SiO2 nanoparticles for using in heating systems*. Case Studies in Thermal Engineering, 42, 102683/ https://doi.org/10.1016/j.csite.2022.102683.
12. Farade, R. A., Wahab, N. I. A., & Mansour, D. E. A. (2023). *The Effect of Nano-Additives in Natural Ester Dielectric Liquids: A Comprehensive Review on Dielectric Properties*. IEEE Transactions on Dielectrics and Electrical Insulation.
13. Qiu, L., Zhu, N., Feng, Y., Michaelides, E. E., Żyła, G., Jing, D., ... & Mahian, O. (2020). *A review of recent advances in thermophysical properties at the nanoscale*: From solid state to colloids. Physics Reports, 843, 1-81/ https://doi.org/10.1016/j.physrep.2019.12.001.

14. Dey, D., Kumar, P., & Samantaray, S. (2017). *A review of nanofluid preparation, stability, and thermo-physical properties. Heat Transfer*—Asian Research, 46(8), 1413-1442/ https://doi.org/10.1002/htj.21282.
15. Hussain, M., Mir, F. A., & Ansari, M. A. (2022). *Nanofluid transformer oil for cooling and insulating applications: A brief review*. Applied Surface Science Advances, 8, 100223/ https://doi.org/10.1016/j.apsadv.2022.100223.
16. Hanif, H., & Shafie, S. (2022). *Impact of al2o3 in electrically conducting mineral oil-based maxwell nanofluid: application to the petroleum industry*. Fractal and Fractional, 6(4), 180/ https://doi.org/10.3390/fractalfract6040180.
17. Mittal, V., Mathur, B., Beniwal, S., & Panwar, A. K. (2022, November). *Investigation of Thermal Battery Management Pack Using Liquid Cooling Systems in 3-D Li-Ion Battery Model*. In Advances in Manufacturing Technology and Management: Proceedings of 6th International Conference on Advanced Production and Industrial Engineering (ICAPIE)—2021 (pp. 569-577). Singapore: Springer Nature Singapore.
18. Sekrani, G., & Poncet, S. (2016). *Further investigation on laminar forced* convection *of nanofluid flows in a uniformly heated pipe using direct numerical simulations*. Applied Sciences, 6(11), 332.

Seismic risk assessment of hazardous materials storage tanks in energy facilities

Ahmad Abo El Ezz[1,a]

[1]École de technologie supérieure, Université du Québec, Montréal, Canada

[a] ahmad.abo-el-ezz@etsmtl.ca

Keywords: seismic risk, hazardous materials release, storage tanks, energy infrastructures.

Abstract. Storage tanks are critical components of oil and gas energy facilities located near coastal and inland communities. Damage to storage tanks caused by natural hazard events such as earthquakes could induce the release of hazardous materials that can have serious consequences on population, infrastructures, and the environment. Risk assessment of potential negative impacts of seismic induced damage to storage tanks and cascading events of chemical releases such as spills, fires and explosions is an essential step for preparing emergency management strategies and implementation of mitigation actions. This paper presents a framework for risk-based seismic assessment and screening of storage tanks in energy facilities in seismic prone regions. The proposed framework consists of the following models: hazard, inventory, damage, and impact. The seismic hazard model generates spatial distribution of seismic intensity for earthquake scenarios; the inventory model provides structural characterization of storage tanks for a given study area; the vulnerability model assesses seismic performance of tanks by applying respective fragility functions represented as probabilistic relationships between seismic intensity and the expected degree of damage, whereas the impact model evaluates the post-earthquake consequences including potential releases and spatial exposure to nearby communities.

Introduction

Storage tanks are critical components of oil and gas energy facilities located near coastal and inland communities. Damage to storage tanks that contain hazardous and flammable materials caused by natural hazard events such as earthquakes could induce the release of hazardous materials that can have serious consequences on population, infrastructures, and the environment [1]. Such releases and cascading consequences such as fires are known as natural hazard-triggered technological (NaTech) events [2]. Releases of hazardous materials into water, ground and air would pose threats to surrounding communities near the facilities. Such releases would cause fires and explosions which pose immediate threats to people and properties [3]. A significant earthquake is likely to impact community emergency services as well as to cause damage water lifelines infrastructures and thus a petrochemical fire poses significant risk to the surrounding areas because containment and suppression resources might not be available immediate in the aftermath of the earthquake. Observations from past earthquake events have demonstrated the impacts of damage to storage tanks and fires following these events such as: the 1964 Niigata earthquake that caused the collapse of a number of tanks at a local oil refinery and the resulting fire caused extensive damage to the plant [4]; the 1999 Kocaeli earthquake that caused significant structural damage to tanks, release of toxic materials and losses due to fires to petroleum refineries [5]; and the 2011 Tohoku earthquake that caused fires and explosion to oil refineries [6]. Typical damage to steel tanks that has been reported from post-earthquake damage surveys included: significant wall buckling at the base of the tank; rupture of piping system interface with the tank; roof damage associated with the sloshing of the fluid inside the tank; and uplifting of the tanks leading to collapse [7]. These observations highlighted the importance of the assessment of risks and identification of structural vulnerabilities of storage tanks for reliable evaluation of potential post-earthquake releases.

Risk assessment of potential negative impacts of seismic induced damage to storage tanks and cascading events of chemical releases such as spills, fires and explosions is therefore an essential step for preparing emergency management strategies and implementation of mitigation actions. This paper presents a framework for risk-based seismic assessment and screening of steel storage tanks in energy facilities in seismic prone regions to identify areas that are susceptible to seismic induced hazardous materials

releases. The proposed framework consists of the following models (Fig. 1): hazard, inventory, vulnerability, and impact. The seismic hazard model generates spatial distribution of seismic intensity for earthquake scenarios with emphasis to seismic zones in Southeastern Canada; the inventory model provides structural characterization of storage tanks for a given study area; the vulnerability model assesses seismic performance of tanks by applying respective fragility functions represented as probabilistic relationships between seismic intensity and the expected degree of damage, whereas the impact model evaluates the post-earthquake consequences including potential releases and spatial exposure to nearby communities.

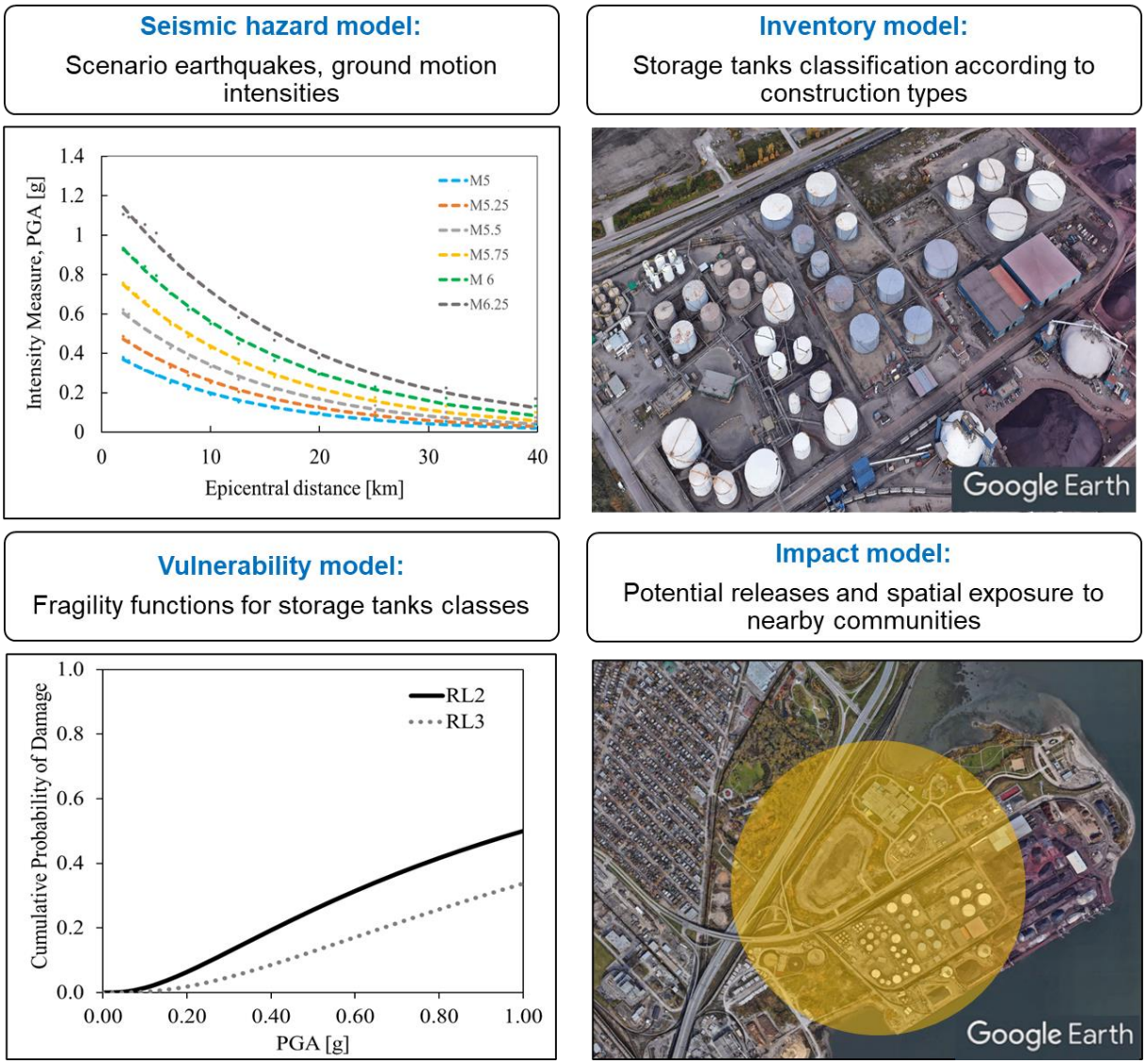

Fig. 1. Framework for risk-based seismic assessment and screening of storage tanks.

Seismic Hazard Model

Seismic hazard modelling includes the estimation of ground motion intensity at energy facilities sites for varies earthquake scenarios. In the context of Southeastern Canada seismic zones along the Saint-Laurence River valley [8], ground-motion prediction models for Peak Ground Acceleration (PGA) on rock are used as a function of earthquake magnitude (M) and epicentral distance [9]. In this study, PGA is considered as the Intensity Measure (IM) for the subsequent steps in the risk modelling since most fragility functions of storage tanks in the literature were developed based on the correlation of damage with increasing levels of PGA. The uncertainty in the IM was captured with the provided upper and lower bounds. At the investigated energy facility, the distance from the epicenter is estimated and the rock IM is automatically modified for local site conditions with amplitude and frequency dependent site

amplification factors as functions of the average shear wave velocity to a depth of 30 m (Vs30) as defined in the National Building Code of Canada (NBCC) [10].

Inventory Model

Structural characterization of existing storage tanks in energy facilities is required to develop a classification system according to physical parameters that are known to impact their seismic vulnerability past on past earthquake damage observations [11]. This classification system is essential for the vulnerability model to simplify the analysis by grouping tanks into main classes with similar seismic response. The following information are collected: the hazardous substance contained within the tank and capacity volume; the date of construction and/or the adopted design code; physical dimensions including height (H) and diameter (D) to estimate the slenderness ratio (H/D) that is known to influence seismic performance, principal roof types either floating or fixed; the foundation including details on anchorage system and type of foundation structure (e.g., gravel or concrete pad, concrete ring, direct base on compacted soil or rock, pile foundation); and the percentage of filling which is a crucial issue for the tank seismic response; and the flammability of stored materials based upon Occupational Safety and Health Administration (OSHA) categories 1 through 4 [12] to identify the ignition potential following a release and to determine the range of air-quality and in-water environmental impacts. Another type of inventory datasets should include information about the community infrastructures, buildings and population surrounding energy facilities that can be impacted by hazardous material releases following an earthquake event.

Vulnerability Model

The vulnerability model consists of a dataset of fragility functions related to the storage tanks classes in the inventory model. Two types of fragility functions have been developed for storage tanks. The first type quantifies the conditional probability representing the likelihood that a given tank will meet or exceed specified level of structural damage for a given IM. Damage states (DS) include: slight damage to tank wall, bottom plate, minor damage to piping system (DS1); damage to roof and upper part of shell due to sloshing (DS2); damage to piping system (DS3); slight elephant foot buckling, damage to the shell-bottom plate junction (DS4) and extensive elephant foot buckling, damage to the shell-bottom plate junction, severe damage to the shell or bottom plate, total failure, tank collapse, overturning (DS5) [11]. The second type of quantify damage in terms of loss of content and it consists of three risk levels of release of hazardous materials [3][11]. Based on the amount of release caused by failure at the shell or at the piping system, each tank has been associated with a risk level, following the criteria given in Table 1 [11]. An example set of fragility functions for storage tanks based on statistical analysis of post-earthquake damage observations is shown in Fig. 2 with respective discrete risk level probabilities obtained for ground motion intensity of PGA=0.4g are 81% of no release, 11% minor leaks, 9% major leaks.

Table 1. Example risk level description of storage tanks [11]

Risk level	Description
RL1	No release, spillages from roof
RL2	Minor leaks from shell tearing or damaged piping
RL3	Major leaks from shell rupture or broken pipe, inlet/outlet pipe or outflow pipe disconnected from tank. Leaks from tearing in correspondence of bottom-shell junction

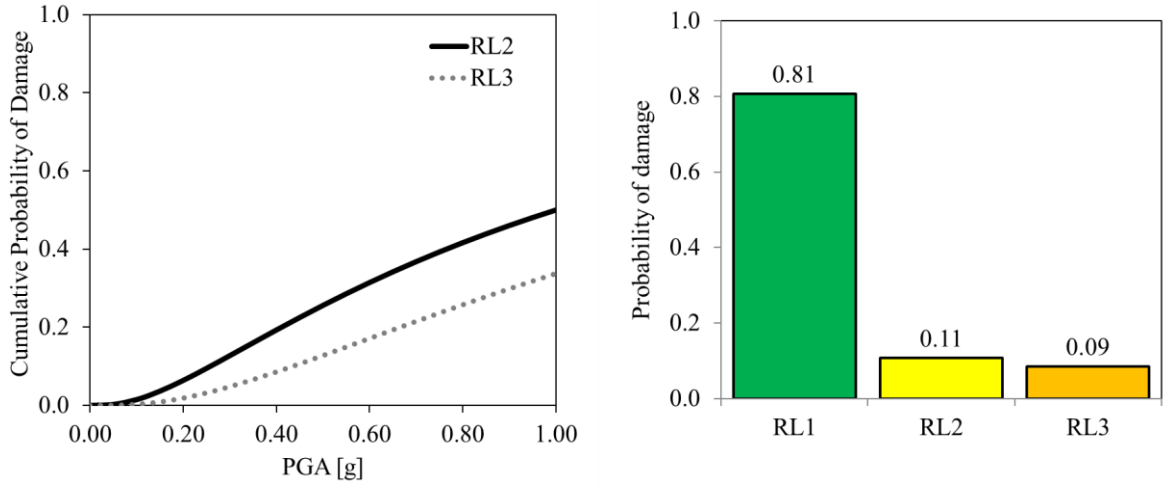

Fig. 2. Example fragility functions for storage tanks based on post-earthquake damage observations [11] (left) and corresponding probabilities of varies risk levels RL at PGA=0.4g.

Impact Model

The direct and cascading impacts are evaluated based on the predicted damage degree to storage tanks and the corresponding risk levels (Table 2). Direct impact indicators include the repair costs of structural damage to tanks and the total volume of material releases [14]. For example, the attainment of RL3 would indicate the rapid total volume release. Release impact scale has also been proposed as a function of the volume of released materials including small (5,000 to 50,000 liters) corresponding to damage to tank resulting in minor leakage; medium (50,000 to 500,000 liters) corresponding to failure of small to medium size tank, with loss of contents and large (greater than 500,000 liters) corresponding to failure of large tank or multiple tanks with loss of contents [7]. Cascading impacts of hazardous materials releases would include toxic gas releases, fire, and explosions. A simplified impact indicator has been proposed based on estimation of the maximum distance that a toxic cloud will travel from its source defined as the maximum distance to an endpoint (MDE) using the off-site consequence Analyses software (RMP*Comp) developed by US Environmental Protection Agency (EPA) [13]. Circles of radius MDE can be drawn around each corresponding storage tank to visualize the potential area of impact [2]. The ALOHA software (Areal Locations of Hazardous Atmospheres) developed by National Oceanic and Atmospheric Administration (NOAA) and EPA can be used to model toxic gas clouds, flammable gas clouds, jet fires, pool fires, and vapor cloud explosions [15]. A threat zone can then be generated to identify an area where a hazard such as toxicity or thermal radiation exceeded specific thresholds.

Table 2. Impact indicator for seismic induced damage to storage tanks.

Impact indicator	Description
Direct economic losses	Repair cost of structural damage to tanks as a function of total replacement cost.
Material releases	Total volume of hazardous material releases.
Cascading impacts of toxic gas releases, fire, and explosions	Maximum distance that a toxic cloud will travel from its source. Threat zones based on exceedance of toxicity or thermal radiation thresholds.

Conclusions

Risk assessment of potential negative impacts of seismic induced damage to storage tanks and cascading events of chemical releases such as spills, fires and explosions is an essential step for preparing emergency management strategies and implementation of mitigation actions. This paper presented a framework for risk-based seismic assessment and screening of steel storage tanks in energy facilities in seismic prone regions to identify areas that are susceptible to seismic induced hazardous materials

releases. The proposed framework consists of developing four models: hazard, inventory, vulnerability, and impact. The seismic hazard model generates spatial distribution of seismic intensity for earthquake scenarios using ground motion prediction equations which are then modified to consider amplification from local site conditions; the inventory model provides structural characterization of storage tanks for a given study area according to a classification system that consider geometrical and anchorage details; the vulnerability model assesses seismic performance of tanks by applying respective fragility functions for structural damage as well as risk level of material releases, whereas the impact model evaluates the post-earthquake consequences including potential releases volumes and spatial exposure to toxic gases or radiant heat from fires. Future works should include numerical implementation of the framework and testing the risk assessment algorithm using case studies of energy facilities located in Southeastern Canada seismic zones.

References

[1] Girgin, S., and Krausmann E. RAPID-N: Rapid natech risk assessment and mapping framework. Journal of loss prevention in the process industries 26, no. 6 (2013): 949-960.
[2] Cruz, A-M, and Okada N. Methodology for preliminary assessment of Natech risk in urban areas. Natural Hazards 46 (2008): 199-220.
[3] Fabbrocino, G., Iervolino I., Orlando F., and Salzano E. Quantitative risk analysis of oil storage facilities in seismic areas." Journal of hazardous materials 123, no. 1-3 (2005): 61-69.
[4] Cooper, T. W. A Study of the Performance of Petroleum Storage Tanks During Earthquakes. (1997). National Institute of Standards and Technology, Gaithersburg, MD, Report No. GCR 97-720.
[5] Yazici, G., and Cili, F., Evaluation of the Liquid Storage Tank Failures in the 1999 Kocaeli Earthquake. 14th World Conference on Earthquake Engineering (2008), Beijing, China.
[6] Zama, S., Nishi, H., Hatayama, K., Yamada, M., Yoshihara, H., and Ogawa, Y., On Damage of Oil Storage Tanks Due to the 2011 Off the Pacific Coast of Tohoku Earthquake (Mw 9.0). 15th World Conference on Earthquake Engineering (WCEE), Lisboa (2012).
[7] Brabhaharan, P., G. K. Bharathy, R. Lynch, and D. Prentice. Natural Hazards Risk Associated with Petroleum Storage in the Wellington Region, New Zealand. In Pacific Conference on Earthquake Engineering. (2003).
[8] NRCAN. Earthquakes in southeastern Canada. https://earthquakescanada.nrcan.gc.ca/pprs-pprp/pubs/GF-GI/GEOFACT_earthquakes-SE-Canada_e.pdf
[9] Atkinson, G. M. and Adams, J. Ground motion prediction equations for application to the 2015 Canadian national seismic hazard maps. Canadian Journal of Civil Engineering, (2013), 40(10), 988-998.
[10] NRC 2020. National Building Code of Canada. National Research Council of Canada. Ottawa, Canada.
[11] D'Amico, Marta, and Nicola Buratti. Observational seismic fragility curves for steel cylindrical tanks. Journal of Pressure Vessel Technology 141, no. 1 (2019).
[12] Occupational Safety and Health Administration: https://www.osha.gov/laws-regs/regulations/standardnumber/1910/1910.106
[13] Offsite consequence analysis software (RMP*Comp). U.S. Environmental Protection Agency (EPA). https://cdxapps.epa.gov/olem-rmp-maintain/action/rmp-comp
[14] Eco Northwest. Impacts of Fuel Releases from the CEI Hub due to a Cascadia Subduction Zone Earthquake. Report prepared for Multnomah County Office of Sustainability and the City of Portland Bureau of Emergency Management (2022).
[15] ALOHA example scenarios. National Oceanic and Atmospheric Administration (NOAA) Office of Response and Restoration and U.S. Environmental Protection Agency (EPA) Office of Emergency Management (2016).

Intensification of the rate of mass transfer in tubular reactors using longitudinal baffles sheets

A. A. Mohamed[†1], A. S. Fathalla[1,a], E.-S. Z. El-Ashtoukhy[1,b],
G.H. Sedahmed1 and M. A. EL-Naggar[1,c]

[1]Chemical Engineering Department, Faculty of Engineering, Alexandria University, Alexandria, Egypt

[†]Corresponding author e-mail: A.ashour.ewinat@gmail.com

[a] ahmed.salah@alexu.edu.eg, [b] el.elashtoukhy@alexu.edu.eg,

[c] m.abbas.elnaggar@alexu.edu.eg

Keywords: Catalyst Support, Diffusion-Controlled Reactions, Mass Transfer, Tubular Reactors.

Abstract. Tubular reactors have proved their efficient applicability in conducting solid-fluid diffusion-controlled catalytic reactions such as immobilized-enzyme biochemical reactions used in wastewater treatment systems. In the present study, the liquid-solid mass transfer behavior was studied for tubular reactors whose inner surface was fitted with chemically active vertical baffles. The well-known diffusion-controlled dissolution of copper in acidified dichromate technique was used to determine the mass transfer coefficient for in terms of different geometric and hydrodynamic variables such as solution flow rate, reactor's height, physical properties of the solution, and number of baffles included. Data analysis was carried out by dimensional analysis, where it was found that the rate of mass transfer in the present tubular reactor was increased by increasing the solution flow rate and decreasing the reactor's height. Compared to the unbaffled reactor, it was found that the volumetric mass transfer coefficient was increased by an amount ranging from 53% to 129% using one vertical baffle and from 134% to 380% using two-cross baffles depending on the reactor's height and flow rate. The contribution of the used baffles to increasing the rate of solid-fluid diffusion-controlled catalytic reactions promoting turbulence and increasing the reaction surface area provided for supporting catalysts was highlighted.

Introduction

The use of tubular reactors for conducting solid-fluid diffusion-controlled catalytic reactions has gained significant attention in recent years due to their efficient performance, ease of operation, and low cost. These reactors are commonly used in various industrial processes, such as (1) wastewater treatment systems for the removal of organic pollutants using immobilized-enzyme biochemical reactions [1,2]. In these systems, the enzymes are immobilized on a solid surface and the wastewater is passed through the tubular reactor, where the mass transfer between the enzymes and the pollutants takes place. This approach can offer advantages over traditional wastewater treatment methods, such as activated sludge processes, by enabling a more efficient and sustainable treatment process. (2) chemical synthesis, where tubular reactors are commonly used for continuous-flow reactions involving mass transfer between a solid catalyst and a fluid phase [3]. Examples of such reactions include hydrogenation, oxidation, and esterification. Tubular reactors can offer advantages over other types of reactors, such as batch reactors, by enabling a more controlled and efficient reaction process. (3) petrochemical processing, where tubular reactors are used for a variety of reactions, including catalytic cracking, hydrocracking, and reforming [4,5].

However, the efficiency of these reactors depends on the mass transfer rate between the solid catalyst and the fluid phase. Thus, the present work aims to enhance the rate of liquid-solid mass transfer behavior in tubular reactors by incorporating chemically active vertical baffles onto the inner surface of the reactor. The contribution of these baffles to optimizing tubular reactors for efficient mass transfer in case of solid-fluid diffusion-controlled catalytic reactions involves improved mixing and turbulence

of the fluid phase [6] and increased reaction surface area on which catalysts may be supported resulting in a higher catalyst utilization, which is an important key factor in improving the efficiency of diffusion-controlled industrial processes. To this end, the diffusion-controlled dissolution of copper in acidified dichromate technique was used to determine the mass transfer coefficient [7,8]. The simplicity, precision, accuracy, versatility, and cost-effectiveness of this technique make it a popular choice for researchers and industrial practitioners alike [9-11].

Experimental Part

The experimental setup (Fig. 1) comprised a tubular baffled reactor and a 30-liter storage tank made of plexiglass, between which the solution was circulated using a plastic centrifugal pump with a 0.5 horsepower rating. The reactor is a plexiglass cylindrical column measuring 70 cm in height and 15 cm in inner diameter, and divided into three sections. The first section, which was 15 cm height, was filled with glass spheres to ensure a fully developed calm flow in the next section. The working section was lined with a copper cylinder of different heights, namely: 15, 25, and 40 cm. The cylinder was fitted either with a vertical copper baffle diving the section into two identical hemi-cylinders or with two-cross copper baffles (Fig. 2). The final section, had an overflow weir from which the solution was recycled to the storage tank.

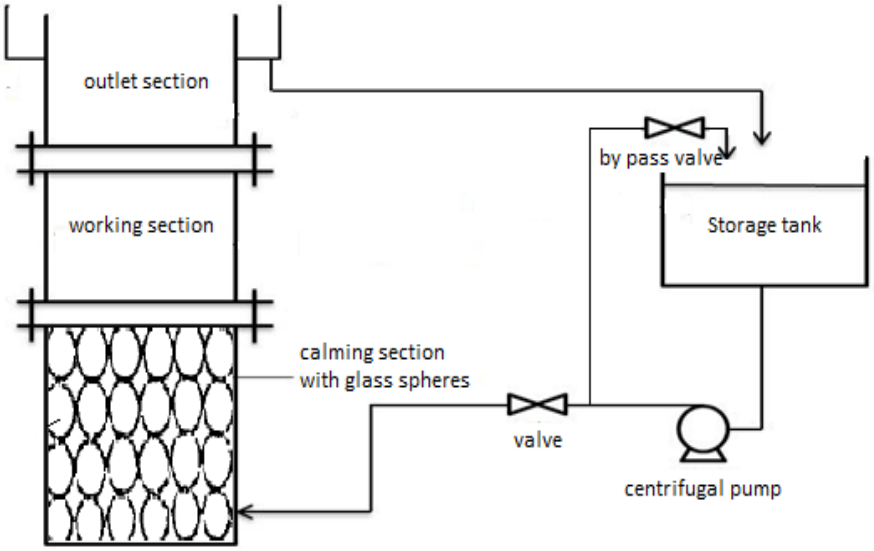

Fig. 1 Expeimental setup.

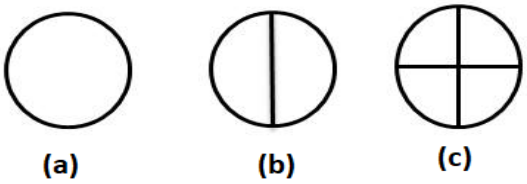

Fig. 2 Plan view of the working section with (a) no baffles introduced, (b) one longitudinal baffle, and (c) two cross baffles.

To start each run, 20 liters of a fresh acidified dichromate solution were prepared and placed in the storage tank. Three different solution compositions were used, namely: 0.003 M $K_2Cr_2O_7$ + 0.5 M H_2SO_4, 0.003 M $K_2Cr_2O_7$ + 1 M H_2SO_4, and 0.003 M $K_2Cr_2O_7$ + 1.5 M H_2SO_4. All solutions were prepared using A.R. grade chemicals and distilled water. The temperature was maintained at 25 ± 2°C

during the runs. The solution density and viscosity required for data correlation were determined at the run temperature using a density bottle and an Ostwald viscometer, respectively [12]. The diffusion coefficient of $K_2Cr_2O_7$ was obtained from the literature [8] and corrected for changes in temperature using Stokes–Einstein equation. Table 1 provides the physical properties of the solutions used at 25°C. The solution velocity (flow rate) was regulated by a bypass equipped with two plastic valves and was measured by a digital flowmeter. To track the rate of reaction, 5 cm^3 of the solution was withdrawn every 3 minutes and analyzed for chromate concentration by titration against standard ferrous ammonium sulfate solution using diphenylamine as an indicator [13].

Table 1 Physical properties of the solutions at 25℃.

Solution composition	Density ρ [g/cm^3]	Viscosity μ [poise]	Diffusivity D*10^6 [cm^2/s]	Sc
0.003 M $K_2Cr_2O_7$ + 0.5 M H_2SO_4	1.026	0.0096	10.147	922
0.003 M $K_2Cr_2O_7$ +1 M H_2SO_4	1.06	0.0105	8.945	1107
0.003 M $K_2Cr_2O_7$ + 1.5 M H_2SO_4	1.117	0.0126	7.662	1472

Results and discussion

Determination of the mass transfer coefficient

The equation governing the rate of the diffusion-controlled liquid-solid reaction in the current batch recirculating reactor is as follows [14,15]:

$$-Q\,(dC/dt) = k\,A\,C \qquad (1)$$

Upon integration, Eq. (1) gives:

$$\ln (C_o/C) = (k\,A/Q)\,t \qquad (2)$$

where k is the mass transfer coefficient, A is the reaction surface area, Q is the solution volume, and C_o and C are $K_2Cr_2O_7$ concentrations at time = 0 and at time t, respectively.

Fig.3 shows a typical plot of ln (C_o/C) Vs. t, where the mass transfer coefficient was calculated from the slope (k A/Q) at different superficial solution velocities.

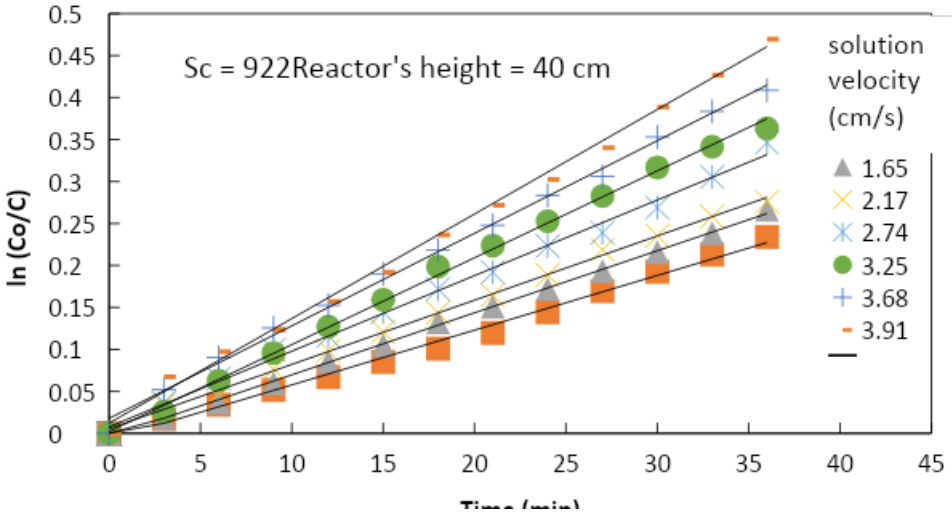

Fig. 3 Typical ln (C_o/C) Vs. t at different superficial solution velocities.

Mass transfer data correlation of unbaffled tubular reactor

Fig. 4 illustrates the effect of superficial solution velocity on the mass transfer coefficient for different Sc, where the data conform to the equation:

$$k = \text{constant } V^{0.73} \quad (3)$$

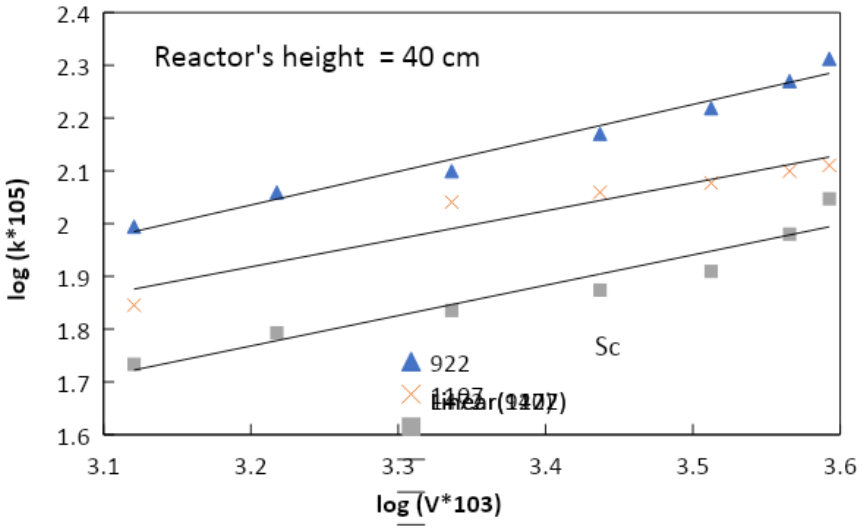

Fig. 4 Effect of superficial velocity on the mass transfer coefficient for different Sc.

The increase in the rate of mass transfer with increasing the superficial solution velocity (V) is attributed to the decrease in the thickness of the hydrodynamic boundary layer and the underlying diffusion boundary layer (δ) as given by the equation [16]:

$$k = \frac{D}{\delta} \quad (4)$$

Additionally, the increase in the superficial solution velocity promotes the formation of more turbulence in the fluid flow, which can increase the degree of mixing of the fluid. This increased mixing can also help to reduce the thickness of the boundary layers and enhance mass transfer [17].

With regard to the effect of the reactor's height on the mass transfer coefficient, Fig. 5 shows that the data fit the equation:

$$k = \text{constant } h^{-0.55} \quad (5)$$

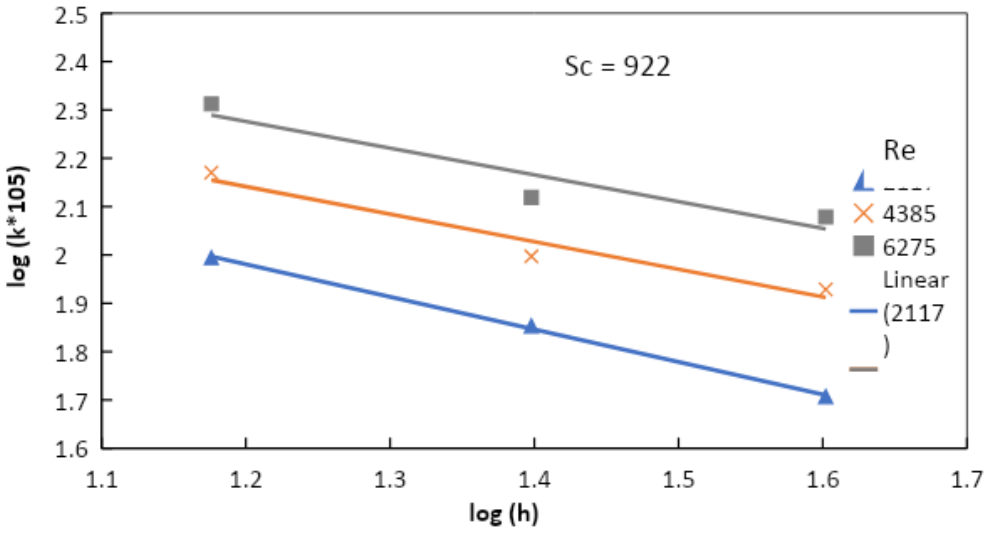

Fig. 5 Effect of reactor height on the mass transfer coefficient.

By increasing the reactor's height, the thickness of the hydrodynamic and diffusion boundary layers increases along the flow direction with a consequent decrease in the mass transfer coefficient (Eq. 4) [17]. Also, the concentration of $K_2Cr_2O_7$ decreases as the solution progresses through the tubular reactor; as a consequence, the driving force for the reaction decreases, with a subsequent decrease in k according to Eq. (1) [10].

To aid in the scale-up and rational design of the present tubular reactor, an overall mass transfer correlation was envisaged in terms of the dimensionless groups Sh, Re, Sc, and (h/d). Fig. 6 shows that for the conditions $922 < Sc < 1472$, $2000 < Re < 6275$, and $1 < h/d < 2.67$, the present data fit the equation:

$$Sh = 0.534\ Sc^{0.33}\ Re^{0.73}\ (h/d)^{-0.55} \quad (6)$$

With an average deviation of ±11%. In obtaining Eq. (6), the exponent of Sc was fixed at 0.33 following previous theoretical and experimental mass transfer studies [14,15].

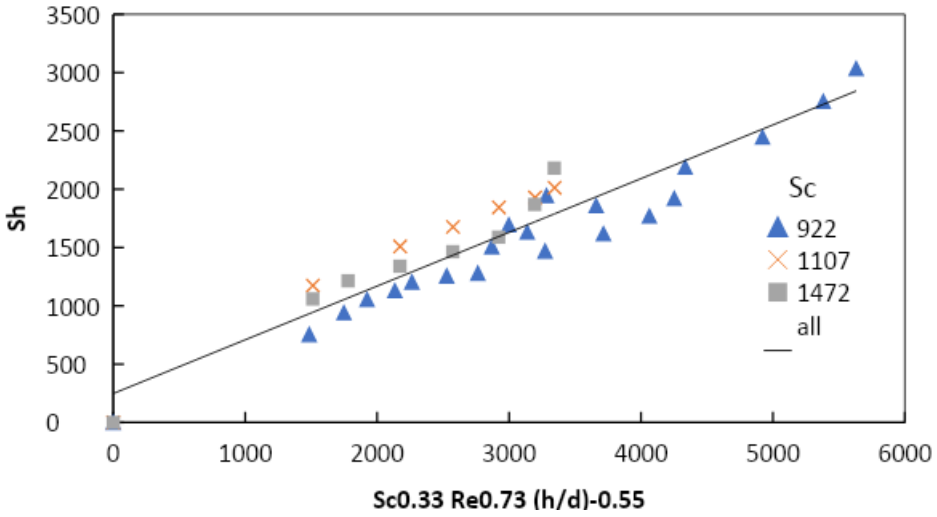

Fig. 6 Overall mass transfer correlation for the present unbaffled tubular reactor.

Effect of longitudinal baffles on the mass transfer coefficient in tubular reactors

Fig. 7 shows that fitting the tubular reactor with a chemically-active vertical baffle enhanced the volumetric mass transfer coefficient at the inner side of the tubular reactor, i.e., the rate of production, by an amount ranging from 53% to 129% depending on the operating conditions. Also, the figure shows that installing two chemically active cross baffles increased the % enhancement in volumetric mass transfer coefficient at the inner side of the tubular reactor by an amount ranging from 134% to 380% on the operating conditions. The high degree of enhancement in the mass transfer behavior may be ascribed to the fact that the installed baffles not only promote turbulence in the direction of solution flow, but also they increase the surface area of the reaction owing to their chemically-active nature [18]. These findings qualify the present tubular baffled reactor to conduct solid-fluid catalytic diffusion-limited reactions where the catalyst is supported on the front and the back sides of the baffles beside the inner periphery of the tubular reactor itself.

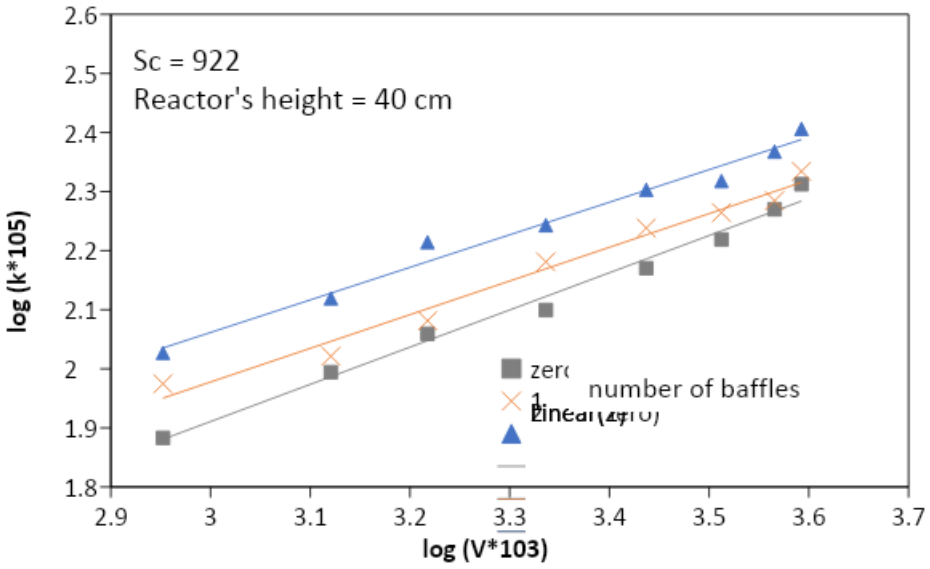

Fig. 7 Effect of the number of bafflers on the mass transfer coefficient.

Conclusions

The present study investigates the liquid-solid mass transfer behavior in a tubular baffled reactor. The results show that increasing the superficial solution velocity and decreasing the reactor height enhanced the rate of mass transfer owing to the reduction in the thickness of the hydrodynamic and the underlying diffusion boundary layer. Additionally, the installation of chemically-active baffles can significantly increase the volumetric mass transfer coefficient up to 380%, depending on the operating conditions due to their ability to promote turbulence and increase the reaction surface area. Overall, these findings provide valuable insights into the design and optimization of tubular reactors for solid-fluid catalytic diffusion-limited reactions.

List of symbols

A	Reaction surface area [m^2]
C_o	Initial concentration [mol/m^3]
C	Concentration at any time [mol/m^3]
d	Dimaeter of the reactor [m]
D	Diffusion coefficient [m^2/s]
h	Reactor's height [m]
k	Mass transfer coefficient [m/s]
Q	Solution volume [m^3]
t	Reaction time [s]
V	Superficial solution velocity [m/s]

Greek letters

δ	Diffusion layer thickness [m]
μ	Solution viscosity [kg/(m. s)]
ρ	Solution density [kg/m^3]

Dimensionless groups

Re	Reynold's number ($\frac{\rho V d}{\mu}$)
Sc	Schmidt number ($\frac{\mu}{\rho D}$)
Sh	Sherwood number ($\frac{k d}{D}$)

References

[1] J.M. Bolivar and F. L.-Gallego: Curr. Opin. Green Sustain. Chem. Vol. 25 (2020), p. 100349
[2] A. Jamie, A.S. Alshami, Z.O. Maliabari, M.A. Ateih and O.C.S. Al Hamouz: Environ. Prog. Sustain. Energy Vol. 35 (2016), p. 1441
[3] A.O. Osikoya, C.W. Dikio, N. Ayawei, D. Wankasi, A.S. Afolabi and E. D. Dikio: Adv. Mater. Sci. Appl. Vo. 4 (2015), p. 53
[4] A.A. Wordu and D.E. Akarolo: European J. Eng. Technol. Vol. 6 (2018), p. 18
[5] M. Ali, L. Zuwei, Y. Yang, S. Jingyuan, J. Binbo, W. Jingdai and Y.Yongrong: China Pet. Process. Petrochem. Technol. Vol. 22 (2020), p. 117
[6] S.M.R. Ahmed, A.N. Phan and A.P. Harvey: Chem. Eng. Process.: Process Intensif. Vol. 130 (2018), p. 229
[7] A.J. Madden and D.C. Nelson: AIChE J. Vol. 10 (1964), p. 415
[8] D.P. Gregory and A.C. Riddiford: J. Electrochem. Soc. Vol. 107 (1960), p. 950.
[9] G.H. Sedahmed, Y.A. El-Taweel, M.H. Abdel-Aziz and H.M. El-Naqeara: Chem. Eng. Process.: Process Intensif. Vol. 80 (2014), p. 43
[10] M.A. El-Naggar, M.H. Abdel-Aziz, A.A. Zatout and G.H. Sedahmed: Chem. Eng. Technol. Vol. 37(2014), p. 1525
[11] A.S. Fathalla, N.K.Amin, E.S.-Z. El-Ashtoukhy and G.H.Sedahmed: Int. J. Electrochem. Sci. Vol. 11 (2016), p. 5207
[12] A. Findlay and J.K. Kitchener: *Practical Physical Chemistry* (Longmans, London 1965).
[13] A.I. Vogel: *A Text Book of Quantitative Inorganic Analysis* (Longmans, London 1961).
[14] T.Z. Fahidy: *Principles of Electrochemical Reactor Analysis* (Elsevier, New York 1985).
[15] F.C. Walsh, *A First Course in Electrochemical Engineering* (The Electrochemical Consultancy, Hants 1993)
[16] H.S.Fogler: *Elements of Chemical Reaction Engineering* (Pearson Education Ltd., London 2020)
[17] W. McCabe, J. Smith and P. Harriott: Unit Operations of Chemical Engineering (McGraw Hill, New York 2005)
[18] A.T. Olson and K.A. Shelstad: *Introduction to Fluid Flow and The Transfer of Heat and Mass* (Prentice Hall Inc., New Jersey 1987)

The future of new Alternative marine fuel for passenger ships

Ahmed Gamal Mohamed Zaki [1, a], Mohamed Morsy Elgohary[2, a,b] and

Ibrahim S. Seddiek[3, c]

[1]Alexandria University, Egypt. [2]Borg El Arab Technological University, Egypt. [3]Arab Academy for Science and Maritime Technology, Alexandria, Egypt.

[a] AhmedGamalzaki91@gmail.com , [b]mohamed.elgouhary@alexu.edu.eg ,[c] prof.isibrahim@gmail.com

Keywords: Alternative Fuel, Marine fuels, Emissions CHG

Abstract. Economic and population growth are the most important drivers of growing global energy demand, Also Emissions from ships are a serious global issue due to their effects on the environment, particularly global warming of the atmosphere. As a result, the international Maritime organization (IMO) places a high priority on environmental Protection by Reducing Emissions at Least 50% by 2050 As per Marine environment protection committee (MEPC 80), Among the IMO's Proposed measures, using alternative marine fuels such as natural gas and methanol instead of conventional Fuels has been applied. in this paper a comparative study between convert diesel engine into Dual engine as a methanol or natural gas is to be carried out. Environmental and economical assessment of both dual engines using either Natural Gas or Methanol is conducted too including Percentages of reduction for different types of Emissions and cost effectiveness of applying dual engines for each type of Alternative fuel. The engines will be compared against their fuel consumption in each state, cost saving as well as emission. Moreover, this article highlights the latest rules and regulations that govern the use of liquified natural gas as marine fuel onboard ships.

Introduction

The emissions produced or arising from maritime industry is become significant during the last decades which most probably contribute to air pollution, The introduction of Marine alternative fuel during the beginning of 2003 summarized on the first trials of using Natural gas in dual fuel engines onboard ships, considered the beginning of Phase of Maritime decarbonization, in parallel with initial strategy of IMO for reducing emissions produced from ships which called greenhouse gas (GHG), through the huge increase on maritime trade in past years, a lot of shipping companies intended to transit to use alternative fuel for examples; Natural gas (LNG), Ammonia, Methanol, Hydrogen, Fuel cells, nuclear power, and wind power. however, the use of Subject alternative marine fuels by those shipping companies ignores the side impact on the marine environment and potential risk from those reduced carbon emissions such as marine fuel spill and fuel vapor dispersion and fuel pool fires [1] The maritime industry is the primary key role asset for the global economy trade , 80% of the total world trade completed by maritime transportation, consequently the maritime industry plays important role in the development of world economy, on the other hand , the restrictions of regulations in the regard of GHG emissions set for making ship owners find new alternative ways of comply with this new requirements .in way of searching for clean, reliable and economic fuel and the existing researches is based on three phases as follows:

First , Now a days researches Focuses on the advantages and applicability of those subject fuels due to regulation of Sulphur and noxious and using the LNG as a standalone marine fuel has been increased and considered highly efficient and clean low carbon energy source and also considered the best solution due to availability of infrastructure and familiarization of usage by ship operators and also good safety records, however, researchers has been intended for searching of other alternatives like methanol, ammonia and hydrogen fuels.

cond, the existing researches also focus on the disadvantages alternative marine fuel, given that are still many obstacles for the continuous application of subject fuels for continuous shipping and not all of them are completely clean and for example LNG could be a dangerous liquid and during the manufacturing of methanol, large amounts of GHG emissions could be produced.
Third, the research proposes the potential ways or directions to solve the existing problems in this regard, taken in consideration the economic cost of alternative marine fuels and researches also recommend that simultaneous operations should be used to reduce costs and to avoid the technical problems of usage [1] .

IMO strategy

Through a long amendments to MARPOL Annex IV convention in the regard of reducing SOX, NOX, CO2 and Soot in addition to clear definition emission control areas in a parallel with local emissions regulations , through different economic aspects like availability of low Sulphur fuel and oil price uncertainty and cost of Sox scrubbers , for example ; SOX emissions reductions included on MEPC 70 with the intention of reducing global fuel Sulphur limit of .5% (Jan 2020) and MEPC 73 in the regard of carriage ban on fuel oils with %S>.5% and for GHG emissions there was MEPC 72 for the purpose of GHG strategy 2018 (-50% GHG by 2050 / -40% CI by 2030) , moreover MEPC 76 was illustrated on the aim of 2% yearly decreasing CI reduction from 2023 to 2026 [2] [15] , The IMO strategy plan is summarized at Fig (1) .

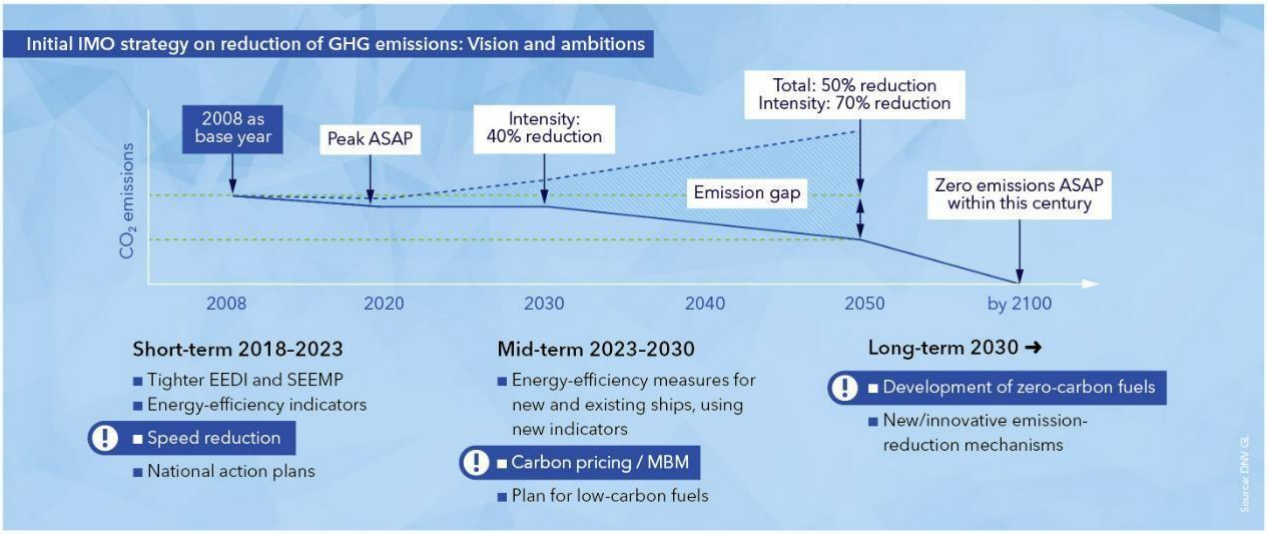

Figure (1)

Fig (1) is summarized the different phases for aim of compliance with IMO strategy by 2050 , through speed reduction Using EPL devices to reach finally development of zero carbon fuels at 2030 .
The initial compliance options in above mentioned regulations is focus on 3 method ; first , using of Distillate or blended fuels like MGO (.1% S) and MDO (.5%S) and Hybrid fuels and VLSFO (.1%<S<.5%) and ULFSO (S<.1%) ; second , using high Sulphur fuels with exhaust gas cleaning systems (sox scrubbers) ; third , using alternative fuels as illustrated on the first paragraph .

Biofuels

Contains many types for example: Biodiesel (Fatty-acid methyl ester(FAME) and renewable diesel like hydrotreated vegetable oil and there advantages can be concluded in their high GHG emissions reduction that meets IMO strategy (-50%) and also applicability for mixing with MGO in dual fuel engines and consequently they considered a clean fuels with no Sulphur and great reduction in NOX

and Soot , however , their disadvantages summarized in High fuel Price and limited availability and also possible effects on fuel systems and engines (FAME) and limitations to mixing amounts (FAME) [3]

LNG (Natural gas)

Considers clean fuel with no sulfur and reduced NOX (-80%) and Soot (-98%) and proven safety records from LNG carriers and low fuel prices and also has a large service experience from 2003 at 4-stroke DF and from 2014 at 2- stroke DF however their disadvantages can be said that it considered a Gaseous fuel that must be stored under cryogenic conditions – CAPEX and their low GHG emissions reductions up to 23 % and finally , their bunkering infrastructure in under development [4]

Methanol

Considered clean with No Sulphur and reduced NOX (-50%) and Soot (-90%) and can stored at atm conditions – Lower CAPEX and their conversation /retrofit is relatively simple and used in service for 5 years however their disadvantages is that they are Toxic and corrosive and bunkering infrastructure is limited and their potential reduction on Low GHG emissions ins considered low (Up to 10 %) [5]

LPG

Clean fuel: No Sulphur, Soot (-90%) and their bunkering infrastructure is available and fuel price is low and there's a possible transition to a carbon free fuel (Ammonia) however, their disadvantages that it must stored under cryogenic conditions and their low reduction of potential GHG emissions (-17%) and their short service duration on maritime field (1 year) [6]

Ammonia

Clean fuel 'carbon free and Sulphur free and strong potential to meet IMO's GHG emission targets and proven to have a good handling record from ammonia carrier and have a true GHG reduction potential through green Ammonia and fuel price is moderate, however they considered Toxic and bunkering infrastructure is limited and have no work experience in the past years and initial trials will be conducted at 24/25 [7]

Applicability of Alternative fuel onboard Ocean going Vessels

2021	IMO's GHG Targets	Fuel Price	Infrastructure (Availability)	Technology Readiness	Regulation & Rules
MDO					
LNG					
Methanol					
LPG					
Amonia					

Notes :

- Red = Low , Green = Strong , yellow = Medium
- Regarding Fuel Prices , Relative differences between Fuels in 2021 , Remain Same at 2022 .
- Infrastructure & Technology and reg& Rules , Development in continuous

Figure (2)

Fig(2) is describing the applicability of alternative fuel on board ocean going vessels through different phases IMO GHG target and economic wise and infrastructure (availability) and technology readiness by ship operators .

Case Study

The case study will give a true example of applicability of IMO 2020, a container vessel that serves the route from port of Panjang in Lampung to port of Singapore, the vessel needs around 3 days for completing such a one trip between the mentioned ports, the ship data is provided below [13], The ship particulars data is illustrated at Table (1) which is used on subject case study

Table (1)

Ship Information	
Ship Name	: Meratus Samarinda
IMO Number	: 9808481
Vessel Type	: Container Ship
MMSI	: 525125029
Call Sign	: YDIZ2
Flag	: Indonesia
GT	: 7542
DWT	: 8139 T
LOA	: 123 m
Breadth	: 24.4 m
Draught	: 5 m
Depth	: 7 m
TEU	: 526
Engine	: 2 x Yanmar 6EY26W
Total Power	: 3840 kW
RPM	: 750 rpm
Speed Max	: 17 knots
Former Name	: PAC Cekap

Reference to Route and vessel data, the analysis will run based on emission types (SOX & NOX), Emissions results in final number of emissions produced by trip in which studies carried out by US Environmental protection Agency (EPA) and Canadian inventory efforts for calculation of total emissions through Eq (1) & (2)

$$\Sigma E\text{total} = \text{total Estandby} + \text{total Emanouvering} + \text{total Ecruise} \quad (1)$$

Where ΣEtotal is the total emissions produced during the different phases of Vessel trading cycle

$$\Sigma E = \text{P LF efd T} \quad (2)$$

Where: E: Emission quantity (g)
P: Engine power at maximum continuous rating (kW)
efd: Emission factor (g/kWh)
LF: Load Factor (per cent)
T: Engine running time (h)

Engine Power is 3840 KW, Engine load factor is utilizing 80% for shipping (Cruising) and 20% for maneuvering and 5 % for standby mode (anchorage area for example) and emissions factors for different phases is illustrated below at table (2) for cruising phase and table (3) for maneuvering and in port operations

Table (2)

Cruising Operation						
	NOx	NOx (with Scrubber)	SOx	SOx (with Scrubber)	CO_2	CO_2 (with scrubber)
HFO	14	14.14	11.5	0.97	677	643.15
MGO	13.2		1		645	
LNG	2.16		0		548.25	

Table (2) summarized the emissions produced through different fuel types during shipping (Cruising phase)

Table (3)

Maneuvering and In-Port Operation (Standby/loading-unloading)						
	NOx	NOx (with Scrubber)	SOx	SOx (with Scrubber)	CO_2	CO_2 (with scrubber)
HFO	11.2	11.312	12.7	0.95	745	707.75
MGO	10.6		1.1		710	
LNG	2.16		0		603.5	

Table (3) summarized the emissions produced through different fuel types during shipping (In port phase)

The best Options to comply with IMO regulations.

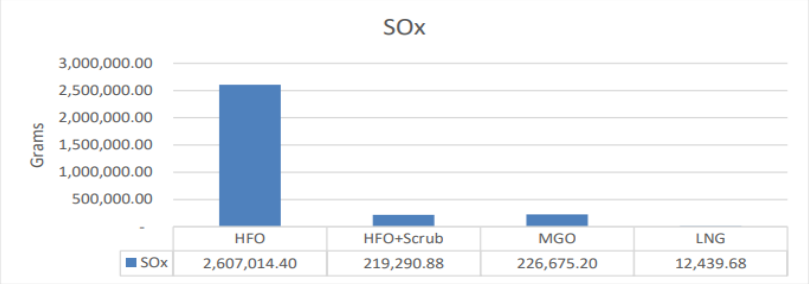

Figure (3)

Fig (3) describe the relations between SOX emissions in grams and 4 different options to comply with IMO strategy target , which resulted in that the best option at this fig is using LNG which gives less SOX emissions grams .

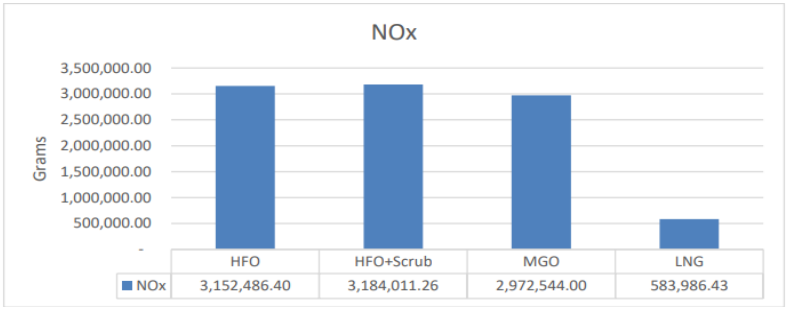

Figure (4)

Fig (4) describe the relations between NOX emissions in grams and 4 different options to comply with IMO strategy target , which resulted in that the best option at this fig is using LNG which gives less NOX emissions grams

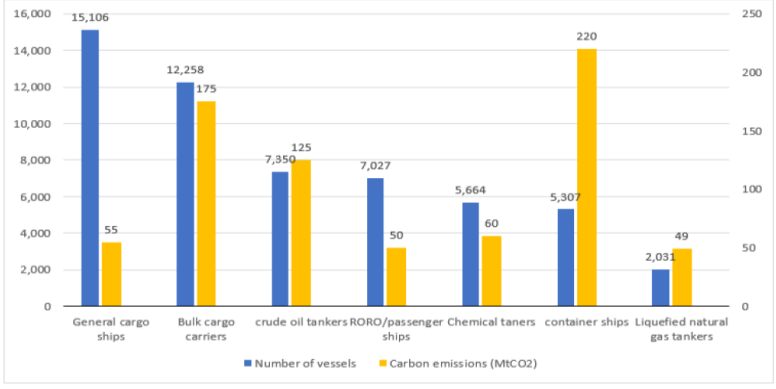

Figure (5)

Figure (5) is used to describe the relation between the different vessel types which specified numbers for each type and also carbon emissions produced In this regard.

References

[1] Elgohary, M.M., Seddiek, I.S. and Salem, A.M., 2015. Overview of alternative fuels with emphasis on the potential of liquefied natural gas as future marine fuel. Proceedings of the Institution of Mechanical Engineers, Part M: Journal of Engineering for the Maritime Environment, 229(4), pp.365-375.
[2] Port-Said Engineering Research Journal Published by Egypts Presidential Specialized Council for Education and Scientific Research Online ISSN: 2536-9377
[3] Kouzelis, K., Frouws, K. and van Hassel, E., 2022. Maritime fuels of the future: what is the impact of alternative fuels on the optimal economic speed of large container vessels. Journal of Shipping and Trade, 7(1), pp.1-29.
[4] Elkafas, A.G., Khalil, M., Shouman, M.R. and Elgohary, M.M., 2021. Environmental protection and energy efficiency improvement by using natural gas fuel in maritime transportation. Environmental Science and Pollution Research, 28(43), pp.60585-60596.
[5] Nasser, M.A., Elgohary, M.M., Abdelnaby, M. and Shouman, M.R., 2022. Environmental and economic performance investigation of natural gas and methanol as a marine alternative fuel.
[6] Akman, M., A techno-environmental and energy efficiency investigation of marine dual-fuel engines. Marine Science and Technology Bulletin, 12(2), pp.128-141.
[7] Zincir, B., 2020. A short review of ammonia as an alternative marine fuel for decarbonised maritime transportation. Proceedings of the ICEESEN2020, Kayseri, Turkey, pp.19-21.
[8] Ibrahim Sadek and Mohamed Elgohary: Environmental Science and Pollution Research volume 27, pages5547–5558 (2020)
[9] Mohamed M Elgohary, Ibrahim S Seddiek, and Ahmed M Salem: sumitted to J Engineering for the Maritime Environment 2015, Vol. 229(4) 365–375
[10] Ibrahim S. Seddiek and Mohamed M. Elgohary: submitted to International Journal of Naval Architecture and Ocean Engineering Volume 6, Issue 3, September 2014, Pages 737 748
[11] Mohamed M Elgohary malgohary, Ibrahim S Seddiek, and Ahmed M Salem: submitted to Proceedings of the Institution of Mechanical Engineers, Part M: Journal of Engineering for the Maritime Environment Volume 229, Issue 4 Pages: 365 - 375
[12] A A Banawan, M M El Gohary, and I S Sadek: submitted to Proceedings of the Institution of Mechanical Engineers, Part M: Journal of Engineering for the Maritime Environment Volume 224, Issue 2 Pages: 103 – 113
[13] Danuja Wijayanto and Gede Bagus Dwi Suasti Antara 2022 IOP Conf. Ser.: Earth Environ. Sci. 1081 012051
[14] Nasser, M.A., Elgohary, M.M., Abdelnaby, M. and Shouman, M.R., 2022. Environmental and economic performance investigation of natural gas and methanol as a marine alternative fuel.
[15] Jarzemskis, A. and Jarzemskiene, I., 2016. The model to assess the implementation of technical conditions defined in Annex IV of MARPOL convention 73/78: the case of the Baltic sea port of Klaipeda. Transport and telecommunication journal, 17(4), pp.335-349.

Green Hydrogen Toward Sustainable Marine Fuel

Ahmed G. Mohamed [1, a], Aya A. Elbauomy [2, b]

[1,2] Arab Academy for Science, Technology and Maritime Transport, Egypt

[a]a.gomaa@aast.edu , [b]ayaa73520@gmail.com

Keywords: *green hydrogen, renewable energy, economic feasibility, solar-powered.*

Abstract. The reduction of emissions from marine engines is an important topic in the marine sector that corresponds with the International Maritime Organization's (IMO) 2030 agenda for the 13th Sustainable Development Goal Climate Action, which states "Take urgent action to combat climate change and its impacts." Green hydrogen is vital to the decarbonization of maritime transportation. This paper investigates the green hydrogen production from renewable energy sources for the Suez Canal ferry boat, the design, and economic feasibility of a sustainable supply chain consisting of a solar-powered electrolysis system that generates hydrogen for powering a fuel cell-based propulsion system installed on a small passenger ferry boat traveling on a short route. The results reveal a comparative assessment between the conventional diesel-electric engine and hydrogen production by using an alkaline electrolysis unit with a total number of roundtrips per year and a comparative assessment of conventional diesel-electric and IMO limits. These findings illustrate the environmental impact of the proposed supply chain, which is based on hydrogen technologies that are already available on the market and can be effectively deployed to promote the maritime sector's decarbonization.

1. Introduction

The International Maritime Organization (IMO) adopted the IMO Initial Strategy for Reducing Greenhouse Gas Emissions from International Shipping (COP 21) in 2018. The goals are highly ambitious, with a call to reduce carbon emissions by at least 40% by 2030 (the "2030 Goal") and 70% by 2050 (compared to 2008 emissions) [1].

Among potential alternative energy sources, hydrogen is seen as a promising fuel, particularly due to its low environmental impact. It emits no carbon dioxide when burned, and depending on how it is produced, the quantity of carbon dioxide released into the atmosphere can be significantly lowered [2].

Hydrogen is appropriate for use in a fuel cell, an innovative technology that converts the chemical energy of a fuel directly into electric energy through electrochemical reactions. Hydrogen storage is one of the main obstacles to its wider application in the marine sector which has led to onboard hydrogen production from hydrogen carriers (i.e., natural gas, methanol, ethanol, etc.)[3].

According to DNV GL-Maritime [4], the investment costs of hydrogen utilization in the maritime sector are relatively high but are projected to go down as fuel cells become more widely available.

Few studies focused on hydrogen as a fuel for shipping. [5] and [6] have observed the building of prototypes created to demonstrate technological feasibility on board a ship, a canal boat, and a small cruise boat. Both examples are currently operational. As stated in [7] and [8], the installation of onboard submarines is another effective example of the practical use of hydrogen technology on board.

Hydrogen storage systems have received special attention. Maximizing the volumetric and gravimetric energy density of stored fuel is a significant obligation. Although high-pressure gas cylinders are the most often utilized hydrogen storage device today, their low volumetric density is seen as a significant drawback to their application on board ships. According to various studies, huge storage cylinders have a volume that is 4-7 times that of standard fuel oil tanks [9], [10]. [11], [12], both considered liquid hydrogen held in a cryogenic state.

2. Methodology

2.1. Case study

The Case Study discusses in this paper is to replace the electric diesel engine propulsion system with a hydrogen fuel cell propulsion system. The assessment process of design and environmental feasibility of a sustainable supply chain is selected to be a cellular port Fouad ferry boat. The ship is powered by conventional power systems, i.e., diesel engines. Their main particulars are presented in (Table 1).

Table 1. Ferry particulars [13].

Ferry particulars	value
Name	Port Fouad Ferry
Length overall (m)	64
Breadth (m)	19
Draught (m)	1.44
Main engine power (KW)	2 * 360
Design speed (Knots)	8
Diesel generator model	AD-360S-T400-R
Rated power	368 kW / 460 kVA
Rated voltage (V)	400
Motor shaft (RPM)	1500
Fuel consumption (Kg/hr)	79.8

The first step is removing the current electric diesel propulsion and calculating its environmental impact. The complete combustion of diesel fuel is calculated using the following equation.

$$C_{12}H_{23} + 17.75(O_2 + 3.76N_2) \rightarrow 12CO_2 + 11.5\ H_2O + 66.74\ N_2 \quad (1)$$

To calculate the emission impact on the surrounding environment. (Fig. 1) presents the fuel's complete combustion process. In this process, the diesel fuel inlets the diesel engine to react with the air (oxygen + nitrogen) to produce power to move the ferry. But power production has an amount of emission effect on the environment as shown in (Eq. 1).

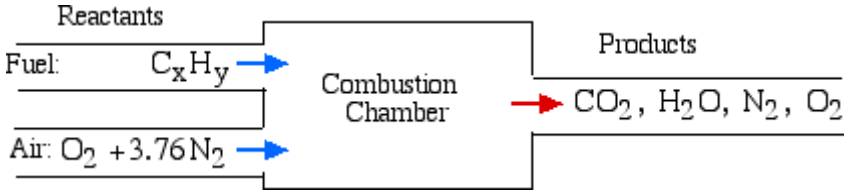

Figure. 1 fuel combustion process.

2.2. Fuel-cell-powered ship

The next step is designing an electric fuel cell propulsion system. A PEMFC is the most commercialized fuel cell, with several uses, including the maritime industry. It has a 50-60% efficiency, but its primary drawback is its sensitivity to contaminants and the need for pure hydrogen [14]. Between the electrodes is a proton-conductive polymer electrolyte membrane. Electrochemical reactions take place between pure hydrogen as a fuel and oxygen. The hydrogen is oxidized, and the created electrons provide electricity, while the formed protons diffuse through the electrolyte to the cathode due to the electrochemical gradient. The oxygen is reduced in the cathode, and its ions react with protons and produce water [15]. (Fig. 2) shows the onboard PEMFC system that is powered by pure hydrogen.

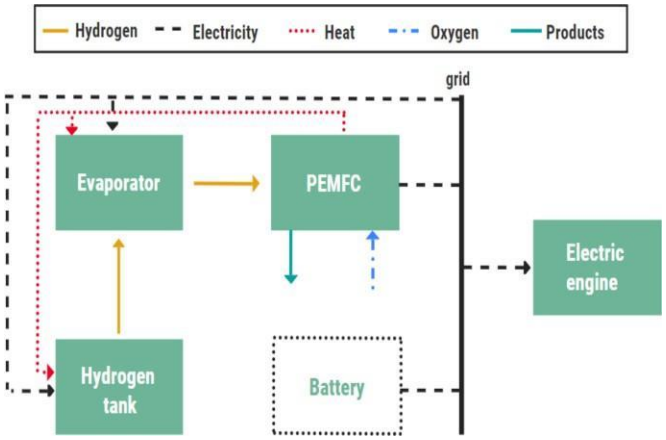

Figure. 2 PEMFC system onboard a ship [19].

Design a fuel cell must be met and optimized among many parameters such as hydrogen storage, oxygen supply, power electronics, and fuel cell stack (heat and water). calculate the amount of hydrogen, and oxygen supplying and stack water as illustrated in the following equations
Equation 2 shows the calculation for the hydrogen usage

$$Rate\ of\ hydrogen\ (Kg/sec) = 1.05 \times 10^{-8} \times \frac{Pe}{Vc}\ Kg/sec \qquad (2)$$

Equation 3 shows the calculation for the hydrogen usage

$$Oxygen\ usage\ (Kg/sec) = 8.29 \times 10^{-8} \times \frac{Pe}{Vc}\ Kg/sec \qquad (3)$$

Equation 4 illustrates the calculation for stack water

$$Water\ production(Kg/sec) = 9.34 \times 10^{-8} \times \frac{Pe}{Vc}\ Kg/sec \qquad (3)$$

2.3. Hydrogen storage

Hydrogen utilization and hydrogen-based fuel-cell systems and applications provide several environmental benefits. A worldwide transition from traditional fuel combustion to hydrogen fuel cell electric vehicles is taking place in the transportation sector, and this transformation is also taking place in aircraft, watercraft, locomotives, and drones. Instead of standard fuel tanks, hydrogen tanks are utilized in fuel-cell electric vehicles, and stored hydrogen is supplied to the hydrogen fuel cell for generating electricity [16].

2.3.1. Compressed Hydrogen Storage

Among the several technologies, compressed hydrogen storage is the most developed and well- tested. The hydrogen is held at extremely high pressures of 350-700 bar, resulting in densities of 23.3 Kg/m^3 and 39.3 Kg/m^3, respectively (Raucci et al.,2015).

2.3.2. Hydrogen tank components

Hydrogen tanks come in a variety of designs and sizes. Spherical shapes are utilized for certain liquid hydrogen tanks, and any form is suitable for holding hydrogen pressures near atmospheric pressure,

although a cylindrical container is the most typical form of a hydrogen tank [18]. (Fig. 3) represents the common components found in most hydrogen tanks.

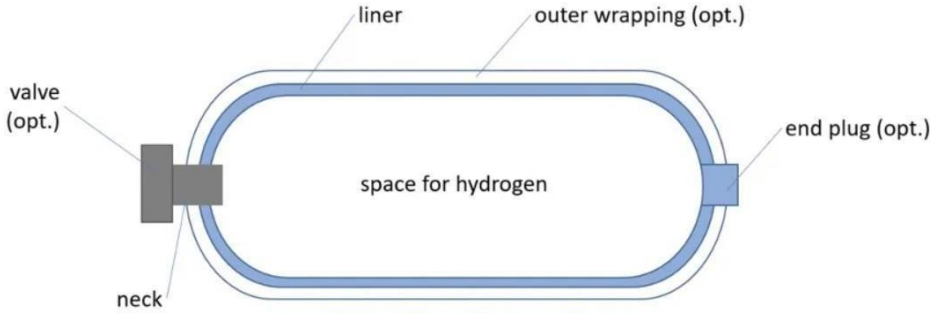

Figure. 3 Hydrogen tank components [18].

The liner holds the hydrogen contained within the tank's storage capacity. The liner may be further encased in an outer wrapping that serves to stabilize the liner against the physical strain exerted on it when storing hydrogen at high pressures and produces a further thermal insulation layer (high- pressure hydrogen tank). The neck is where the hydrogen enters and exits the tank, and it links to a hydrogen tank valve or tubing, which allows for regulated input and outflow of the hydrogen. It usually includes a safety valve, as well as sensors or a more complicated hydrogen tank valve structure that allows for extra pressure adjustment. The optional end plug is a supplemental tank opening [18].

3. Results

Investigating the green hydrogen production from renewable energy sources for the port Fouad ferry boat and analyzing the exhaust emission rates every hour allows for the evaluation of the environmental performance. NOx and SOx emission rates have been compared with the IMO 2016 and 2020 emission-limit rates, respectively. The IMO 2020 SOx and tier III 2016 NOx limits 1.555 kg/min and 2.008 kg/n, respectively. Fig. 4 can be noticed that SO_x emission rate (Kg/hr) from the conventional diesel-electric propulsion system is comply with IMO 2020 limit but in the other hand
NO_x higher than the IMO 2016 limit, therefore, it is recommended to use selective catalytic reduction (SCR) technique which can reduce NOx emission rate from the proposed diesel electric engine. and the comparative study between the conventional diesel-electric propulsion system operated and the hydrogen fuel cell with the NO_x, SO_x, and H_2O exhaust rate. as illustrated in (Fig. 5) it can be noticed that NO_x, and SO_x reduce to lowest value when using a hydrogen fuel cell and amount of extracted water is decreased also.

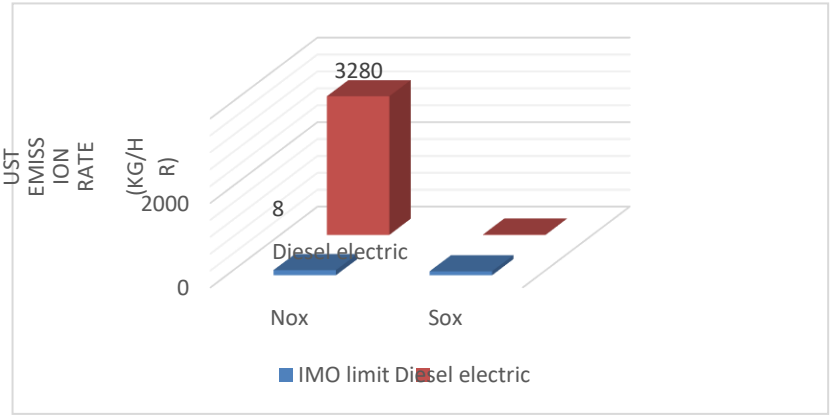

Figure. 4 exhaust emission rate.

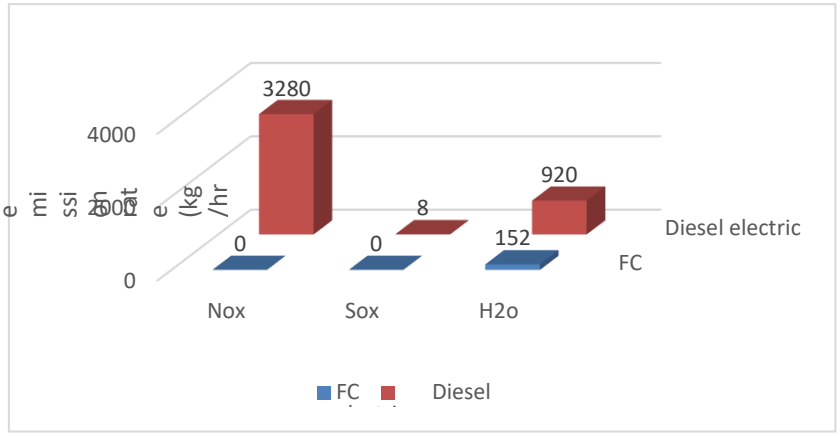

Figure. 5 exhaust emission rate of diesel electric and fuel cell.

4. Conclusion

Since hydrogen is a non-carbon clean fuel, it has a far lower operating impact on global warming than other fuels used in ship engines. The following is a list of the study's principal conclusions:

- Conventional diesel electric-driven maritime vehicles emit high GHGs and cause environmental pollution which can significantly be reduced when hydrogen which is carbon-free fuel is utilized.
- Comparative assessment of the exhaust emission rate of NO_x, and SO_x of conventional diesel electric-driven and IMO limit are obtained as 3280 Kg/hr and 8 Kg/hr while the IMO limit is obtained as 120.48 Kg/hr, and 93.3 Kg/hr .
- Comparative assessment of the exhaust emission rate of NO_x, and SO_x of conventional diesel electric-driven with hydrogen fuel cell are obtained as 3280 Kg/h , 8 Kg/hr when using hydrogen fuel cell NO_x , SO_x become net zero, and H_2O 920 Kg/hr while using hydrogen fuel cell decrease till 152 Kg/hr.

References

[1] IMO, “IMO’s work to cut GHG emissions from ships.” https://www.imo.org/en/MediaCentre/HotTopics/Pages/Cutting-GHG-emissions.aspx (accessed Jun. 09, 2023).

[2] R. W. Dorner, D. R. Hardy, F. W. Williams, and H. D. Willauer, “Heterogeneous catalytic CO 2 conversion to value-added hydrocarbons,” *Energy Environ Sci*, vol. 3, no. 7, pp. 884–890, 2010.

[3] L. van Biert, M. Godjevac, K. Visser, and P. V Aravind, “A review of fuel cell systems for maritime applications,” *J Power Sources*, vol. 327, pp. 345–364, 2016.

[4] DNVGL-Maritime, “Assessment of selected alternative fuels and technologies,” 2018.

[5] A. I. Bevan, A. Züttel, D. Book, and I. R. Harris, “Performance of a metal hydride store on the ‘Ross Barlow’ hydrogen powered canal boat,” *Faraday Discuss*, vol. 151, pp. 353–367, 2011.

[6] Bulletin, “First hydrogen fuel cell powered ferry in UK demos green tech,” *Fuel Cells Bulletin*, vol. 2013, no. 7, p. 4, 2013, doi: https://doi.org/10.1016/S1464-2859(13)70249-9.

[7] G. Sattler, “PEFCs for naval ships and submarines: many tasks, one solution,” *J Power Sources*, vol. 71, no. 1–2, pp. 144–149, 1998.

[8] A. Psoma and G. Sattler, “Fuel cell systems for submarines: from the first idea to serial production,” *J Power Sources*, vol. 106, no. 1–2, pp. 381–383, 2002.

[9] M. Taljegard, S. Brynolf, M. Grahn, K. Andersson, and H. Johnson, "Cost-effective choices of marine fuels in a carbon-constrained world: results from a global energy model," *Environ Sci Technol*, vol. 48, no. 21, pp. 12986–12993, 2014.
[10] F. Vogler and G. Würsig, "New developments for maritime fuel cell systems," *Germany: Germanischer Lloyd AG*, 2010.
[11] I. J. S. Veldhuis, R. N. Richardson, and H. B. J. Stone, "Hydrogen fuel in a marine environment," *Int J Hydrogen Energy*, vol. 32, no. 13, pp. 2553–2566, 2007.
[12] J. Han, J. F. Charpentier, and T. Tang, "State of the art of fuel cells for ship applications," in *2012 IEEE international symposium on industrial electronics*, IEEE, 2012, pp. 1456–1461.
[13] port said for Engineering works & naval constructions co., "FERRY BOAT ." http://cncshipyard.com/project/ferry-boat/ (accessed Jun. 26, 2023).
[14] EMSA, "EMSA Study on the use of Fuel Cells in Shipping," 2017. https://www.emsa.europa.eu/publications/item/2921-emsa-study-on-the-use-of-fuel-cells-in-shipping.html (accessed Jun. 09, 2023).
[15] Y. Wang, D. F. R. Diaz, K. S. Chen, Z. Wang, and X. C. Adroher, "Materials, technological status, and fundamentals of PEM fuel cells–a review," *Materials today*, vol. 32, pp. 178–203, 2020.
[16] H. Ishaq, I. Dincer, and C. Crawford, "A review on hydrogen production and utilization: Challenges and opportunities," *Int J Hydrogen Energy*, vol. 47, no. 62, pp. 26238–26264, Jul. 2022, doi: 10.1016/j.ijhydene.2021.11.149.
[17] C. Raucci, J. Calleya, S. S. De, L. Fuente, and R. Pawling, "HYDROGEN ON BOARD SHIP: A FIRST ANALYSIS OF KEY PARAMETERS AND IMPLICATIONS."
[18] Hyfindr, "Hydrogen Tank." https://hyfindr.com/hydrogen-tank/ (accessed Jun. 26, 2023).
[19] M. Perčić, N. Vladimir, I. Jovanović, and M. Koričan, "Application of fuel cells with zero- carbon fuels in short-sea shipping," *Appl Energy*, vol. 309, Mar. 2022, doi: 10.1016/j.apenergy.2021.118463.

Modelling and Simulation of CO2 Removal from Natural Gas by Membranes

Ahmed Wahba Gabr [1 a], Abbas Anwar Ezzat [2 b], A.H. EL-Shazly[3 c], Wael Bakr [1 d], Mohammed Shamakh [1 e] and N.S. Yousef [2 f]

[1] Khalda Petroleum Co., Egypt

[2] Petrochemical Department, Faculty of Engineering, Pharos University, Alexandria, Egypt

[3] Chemicals and Petrochemicals Engineering Department, Egypt-Japan University of Science and Technology, Alexandria Egypt

[a]5320002@pua.edu.eg , [b]abbas.ezzat@pua.edu.eg , [c]Elshazly_a@yahoo.com, [d]Waelbakr123@gmail.com, [e]Mohamed.shamakh@khalda-eg.com, [f]noha.said@pua.edu.eg

Keywords: Membrane, Gas Separation, Spiral Wound, Mathematical Model, Forward Finite Difference, 1D model, 2D model.

Abstract. This paper presents an improved model for modelling membrane separation processes. Several changes have been made to our model to improve accuracy and computational performance. The addition of a new dimensionless parameter, the simplification of equations for selectivity, permeate flow rate, and the adoption of speedier methods for calculating critical variables are among the changes. Furthermore, the new model is built to accommodate membrane package data, allowing for a more in-depth sensitivity analysis of system parameters. The model is an easily expandable approach utilizing the Python programming language and Object-Oriented Programming (OOP) with descriptive and sample code. Our suggested model has estimated the effect of a variety of parameters including flow rate, pressure ratio, carbon dioxide composition, membrane active area, and membrane thickness on both product purity and CO2 selectivity. It provides a more thorough understanding of membrane separation processes and can be utilized as a base to build and optimize such systems in a variety of industries.

Introduction

Many industrial processes, such as gas purification, natural gas processing, hydrogen production, and carbon capture, are relying on gas separation processes [1]. Membrane gas separation technology is one of the developing technologies that has gotten a lot of attention because of its appealing characteristics, such as low energy consumption, ease of operation, and environmental friendliness [2][3][4]. Gas-transport mechanisms via membranes are crucial in determining the efficiency of a membrane separation process [5]. Spiral-wound permeators can be used to improve natural gas mixing, which is an important application in natural gas treatment and enhanced oil recovery [6]. On the other hand, the lack of proper permeator models is a fundamental impediment to effective simulation and design of membrane processes. In other words, in order to simplify the basic transport models and make the procedure more efficient, approximate models consisting of a collection of nonlinear algebraic equations have been constructed [7][8].

Mathematical Model Development

Using fundamental molar balancing equations and the solution-diffusion assumption, the researchers developed a 1-D model that explains gas penetration via a membrane. The model is based on gas equilibrium and constant stream pressures, and it expresses the chemical potential gradient across the membrane as a concentration gradient. For the suggested model, the study makes numerous reasonable assumptions, which include steady state circumstances, which indicate that the system remains stable over time with no changes in factors affecting the separation process. Fast gas penetration through the membrane, with no mass building in the membrane. There are no pressure decreases along the membrane leaf. The solution-diffusion model describes the permeation mechanism. Gas adheres to the ideal gas law. The membrane's characteristics and thickness are consistent. The permeabilities of gaseous components are determined by temperature rather than pressure or concentration. The

feed stream is uniform. Thermal, thermodynamic equilibrium, and mass transfer effects are all considered. The elemental area of the spiral wound membrane module employed in the proposed model is depicted in Figure 1. The retentate and permeate parts, as well as the membrane layer, comprise the module.

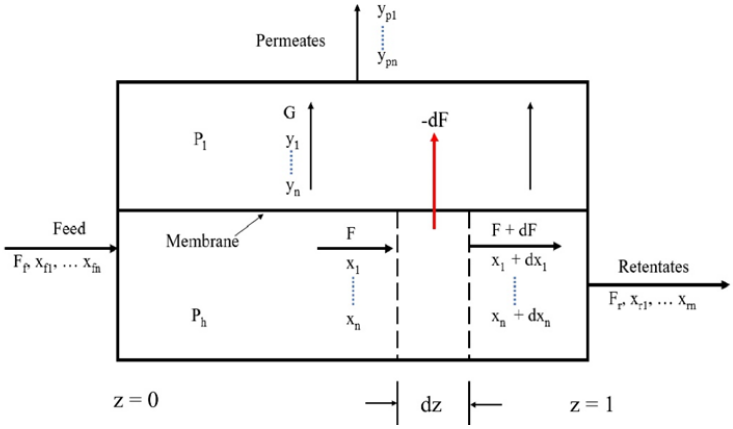

Fig. 1. Single permeation stage with cross flow

By applying material balance over the differential area equations 1 and 2 are obtained:

$$-dF = dG \tag{1}$$

$$= dA\frac{Q_i}{l}\sum_{k=1}^{NC} \quad (P_h x_k - P_l y_k) \tag{2}$$

Material balance for component i yields the following:

$$-d(x_i F) = d(y_i G) \tag{3}$$

$$= dA\frac{Q_i}{l}(P_h x_i - P_l y_i) \tag{4}$$

Several variables are included in the equation: F, which represents the flow rate on the high-pressure feed stream; G, which represents the flow rate on the low-pressure permeate stream that runs perpendicular to the feed stream; NC, which represents the number of gaseous components in the system. P_h and P_l are the feed and permeate pressures, respectively; Q_i is the permeability of component i; and l is the membrane thickness. The mole fractions of component i on the feed and permeate sides denoted as x_i and y_i, respectively. There are certain conditions that must be satisfied, which are as follows:

$$\sum_{k=1}^{NC} \quad x_k = 1 \tag{5}$$

$$\sum_{k=1}^{NC} \quad y_k = 1 \tag{6}$$

Instead of solving for dx_i, new term F_i, is used and defined by

$$F_i = x_i F \tag{7}$$

Where F_i the flow rate of each component i, this eliminates summation term in Eq. (2) and keeps the solution simple. The integration of Eqs. (1) and (3) from the inlet point to an arbitrary point yields the following:

$$G = F_f - F \tag{8}$$

$$y_i = \frac{x_{f_i} F_f - x_i F}{F_f - f}, \qquad G \neq 0 \tag{9}$$

where F_f, is the feed flow rate at the inlet, and x_{f_i}, is the feed mole fraction of component i. It is assumed that permeate flow rate G is zero at $A = 0$. The mole fraction y_i at $G = 0$ is obtained by a limiting process of the L'Hospital rule [32] as $F \to F_f$.

$$y_i = \frac{\frac{Q_i}{l}(P_h x_i - P_l y_i)}{\sum_{k=1}^{NC} \frac{Q_k}{l}(P_h x_k - P_l y_k)}, \qquad G = 0 \tag{10}$$

The mole fractions on the permeate stream at $G = 0$ can be obtained by solving the simultaneous equations, Eq. (10), for every component. The ratio of any two members of Eq. (10) becomes:

$$\frac{y_i}{y_j} = \frac{Q_i (P_h x_i - P_l y_i)}{Q_j (P_h x_j - P_l y_j)} \tag{11}$$

solving for y_i yields:

$$y_j = \frac{x_j \frac{Q_j}{Q_i}}{\frac{P_h}{P_l}\left(\frac{Q_j}{Q_i} - 1\right) + \frac{x_i}{y_i}} \tag{12}$$

Substituting Eq. (12) into Eq. (6) gives:

$$\sum_{k=1}^{NC} \frac{x_k \frac{Q_k}{Q_i}}{\frac{P_h}{P_l}\left(\frac{Q_k}{Q_i} - 1\right) + \frac{x_i}{y_i}} = 1, \qquad G = 0 \tag{13}$$

Eq. (13) can be solved by Bisection's iterative procedure for initial y_{0_i} only. The values of y_i for the other components can calculated with the aid of Eq. (12). After passing through the membrane A , y_i is obtained from Eq. (9) assuming $G \neq 0$.Dimensionless variables are given by the following equations:

$$s_t = A_t \frac{Q_m P_h}{F_f l}, \quad z = \frac{h_x}{L} \tag{14}$$

$$f = \frac{F}{F_f} \qquad f_r = \frac{F_r}{F_f} \tag{15}$$

$$\theta = 1 - f \tag{16}$$

$$g = \frac{G}{F_f} = \theta \tag{17}$$

$$q_i = \frac{Q_i}{Q_m} \tag{18}$$

$$\gamma = \frac{P_l}{P_h} \tag{19}$$

$$f_i = \frac{x_i}{f} \qquad g_i = \frac{y_i}{g} \tag{20}$$

Where $s_t, z, f, f_i, f_r, \theta, g, g_i, q_i, \gamma$ are dimensionless parameters defined by Eq. (14) to Eq. (20) where Q_m is the permeability of the base component, usually the most permeable component; F_r is the flow rate of the retentate stream; and θ is the stage cut, h_x is transversal lengths of retentate flux, L length of the membrane element. In terms of these dimensionless variables, the following governing equations for the crossflow are obtained from Eqs. (2), (5) to (8), (10), (12), and (13):

$$\frac{df_i}{dz} = -s_t q_i (x_i - \gamma y_i) \tag{21}$$

$$x_{NC} = 1 - \sum_{k=1}^{NC-1} x_k \tag{22}$$

$$\sum_{k=1}^{NC} \frac{x_k \frac{q_k}{q_i}}{\gamma\left(\frac{q_k}{q_i} - 1\right) + \frac{x_i}{y_i}} = 1 \qquad g = 0 \tag{23}$$

$$y_j = \frac{x_j \frac{q_j}{q_i}}{\gamma\left(\frac{q_j}{q_i} - 1\right) + \frac{x_i}{y_i}}, \qquad j \neq i, NC \tag{24}$$

$$y_{NC} = 1 - \sum_{k=1}^{NC-1} \quad y_k \tag{25}$$

$$y_i = \frac{x_{fi} - x_i f}{1-f} \ , \ G \neq 0 \tag{26}$$

The Forward Finite Difference Method (FFDM) was used to solve a proposed 1D model of gas separation using a spiral wound membrane. By applying the discretization method, the model Equations are as following:

$$\frac{f_i(n+1) - f_i(n)}{\Delta z} = -s_t \, q_i\big(x_i(n) - \gamma \, y_i(n)\big) \tag{27}$$

$$f(n+1) = \sum_{k=1}^{NC} \quad f_k(n+1) \tag{28}$$

$$x_i(n+1) = \frac{f_i(n+1)}{f(n+1)} \tag{29}$$

Where n is a discretization step. This is a simple initial value problem with following boundary condition.

$$\{z = 0 \ \rightarrow f = 1 \ ; \ x_i(z=0) = \ x_i^f \ \ z = 1 \ \rightarrow f = \ f_r ; \ x_i(z=1) = \ x_i^r \tag{30}$$

Model Validation

A two-stage membrane separation unit was used to validate our mathematical model. Table 1 shows the input data used for model validation.

Table 1. Input data used for validation.

Component	Q_i(mol/(m.s.Pa))	x_f
CO_2	4.35 x 10^{-11}	9.63
CH_4	1.56 x 10^{-12}	78.58
C_2H_6	7.03 x 10^{-13}	7.21
C_3H_8	2.14 x 10^{-13}	2.50
iC_4	9.44 x 10^{-14}	0.38
nC_4	1.11 x 10^{-13}	0.66
iC_5	1.13 x 10^{-13}	0.16
nC_5	1.26 x 10^{-13}	0.15
C_6^+	1.89 x 10^{-14}	0.10
N_2	1.50 x 10^{-12}	0.63
	γ = 0.033	
	F_f=141.9 $k(Nm^3)/hr$	
	A = 37 m^2	

The validation data for 1D and 2D models are summarized in Table 2. The mean absolute percentage error (MAPE) and the coefficient of determination (R2) were used to calculate the percentage error between the data obtained from the gas plant and the predictions from the mathematical model.

Table 2. show validation data for 1D and 2D models.

Stages	F_r $k(Nm^3)/hr$			x_r (CO_2)			y_o (CO_2)		
	Exp.	Model	Err. %	Exp.	Model	Err. %	Exp.	Model	Err. %

1st	112.46	112.61	0.13	2.97	2.84	4.38	35.06	34.96	0.29
2nd	112.43	112.38	0.39	9.70	9.78	0.82	72.72	70.15	3.53

The validation study results, shown in Table 2, demonstrated that the data received from the gas plant agreed well with the predictions from the suggested mathematical model. The MAPE was less than 4%, indicating that the disparity between the observed data and the predicted data are within an acceptable range. Furthermore, R^2 was greater than 0.9, indicating a strong correlation between the real data and the model predictions.

Results and Discussions

Effect of Feed Flow rate. The product purity diminishes as the gas feed flow rate increases as shown in Figure 2 (a). Increasing feed rate, increases the amount of hydrocarbon present in the feed, and on the other hand the residence time decreases, resulting in decreasing the amount of hydrocarbon in permeate, accordingly product purity decreases. Figure 2 (b) shows that CO_2 selectivity diminishes with increasing gas feed flow rate. Increasing the feed flow rate promotes the reduction in residence time, which leads to smaller variations of the CO_2 compositions in the membrane, and promotes higher CO_2 final molar compositions resulting in lowering CO_2 selectivity.

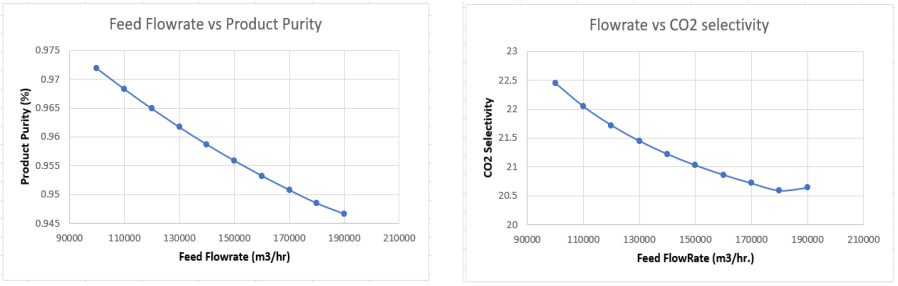

(a) (b)

Fig. 2. effect of feed flowrate

Effect of Pressure ratio. Pressure ratio is a very important parameter for the separation process, since the pressure gradient between the streams controls the mass transfer phenomena. High pressure ratios result in small pressure gradient, and in decreasing the permeation rate and accordingly decreasing product purity as shown in Figure 3(a). Also Increasing the pressure ratio causes an increase in the final molar fraction of carbon dioxide in permeate, since the pressure gradient across the membrane decreases, resulting in decreasing CO_2 selectivity as shown in Figure 3(b).

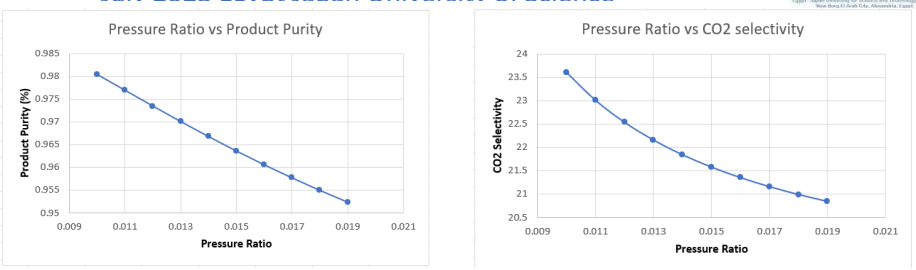

(a) (b)

Fig. 3. effect of pressure ratio

Effect of Mole fraction of CO_2 in feed. The transport mechanism favors the surface diffusion, since one of the permeating molecules is adsorbed on the pore wall. This behavior reduces the effective pore dimensions obstructing the transfer of other molecular species. As the CO_2's affinity is higher towards the membrane, larger surface area is adsorbed by CO_2 leaving very little space for other gases. Another reason that can be associated with the CO_2 selectivity is the diffusion mechanism. Diffusion occurs across a semi permeable membrane, in which the driving force of diffusion is the concentration gradient. When a CO_2 rich feed gas is used, the driving force for CO_2 is higher compared to the other gases. Hence it moves across the membrane more readily than other gases.

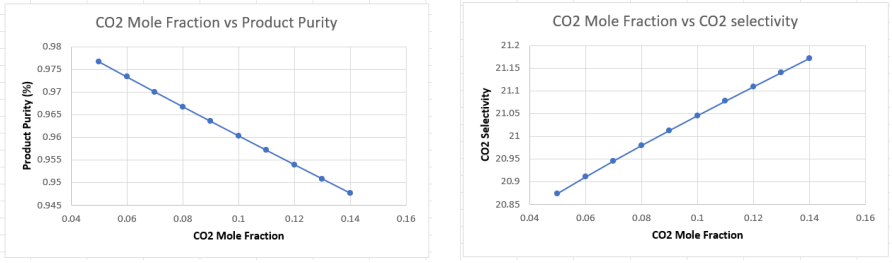

(a) (b)

Fig. 4. effect of mole fraction of CO_2

Conclusions

A mathematical model is built to predict the operation of a Membrane Separation Unit (MSU) that removes carbon dioxide (CO_2) from natural gas using spiral wound membranes. The model was created using forward finite difference methods in one and two dimensions, and it was validated using field data from a real plant. The validation results demonstrated that the model could properly predict MSU performance with an error of less than 3%. The influence of feed rate, pressure ratio, mole fraction of CO_2, membrane active area, membrane thickness on product purity and CO_2 selectivity were studied. Product purity decreased with increasing the following parameters: feed rate, pressure ratio, Mole fraction of CO_2 and membrane thickness, while it increased with increasing membrane area. Also, there exists a direct proportionality between CO_2 mole fraction and CO_2 selectivity.

References

Bernardo, P., Drioli, E., & Golemme, G. (2009). Membrane gas separation: A review/state of the art. Industrial & Engineering Chemistry Research, 48(10), 4638-4663. DOI: 10.1021/ie8019032

Baker, R.W. (2012). Membrane technology and applications (3rd ed.). John Wiley & Sons. ISBN: 978-0-470-74664-4

Li, Y., & Chen, H. (2018). Gas separation membranes: Polymeric and inorganic. Springer International Publishing. DOI: 10.1007/978-3-319-68255-6

Caro, J., Noack, M., Kölsch, P., & Schäfer, R. (2010). Zeolite membranes – Recent developments and progress. Microporous and Mesoporous Materials, 131(1-3), 215-246. DOI: 10.1016/j.micromeso.2009.06.024

Liang, W., Bajpai, R., & Huang, Y. (2017). Metal–organic framework membranes for gas separation. Chemical Society Reviews, 46(12), 3357-3385. DOI: 10.1039/C6CS00859A

Fontoura, T.B., de Sá, M.C.C., de Menezes, D.Q.F., Oechsler, B.F., Melo, A., Campos, L.F.O., Anzai, T.K., Diehl, F.C., Thompson, P.H., & Pinto, J.C. (2022). Modeling of spiral wound membranes for gas separations. Part III: A nonisothermal 2D permeation model. Chemical Engineering Research and Design, 177, 376-393. DOI: 10.1016/j.cherd.2021.10.036

Alshehri, A.A. (2015). Modeling and simulation of spiral wound membrane modules for natural gas sweetening (Doctoral dissertation). University of Waterloo. DOI: 10.20381/ruor-3459

Alshehri, A.A., & Lieuwen, D. (2021). Multicomponent spiral wound membrane model for natural gas sweetening applications. Membranes, 11(9), 654. DOI: 10.3390/membranes11090654

Removal of Phenol from Wastewater by Different Polymeric Membranes Using Pervaporation Technique

Alaa Dandash[1, a], Shaban Nosier[2], Heba Abdallah[3,b], Samah A. Hawash[4- 5,c] and Usama Eldemerdash[6,d]

[1]Menoufia Higher Institute of Engineering and Technology , El-menoufia, Egypt
[2]Faculty of Engineering, Alexandria University, Alexandria, Egypt
[3]National Research Centre, Giza, Egypt
[4] Higher Technological Institute, Ash Sharqia, Egypt
[5]Egypt-Japan University of Science and Technology, Alexandria, Egypt

[a]*alaaa_ayman@yahoo.com*, [b]heba_nasr94@yahoo.com, [c]samah.mohamed@bie.edu.eg,

[d]usama.nour@bhit.bu.edu.eg

Keywords: pervaporation, sodium alginate, polyvinyl alcohol membrane, cellulose acetate membrane, wastewater treatment.

Abstract. Phenolic compounds are regarded as a primary pollutant. Due to their high toxicity, even at low concentrations, phenols usually exist in the wastewater discharged in the effluents of numerous industries, including petrochemicals, medications, pesticides, and the paper industry. In this study, a phenol–water mixture was separated by utilizing the pervaporation process for removing phenols from wastewater using different polymeric membranes prepared from polyvinyl alcohol (PVA) and cellulose acetate (CA), and the performance of each membrane was investigated. The key factors affecting the membrane separation were the membrane selectivity towards the water, evaporation temperature, and feed concentration. Experiments conducted to study the separation factor concerning the feed concentration found that as the phenol concentration increased, the separation factor was enhanced and could reach as high as 38.18 for CA and 10.258 for PVA. The results also showed that the CA membrane has a higher separation factor than PVA. The pervaporation performance is effectively higher than that of PVA at a flow rate of 6 L/h, an optimum operating temperature of 55 °C, and a higher feed concentration of about 9000 ppm. The membranes were found to permeate water selectively, and scanning electron microscopy observed the morphology of the membranes.

Introduction

One of the most common pollutants in effluents from oil refining, petrochemicals, pharmaceuticals, coking operations, resin manufacturing, plastics, paint, pulp, paper, and wood products is phenolic compounds. They can be harmful to humans, animals, and the environment even at low concentrations. The EPA's water purity standards set a limit of 1 ppb for phenol. The toxicity level for humans and marine life is 9-25 mg/L. Protein degradation, tissue erosion, central nervous system paralysis, kidney, liver, and pancreatic damage are all caused by phenol-contaminated water, which should be less than 0.1 g/L [1] Solvent extraction, adsorption with activated carbon and polymers, and precipitation are all traditional methods for recovering phenol from wastewater [2]. Unfortunately, when the phenol components are present in low concentrations, these approaches are usually uneconomical. Membrane processes have recently gained popularity as an alternative technique for removing low volatile organic compounds from wastewater.

Membrane technologies that deal with azetropic separation problems have been competing with other methods for decades. Pervaporation membranes are a popular technique for extracting

low-volatility organics from wastewater because they consume little energy, require no regeneration, have little secondary contamination, are highly efficient, and are simple to operate.
Many researchers used solution-diffusion principles to explain the diffusion coefficient and Pervaporation results. The success of the pervaporation process is dependent on membranes with high permeability, good selectivity, and adequate mechanical strength [3]

M. Kondo et al. (1994) [4] studied the treatment of wastewater from phenolic resin process by pervaporation with a polyether block amide (PEBA) membrane and the result showed the concentration of phenol reduced from 5% up to less than 300 ppm. Xiaogang Hao et al (2009) [5] studied the pervaporative separation of phenol from dilute aqueous solutions using PEBA 2533 membrane. It showed that the good permeation separation factor of the membrane for phenol/water separation derived from the solubility separation factor. Xiaogang found that At 80 °C and over feed concentrations from 300 to 8000 ppm, phenol fluxes from 0.017 to 0.26 kg/ (m^2.h), permeate phenol concentrations from 1.7 to 19.7 wt%.

In the present work PVA/SA and CA were prepared to investigate the pervaporation separation of phenol from aqueous solutions with high flux and separation factor for phenol-water separation. The effects of temperature, feed concentration and flow rate on the membrane performance were evaluated.

Experimental

Materials. PVA powder with an average molecular weight of 50,000 and assay (min) 98% was supplied by alpha chemika, sodium alginate bulk density 1.6 g/cm^3 at 25℃, acetone, glutaraldehyde, dimethylformamide and Phenol were purchased from El-Gomhouria Co. for chemicals trading. Cellulose acetate was purchased from Sigma Aldrich Company.

Membrane preparation. For PVA membrane it was prepared by the solution-casting technique as 2.5% PVA and 2% SA was dissolved in distilled water to form a solution, with continuous stirring to ensure a homogenous solution was formed. The solution was then allowed to stand still at room temperature overnight to release any entrapped gas bubbles before being cast onto a polyester support, Followed by heating in an oven at 100◦C for 2 h to evaporate the solvent. Finally, the membrane was detached from the glass plate. and immersed in a reaction solution that contained 10 vol % of GA and 0.05 vol % of HCl in an acetone crosslinking reaction for an hour and half, the membrane was taken out of the reaction solution, washed out several times with pure methanol, immersed in methanol for 24 h eliminate any possible residual HCl and GA, and then washed by water and then dried under vacuum for 24 h**.**
For CA membrane the phase inversion approach was utilized in the production of cellulose acetate membrane. A combination solvent consisting of a 1:1 ratio of acetone to dimethylformamide was used to dissolve 25 weight percent of CA. A total of eight hours were spent stirring the mixture. After waiting for 24 hours, any bubbles that may have been present in the polymeric mixture were eliminated. The polyester support served as the working surface for the casting process. After that, coagulation in a bath of cold water at 5 degrees Celsius. The produced membrane was then annealed in a water bath at 85 degrees Celsius for five minutes.

Pervaporation experiment. The Pervaporation experiments were conducted in a lab-scale setup, as illustrated in Fig.1 The membrane cell is made of stainless steel. To control the operating temperature, the feed tank was heated with a water bath, and the feed temperature was measured with a thermometer. A peristaltic pump was used to continuously circulate the feed solution through the membrane cell with a membrane area equal to 16 cm^2. The pervaporation process was carried out with a temperature ranging from 25 to 55°c, the phenol concentration in the feed tank varied from 1000 to 9000 ppm. A feed mixture enters the cell through the center opening, flows radially

through the thin channel, and leaves the cell through the side opening, which allows relatively high fluid velocity parallel to a membrane. During experiments, the upstream pressure was maintained at the atmospheric pressure, while the downstream pressure was kept below 4 bar using a vacuum pump and permeate was obtained by condensing the downstream using cold water fed to the condenser. Permeation fluxes were determined by weighing permeate collected over a given period of time in the permeate tank. Composition of both the feed and permeate mixtures was determined by using Agilent UV-VIS spectrophotometer device. Separation factor for concentrate ( ) and flux (J) was calculated by the following equation

$$a = \frac{\text{Yphenol /Ywater}}{\text{Xphenol /Xwater}}$$

Where X and Y are the weight fractions of each component in feed and permeate, respectively.

$$J = \frac{W}{Am \times time}$$

Where, W represent weight of the permeate (kg), Am is the effective membrane area (m^2)

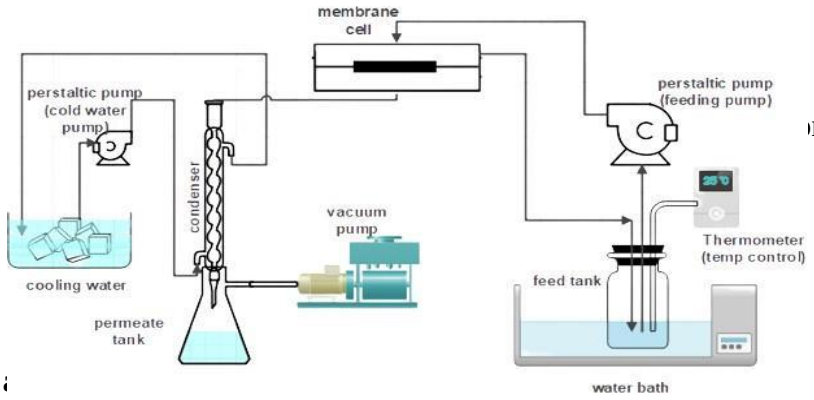

ıration Setup.

Result a

Scanning Electron Microscopy (SEM). Fig. 2 (a-b) depicted the cross-section morphology of the hollow-fiber CA membrane, revealing that it comprises three layers with varying pore sizes. The resulting membrane is anisotropic, with smaller pores in the outer layer (1) and slightly larger pores in the inner layer (2). When compared to the thickness of the inner supporting layer, outer skin layer is thin. A high concentration of pores next to the skin supported with a spongy microporous is desirable because it increases membrane permeability [6].

Meanwhile, the morphology of the optimized PVA/SA nanofiber membranes was shown in Fig.2 (c-d), indicating that the nanofibers were heterogeneously arranged, with a smooth surface and numerous voids between the fibers. Because more molecular chains participated in the crosslinking reaction, formed a dense network structure with a relatively small pore size [7].

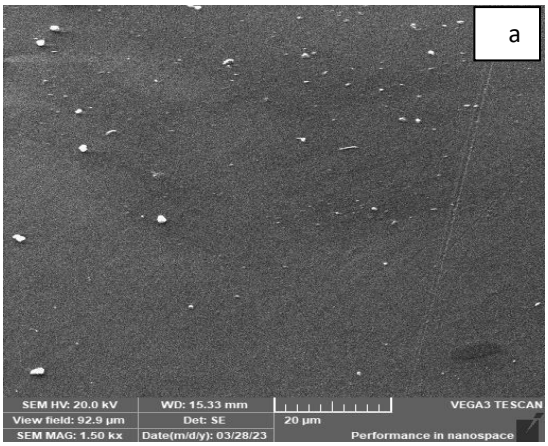

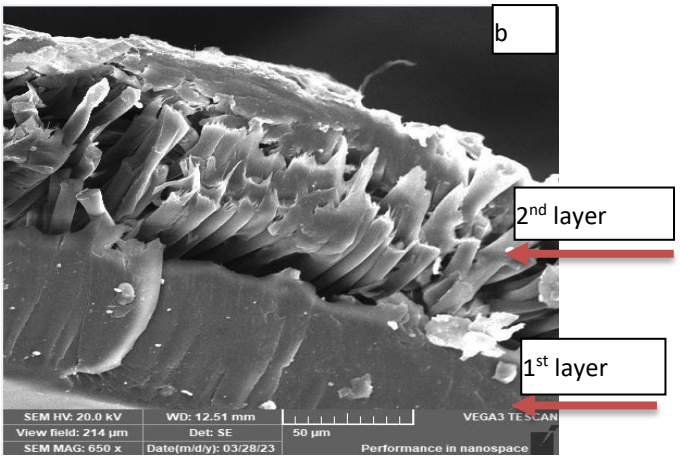

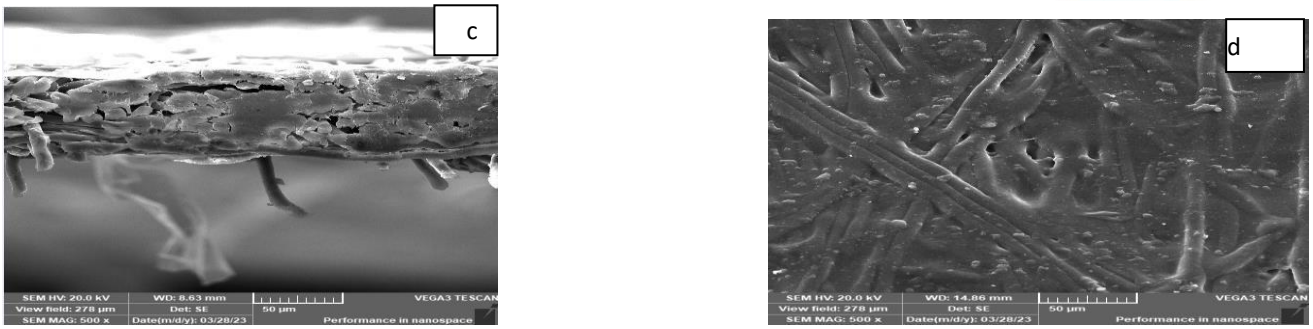

Fig.2 (a-b) SEM Images of CA membrane & (c-d) SEM Images of PVA-SA membrane.

Effect of Temperature on Removal of Phenol. The effect of temperature in the separation factor of concentrate, fluxes of water and phenol using PVA/SA and CA membranes were investigated at a temperature ranging from 25 to 65 °C and phenol concentration of 1000 ppm. Fig. 3.1 and 3.2 showed that the optimal separation factor of the CA membrane and higher water flux was achieved at 65°C. The separation factor of CA increases rapidly from 2.1 to 6 at 65 ° C. Meanwhile, the separation factor of PVA/SA is slightly raised and almost constant. Moreover, the water flux curves increased in the CA membrane with increasing temperature than in PVA/SA membrane. The temperature influenced the permeate transport and the ease of swelling in the membrane structure. the vapor pressure of permeating molecules increases at higher temperatures. Furthermore, At higher temp, the increase of free volume and lower the degree of swelling in CA membrane facilitate permeate transport and increase the permeation flux. At the same time, SA has a higher tendency to absorb water and causes a high degree of swelling which affect the PVA pores, and water flux rate [8].

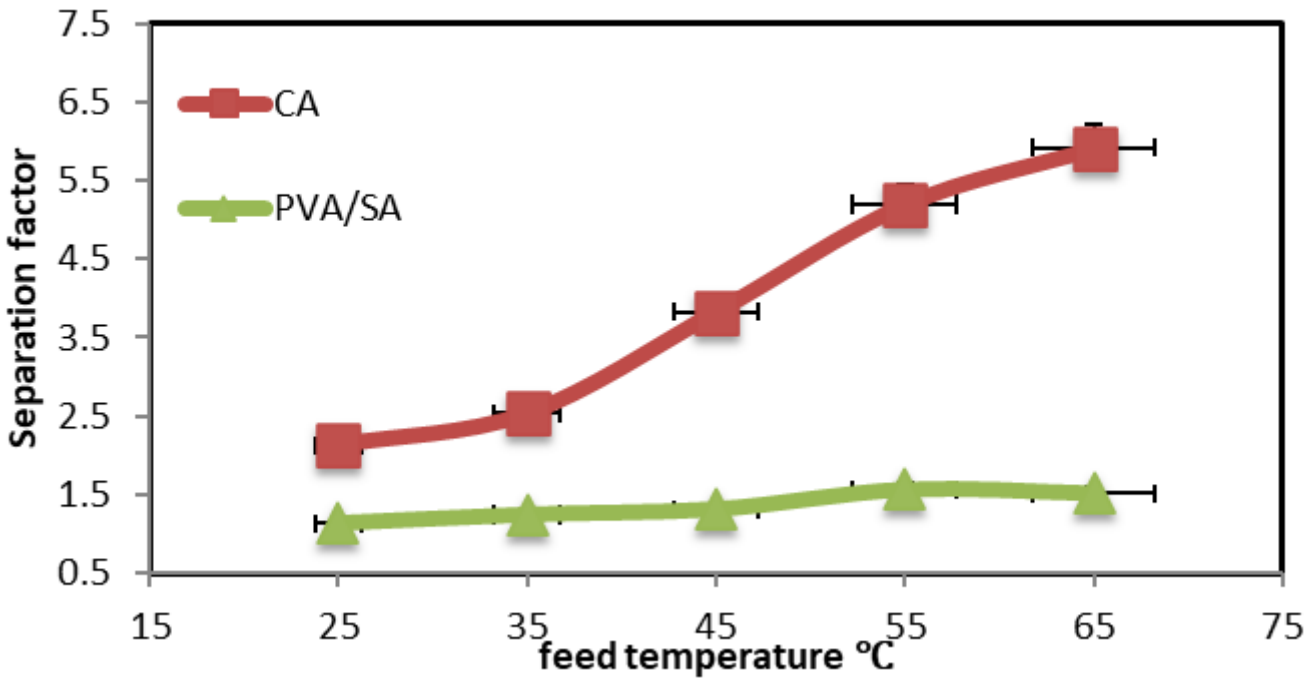

Fig. 3.1 Effect of Feed Temperature on Phenol Separation Factor Using CA and PVA/SA Membranes50

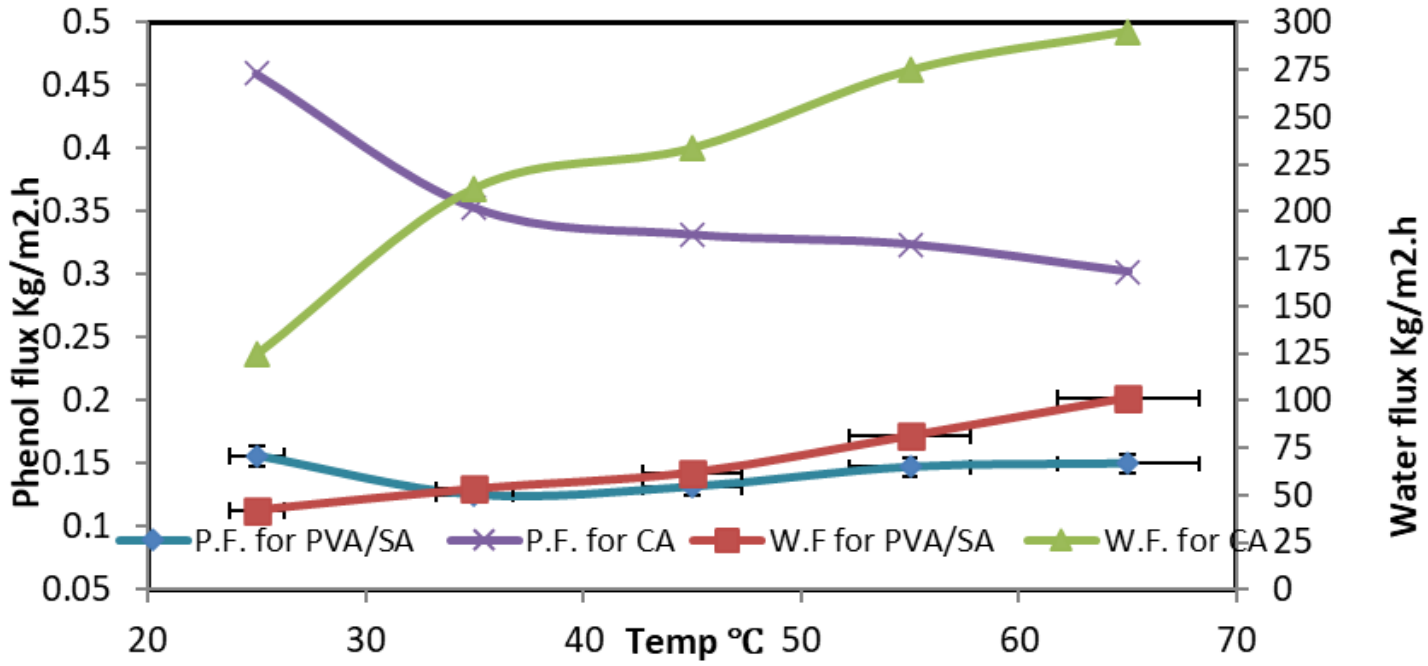

Fig.3.2 Effect of Feed Temperature on Phenol and Water Flux Using CA and PVA/SA Membranes

Effect of feed concentration on different membranes. Fig.4.1 illustrated the effect of the separation factor at different feed concentrations ranging from 1000 to 9000 ppm at 65°C. The separation factor of the CA membrane increased rapidly from 38.2 to 52 in increasing the feed concentration of phenol from 1000 to 9000 ppm. The separation factor depends both on the membrane properties and on the driving force, which in turn depends on the pressure. For dilute solutions, the increase in feed concentration increased both the driving force and the membrane permeability and hence, the separation factor of concentrate. The increase in the separation factor of the CA membrane from PVA/Sa was due to the spongy microporous structure of the inner layer, which increases the membrane's permeability and therefore increases the flux [9].

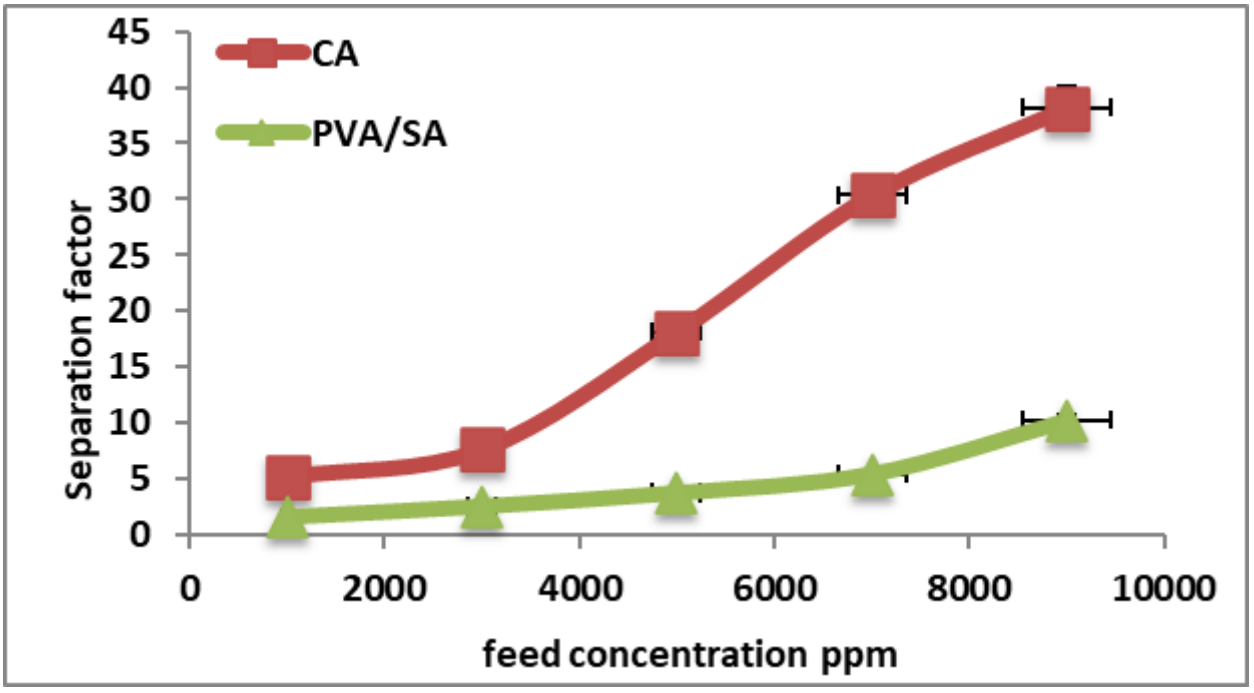

Fig.4.1 Effect of Feed Concentration on Phenol Separation Factor Using CA and PVA Membranes

At a given temperature of 65°C, Fig. 4.2 showed that the permeate phenol concentration was found to increase significantly with an increase in the feed phenol concentration. The permeated phenol concentration was as high as 1.3 Kg/m^2.h in the CA membrane and 1 Kg/m^2.h in PVA/SA membrane. These results are based on the solution-diffusion mechanism. A higher phenol concentration in the feed increases the driving force for permeation. For dilute solutions, with an increase in the phenol concentration in the feed, both the driving force and the membrane permeability for the permeation of phenol increased. For water permeation, the driving force tends to decrease with an increase in the feed phenol concentration. Still, the decrease is relatively insignificant because phenol is the minor component over the feed concentration range studied. The feed concentration is thus expected to affect phenol permeation more significantly than that of water [10].

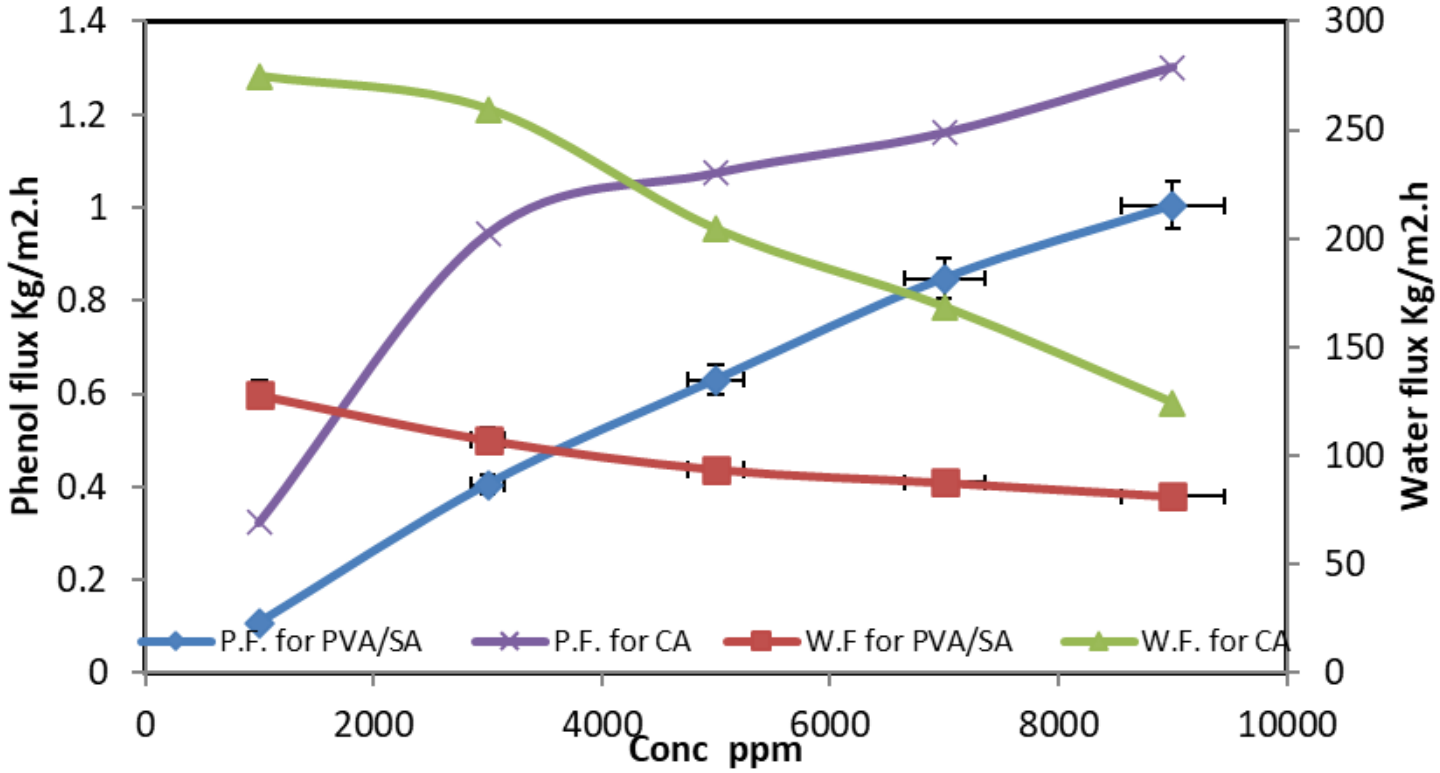

Fig.4.2 Effect of Feed Concentration on Phenol and Water Flux Using CA and PVA/SA Membranes

Conclusion

The pervaporation separation of phenol from water using PVA/SA and CA membranes was studied.

- It was shown that the good permeation separation factor of the membranes for phenol/water separation was derived from the solubility separation factor.
- The membrane performance was affected by phenol concentration in the feed, especially at elevated temperatures. The CA membrane possessed a higher water flux and separation factor compared to PVA/Sa at 65°C.
- The permeation flux of phenol rose to 1.3 kg/m^2.h in the CA membrane with an increase in feed phenol Concentration to 9000 ppm at 65°C, on the other hand, the permeation flux of phenol in the PVA/SA membrane was small, and reached 1 kg/m^2.h.

References

[1] Information from Environmental protection agency on https://www.epa.gov/sites/default/files/2016-09/documents/phenol.pdf

[2] H. Yamasaki, Y. Makihata, K. Fukunaga, Efficient phenol removal of wastewater from phenolic resin plants using crosslinked cyclodextrin particles, J. Chem. Technol. Biotechnol. 81 (2006) 1271–1276.

[3] Satyanarayana, S. Sridhar, Carbohydrate Polymers, 87 (2012)1569– 1574.

[4] M. Kondo, H. Sato,Treatment of wastewater from phenolic resin process by pervaporation, Desalination,Volume 98 (1994) Pages 147-154.

[5] Xiaogang Hao, Mark Pritzker, Xianshe Feng, Use of pervaporation for the separation of phenol from dilute aqueous solutions, Journal of Membrane Science 335, (2009)

[6] Hoshi, M., Kogure, M., Saitoh, T. and Nakagawa, Separation of aqueous phenol through polyurethane membranes by pervaporation. Journal of Applied Polymer Science, 65 (1997) 469-479.

[7] Tai Shung Chung, Kai-Chee Loh, Sock Khiang Goh, Development of Cellulose Acetate Membranes for Bacteria Immobilization to Remove Phenol, Journal of Applied Polymer Science, Vol. 68, 1677–1688 (1998).

[8] Asma Rhimi, Khira Zlaoui, Bart Van der Bruggen, Karima Horchani-Naifer, Dorra Jellouli Ennigrou, Synthesis and characterization of crosslinked membranes based on sodium alginate/polyvinyl alcohol/graphene oxide for ultrafiltration applications, Desalination and Water Treatment, 204–218, (2021), doi: 10.5004/dwt.2021.27434

[9] H K Dave and K Nath, Effect of Temperature on Pervaporation Dehydration of Water-Acetic Acid Binary Mixture, Journal of Scientific & Industrial Research, vol. 76, (2017).

[10] Muhammad Zafar, Muddassir Ali, Shahzad Maqsood Khan, Tahir Jamil, Muhammad Taqi Zahid Butt, Effect of additives on the properties and performance of cellulose acetate derivative membranes in the separation of isopropanol/water mixtures, Desalination 285 (2012) 359–365

Comparative and optimization study of utilizing alginate and agar flocculants for water treatment

Nagat A. Mostafa[1] and Aliaa M. Monazie[†2]
[1] [1]Faculty of Engineering, Minia University, Minia, Egypt
[2] [2]Faculty of Engineering, Fayoum University, Fayoum, Egypt
[3] [†]E-mail: amm17@fayoum.edu.eg

Keywords: water treatment, bio-flocculant, alginate, agar

Abstract. Recently, bio-based flocculants such as organic polymers have gained lots of consideration in water treatment technology owing to their superior advantages in excess of conventional synthetic inorganic polymers. A comparative study of two organic flocculants (sodium alginate and agar) for the treatment of surface water is aimed in this study. The influence of adding dry yeast (1, 2 & 3%) on the turbidity removal was studied. Adding 1% dry yeast improved the performance of both alginate and agar as a flocculating agent (percent removal of turbidity 62% and 60% after 60 min, respectively), but increasing the amount of dry yeast was not helpful. Optimal conditions for the turbidity removal process were obtained using response surface methodology. Based on the predicted linear models, the optimum parameters were 1.3 g alginate and 1.6 g agar for 59 min. Maximum turbidity removal achieved at these conditions were 62.4 and 59.7%, respectively. Thus, it is important to have further research on this natural coagulant for the future development of green technology in the water treatment process.

`

Introduction

The quality of water for the purpose of human consumption has been of interest since its effects on health was first discovered. Considering the increase in demand and the decrease in resources, water as essential fluid of life is a scare commodity [1]. Suspended and colloidal matters in water result in turbidity, they form a stable colloidal suspension that do not settle readily but remain in suspension [2]. Not only due to the appearance reasons but also its potential health risks turbidity is an important parameter stated in drinking water quality criteria. Primary contributors to turbidity include clay, silt, finely divided organic and inorganic matter, soluble colored organic compounds, plankton, and microscopic organisms [3,4].

For water treatment facilities to produce safe drinking water from river water, removing turbidity from the water is a challenge [5], particularly during the dry season when silt is carried into the pumping well. Coagulation and flocculation are the most economic methods for turbidity removal from water [6]. For the traditional reduction of turbidity in raw water, inorganic coagulants like alum and lime were used. The sludge obtained from such treatment poses disposal problems and tends to accumulate in the environment [7,8].

Recently, bio-based flocculants have received a lot of attention due to their superior advantages over conventional synthetic polymers or inorganic agents. Among natural polymers, polysaccharides show many benefits such as biodegradability, non-toxicity, ability to undergo different chemical modifications, and wide accessibility from renewable sources [9,10]. Several studies have tested different types of natural flocculants such as plant based coagulants [11-13], and different polysaccharides such as sago and chitin [14]. Although many studies have been conducted on the use of alginate as a flocculating agent, it is still in its infancy [15].

Alginate and agar are natural polymers with promising challenges as flocculating agents for water and wastewater treatments due to their biodegradability and non-toxicity. The present study is an attempt to compare and optimize the efficacy of using these natural polymers as a natural flocculants with a view to achieving the best results in moving towards a treatment for drinking water that meets the sustainable developing goals.

Materials and Methods

Materials. Sodium alginate powder, calcium chloride and agar powder were purchased from El-Gomhouria Pharmaceuticals and Chemicals Company, Cairo, Egypt.

Synthetic water. Synthetic water was prepared by adding garden soil to tap water and left mixing by magnetic stirrer for 1 hour. The suspension was then allowed to stand for 2 hours and after that, the supernatant was taken and served as the sample for the experiments. Table 1 shows the main features of the prepared synthetic water.

Table 1. Features of the prepared synthetic water

Parameter	Water
PH	7.14
Turbidity	88-92 NTU
Temperature	25-26 °C

Alginate and agar beads preparation

Alginate beads preparation. Alginate beads were prepared using sodium alginate solution (4%w/v) dripped into calcium chloride solution (4%w/v) using a syringe, then the solution of calcium chloride with drops of alginate solution is put into the fridge for 1 hour. Then the alginate beads are washed with distilled water in order to be used for the flocculation experiment. Alginate beads with dry yeast were prepared by adding 1, 2 and 3% dry yeast.

Agar beads preparation. Agar beads were prepared using 3 g of agar powder/100 ml of distilled water and left the flask with a solution in hot water bath with a temperature 100 °C for 1 hour. Then the agar solution is poured into a plate after this the solution of agar in the plate is left to cool for 10 min out the fridge and then for 30 min in the fridge. Then the plate of agar is gotten out from the fridge, cut the agar to small beads in order to be used for the flocculation experiment. Agar beads with dry yeast were prepared by adding 1, 2 and 3% dry yeast.

Flocculation procedure. For different types of prepared beads (alginate beads, alginate with yeast beads, agar beads and agar with yeast beads); different amounts (1, 2, 3 and 4g) of beads were put each weight in a beaker with 100 ml of synthetic water with initial turbidity 90 NTU and then allow mixing at high speed for 2 min then mixing at slow speed for 10 min then allowed for settling through different time periods (30, 40, 50 and 60 min), then the final turbidity was measured using turbidity meter.

Analytical methods. Final turbidity was measured using turbidity meter (Lutron TU-2016).

Experimental design and data analysis

Response surface methodology was utilized to optimize the process response (turbidity removal percent). Central composite design (face centered) with three coded levels leading to nine sets of experiments was performed to evaluate the effect of the independent process variables (grams of beads/100 ml turbid water, and settling time). Experimental process variables and levels for the design are given in Table 2. Design-Expert 10.0.1 software was used for the statistical analysis.

Table 2. Experimental range and levels of the independent process variables

Independent variable	Symbol	Range and levels

		-1	0	+1
Grams of beads/100 ml turbid water	X_1	1	2	3
Settling Time (min)	X_2	40	50	60

Results and Discussion

Effect of alginate beads on turbidity of water. Fig. 1 shows that by increasing the amount of alginate beads in the turbid water, the turbidity decreased and by increasing the time of settling, turbidity of water decreased too. Also, Fig. 2 shows that adding 1 g of dry yeast help to improve the ability of alginate beads to remove turbidity from water but increasing the amount of dry yeast in the prepared alginate beads is not more helpful in turbidity removal as shown in Table 3.

Effect of agar beads on turbidity of water. Fig. 3 shows that by increasing the quantity of agar beads in the turbid water, the turbidity decreased slightly. But, increasing the settling time decreases the turbidity of water. So, agar is not a better choice to eliminate turbidity of water at these conditions. Fig. 4 shows that adding 1 g of dry yeast help to increase the ability of agar to eliminate turbidity from water but increasing the quantity of agar with 1g dry yeast in water is not more helpful in the turbidity removal. Also, increasing the quantity of dry yeast doesn't help to improve the ability of agar to eliminate turbidity of water (Table 3).

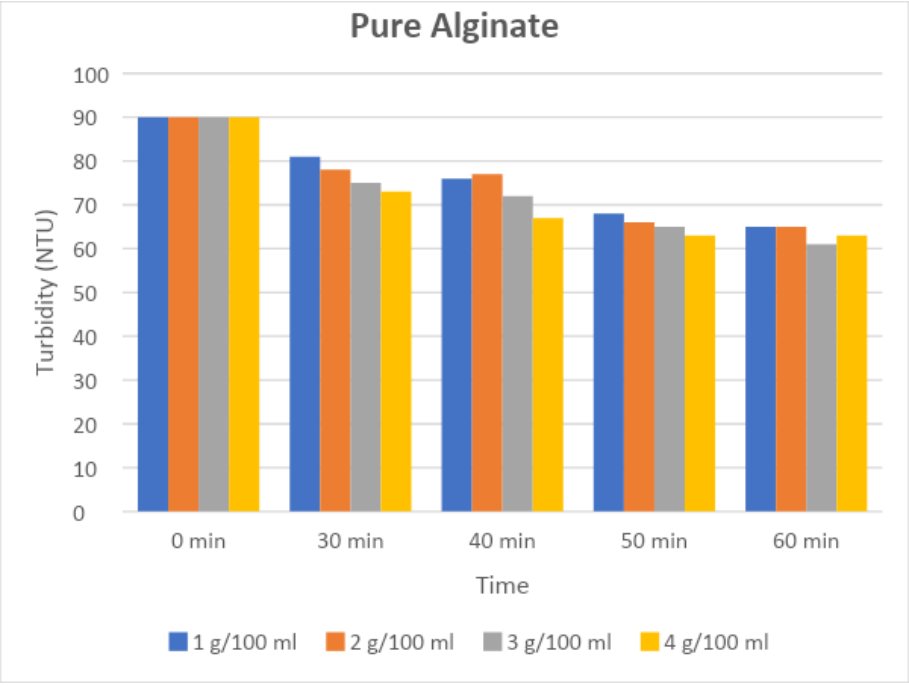

Fig. 1. Turbidity removal using alginate beads

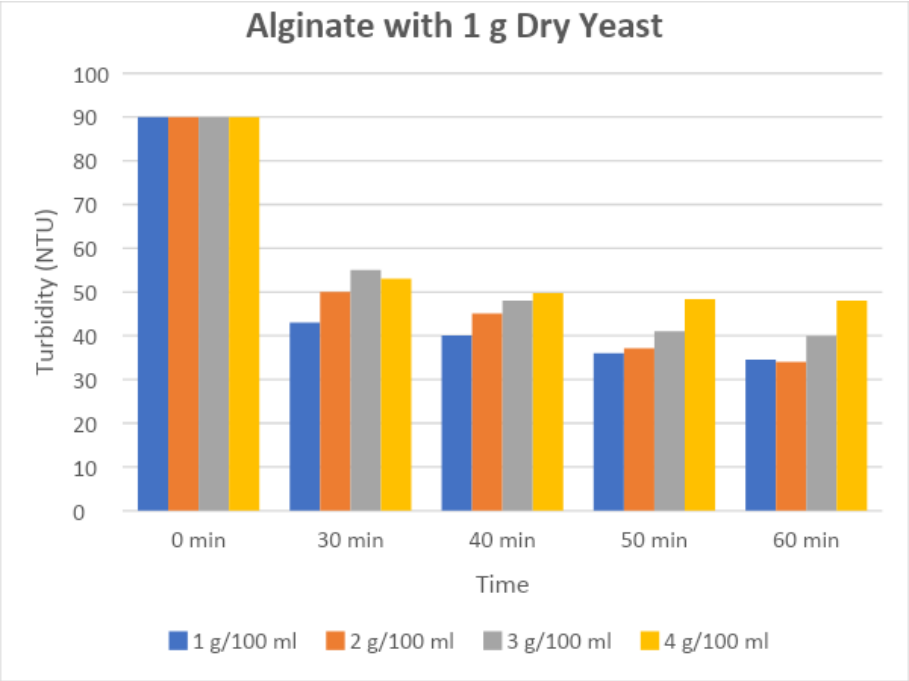

Fig. 2. Turbidity removal using alginate beads with 1% dry yeast

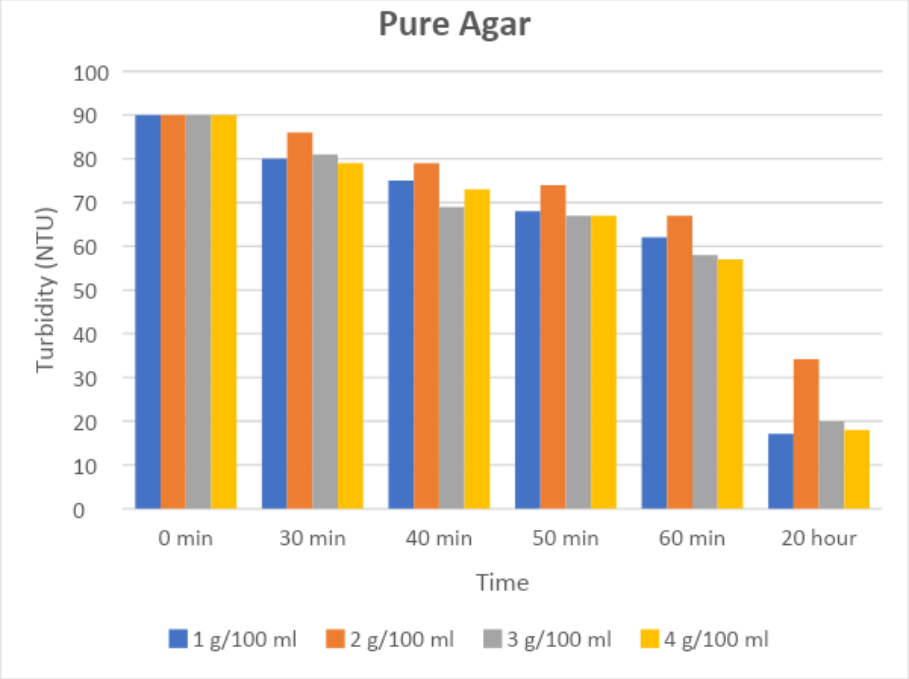

Fig. 3. Turbidity removal using agar beads

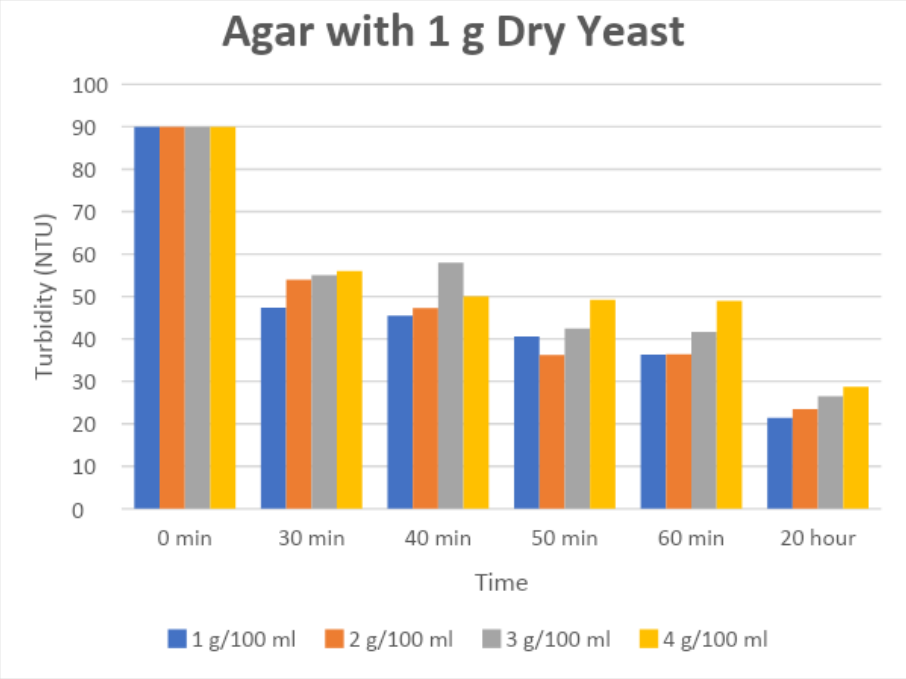

Fig. 4. Turbidity removal using agar beads with 1% dry yeast

Table 3. Effect of dry yeast concentration on turbidity removal using 1 g beads/ 100 ml turbid water

Dry yeast concentration (%)	Final turbidity (NTU)					
	Alginate	Agar	Alginate	Agar	Alginate	Agar
	40 (min)		50 (min)		60 (min)	
1	40.08	45.46	36	40.54	34.53	36.31
2	52	58	48.64	55	39.88	47.68
3	61.33	75	55.5	59	58.12	56

Statistical Modeling

Response surface model of the percent turbidity removal outcome. The experimental values for turbidity removal response at the design points and all the three uncoded independent variables for both alginate and agar models are given in Table 4.

Table 4. Experimental design and results for the developed turbidity removal model

Runs	Coded variables		Natural variables		Response (%Turbidity removal)	
	X_1	X_2	g beads/100 ml turbid water	Settling Time (min)	Y_1	Y_2
1	+1	-1	3	40	46.7	35.6
2	+1	+1	3	60	55.6	53.7
3	-1	0	1	50	60	55
4	0	-1	2	40	49.9	47.4
5	0	+1	2	60	62.2	59.6
6	0	0	2	50	58.8	59.7
7	-1	+1	1	60	61.6	59.7
8	+1	0	3	50	54.4	52.8
9	-1	-1	1	40	55.5	49.5

Where, Y_1 and Y_2 represent the percent turbidity removal response for alginate and agar beads, respectively. The predicted models for turbidity removal percent in terms of coded variables are expressed in Eq. 1 and Eq. 2 representing alginate response (Y_1) and agar response (Y_2) as a function of grams of beads/100 ml turbid water (X_1) and settling time (X_2):

$$Y_1 = 56.08 - 3.40X_1 + 4.55X_2 \quad (1)$$

$$Y_2 = 52.56 - 3.68X_1 + 6.75X_2 \quad (2)$$

The given linear equations in terms of coded variables can be used to make predictions about the percent turbidity removal response for the specified levels of each independent process variables (g beads/100 ml turbid water, and settling time). Fig. 5 and Fig. 6 display the response surface plots designed for the predicted responses for turbidity removal process using alginate and agar beads.

The statistical significance for the developed models for percent turbidity removal response was evaluated by Analysis of variance (Table 5). Table 5 indicates that the p-values of the predicted models were 0.0018 and 0.0185 for alginate and agar, respectively, implying that the two models are significant. Also, the R-squared values for the two developed models equations were 0.88 and 0.74 displayed that the fitting degree of the predicted models were reasonable. So, the two developed mathematical models for both alginate and agar responses can be used to navigate the design space.

Table 5. Analysis of variance (ANOVA) for alginate response (Y_1) and agar response (Y_2)

	Sum of squares		Mean squares		F-value		p-value prob>F		R^2	
	Y_1	Y_2	Y_1	Y_2	Y_1	Y_2	Y_1	Y_2	Y_1	Y_2
Model	193.58	354.78	96.79	177.39	21.77	8.34	0.0018	0.0185	0.88	0.74
Residual	26.68	127.69	4.45	21.28						
Total	220.26	482.46								

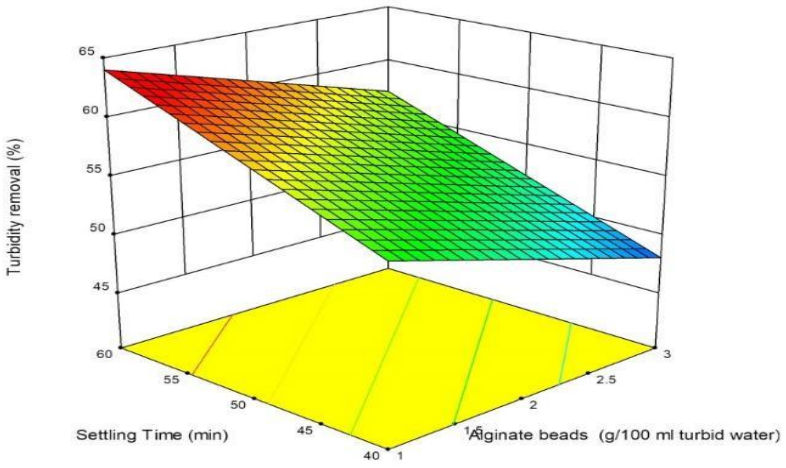

Fig. 5. The response surface plot for the alginate beads model

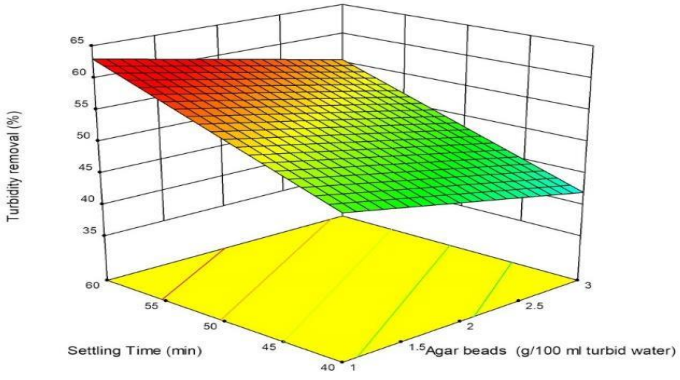

Fig. 6. The response surface plot for the agar beads model

Optimization for the process parameters (g beads/100 ml turbid water and settling time)

Based on the significant predicted mathematical models, the optimum operating parameters for turbidity removal process were identified to maximize the percent turbidity removal. The optimum values were 1.3 g alginate and 1.6 g agar per 100 ml turbid water for 59 min. Maximum turbidity removal percent achieved at these conditions were 62.4 and 59.7%, respectively.

Conclusions

Based on this study, it can be concluded that: 1- Adding 1 g of dry yeast help to improve the ability of alginate and agar beads to remove turbidity from water. 2- Increasing the amount of dry yeast doesn't help to improve the ability of beads to remove turbidity from water. 3- Agar is not a better choice to remove turbidity from water at these conditions. 4- For high turbidity water, the calcium-alginate system is more effective than for low turbidity water. Moreover, as the initial turbidity decreases the required concentration of alginate and calcium increases.

So, alginate is a high potential to be used as an alternative flocculant for water treatment purposes. This natural flocculant is safer to be used compared to the chemical flocculants and has potential to be commercialized. Thus, it is significant to have additional research on this natural flocculant for the future development of green technology in the water treatment process.

References

[1] Z. Tian, L. Zhang and C. Ni: Preparation and flocculation properties of modified alginate amphiphilic polymeric nano-flocculants, Environmental Science and Pollution Research 26 (2019), p. 32397

[2] B.G. Kitchener, J. Wainwright and A.J. Parsons: A review of the principles of turbidity measurement, *Progress in Physical Geography 41*(5) (2017), p. 620

[3] S.D. Faust and O.M. Aly: *Chemistry of water treatment* (CRC press 1998).

[4] S.N. Bakar, H.A. Hasan, S.R. Abdullah, N.A. Kasan, M.H. Muhamad and S.B. Kurniawan: A review of the production process of bacteria-based polymeric flocculants, *Journal of Water Process Engineering 40* (2021), p.101915

[5] D.S. de Oliveira and E. Costa Teixeira: Experimental evaluation of helically coiled tube flocculators for turbidity removal in drinking water treatment units, *Water SA 43*(3) (2017), p. 378

[6] A.M. Yüksel: *Use of calcium-alginate as a coagulant for low turbidity waters* (Master's thesis, Middle East Technical University 2007).

[7] Z. Tian, L. Zhang, X. Sang, G. Shi, and C. Ni: Preparation and flocculation performance study of a novel amphoteric alginate flocculant, *Journal of Physics and Chemistry of Solids 141* (2020), p. 109408

[8] R.A. Wahaab and M.I. Badawy: Water quality assessment of the River Nile system: an overview, *Biomedical and environmental sciences 17*(1) (2004), p. 87

[9] P. Maćczak, H. Kaczmarek and M. Ziegler-Borowska: Recent achievements in polymer bio-based flocculants for water treatment, *Materials 13*(18) (2020), p. 3951

[10] R.A. Hassan, N. Kasmuri, R. Ahmad, R. Santiagoo and S. Ramasamy: Enhancement of water quality using natural coagulant in Shah Alam Lakes, Malaysia, In *IOP Conference Series: Earth and Environmental Science* Vol. 646 No. 1 (2021), p. 012051

[11] A. Iqbal, G. Hussain, S. Haydar and N. Zahara: Use of new local plant-based coagulants for turbid water treatment, *International Journal of Environmental Science and Technology 16* (2019), p. 6167

[12] A. Latha, R. Ganesan, B. Krisnakumari and S. Theerkadarsin: Comparative Study of Organic Coagulants in Water Treatment, *ECS Transactions 107*(1) (2022), p.7997

[13] B. Othmani, M.G. Rasteiro and M. Khadhraoui: Toward green technology: a review on some efficient model plant-based coagulants/flocculants for freshwater and wastewater remediation, *Clean Technologies and Environmental Policy 22* (2020), p. 1025

[14] V. Saritha, M.K. Karnena and B.K. Dwarapureddi: "Exploring natural coagulants as impending alternatives towards sustainable water clarification"–a comparative studies of natural coagulants with alum, *Journal of Water Process Engineering 32* (2019), p. 100982

[15] P. Saranya, S.T. Ramesh and R. Gandhimathi: Coagulation performance evaluation of alginate as a natural coagulant for the treatment of turbid water, *Water Practice and Technology 17*(1) (2022), p. 395

Comparative assessment of hydrogen and ammonia fuel for reducing ship emissions

Aya A. Elbauomy[1, a], Mohamed R. Shouman[2, b] and Mohamed M. Elgohary [3, c]

[1,2] Arab Academy for Science, Technology and Maritime Transport, Egypt

[3] Borg El Arab Technological University, Egypt

[a]ayaa73520@gmail.com , [b]shouman85@aast.edu , [c]Mohamed.elgouhary@alexu.edu.eg

Keywords: alternative fuel, hydrogen, ammonia, zero-carbon shipping.

Abstract. Global warming, the greenhouse effect, acid rain, the depletion of traditional energy sources (i.e., fossil fuels), price fluctuations in conventional energy sources, the growing population, and increased energy use are all factors to consider. However, marine transport accounts for 3.1% of total CO_2 emissions worldwide, and the International Marine Organisation (IMO) predicts that this will continue to rise if no action is taken. All of these reasons indicate that it is critical to discover new energy sources and alternative power plants. Hydrogen and ammonia as alternative fuels have great potential given their higher efficiency when compared to other sources of energy. This paper investigates the comparison between both alternative fuels according to different criteria: safety, cost, storage, and environmental impact. The result of the criteria used in this study; ammonia performed slightly better than hydrogen for transportation. This study shows that on the road to decarbonization, shipping has powerful possibilities such as ammonia and hydrogen, and ammonia may play a major part in the transition to zero-carbon shipping.

Introduction

As global climate change concerns grow due to the massive quantity of pollution from industrial sources, the maritime industry is also facing more strict control regulations for emissions from seagoing commercial vessels. The International Maritime Organization (IMO) established standards for the avoidance of air pollution from ships in the International Convention for the Avoidance of Pollution from Ships, including the establishment of Emission Control Areas (ECAs). The limit on SO_X emissions is determined by the sulphur content of the fuel, but the limit on NO_X emissions is determined by the engine's maximum speed of operation. The standards for SO_X and NO_X regulations vary based on the region of navigation (global or ECA) [1].

CO_2 is the most significant Greenhouse Gas (GHG), and its quantity in the atmosphere causes global warming. Within the scope of the 2015 Paris Agreement, which argues for GHG reductions. IMO established a goal of reducing GHG emissions from international shipping by 50% by 2050 compared to 2008 levels [2].

Alternative fuels having lower carbon content than conventional marine fuels, such as liquefied natural gas (LNG) and methanol, are utilized for the short-term and will continue to be used for medium-term initiatives in maritime transportation. Long-term, on the other hand, include zero-carbon fuels and electric ships. As a result, ammonia and hydrogen are viable alternative fuels for the total decarbonization of maritime transportation [3] [4]. Ammonia and hydrogen must be utilized to produce energy in order to generate electricity for full-electric propulsion aboard ships. As a long-

term measure, ammonia and hydrogen are ideal fuels for fuel cells to be used to provide full-electric propulsion [5], [6].

Methodology

Ammonia

Ammonia is a colorless gas with a strong odor that may be recognized in the air at 5 parts per million (ppm) [7]. Ammonia is a compound that has no carbon in its structure. It is formed of one nitrogen and three hydrogen atoms. Ammonia is a hydrogen energy transporter with a hydrogen concentration of 17.6% by weight, and liquid ammonia has a greater volumetric energy density than liquid hydrogen [8]. In 2019, global annual ammonia production was 150 million tonnes [9]. Currently, the Haber-Bosch (HeB) method, created almost 100 years ago by Fritz Haber and Carl Bosch, is used to produce the majority of ammonia [10].

The toxicity of ammonia is a significant concern for shipboard storage and usage. It is three times as toxic as methanol and gasoline [11]. The toxicity of ammonia is widely recognized, and spilling ammonia into the water may pose risks to aquatic life. When ammonia dissolves in water, it produces ammonium hydroxide NH_4OH and ammonium ions NH_4 [7].

The reason of its hydrogen-carrying capability, ammonia is one of the chosen fuels for fuel cells. Ammonia may be used directly in the stacks of alkaline fuel cells (AFCs) and solid oxide fuel cells (SOFCs) to generate energy. AFCs are impacted by CO_2 in the air Because of their limited durability, [12]. SOFCs provide significant power capacity and fuel flexibility [13].

Hydrogen

As a maritime fuel, hydrogen may provide zero-emission shipping. Although it can be used in gas turbines and internal combustion engines (albeit with low efficiency), hydrogen is best suited for use in fuel cells due to its electrochemical kinetics, an innovative technology based on the direct conversion of fuel's chemical energy into electric energy via electrochemical reactions.

Hydrogen is produced from a variety of feedstocks, 96% of which are fossil fuels (natural gas 48%, oil 30%, and coal 18%) and 4% of which are renewable resources. The annual worldwide energy consumption of hydrogen production equals 2% of global energy demand [15]. Hydrogen can be classified into three varieties based on its cleanliness and the type of energy utilized to produce it: grey, blue, and green hydrogen. Grey hydrogen is produced using fossil fuels, which results in significant CO_2 emissions. Blue hydrogen is similarly made from fossil fuels, but Carbon Capture and Storage (CSS) technology reduces CO_2emissions, whereas green hydrogen is a sustainable and clean fuel produced from Renewable Energy Sources (RES) [16]. Hydrogen storage is one of the major barriers to its widespread application in the maritime industry, leading to onboard hydrogen production from hydrogen carriers (e.g., natural gas, methanol, ethanol, etc.) [17].

Table 1 illustrated the properties of Ammonia and Hydrogen.

Properties	Ammonia	Gaseous Hydrogen	Liquid Hydrogen
Auto-ignition temperature (C)	651	571	571
Flammability limits (Vol. %)	16-25	4-75	4-75
Flame speed (m/s)	0.15	3.51	3.51
Octane number	110	>130	>130
Density $kg\ /\ m^3$	602.8	17.5-20.54	70.85-71.1

Energy density MJ / m^3	11,333	2101	8539
Storage pressure (bar)	10.3	300	1
Storage type	Compressed liquid	Compressed gas	Cryogenic liquid
Storage temperature (C)	25	25	-253

Table 1.properties of Ammonia and Hydrogen [18], [19].

Criteria

Safety. Explosion/fire risk, toxicity, corrosiveness, and cryogenic properties of hydrogen and ammonia are all taken into consideration. During the comparison, the physical and chemical properties of hydrogen and ammonia are used, (Table 1). Hydrogen has a high auto-ignition temperature (571 C), a wide range of flammability (4-75%), and a fast flame speed (3.51 m/s) [20]. Auto-ignition of hydrogen is difficult during onboard storage, but the air's large flammability limitations result in a substantial explosion/fire danger on a ship. Furthermore, fast flame speed allows for the rapid spread of difficult-to-extinguish hydrogen fires. Ammonia, on the other hand, has a higher auto-ignition temperature (651 C) than hydrogen, narrower flammability limits (16-25%), and a low flame speed (0.15 m/s) [20].
Hydrogen performs better than ammonia in terms of toxicity and corrosiveness. Hydrogen is neither a poisonous chemical, nor is it corrosive to materials. However, storing hydrogen as a cryogenic liquid poses a cold burn danger to the ship's crew. However, ammonia is a poisonous toxin that, if breathed at a concentration of 2000 to 3000 ppm, can cause death within half an hour, and death can occur when exposed to more than 5000 ppm [12].

Cost. In this analysis, the cost covers fuel and onboard storage. The fuel cost of hydrogen is 153 $€ / KWh$, while the fuel cost of ammonia is 120 $€ / KWh$. Furthermore, the onboard storage operation costs range between 1.29 and 1.71 $€ / KWh$ for hydrogen and 0.23-0.29 $€ / KWh$ for ammonia [18]. The cost of fuel is determined by the price of electricity and the infrastructure. Even ammonia production necessitates producing hydrogen and nitrogen capture from the air, which consumes more electrical energy than hydrogen production; also, a substantial amount of hydrogen produced must be stored in cryogenic tanks. Cryogenic storage necessitates higher electrical consumption and distinct infrastructure. As a result, hydrogen is more expensive to fuel than ammonia. As shown in (Table 1), Because ammonia can be easily kept at 10 bar and 25 C, hydrogen is generally stored as a cryogenic liquid, resulting in a greater onboard storage cost than ammonia.

Storage. The most significant difference between these two types of fuel is the necessity to store enough fuel for a single voyage in terms of weight and volume per power. Hydrogen storage systems can be categorized into four types: compressed, liquid, solid-state, and alternate carriers [21]. Ammonia can be stored in two ways. It may be kept as a liquid at 1 bar at -33 degrees Celsius or 10 bars at a normal temperature [7]. Ammonia is significantly easier to store on a ship than hydrogen, which is generally kept as a compressed gas in high-pressure tanks (300 bar) or as a cryogenic liquid at -253 C temperature [22].

Environmental impact. The investigation of this paper was the path toward the decarbonization of shipping. In addition, hydrogen and ammonia were discovered to be the best short-term alternatives. As a result, as the basic concept suggests, using hydrogen and ammonia in fuel cells produces no CO_2. Hydrogen has a lifecycle emission of 139 $gCO_2 / MJ$when produced by grid energy, 2.59-20.74 $gCO_2 / MJ$when produced with wind power, and 6.67-66.67 gCO_2 / MJ when produced with solar

PV

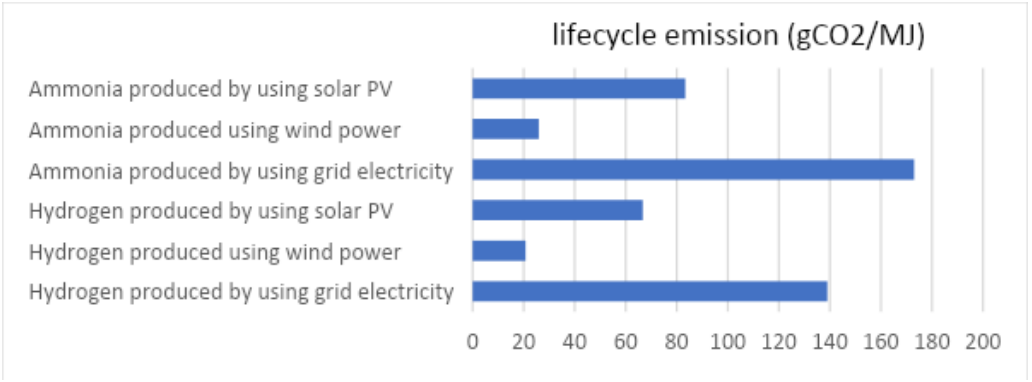

electricity. At the same kind of electrical consumption, ammonia has a lifecycle emission of 173 gCO_2 / MJ, 3.24-25.93 gCO_2 / MJ, and 8.83-83.33 gCO_2 / MJ [19].

Result

The Ideal shipping fuels should have a certain set of characteristics:

- The high energy density MJ / m^3 and specific energy reduce fuel volume and mass while enabling long-distance travel.
- In order to ensure compliance with IMO ECA requirements, produce a minimum quantity of local emissions (SO_x, NO_x, PM).
- Low life cycle GHG emissions gCO_2 / MJ, in order to meet the IMO objective of reducing shipping emissions by 50% by 2050.

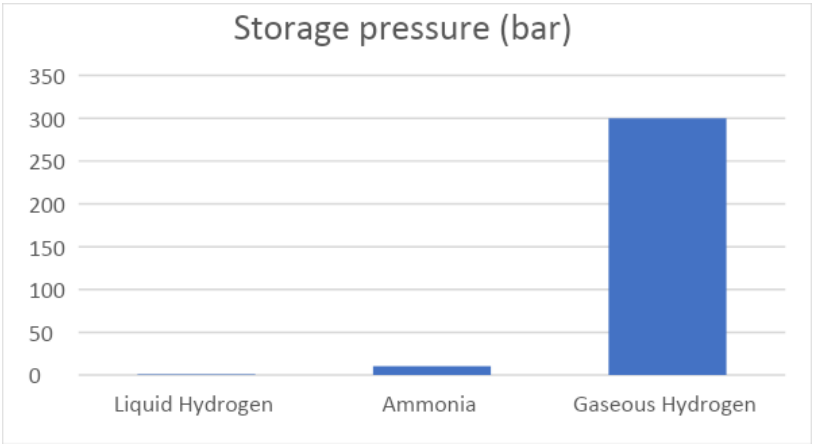

- Low cost of energy$(€ / KWh)$, in order to compete with low-quality remaining fossil fuels.
- Widespread bunkering infrastructure is necessary to ensure that vessels can refill at ports across the world.

Since ammonia and hydrogen are carbon-free alternative fuels for fuel cells, the environmental impact criteria take into account emissions from the production phase.

The storage criteria provide ammonia and hydrogen performance points based on the consideration of storage technologies and volumetric energy density.

The cost criteria determine performance points for ammonia and hydrogen based on the fuel cost and onboard storage cost.

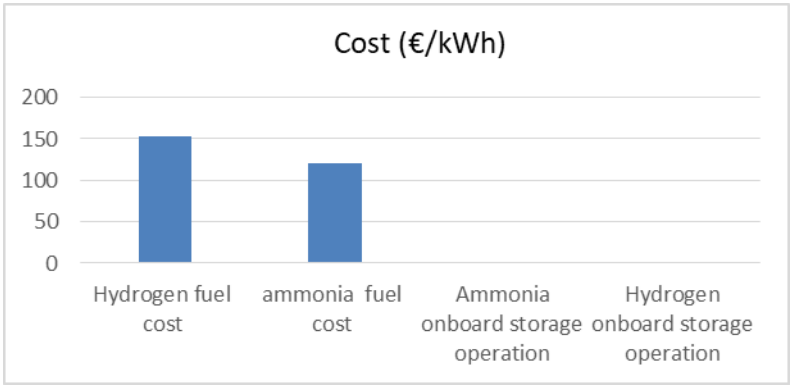

Conclusion

The purpose of this paper is to identify the most promising and appropriate zero-carbon fuel for the maritime sector. The criteria were developed utilizing knowledge from the literature. The explanations for each criterion and fuel performance are mostly based on marine perspectives and shipping experiences. When ammonia and hydrogen are compared, ammonia is a safer fuel with cheaper costs and lower storage issues. The only potentially negative aspect of ammonia is its environmental effect. Despite the little difference, ammonia has higher well-to-wheel emissions than hydrogen, leading to a greater environmental impact. Finally, based on the comparison, ammonia is determined to be a better fuel than hydrogen for decarbonized shipboard fuel cell applications. The primary issue to be addressed is shipping decarbonization, and ammonia and hydrogen are two major potential fuels for the shipping industry's future. It should be highlighted that when costs fall and storage conditions improve, hydrogen may play a larger role. However, technical advancements now provide greater opportunities for ammonia than hydrogen under marine conditions in terms of a sustainable and dependable shipping cost. To accomplish the zero-carbon goal, both fuels are elaborated using fuel cell systems; so, the power generation phase is relatively identical for both.

References

[1] IMO, “Emission Standards: IMO Marine Engine Regulations.” https://dieselnet.com/standards/inter/imo.php#s (accessed Jun. 20, 2023).

[2] J. Chen, Y. Fei, and Z. Wan, “The relationship between the development of global maritime fleets and GHG emission from shipping,” J Environ Manage, vol. 242, pp. 31–39, Jul. 2019, doi: 10.1016/j.jenvman.2019.03.136.

[3] O. B. Inal and C. Deniz, “Fuel cell availability for merchant ships,” in Proceedings of the 3rd International Naval Architecture and Maritime Symposium, 2018, pp. 907–916.

[4] B. Zincir, “A SHORT REVIEW OF AMMONIA AS AN ALTERNATIVE MARINE FUEL FOR DECARBONISED MARITIME TRANSPORTATION,” 2020.

[5] M. Rivarolo, D. Rattazzi, and L. Magistri, “Best operative strategy for energy management of a cruise ship employing different distributed generation technologies,” Int J Hydrogen Energy, vol. 43, no. 52, pp. 23500–23510, 2018.

[6] L. Balestra and I. Schjølberg, “Modelling and simulation of a zero-emission hybrid power plant for a domestic ferry,” Int J Hydrogen Energy, vol. 46, no. 18, pp. 10924–10938, 2021.

[7] T. Ayvali, S. C. E. Tsang, and T. Van Vrijaldenhoven, “The position of ammonia in decarbonizing maritime industry: an overview and perspectives: Part II: costs, safety and environmental performance and the future prospects for ammonia in shipping,” Johnson Matthey Technology Review, vol. 65, no. 2, 2021.

[8] P. Dimitriou and R. Javaid, "A review of ammonia as a compression ignition engine fuel," International Journal of Hydrogen Energy, vol. 45, no. 11. Elsevier Ltd, pp. 7098–7118, Feb. 28, 2020. doi: 10.1016/j.ijhydene.2019.12.209.

[9] F. Y. Al-Aboosi, M. M. El-Halwagi, M. Moore, and R. B. Nielsen, "Renewable ammonia as an alternative fuel for the shipping industry," Current Opinion in Chemical Engineering, vol. 31. Elsevier Ltd, Mar. 01, 2021. doi: 10.1016/j.coche.2021.100670.

[10] P. Dimitriou and R. Javaid, "A review of ammonia as a compression ignition engine fuel," International Journal of Hydrogen Energy, vol. 45, no. 11. Elsevier Ltd, pp. 7098–7118, Feb. 28, 2020. doi: 10.1016/j.ijhydene.2019.12.209.

[11] N. Morlanés et al., "A technological roadmap to the ammonia energy economy: Current state and missing technologies," Chemical Engineering Journal, vol. 408, Mar. 2021, doi: 10.1016/j.cej.2020.127310.

[12] Z. Wan, Y. Tao, J. Shao, Y. Zhang, and H. You, "Ammonia as an effective hydrogen carrier and a clean fuel for solid oxide fuel cells," Energy Convers Manag, vol. 228, p. 113729, 2021.

[13] Ö. B. İNAL and C. Deniz, "Emission analysis of LNG fuelled molten carbonate fuel cell system for a chemical tanker ship: a case study," Mar Sci Technol Bull, vol. 10, no. 2, pp. 118–133, 2021.

[14] C. G. Vayenas and R. D. Farr, "Cogeneration of electric energy and nitric oxide," Science (1979), vol. 208, no. 4444, pp. 593–594, 1980.

[15] E. Taibi, R. Miranda, W. Vanhoudt, T. Winkel, J.-C. Lanoix, and F. Barth, "Hydrogen from renewable power: Technology outlook for the energy transition," 2018.

[16] F. Dawood, M. Anda, and G. M. Shafiullah, "Hydrogen production for energy: An overview," Int J Hydrogen Energy, vol. 45, no. 7, pp. 3847–3869, 2020.

[17] L. van Biert, M. Godjevac, K. Visser, and P. V Aravind, "A review of fuel cell systems for maritime applications," J Power Sources, vol. 327, pp. 345–364, 2016.

[18] A. D. Korberg, S. Brynolf, M. Grahn, and I. R. Skov, "Techno-economic assessment of advanced fuels and propulsion systems in future fossil-free ships," Renewable and Sustainable Energy Reviews, vol. 142, May 2021, doi: 10.1016/j.rser.2021.110861.

[19] N. Gray, S. McDonagh, R. O'Shea, B. Smyth, and J. D. Murphy, "Decarbonising ships, planes and trucks: An analysis of suitable low-carbon fuels for the maritime, aviation and haulage sectors," Advances in Applied Energy, vol. 1. Elsevier Ltd, Feb. 23, 2021. doi: 10.1016/j.adapen.2021.100008.

[20] D. Erdemir and I. Dincer, "A perspective on the use of ammonia as a clean fuel: Challenges and solutions," International Journal of Energy Research, vol. 45, no. 4. John Wiley & Sons, Inc. Chichester, UK, pp. 4827–4834, 2021.

[21] L. Van Hoecke, L. Laffineur, R. Campe, P. Perreault, S. W. Verbruggen, and S. Lenaerts, "Challenges in the use of hydrogen for maritime applications," Energy and Environmental Science, vol. 14, no. 2. Royal Society of Chemistry, pp. 815–843, Feb. 01, 2021. doi: 10.1039/d0ee01545h.

[22] C. Deniz and B. Zincir, "Environmental and economical assessment of alternative marine fuels," J Clean Prod, vol. 113, pp. 438–449, Feb. 2016, doi: 10.1016/j.jclepro.2015.11.089.

Reduction of hexavalent chromium to trivalent chromium by using a fixed bed of iron solid cylinders

D.N. Shaaban[†1], M.A. El-Naggar[1], S.A. Nosier[1], G.H. Sedahmed[1] and A.S. Fathalla[1] [1]Chemical Engineering Department, Faculty of Engineering, Alexandria University, Alexandria, Egypt

[†]E-mail: eng.dinanagy112@gmail.com

Keywords: Agitated Vessels, Fixed Bed, Hexavalent Chromium, Mass Transfer, Wastewater Treatment.

Abstract. In view of their high space-time yield resulting from their high specific area and high mass transfer coefficient, the present work studies the rate of liquid-solid mass transfer on a fixed bed of randomly-packed scrap iron solid cylinders located at the bottom of an agitated vessel. The rate of the reaction was determined in terms of the mass transfer coefficient using the diffusion-limited dissolution of iron in acidified dichromate technique. Variables studied were impeller rotational speed, impeller geometry, physical properties of the solution, bed thickness, and diameter of cylinders. Also, the effect of a galvanic coupling of carbon (graphite)-iron fixed bed on the rate of mass transfer was investigated. The data were correlated by dimensionless equations which reported that for a given set of conditions, the rate of mass transfer for the radial flow impeller was higher than that for the axial flow impeller. Also, it was found that the rate of mass transfer increased by increasing the speed of rotation and decreasing the cylinder diameter and bed height. The galvanic action of adding carbon cylinders with the iron cylinders increased the dissolution rate of iron cylinders with a subsequent increase in the mass transfer coefficient by an amount ranging from 4.4% to 12.7% and from 3% to 15.8% for the axial and radial flow impellers, respectively depending on the operating conditions. The advantages of supporting the catalyst on the outer surface of the fixed bed instead of being fluidized as in stirred slurry reactors were pointed out.

1. Introduction.

Hexavalent chromium (Cr(VI)) is a toxic and carcinogenic pollutant that poses a significant risk to human health and the environment. It is commonly found in industrial wastewater streams, particularly in industries such as electroplating, leather tanning, and textile manufacturing. The reduction of Cr(VI) to trivalent chromium (Cr(III)) is an important step in the treatment of these wastewaters, as Cr(III) is less toxic and more stable than Cr(VI). [1 – 6]**.**

Agitated vessels are commonly used in industrial processes to enhance mass transfer and promote mixing, which can improve the efficiency of chemical reactions and other processes. In recent years, researchers have investigated the use of agitated vessels for the reduction of Cr(VI) to Cr(III) using iron-based materials. [7 – 16]

Using the agitated vessel wall as a catalyst support has the drawback of limited surface area on the vessel wall, resulting in low productivity of the reactor. To address this limitation, an effort has been made to overcome this shortcoming, El-Naggar et al. [17] studied the liquid-solid mass transfer behavior of a stirred-tank reactor with a fixed bed at its bottom. An equation was formulated by the authors to correlate their data for an agitated vessel with a radial-flow turbine, using Raschig rings placed at the bottom of the vessel:

$$Sh = \mathbf{0.046Sc^{0.33}Re^{0.78}d_h^{0.45}} \quad (1)$$

where h is the bed thickness and d is the particle diameter. When computing Sh, the impeller diameter was utilized as a characteristic length, however when calculating Re, the particle diameter was employed. Fouad et al. [18] conducted a study aimed at developing a liquid-solid stirred-tank catalytic reactor capable of performing diffusion-controlled reactions involving heat-sensitive catalysts or products. To achieve this, they measured the mass transfer rate at a vertical square array of tubes

placed within a square agitated vessel. The outer surface of the tubes served as the catalyst support, while the inner surface acted as a cooler, which was circulated with cold water.

Building on the aforementioned research, the present work sought to investigate the effectiveness of a stirred tank reactor that incorporates a stationary bed at the bottom in facilitating diffusion-controlled liquid-solid reactions.

In addition to facilitating liquid-solid diffusion-controlled reactions, the recommended reactor is highly appropriate for carrying out liquid-solid reactions that require initial dispersion of the reactant, such as gases, sparingly soluble particles, and immiscible liquid reactants. It is versatile enough to be utilized for conducting various types of reactions, including immobilized enzyme-catalyzed biological reactions, photocatalytic reactions, and catalytic chemical liquid-solid reactions like wet oxidation and organic synthesis.

2. Experimental Part

2.1. Set up

The present study utilized an experimental setup comprising a 15 cm diameter and 25 cm height cylindrical Plexiglas container. A fixed bed of randomly oriented iron spheres was positioned at the bottom of the container, as depicted in Figure 1. The reactor was agitated using either a 4-blade 45opitched-blade stainless-steel turbine (axial-flow impeller) or a 90oflat-blade turbine (radial-flow impeller) affixed to a 0.5-cm stainless-steel shaft rotated by a variable-speed motor ranging from 100 RPM to 450 RPM. To prevent vibration and eccentric motion, the motor was securely mounted against a brick wall. The impellers and shafts were coated with epoxy resin to protect against corrosion. The reactor dimensions were designed according to standard agitated vessel design specifications [19], with an impeller diameter of 5 cm and a clearance of 5 cm between the impeller and vessel bottom. Three bed heights were employed, consisting of a single layer, two layers, and three layers of randomly oriented iron spheres. The impeller geometry and dimensions used in the study are illustrated in Figs. 1a and 1b.

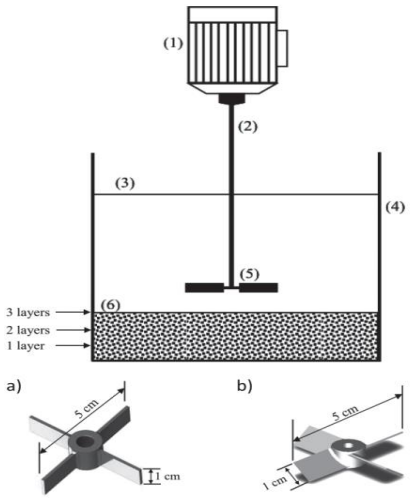

Figure 1 Apparatus with impeller drawing and dimensions. (1) Variable-speed motor, (2) isolated steel shaft, (3) solution level, (4) Plexiglas tank, (5) isolated impeller, (6) fixed bed of iron sphere. a) 4-Blade **90o** turbine impeller; b) 4-blade **45o** pitched turbine

2.2. Procedure

Prior to each experimental run, 3000 mL of acidified dichromate was introduced into the reactor, and the impeller speed was adjusted to the desired value using a variac, while the digital tachometer was employed to measure the impeller speed. To monitor the reaction rate, 5 mL samples were extracted from the solution at intervals ranging from 1 to 3 minutes for analysis. Residual dichromate was assessed by titrating the solution against a standard ferrous ammonium sulfate solution, with diphenylamine serving as an indicator [20]. Three different solution compositions were employed, consisting of 0.03 M $K_2Cr_2O_7$ + 0.5 M H_2SO_4, 0.03 M $K_2Cr_2O_7$ + 1 M H_2SO_4, and 0.03 M $K_2Cr_2O_7$ + 1.5 M H_2SO_4. All solutions were prepared using A.R. grade chemicals and distilled water. The viscosity and density of each solution were determined using an Ostwald viscometer and a density bottle, respectively [21]. The diffusivity of K2Cr2O7 was obtained from relevant literature sources [22]. Table 1 presents the physical properties of the solutions used in data correlation, where the temperature was maintained at 20 ± 1 °C.

Table.1 Physical properties of the solution used at 20°C.

Solution composition	ρ [kg m^{-3}]	μ x 103[kg m^{-1} s^{-1}]	D x 1010[m^2 s^{-1}]	Sc
0.03 M $K_2Cr_2O_7$ + 0.5 M H_2SO_4	1029.2	1.01	9.476	937
0.03 M $K_2Cr_2O_7$ + 1 M H_2SO_4	1060.5	1.09	8.778	1095
0.03 M $K_2Cr_2O_7$ + 1.5 M H_2SO_4	1070	1.095	8.282	1217

3. Results and Discussion

The fixed bed's mass transfer coefficient was determined for diffusion-controlled reactions by utilizing the batch reactor rate equation, while varying the conditions [23, 24]

$$-QdCdt=kAC \quad (2)$$

which integrates to

$$QlnC0C=kAt \quad (3)$$

In the equation, C represents the concentration of dichromate. Figure 2 demonstrates a good fit between the obtained dichromate concentration-time data and Equation (3), with the reaction rate escalating as the degree of stirring intensifies. This finding verifies that the dissolution of the fixed bed of iron cylinders in acidified $K_2Cr_2O_7$ is diffusion-controlled, similar to other geometries under varying hydrodynamic situations [25, 26]. The slope of the graph of ln(C_0/C) versus t was utilized to determine the mass transfer coefficient.

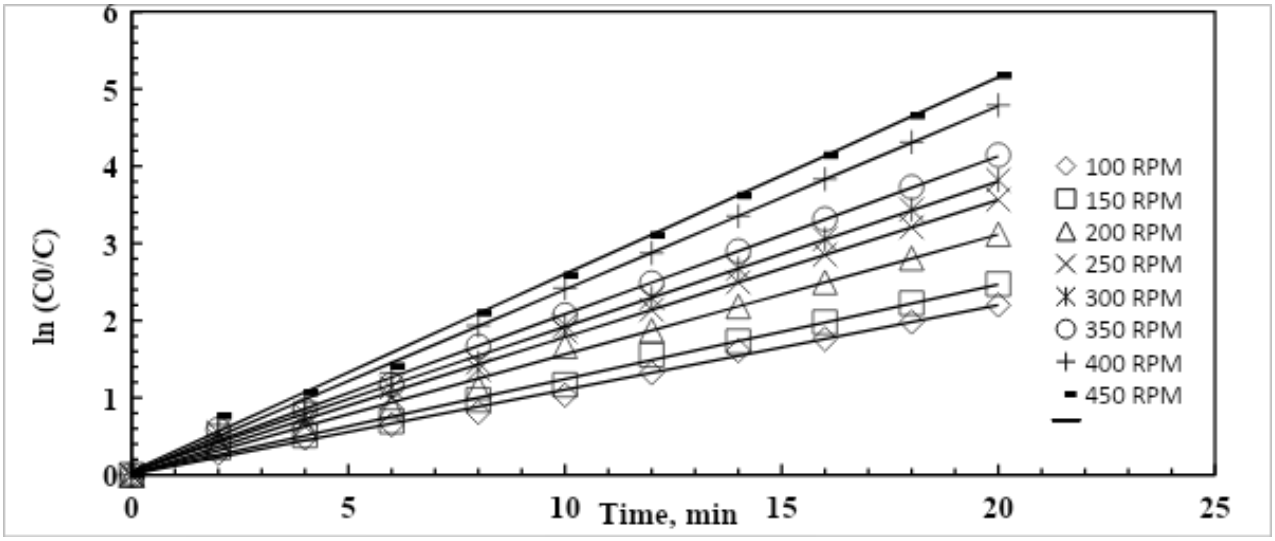

Figure 2. Typical plot of ln(C_0/C) versus t

Prior to discussing the results of the study, it is worth noting that despite using an unbaffled cylindrical agitated vessel, no vortex was observed on the solution surface within the range of conditions tested. It appears that the fixed-bed particles settled on the bottom of the tank acted as a horizontal baffle [27], which transformed the tangential component of the flow velocity into more favorable axial and radial components, respectively, for the pitched-blade and the flat-blade turbine. Kato et al. [27] proposed that a protruding surface located on the bottom of the tank functions as a baffle that converts rotational (swirl) flow into axial and radial flow.

Figure 3 depicts the impact of the dimensionless impeller rotation speed (Re) on the dimensionless mass transfer coefficient (Sh) for various bed heights. The data for the 90° flat-plate turbine (radial flow) were fitted to the following equation:

$$Sh = a\ Re^{0.99} \quad (4)$$

The data for the 45° pitched-blade turbine (axial flow) resulted in a comparable graph, which was fitted to the following equation:

$$Sh = a_1\ Re^{0.94} \quad (5)$$

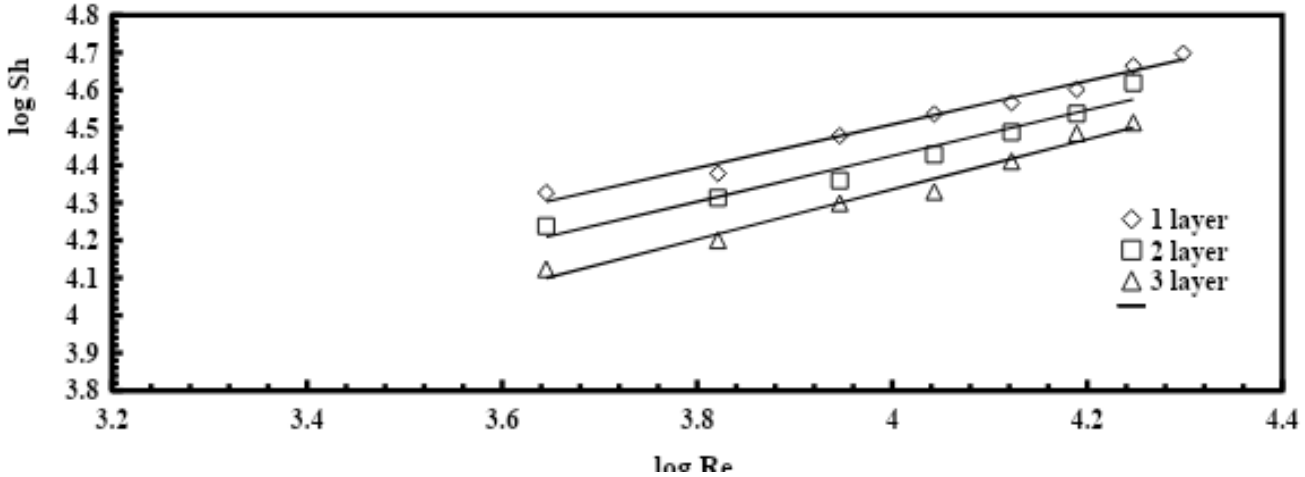

Figure 3. Effect of Re on Sh at different bed heights.

As in the case of ordinary fixed beds, the particle diameter d was used as a characteristic length in calculating Sh (Sh = kd/D); for agitated vessels, $Re = \rho Ndi2$, where di is the impeller diameter.

The obtained data reveals a decrease in the mass transfer coefficient for a given Reynolds number as the bed height increases. However, the increase in impeller speed results in an increase in the mass transfer coefficient due to the induced solution velocity that penetrates the bed, leading to a decrease in the thickness of both the hydrodynamic boundary layer and the underlying diffusion layer around each cylinder. This decrease ultimately translates to an increase in the rate of mass transfer. Furthermore, the possible formation of turbulent wakes behind horizontally oriented cylinders can lead to the separation of the hydrodynamic boundary layer, further enhancing mass transfer [28]. In multilayered beds, the successive buildup and destruction of the developing hydrodynamic boundary layer also contribute to enhancing the rate of mass transfer. The observed Re exponents of 0.78 and 0.81 are consistent with previous studies on turbulent-flow mass transfer in fixed beds [29-31]. However, the decrease in mass transfer coefficient with increasing bed height, as seen in Figure 3, can be attributed to reduced active area and solution momentum in contact zones between cylinders [32], as well as a decrease in reactant concentration as the solution progresses through the bed, leading to a subsequent decrease in the driving force for the reaction. Figure 4 expresses the effect of bed height on the dimensionless mass transfer coefficient (Sh) for the radial-flow turbine (90° flat-blade turbine) which can be expressed by the equation:

$$Sh=a2hd-0.29 \quad (6)$$

For the axial-flow turbine (45° pitched-blade turbine):

$$Sh=a3hd-0.32 \quad (7)$$

The reduction in the mass transfer coefficient observed with increasing cylinder diameter can be attributed to two factors: the increase in the average thickness of the developing hydrodynamic and diffusion layers along the vertical and around the horizontal cylinders, and the increase in bed porosity as the cylinder size increases. The latter factor leads to an increase in axial dispersion, which subsequently decreases the driving force for the reaction [32].

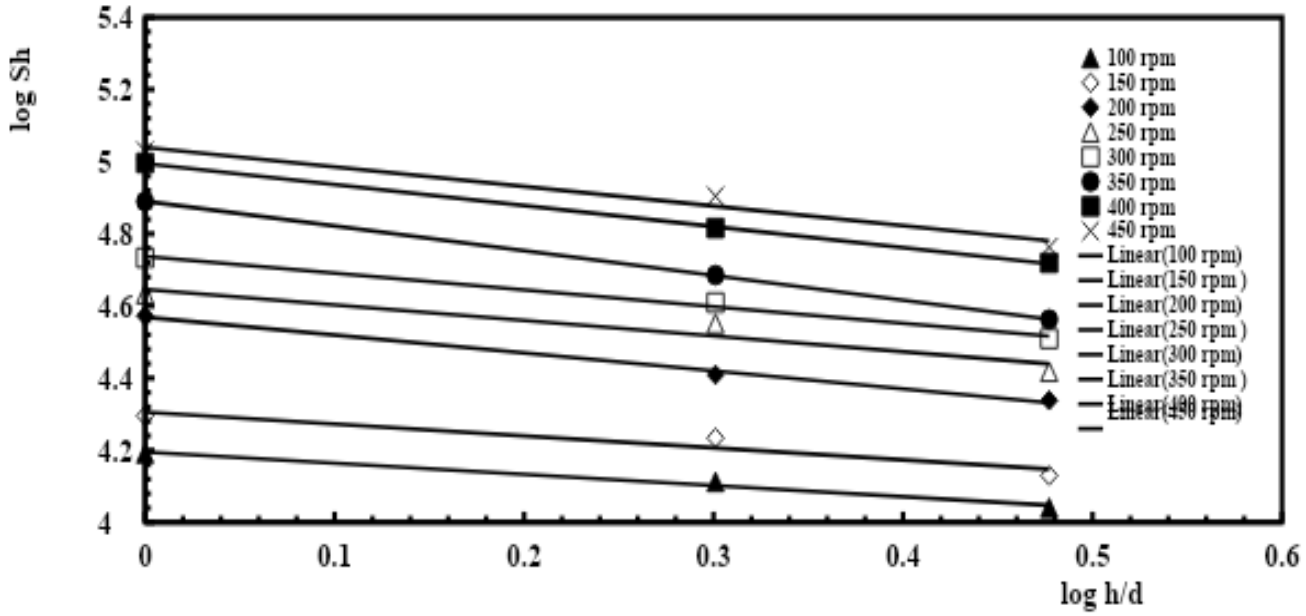

Figure 4. Effect of h/d on Sh.

A correlation for mass transfer was developed using dimensionless parameters including Sh, Sc, Re, and h/d. Figure 5 illustrates that the data from radial-flow turbines under specific conditions ($937 < Sc < 1217$, $3990 < Re < 19,880$, and $1 < h/d < 3$) conforms to the equation:

$$Sh=0.23\ Sc^{0.33}Re^{0.99}h d^{-0.29} \quad (8)$$

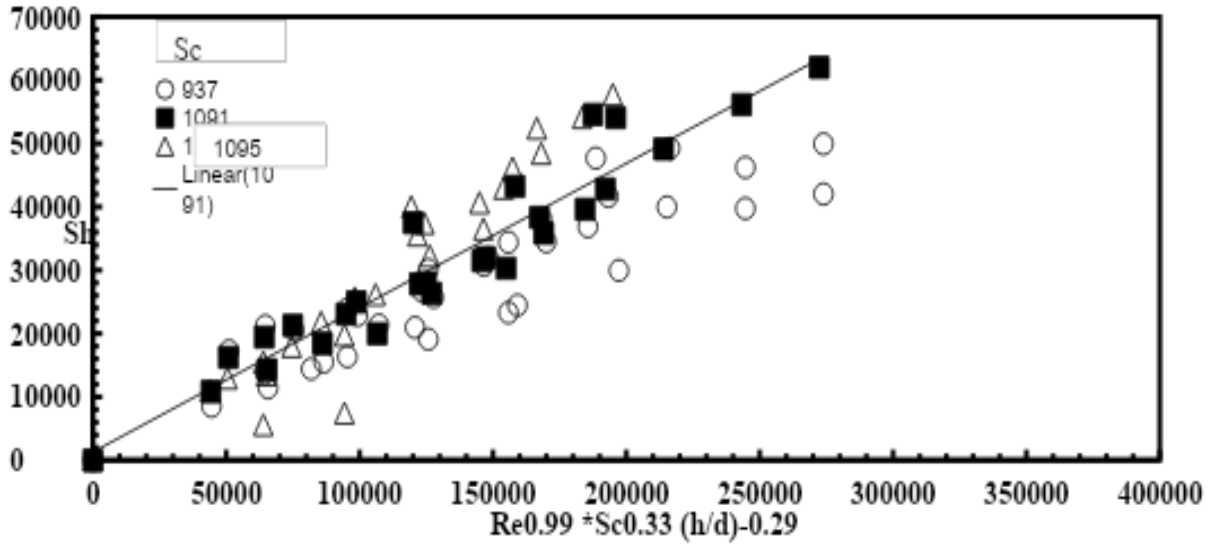

with an average deviation of ±16 %.

A correlation for mass transfer was developed using dimensionless parameters including Sh, Sc, Re, and h/d. Figure 6 illustrates that the data from axial-flow turbines under specific conditions (937 < Sc < 1217, 3990 < Re < 19,880, and 1 < h/d < 3) conforms to the equation:

$$Sh=0.29\ Sc^{0.33}Re^{0.94}h d^{-0.32} \quad (9)$$

with an average deviation of ±15 %.

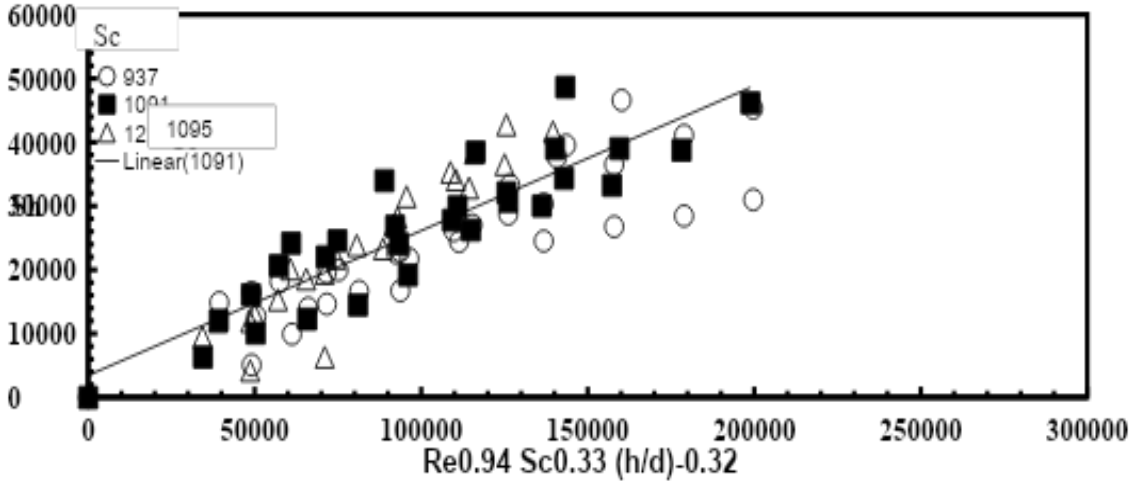

4. Conclusion.

The results of this study demonstrate a high rate of mass transfer in a stirred fixed bed, which supports the use of a fixed-bed reactor with a stirred tank as an effective means of conducting liquid-solid diffusion-controlled catalytic reactions. The dimensionless mass transfer equation derived from this work can aid in the design and scale-up of such reactors. This reactor design offers significant advantages, as it can disperse reactants that require prior dispersion, including gaseous reactants, sparingly soluble solid particles, and reactants dissolved in immiscible solvents. The multifunctional nature of the reactor can reduce the costs associated with processes that require prior reactant dispersion. Future studies should explore the effects of other phases, such as gas bubbles and immiscible solvents on mass transfer rates in the fixed bed. This reactor can operate in batch or

continuous mode at low feed rates to increase residence time, and the high mass transfer coefficient resulting from stirring and extended residence time can increase the degree of conversion [18].

Symbols Used.

A	[m2]	Area of iron cylinders
a, a1, a2, a3	[-]	Constants
C_0, C	[mol m-3]	Initial $K_2Cr_2O_7$ concentration., and concentration at any time.
D	[m2s-1]	Diffusivity.
d	[m]	Iron cylinders diameter
d_i	[m]	impeller diameter
h	[m]	Bed thickness.
k	[m s-1]	Mass transfer coefficient.
L	[m]	Bed Height
N	[rps]	Rotation Speed
T	[m]	Tank diameter
Re	[-]	Reynolds number
Sc	[-]	Schmidt Number
Sh	[-]	Sherwood Number
t	[s]	Time
V	[m s-1]	Superficial solution velocity in fixed bed
α, β	[-]	Constants
Ɛ	[N kg-1]	Specific power consumption
μ	[kg m-1 s-1]	Dynamic viscosity of solution
υ	[m2 s-1]	Kinematic solution viscosity

References

[1] P. Sharma, S. P. Singh, S. K. Parakh and Y. W. Tong: Bioengineered Vol. 13 (2022), p. 4923.
[2] A. Baral, R. Engelken, W. Stephens, J. Farris and R. Hannigan: Archives of Environmental Contamination and Toxicology Vol. 50 (2006), p. 496.
[3] B. Dhal, H. Thatoi, N. Das and B. Pandey: Journal of hazardous materials Vol. 250 (2013), p. 272.
[4] P. Chowdhary, R. N. Bharagava, S. Mishra and N. Khan: Environmental Concerns and Sustainable Development: Volume 1: Air, Water and Energy Resources Vol. (2020), p. 235.
[5] Modified biochar as a green adsorbent for removal of hexavalent chromium from various environmental matrices: Mechanisms, methods, and prospects
[6] W. Jin, H. Du, S. Zheng and Y. Zhang: Electrochimica Acta Vol. 191 (2016), p. 1044.
[7] A. Ghanem, T. Lemenand, D. Della Valle and H. Peerhossaini: Chemical engineering research and design Vol. 92 (2014), p. 205.
[8] W. S. Askew and R. B. Beckmann: Industrial & Engineering Chemistry Process Design and Development Vol. 4 (1965), p. 311.
[9] W. S. Askew and R. B. Beckmann: Industrial & Engineering Chemistry Process Design and Development Vol. 5 (1966), p. 268.
[10] M. Major-Godlewska and J. Karcz: Chemical Papers Vol. 65 (2011), p. 132.
[11] K. Suzukawa, S. Mochizuki and H. Osaka: Chemical engineering science Vol. 61 (2006), p. 2791.
[12] M. Major-Godlewska and J. Karcz: Chemical Papers Vol. 72 (2018), p. 1081.
[13] M. Abdel-Aziz: Chemical engineering research and design Vol. 91 (2013), p. 43.
[14] N. Amin, E.-S. El-Ashtouky and O. Abdelwahab: Environmental technology Vol. 35 (2014), p. 1208.
[15] M. Major-Godlewska and J. Karcz: Chemical Papers Vol. 72 (2018), p. 2933.
[16] A. S. Fathalla, N. K. Amin, E.-S. Z. El-Ashtoukhy and G. H. Sedahmed: Alexandria Engineering Journal Vol. 60 (2021), p. 4775.

[17] M. A. El-Naggar, M. H. Abdel-Aziz, A. A. Zatout and G. H. Sedahmed: Chemical Engineering & Technology Vol. 37 (2014), p. 1525.
[18] Y. Fouad, G. Malash, A. Zatout and G. Sedahmed: Chemical engineering research and design Vol. 91 (2013), p. 234.
[19] W. L. McCabe, J. C. Smith, P. Harriot, Unit Operation of Chemical Engineering, McGraw Hill, New York 1965.
[20] A. I. Vogel, A Textbook of Quantitative Inorganic Analysis, Longman, London 1961.
[21] A. Findlay, J. K. Ketchener, Practical Physical Chemistry, Longman, London 1965.
[22] D. P. Gregory, A. C. Riddiford, J. Electrochem. Soc. 1960, 107, 950.
[23] T. Z. Fahidy, Principles of Electrochemical Reactor Analysis, Elsevier, New York 1985.
[24] F. Walsh, A First Course in Electrochemical Engineering, The Electrochemical Consultancy, Hants 1993.
[25] J. Knop: Journal of the American Chemical Society Vol. 46 (1924), p. [263].
[26] Z. Lu, D. Huang and W. Yang: Corrosion science Vol. 47 (2005), p. 1471.
[27] Y. Kato, S. Hiraoka, Y. Tada, M. Ohnishi, T. Naganawa, R. Yamauchi and K. Shiobara: Journal of chemical engineering of Japan Vol. 35 (2002), p. 208.
[28] F. P. Incropera, D. P. Dewitt, Fundamentals of Heat and Mass Transfer, 3rd ed., John Wiley & Sons, New York 1990.
[29] P. N. Dwivedi, S. N. Upadhyay, Ind. Eng. Chem. Proc. Des. Dev. 1977, 16, 157.
[30] S. V. Potnis, T. G. Lenz, Ind. Eng. Chem. Res. 1996, 35, 4185.
[31] E. Ruckenstien, Adv. Chem. Eng. 1987, 13, 11.
[32] I. Colquhoun-Lee, J. Stepanek, Chem. Eng. 1974, 282, 108.

Algae-bacterial granular sludge for domestic wastewater treatment: A sustainable development approach

Hani Ezz[1,a], Mona G. Ibrahim[1,2,b], Mahmoud Nasr[1,3,c]
[1]Environmental Engineering Department, Egypt-Japan University of Sciences and Technology (E-JUST), New Borg Al Arab City, Alexandria 21934 Egypt
[2]Environmental Health Department, High Institute of Public Health, Alexandria University, Alexandria 21544, Egypt
[3]Sanitary Engineering Department, Faculty of Engineering, Alexandria University, 21544, Alexandria, Egypt
[a]hani.ezz@ejust.edu.eg, [b]mona.gamal@ejust.edu.eg, [d]mahmoud.nasr@ejust.edu.eg

Keywords: algae-bacterial granular sludge, bacterial granular sludge, domestic wastewater treatment, sustainable development goals

Abstract. The field of biological wastewater treatment has witnessed a remarkable surge of interest in utilizing algae-bacteria granular sludge (ABGS) technology. This study aims to comprehensively compare the performance of ABGS with bacteria granular sludge (BGS) in the treatment of synthetic domestic wastewater, with a specific focus on the removal of chemical oxygen demand (COD), ammoniacal nitrogen, and phosphate. The correlation between ABGS and sustainable development goals (SDGs) is also investigated. To evaluate these aspects, two lab-scale sequencing batch reactors were employed to treat the synthetic domestic wastewater. The results revealed that both ABGS and BGS exhibited highly efficient COD removal, with ABGS achieving a removal efficiency of 94.5% and BGS achieving 96.5%. ABGS achieved better NH_4^+-N (96.5%) and PO_4^{3-}-P (83.5%) removal rates compared to BGS (92.5% and 75.4%, respectively). ABGS aligns with SDGs 7, 9, and 12 by enabling biomass and bioenergy production. Furthermore, it contributes to the realization of SDGs 6 and 14 by significantly reducing water pollution and safeguarding aquatic ecosystems. This study demonstrates the exceptional potential of ABGS for domestic wastewater treatment, particularly in nutrient removal, where it surpasses the performance of BGS. Additionally, this approach contributes to multiple SDGs, emphasizing sustainable wastewater treatment practices.

Introduction

The relentless growth in human population and industrial activities has led to an alarming surge in wastewater production and greenhouse gas emissions [1]. These pressing environmental challenges pose significant threats to global sustainability in the modern era. Domestic wastewater is notorious for its high carbon, nitrogen, and phosphorus levels, which can cause detrimental consequences such as oxygen depletion, toxicity, and eutrophication in natural water bodies [2]. Despite the availability of numerous biological and physical/chemical technologies for carbon and nutrient removal in wastewater treatment plants (WWTPs), these approaches often come with substantial investment and operational costs. Moreover, they frequently fall short of facilitating cost-effective nutrient recovery, especially in the case of domestic and industrial wastewater [3]. As a result, there is an urgent need to explore innovative approaches that bridge the gap between wastewater treatment and the circular economy, ensuring sustainable resource management and economic viability.

The BGS wastewater treatment strategy emerges as an efficient and innovative solution. It employs self-immobilized cells bound together by an exo-polymeric matrix, forming compact granules. This approach surpasses traditional methods by significantly reducing settling time and eliminating the need for large tanks [1]. Notably, Sarma et al. [4] discovered that BGS plants occupy only one-fifth

of the space required by conventional systems while treating the same volume of wastewater. This remarkable space-saving attribute, coupled with its high efficacy in removing pollutants such as chemical oxygen demand (COD), nutrients, and toxic compounds from diverse wastewater, leads to a marked improvement in water quality [5].

On the other hand, ABGS presents a compelling and cost-effective solution that not only tackles wastewater treatment but also enhances nutrient recovery [1]. Leveraging the oxygen generated through microalgae photosynthesis, these processes facilitate the efficient oxidation of organic pollutants by aerobic heterotrophs and ammonium by nitrifiers [6]. As a result, the reliance on conventional mechanical aeration in wastewater treatment plants (WWTPs) is significantly reduced, leading to lowered operating costs and minimized environmental impacts [7]. The true power of this approach lies in the synergistic relationship between algal-bacterial consortia, which enables the utilization of both the organic carbon naturally present in wastewater and the inorganic carbon derived from the biological oxidation of organic carbon. This integrated approach optimizes the use of carbon sources, such as alkalinity in wastewater or external carbon dioxide (CO_2) supply, resulting in increased biomass productivity and fostering enhanced nutrient recovery. By harnessing the combined potential of algae and bacteria, this innovative strategy paves the way for a sustainable and efficient future in wastewater management [8].

Despite the considerable research on the ABGS for domestic wastewater treatment, there is still a lack of clarity regarding its alignment with the three pillars of sustainability. Therefore, the main objectives of this study are twofold. Firstly, to compare the performance of ABGS and BGS in reducing COD, NH_4-N, and PO_4^{3-}-P in domestic wastewater treatment. Secondly, to establish the connection between the ABGS and the three pillars of sustainability, thereby highlighting the holistic impact of ABGS in domestic wastewater treatment.

Materials and methods

Seed sludge. Both mature BGS and ABGS were cultivated in the laboratory, which has been stably operated for more than 90 days. The size of the seed ABGS and BGS mainly ranged between 1.0 and 5.0 mm. The initial biomass concentrations in the two reactors (R_B for control and R_{A-B} for testing) were around 4.50 ± 0.03 g/L of mixed liquor volatile suspended solids (MLVSS) with a sludge volume index (SVI_{30}) of 37.9 ± 0.3 ml/g.

Synthetic wastewater. Synthetic domestic wastewater with the following compositions was applied including chemical oxygen demand (COD, as NaAc) of about 400 mg/L, NH_4^+-N (as NH_4Cl) of about 50 mg/L, PO_4^{3-}-P (as KH_2PO_4) of about 10 mg/L, 52 mg/L MgSO4.7H2O, 25 mg/L $FeSO4.7H_2O$, 40 mg/L $CaCl_2$ and 1 mL/L trace element solution [9]. The pH values were adjusted to be 7.2 to 7.5.

Experimental set-up. The experiment involved the use of two identical column-photo sequencing batch reactors constructed from transparent acrylic plastic. These reactors had the same dimensions: an inner diameter of 84 mm, a height of 200 mm, and a working volume of 1 L. The first reactor, R_B, served as a control and was inoculated solely with BGS. In contrast, the second reactor, R_{A-B}, was inoculated with ABGS. During the operation, R_{A-B} was exposed to white LED tubes with an intensity of 4000 Lux, following a 12-hour light-dark cycle. On the other hand, R_B was covered with a light-blocking plastic bag. Aeration was accomplished by introducing air at a rate of 4.00 L/min through a porous diffuser positioned at the bottom of the reactors. The reactor's cycle lasted for 6 hours, including a feeding period of 2 minutes, non-aeration phase of 60 minutes, aeration period of 285 minutes, and settling phase of 10 minutes. Additionally, a discharge point was included at the midpoint of the reactor to facilitate a 50% exchange ratio, with a hydraulic retention time of 12 hours.

Analytical methods. Every three days, water samples were taken at the end of the operation cycle. The filtrates were used for analysis after filtration through a 0.22 m membrane. Wastewater samples were analyzed for COD, $NH_4^+ - N$, PO_4^{3-}-P according to the standard methods [10].

Results and discussion

COD Removal. Both reactors exhibited consistent and impressive results in effectively reducing COD, with maximum removal of 96.5% for R_B and 94.5% for R_{A-B} and no notable distinction ($p > 0.05$) (Fig. 1a). R_B displayed a slightly better capability for removing COD compared to R_{A-B}, implying that ABGS may require fewer organic carbon sources compared to conventional BGS. This discovery supports the assertion made by Zhao et al. [11], highlighting the substantial potential of algal-bacterial AGS for treating wastewater with limited carbon sources.

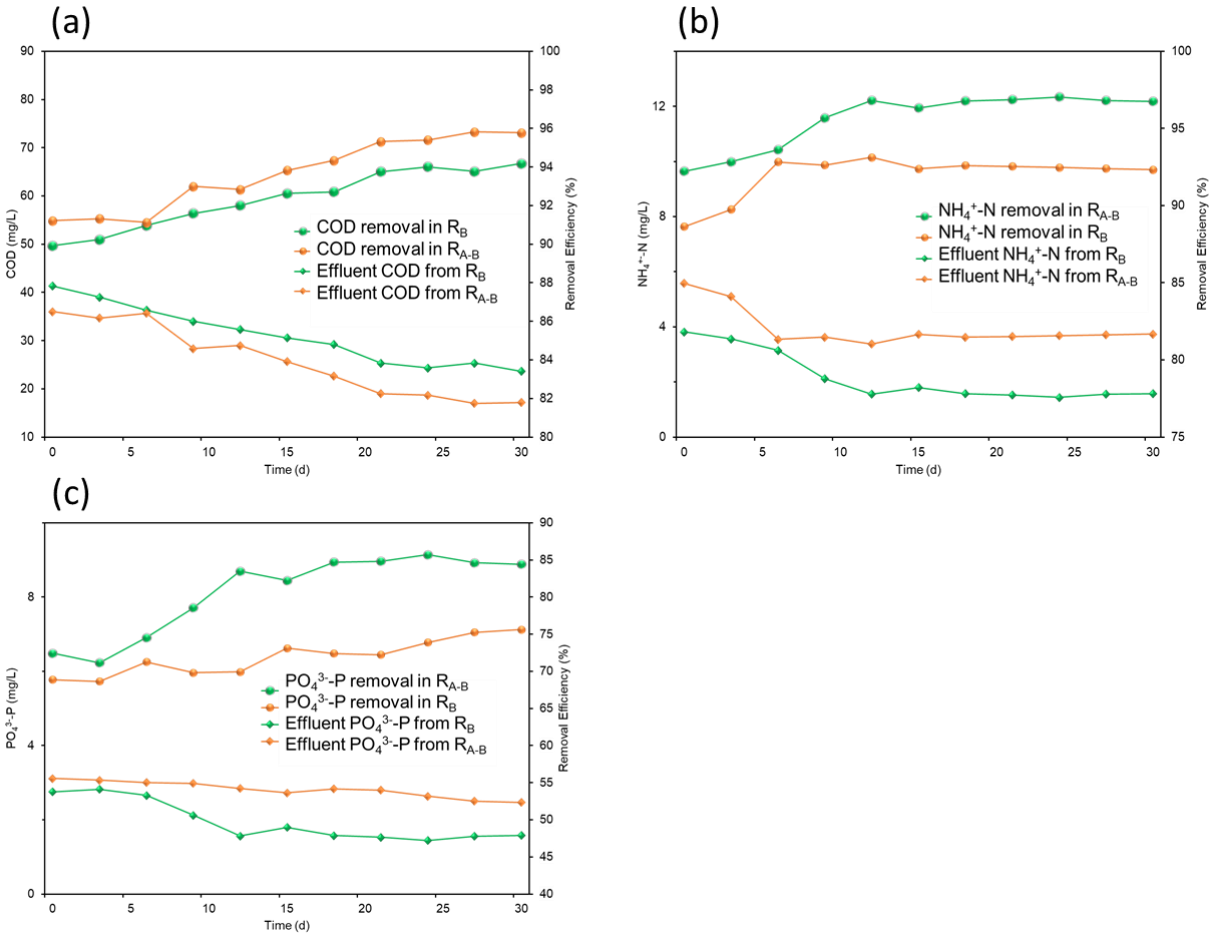

Sustainable Development Goals (SDGs) Linked to domestic Wastewater with ABGS.

Nitrogen and phosphorus removals

The maximum removal efficiency of removing NH_4-N was approximately 96.5% after a 30-day experimental period for reactor R_{A-B}, while reactor R_B achieved maximum removal of 92.5% (Fig. 1b). In both reactors, the concentration of ammoniacal nitrogen rapidly decreased within five days of the cultivation period and remained below 5 mg/L throughout the experiments. The higher removal observed in reactor R_{A-B} is attributed to the activity of ammonia-oxidizing bacteria (AOB) and the

direct assimilation of ammoniacal nitrogen by algae. During the process of ammonia oxidation, AOB converted ammoniacal nitrogen into nitrite (NO_2^-) and nitrate (NO_3^-), while algae directly assimilated ammoniacal nitrogen from the wastewater.

Examining the changes in effluent PO_4^{3-}-P concentration and PO_4^{3-}-P removal rate (Fig. 1c), it was evident that R_{A-B} consistently achieved significantly higher and more stable PO_4^{3-}-P removal (83.5%) compared to R_B (75.4%) ($p<0.05$). Initially, both reactors experienced a slight decrease in P removal, which could be attributed to the adaptation of granules to the new environment. However, they quickly recovered and resumed their efficient P removal. Notably, the presence of mature algal-bacterial AGS in R_{A-B} likely facilitated the recovery process and consistently
contributed to higher P removal capability compared to RB. This finding suggests that the co-existing algae in R_{A-B} significantly contribute to P removal from wastewater.

Environmental-related SDGs. The implementation of domestic wastewater treatment systems using ABGS aligns with several environmental-related SDGs and their associated targets. Firstly, SDG 6, Clean Water and Sanitation, is directly addressed by utilizing ABGS systems. These systems contribute to achieving Target 6.3, which aims to improve water quality by reducing pollution, eliminating dumping, and minimizing the release of pollutants in waterbodies. Additionally, Target 6.4 is supported through the implementation of these systems as they help increase water-use efficiency and ensure sustainable withdrawals and supply of freshwater, thus addressing water scarcity. Moreover, domestic wastewater treatment with ABGS systems contributes to SDG 13, Climate Action. The algae Play a crucial rule in capturing and stabilizing CO_2, assisting in the reduction of greenhouse gases (Target 13.2 Climate change policy) [12]. Furthermore, Target 13.3 is addressed as the implementation of sustainable wastewater treatment practices enhances education, awareness, and capacity building on climate change mitigation and adaptation. SDG 14, Life Below Water, is promoted through the application of algae-bacteria granular sludge systems for domestic wastewater treatment. These systems assist in achieving Target 14.1 by preventing and significantly reducing marine pollution of all kinds. Additionally, Target 14.2 is supported as the proper treatment of wastewater helps sustainably manage and protect marine and coastal ecosystems, avoiding significant adverse impacts. In line with SDG 15, Life on Land, the use of ABGS systems helps in achieving Target 15.3, which aims to combat desertification, restore degraded land, and soil affected by desertification, drought, and floods. Furthermore, Target 15.5 is addressed by the systems' contribution to the reduction of degradation of natural habitats and the preservation of biodiversity. Lastly, SDG 12, Responsible Consumption and Production, is advanced through the utilization of ABGS systems for domestic wastewater treatment. Target 12.2 is supported as these systems promote sustainable management and efficient use of natural resources. Additionally, Target 12.4 is addressed by achieving the environmentally sound management of chemicals and waste throughout their life cycle.

Economic-related SDGs. SDG 8, Decent Work and Economic Growth, is avancier through the creation of employment opportunities in the design, construction, operation, and maintenance of these ABGS technology, as outlined in Target 8.3. Additionally, the adoption of ABGS technology contributes to Target 8.4 by improving resource efficiency in consumption and production, thus promoting sustainable economic growth. SDG 9, Industry, Innovation, and Infrastructure, is supported by the use of ABGS systems. These systems foster innovation in the wastewater treatment sector, aligning with Target 9.2, and contribute to sustainable industrialization by upgrading infrastructure and retrofitting wastewater treatment facilities for increased resource-use efficiency and the adoption of clean technologies, as highlighted in Target 9.4. Furthermore, the application of ABGS in domestic wastewater treatment promotes Target 12.2 of SDG 12, Responsible Consumption and Production. By achieving sustainable management and efficient use of natural resources, these systems contribute to reduced resource consumption and waste generation, leading to cost savings

and improved economic efficiency. Additionally, Target 12.5 is advanced by substantially reducing waste through prevention, reduction, recycling, and reuse in the wastewater treatment process. Collaboration and partnerships among various stakeholders, including public, private, and civil society organizations, are essential for the successful implementation and scaling up of ABGS systems. This aligns with Target 17.17 of SDG 17, Partnerships for the Goals, as effective partnerships are encouraged to leverage resources, expertise, and knowledge for sustainable economic development.

Social-related SDGs. SDG 3, Good Health and Well-being, is advanced as these systems effectively treat wastewater, reducing hazardous chemicals and pollution, thereby contributing to the reduction of illnesses and deaths related to contaminated water and soil (Target 3.9). Additionally, SDG 6, Clean Water and Sanitation, is supported as ABGS systems help achieve universal access to safe drinking water (Target 6.1) and adequate sanitation and hygiene facilities (Target 6.2), ensuring improved health and well-being for all. By addressing the needs of vulnerable populations and promoting inclusive access to sanitation and water services, these systems also contribute to SDG 10, Reduced Inequalities (Target 10.2). Furthermore, the adoption of algae-bacteria granular sludge systems aids in creating sustainable cities and communities (SDG 11) by reducing the environmental impact of wastewater management, including waste generation (Target 11.6). Overall, these systems promote social well-being, improve public health, enhance access to clean water and sanitation, reduce inequalities, and foster sustainable communities, aligning with various social-related SDGs and their targets.

Conclusions

In conclusion, the results of this study highlight the effectiveness of ABGS systems for domestic wastewater treatment. Both ABGS and BGS demonstrated impressive performance in reducing COD, with a maximum removal of 95.4% for ABGS and 96.5% for BGS. While ABGS exhibited a higher removal efficiency in NH_4^+-N (96.5%) compared to BGS (92.5%). Additionally, ABGS consistently outperformed BGS in PO_4^{3-}-P removal, with significantly higher and more stable removal rates. Furthermore, the implementation of ABGS systems aligns with several Sustainable Development Goals (SDGs) related to the environment, economy, and society. These systems contribute to SDG 6 (Clean Water and Sanitation) by improving water quality and addressing water scarcity. They also support SDG 13 (Climate Action) through CO_2 capture and reduction of greenhouse gases. Additionally, ABGS systems promote SDG 14 (Life Below Water) by reducing marine pollution and SDG 15 (Life on Land) by combating desertification and preserving biodiversity. In terms of economic-related SDGs, ABGS systems create employment opportunities (SDG 8) and foster innovation in wastewater treatment (SDG 9). They also contribute to responsible consumption and production (SDG 12) by reducing resource consumption and waste generation. Finally, ABGS systems advance social-related SDGs, including SDG 3 (Good Health and Well-being), SDG 10 (Reduced Inequalities), and SDG 11 (Sustainable Cities and Communities), by improving public health, reducing inequalities, and promoting sustainable communities. Overall, the study highlights the potential of ABGS systems as an innovative and sustainable solution for domestic wastewater treatment, addressing environmental challenges and aligning with key sustainability goals. Further research and implementation of ABGS systems are necessary to fully leverage their benefits and achieve a sustainable future in wastewater management.

References

[1] M. Zhang, B. Ji, and Y. Liu: *Sci. Total Environ.*, vol. 752 (2021), p. 141957.
[2] L. Dina *et al.*: *J. Environ. Manage.*, vol. 333 (2023), no. February, p. 117374.
[3] B. Ji, M. Zhang, J. Gu, Y. Ma, and Y. Liu: *Water Res.*, vol. 179 (2020), p. 115884.
[4] S. J. Sarma, J. H. Tay, and A. Chu: *Trends Biotechnol.*, vol. 35 (2017), no. 1, pp. 66–78.
[5] Y. Li, J. Zou, L. Zhang, and J. Sun: *Bioresour. Technol.*, vol. 154 (2014), pp. 178–184.
[6] Z. Liu *et al.*: *SSRN Electron. J.*, vol. 410 (2022), no. 13, p. 137327.
[7] Z. Liu *et al.*: *Bioresour. Technol.*, vol. 376 (2023), no. 13, p. 128851.
[8] Q. He *et al.*: *J. Hazard. Mater.*, vol. 359 (2018), no. June, pp. 222–230.
[9] Y. Zhang *et al.*: *J. Water Process Eng.*, vol. 34 (2019), no. August 2019, p. 101073.
[10] USEPA, "Standard Methods for the Examination of Water and Wastewater 22th Edition," *Am. Public Heal. Assoc. Am. Water Work. Assoc. Water Environ. Fed.*, 2012, [Online].
[11] L. Sun, S. Wan, and W. Luo,: *Bioresour. Technol.*, vol. 140 (2013), pp. 406–413.
[12] F. A. Ansari, M. Nasr, I. Rawat, and F. Bux,: *J. Water Process Eng.*, vol. 40 (2021), no. July 2020, p. 101761.

Advanced Nanotechnology-based Techniques for LIB Performance Improvement

A. El-Tayeb[*,1], Asmaa A. Mohamed[1,*], Esam H. Abdelhameed[1], Adel Z. El-Dein[1,2], Ibrahim Moukhtar[1]

[1]*Electric Engineering Department, Faculty of Energy Engineering, Aswan University, Aswan, Egypt.*

[2]*Faculty of Technological Industry and Energy, Thebes Technological University, Thebes, 85863, Luxor, Egypt.*

[*]E-mail: *Ahmed_al_tayeb@aswu.edu.eg; Abdelhamidasmaa3@gmail.com*

Keywords: LIBs, Nanotechnology, anode, silicon, low cost.

Abstract. Rechargeable lithium-ion batteries are the most prominent candidate for the power supply for a wide range of modern commercial portable electronic devices and electric vehicles. Accordingly, lithium-ion batteries have attracted more attention from researchers around the world. Therefore, the researchers have focused on anode materials and nanotechnology techniques to increase the energy density of lithium-ion batteries and improve their performance. Silicon as an anode material has great promise to realize high energy density for lithium-ion batteries since it has an exceptional theoretical charge capacity, high stability, abundant availability, and is environmentally friendly. However, silicon anode materials face some challenges, such as low electrical conductivity, large volume expansions, and unstable solid electrolyte interphases, which result in poor cycling performance. Nanostructured silicon and silicon composites, as well as novel coating strategies, exhibit effective methods to enhance the electrochemical and physical properties of anode materials. This paper presents a brief overview of high-performance nanostructured silicon-based anodes with low-cost facile synthesis processes as well as their coating structures.

1. Introduction

Batteries are electrochemical devices which store electrical energy in the form of chemical energy and can later convert it into electricity during both the charging and discharging processes. Over the past decade, there has been significant interest in lithium-ion batteries (LIBs) due to their potential to serve as power sources, potentially driving the electric vehicle (EV) revolution within the next five years [1]. LIBs have become a popular energy storage technology due to their remarkable properties, which include relatively high gravimetric and volumetric energy densities, high power densities, long cycle life, lightweight nature, good rate capabilities, and low self-discharge rates. The battery cell, which represents the smallest unit within a battery pack or acts as a standalone unit, plays a crucial role. In electric vehicles (EVs), three types of battery cells are commonly employed: cylindrical cells, pouch cells, and prismatic cells. Notably, cylindrical cells find extensive use in various models of Tesla cars[2, 3]. LIBs consist of an anode, cathode, electrolyte, separator, and current collectors [4, 5]. Fig. 1 illustrates the working mechanism of LIBs cell. Initially, the lithium (Li) cations are

assembled in the cathode. Under the external voltage, Li cations will be extracted from the cathode to the electrolyte and then intercalate into the anode. At the same time, equivalent electrons move from the cathode to the anode through the outside circuit. Afterward, the chemical potential of the anode will be much higher than that of the cathode, which means the electric energy is stored. While reversing the above process, the discharging of the cell will release the electric energy to electrical appliances. It is noted that there has a separator between the cathode and anode region, which is a micro-porous membrane enabling the Li+ to pass and preventing the short circuit between the electrodes [6].

Anodes, which serve as negative electrodes, play a crucial role in enhancing the energy density of LIBs. Various materials, including carbon, alloy, transition metal, and silicon (Si), are utilized as anodes, each with its own advantages and disadvantages. Among these materials, Si-based nanomaterials have gained popularity among researchers aiming to meet the increasing energy demands of the market [8]. This is primarily due to Si has desirable properties, such as its high theoretical storage-specific capacity, abundance in nature, low cost, environmental friendliness, and low working potential, making it an attractive choice for energy storage applications. However, successful applications of Si-based anodes in LIBs are hindered by some critical challenges. As presented in Fig. 2, one of the biggest Si issues is the severe volume change (~400%) that occurs upon cycling, which can induce cracking and pulverization of the Si anode [9]. This can lead to a significant reduction in battery performance and lifespan. Another issue is the continuous growth of unstable solid electrolyte interphase (SEI) films on the surface of Si. This phenomenon occurs due to the anode's reaction with the electrolyte, leading to the formation of a passivating layer that prevents Li ions diffusion.

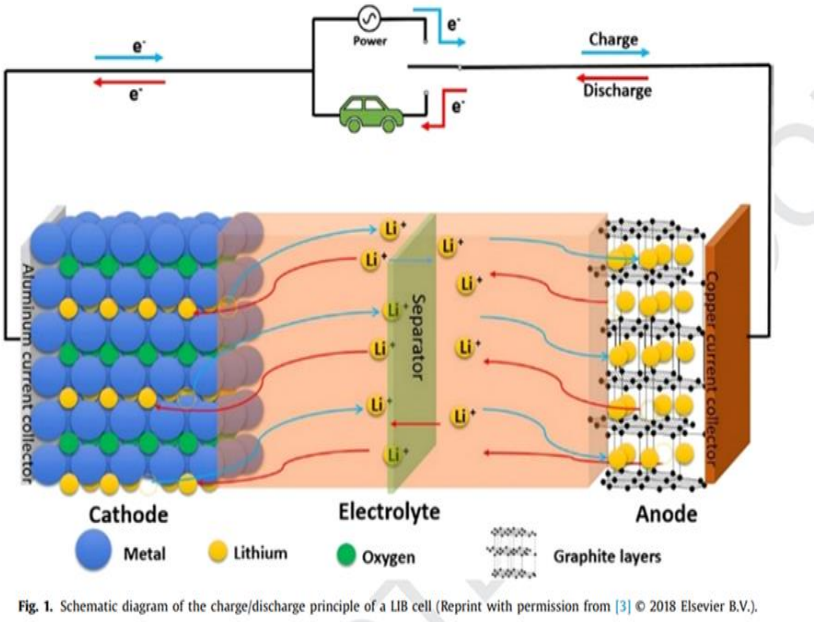

Fig. 1. Schematic diagram of the charge/discharge principle of a LIB cell (Reprint with permission from [3] © 2018 Elsevier B.V.).

Fig. 1 Schematic diagram of the Li cell's charge/discharge process [7].

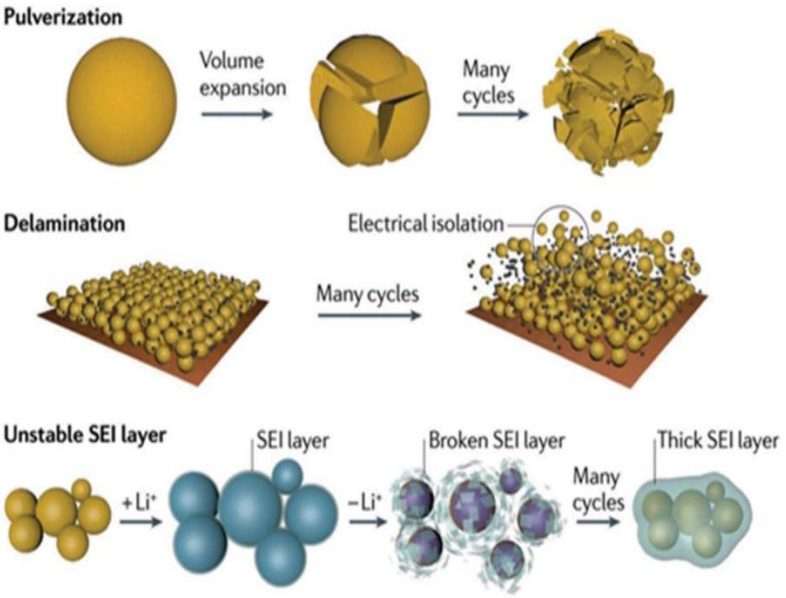

Fig. 1 Cell failure mechanisms of silicon.[25]

Fig. 2 Cell failure mechanisms of silicon [10]

Extensive efforts have been devoted to significantly enhance the performance of Si anodes [11]. Nanotechnology, which focuses on manipulating matter at the nanoscale level, has been utilized by researchers[12]. Nanomaterials possess exceptional properties that find wide applications in various research and industrial domains [13]. In batteries, nanomaterials offer a larger electrode or electrolyte contact area, resulting in heightened charge/discharge rates and shorter paths for electronic and Li-ion transportation. These characteristics enable the introduction of new active reactions, reduction of specific surface current rate, improvement in stability, and enhancement of specific capacity [14]. To overcome the limitations of Si, nanomaterials and composite materials containing conductive additives like carbon are employed [15]. The reduced particle size helps mitigate damage and minimize diffusion path length, while carbon serves as a buffer to eliminate volume changes and maintain stable contact between particles [16]. Currently, nanocoatings are divided into three types: amorphous carbon, metal and metal oxide, and polymer [17]. This paper discusses some techniques to accommodate the volume variation of Si during cycling and enhance LIBs performance. In addition, it presents a low-cost facile synthesis process scalable and provides a promising alternative way to large-scale production of inexpensive high-performance Si-based materials for next-generation LIBs.

0. Nano-structured silicon and silicon-based composites

Various effective approaches have been developed to address the challenges associated with Si-based anodes for high-energy-density LIBs. One such approach involves utilizing well-designed Si nanostructures, including 0D Si nanoparticles, 1D-like nanowires, hollow nanospheres, yolk shells, and nanotubes. 2D like a thin film, nanosheets, silicene, and 3D porous structures [18, 19]. The 3D porous structure of the Si-based materials provides a large surface area for Li-ion insertion and extraction, which enhances the overall electrochemical performance of the material. This structure also facilitates the efficient transport of Li ions, enabling faster charging and discharging of the battery. Furthermore, 3D porous Si-based materials have been found to be highly stable and can withstand repeated cycling without any significant degradation in their electrochemical performance. This is due to their ability to accommodate the volume expansion and contraction that occurs during cycling, which is a major challenge faced by conventional Si-based anode materials. In conclusion, 3D porous Si-based materials are a promising approach to improving the electrochemical

performance of Si-based anode materials. For the Si-based composites, Si/C composites in which Si particles are distributed in a conductive carbon matrix. Si/C composites with yolk–shell structures have also been proposed as alternative candidates that can maintain both high cycling performance. Also, Si@void@C nanocomposites offer sufficient space for accommodating the volume expansion of Si, and the porosity of the carbon shell enabled fast transport of Li + between the electrolyte [19, 20]. Carbon nanotubes, and carbon nanofibers have attracted a great deal of attention due to their unique properties and applications in the field of nanotechnology and are also alternative materials that can be composited with Si to improve the electrochemical performance of electrodes for LIBs [21, 22]. Si/metal composites are metallic materials with features including good malleability, high electronic conductivity, and high mechanical strength. For Si/metal composites, the SiNPs are dispersed in the metal matrix or coated with the metal particles to improve the electrochemical properties of Si anodes. Si/transition metal oxide composites with Si are also found to be potential candidates to improve the electrochemical performance of anode materials in LIBs. Si/metal oxide composites usually exhibit a core–shell structure with a similar working mechanism to Si/C core–shell composites. Fig. 3 illustrates different representative strategies to solve the major issues of Si-based anodes. All these various strategies to overcome the challenges of Si-based anodes for LIBs that shortened Li-ions and electron diffusion pathways, fast diffusion rates and electron transfer, large surface areas, high rate performance, long charge/discharge cycle life, accommodate volume changes during Li insertion/extraction.

0. Silicon coating strategies

The surface coating prevents direct contact between Si and the electrolyte, enhancing Si electrochemical performance. To ensure benign electrochemical stability, the coating layer may be tough or flexible to buffer the stress, thereby providing fast transport channels for Li-ion/electrolyte. Nanocoatings are divided into three types: amorphous carbon, metal, metal oxide, and polymer. surface coating methods (high-energy ball milling, hydrothermal or solvothermal, CVD, electrospinning, sol-gel, spray drying. the Si/C composites can be divided into 0D (monodisperse nanoparticles), 1D (nanofibers and nanotubes), 2D (graphene sheet) and 3D (graphene shell and porous structure). By coating the Si structures with these carbon-based materials, the carbon can be derived by carbonization of various sources such as polydopamine, pyridine, sucrose, toluene, pitch, and glucose. Si/metallic or nonmetallic composites are metals, metal compounds, metal silicides, metal sulfides, Si oxides, and natural metal oxides as surface coatings. To buffer the volume expansion of Si during cycling, the coating can be tough or flexible they can better withstand the volume variation that occurs during cycling, can improve the conductivity of Si, prevent the contact of Si with electrolytes, and reduce the agglomeration of Si particles. But carbon materials, metals, and metal oxides have significant disadvantages, such as the "dead weight" of the binding and conducting phases. which reduces the theoretical specific capacitance of the electrode by up to 50 %. Many research approaches have recently been directed toward conducting polymers. For example, polypyrrole, polyacrylic acid, and poly have been used as coatings for electrode materials due to their excellent chemical stability, and high structural stability, excellent electrical that can improve the conductivity and stress buffer properties of Si anodes due to their outstanding properties, including tunable electrical properties, optical and high mechanical properties, easy synthesis, and effortless fabrication and high environmental stability over conventional inorganic materials [3, 9, 11, 23].

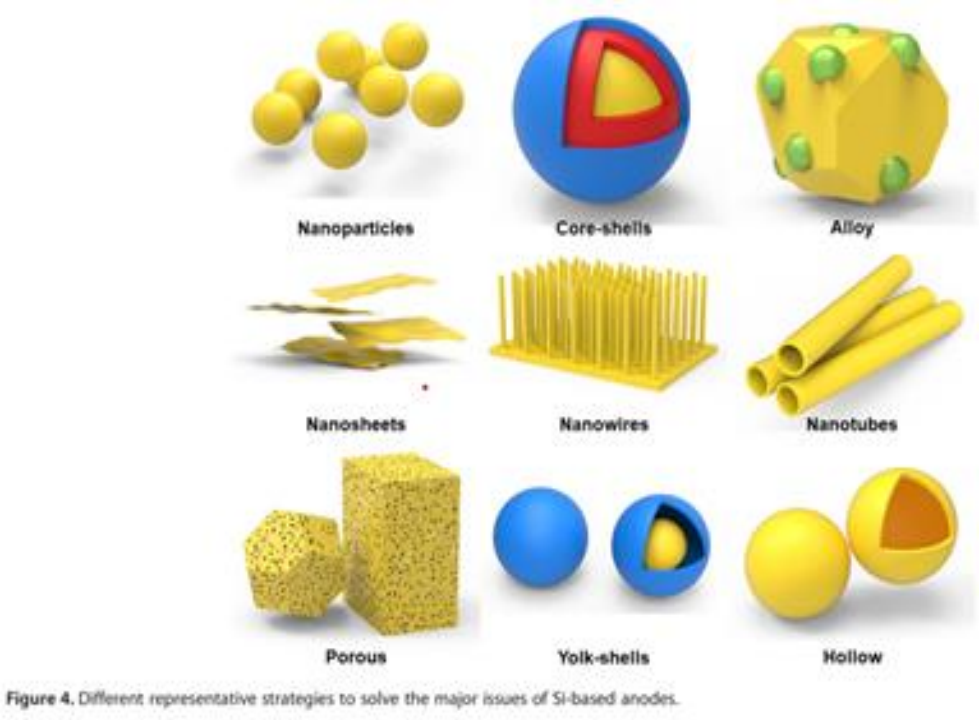

Figure 4. Different representative strategies to solve the major issues of Si-based anodes.

Fig. 3 Different techniques to overcome the challenges of Si-based anodes [3].

0. Silicon preparation

Controllable synthesis of 3D porous Si/SiO_2/C composites as anode for high-performance LIBs. to get nanosized Si fully embedded in mesoporous carbon layers successfully prepared from commercially available, low-cost, microsized Si as starting materials via a simple and low-cost High energy mechanical milling technique. Preparation of SiO_2 from biosources like rice husks or wheat hay as presented in Fig. 5. SiO_2 which has a higher theoretical capacity than commercial carbon, lower cost, and easier synthesis process. Despite this, SiO_2 has disadvantages that limit its widespread use as an anode material for LIBs due to low electrical conductivity and short cycling life associated with volume changes during charge and discharge processes. We will propose an inexpensive and simple method for obtaining amorphous SiO_2 particles in a carbon shell to solve these shortcomings. SiO_2 was synthesized from biological waste material [24, 25]. The process steps of Si/ SiO_2/c preparation are as follows: The amounts of glucose and melamine are dissolved in distilled water under constant stirring to form a uniformly dispersed solution. Si/SiO_2 amounts are added into the solution under vigorously stirred for 30 min to form a homogeneous precursor solution and then quickly transferred to a polytetrafluoroethylene (PTFE) container. After that, the container is sealed and maintained at 160 ◦C for 16 h. When the autoclave cooled to room temperature, the black precursor is obtained by filtering and drying at 60 ◦C for 12 h. The black precursor is successively named P1. Subsequently, the precursor is mixed with magnesium powder. Then the mixed powder is placed in a vacuum tube furnace, and an Ar atmosphere is maintained. Keep the heating rate at 5 ◦C min− 1 and heat at 650 ◦C for 2 h. After cooling down to room temperature, the obtained powders are immersed in HCl for 6 h to eliminate MgO and excessive Mg. Subsequently filtered, washed with deionized water, and then dried under vacuum at 60 ◦C for 12 h. With the mass of Si/SiO_2/c nanospheres increasing, the products are successively named S1.

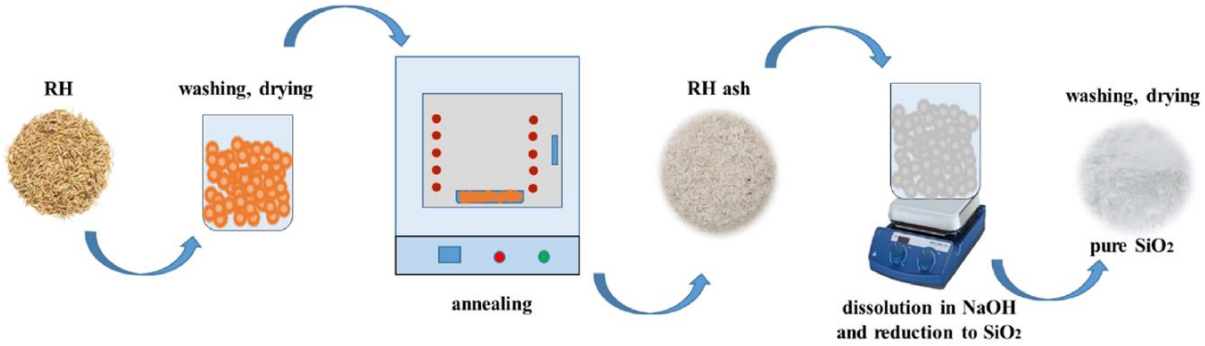

Fig(5) The scheme of the process for obtaining SiO_2 [24]

0. Conclusion

Silicon is used as an anode material to achieve high energy density for LIBs. This paper presents anode materials, nanotechnology, and coating techniques that can increase energy density and improve the performance of LIBs. Additionally, it discusses Si challenges such as large volume expansions and their solution. 3D porous honeycomb $Si/SiO_2/C$ can accommodate the volume change of si anodes and can shorten the electron and Li diffusion pathways, enable fast relaxation of mechanical stress, and are favorable for a long-cycle lifetime of Si electrodes. Si with Nanostructured and Si composites, as well as novel coating strategies, offer effective procedures for enhancing the physical/electrochemical properties of anode materials. The low-cost preparation is a simple and effective method. The process does not require expensive or hazardous reagents or specialized equipment. Hence, it is extremely appealing for large-scale manufacturing and industrial application. As well, this simple synthesis method may provide a pathway for SiO_2-based anodes in the commercialization of LIBs for the next generation.

0. Acknowledgment

The authors appreciatively recognize the Egyptian Science and Technology Development Fund (STDF) for subsidizing this work among the STDF project with ID no. 43247.

0. References

[1] Y. Abu-Lebdeh and I. Davidson, *Nanotechnology for lithium-ion batteries*. Springer Science & Business Media, 2012.

[2] A. J. A. c. s. Manthiram, "An outlook on lithium ion battery technology," vol. 3, no. 10, pp. 1063-1069, 2017.

[3] J. Nzabahimana, Z. Liu, S. Guo, L. Wang, and X. J. C. Hu, "Top-down synthesis of silicon/carbon composite anode materials for lithium-ion batteries: mechanical milling and etching," vol. 13, no. 8, pp. 1923-1946, 2020.

[4] T. J. P. o. t. I. Horiba, "Lithium-ion battery systems," vol. 102, no. 6, pp. 939-950, 2014.

[5] P. N. Halimah, S. Rahardian, and B. A. J. I. J. o. S. T. T. Budiman, "Battery cells for electric vehicles," vol. 2, no. 2, pp. 54-57, 2019.

[6] P. Guan *et al.*, "Recent progress of surface coating on cathode materials for high-performance lithium-ion batteries," vol. 43, pp. 220-235, 2020.

[7] G. Zubi, R. Dufo-López, M. Carvalho, G. J. R. Pasaoglu, and S. E. Reviews, "The lithium-ion battery: State of the art and future perspectives," vol. 89, pp. 292-308, 2018.

[8] W. Qi, J. G. Shapter, Q. Wu, T. Yin, G. Gao, and D. J. J. o. M. C. A. Cui, "Nanostructured anode materials for lithium-ion batteries: principle, recent progress and future perspectives," vol. 5, no. 37, pp. 19521-19540, 2017.

[9] Z. Bitew, M. Tesemma, Y. Beyene, M. J. S. E. Amare, and Fuels, "Nano-structured silicon and silicon based composites as anode materials for lithium ion batteries: recent progress and perspectives," vol. 6, no. 4, pp. 1014-1050, 2022.

[10] J.-Y. Li, Q. Xu, G. Li, Y.-X. Yin, L.-J. Wan, and Y.-G. J. M. C. F. Guo, "Research progress regarding Si-based anode materials towards practical application in high energy density Li-ion batteries," vol. 1, no. 9, pp. 1691-1708, 2017.
[11] K. Xu *et al.*, "Research Progress on Coating Structure of Silicon Anode Materials for Lithium-Ion Batteries," vol. 14, no. 23, pp. 5135-5160, 2021.
[12] N. Patil, R. Bhaskar, V. Vyavhare, R. Dhadge, V. Khaire, and Y. J. I. J. o. C. P. R. Patil, "Over View on Methods of Synthesis of Nanoparticles," vol. 13, no. 2, pp. 11-16, 2021.
[13] N. Baig, I. Kammakakam, and W. J. M. A. Falath, "Nanomaterials: A review of synthesis methods, properties, recent progress, and challenges," vol. 2, no. 6, pp. 1821-1871, 2021.
[14] E. Kianfar, A. Hassanijoshaghani, and S. A. Razavikia, "Introducing the Application of Nanotechnology in Lithium-Ion Battery," 2020.
[15] C. Jiang, E. Hosono, and H. J. N. t. Zhou, "Nanomaterials for lithium ion batteries," vol. 1, no. 4, pp. 28-33, 2006.
[16] A. B. Yaroslavtsev and I. A. J. S. I. Stenina, "Carbon coating of electrode materials for lithium-ion batteries," vol. 9, no. 2–3, pp. 92-110, 2020.
[17] J. Lu, Z. Chen, Z. Ma, F. Pan, L. A. Curtiss, and K. J. N. n. Amine, "The role of nanotechnology in the development of battery materials for electric vehicles," vol. 11, no. 12, pp. 1031-1038, 2016.
[18] F. Wang *et al.*, "Construction of structure-tunable Si@ void@ C anode materials for LIBthrough controlling the growth kinetics of resin," vol. 13, no. 10, pp. 12219-12229, 2019.
[19] J. Nzabahimana, S. Guo, and X. J. A. S. S. Hu, "Facile synthesis of Si@ void@ C nanocomposites from low-cost microsized Si as anode materials for lithium-ion batteries," vol. 479, pp. 287-295, 2019.
[20] S. Guo, X. Hu, Y. Hou, Z. J. A. a. m. Wen, and interfaces, "Tunable synthesis of yolk–shell porous silicon@ carbon for optimizing Si/C-based anode of lithium-ion batteries," vol. 9, no. 48, pp. 42084-42092, 2017.
[21] A.-H. Liang, T.-H. Xu, S. Liou, Y.-Y. J. E. Li, and Fuels, "Silicon single walled carbon nanotube-embedded pitch-based carbon spheres prepared by a spray process with modified antisolvent precipitation for lithium ion batteries," vol. 35, no. 11, pp. 9705-9713, 2021.
[22] Y. Zhao *et al.*, "Facile synthesis of SiO 2@ C nanoparticles anchored on MWNT as high-performance anode materials for Li-ion batteries," vol. 12, pp. 1-7, 2017.
[23] K. Namsheer and C. S. J. R. a. Rout, "Conducting polymers: A comprehensive review on recent advances in synthesis, properties and applications," vol. 11, no. 10, pp. 5659-5697, 2021.
[24] K. Askaruly *et al.*, "A facile synthesis of graphite-coated amorphous SiO2 from biosources as anode material for libs," vol. 34, p. 105136, 2023.
[25] A. Jumari *et al.*, "SiO2/C composite as a high capacity anode material of LiNi0. 8Co0. 15Al0. 05O2 battery derived from coal combustion fly ash," vol. 10, no. 23, p. 8428, 2020.

A Life Cycle Assessment for Environmental Evaluation of Concrete Mixes with Water Treatment Sludge

Khadiga M. Mekky[1], Mahmoud Nasr[1,2], Kamal Sharobim[3], Manabu Fujii[4], and Mona G. Ibrahim[1,5]

[1] *Environmental Engineering Department, Egypt-Japan University of Science and Technology (E-JUST), Alexandria, Egypt*

[2] *Sanitary Engineering Department, Faculty of Engineering, Alexandria University, Alexandria 21544, Egypt*
[3]*Tokyo Institute of Technology, Tokyo, Japan*

[3] *Civil Engineering Department, Faculty of Engineering, Suez Canal University, Ismailia, Egypt*

[4] *Civil and Environmental Engineering Department, Tokyo Institute of Technology, Meguro-Ku, Tokyo, Japan*

[5] *Environmental Health Department, High Institute of Public Health, Alexandria University, Alexandria, Egypt*

†*E-mail: khadiga.mekky@ejust.edu.eg*

Keywords: Global warming, SimaPro, Raw sludge**.**

Abstract. The usage of water treatment sludge as a supplementary cementitious material to concrete has positive effects on the environment, and lead to achieve the sustainability goals. In this study, a life cycle assessment (LCA) model has been used to evaluate and quantify the possible environmental impacts of using raw sludge (RS) and thermally activated alum sludge (TAAS) as partial cement replacement for concrete mixtures. The paper compares the environmental effects of three scenarios: ordinary concrete and sludge landfilling, RS mixture, and TAAS mixture. LCA model was prepared using SimaPro LCA software, which presented through a cradle-to-gate LCA boundary based on collected data from site, and the functional unit is the unit volume (1 m3). In comparison to TAAS and OPC mixtures, the results demonstrated that RS mix has the least negative effects on the environment. By using RS, the global warming potential (GWP) in kilograms of carbon dioxide equivalent (kg CO2 eq) is reduced by approximately 90%. The negative environmental impact is due to the use of fossil fuel in OPC production and the burning process for preparation of TAAS and disposal of sludge to landfill. Therefore, in order to save landfill space and create ecologically friendly concrete, using RS as a partial replacement for cement will help meet sustainability goals connected to health, economic development, and climate action.

Introduction

Large quantities of water treatment sludge, also known as alum sludge, are generated from water treatment plant and transferred to rivers and landfills, which causes considerable environmental pollution [1]. Hence, water treatment sludge disposal should be managed to preserve the landfills and decrease the negative environmental effects.

Numerous studies examined the use of alum sludge as an additional cementitious material in the construction industry. Aluminum and silicates are the main component of raw sludge (RS), which can be classified as a pozzolanic material [2]. The effect of thermally activated alum sludge ash (AASA) as a partial replacement of cement on properties of binary and ternary blended binders' concretes was studied by Owaid et al [3]. The results indicated that AASA has a pozzolanic behavior and by 15 % AASA replacement of cement, there was an increase in compressive strength and split tensile strength, and more than 15% AASA, there was a reduction in strengths. Singh et al [4] studied the usage of sewage sludge as a partial sand replacement. The findings showed that 5% of dry sewage sludge is acceptable without having a significant negative effect on concrete characteristics and the cost of concrete production may be reduced by 1.63%. Since, sludge is used a lot in construction sector, it must be environmentally evaluated.

Life cycle assessment (LCA) is the best method for quantifying and evaluating environmental impacts [5]. According to ISO 14040, LCA is a comprehensive approach that used to evaluate the potential environmental impacts ensures its reproducibility [6]. Nakic [7] compared the environmental effects of ordinary concrete and sludge landfilling with 10% sewage sludge ash (SSA) concrete as a partial cement replacement. The results demonstrated that 10% SSA as a replacement of cement could produce concrete with the same technical and environmental properties as the control mixture, and there is a reduction in global warming by 9%.

- Main objective of this paper is to examine and evaluate the potential environmental effects of using RS and TAAS as a partial cement replacement in concrete, which achieve the same performance based on information gathered from manufacturing plant.
-

Methodology

Preparation of concrete mixtures. Concrete mixes were designed according to American Concrete Institute (ACI 211.1-91) [8], then the required quantities of materials are calculated related to the functional unit, which is the unit volume of ready-mixed concrete (1 m3). Table 1 shows the concrete mixes with their proportions.

-

Table 1: Concrete mix proportions for 1 m^3

Mix description	Cement (kg)	Sand (kg)	Gravel (kg)	Water (liter)	Superplasticizer (%)	Supplementary cementitious material
OPC mix	380	678	1016	190	1.75	0
RS mix	361	678	1016	190	2.62	19
TAAS mix	361	678	1016	190	2.73	19

LCA of production of concrete mixes with sludge. Firstly, the goal and scope of this study was identified, and the goal is to evaluate and compare the environmental effects of using various forms of water treatment sludge as a partial cement replacement to prepare concrete mix with same compressive strength. Then, the functional unit was determined which is the volume unit of concrete (1 m^3). The system boundary was presented through cradle-to-gate system boundary. This approach starts with extraction of natural resources and ends with the production of concrete, not considering the usage phase and end of life of the product.

SimaPro is the LCA software that is used for all calculations. LCA model was created to compare the potential environmental impacts for three scenarios, which are the production of 1 m^3 for plain concrete element with ordinary Portland cement, 5% RS as a partial cement replacement, 5% TAAS as a partial cement replacement.

For the inventory data, the location of the water treatment plant was determined in Ismailia (Egypt), where the sludge was obtained, and transported to the concrete plant in El halos, Ismailia. Also, all the required sites were determined (quarry for sand in El salheya, quarry for coarse aggregate in El Galala, cement plant in El Katameya , and superplasticizer plant in El Oubour city) to identify the distance and means of transportation to the concrete plant. Table 1 and 2 presented the inventory data of this study. IMPACT 2002+ V2.05 is method that used to calculate LCA. Used type of sludge is from anaerobic digestion plant, sewage sludge, and the data of sludge include infrastructure of the digestion tank, gas holder, land occupation, and land transformation.

Table 2: Inventory data of system.

Concrete Mixture Types	FU=1 m3	For OPC Mix, RS mix, TAAS mix
Processing		
Generator Diesel	Liter/m3	0.65
Transportation to Concrete plant (Truck 16)		

From Water treatment plant	km	8.7
From Sand quarry	km	67.9
From Coarse aggregate quarry	km	144
From Cement factory	km	126
From Superplasticizer plant	km	105

Results and discussion

Life cycle assessment (LCA)

Concrete mixtures environmental impacts. The results for comparing 1 m^3 of concrete that gives 35 MPa compressive strength for three different concrete scenarios (OPC mix and sludge landfilling, RS mix, and TAAS mix) are presented in Fig. 1 and listed in Table 2. The IMPACT 2002+ V2.05 methodology by SimaPro 9.0 was selected.

The main environmental impacts are Global warming potential (GWP), respiratory inorganics, and non-renewable energy. The global warming was calculated based on the equivalent carbon dioxide emissions to the air measured in Kg CO_2 eq. The OPC mixture and landfilling case resulted in 28300 a total GWP of kg CO_2 eq. In contrast, the total GWP for the other two scenarios which are RS mix and TAAS were 2520 and 4670 of kg CO2 eq, respectively. In another words, using RS and TAAS in concrete resulted in reduction 91% and 83% compared with the OPC mixture and sludge landfilling. This result is similar to a previous study that used sewage sludge ash (SSA) [7].

For non-renewable energy, there is a higher reduction by using RS and TAAS compared with the usage of OPC. The reduction in non-renewable energy using RS and TAAS was 91% and 83%, respectively. Likewise, the RS mix has the least respiratory inorganics impact with reduction 92% compared with OPC mixture impact.

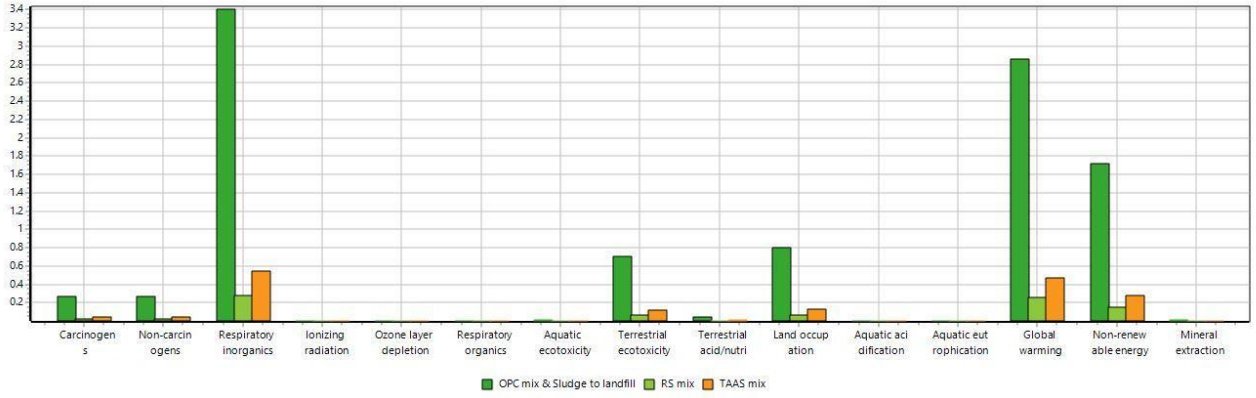

Fig. 1. Comparison between environmental impacts of OPC mixture & landfilling, RS mixture, and TAAS mixture.

Table 3: : The potential environmental impacts categories for OPC mixture & landfilling, RS mixture, and TAAS mixture.

Impact category	**Unit**	**OPC mixture & landfill**	**RS mixture**	**TAAS mixture**
Carcinogens	kg C_2H_3Cl eq	663	53	104

Non-carcinogens	kg C_2H_3Cl eq	668	56.1	107
Respiratory inorganics	kg PM2.5 eq	34.5	2.87	5.51
Ionizing radiation	Bq C-14 eq	129000	13200	22900
Ozone layer depletion	kg CFC-11 eq	0.0017	0.000148	0.000278
Respiratory organics	kg C_2H_4 eq	12.9	1.04	2.03
Aquatic eco-toxicity	kg TEG water	3360000	288000	545000
Terrestrial eco-toxicity	kg TEG soil	1220000	103000	196000
Terrestrial acid/nutria	kg SO_2 eq	531	46.5	87
Land occupation	m2org.arable	10000	775	1550
Aquatic acidification	kg SO_2 eq	109	9.47	17.8
Aquatic eutrophication	kg PO_4 P-lim	2.55	0.225	0.419
Global warming	kg CO_2 eq	28300	2520	4670
Non-renewable energy	MJ primary	261000	22800	42700
Mineral extraction	MJ surplus	2230	175	347

Interpretation. In this section, the interpretation of impact categories for each situation was examined in order to understand the variation of each mixture. According to the results of the GWP, using RS and TAAS as a partial cement replacement has environmental benefits compared to using OPC, where scenarios 1 and 2 have lower GWP due to preventing waste from going to the landfill and reusing RS and TAAS in concrete. The results of the environmental impact categories for the three scenarios are shown in Fig. 2 and listed in table 3. Additionally, the production of cement accounts for 5-7% of the world's CO2 emissions [9]; hence, employing RS and TAAS as supplemental cementitious materials to reduce the amount of cement helps to lower GWP. The findings in table 2 show that OPC mixture and sludge landfilling has the greatest negative effects on non-renewable energy because they use fossil fuels to heat kilns used to create OPC and provide heat energy for the manufacturing of cement.

□

Conclusion

□ The partial replacement of OPC by RS will promote both economic and environmental sustainability. The environmental effect categories are lower in the RS mixed scenario because less fuel is used for shipping and there is no heating or incineration, as opposed to how much fossil fuel is used to maintain the kiln's temperature during OPC production. Due to the use of less energy and the decrease in the quantity of waste transported to landfills, RS also led to a 91% reduction in the harmful greenhouse emissions.

References

[1] A. M. Hussein, R. K. Mahmoud, M. Sillanpää and M. S. A. Wahed, "Impacts alum DWTPs sludge discharge and changes in flow regime of the Nile River on the quality of surface water and cultivated soils in Fayoum watershed, Egypt," *Science of the Total Environment*, vol. 766, p. 144333, 2021.

[2] H. M. Owaid, R. Hamid and M. R. Taha, "Durability properties of multiple-blended binder concretes incorporating thermally activated alum sludge ash," *Construction and Building Materials,* vol. 200, pp. 591-603, 2019.
[3] H. M. Owaid, R. Hamid and M. R. Taha, "Influence of thermally activated alum sludge ash on the engineering properties of multiple-blended binders concretes," *Construction and Building Materials,* vol. 61, pp. 216-229, 2014.
[4] J. Singh, A. Chaudhary, V. K. Dhiman, A. Kumar and A. Goyal, "Impact of dry sewage sludge on characteristics of concrete," *Materials Today: Proceedings,* vol. 52, pp. 818-824, 2022.
[5] A. P. Gursel, E. Masanet, A. Horvath and A. Stadel, "Life-cycle inventory analysis of concrete production: A critical review," *Cement and Concrete Composites,* vol. 51, pp. 38-48, 2014.
[6] ISO14040, in *Environmental management—life cycle assessment—principles and framework,* 2006, pp. 235-248.
[7] D. Nakic, "Environmental evaluation of concrete with sewage sludge ash based on LCA," *Sustainable Production and Consumption,* vol. 16, pp. 193-201, 2018.
[8] D. E. Dixon, J. R. Prestrera, G. R. Burg, S. A. Chairman, E. A. Abdun-Nur, S. G. Barton and S. H. Lee, "Standard Practice for Selecting Proportions for Normal, Heavyweight, and Mass Concrete," in *ACI 211.1-91*, Farmington Hills, MI, USA, American Concrete Institute, 1991.
[9] L. K. Turner and F. G. Collins, "Carbon dioxide equivalent (CO2-e) emissions: A comparison between geopolymer and OPC cement concrete," *Construction and building materials,* vol. 43, pp. 125-130, 2013.

Enhancing the heat transfer of gases in PTC absorber tubes using porous twisted tape inserts

Kareem Wagdy[1, a], Osama A. Elsamni[1,b], Mohamed Shawky[1,c], Sami Elsherbiny[1,d]

[1]Mechanical Engineering Department, Faculty of Engineering, Alexandria University, El-Chatby, Alexandria, 21544, Egypt

[a]kareem-wagdy@alexu.edu.eg, [b]elsamni@alexu.edu.eg, [c]eng.mh2005@yahoo.com, [d]samymelsherbiny@yahoo.com

Keywords: Solar energy, solar collectors, parabolic trough, concentrator, porous inserts, porous material, twisted tapes.

1. Abstract

Using gases as the heat transfer fluid inside the absorber tube of parabolic trough solar collectors is preferable in some applications that need higher temperature levels. However, gases suffer from low convective heat transfer coefficients. Enhancing the heat transfer passively, via employing inserts, roughness, or internal fins is more efficient and reliable since no external power input is needed. Numerous studies have been conducted to increase the rate of heat transfer using various insert shapes and a considerable increase in Nusselt number has been observed. In the present study, the effect of inserting four different porous inserts in the absorber tube of a parabolic trough collector to enhance heat transfer by reducing the entire weight of the inserts is studied numerically. A 2D-axisymmetric numerical model is developed to simulate the forced convection heat transfer in the air flowing through a copper tube subjected to a uniform heat flux on its outer surface with a porous insert inside. A fully developed turbulent flow is considered in the study with Reynolds numbers ranging from 4000 to 20000. The $k-\varepsilon$ model is used to solve the problem of turbulence closure. The validation

of numerical results of the Nusselt number and friction factor with the experimental data obtained from the literature revealed excellent agreement. Nusselt number and friction factor are compared for the different configurations. The results revealed that inserting a porous insert significantly improves heat transfer since using an annular porous insert to the inner wall of the tube resulted in a significant increase in Nu with an acceptable rise in friction factor and proved to be effective at low and high Reynolds numbers and achieved performance evaluation criteria (PEC) of 2.18.

2. Introduction

Improving heat transfer without considerably raising the coefficient of friction is one of the research areas that has received a lot of attention, especially with gases due to their low heat transfer coefficients. Because of their low weight and high thermal conductivity, porous inserts have been widely employed in enhancing heat transfer and showed great potential.

Recently, several research on porous material inserts have been conducted both experimentally and numerically to make the most of it. Valizade et al. [1] experimentally studied the behavior of copper metal foam as a volumetric absorber for parabolic trough collector in three different configurations: full porous, semi-porous, and without porous. They found that employing porous foam significantly increases the friction factor. Furthermore, the maximum thermal efficiency rises from employing full metal and semi-metal foam over free metal foam by 171.2% and 119.6%, respectively. An experimental study on an absorber tube filled with metal foam was conducted by Jamal-Abad et al. [2] in order to enhance the heat transfer and the efficiency of the parabolic trough collector. They showed that when an absorber is filled with metal foam, the overall loss coefficient UL lowers by 45%, increasing efficiency since less energy is wasted.

Furthermore, various numerical research focused on porous media for heat transfer augmentation. Ghafarian et al. [3] numerically investigated forced convection heat transfer in a conduit filled with metal foam that was exposed to a uniform heat flux. The numerical analysis findings showed that inserting metal foam into the channel improved the heat transfer significantly. Yang et al. [4] investigated forced convection in a tube partially filled with porous media in the tube center and along the tube's walls. The heat transfer performance of the tube with a porous medium core was superior to that of the tube with a porous medium layer on the wall at a comparatively low range of Re. However, in a wide range of Re, the latter outperforms the former. Huang et al. [5] implemented a porous media with a slightly smaller diameter to a tube subjected to a uniform heat flux at the walls. The results revealed that the convective heat transfer is significantly improved by the porous inserts of approximately similar diameter to the tube, and the flow resistance increases to an acceptable level, particularly in the laminar flow range. The porous disc line receiver for the solar parabolic trough collector was analyzed by Kumar et al. [6] using a 3D numerical model. They investigated the effect of many geometrical parameters including angle, orientation, the height of the disc, and the axial distance between the discs for different heat fluxes imposed on the tube surface. They noticed an increase in Nusselt number by 64.3% compared with the plain tube. Wang et al. [7] studied the effect of inserting semi-circular cross-section metal foams in the receiver tube of a parabolic trough collector under non-uniform heat flux conditions. The impacts of metal foam arrangement (top/bottom), geometrical parameters, and porosity on flow resistance, and heat transfer were investigated. They concluded that insert height has a significant impact on thermal performance. However, porosity has a minor impact on it. Furthermore, the arrangement in view of the non-uniform heat flux border has a major impact on heat transmission. Xu et al. [8] obtained solutions for velocity and temperature using several approaches, including numerical, analytical, and fin-analysis methods. They established the momentum equations for metal foams using the Forchheimer/Brinkman/Darcy models, while the energy equations were established using the local thermal non-equilibrium (LTNE)/local thermal equilibrium (LTE) models. Ahmed et al. [9] proposed a new design of a circular pipe partially filled with grooved metallic foam in order to improve hydraulic and thermal performance. They

investigated the effect of various parameters such as the pitch of the helical grooves, the number of grooves, and the aspect ratio. The results indicated that at Re of 1000, the case of four helical grooves with two pitches gives the best increase in the Nu number by 7%.

In this project, the heat transfer augmentation with less penalty in the pressure drop is targeted for airflow inside the absorber of parabolic trough and Fresnel-type heat exchanger used for industrial applications. The aim is to study the effect of various porous inserts including twisted tapes which is considered a three-dimensional complex problem. So, as a preliminary phase before carrying out heavy 3D simulations for the twisted tapes at a wide range of geometrical specifications, a series of 2D axisymmetric simulations are performed on a tube with different porous simplified insert shapes under uniform heat flux condition in order to understand the associated phenomena and to narrower the range of parameters of the twisted tapes in the second phase. Several aspects will be explored such as the thickness and spacing of the simplified inserts.

3. Mathematical Modeling

In this study, a 2D axisymmetric model including the basic continuity, momentum, and energy conservation equations is developed to investigate the effect of various porous inserts with a porosity (ε_p) of 0.9 on Nusselt number and the friction factor in a tube of dimensions ($D_i = 45mm, D_o = 50mm$) subjected to a uniform heat flux ($q_{in} = 700\ W/m^2$). The flow is considered turbulent where the Reynolds number is ranged between 4000 and 20000. Four different configurations for the porous inserts are studied including: an annular insert to the inner wall, concentric cylindrical insert, circumferential fins, and central concentric disks as depicted in Fig. 1. For all inserts the height (L_f) is taken to be $D_i/4$. Air is used as the heat transfer fluid with inlet temperature $T_{in} = 25$℃.

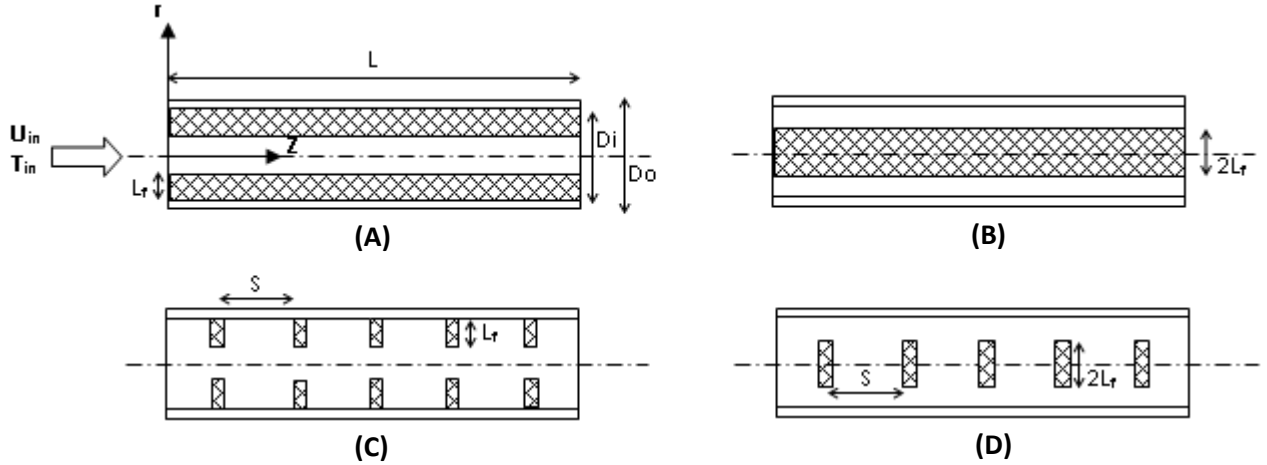

Fig. 1 – The different configurations used in simulaton: (A) with boundary layer insert, (B) with concentric cylinderical insert, (C) with circumferential fins, (D) with central disk inserts

3.1. Governing equation

3.1.1.Fluid domain

The three basic conservation equations are all solved simultaneously for the fluid domain to obtain the velocity and temperature distributions needed for further calculations of the Nusselt number and friction factor. For steady, turbulent flow the mass, momentum, and energy equations are represented respectively as follows:

$$\rho \nabla . u = 0. \quad (1)$$

$$\rho (u. \nabla) u = \nabla . [-pI + \mu(\nabla u + (\nabla u)^T)]. \quad (2)$$

$$\rho C_p u. \nabla T + \nabla . (-k \nabla T) = 0. \quad (3)$$

Where ρ is the fluid density, μ is the fluid viscosity, u is the velocity field, and p is the pressure.

3.1.2. Porous domain

The Brinkmane-Forchheimer model with accompanying energy equations was used to simulate the flow field and heat transfer in the porous media. The equations are written as follows:

$$\rho \nabla . u = 0. \tag{4}$$

$$\frac{1}{\varepsilon_p}\rho(u.\nabla)u\frac{1}{\varepsilon_p} = \nabla.\left[-pI + \mu\frac{1}{\varepsilon_p}(\nabla u + (\nabla u)^T) - \frac{2}{3}\mu\frac{1}{\varepsilon_p}(\nabla . u)I\right] - \left(\mu K^{-1} + \frac{C_F}{K}\rho|u|\right). \tag{5}$$

$$\rho C_p u.\nabla T = \nabla.(k_{eff}\nabla T). \tag{6}$$

Where T is the temperature, ε_p is the porosity, K is the permeability, C_p is fluid heat capacity at constant pressure, and k_{eff} is the effective thermal conductivity which can be calculated using the following equation:

$$k_{eff} = \varepsilon_p k_f + (1 - \varepsilon_p)k_s. \tag{7}$$

Where k_f and k_s are the fluid and the solid matrix thermal conductivities, respectivly.
And C_F is the forchheimer coefficient that is calculated as:

$$C_F = \frac{1.75}{\sqrt{150\ \varepsilon_p}}. \tag{8}$$

3.1.3. The tube wall

To obtain the temperature distribution through the tube wall, Fourier's equation for conduction as follows is applied domain:

$$\nabla.(-k_w \nabla T_w) = 0. \tag{9}$$

Where T_w is the wall temperature, and k_w is the tube wall thermal conductivity.

3.2. Boundary conditions

the boundary conditions used in the model for the three domains is shown in Table 1

Table 1 – boundary conditions applied to the problem

Position	Mass and momentume equations	Energy equation
$z = 0$	$u = U_{in}, v = 0$	$T = T_{in}$
$z = L$	$\frac{\partial u}{\partial z} = 0, v = 0$	$\frac{\partial T}{\partial z} = 0$
$r = 0$	$\frac{\partial u}{\partial r} = 0, v = 0$	$\frac{\partial T}{\partial r} = 0$
$r = Di/2$	$u = 0, v = 0$	$T_w = T_f$
$r = Do/2$	–	$k_f \frac{\partial T}{\partial r} = q_{in}$

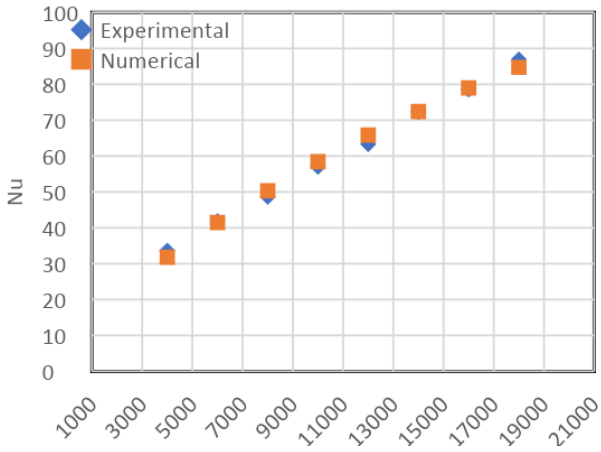

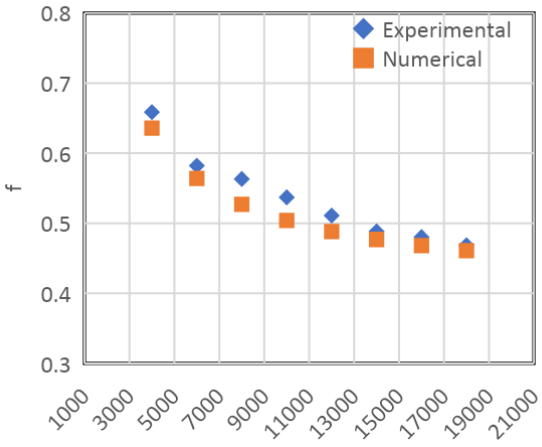

3.3. Numerical simulation

The previous system of equations coupled with the boundary conditions are solved numerically using the finite element method by COMSOL Multiphysics software with K-ε turbulence model applied to the problem. After determining the velocity and temperature fields, the heat transfer coefficient (h), Nusselt number (Nu), and friction factor (f) can be determined as follows:

- $h = \frac{q_{in}}{(T_w - T_b)}$, $Nu = \frac{hD}{k_f}$, $f = \frac{\Delta P}{L}\frac{2D}{\rho u^2}$.

Where: T_w is the tube wall average temperature and T_b is the bulk fluid temperature.

The model is validated by comparing both Nusselt number and friction factor with experimental data obtained by Huang et al. [5] The results showed good agreement as illustrated in *Fig. 2* with a maximum error of 5.5% for Nusselt number and 6.45% for the friction factor.

4. Results and Discussion

The results for Nusselt number and friction factor are shown in Fig. 3 and Fig. 4, respectively. Figures show that, except for case (D), all cases caused a significant increase in Nu. Case (D) of the concentric disc inserts had a minor effect on the Nusselt number compared to the other configurations. For case (C), the effect of the circumferential fins was minimal at low Re, but it improved with rising Re. Cases (A) and (B), on the other hand, resulted in a large increase in Nusselt number, and the percentage increase in Nu for case (A) seems to rapidly grow with Re.

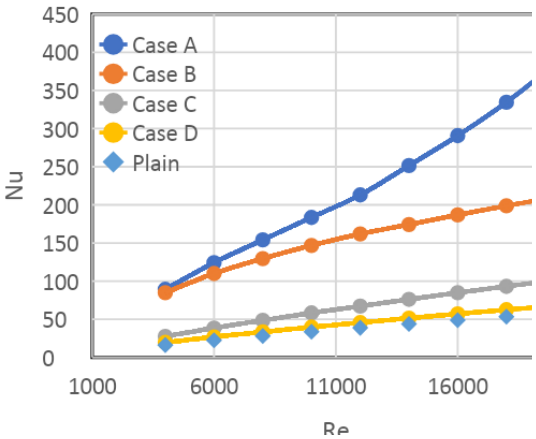

Fig. 3 – Numerical rsults of Nu for different insert configurations

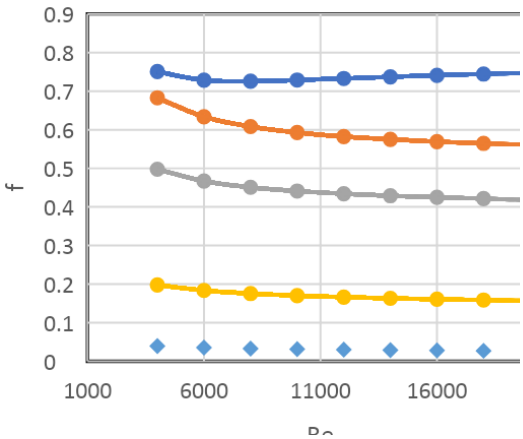

Fig. 4 – Numerical results of friction factor for different insert configuration

On the other side, Case (D) greatly increased the friction factor when compared to its effect on Nu. Also, the outstanding enhancement in Nu acheived by cases (A) and (B) was accompanied by a noticeable increase in friction factor.

To compare between the cases, the following performance evaluation criteria (PEC) formula [10] is used to analyse heat transfer enhancement under constant pumping power:

$$PEC = \frac{(Nu/Nu_s)}{(f/f_s)^{\frac{1}{3}}.} \quad (10)$$

Fig. 5 showes that case (A) outperfoms all other cases in terms of PEC; However, for low Reynolds numbers, case (C) is preferable because it provides comparable performance with less material volume, resulting in a reduced total weight and cost.

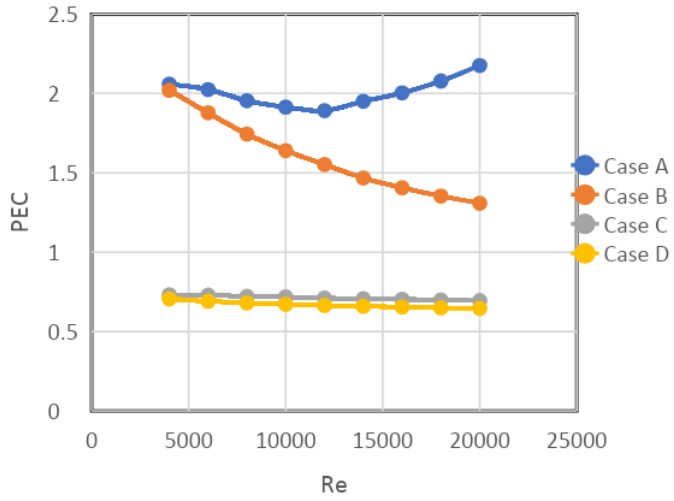

Fig. 5 – Variation PEC with Re

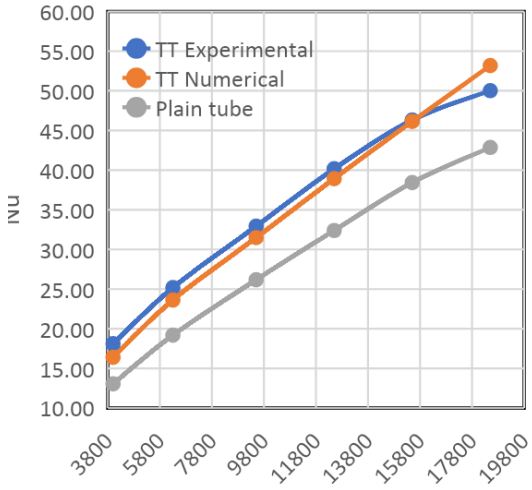

Fig. 6 – The effect of inserting a twisted tape insert on Nu

A 3D numerical model for a tube with a twisted tape (TT) insert is also developed and validated with the experimental results from [11] as depicted in Fig. 6 and showed good agreement for Nu and f. The results showed good enhancement in Nu over the plain tube case. Further research will be carried out to investigate the effect of various parameters in the twisted tape such as twist ratio, width ratio, porosity, etc.

5. Conclusion

Using porous inserts in a tube can greatly enhance heat transfer without adding much weight to the structure of the heat exchanger; However, there is a corresponding rise in friction factor. The configurations with full-tube-length inserts outperformed the cases with intermittent inserts as their PEC values were always larger than 1 that is, the rise in Nu is significantly more than the increase in *f*. The Nusselt number in a tube with an annular porous insert is approximately $5.5 - 6.6$ times greater than the plain tube case in turbulent flow, therefore using the annular insert is recommended especially at high Re where the PEC value is larger than 2. While at low Re, the concentric cylindrical insert is recommended since it provides acceptable performance while being much lighter and less expensive.

6. Acknowledgment

The authors acknowledge the support provided by Science, Technology & Innovation Funding Authority (STIFA), project ID. 33541.

7. References

[1] Valizade, M., M.M. Heyhat, and M. Maerefat, *Experimental study of the thermal behavior of direct absorption parabolic trough collector by applying copper metal foam as volumetric solar absorption.* Renewable Energy, 2020. **145**: p. 261-269.
[2] Jamal-Abad, M.T., S. Saedodin, and M. Aminy, *Experimental investigation on a solar parabolic trough collector for absorber tube filled with porous media.* Renewable Energy, 2017. **107**: p. 156-163.
[3] Ghafarian, M., D. Mohebbi-Kalhori, and J. Sadegi, *Analysis of heat transfer in oscillating flow through a channel filled with metal foam using computational fluid dynamics.* International Journal of Thermal Sciences, 2013. **66**: p. 42-50.
[4] Yang, C., A. Nakayama, and W. Liu, *Heat transfer performance assessment for forced convection in a tube partially filled with a porous medium.* International Journal of Thermal Sciences, 2012. **54**: p. 98-108.
[5] Huang, Z.F., et al., *Enhancing heat transfer in the core flow by using porous medium insert in a tube.* International Journal of Heat and Mass Transfer, 2010. **53**(5-6): p. 1164-1174.
[6] Ravi Kumar, K. and K.S. Reddy, *Thermal analysis of solar parabolic trough with porous disc receiver.* Applied Energy, 2009. **86**(9): p. 1804-1812.
[7] Wang, P., D.Y. Liu, and C. Xu, *Numerical study of heat transfer enhancement in the receiver tube of direct steam generation with parabolic trough by inserting metal foams.* Applied Energy, 2013. **102**: p. 449-460.
[8] Xu, H., et al., *Non-equilibrium heat transfer in metal-foam solar collector with no-slip boundary condition.* International Journal of Heat and Mass Transfer, 2014. **76**: p. 357-365.
[9] Ahmed, H.E., O.T. Fadhil, and W.A. Salih, *Heat transfer and fluid flow characteristics of tubular channel partially filled with grooved metal foams.* International Communications in Heat and Mass Transfer, 2019. **108**: p. 104336.
[10] Z.Y. Guo, W.Q. Tao, R.K. Shah, The field synergy (coordination) principle and its applications in enhancing single phase convective heat transfer, Int. J. Heat Mass Transfer 48 (2005) 180–1797
[11] EIAMSA-ARD, Smith, et al. Convective heat transfer in a circular tube with short-length twisted tape insert. International communications in heat and mass transfer, 2009, 36.4: 365-371.

Evaluating the Carbon Footprint (CFP) of a Refinery and Suggested Decarbonization Measures

Lamiaa Abdallah[1, a] and Tarek El-Shennawy[2,b]

[1]Alexandria higher Institute of Engineering & Technology (AIET), Alexandria, Egypt

[2]Alexandria National Refining & Petrochemicals Co. (ANRPC), Alexandria, Egypt

[a]Lamiaa_abdallah@yahoo.com, [b]tshennawy@yahoo.com

Keywords: Carbon Footprint, Climate Change, Sustainability, Decarbonization, Industry.

Abstract. The Carbon Footprint (CFP) is a tool to measure the impact of an organization on the environment by calculating the annual amount of greenhouse gases (GHGs) emitted into the atmosphere due to the activities of that organization, expressed in tons of carbon dioxide equivalent (CO_2eq). Organizational emissions are divided into three “scopes”. Scope 1 includes direct emissions

that occur inside the organization due to its activities. Scope 2 includes indirect emissions of the organization, mainly due to energy (for example, electricity) purchased from outside the organization. Scope 3 includes other indirect emissions not included in scope 2. Alexandria National Refining & Petrochemicals Co. (ANRPC) is a refinery in Alexandria, Egypt, which refines gasoline with low-octane number (80) to produce gasoline with high-octane number (92 & 95). This study aims to analyze the CFP of the refinery and to suggest actions to reduce the CFP (decarbonization). Results show that approximately 53% of the refinery emissions results from burning of the natural gas to produce steam in the boiler (scope 1). Approximately 32% of the emissions results from the purchased electricity from the utility (scope 2). Approximately 15% are from other sources, mainly transportation (commuting) of employees (scope 3). Several recommendations are suggested to decrease the CFP of the refinery. This study provides a model that can be followed and developed by other companies in the industrial sector to evaluate their CFPs and therefore, apply action plans to gradually de-carbonize this sector.

Introduction

GreenHouse Gases (GHGs), Global Warming & Climate Change. Climate change is one of the greatest global threats to the world in the 21st century [1,2]. Climate change refers to altered climate and weather patterns, resulting from global warming – which is caused by GHGs. The main GHG is the Carbon dioxide (CO_2). Other gases include methane, nitrous oxides and fluorinated gases. GHGs form a spherical thin layer that surrounds the planet Earth and keeps it warm at an average global temperature of 15°C. Without this GHG layer, the Earth's average temperture would be -18°C. For hundreds of thousands of years, this global ecosystem was in a natural balance. Starting from the industrial revolution in the late 19th century, massive burning of fossil fuels to generate heat, steam and power have caused a dramatic increase in GHG emissions in the atmosphere, intensifying the GHG layer that traps more and more heat, leading to global warming, which is the main cause of climate change. If the world does not take actions to stop emitting GHG emissions in the atmosphere, the increase in the aveage global temperature is expected to reach 4°C by 2100 relative to pre-industrial levels, with several catastrophic sequences on humanity [3,4].

Climate Action. Each year, the leaders of the world countries and relevant organizations meet in a Conference of Parties (CoP) to discuss how to combat climate change. During CoP 21 held in Paris in 2015, the world leaders announced the Paris Agreement (PA) to do every possible action to limit global warming to well below 2°C (preferably 1.5°C) compared to pre-industrial levels. Developped countries, which are responsible for most of the global GHG emissions, pledged to finance climate action by 100 billion dollars annually. However, these pledges are not fulfilled. In response to their committments to PA, countries submitted their voluntary or Nationally Determined Contributions (NDCs) to decrease the GHG emissions. Most of the NDCs of the developing countries are conditional on financial aids from developed countries [5].

In 1988, the United Nations (UN) established the Intergovernmental Panel on Climate Change (IPCC), which includes scientists from all over the world, and which publishes scientific reports about climate change. In the IPCC Sixth Assessment Report (AR6) published in 2023, there was a clear bold warning; "Pace and scale of climate action are insufficient to tackle climate change". By 2022, human activities have caused about 1.1°C increase in the Earth's average temperature above the pre-industrial level. To limit global warming to 1.5°C above pre-industrial levels, as set out in the PA, global GHG emissions will need to peak before 2025, then they must decline to net zero by 2050 [6].

Goal 13 0f the UN 17 Sustainable Development Goals (SDGs), which were announced in 2015 to be acheived by 2030, is dedicated to climate action; "Take urgent action to combat climate change and its impacts". Now, almost halfway between 2015 and 2030, current NDCs are not sufficient to meet the PA targets [7].

Carbon footprint (CFP). CFP is defined as the quantity of GHGs in terms of carbon dioxide equivalents (CO_2e) emitted into the atmosphere by individuals, organizations, processes, products or events within specified boundaries. Calculating CFP allows to better understand how the corporate contributes to climate change, identify where emissions are created, and understand which areas are needed to be addressed to reduce emissions [8]. Up till now, there is no obligation for corporates to calculate and disclose their GHG emissions. However, companies that manage their carbon emissions responsibly can enhance their brand value, and make themselves more attractive to potential customers and investors. They can also use the information to manage long-term business risks [9].

Corporates who want to manage their GHG emissions can follow the international standard ISO 14064-1:2018 [10] or alternatively, the scheme given by the World Resources Institute and the World Business Council on Sustainable Development "The GHG Protocol: A Corporate Accounting and Reporting Standard" [11]. This protocol categorizes the GHG emissions into three scopes:

- Scope 1: Direct GHG emissions from the corporate's activities that they own and control.
- Scope 2: Indirect GHG emissions from purchased energy, steam, heat, and air conditioning.
- Scope 3: Other indirect GHG emissions from up- and downstream activities along the value chain that are not covered by scope 2.

The difference between the ISO standard and the GHG protocol lies in scope 3. The standard requires the corporate to calculate scopes 1 and 2, and preferably, but not mandatory, scope 3. The standard subcategorize scope 3 into a) emissions from transportation; b) emissions from upstream supply chain; c) emissions from downstream supply chain; and d) emissions from other sources. The protocol insists on including scope 3 emissions, and it subcategorize scope 3 into 15 sub-scopes. In fact, scope 3 or value chain emissions fall outside of the organisations' direct control. This makes them the most challenging emissions to manage [12].

CFP of Petroleum Refineries: If the world is to come anywhere near to meeting its climate-change goals, the oil and gas (O&G) industry will have to play a big part. The industry's operations account for 9% of all human-made GHG emissions. In addition, it produces the fuels that create another 33% of global emissions, so it is at the forefront of the energy transition and net zero pathways [13]. The refining industry alone accounts for nearly 5% of the global GHG emissions. Cumulative GHG emissions from refineries reached approximately 34 gigatons (Gt) in the period 2000–2021 with an average annual increasing rate of 0.7% [14].

In refineries, scope 1 includes direct emissions, such as fuel combusted at a refinery. Scope 2 includes indirect emissions from energy purchases, such as purchased electricity used in facility operations. Scope 3 emissions are emissions that result from value chain activities, such as emissions that result from purchased goods, equipment, materials, or emissions that result from employees commutting. Scope 3 GHG emissions depend on a company's organizational and operational boundaries. It is important, if choose to include scope 3, to include all the activities that emit GHG throughout the up and downstream value chain [15].

Case Study & Methodology

Case Study. Alexandria National Refining & Petrochemicals Co. (ANRPC) is a refinery established in 1999 in Alexandria, Egypt, with the purpose of refining low-octane gasoline (80) into high-octane gasoline (92 & 95) and that is free from lead. The production quantity is approximately 1.8 million ton/year. Approximately 30% of the high-octane gasoline produced in Egypt. The company wants to calculate its CFP during 2022 for the first time. This will be the "base year". All the subsequent assessments of its CFP will be compared with this reference one. The reporting period will be a calendar year, from 1 Jan. 2022 to 31 Dec. 2022.

Methodology. The company decided to apply the GHG protocol, with inclusion of scope 3 emissions. It should be noted that since the main feed to the company is gasoline 80, and the main products of the company are gasoline 92 and gasoline 95, therefore, it was decided to exclude these

feed / products from the value chain. In fact, the company is a refinery, which adds value to the feed. Without the refining process, car-owners would fuel their cars with gasoline 80, which will advesely affect both the cars' engines and the environment.

Different GHGs vary both in how much they warm the atmosphere and how long they remain in the atmosphere. For example, N_2O has a warming effect 273 times more than CO_2 during a time frame of 100-years. This relative index is called Global Warming Potential (GWP), which expresses how much warming a gas will provide over some time frame, typically 100-years. the combustion of natural gas in a boiler or a furnace releases CO_2, CH_4 and N_2O. Air conditioning systems use refrigerants such as Hydro-Fluoro-Carbons (HFC) or, as commercially known, R134a, a GHG with high GWP (1500 times more than CO_2), and which may be leaked into the atmosphere during normal operation, re-filling, maintenance and end of life of the air conditioners. High voltage electrical switchgear uses Sulfur hexafluoride (SF6) for insulation and arc supression during switching operations. This is also a GHG gas with very high GWP (25000 times more than CO_2), which can be released during leakage, re-filling, maintenance and end of life processes. Fortunately, these gases, if released to the atmosphere, are emitted in very small quantities, that are negligible, even when multiplied by their GWP, to be expressed as CO_2 equivalent. GWP of the GHGs that are emitted in the refinery under study are shown in Table 1 [16].

Emission factors describe the rate at which a given activity releases GHGs into the atmosphere. They are also referred to as conversion factors, emission intensity and carbon intensity. For example, burning 1 kg of natural gas will release 2.7 kg of CO_2 into the atmosphere. Therefore, the emission factor of this activity is 2.7 kg CO_2/kg of natural gas. Emission factors for relevant GHG inventories from scope 1 are derived from [17]. As for scope 2 emissions, the refinery purchases electricity from the national grid, with no self-generation. According to the data from the national electricity company, the emission factor for the current energy mix is approximately 460 gCO_2/kWh [18]. Emission factors for scope 3 are derived from [19].

For each source of emission, the quantity of the source of GHG is multiplied by the emission factor, and then transferred to the equivalent CO_2 emissions, according to the template recommended by the protocol [20].

Table 1. Global Warming Potential (GWP) of relevant GHGs [16]

GHG	Formula	GWP
Carbon Dioxide	CO_2	1
Methane	CH_4	27.9
Nitrous Oxide	N_2O	273
Refrigerant (Freon) HFC-134a	CHF_2CHF_2	1530
Sulfur hexafluoride	SF_6	24300

Results & Discussions

The results of applying the CFP calculation methodology are presented in Table 2. The results show that during the reporting year (2022), the most significant GHG source was the natural gas combustion in the process facilities, especially inside the steam boiler (scope 1). It accounts for approximately 53% of the total GHG emissions. The second significant GHG source was the purchased electricity (scope 2). It accounts for approximately 32% of the total GHG emissions. Scope 3 emissions aggregate to approximately 15% of the total GHG emissions, as shown in Figure 1. These results will serve as reference or base values, so that all subsequent CFPs for the refinery will be compared with these values, to assess any improvements (reductions in the GHG emissions). It can also help the decision makers to focus on areas with intensive GHG emissions. Perhaps more important than the

abstract quantity of GHG emissions (194,200 Tons) is the emissions / Ton of production. For a production quantity of 1.8 Million Tons in 2022, this indicator will be approximately 0.108 Ton CO_2 / Ton of gasoline produced (refined).

Table 2. GHG emissions of the refinery under study

Scope 1: Direct emissions from owned/controlled operations	Ton CO_2e	Total
Steam boiler, process furnaces, heaters and the flare use natural gas with quantity of approximately 38,000 tons.	102,600	102,700
Emergency diesel generators.	4	
On-site cars, Cranes, fork-lifts and basket trucks.	20	
Air conditioning systems use refrigerant R134a.	76	
Scope 2: Indirect emissions from the use of purchased energy		
Annual consumed electrical energy was approximately 132 Million kWh.	60,700	61,900
Purchased steam during boiler shutdown	900	
Purchased nitrogen for cooling	300	
Scope 3: Indirect emissions from the value chain		
Emissions from supplied equipment (machinery, spare parts, tools, etc)	8,240	29,600
Emissions from supplied chemicals (catalyst, lubricants, grease, etc)	2,060	
Emissions from supplied materials (steel, concrete, wood, paper, etc)	2,500	
Emissions from supplied goods (cables, lighting fixtures, air conditioners, personal protective equipment, furniture, etc)	4,000	
Emissions from transportation and distribution of purchased products	1,000	
Emissions from purchased electricity losses in transmission & distribution	4,860	
Emissions from generated waste (waste water, plastics, wood, glass, paper, garbage, etc.)	2,000	
Emissions from employee commuting	2,820	
Emissions from business travel	1,000	
Emissions from downstream transportation and distribution of products.	1,120	
Total scope 1 + scope 2 + scope 3 emissions (in Tons of CO_2 equivalent)		194,200

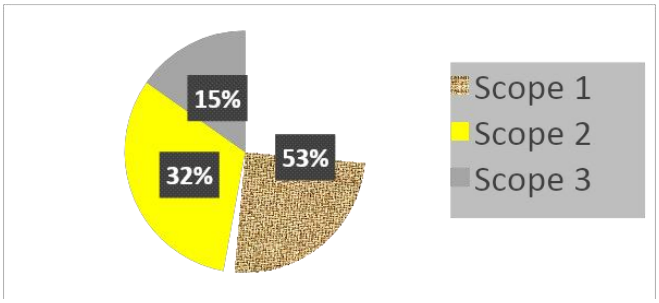

Figure 1. GHG emissions from the refinery under study

Recommendations

General recommendations. As the pressure to act on climate change increases, the refining industry should consider a range of options to decrease its CFP in line with the global efforts. Several recommendations exist in literature which include [13, 21-23]:

- Fuel Switching from fossil fuel to hydrogen
- Energy Efficiency, including high efficient equipment, variable speed drives, LED lighting, use of process optimization techniques, digitalization, etc.

- Use of electricity from renewable energy (on site generation or purchased)
- Combined Heat and Power generation (CHP Co-generation)
- Electrification of fuel-fired heaters and furnaces
- No flaring schemes
- Abatement of fugitive (methane) emissions using Vapor Recovery Units (VRUs)
- Change refinery feedstock from crude to vegetable oil
- Consider green hydrogen for heavy transport
- Carbon Capture and Storage (CCS). This option, which is now somewhat expensive (approximately 50$/ton of CO_2) seems to be the last mile solution for deep de-carbonization of the industry.

Recommendations for the case study. As for the refinery subject to case study, since it was found that the most significant GHG emissions came from combustion of natural gas in the steam boiler (scope 1) and purchasing of electricity (scope 2), summing up to approximately 85% of the total CFP of the refinery, then we will focus on these two categories for improvements.

It was found that there exists an amount of excess hydrogen gas that is the byproduct of the chemical processes in the refinery and that has no users in the refinery or in the nearby facilities. The amount of the excess hydrogen gas (now flared) is approximately 20,000 tons annually. It is recommended to modify the burners of the steam boiler to allow for burning a mixture (50:50) of natural gas / hydrogen. This may lead to decreasing the scope 1 emissions by approximately 50%.

As for the purchased electricity, there are several recommendations, including replacing standard motors with high efficient ones, installing variable speed drives to motors, replace conventional lighting systems with LED, on-site cogeneration of steam and power, on-site generation of electrical power from solar panels, solar systems for pre-heating water inlet to the boiler, purchasing electricity from renewables. Some of these options may require high investments and should undergo a feasibility study that also takes the environmental issue into consideration.

The option of applying CCS technology will be costly for the refinery as long as no obligations or binding regulations exist to force the refineries to cap (or limit their emissions) under specific thresholds. However, this solution can be taken into consideration in any upcoming revamp or rehabilitation of the refinery, at least to make the necessary infrastructure and tie-ins.

Conclusions

Global warming due to the intensified release of the GHGs in the atmosphere is causing climate changes, one of the major threats to the future of the humans on the planet Earth. Immediate actions are required to gradually decrease our CFP on the planet due to our activities and move to a more sustainable, carbon-neutral life. The first step towards these actions is to calculate the CFP of our activities, in order to decrease it through a set of feasible action plans. In this paper, the CFP of a refinery in Alexandria, Egypt was calculated for the first time. Scope 1 (direct and controlled emissions) accounts for 53% of the total emissions. Scope 2 (indirect emissions from purchased electricity) accounts for 32% of the total emissions. Scope 3 (indirect emissions from up and downstream value chain) accounts for 15% of the total emissions. The emission intensity of the refinery is 0.108 Ton CO_2 / Ton of gasoline produced. Some general and specific recommendations are suggested to successfully manage the CFP of the refinery.

References

[1] S. Heading and S. Zahidi. The global risks report 2023, 18th Edition, World Economic Forum, 2023.

[2] M. Romanello et al., The 2022 report of the Lancet countdown on health and climate change: health at the mercy of fossil fuels, Lancet, 400: 1619–54, 2022.

[3] Intergovernmental Panel on Climate Change (IPCC). Climate change 2021: Summary for all, Ver. 3, 2022.
[4] United Nations Environment Programme (UNEP). Emissions gap report 2022: The closing window — Climate crisis calls for rapid transformation of societies. Nairobi, 2022.
[5] World Economic Forum. The "No-Excuse" framework to accelerate the path to net-zero manufacturing and value chains, World Economic Forum, 2023.
[6] Intergovernmental Panel on Climate Change (IPCC). Climate change 2023: Summary for policymakers, 2023.
[7] United Nations (UN). The Sustainable Development Goals (SDGs) report, 2022.
[8] M. G. G. Awanthia and C. M. Navaratne. Carbon footprint of an organization: A tool for monitoring impacts on global warming, Procedia Engineering, Vol. 212, pp. 729-735, 2018.
[9] Carbon Trust. A guide to carbon footprinting for businesses, United Kingdom, 2022.
[10] International Standardization Organization (ISO). ISO 14064-1:2018(E), Greenhouse gases — Part 1: Specification with guidance at the organization level for quantification and reporting of greenhouse gas emissions and removals. 2nd edition, Dec. 2018.
[11] World Business Council on Sustainable Development and World Resources Institute. The GHG protocol. A corporate accounting and reporting standard, revised version, 2015.
[12] L. Klaaben and C. Stoll. Harmonizing corporate carbon footprints, Nature Communications, Vol. 12:6149, 2021.
[13] C. Beck, S. Rashidbeigi, O. Roelofsen and E. Speelman, The future is now: How oil and gas companies can decarbonize, McKinsey & Company, 2020.
[14] S. Ma et al., Global oil refining's contribution to greenhouse gas emissions from 2000 to 2021. The Innovation, 4(1), 100361, 2023.
[15] International Petroleum Industry Environmental Conservation Association (IPIECA), American Petroleum Institute (API) and International Association of Oil & Gas Producers (OGP). Petroleum industry guidelines for reporting greenhouse gas emissions, 2011.
[16] C. Smith et al., The Earth's energy budget, climate feedbacks, and climate sensitivity supplementary material. In: Climate change 2021: The physical science basis. AR6 of the IPCC, 2021.
[17] US Environmental Protection Agency (EPA). Emission factors for Greenhouse Gas Inventories, 18 Apr. 2023.
[18] Egyptian Electricity Regulation Authority (Egyptera), Electricity Observatory Reports [in Arabic], 2022.
[19] International Petroleum Industry Environmental Conservation Association (IPIECA) and American Petroleum Institute (API). Estimating petroleum industry value chain (scope 3) greenhouse gas emissions, 2016.
[20] World Business Council on Sustainable Development and World Resources Institute. GHG Protocol Reporting Template, 2017.
[21] N. Sunny et al., A pathway towards net-zero emissions in oil refineries. Frontiers in Chemical Engineering, Vol. 4, Article 804163, 2022.
[22] Environment and Climate Change Canada, Options to cap and cut oil and gas sector greenhouse gas emissions to achieve 2030 goals and net-zero by 2050, 2022.
[23] V. Fetisov et al., On the integration of CO_2 capture technologies for an oil refinery. Energies, 16, 865, 2023.

Synthesis and characterization of ZnO nanoparticles and how temperature variation affects their morphological structure

Lengu Peter Tuok 1, a , Marwa Elkady 2,c , Abdelrahman Zkria 2,3 , Tsuyoshi Yoshitake 2,c , Usama Nour Eldemerdash 5,b

[1]Department of Chemical and Petrochemical Engineering, Egypt Japan University of Science and Technology (E-JUST), New Borg El- Arab City, 21934, Alexandria, Egypt

[2]Department of Chemical and Petrochemical Engineering, Egypt Japan University of Science and Technology (E-JUST), New Borg El- Arab City, 21934, Alexandria, Egypt

[3]Center for Japan-Egypt Cooperation in Science and Technology (E-JUST Center), Kyushu University, Japan

[4]Department of Advanced Energy Science and Engineering, Faculty of Engineering Sciences, Kyushu University, Kasuga, Fukuoka 816-8580, Japan

[5]Department of Chemical and Petrochemical Engineering, Egypt Japan University of Science and Technology (E-JUST), New Borg El- Arab City, 21934, Alexandria, Egypt

[1,a] lengu.gatluak@ejust.edu.eg, [5,b]usama.nour@ejust.edu.eg, [2,3] abdelrahman@ejust.kyushu-u.ac.jp
[2,c]marwa.elkady@ejust.edu.eg [2,c]tsuyoshi_yoshitake@kyudai.jp

Keywords: ZnO nanoparticles, Sol-gel method, Synthesis, Calcination, FTIR, XRD, TEM.

Abstract.
ZnO oxide (ZnO) nanoparticles have gained great attention in their applications because of their robust properties such as great energy band, chemical stability, good transparency, and environmentally friendly. In this research, ZnO nanoparticles were successfully synthesized via sol-gel method. This synthesis method was chosen due to its ability to control the nanoparticles' size and their morphological properties. The particles' morphology and the size of their distribution were examined using TEM, FTIR, XRD, and Zeta Potential to determine the effect of synthesis processes and condition used. Based on various characterization results, the calcination temperature has a higher influence on ZnO nanoparticles size and morphological structure. As the calcination temperature increases, the intensity of ZnO nanoparticles becomes higher and this leads to shift and increase in absorption peaks. XRD results revealed that ZnO nanoparticles show hexagonal wurtzite structure however, TEM images indicate that the morphological appearance of ZnO nanoparticles in low calcination temperature is plate like shape with high agglomeration but a higher temperature the shape become smooth hexagonal without agglomeration. The size of the ZnO nanoparticles were found at range of 30-50 nm. The mean zeta potential measurement was in the range of 2.0 to -45 mV exhibiting high stability in suspension at different calcination temperatures.

1. Introduction

The distinctive properties of Zinc oxide nanoparticles have created a great interest in synthesizing them for various applications. These properties include unique optical properties, wider band gap ratio, and other physical and chemical properties which have them main subject to many research (Pratap *et al.*, 2023). The Sol-gel method is an effective synthesis technique because it is efficient since the morphology and size of nanoparticle can easily be controlled. In addition, sol gel technique

is known for it repeatability, low cost, reliability and simplicity (Singh *et al.*, 2022). Nanoparticles have been studied and applied in different fields such as nanofluids for enhanced oil recovery, gas sensors, biosensors, and photocatalysis due to their superior chemical and physical properties. Zinc oxide nanoparticles are also known for excellent electrochemical coefficient and better stability in the base fluids when suspended as colloids (Al-luhaibi and Sendi, 2022).

2. Materials and Methods

2.1 Preparation of Zinc Oxide nanoparticles

Sol-gel technique was used for the synthesis of zinc oxide nanoparticles due to its versatility and because it also provides precise control conditions over the morphology and composition of the material. 10g of zinc acetate was dissolved in 150 ml of ethanol under constant stirring with a magnetic stirrer until the mixture formed a clear solution. 3g of sodium hydroxide was added dropwise while stirring for three hours, and the mixture was allowed to age overnight at room temperature to form a gel. The mixture was sonicated for 15 minutes at a rate of 6000 rpm and put into an oven to dry at 80 ^{o}C. The sample was calcined for 2 hours in a muffle furnace at different temperatures of 500 and 700 ^{o}C, respectively, and was allowed to cool.

2.2 Characterization techniques

X-Ray Diffraction (XRD), Panalytical Xpert3 powder model, Transmission Electron Microscope (TEM), JEOL's JEM 2100F, Fourier Transform Infrared Spectroscopy (FTIR), Bruker Vertex 70V, and Zeta Sizer Malvern nano series were used to analyze the physical and chemical characteristics of synthesized zinc oxide nanoparticles.

3. Results and Discussion

3.1 FTIR analysis

The functional groups in Zinc oxide nanoparticles were analyzed and determined using FTIR analysis. It was observed that the peak at 3414.69 cm-1 is associated with O-H groups while C=O is located at the peaks of 1619.22 cm-1 which indicates the bond of non-ionic carbonylic group. Based on temperature increase the FTIR spectra of zinc oxide nanoparticles shifted slightly to the right and there was significant shift in the position of intensity at 700 ^{o}C temperature compared to 500 ^{o}C. The result of bands shifting is due to thermal expansion of crystal lattice(Goswami, Adhikary and hattacharjee, 2018).

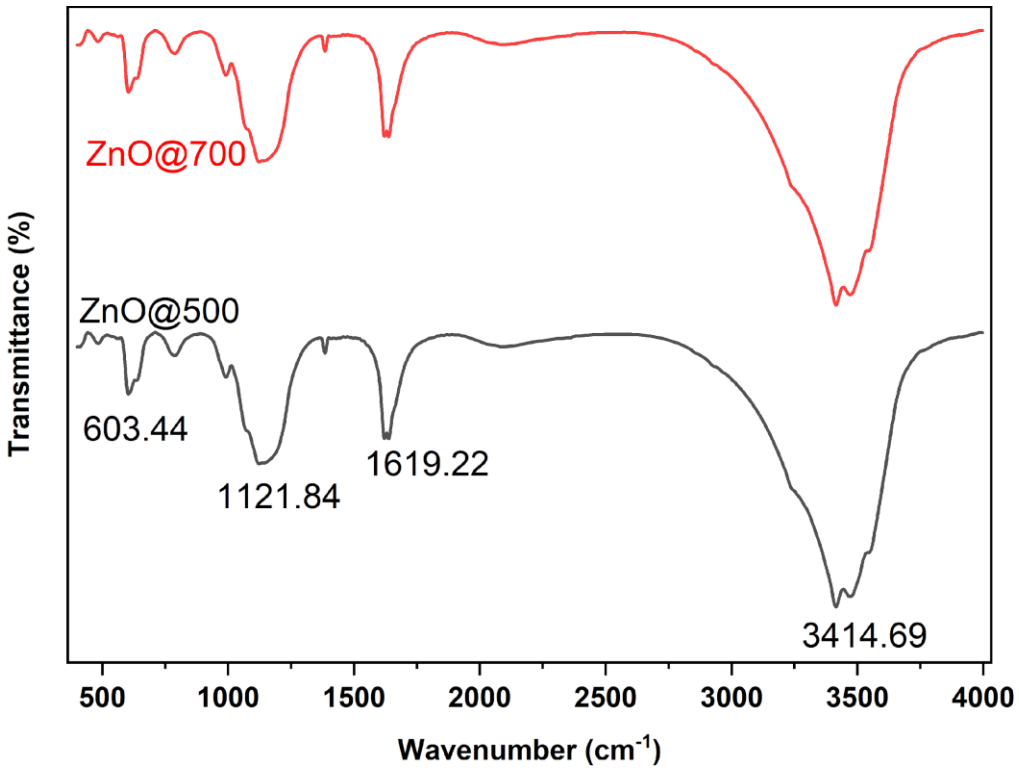

Figure 1 FTIR patterns of Zinc oxide annealed at 500 °C and 700 °C.

3.2 XRD Analysis

The structure of synthesized zinc oxide nanoparticles was determined using XRD and the patterns were captured between 20 and 80 degrees (2) at a scan rate of 12 o/min. The value of sharp peaks was 36.1, 3.71, and 56.5 which were aligned to (101), (100), and (110). This arrangement matches work done by (Lavanya, Aparna and Ramana, 2023). Based on XRD analysis, the mean crystal size of zinc oxide nanoparticles is 40 nm which was determined using Scherer equation and our results were in line with literature. It was found that as calcination temperature increases from 500 °C to 700 °C zinc oxide XRD peaks get intense and sharpened. The prepared zinc oxide nanoparticle exhibits a Wurtzite hexagonal structure which can be indexed to JCPDS card no. 79-0205. There is an unwanted peak at XRD of 500 °C which indicates that some precursors are not decomposed during calcination process and when temperature was increased to 700 °C the unwanted peak disappeared showing that there were no secondary peaks in the XRD spectra.

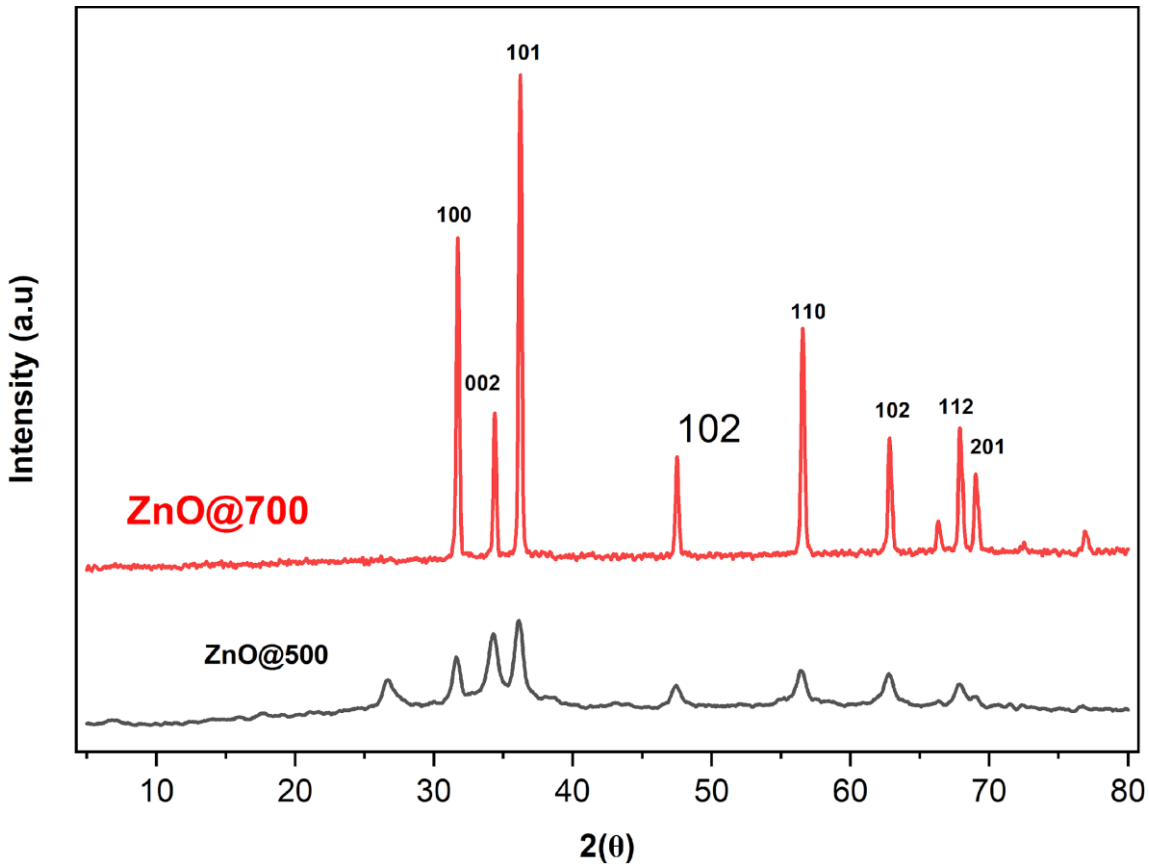

Figure 2 XRD patterns of Zinc oxide annealed at 500 °C and 700 °C.

3.3 TEM analysis

Transmission Electrons Microscope (TEM) JEOL's JEM 2100F Japan was used to determine the physical and chemical composition of Zinc oxide nanoparticles. The TEM results show that temperature increase plays a significant role on structure and agglomeration of ZnO nanoparticles. On Fig () it can be seen that at 500 °C ZnO nanoparticles agglomerated, and clusters were formed in some region while when calcination temperature was increased to 700 °C the shape of nanoparticles became clear without agglomeration. The agglomeration of ZnO nanoparticles is due to the Van der Waals attraction among the particles. The structure of ZnO nanoparticles in both temperature ranges is spherical and the average particles size is between 30-45 nm which is in good agreement with the literature. However, based on the temperature difference it can be concluded that particles size, agglomeration, and structure are heavily influenced by the calcination temperature variation.

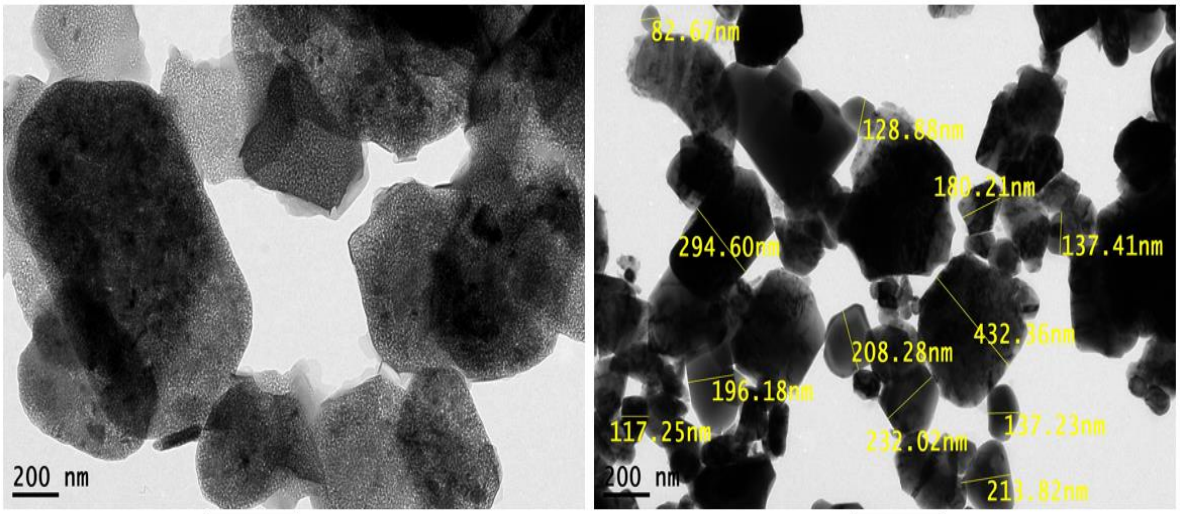

Figure 3 TEM images of Zinc oxide annealed at 500 °C and 700 °C

3.4 Zeta potential analysis

Zeta potential analysis was carried out to determine the effects of calcination temperature on zeta potential values. Zeta potential is one of the important factors to be analyzed critically when nanoparticles are suspended in the base fluids because it has a high influence on nanoparticles stability and aggregation behavior. Since it measures the surface charges of nanoparticles it is considered as a key parameter for understanding the behavior of zinc oxide nanoparticles when suspended in the base fluids. At temperature 500 °C the zeta potential at the highest peak was ±3.8 (mV) but when the temperature was increased to 700 °C the zeta potential increased to ±43.7 (mV). Based on these observations, increase in annealing temperature increases zeta potential of Zinc oxide nanoparticles and this effect can be attributed to increase of oxygen vacancies and decrease in surface hydroxyl group at higher temperatures(Verma *et al.*, 2022).

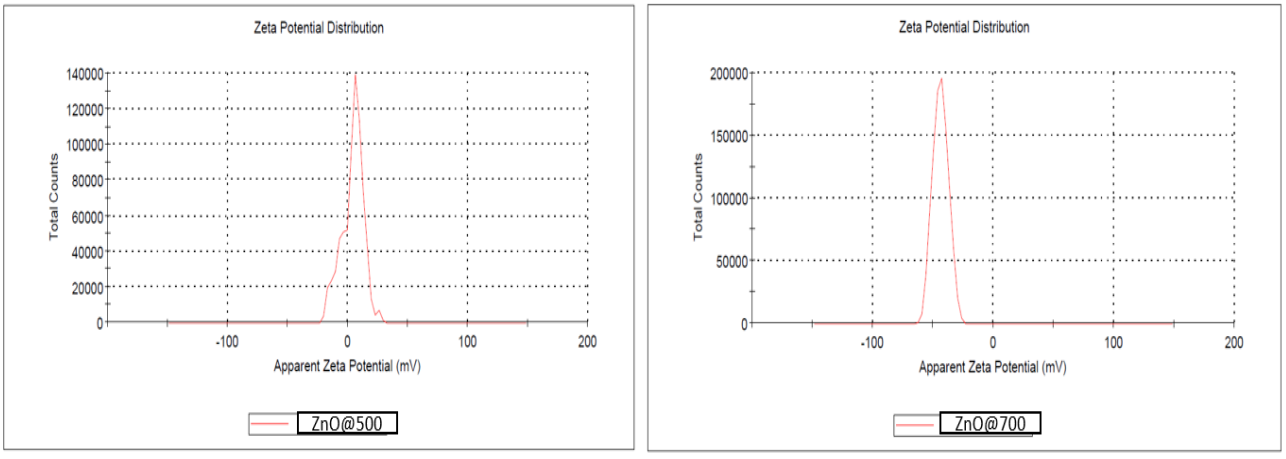

Figure 4 Zeta potential of Zinc oxide annealed at 500 °C and 700 °C.

4. Conclusion

Based on the obtained results, zinc oxide nanoparticles were successfully prepared using sol-gel method and it was calcined at different temperatures (500 ºC & 700 ºC). Four different characterization techniques were used, and they included XRD, TEM, FTIR, and zeta potential to determine the effect of temperature increase on chemical and physical properties ZnO nanoparticles. Based on XRD analysis the peaks get intense at higher temperatures compared to lower temperatures. However, zinc oxide zeta potential increases with increasing temperatures and the same effect were also observed with TEM image as nanoparticles become less agglomerated at high temperatures. However, the results suggest the positive potential application of the synthesized zinc oxide nanoparticles for enhanced oil recovery.

References

Al-luhaibi, A.A. and Sendi, R.K. (2022) 'Synthesis, potential of hydrogen activity, biological and chemical stability of zinc oxide nanoparticle preparation by sol–gel: A review', *Journal of Radiation Research and Applied Sciences*, 15(3), pp. 238–254. Available at: https://doi.org/https://doi.org/10.1016/j.jrras.2022.07.008.

Goswami, M., Adhikary, N.C. and Bhattacharjee, S. (2018) 'Effect of annealing temperatures on the structural and optical properties of zinc oxide nanoparticles prepared by chemical precipitation method', *Optik*, 158, pp. 1006–1015. Available at: https://doi.org/https://doi.org/10.1016/j.ijleo.2017.12.174.

Lavanya, B., Aparna, Y. and Ramana, M. V (2023) 'Synthesis, characterization of zinc oxide nanoparticles using Terminalia mantaly leaf extract and their antibacterial activity', *Materials Today: Proceedings* [Preprint]. Available at: https://doi.org/https://doi.org/10.1016/j.matpr.2023.05.001.

Pratap, R. *et al.* (2023) 'Study on structural, microstructural and dielectric properties of zinc oxide nanostructure synthesized by Sol-gel technique', *Materials Today: Proceedings*, 82, pp. 369–374. Available at: https://doi.org/https://doi.org/10.1016/j.matpr.2023.03.091.

Singh, M. *et al.* (2022) 'Synthesis, optimization and characterization of zinc oxide nanoparticles prepared by sol–gel technique', *Materials Today: Proceedings*, 48, pp. 690–692. Available at: https://doi.org/https://doi.org/10.1016/j.matpr.2021.08.145.

Verma, N. *et al.* (2022) 'Characterization of Fabricated Gold-Doped ZnO Nanospheres and Their Use as a Photocatalyst in the Degradation of DR-31 Dye', *Journal of Nanomaterials*. Edited by S.J.S. Chelladurai, 2022, p. 7532332. Available at: https://doi.org/10.1155/2022/7532332.

Experimental research for reducing emissions in maritime industry

Mahmoud A. Farouk [1.2] , Mohamed M. Elgohary[1] , Ashraf A. Zahran [3] , Mohamed R. Shouman [2]

[1]Department of Naval Architecture and Marine Engineering, Faculty of Engineering, Alexandria University, Alexandria 21544, Egypt

[2]Department of Marine Engineering Technology, College of Maritime Transport & Technology, Arab Academy for Science, Technology and Maritime Transport, Alexandria 1029, Egypt

[3]Institute of Environmental Studies and Research, University of Sadat City, Sadat City, Egypt

Academic Author: Mahmoud Ashraf farouk

Email: eng.mahmoud219@gmail.com

Keywords: shipping transportation, emission reduction, selective catalytic reduction, liquefied natural gas and air pollution.

ABSTRACT: In terms of global coordination, shipping transportation is the most crucial mode. On show, shipping transportation contributes for more than 2/3 of the total volume of global commerce. Large-power diesel motors with exhaust, which are the most damaging pollutants detected in the environment from ships, are used on ships as a means of marine shipping. Large-scale exhaust gas emissions from ships are becoming a major source of air pollution in oceans, harbors, and coastal areas. The International Maritime Organization (IMO) has therefore set regulations to lower this pollution. In this experiment, marine diesel oil fuel (MDO)-powered Aida IV ship's main engine exhaust gases were measured. Sensonic2000 device measurement at 85% load, which is the primary sailing weight. The installation of liquefied natural gas (LNG) to the system and the implementation of selective catalytic reduction (SCR) to the marine diesel oil (MDO+SCR) are the emission reduction methods that have been studied. Because they have the greatest impact on the environment, the experiment measures the amounts of exhaust emitted by the ship. identical ship engine driving the exact same load was used using the reduction technologies. Finally, the experiment discovered that MDO+SCR is the more effective technologies for the Aida 4 ship because of its low consumption and lack of need for engine modification; all that is required is to add the selective catalytic reduction exhaust line reduction system, known as the simplest and least expensive solution. Additionally, there aren't many differences between them in terms of emission.

Introduction

The most significant mode of transportation in global logistics is maritime. Currently, more than two thirds of all international trade is carried out via marine transportation [1]. The primary detrimental pollutants present in the exhaust gas released by marine power plants are sulfur oxides (SOx), particulate matter (PM) and nitrogen oxides (NOx). Ships are utilized as a mode of sea transportation and are equipped with powerful diesel engines[2]. In coastal areas and ocean, harbor ships that produce significant amounts of exhaust gas pollutants are becoming a major cause of air pollution [3]. Recent years have seen the development of stringent ship emission laws and the enforcement of tougher emission limits inside specified emission control areas (ECAs) by the IMO the USA, China, Europe and other nations. The need for exhaust gas treating devices has grown quickly since the

maritime industry is under intense pressure to reduce pollution emissions[4]. oil-fired boilers, auxiliary diesel engines, and Low-speed diesel engines are the main components of marine power plants. Due to the fact that these engines often utilize subpar heavy fuel oil (HFO), which contains a lot of sulfur (up to 3.5% m/m), the burning of this fuel unavoidably produces large amounts of SOx emissions [5]. The primary source of NOx is the airborne combustion of N2 and O2, which is mostly influenced by the combustion temperature in the cylinder. Diesel engine fuel quality and combustion conditions have an impact on PM production, and there is a trade-off between NOx and PM production [6]. Due to its advantages of being a plentiful supply, affordable fuel, and environmentally friendly product, liquefied natural gas (LNG) will be a major player in fuel development in coming years [7]. Combining LNG combustion with engine combustion control technologies may result in simultaneous elimination of SOx, NOx, and PM. Its development and use, however, have been constrained by a number of difficulties, including safety, expensive equipment investment costs, continuous operation capabilities, and methane leakage. As a result, it is presently largely utilized in offshore inland ships and natural gas carriers [8]. Low-sulfur fuel is more expensive than traditional HFO and has less viscosity, which may wear down cylinders, but it reduces SOx emissions directly and effectively at the source [9].The Exhaust Gas Cleaning (EGC) system is recognized by the International Maritime Organization (IMO). as the equivalent technique for reducing SOx emissions because it uses alkaline or pure saltwater as a substance that absorbs SOx from exhaust emissions. It operates on a simple concept, effectively removes SOx, and can also remove some PM (particulate matter) [10]. Another exhaust gas after-treatment technique, selective catalytic reduction (SCR), uses a catalyst and reductant urea pyrolysis to efficiently convert NOx into N2 [11]. The utilization of EGC and SCR share some disadvantages, such as higher volume and expensive initial investment costs. SCR does have several other weaknesses that are known, such as low effectiveness at low temperatures and catalyst sulfur poisoning [12]. Additionally, EGC is more adaptable to exhaust gas than SCR. The best engine in cylinder technique exhaust gas recirculation (EGR) is a technology that can satisfy IMO Tier 3 standards. technology. The MAN Company pioneered the use of EGR technology in maritime low speed engines, and this technique effectively inhibits the creation of NOx by forcing cooled and cleansed exhaust gas to lower the combustion temperature, into the cylinder [13]. All currently achievable reductions in marine exhaust gas emission devices are capable of eliminating a single pollutant section, and while single pollutant elimination machinery connected in sequence directly can satisfy the current pollution regulation, the application of this technique to ships is constrained due to the price, quantity, effect on the engine's efficiency, and other factors. Low-sulfur fuel and SCR can reduce NOx and SO2 at the same time, but using integrated technology will considerably increase transportation costs, and engine and upon-treatment system dependability is another tricky problem [14]. Low-sulfur gasoline and EGR work together to immediately eliminate SO2 and NOx but the technology's use also makes engines consume expensive low-sulfur fuel and necessitates the addition of an EGR device. Additionally, the EGR system alone has a significant impact on engine fuel efficiency and increases HC and CO emissions [15]. In order to simultaneously remove SOx, NOx, and certain particulates, EGC in conjunction with SCR technology has been utilized in land-based coal-fired power facilities to treat exhaust gases. But it cannot be used in ships due to the drawbacks of a complex system and larger volume. Although the above method is more ship-practical, EGR combined with EGC technology still has the drawbacks of a complex system and poor fuel efficiency [16]. The thorough analysis of the technical plan above shows that at least one additional piece of equipment is required to meet the goal of

simultaneously eliminating NOx and Sox from marine exhaust gas. Ships frequently use EGC systems because of their excellent flexibility to exhaust gas requirements and minimal effects on engine achievement. The EGC system's investment cost payback period is shortened for marine diesel engines with greater power [17]. To be able to comply with emission restrictions, modern technology that can simultaneously remove SOx and NOx in a single piece of equipment based on maritime EGC technology is needed. conventional EGC technology cannot remove NOx, which generates almost 90% of the emissions of NOx and is exceedingly difficult to break down in water, hence it is mostly used to remove SOx. Due to this problem, dry oxidation absorbing technology has been researched [18]. This technique can be used in conjunction with EGC technology to simultaneously remove SOx and NOx from a piece of machinery [19]. The key concept is that high valence NOx, which has superior water solubility, can be produced when an oxidant oxidizes NO, and that high covalent NOx is able to be absorbed by the dry scrubbing technique. However, the International Maritime Organization (IMO) requires that the quantity of nitrate in scrubber wastewater not go above 60 mg/L or that the correspondingly decreased amount of NOx not go above 12% of total NOx, whichever is greater [20]. Nitrate is typically the final product of the process of oxidative absorption. According to IMO emission standards, As the calculated value of NOx reduces from Tier 2 to Tier 3 (from 14.4 to 3.4 kWh), the NOx elimination rate must be better than 77%, and the amount of nitrate related to this NO removal efficiency surely exceeds the permissible value. The three main problems that need to be handled are nitrate inhabitation, NO oxidation degree control, and oxidant selection [21]. Even so, nitrate cannot be eliminated from the liquid stage and NOx can simply be overoxidized. The wet approach is more effective at removing NOx from some common oxidants, including sodium hypochlorite (NaClO), hydrogen peroxide (H2O2), sodium persulfate (Na2S2O8), sodium chlorite (NaClO2), and other oxidants. The primary factor causing metal corrosion in scrubbers is Cl in liquid [22]. The amount of NO oxidation and the amount of reductant have a direct impact on the diminished efficiency of NOx, and adding reductant will reduce NOx to N2, which is preferable to the one fold oxidation absorbing method [23]. Urea (CO(NH2)2) and sodium sulfite (Na2SO3) are a couple of the principal reductants. Strong oxidants are typically used with caution because they can produce issues including excessive NOx oxidation and mutual oxidant and reductant consumption, which wastes a lot of absorbent and raises operating costs [24]. Currently, studies on dry oxidation absorbing technology have mostly focused on the effectiveness and efficiency of SOx and NOx removal., failing to address issues with NO oxidation control and large waste liquid nitrate contents. In light of this, preliminary research has been used to examine all available oxidation absorption techniques, and urea peroxide (CO(NH2)2H2O2) with oxidation reduction properties has been chosen as an absorbent to carry out experimental experiments on SOx and NOx removal. Its advantages over other inorganic peroxides include a high concentration of active oxygen species, increased solubility, improved stability, manageable oxidation, and a lengthy action duration[25,26]. As a new green oxidant, urea peroxide watery solution combines the characteristics of urea and hydrogen peroxide while outperforming hydrogen peroxide in terms of stability and oxidation [29,30]. Urea peroxide is inexpensive and ought to be effective at removing NOx and Sox. The reaction's byproducts won't pollute the ocean's ecology in a secondary way. Additionally, temperature and metal ions can have an impact on urea peroxide's ability to absorb oxygen, and this property can be used to modify the degree of NO oxidation and enhance solution absorption [27]. The research additionally developed a novel absorption technique for marine exhaust gas pollutants. The effectiveness of urea peroxide aqueous

solution in reducing NOx and SOx was also investigated. The goals of this study are to determine how well NO is removed from urea peroxide solution and to investigate how operational conditions may impact the effectiveness of nitrate inhibition and NO removal [28].

EXPERIMENTAL METHODS

Due to their significant contribution to transportation, ships have become more numerous in the past few years. The result is the amount of emissions rose, and in this research, we investigate the best strategy for cutting emissions on the ship Aida 4 (Fig. 1). Selective Catalytic Reduction (SCR) was added to the exhaust line of the ship, which was utilizing MDO (Marine Diesel Oil), and the emissions were compared to those of a standard system without SCR. In order to determine whether system is more effective in reducing emissions, we also added an SCR system with MDO compared it to a liquefied natural gas LNG system. All measurement was done at 85% of load. The key ship technical information is shown in Table 1.

Figure (1) Aida 4 Training ship

able 1 Aida IV ship technical data.

ITEMS	Description
Ship Type	SUPPLY VESSEL/ SEA TRAINING
Ship builder	Shipyard Miho Ltd.
NO. of engine	TWO DIESEL ENGINE
ENGINE TYPE	4 STROKE AND 6 CYLINDER

BORE	210.0 mm
STROKE	310.0 mm
Power (kW)	2,650 (1,340 x 2)
RPM	1000.0
Manufacturer	Yannmar

The measurement tool (Sensonic2000) that measures exhausts produced by these fuel types (MDO, MDO+SCR, and LNG). the sampling of exhaust gases taken from the engine's exhaust stack. The sample port, which is depicted in Fig. 2, is located in the exhaust line, where the sampling was conducted. The same stable circumstances, such as humidity and room temperature, were used for all of the measurements. Additionally, the Sensonics device measures the amount of nitrogen oxides (NOx), sulfur oxide (SOx) and exhaust temperature (Text) while the engine is running under load for 20 minutes to detect any reading instability.

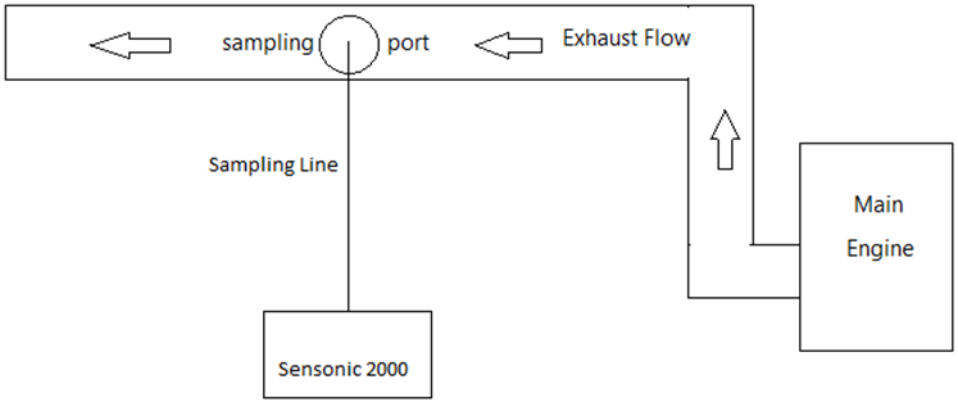

Figure (2) Experimental RIG

The instrument was calibrated, but we conducted a test using a small generator with a single-stage, air-cooled engine that had 1600 rpm and 7.6 brake power (BW) represented in (Fig 3). The measurement tool (Sensonic2000), which measures the exhaust gases produced by the main engine and for the generator, is shown in (Fig 4). Table 2 displays the generator's specifications.

Table 2 Specification of engine

ITEMS	Specifications
TYPE	India Apan
BW	7.6
REVOLUTION (rpm)	1600
NO. of cylinder	1 cylinder
Bore	103 mm
Stroke	120 mm
ENGINE TYPE	Four stroke
Cooling	Air cooled

Compression Ratio	17.5

Figure 3 Generator -engine

Figure 4 the measurement device

The generator was measured using four loads, which are indicated as (0%-25%-50%-75%-100%).In order to ignore any inconsistent readings, the engine must be operating on diesel oil for 20 minutes at a time. The nitrogen oxide (NOx) using result was calculated close to reference [33], as shown in (Fig 5). The NOx was rising close to the referenced research until reach 50% load, then because of a slight variance between the two engines you'll discover a gap in outcomes at 70% to 75% load, then they are going to near again at 80% load until the engine is fully loaded. In addition, the results of sulfur dioxide (SO2) measurements were made in close range to the reference [34], as shown in (Fig 6).

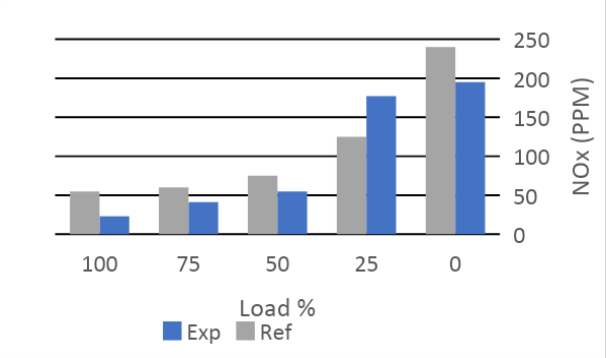

Figure 5 validation of NO_x measurement [15]

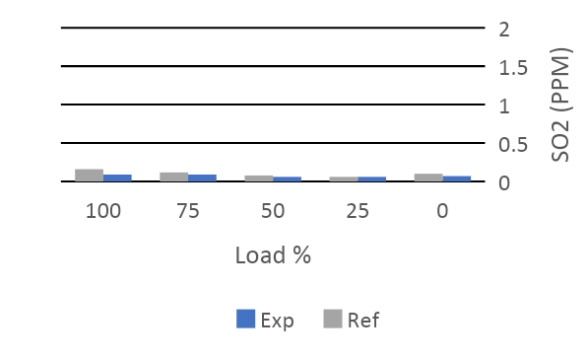

Figure 6 validation of SO_2 measurement [29]

RESULTS AND DISCUSSIONS

According to the generator test, we began our experiment by monitoring the exhaust of the main engine of the Aida IV ship using its primary system of fuel, Marine Diesel Oil (MDO). We let the engine run for 40 minutes to warm up before increasing the load to 85%, This is the ship's primary load while sailing, and then we started to measures the emissions (carbo di-oxide CO2, nitrogen oxide NOx, slufer oxide SOx, hydrocarbon HC, particular matter PM10, and carbon The volume of exhaust produced by MDO is displayed in Table 3.

Table 3 emission emitted by MDO

Engine fuel	**Load 85% (KW)**	**Fuel consumptions**	**Engine emission factor**					
		MDO(m3/hr)	**NO_x**	**SO_x**	**CO_2**	**PM_{10}**	**HC**	**Co**
Diesel engine	2261	0.37	4.9	0.94	254.5	0.2	0.19	0.6

Using alternative fuel (LNG)

Ventilation systems, storage bottles with supply lines, gas monitoring systems with alarm to detectors any LNG leakage, and numerous parts (such as valves, fuel injectors, etc.) must be replaced or added. Liquefied natural gas (LNG) was used to start the engine, and after 45 minutes, the reading remained steady as indicated in Table 4.

Table 4 emission emitted by LNG

Engine fuel	**Load 85% (KW)**	**Fuel consumptions**	**Engine emission factor**				
		LNG (m3/hr)	**NO_x**	**SO_x**	**CO_2**	**PM_{10}**	**HC**
LNG engine	2261	450.7	0.95	0.098	204.3	0.0055	0.33

Using reduction technology

Selective Catalytic Reduction (SCR) technology uses a straightforward chemical procedure to neutralize NOx in the exhaust. The catalyst makes it easier for NOx to interact with a reducing substance, like ammonia, in an exhaust stream at the comparatively low temperatures. The nitrogen oxides in the exhaust gases are chemically reacted with when a water and urea solution is injected into the exhaust line [30]. The high emission temperature leads the solution to evaporate. The dangerous substances in exhaust fumes are converted by a catalytic converter into innocuous water vapor and harmless nitrogen gas. A titanium and vanadium catalyst and a nozzle that spray urea water over the catalyst's top side make up the SCR system, as depicted in (fig 7). Up to 99 percent of NOx emissions can be removed by the highly effective SCR technologyThe technique has been widely used to reduce NOx emissions from power plants and has become the industry standard for removing NOx emissions from transportation engines. SCR has been used in maritime applications since the 1990s and has emerged as one of the most popular technologies [31].

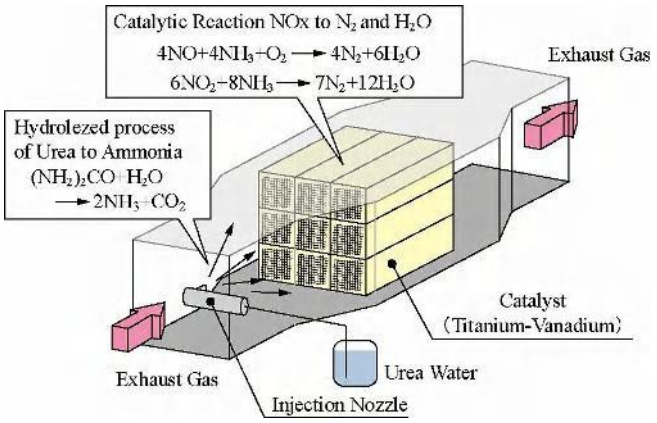

Figure 7 SCR system

The design flowchart for the SCR system is shown in Figure 8. Temperature, NOx content of exhaust gas, and flow rate are required as design criteria for the SCR system. We used assumed values to assess the SCR performance because certain data couldn't be acquired because of the early design stage [32]. The space velocity (SV), which is based on the ratio of catalyst volume (m3) to exhaust gas flow rate (m3/h), is calculated at 12000 h-1 at rated

power. The diameter of the emission tube and the available experimental space influence the number and length of catalysts. The SCR's expected performance and characteristics are listed in Table 5.

Table 5 Predicted performance and characteristics of SCR

Catalytic Type	Vanadium - Titanium
Number	8
Size	60x60x90mm
Cell /MeshNum.	20 / 1
Number	8
Velocity (SV)	12000h^{-1}
Flow Rate (Urea)	25~ 50 mL/min
Mixture	40% Urea Water
NOx conversionrate	60~ 65% (at 65.5% of equivalent ratio)
Solution	45%UreaWater
Catalytic Type	Vanadium - Titanium

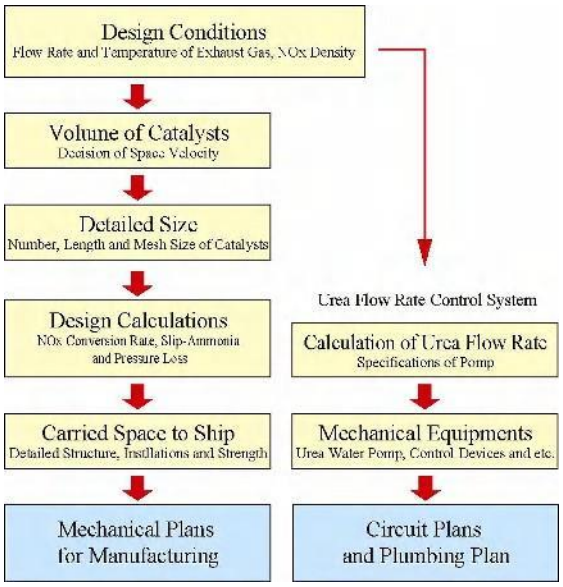

Figure 8 design flowchart for the SCR system

To achieve IMO tier3 NOx restrictions by reducing the amount of NOx in Aida IV ships utilizing (MDO + SCR) The connection between the ship's main engine and the selective catalytic reduction (SCR) is shown in (Fig 9) On the upper side of the engine, in the straight section of the exhaust pipe, are a urea injection nozzle and a catalyst case. The space between the catalysts and the nozzle needs to be as large as possible to allow ample time for urea to be converted to ammonia. However, because of the length of the exhaust tube and the limited amount of available space in the engine room, the nozzle and catalysts must both be positioned in the 1 m's straight section.

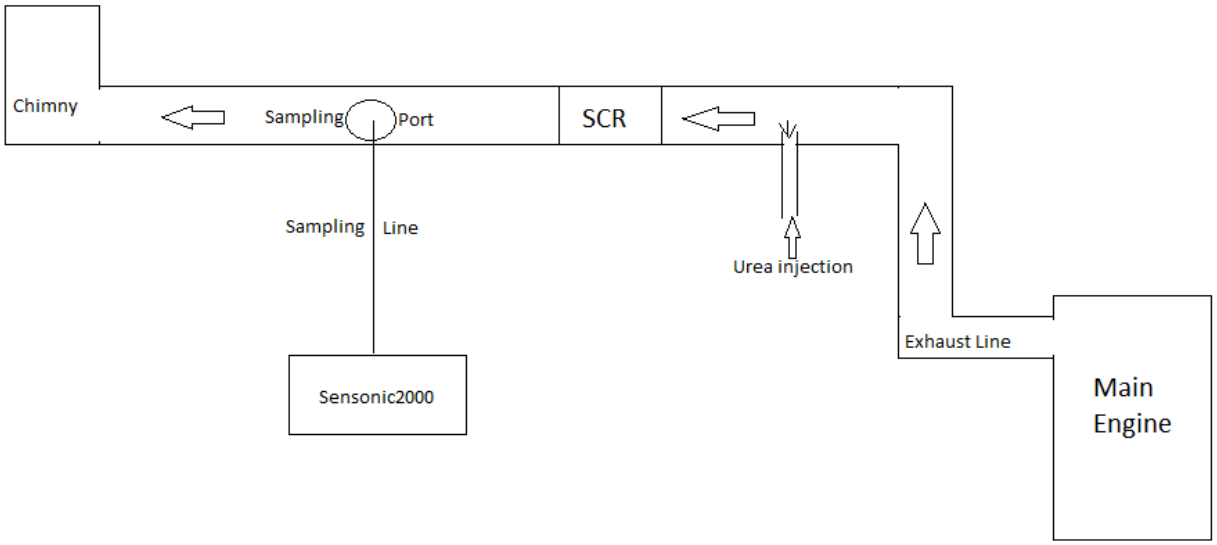

Figure 9 SCR rig

We tested the urea nozzle before installing the SCR to make sure it functions flawlessly and to check all the characteristics of the diesel engine.

Engine fuel	Load 85% (KW)	fuel consumption	Engine emission factor					
		MDO(m 3/hr)	No_x	So_x	CO_2	PM_{10}	HC	CO
MDO	2261	0.37	4.9	0.94	25 4.5	0.2	0.19	0.6
LNG		450.7	0.95	0.098	20 4.3	0.0055	0.33	0.2
MDO+ SCR			0.58 8	0.063	25 4.5	0.0023	0.19	0.6

Table 6 displays the emissions produced by the main engine of the Aida IV ship using both reduction methods and standard ship systems (LNG, MDO+SCR, and MDO).

According to (fig 10), the main engine of the Aida IV ship's emissions of nitrogen oxides (NOx), sulfur oxides (SOx), carbo di-oxide (CO2), particulate matter (PM10), hydrocarbons (HC), and carbon monoxide (CO) were reduced by a percentage by using various types of alternative fuels, which are represented Liquefied natural gas (LNG), which is represented in this work by selective catalytic reduction (MDO+SCR), and reduction technology.

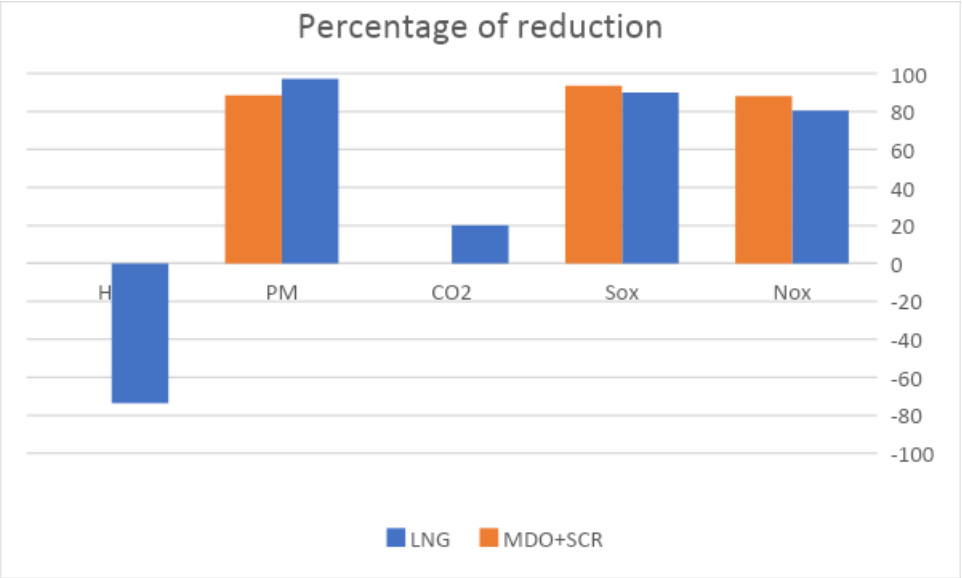

figure 10 the percentage of reduction

From an economic standpoint, we discovered that LNG is substantially less effective than marine diesel oil with selective catalytic reduction (MDO+SCR). Due to the high rate of consumption of LNG, engines must be modified to include new valves, pistons, compressors, pipe lines, and fuel injectors. Additionally, Bottle storage space and alarm-equipped detectors are required for safety. Furthermore, maritime diesel fuel with selective catalytic reduction has an inexpensive consumption rate, and the most straightforward and inexpensive method to use it without modifying the engine is to add an SCR system to the exhaust line. Furthermore, as demonstrated in this paper, there aren't as many differences between them in terms of emission.

Acknowledgements

The Arab Academy for Science, Technology, and Maritime Transport's support is acknowledged by the writers, who also like to express their gratitude. The workshops and lab with all engineers and technicians who support and supply safety equipment for this experimental project.

Conclusions

Ship emissions, which have a negative impact on the marine ecosystem, are one of the most urgent concerns among those working in the maritime industry. The current study looked at various methods that could be used to reduce those emissions, including alternative fuels like liquefied natural gas (LNG) and reduction technologies like selective catalytic reduction (MDO+SCR), which is the most widely used. However, as shown in this study, there are requirements to use one of these techniques, including cost, main engine free space, and time. We discovered that MDO+SCR is the more effective technology as a training and supply ship after conducting our trial on the Aida IV ship. Due to their impact on the environment, the experiment examined the levels of nitrogen oxides (NOx), carbon monoxide (CO), and sulfur dioxide (SO2). However, in order to adhere to IMO standards and the obligation to reduce ship emissions by 50% by 2030, equivalent to 2008, the study includes Selective Catalytic Reduction (SCR) into the exhaust line to reduce Nitrogen Oxide (NOx) emissions. The experiment shows that large emission reduction percentages can be achieved on board ships by using marine diesel oil (MDO) with low sulphur and the Selective Catalytic Reduction (SCR) as a treatment method. The MDO + SCR system can

also be upgraded with a sea water scrubber system to further reduce sulphur oxide SOx levels and achieve further emission reductions.

References

[1] L. Huang, Y. Wen, X. Geng, C. Zhou, C. Xiao, Integrating multi-source maritime information to estimate ship exhaust emissions under wind, wave and current conditions, Transp. Res. Part D Transp. Environ. 59 (2018) 148–159. https://doi.org/10.1016/j.trd.2017.12.012.

[2] P.S. Yau, S.C. Lee, Y. Cheng, Y. Huang, S.C. Lai, X.H. Xu, Contribution of ship emissions to the fine particulate in the community near an international port in Hong Kong, Atmos. Res. 124 (2013) 61–72. https://doi.org/10.1016/j.atmosres.2012.12.009.

[3] S. Woo, W. Kim, J. Lee, K. Lee, Fuel properties of water emulsion fuel prepared using porous membrane method for low pollutant engine at various temperatures, Energy Reports. 7 (2021) 6638–6650. https://doi.org/10.1016/j.egyr.2021.09.082.

[4] M. Latarche, Explaining the types of fuel used on ships, ShipInsight. (2017) 1–11. https://shipinsight.com/articles/explaining-the-types-of-fuel-used-on-ships.

[5] J. Verschuur, E.E. Koks, J.W. Hall, Global economic impacts of COVID-19 lockdown measures stand out in highfrequency shipping data, PLoS One. 16 (2021) 1–16. https://doi.org/10.1371/journal.pone.0248818.

[6] E.S. Han, A. goleman, daniel; boyatzis, Richard; Mckee, Review of Maritime Transport 2020, 2020. https://unctad.org/system/files/official-document/rmt2020_en.pdf.

[7] B. Beškovnik, M. Zanne, M. Golnar, Dynamic Changes in Port Logistics Caused by the COVID-19 Pandemic, J. Mar. Sci. Eng. 10 (2022). https://doi.org/10.3390/jmse10101473.

[8] B. Zondag, P. Bucci, P. Gützkow, G. de Jong, Port competition modeling including maritime, port, and hinterland characteristics, Marit. Policy Manag. 37 (2010) 179–194. https://doi.org/10.1080/03088831003700579.

[9] D. Hummels, L. Puzzello, Trade and the Greenhouse Gas Emissions from Anca Cristea , University of Oregon, (2011) 1–47.

[10] M. Lenzen, A. Geschke, M.D. Abd Rahman, Y. Xiao, J. Fry, R. Reyes, E. Dietzenbacher, S. Inomata, K. Kanemoto, B. Los, D. Moran, H. Schulte in den Bäumen, A. Tukker, T. Walmsley, T. Wiedmann, R. Wood, N. Yamano, The Global MRIO Lab–charting the world economy, Econ. Syst. Res. 29 (2017) 158–186. https://doi.org/10.1080/09535314.2017.1301887.

[11] D. Kim, H. Ahn, W. Yang, K.Y. Huh, Y. Lee, Experimental analysis of CO/H2 syngas with NOx and SOx reactions in pressurized oxy-fuel combustion, Energy. 219 (2021) 119550. https://doi.org/10.1016/j.energy.2020.119550.

[12] H. Zan, X. Chen, J. Ma, D. Liu, Y. Wu, Experimental Study of NO xFormation in a High-Steam Atmosphere during a Pressurized Oxygen-Fuel Combustion Process, ACS Omega. 5 (2020) 16037–16044. https://doi.org/10.1021/acsomega.0c01480.

[13] N.N. Choudhury, B. Padak, An investigation of the interaction between NOx and SOx in oxy-combustion, Environ. Sci. Technol. 51 (2017) 12918–12924. https://doi.org/10.1021/acs.est.7b02064.

[14] L. Ying, Marine diesel engine energy saving and emission reduction technology, IOP Conf. Ser. Earth Environ. Sci. 242 (2019). https://doi.org/10.1088/1755-

1315/242/5/052039.

[15] D. Agarwal, S. Sinha, A.K. Agarwal, Experimental investigation of control of NOx emissions in biodiesel-fueled compression ignition engine, Renew. Energy. 31 (2006) 2356–2369. https://doi.org/10.1016/j.renene.2005.12.003.

[16] L. Johansson, J.P. Jalkanen, J. Kalli, J. Kukkonen, The evolution of shipping emissions and the costs of regulation changes in the northern EU area, Atmos. Chem. Phys. 13 (2013) 11375–11389. https://doi.org/10.5194/acp-13-11375-2013.

[17] K. Andersson, H. Winnes, Environmental trade-offs in nitrogen oxide removal from ship engine exhausts, in: Proc. Inst. Mech. Eng. Part M J. Eng. Marit. Environ., 2011. https://doi.org/10.1243/14750902JEME223.

[18] S. Bengtsson, K. Andersson, E. Fridell, A comparative life cycle assessment of marine fuels: Liquefied natural gas and three other fossil fuels, Proc. Inst. Mech. Eng. Part M J. Eng. Marit. Environ. 225 (2011) 97–110. https://doi.org/10.1177/1475090211402136.

[19] A. Andreasen, S. Mayer, Use of seawater scrubbing for SO2 removal from marine engine exhaust gas, Energy and Fuels. 21 (2007) 3274–3279. https://doi.org/10.1021/ef700359w.

[20] A.A. Banawan, M.M. El Gohary, I.S. Sadek, Environmental and economical benefits of changing from marine diesel oil to natural-gas fuel for short-voyage high-power passenger ships, Proc. Inst. Mech. Eng. Part M J. Eng. Marit. Environ. 224 (2010) 103–113. https://doi.org/10.1243/14750902JEME181.

[21] M.I. Lamas, C.G. Rodríguez, Emissions from marine engines and NOx reduction methods, J. Marit. Res. 9 (2012) 77–82.

[22] L. Ying, Marine diesel engine energy saving and emission reduction technology, in: IOP Conf. Ser. Earth Environ. Sci., Institute of Physics Publishing, 2019: p. 052039. https://doi.org/10.1088/1755-1315/242/5/052039.

[23] M.I. Lamas, C.G. Rodríguez, J.D. Rodríguez, J. Telmo, Internal modifications to reduce pollutant emissions from marine engines. A numerical approach, Int. J. Nav. Archit. Ocean Eng. 5 (2013) 493–501. https://doi.org/10.2478/IJNAOE-2013-0148.

[24] K. Andersson, H. Winnes, Environmental trade-offs in nitrogen oxide removal from ship engine exhausts, in: Proc. Inst. Mech. Eng. Part M J. Eng. Marit. Environ., SAGE PublicationsSage UK: London, England, 2011. https://doi.org/10.1243/14750902JEME223.

[25] A.A. Banawan, M. Mosleh, I.S. Seddiek, Prediction of the fuel saving and emissions reduction by decreasing speed of a catamaran, J. Mar. Eng. Technol. 12 (2013) 40–48. https://doi.org/10.1080/20464177.2013.11020287.

[26] I.S. Seddiek, Application of fuel-saving strategies onboard high-speed passenger ships, J. Mar. Sci. Technol. 21 (2016) 493–500. https://doi.org/10.1007/s00773-016-0371-4.

[27] M.M. Elgohary, I.S. Seddiek, A.M. Salem, Overview of alternative fuels with emphasis on the potential of liquefied natural gas as future marine fuel, Proc. Inst. Mech. Eng. Part M J. Eng. Marit. Environ. 229 (2015) 365–375. https://doi.org/10.1177/1475090214522778.

[28] D. Gritsenko, J. Yliskylä-Peuralaht, Governing shipping externalities: Baltic ports in the process of SOx emission reduction, Marit. Stud. 12 (2013) 1–21. https://doi.org/10.1186/2212-9790-12-10.

[29] M. Durmaz, S. Ergin, Experimental Study on the Effects of Ultra-Low Sulfur Diesel Fuel

to the Exhaust Emissions of a Ferry Fire Safety of Ships View project Underwater Acoustics-Flow Noise View project, n.d. https://www.researchgate.net/publication/320215729.

[30] S. Yang, X. Pan, Z. Han, D. Zhao, B. Liu, D. Zheng, Z. Yan, Removal of NOx and SO2 from simulated ship emissions using wet scrubbing based on seawater electrolysis technology, Chem. Eng. J. 331 (2018) 8–15. https://doi.org/10.1016/j.cej.2017.08.083.

[31] L. Bilgili, U.B. Celebi, Developing a new green ship approach for flue gas emission estimation of bulk carriers, Meas. J. Int. Meas. Confed. 120 (2018) 121–127. https://doi.org/10.1016/j.measurement.2018.02.002.

[32] S. Kouravand, A.M. Kermani, Clean power production by simultaneous reduction of NOx and SOx contaminants using Mazut Nano-Emulsion and wet flue gas desulfurization, J. Clean. Prod. 201 (2018) 229–235. https://doi.org/10.1016/j.jclepro.2018.08.017.

Sustainable techniques of retrofitting non-ductile reinforced concrete beam-to-column joints subjected to cyclic loading

Manal Wael[1, a], Sally Hosny[1], Ehab Lotfy[1] and Erfan Abd El Latif[1]

[1]Department of Civil Engineering, Suez Canal University, Ismailia, Egypt

[a]UGS.160071@eng.suez.edu.eg

Keywords: Engineered cementitious composites, External fiber reinforced polymer wrapping, Steel jacketing, life cycle assessment, SimaPro®

Abstract. Existing reinforced concrete (RC) structures may need to be repaired or strengthened as a consequence of material deterioration, changes in usage, new building codes, or new design requirements. The experience of past earthquakes has shown that the beam-to-column joints in moment frames are one of the key members in the path of lateral load transfer and their poor performance results in the total collapse of the building. Hence, retrofitting of existing buildings has become a prominent activity in the construction sector. This study aims to select an eco-friendly strengthening method for non-ductile beam-column joints. Three methods have been proposed, 1-CFRP grid and engineered cementitious composites (ECC), 2-External fiber reinforced polymer wrapping (EBR) and steel anchor bolts, and 3-Steel jacketing. The paper aims to assess the environmental impacts of these three methods using life cycle assessment (LCA). The analyses are carried out using SimaPro® considering a cradle-to-gate system boundary. The results indicate that the primary environmental burden is associated with using external fiber reinforced polymer wrapping sheets (EBR) and steel anchor bolts, concerning aspects such as human health, ecosystem quality, and climate change. Steel jacketing (The steel plates and anchor bolts) solution has the lowest impact on climate change. It is crucial to emphasize that the decision-making of designers has to depend not only on mechanical performance and cost but also considering environmentally sustainable strategies.

Introduction

In recent years, numerous studies have been focused on assessing the global environmental impacts in both developed and developing countries [1,2]. The gradual accumulation of greenhouse gases (such as CO2, CH4, N2O) in the atmosphere is the underlying cause of global warming, which has the potential for diverse repercussions on a global scale [3]. Consequently, it is crucial for future generations to prioritize sustainable development practices across all sectors to prevent detrimental effects on the environment [4]. To achieve the goal of sustainability, a multidisciplinary strategy encompassing various aspects is essential. This includes reducing energy consumption, maximizing material utilization, promoting material recycling, and implementing effective emission control measures[5].

- The seismic activity is widely recognized as the greatest threat to structures, often resulting in substantial destruction. When it comes to retrofitting operations, the decision-making process should be approached as a multi-objective, multi-criteria optimization complex problem.[6]. Indeed, as reported the best technique should be chosen by considering several matters such as energy consumption, economics, technical and environmental factors, relevant regulations, and social effects, while the overall process of a construction retrofit could be divided into three main steps. The first step consists of a structural analysis of a facility to assess capacity and identify the strengthening solution aimed at extending its lifetime. In the second step, these retrofit techniques should be evaluated using appropriate criteria, with given consideration to financial, environmental, social, and structural factors [7,8].
- The selection of the ideal retrofit solution is the third and last phase. If this strategy is pursued, structural and sustainability requirements are both implemented throughout the retrofit process.

Designers usually consider a small number of factors while making decisions such as cost, the performance of the structure, the installation's speed, the Period of suspension, and the strategies for maintenance's feasibility. Due to the complexity of evaluating some factors, designers hardly ever consider environmental consequences when making decisions.

The life-cycle assessment (LCA) is a decision-making support tool in the building industry, which provides an account of the materials and energy used in a product and evaluates the associated environmental impact [9].

LCAs have been used in the construction sector for twenty years [10–12], two different strategies have been used when applying an LCA [13,14]: bottom-up LCA for various building material and component combinations, and top-down LCA for the entire construction process [6].

LCA Methodology

The LCA takes into account a product's complete life cycle, from the extraction and acquisition of raw materials (through energy and material production and manufacturing) to usage and end-of-life disposal [15]. The LCA has the chance to examine the environmental effect of a facility across its many life-cycle stages thanks to this analytical approach. The LCA methodology is increasingly being applied to the construction industry in order to quantify the impacts of energy use, CO2 emissions, the use of renewable and non-renewable resources, and the emission of organic and non-organic materials.

Given these features, an environmental impact assessment in the construction industry using LCA could be usefully adopted for the development of databases and tools to track the effects of various systems, technologies, and processes, the selection of construction materials, and assessing construction procedures and systems [16].

The LCA is part of ISO 14040:2006 (Environmental management—life-cycle assessment—principles and framework) [15] and ISO 14044:2006 (Environmental management—life-cycle assessment—requirements and guidelines) [17]. The methodology is an iterative technique and consists of four main steps, as reported in Fig.1: (a) Definition of goal and scope, (b) Life-cycle inventory (LCI), (c) Life-cycle impact assessment (LCIA), and (d) The results interpretation.

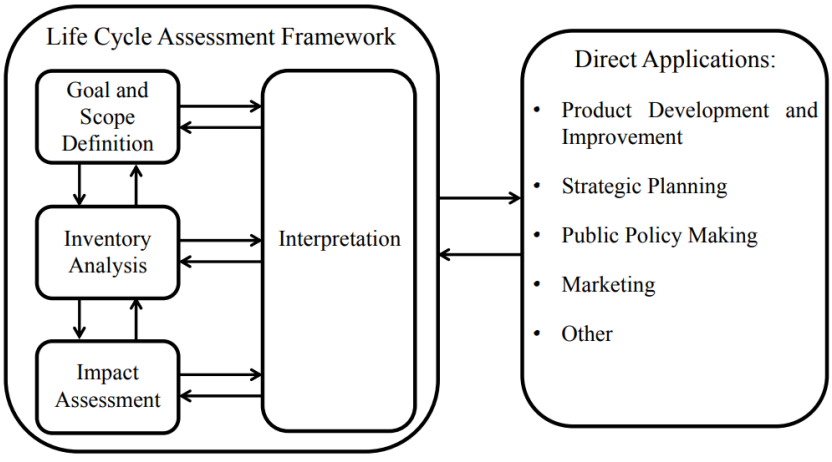

Fig. 1. Phases and applications of a life-cycle assessment (LCA) (based on ISO 14040, 2006) [15].

Goal and Scope

The scope and goal phase defines the purpose of the study, its application, the products to be used,

the system boundaries, and the functional unit. The functional unit is an essential step that enables the comparison and analysis of different products and services. In this research, the LCA

methodology described is implemented in a case study of the sustainability of three retrofit techniques in three exterior beam–column joints through using 1-CFRP grid and engineered cementitious composites (ECC), 2-External fiber reinforced polymer wrapping (EBR) and steel anchor bolts, and 3-Steel jacketing, and the function unit in this research is the amount of each material needed for a beam-column joint to reach a capacity of 27 KN.

- **Life-Cycle Inventory**

In the LCI phase, all environmental inputs at each stage of the life cycle are thoroughly described in Table 1. Therefore, the LCA practitioner evaluates emissions and resource consumption throughout the entire life cycle of the product (from "cradle to grave").

- **Life-Cycle Impact Assessment**

In the LCIA phase, all environmental impacts and resource usage are quantified. The LCIA aims to assess the corresponding environmental impact based on the findings of the prior phase. LCI results are categorized into impact categories (such as climate change, toxicological stress, noise, and land use) in accordance with ISO 14042 [18], Impact categories (such as climate change, toxicological stress, noise, and land use) are used to categorize LCI results.

- **Interpretation**

The life-cycle phases and the products with the most environmental impact are found in the final step, which is the interpretation of the findings. Overall, every stage of an LCA involves life-cycle interpretations. Thus, if two product alternatives are compared, a practitioner will be able to decide which is the best option following the LCI phase. LCA is a relative methodology that is dependent on the functional unit of choice. In fact, the functional unit affects every input and output during the LCI stage, which in turn affects the outcomes of the LCIA.

Table 1. Life-cycle inventory (LCI) of the studied cases.

Material	Retrofitting type		
	CFRP grid and ECC	CFRP sheets and anchor bolts	Steel plates and anchor bolts
Cement (Kg)	123.86056	125.34430	125.34430
Sand (Kg)	139.40826	140.14189	140.14189
Aggregate (Kg)	276.36864	307.44170	307.44170
Water (Kg)	55.77694	52.00070	52.00070
Steel (Kg)	22.44	22.44	22.44
Fly ash (Kg)	4.34072	-	-
Polycarboxylic superplasticizer (Kg)	0.06511	-	-
Hydroxypropyl methylcellulose (Kg)	0.04341	-	-
Defoamer (Kg)	0.02169	-	-
PVA (Polyvinyl alcohol) fibers (Kg)	1.01568	-	-
CFRP (Kg)	0.05094	0.04429	-
Epoxy (Kg)	1.60820	3.44040	0.1
Steel plates (Kg)	-	-	0.0022182865
Anchor bolts (Kg)	-	0.823	1.45
Diesel (Litre)	0.130030555	0.1469585	0.1469585
Failure load	27 KN		
Transportation	Truck 16 t		
	Distance to plant		
Cement factory	126		Km
Sand quarry	67.9		Km
Aggregate quarry	144		Km
Steel factory	68		Km
Concrete addmixtures factory	99		Km
CFRP factory	99		Km
Epoxy factory	99		Km

Retrofit Strategies

This study aims to compare the environmental impact of materials and processes related to the three options set out above, with a cradle-to-gate system boundary. This system boundary allows a partial assessment that takes into consideration environmental impacts from the resource extraction to the installation phase [19].

The specimens were fabricated using deformed bars which were used as stirrups and main reinforcements. The height of the column is 2050 mm and the cross-sectional area is 230 × 230 mm^2 as shown in Fig. 2. Each column is reinforced with six 10-mm diameter longitudinal rebars.

The stirrup spacing was 50 mm at the loading and support areas and 100 mm near the joint. The length of the beam is 1550 mm and the cross-section is 230 (width) × 330 mm (depth).

The beam is reinforced with eight 10-mm diameter longitudinal rebars (four at the bottom and four at the top). The stirrup spacing is 133 mm for the entire beam except for the support (the end of the beam where the spacing is only 50 mm). The stirrups in both beam and column are 6-mm diameter bars. The specimen's concrete cover thickness is 30 mm for both the beam and column. The mechanical properties of all the used materials are listed in Table 2.

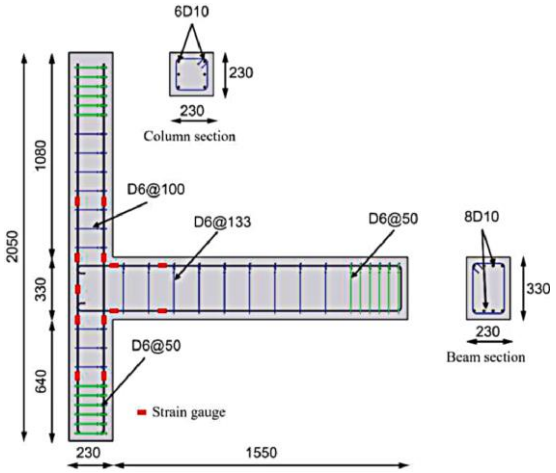

Fig. 2. Specimen detailing.

Table 2. Materials properties.

Material	Yield strength	Compressive Strength (Mpa)	Tensile Strength (Mpa)	Elastic Modulus (Mpa)	Thickness (mm)
Concrete	-	26.13	-	-	-
Main Reinforcement	400	-	-	-	-
Stirrups	300	-	-	-	-
Anchor bolts	400	-	-	-	-
Steel Plates	400	-	-	-	16
ECC	-	47.5	2.43	15451	30
CFRP	-	-	3650	238000	0.13
Epoxy Sika330	-	-	30	3800	1

Three retrofitting types were applied to the specimens. The specimen with type "CFRP grid and ECC" [20] is obtained by removing the concrete cover on all sides of the joint plus the two side covers of the beam and column. Then, two layers of X-shaped CFRP grid were placed on three faces of the columns, then two layers of L-shaped CFRP grid were placed on the fourth face of the column and the top and bottom face of the beam. Finally, ECC was cast into the specimen.

The specimen with type "EBR" [21] is obtained by wrapping the specimen with two layers of CFRP sheets. In addition to four steel anchor bolts on two sides of the column with 12 mm diameter, and 100 mm length.

The specimen with type "Steel Jacketing" [22] is obtained by using steel plates with 16 mm thickness and steel anchor bolts with 12 mm diameter and 120 mm length. The retrofitting schemes are shown in Fig. 3.

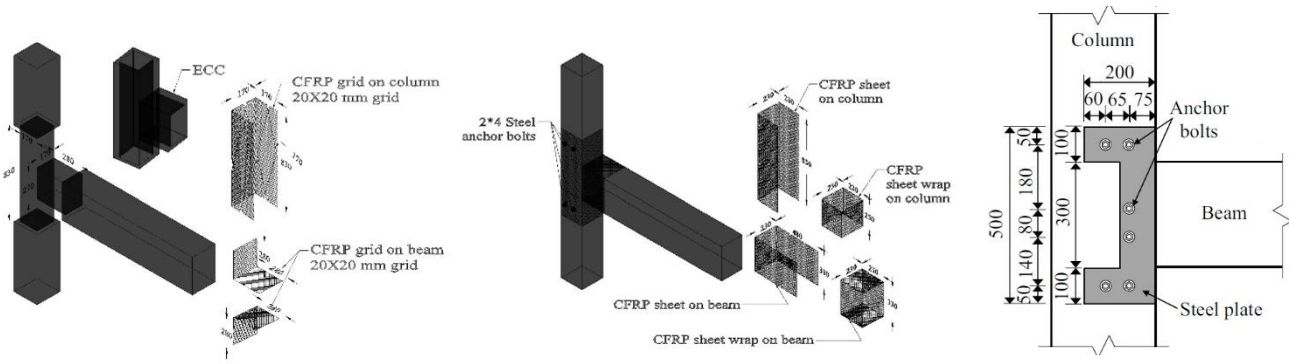

(b) (c)

Fig. 3. a: Details of CFRP grid and ECC retrofitting technique, b: Details of CFRP and steel anchor bolts retrofitting technique, c: Details of steel jacketing retrofitting technique.

Life-Cycle Assessment of the Strengthening Strategies

Fig. 4 shows the LCIA of the CFRP grid and ECC solution [23]. The cement, reinforcing steel and epoxy resin have the highest impact on both global warming and non-renewable energy, while the cement and reinforcing steel have the highest impact on human health due their effect on respiratory inorganic.

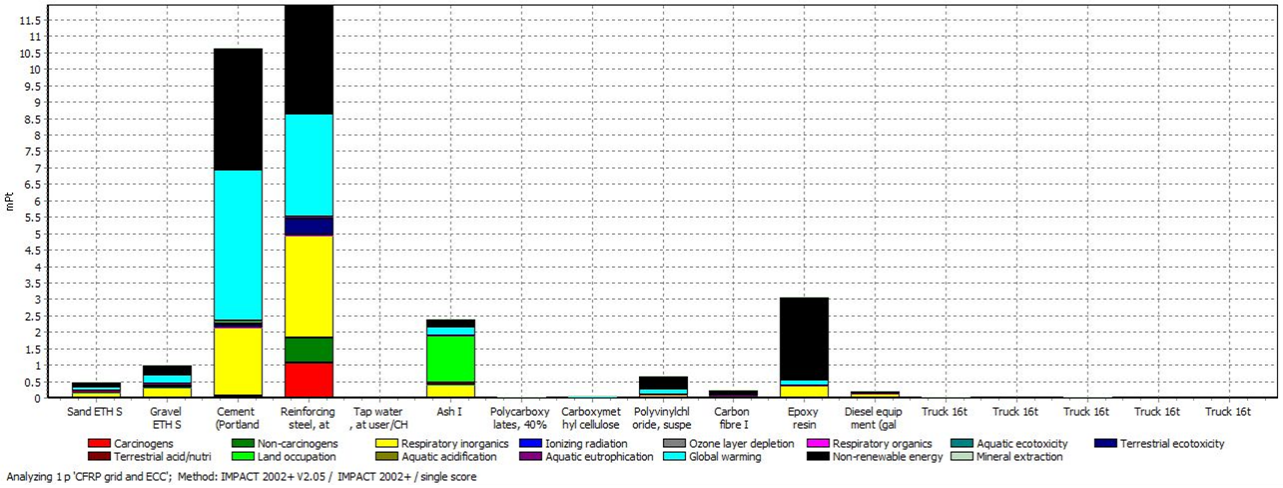

Fig. 4. Life-cycle assesment of "CFRP grid and ECC" retrofit strategy.

Note: X-Axis represents the environmental impact of every used material, and Y-Axis represents the magnetic particle tracking

The environmental results following the CFRP sheets and anchor bolts strategy are reported in Fig. 5. The cement and reinforcing steel strategy have the highest impact on global warming and respiratory inorganic which increase the respiratory inorganic effect with approximately 20% compared to the other two strategies due to the amount of cement. On the other hand, the cement and reinforcing steel have the same high impact on non-renewable energy as the CFRP grid and ECC strategy, while the epoxy resin has the highest non-renewable energy impact of all the retrofit strategies.

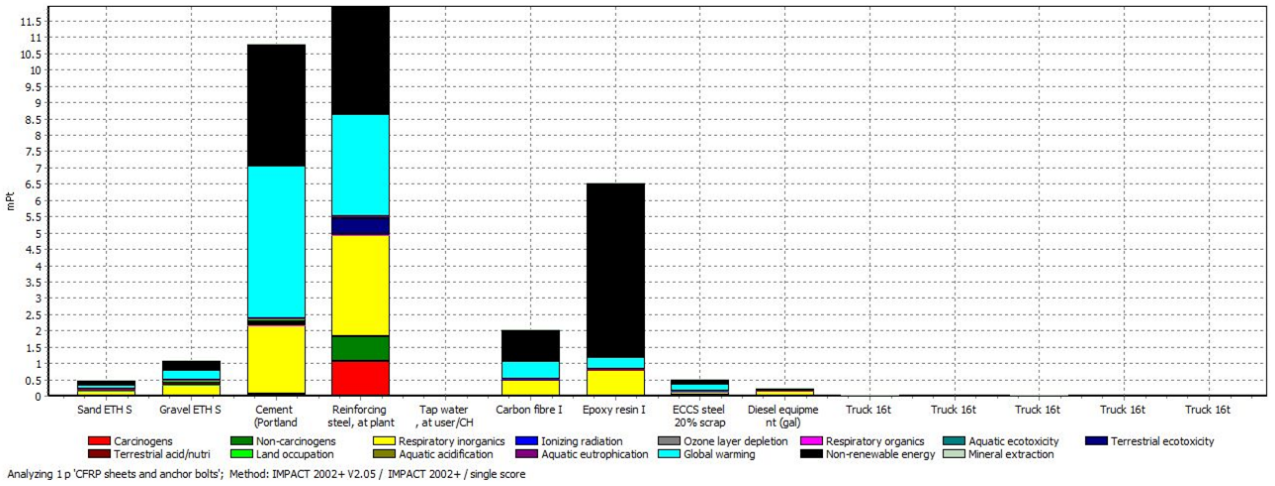

Fig. 5. Life-cycle assesment of "CFRP sheets and steel anchor bolts" retrofit strategy.

Note: X-Axis represents the environmental impact of every used material, and Y-Axis represents the magnetic particle tracking

Fig. 6 shows the LCIA related to the steel plates and anchor bolts strategy. For this strengthening technique, the environmental results reveal high impact on both global warming and non-renewable energy. These environmental effects are due to the amount of concrete and steel reinforcement carried out.

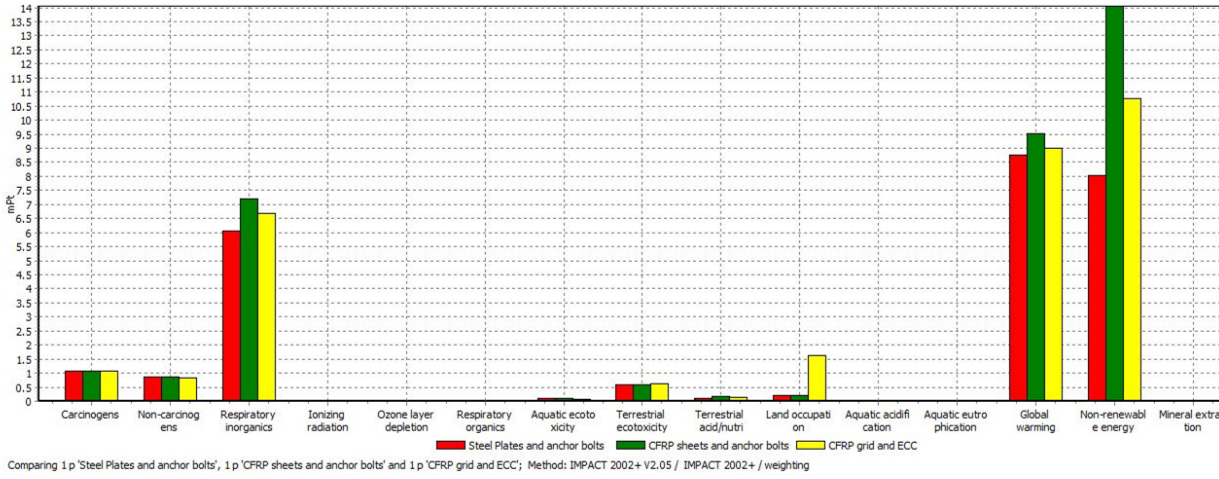

Fig. 6. Life-cycle assesment of "steel plates and anchor bolts" retrofit strategy.

Note: X-Axis represents the environmental impact of every used material, and Y-Axis represents the magnetic particle track

Fig. 7 shows the LCIA of the studied solutions. The environmental results following the CFRP sheets and anchor bolts strategy has the greatest environmental impact that matches same results [24], which affects respiratory inorganics, global warming, and non-renewable energy, while the environmental results related to the steel plates and anchor bolts strategy has the least environmental impact on global warming, non-renewable energy, and respiratory inorganics.

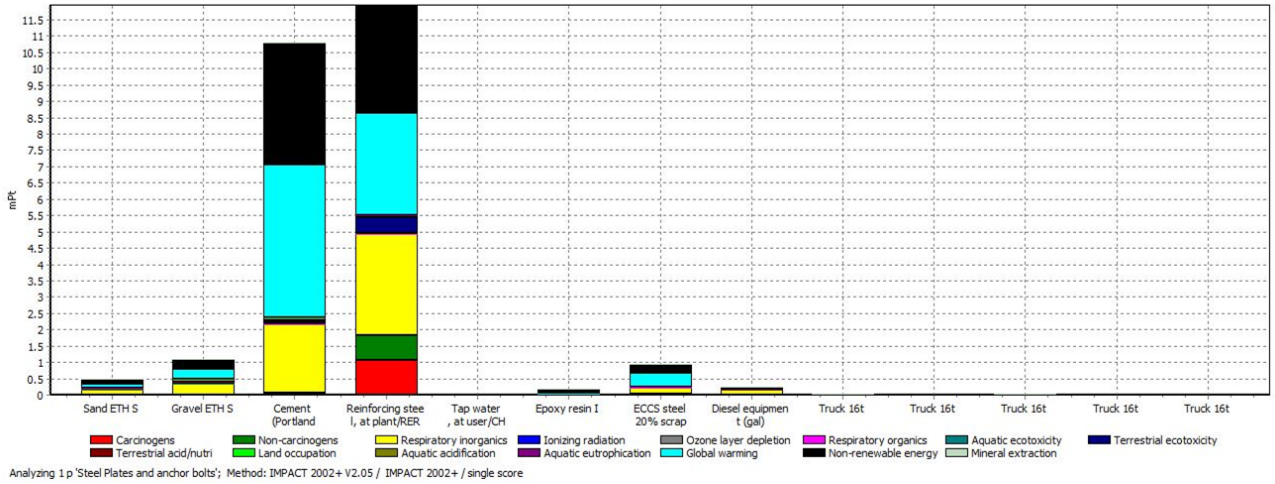

Fig. 7. Life-cycle assessment comparative analysis of the retrofit strategies.

Note: X-Axis represents the environmental impact of every used material, and Y-Axis represents the magnetic particle tracking

Conclusion

It can be concluded that the major environmental load is related to the CFRP sheets and anchor bolts strengthening solution. In particular, the CFRP sheets and anchor bolts strategy has the highest environmental burden in terms of human health, ecosystem quality and climate change. Finally, the steel jacketing strategy has the lowest impact on all the damage categories. Data obtained from these environmental analyses are related to this case study alone and cannot be extended to other scenarios. In fact, the environmental impact depends on several factors such as the vulnerability of the facility, the seismic hazard of the building site and the databases used. Overall, it's important to point out that this kind of outcome raises designers' awareness of the most ecologically friendly retrofit technique. Other considerations, such costs and the social impact, have to be considered during the decision-making process for the strengthening procedures.

References

[1] M. Dijk, I. Blom, T. Salet, and P. Marinus, “Environmental impact as a parameter in concrete structure parametric associative models,” *Constr Build Mater*, vol. 67, no. PART C, pp. 360–365, Sep. 2014, doi: 10.1016/j.conbuildmat.2014.01.006.

[2] Y. Pamu and S. Alugubelli, “A comparative study of environmental impacts due to conventional and sustainable concrete,” *Mater Today Proc*, 2023, doi: 10.1016/j.matpr.2023.03.817.

[3] H. H. Ghayeb, H. A. Razak, and N. H. R. Sulong, “Evaluation of the CO2 emissions of an innovative composite precast concrete structure building frame,” *J Clean Prod*, vol. 242, Jan. 2020, doi: 10.1016/j.jclepro.2019.118567.

[4] L. Guardigli, F. Monari, and M. A. Bragadin, “Assessing environmental impact of green buildings through LCA methods:Acomparison between reinforced concrete and wood structures in the European context,” in *Procedia Engineering*, Elsevier Ltd, 2011, pp. 1199–1206. doi: 10.1016/j.proeng.2011.11.2131.

[5] M. Asif, T. Muneer, and R. Kelley, “Life cycle assessment: A case study of a dwelling home in Scotland,” *Build Environ*, vol. 42, no. 3, pp. 1391–1394, Mar. 2007, doi: 10.1016/j.buildenv.2005.11.023.

[6] C. Menna, D. Asprone, F. Jalayer, A. Prota, and G. Manfredi, “Assessment of ecological sustainability of a building subjected to potential seismic events during its lifetime,” *International Journal of Life Cycle Assessment*, vol. 18, no. 2, pp. 504–515, Feb. 2013, doi: 10.1007/s11367-012-0477-9.

[7] S. Stefanidou, "Optimum selection of bridge pier retrofit measures considering performance, cost and sustainability criteria," *Structures*, vol. 53, pp. 98–108, Jul. 2023, doi: 10.1016/j.istruc.2023.04.052.
[8] J. A. Dauda and S. O. Ajayi, "Understanding the impediments to sustainable structural retrofit of existing buildings in the UK," *Journal of Building Engineering*, vol. 60, Nov. 2022, doi: 10.1016/j.jobe.2022.105168.
[9] M. M. Khasreen, P. F. G. Banfill, and G. F. Menzies, "Life-cycle assessment and the environmental impact of buildings: A review," *Sustainability*, vol. 1, no. 3, pp. 674–701, 2009, doi: 10.3390/su1030674.
[10] V. Montoro Taborianski and R. Prado, "Comparative evaluation of the contribution of residential water heating systems to the variation of greenhouse gases stock in the atmosphere," *Building and Environment - BLDG ENVIRON*, vol. 39, pp. 645–652, Jun. 2004, doi: 10.1016/j.buildenv.2003.12.007.
[11] L. Gustavsson and R. Sathre, "Variability in energy and carbon dioxide balances of wood and concrete building materials," *Build Environ*, vol. 41, pp. 940–951, Jul. 2006, doi: 10.1016/j.buildenv.2005.04.008.
[12] R. Mora, G. Bitsuamlak, and M. Horvat, "Integrated life-cycle design of building enclosures," *Build Environ*, vol. 46, pp. 1469–1479, Jul. 2011, doi: 10.1016/j.buildenv.2011.01.018.
[13] O. Ortiz, F. Castells, and G. Sonnemann, "Sustainability in the construction industry: A review of recent developments based on LCA," *Construction and Building Materials*, vol. 23, no. 1. pp. 28–39, Jan. 2009. doi: 10.1016/j.conbuildmat.2007.11.012.
[14] M. Erlandsson and M. Borg, "Generic LCA-methodology applicable for buildings, constructions and operation services—Today practice and development needs," *Build Environ*, vol. 38, pp. 919–938, Jul. 2003, doi: 10.1016/S0360-1323(03)00031-3.
[15] "Environmental management-Life cycle assessment-Principles and framework Management environnemental-Analyse du cycle de vie-Principes et cadre," 2006.
[16] M. C. Caruso, C. Menna, D. Asprone, A. Prota, and G. Manfredi, "Methodology for life-cycle sustainability assessment of building structures," *ACI Struct J*, vol. 114, no. 2, pp. 323–336, Mar. 2017, doi: 10.14359/51689426.
[17] "ISO 14044 Environmental management-Life cycle assessment-Requirements and guidelines Management environnemental-Analyse du cycle de vie-Exigences et lignes directrices," 2006.
[18] "Environmental management-Life cycle assessment-Life cycle impact assessment(E) PDF disclaimer," 2000. [Online]. Available: www.iso.ch
[19] U. Vitiello, A. Salzano, D. Asprone, M. Di Ludovico, and A. Prota, "Life-cycle assessment of seismic retrofit strategies applied to existing building structures," *Sustainability (Switzerland)*, vol. 8, no. 12, 2016, doi: 10.3390/su8121275.
[20] C. Lim, Y. Jeong, J. Kim, and M. Kwon, "Experimental study of reinforced concrete beam-column joint retrofitted by CFRP grid with ECC and high strength mortar," *Constr Build Mater*, vol. 340, Jul. 2022, doi: 10.1016/j.conbuildmat.2022.127694.
[21] S. Sasmal *et al.*, "Seismic retrofitting of nonductile beam-column sub-assemblage using FRP wrapping and steel plate jacketing," *Constr Build Mater*, vol. 25, no. 1, pp. 175–182, Jan. 2011, doi: 10.1016/j.conbuildmat.2010.06.041.
[22] G. T. Truong, N. H. Dinh, J. C. Kim, and K. K. Choi, "Seismic Performance of Exterior RC Beam–Column Joints Retrofitted using Various Retrofit Solutions," *Int J Concr Struct Mater*, vol. 11, no. 3, pp. 415–433, Sep. 2017, doi: 10.1007/s40069-017-0203-x.
[23] S. Z. Qian, V. C. Li, H. Zhang, and G. A. Keoleian, "Life cycle analysis of pavement overlays made with Engineered Cementitious Composites," *Cem Concr Compos*, vol. 35, no. 1, pp. 78–88, Jan. 2013, doi: 10.1016/j.cemconcomp.2012.08.012.
[24] N. Stoiber, M. Hammerl, and B. Kromoser, "Cradle-to-gate life cycle assessment of CFRP reinforcement for concrete structures: Calculation basis and exemplary application," *J Clean Prod*, vol. 280, Jan. 2021, doi: 10.1016/j.jclepro.2020.124300.

Bio-active glass (S45P0) for waste water treatment

Marwa Nabil[1, a]

[1]Advanced Technology and New Materials Research Institute, City of Scientific Research and Technology Applications, New Borg El-Arab City, Alexandria, Egypt

[a] marwamoh2000@yahoo.com

Keywords: Bioactive glass, melt-quenching technique, heavy metal removal

Abstract. Bioactive glass (BAG) consists of known biocompatible and bioactive minerals. Bioactive Glasses are amorphous solids with the irregular organization of atoms, optically transparent, and brittle consisting of silica networks. Bioactive glass is used as cheap and eco-friendly adsorbents for the removal of Copper ions from water.
The present work aims a new, low cost, and fast regime for water purification using bioactive glass (S45P0). This synthesized (BAG-S45P0) composition consists of 50%SiO_2-25%CaO-25%Na_2O. (S45P0) was synthesized by melt-quenching process. Silicon leftovers powder was as SiO_2 source, it was prepared using wet alkali chemical etching due to the ultra-sonication technique. White sand {Sands of the northern coast of the Mediterranean Sea} was as CaO source, it was prepared using wet alkali chemical etching. And, Sodium silicate (Na_2SiO_3) with 99.9% purity was as Na_2O precursor.
(S45P0) powder can be used effectively for the adsorption of Cu (II) ions from aqueous solutions. The maximum Cu (II) ion adsorption capacity for the (BAG) powder reached to 1383 mg/g under an initial Cu (II) concentration 200 mg/L and adsorption time is 10 min, in addition, no effect of pH and at adsorption temperature. Only using 0.09 g of adsorbent (S45P0) in a 1L solution of 50 mg/L of Cu (II) concentration at contact time 10 min, which produce Cu removal percent is 92.5 %.

Introduction

Bioactive glass (BAG) consists of known biocompatible and bioactive minerals. BAGs are amorphous solids with the irregular organization of atoms, optically transparent, and brittle consisting of silica networks. The BAGs bioactivity involves several steps; BAGs immediately undergo ionic dissolution and glass degradation via the exchange of H^+ ions in the solution and Na and Ca from the glass network [1]. Soda-lime-silica is the most important glass family in daily life because 90 % of the manufactured conventional glasses in the world belong to the Na_2O-CaO-SiO_2 system [2].
The present work aims to introduce a new, low cost, and fast regime for water purification using a specific type of bio-glass S45P0 with nominal composition 50SiO_2: 25CaO: 25Na_2O (mol %).

Methods

1) Silica preparation

For the preparation of SiO_2 NPs powder, 7 g silicon powder (99%, Sigma-Aldrich) was used. It was prepared by wet alkali chemical etching with the ultra-sonication technique. [3]

2) Extraction of calcium oxide from white sand {Sands of the northern coast of the Mediterranean Sea}

For the preparation of CaO powder, 3 g of white sand was used. It was prepared by wet alkali chemical etching with the stirring technique. Briefly, the appropriate amount of white sand was dispersed in a solution containing different (17 wt % KOH), 1-propanol (30 vol %), and water for different sonication time; 4.5 hr. The synthesized CaO powder was filtered washed using distl. Water, and then dried at 60°C overnight.

3) Synthesis of bio-active glass (S45P0) preparation

The glass with composition $50SiO_2$: 25CaO: $25Na_2O$ (mol %) was synthesized by melt-quenching process using silicone leftovers powder as silica source, Sands of the northern coast of the Mediterranean Sea (white sand) as calcium oxide source and sodium silicate (Na_2SiO_3; Assay 90%, Sigma Aldrich) with 99.9% purity as Na_2O precursor. The mixture of powders was melted at a temperature range of 900 °C for 3 h in muffle furnace. The molten mixture was then quenched into brass molds. The glass powder was obtained by grinding the resulting glass pieces. The formation of the chemical bonds for the process was determined by FTIR (Fourier Transform Infrared Spectrophotometer- Shimadzu FTIR-8400s, Japan). Various vibration modes were performed by Fourier transmission infrared spectroscopy with each IR spectra was collected from 400 to 4000 cm^{-1}.

4)Using (S45P0) for heavy metal removal

(4-1) Preparation of Metal Ion Solutions

The Cu is synthesized using standard methods. The double distilled water was used for all the analyses. The concentrations of the metal ions are estimated using UV-Visible Spectrophotometer Double Auto cell (Labomend. INC, USA). Standard Copper Solution: Cu solution is prepared by using Copper sulfate; 0.15 g of Copper sulfate is taken into a 1000 ml volumetric flask [4].

(4-2) Batch Procedure for Cu Element Removal

Batch Equilibrium Method: Batch mode is selected because of its simplicity and reliability. The experiments are carried out by taking 40 ml metal ion sample in a 100 ml Erlenmeyer flask and after pH adjustments; a known quantity of solution dried adsorbent (S45P0) is added. The flasks are agitated at 200 RPM for predetermined time intervals using a mechanical shaker until equilibrium conditions are reached. The residual biomass adsorbed with metal ions, the filtrate is collected and subjected for metal ion estimation using UV- Visible Spectrophotometer Double Auto cell (Labomend. INC, USA). The values of percent metal uptake by the sorbent (Sorption efficiency) and the amount of metal ion adsorbed has been calculated using the mathematical relationships. [5]

Results

FTIR spectra of the bioactive glass (S45P0) are presented in Fig.1. According to the references, the synthetic bioactive glass (S45P0) is indicated the majority of characteristic bands of silica network. The bands at 450, and 680 cm^{-1} were attributed to the deformation vibration of Si–O–Si bridging bonds in the SiO_4 tetrahedrons which have four oxygen atoms linked to four Si neighbors; these tetrahedrons are noted as $Q_4(Si)$ [6].

The bands at 800, 930 and 1040 cm^{-1} correspond to the stretching vibration of Si–O–Si bonds in the Q_1(Si), Q_2(Si) and Q_3(Si) tetrahedrons, respectively, which include 1, 2 and 3 bridging oxygen atoms [7]. The band at 940 cm^{-1} relates to the Stretching in non-bridging Oxygen bonds (NBO) of (Si-O-NBO) in the Q_0(Si) units which have non-bridging oxygen atoms [8]. In addition, band at 1339 corresponds to Na_2O and (1418-1468) cm^{-1} were accompanied by a small shoulder at ≈875 cm^{-1} correspond to C-O stretching of the carbonate group (CO_3^{-2}). [9]

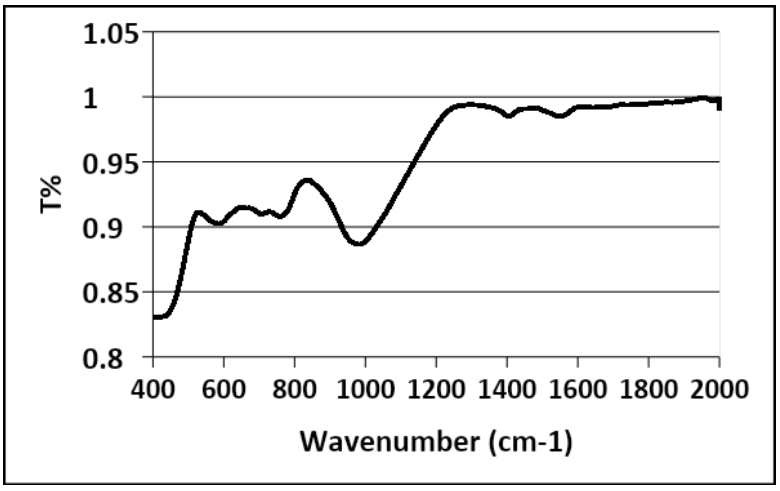

Fig.1. FTIR spectra of bioactive glass S45P0

Adsorption Study

Uptake of the Cu (II) by (S45P0) as a function of contact time in different Cu concentrations; in all of the Cu concentrations (30, 50, 100, 200 ppm), removal process took place. Cu (II) is removed faster; it exhibited a subsequent removal until equilibrium is reached. The main reason for the appearance of rapid process, the plenty active sites on (S45P0) powder and gradual occupancy of these sites causes of emerging [10]. In fact Cu ions, form a molecule (actually ion) layer on the adsorbent surface. After that, the uptake rate is controlled by the rate at which the Cu (II) ions are transported from the exterior to the interior sites of (S45P0) powder particles.

- Effect of initial Cu (II) concentration on adsorption:

The initial Cu (II) concentration serves as an important driving force for overcoming mass transfer resistance of Cu (II) between the aqueous and solid phases. The effects of different initial Cu (II) concentrations on the (S45P0) adsorption capacity are shown in Fig. 2. The adsorption capacity of the (S45P0) powder toward Cu (II) is directly proportional to the initial Cu (II) concentrations at a constant value of (S45P0) dose. As shown in fig. 2.b, the adsorption capacity value at (S45P0) dose = 0.07 gm/l is the best one (1383 mgm/gm) at 10 min.
Noticeable, the removing percent of Cu (II) at several concentrations is nearly similar values at a time (10 min). Studies are carried out to obtain optimum conditions for the adsorption of Cu (II) using 0.09 g of adsorbent (S45P0) in a 1L solution of 50 ppm of Cu (II) concentration adjusted to different contact time values from 2 to 10 min, which produce Cu removal percent is 92.5% and the value of the adsorption capacity of (S45P0) is 513.9 mg/g. This result is observed because higher Cu (II) concentrations result in an increased con-centration gradient, which, leads to a higher probability of collision among Cu (II) ions and the active adsorption sites on the (S45P0) powder, thereby increasing adsorption capacity. With further increases in Cu (II) concentration

than 50 ppm, the adsorption capacity remained constant because the active adsorption sites became saturated [11], as shown in fig. 3.

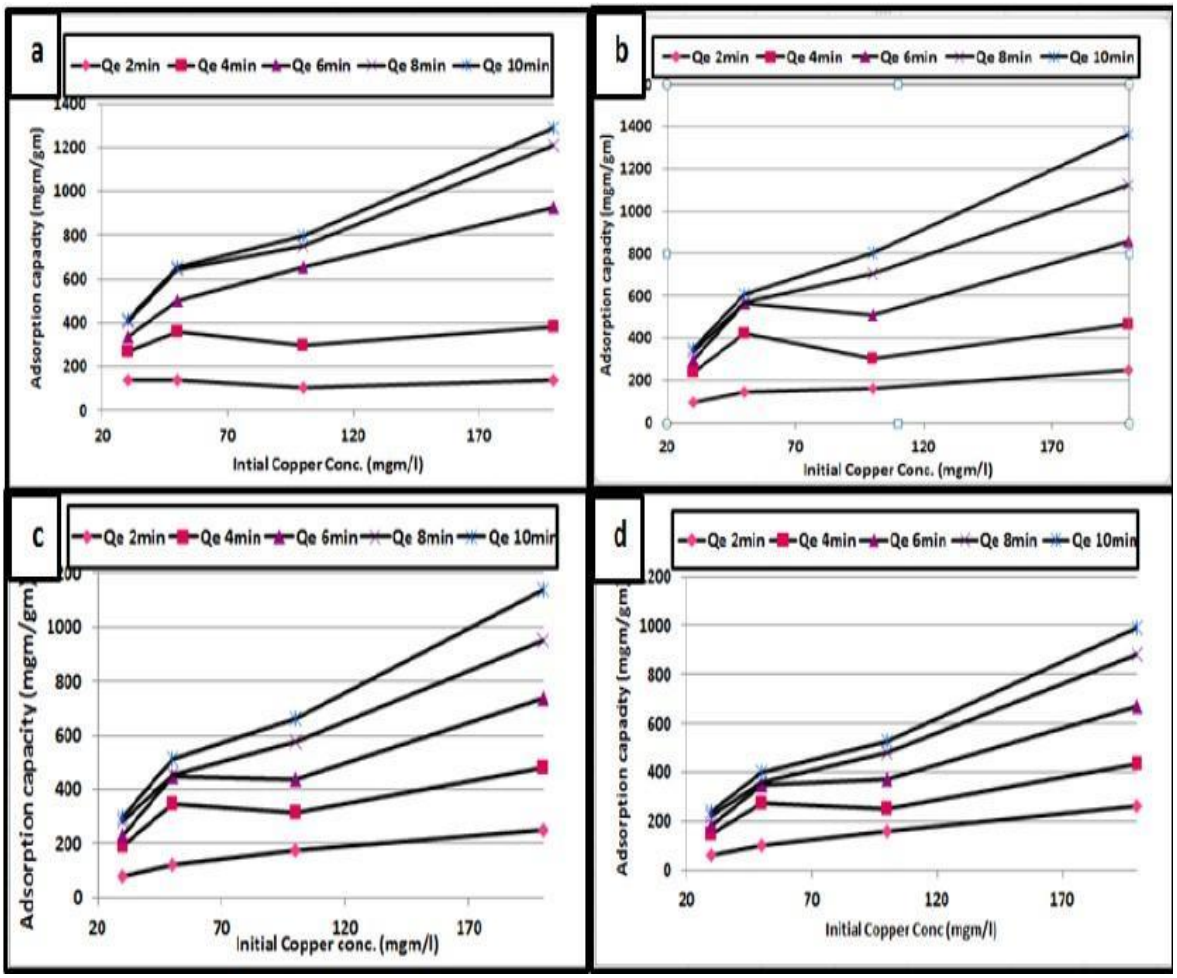

Fig. 2: The effect of the initial copper concentrations on the values of the adsorption capacity value of (S45P0) each gm; initial copper concentration (Cu_{conc}) = (a) 0.05; (b) 0.07; (c) 0.09 and (d) 0.12 gm/l.

In addition, the effect of acidity and temperature on the adsorption value of copper is studied. It has been shown that by changing the pH value and temperature values, there is no obvious effect at the varying process of the Cu adsorption values, which are the same as in case of the room temperature and pH = 7.

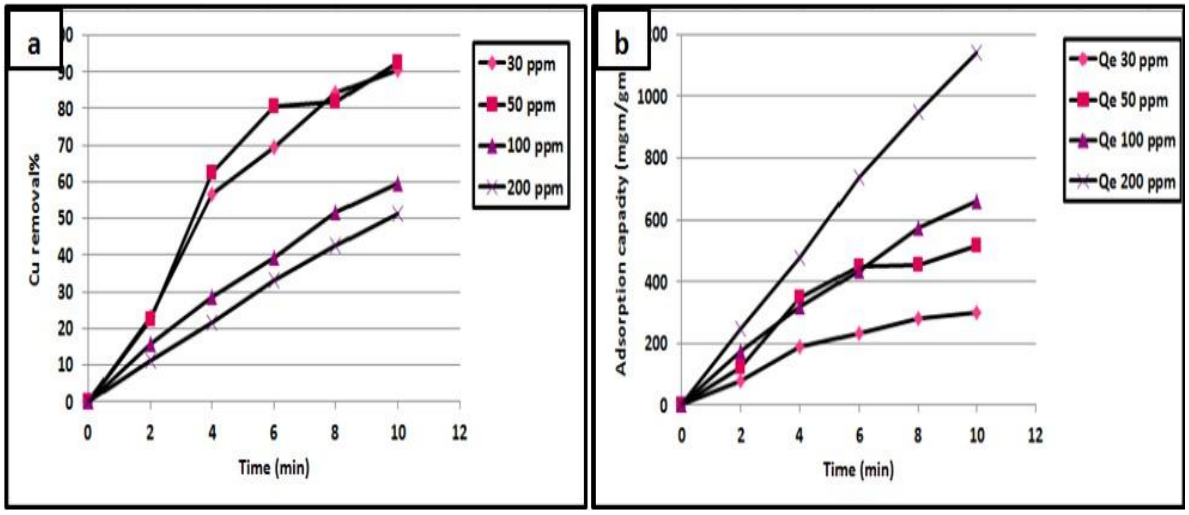

Fig. 3: At the (S45P0) powder dose 0.09 g/L, a) Cu removal concentration percent as a function of contact time (min), b) Effect of contact time on desorption capacity of (S45P0).

Conclusion

We developed an innovative idea by using the glass-ceramic derivatives of S45P0 in water treatment and purification. The novelty of this idea is the usage of a very powerful tool in bone tissue engineering and medical application as a very important weapon in water purification. We concluded from UV-Vis measurements that the purification process of contaminated water with S45P0 had more efficiency in the first 10 min. We concluded that S45P0 provides low-cost efficient adsorbents for heavy metals specifically (copper sulfate)

References

[1] H.E. Skallevold, D. Rokaya, Z. Khurshid, M.S. Zafar: Int. J. Mol. Sci. Vol. 20 (2019), p. 5960-2983

[2] I. Santoso, M. Riihim¨aki, D. Sibarani, P. Taskinen, L. Hupa, Min-Kyu Paek, D. Lindberg: J. Eur. Ceram. Vol. 42 (2022), p. 2449–2463.

[3] M. Nabil, K.R. Mahmoud, A. El-Shaer, H.A. Nayber: J. Phys. Chem. Solids. Vol. 121 (2018), p. 22–26.

[4] A.M. Abdelghany, A.H. Oraby, M. Abdelbaky: Silicon. Vol. 11 (2019), p. 1835–1843.

[5] M. Nabil, H.A. Motaweh: AIP Conference Proceedings. Vol. 1957 (2018), p. 020005-020011

[6] P. Innocenzi: J. Non-Cryst. Solids.Vol. 316 (2003), p. 309–319.

[7] C.I. Merzbacher, W.B. White: Am. Mineral. Vol. 73 (1988), p. 1089–1094.

[8] A.G. Kalampounias: Bull. Mater. Sci. Vol. 34 (2011), p. 299–303.

[9]H.S. Costa, M.F. Rocha, G.I. Andrade, E.F. Barbosa-Stancioli, M.M. Pereira, R.L. Orefice: J. Mater. Sci. Mater. Med. Vol. 43 (2008), p. 494-502

[10] Y. Wang, M. luo, T. Li, C. Xie, S. Li, B. Lei: Bioact. Mater. Vol. 25 (2023), p. 319-332

[11] A. Kashyout, H. Soliman, M. Nabil, A. Bishara: Sens. Actuators B Chem. Vol. 216 (2015), p. 279–285.

New Alternative Marine Fuels

Marwan Magdy Abdelfattah[1, a], Mohamed Morsy Elgohary[2, a,b] and Ibrahim S. Seddiek[3, c]

[1]Alexandria University, Egypt. [2]Borg El Arab Technological University, Egypt. [3]Arab Academy for Science and Maritime Technology, Alexandria, Egypt.

[a]eng-marwan.magdy1318@alexu.edu.eg, [b]mohamed.elgouhary@alexu.edu.eg, [c]prof.isibrahim@gmail.com

Keywords: Alternative fuels, Marine Fuels, Emissions, GHG.

Abstract. The maritime industry is facing increasing pressure to reduce its environmental impact and comply with stricter regulations. One of the major contributors to the industry's emissions is the use of fossil fuels in ships. To address this issue, alternative marine fuels are being developed and tested as a more sustainable and eco-friendly option. **Biofuels** are one such alternative fuel that can be derived from various sources such as algae, vegetable oil, and animal fat. They are considered a promising option as they can be blended with traditional fuels and used in existing engines with minor modifications. However, their production cost and availability are still a challenge. **Hydrogen** is another alternative fuel that has gained attention in recent years. It can be produced using renewable energy sources and has the potential to significantly reduce emissions. However, the infrastructure required for its production and distribution is currently lacking, which makes it costly and challenging to implement. **Ammonia** and **methanol** are other alternative marine fuels that are being explored. They both have lower carbon emissions than traditional fuels, but their production and transport also present challenges.
Overall, the use of alternative marine fuels is essential to reduce the environmental impact of the maritime industry. While each fuel type has its advantages and challenges, a combination of different options may be necessary to achieve the industry's sustainability goals. It is crucial to continue research and development in this area to create a more sustainable future for the maritime industry.

Introduction

The problem of finding fuel alternatives is being tackled in most countries around the world at a time when fuel reserves are rapidly depleting and demand for them is increasing. Ships engaged in international trade face hurdles in reducing exhaust gas emissions and greenhouse gases, particularly carbon dioxide. Coal, peat, lignite, petroleum, and natural gas are examples of the "completely oxidized and decayed animal and vegetable materials" that make up fossil fuels. It is officially defined as "material that can be burned or otherwise consumed to produce heat". The major contributor to the atmospheric release of greenhouse gases is the burning of these fossil fuels. [1]

Many countries' national environmental agencies and the major regulatory agency, the International Maritime Organization (IMO), have enacted laws that substantially reduce emissions from marine sources. These new regulations will compel ship owners and directors to seek other sources, such as alternative fuels. Alternative fuels differ in origin and manufacturing process, but they all have one thing in common: they are produced in a sustainable and environmentally friendly manner, with no additional carbon dioxide emissions (CO2).
The two basic approaches for the synthesis of alternative fuels are the direct use of extra power and thermochemical conversion of raw materials. Liquid fuels like methanol, ethanol, bioliquid

fuel, and biodiesel, as well as gaseous fuels like propane, hydrogen, and natural gas, are available as alternative fuels that can be utilized in marine diesel engines. [2] Here is a review for the recent new alternative marine fuels.

Biofuels

Early in the new millennium, the industry for biofuels had an acceleration in growth because of high oil prices, worries about energy security, and the requirement to cut greenhouse gas emissions. The Renewable Fuel Standard (RFS) of 2007 and the Energy Policy Act of 2005 both established requirements and incentives for the development of biofuels in the United States, which stimulated an upsurge in the production of ethanol and biodiesel. [3] Currently, the only financially viable alternatives for transportation and industry are biofuels, particularly biodiesel and solid biomass. They will be used more frequently in the future, which calls for the creation of new strategies for sustainability. [4] First-generation biofuels include biodiesel and bioethanol, whereas second- generation biofuels are created from forestry byproducts and agricultural waste, including rice husks, wheat straw, and woody biomass, which comprise cellulosic, hemi-cellulosic, and lignin components.
[5] Algae, which is viewed as a crop developed for use as an energy source, creates another third- generation biofuel. Oil is recovered from algae that have been grown using advanced procedures in the proper environments. Through a trans-esterification process, the extracted oil can be transformed into biodiesel, which is then used in diesel engines with or without mixing with Petro-diesel. Algal biofuel use reduces the overuse of petroleum crude oil and offers a sustainable substitute. [5] The benefits of biodiesel include biodegradability, efficient engine lubrication, extremely low greenhouse gas emissions, and effective combustion. Therefore, it is a suitable choice for diesel engine pollution reduction. [5] The flash point is a crucial indicator for fuel storage, transportation, and combustion. According to SOLAS regulations, conventional marine gasoline cannot be kept below the main deck since it has a flash point below 60 degrees Celsius. Biodiesel has a higher flash point than fuels derived from petroleum, such as soy oil, which has a flashpoint of about 138 °C. [6] Since biodiesel has a very low Sulphur content, using it with any marine fossil fuel can greatly reduce deposit development and SOx emissions after combustion. Based on the component weight ratios, the sulphur content of the mix is determined. For instance, if a 23% volume of biodiesel is added to the residual fuel, the 4.5% Sulphur level can be lowered to 3.5%, in compliance with Annex VI of MARPOL's Sulphur emission requirements starting in 2012. [6] The Environmental Protection Agency of the United States has registered biodiesel fuel with annual production rates as shown in fig 1. [5]

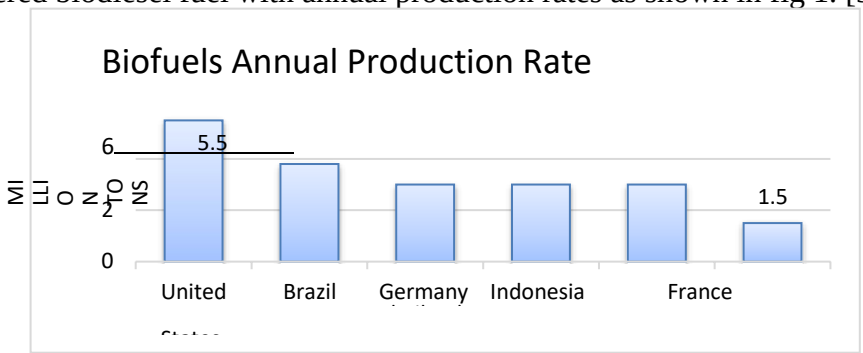

Figure 1

Compared to petroleum diesel, biodiesel is a 75% cleaner energy source since it doesn't contain Sulphur and produces very little incompletely burned hydrocarbon, carbon monoxide, or particulate matter. When compared to the combustion of petroleum fuel, biodiesel creates roughly 50% less particle pollution. To lower the levels of particulate matter, carbon monoxide,

hydrocarbons, and hazardous agents in the exhaust gases of diesel-powered cars, biodiesel is typically employed as a conventional diesel supplement to decrease the amounts of hazardous substances, hydrocarbons, carbon monoxide, and particulate matter in the exhaust gases of diesel-powered engines. [5] Today, we estimate that biofuels currently account for approximately 5-10% of all fuel supplied at the Port of Rotterdam. The aim is for biofuels to represent 20% to 30% of the marine bunker fuel market by 2050. [7]

Hydrogen is classified into three groups: Grey hydrogen is created using a hydrocarbon-based fuel, which implies that CO_2 emissions were produced along with it. Blue hydrogen was created using carbon capture technology. Green hydrogen is created using renewable energy sources and emits no emissions. Now, most of the hydrogen produced comes via methane reforming, where methane is typically sourced from natural gas. However, coal and oil are also occasionally used to manufacture hydrogen.[8] Hydrogen fuel cells are incredibly efficient from the perspective of "green" energy, with a 60% efficiency rate. For instance, the best internal combustion engines have an efficiency of 35– 40%. [9] As a future bunker fuel, hydrogen is still a good choice because it produces more energy per unit mass than traditional maritime fuel and emits less greenhouse gases. However, some barriers, such the price of production and the unique handling needs for storage and transportation, prevent the widespread use of hydrogen fuel. [8] Only a small number of naval vessels have used hydrogen as a fuel thus far. Zemships was the second vessel to use hydrogen after Hydra, which did so in 2000. The fuel for both vessels was compressed hydrogen (CH_2). The ship Energy Observer, which has been in service since 2017, is another well-known CH_2 demonstration project. For many years, LH_2 has been utilized as rocket fuel in the space industry [10]

Due to the low density, a 700-bar hydrogen storage method might be developed, which would limit the amount of hydrogen kept in a single tank. The term "Liquid Organic Hydrogen Carrier" refers to a method of storing hydrogen that makes it non-flammable, allows for atmospheric pressure storage, and provides up to three times the storage capacity of a tank holding the same amount of hydrogen. While enhancing air quality and lowering noise levels, using hydrogen as a fuel can aid in lowering greenhouse gas emissions. Hydrogen is therefore increasingly making its way into all modes of transportation and entering the European Union market with the help of the European Commission.
[11] The fundamental benefit of hydrogen is its potential to be a fuel with zero emissions if it is produced using renewable resources. Future hydrogen production capacity will also be compatible with the planned energy shift to land-based renewable energy sources. The expenses and the lack of bunkering infrastructure are the two main obstacles to hydrogen. [12] Simple illustration for hydrogen production is shown in fig.2.

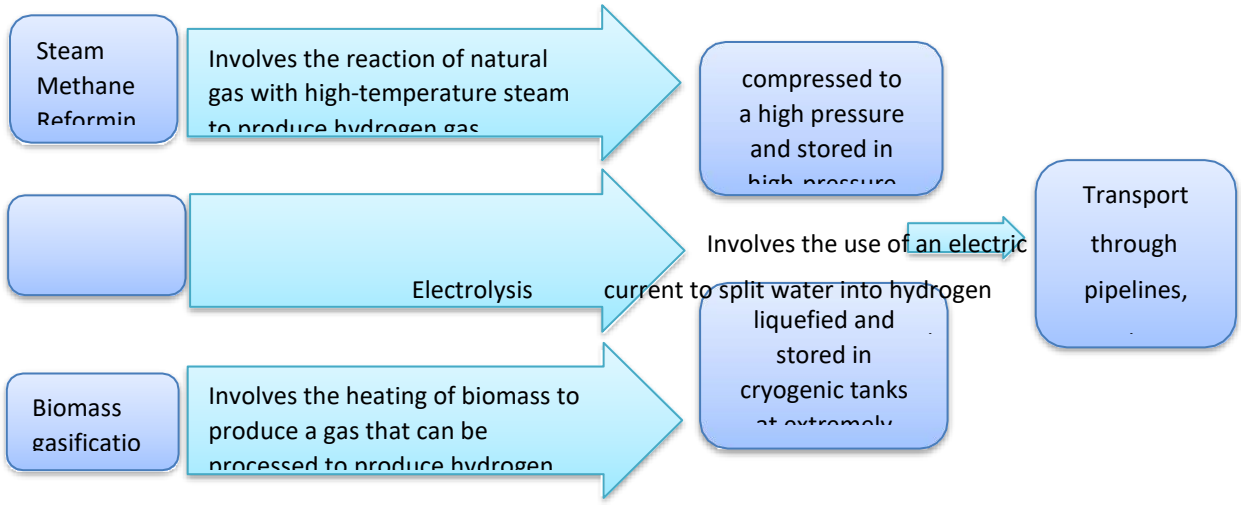

Figure 2

Fuel cell propulsion: In a hydrogen-powered vessel, the stored hydrogen is fed into a fuel cell system, where it reacts with oxygen from the air to produce electricity. This electricity is used to power the ship's propulsion system, with water and heat being the only byproducts. Alternatively, hydrogen can be burned in an internal combustion engine to generate power.

Ammonia

Ammonia is created via the Haber-Bosch (HB) process, which combines nitrogen and hydrogen to accomplish NH_3. Natural gas, coal, and oil gasification, together with steam reforming of natural gas, are the main sources of hydrogen used in the process. [13] Around 180 million tonnes of ammonia are produced annually across the globe. [13] Ammonia is easily stored on a ship because it is liquid at ambient temperature and has 10 bars of pressure. However, it takes 4.1 times more volume than conventional fuels like HFO and MGO, despite being easy to handle and store on a ship. [13]

The production cost of ammonia is primarily influenced by the cost of feedstock, energy, and capital investments. Natural gas is the most common feedstock used, and its price plays a significant role. As of September 2021, the production cost of ammonia was estimated to be around $300-$400 per metric ton. Ammonia is difficult to burn in a standard diesel engine due to its high auto-ignition resistance. For the sole ammonia combustion, alternate combustion techniques must be presented, or a pilot fuel for the combustion initiator may be used. [13] High NOx emissions, N_2O emissions, and ammonia slip are the main problems following ammonia combustion. To lessen or eliminate these pollutants entirely, an ideal combustion must be offered. The NOx emissions can be handled by the after-treatment systems. [13] Within five to ten years, ammonia-powered internal combustion engines should be available for purchase, but adoption won't effective until prices are competitive. [12] Production cost can be estimated as follows in fig.3.

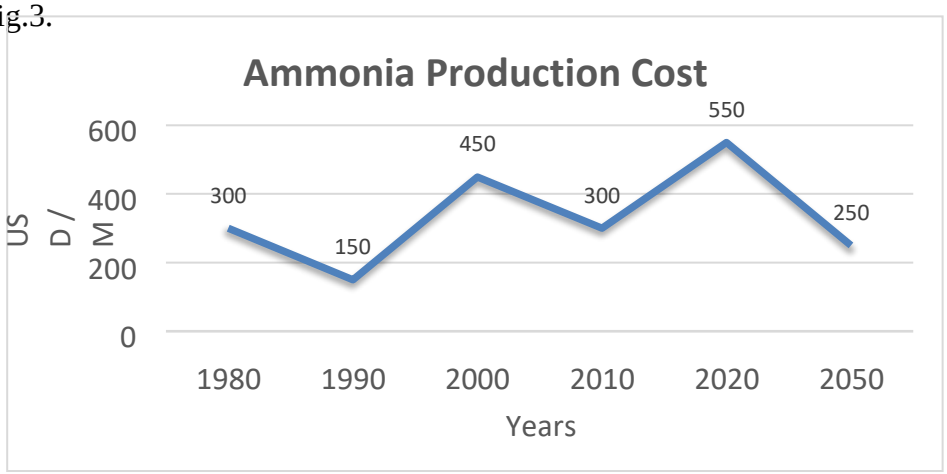

Figure 3

Ammonia is becoming a carbon-free energy carrier with a higher density than hydrogen and, in theory, deep-sea technical viability with the shift to renewable energy sources. Green ammonia's affordability and low maturity, however, limit its viability as an alternative fuel. An obstacle to using ammonia as a substitute marine fuel is also the absence of bunkering infrastructure, and this barrier is expected to last for a while as the market develops. Like hydrogen, until the switch to renewable energy sources is well underway, ammonia production from fossil fuels without carbon capture and storage results in substantial GHG emissions. [12] More than 170 Mt/yr. of

NH_3 are produced globally by several large-scale ammonia manufacturing facilities, the majority of which use natural gas. This has the same amount of energy as 76 million tonnes of fuel oil. China accounted for 32% of global output, followed by Russia (9%), India (8%), and the United States (8%). Electrolysis may be used to manufacture ammonia from renewable sources. Previously, ten facilities that used hydropower to generate energy were claimed to have produced it using electrolysis. The amount of power consumed, and the expense of processing equipment have harmed the older facilities, and just three may still be operational. Ammonia generated from wind or solar energy is another possible early-stage development approach. [12]

Methanol. The purest alcohol is methanol (CH_3OH), which consists of a methyl group (CH_3) joined to a hydroxy group (OH). At -94°C, it solidifies and boils at 65°C [10]. It is colorless and smells somewhat like ethyl alcohol. It has a high hydrogen concentration and a low carbon content. [14] Methanol's price is influenced by the price of natural gas because it is mostly manufactured from that fuel. If methanol is produced from coal, the cost may be cheaper. The latter, nevertheless, could have negative consequences like higher greenhouse gas emissions. Creating methanol from hydrogen and CO_2 has greater production costs than creating methanol from methane. [3] Methanol is a marine fuel with clean-burning properties that may cut sulphur oxide emissions by 99%, nitrogen oxide emissions by up to 60%, and particulate matter emissions by 95%. [14]

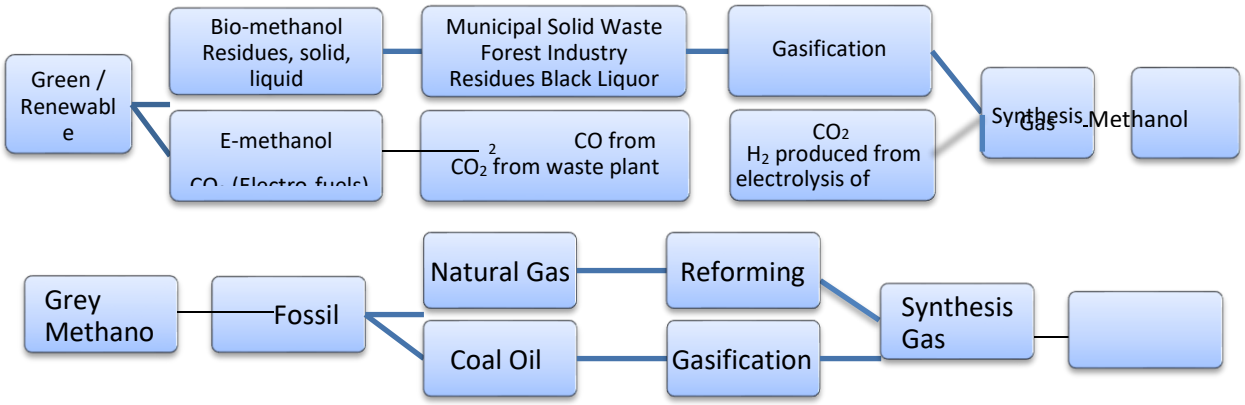

Figure 4

Installing methanol systems onboard the ships (such as internal combustion engines, fuel tanks, and pipes) is three times less expensive than installing LNG systems. No requirement for pressurised fuel tanks and cryogenic temperatures, like with LNG. [14] The type of resource (such as natural gas, coal, or biomass) utilised as a feedstock affects the cost of producing methanol. The cost of methanol is higher than that of LNG and HFO, though. Despite the fact that this methanol is sulphate-free and has the ability to fulfil the current 0.1% SOx emission in the Control Area standards, it is becoming more and more popular on the market. As a low flash point fuel, methanol must adhere to current regulations, such as the International Code of Safety for Ships using Gases or other Low-flashpoint Fuels (IGF), which the IMO is still working to enhance and expand. [14] These fuels may be utilized in diesel engines in two distinct ways. One of them is premixed fuel, which combines methanol or ethanol with diesel or fuel oil and does not contain any debatable information concerning its usage with alcohols. Alcohol phase separation is the fundamental issue with fuel mixtures that have been pre-mixed. The solution is the addition of the appropriate solvent. The alternative method involves injecting methanol or

ethanol on its own into diesel or fuel oil. Depending on the technique used, the injection area might change. Methanol or ethanol are pumped into the diesel engine's intake manifold during the fumigation technique; with the dual-fuel approach, they are injected into the cylinder via a separate injector. At the dual-fuel approach, the primary fuel is either methanol or ethanol, while diesel fuel is utilized as a pilot fuel to ignite the main fuel in the fumigation process. [3] The production procedures can be explained as follows in fig.4.

The key benefits of methanol are its relatively good application, the ability to use current converter technology, and its affordable tanks, all of which translate into inexpensive capital expenditures. On the other hand, methanol's environmental impact when manufactured from fossil sources is a significant drawback to its use as an alternative fuel. [31] Methanol may be utilised as a fuel in two- stroke diesel-cycle engines or four-stroke, lean-burn Otto-cycle engines, which are the two most common alternatives for traditional ship engines. [12] If the demand for methanol as ship fuel grows gradually at first and stays at a modest level, the existing output should be able to safely meet the shipping need by 2030. [12]

References

[1] C. Sakthivel, V. Jethose, K. Selvakumar, S. Pradeep Kumar, E. Parimalasundram: *A Review of Alternate Fuels* submitted to Global Research and Development Journal for Engineering (2018)

[2] Cengiz Deniz, Burak Zincir: *Environmental and economical assessment of alternative marine fuels* submitted to Journal of Cleaner Production (2015)

[3] Information on https://afdc.energy.gov

[4] Nagulash Rahul B, R.V. Nanditta: *Review on Alternate Fuels: Need for Cleaner Fuels to Meet Future Energy Demands* submitted to Turkish Online Journal of Qualitative Inquiry (TOJQI)
Volume 12, Issue 9, August 2021: 805-819

[5] Chandra Bhan, Lata Verma, and Jiwan Singh: Chapter 16 *Alternative Fuels for Sustainable Development* (2020)

[6] Beazit ALI, Levent ALI, Adrian POPA, Anastase PRUIU: *ALTERNATIVE FUELS FOR THE MARINE MARKET* submitted to Naval Academy Scientific Bulletin, Volume XIX – 2016 – Issue 1

[7] Information on https://www.goodfuels.com/faq

[8] Ahad Al-Enazi, Eric C. Okonkwo, Yusuf Bicer, Tareq Al-Ansari: *A review of cleaner alternative fuels for maritime transportation* submitted to Energy Reports on Scince Direct (2020)

[9] Tillahodjaev R.R., Turdiev J.P., Kurbanov A.M.: *ALTERNATIVE FUELS AND ENVIRONMENTAL EFFICIENCY* submitted on International scientific and technical journal INNOVATION TECHNICAL AND TECHNOLOGY (2021)

[10] Ann Rigmor Nerheim, Vilmar Æsøy and Finn Tore Holmeset: *Hydrogen as a Maritime Fuel– Can Experiences with LNG Be Transferred to Hydrogen Systems?* submitted on Journal of Marine Science and Engineering (2021)

[11] Sandro Vidas, Marijan Cukrov, Valentina Šutalo, and Smiljko Rudan: *CO2 Emissions Reduction Measures for RO-RO Vessels on Non-Profitable Coastal Liner Passenger Transport* Submitted to Sustainability MDPI (2021)

[12] DNV-GL Report No.: 2019-0567, Rev. 3 Document No.: 11C8I1KZ-1 Date: 2019-07-05.

[13] B. Zincir in: *A Short Review of Ammonia as an Alternative Marine Fuel for Decarbonised Maritime Transportation* on Proceedings of ICEESEN2020, 19-21 November 2020, Kayseri-
Turkey

[14] Şevket Süleyman İrtem in: Chapter: *A Review of Alternative Marine Fuels* From the edited volume Environmental Health on IntechOpen (2021)

Performance analysis of combined waste heat recovery cycle for improving the energy efficiency

Medhat Aboelkheir[1, a], Mohamed.M.El Gohary[1,b] ,Ibrahem Sadek[2,c]

[1] Department of Naval Architecture and Marine Engineering, Faculty of Engineering, Alexandria University, 21544, Alexandria, Egypt.

[2] Department of Marine Engineering Technology, College of Maritime Transport & Technology, Arab Academy for Science, Technology and Maritime Transport,1029, Alexandria, Egypt.

amedhat_aboelkheir@hotmail.com , b prof.Elgohary@gmai.com , cprof.isibrahim@gmail.com

Keywords: Waste heat recovery; Energy efficiency; Cascade utilization; combined cycle; Evaporation pressure.

Abstract

The world's energy consumption is increasing, and it is already obvious how current energy use affects the environment. Given that shipping accounts for more than 90% of world trade and is the most practical means of moving raw materials and large quantities of goods, the issue of energy and emissions for ships is also one that needs to be tackled. Among the most promising technologies For enhancing energy efficiency and reducing ship emissions is combined cycle between thermoelectric power generation (TEG) and organic Rankine cycle (ORC). The purpose of this study is to use an organic working fluid (R245fa) to investigate the change of key parameters such as system net power output, system thermal efficiency, power-production cost, and waste heat utilization of main engine flue gas at various evaporation pressures. The results showed that the increase in evaporation pressure led to increase in net power output, system efficiency and decrease production cost. Also, the optimum performance of the system is found to be at 0.75 MPa, in which system net power output is 483.25 W. The performance of the combined cycle system was improved by employing R245fa organic working fluid while being environmentally friendly. This study serves as a resource for further understanding and the coupled cycle mechanism's optimization.

1. Introduction

Due to the increasing concern for the environment and economy, the higher requirements are put forward on the carbon emissions of the ships. International Maritime Organization (IMO) has formulated strict laws and regulations to limit carbon emissions from ships [1-2]. Based on the demands for reducing carbon emissions, the recycle of ships waste heat has become an important issue. Waste heat varies according on the features of distinct ships, there are many technologies to recover waste heat recovery. The thermoelectric power generation (TEG) technology has a lot of potential for waste heat recovery. Jovanovic et al. [3] designed a thermoelectric converter for energy recovery employing TEG. They powered wireless sensors used for health monitoring on ships by utilizing the ships waste heat. Georgopoulou et al. [4] proposed a TEG model for ships application. This model captured the complete thermodynamic and thermoelectric conversion process phenomena and characterized the dynamic behavior of ship thermoelectric conversion components. Wang et al. [5] implemented an experimental study and numerical model optimization of the cooling system by employing the TEG device. The thermoelectric model was modified with the measured data, and the design of the cooling plate was optimized by simulation. Finally, The TEG system's capacity to recover waste heat for use

in offshore applications was verified.. Eddine et al. [6] and Hoang et al. [7] carried out theoretical simulations of TEG devices on ships and the TEG efficiency was improved by modifying the internal structure. However, the conversion efficiency of the TEG is not high, and the cost of recovering waste heat from ships is expensive.

- As a more developed technology, Organic Rankine Cycle (ORC) may carry out a range of waste heat recovery methods. Lion et al. [8] and Ng et al. [9] used software to model marine engines, and simulation results confirmed that integrating the ORC system to ships could reduce the operating costs. Yang et al. [10] and Chen et al. [11] improved the waste heat utilization rate of ships by designing a combined ORC system. Based on the complexity of the ORC systems for vehicle applications, a two-stage expansion with an inter-heating ORC system was designed by Liu et al. [12] It made use of a simple system to realize multi-stage heat utilization of diesel engines. Zhu et al. [13] introduced the ORC system to recover marine engine flue gas waste heat. The multi-objective evaluation scheme was numerically simulated to ensure the optimal temperature, and the proper working fluid was chosen to realize the ORC system's thermal economic optimization. Yang et al. [14] and Tian et al. [15] explored the characteristics of various working fluids and conducted parameters selection and realized the thermal economic optimization. But the ORC equipment is large in volume, and The occupied cabin capacity can only be used for waste heat at medium and low temperatures.
- Given the limitation that a single system could only recover a single kind of waste heat, Miller first presented the ORC system with TEG unit in 2009. [16-17] Qiu et al. [18], Shu et al. [19], Zhang et al. [20], Wang et al. [21], Johansson et al. [22], and Kumar et al. [23] studied the performance of the system in theory and experiments. Therefore, the current paper proposes to employ an organic fluid (R245fa) and study the combined cycle's (TEG-ORC) effectiveness for waste heat recovery under various evaporation pressure conditions.

2. Thermodynamic model description

The TEG bottom cycle, despite its low thermal efficiency, can recover high-temperature waste heat at a low cost. ORC technology has a high efficiency in recovering medium and low temperature waste heat, but its size is considerable and the system power generating cost (Cg) is comparatively high. Ship waste heat has a strong temperature gradient, a considerable amount that can be recovered, and a number of other characteristics. It is difficult to recover ship waste heat with a single technology. [24-25]. The flow schematic of the TEG-ORC combined cycle system can be seen in the first diagram.

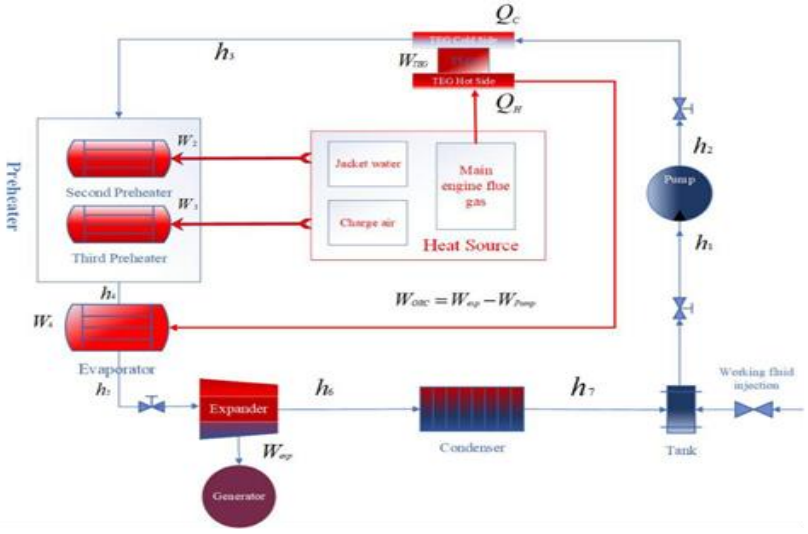

Figure 1 System flow diagram

Eq 1 is used to compute the pump power consumption:

$$P_{pump} = m \times (h_2 - h_1) \quad (1)$$

The TEG unit's absorption of heat is calculated by using Eq. (2) where For the first time, the working medium is preheated.

$$W_C = W_{TEG} = m \times (h_3 - h_2) \quad (2)$$

After that, the medium of operation is preheated by second and third preheaters where the heat absorption can be calculated as shown in Eq. (3)

$$W_2 + W_3 = W_{preheater} = m \times (h_4 - h_3) \quad (3)$$

In the fourth stage, At the evaporator, the working medium absorbs heat to become a saturated liquid with a constant pressure. then it changes the absorption to be at constant temperature and converted to be a saturated gas state. The evaporator rate of heat absorbing can be expressed as shown in Eq. (4).

$$W_4 = m \times (h_5 - h_4) \quad (4)$$

The expander is responsible for the expansion process of steam working medium and an expander's output of power can be expressed as:

$$W_{exp} = m \times (h_6 - h_5) \quad (5)$$

The exhaust steam is recondensed into saturated liquid in the condenser, and the heat is released. is shown as:

$$Q_{cond} = m \times (h_7 - h_6) \quad (6)$$

The power output of a TEG unit can be represented as：

$$W_{TEG} = W_H - W_C \quad (7)$$

The thermoelectric generation unit efficiency is represented as:

$$\eta_1 = 1 - \frac{W_C}{W_H} \quad (8)$$

The power output of the ORC unit can be represented as follows:

$$W_{ORC} = W_{exp} - P_{pump} \quad (9)$$

The organic Rankine cycle unit efficiency is shown as:

$$\eta_2 = \frac{W_{ORC}}{W_1 + W_2 + W_3 + W_4} \quad (10)$$

The net power production of the system is shown as：

$$W_{net} = W_{TEG} + W_{ORC} \quad (11)$$

The thermal performance of the system is stated as：

$$\eta_2 = \frac{W_{net}}{W_H + W_2 + W_3 + W_4} \quad (12)$$

h1, h2 are the enthalpies before and after increasing the ORC working fluid, in kJ/kg. h3, h4 are the enthalpies before and after the preheater, expressed in kJ/kg. h5, h6 are the enthalpies of the wasted steam before and after expansion, expressed in kJ/kg. h7 is the condenser's enthalpy in kJ/kg, and m is the working fluid flow rate in kg/s.

3. Economic model for thermal energy.

□

Cost of ORC unit per kilowatt-hour of power output (EPC_{ORC}) is expressed as [28-30]:

$$EPC_{ORC} = (C_{ORC} * C_{RF} + C_{pl,ORC})/(W_{ORC} * t_{op}) \quad (13)$$

Of them, C_{ORC} is the cost of ORC unit equipment investment. The cost of ORC unit maintenance is defined as $C_{pl,ORC}$. According to the experiment's costs, the annual maintenance cost is 465.31 on average. The system's annual operational hours are classified as t_{op}. According to the experiment development, 500 hours are required. C_{RF} is an abbreviation for fund recovery coefficient., and its computation formula is as follows:

$$C_{RF} = \frac{b * (1+b)^{T_{pl}}}{(1+b)^{T_{pl}} - 1} \quad (14)$$

Among these, the annual interest rate on the loan is represented by b. According to research, the five-year interest rate on commercial loans is roughly 9.5%. Tpl is the number of working years of the system, and the minimum operational life for the purposes of this article is ten years. ORC device costs can be calculated as follows:

$$log\ log\ C_p = K_1 + K_2 * log\ log\ Z + K_3 * (log\ log\ Z)^2 \quad (15)$$

The primary device cost is denoted as C_p, and *The key equipment cost coefficients are K1, K2, and K3, and Appendix B contains their values. Z is the heat exchange area for all heat exchangers., which equals the total heat transfer of the heat exchanger. Z calculates the real work done by the pump. Z handles the expansion work for the scrolled expander.* C_{BM} *displays the material and pressure costs associated with altering equipment. The formula for calculating is as follows:*

$$C_{BM} = C_p(B_1 + B_2 * F_M * F_P) \quad (16)$$

F_p denotes the amount of pressure correction factor.:

$$log\ log\ F_p = A_1 + A_2 * log\ log\ P + A_3 * (log\ log\ P)^2 \quad (17)$$

The pressure correction auxiliary coefficients are A1 A2 A3., and B1 B2 is the cost of equipment modification. FM and Fp are the material and pressure correction factors, respectively. The ORC unit's equipment investment modification cost is shown as：

$$C_{BM,ORC} = C_{BM,2} + C_{BM,3} + C_{BM,eva} + C_{BM,exp} + C_{BM,cond} + C_{BM,pump} \quad (18)$$

The preheaters correction expense is described in the formula as $C_{BM,2}$, $C_{BM,3}$. The cost of evaporator rectification is given as $C_{BM,eva}$. The cost of expander adjustment is defined as $C_{BM,exp}$. $C_{BM,cond}$ is the condenser correction cost. $C_{BM,pump}$ is the pump correction cost.
Organic Rankine cycle unit equipment investment costs are represented as:

$$C_{ORC} = C_{BM,ORC} * \frac{CEPCI_{2020}}{CEPCI_{1996}} \quad (19)$$

CEPCI is a chemical cost index, $CEPCI_{1996} = 382$, $CEPCI_{2020} = 668$.
The only factors taken into account while calculating TEG are the TE modules and the flue gas pipeline equipment. The per-kilowatt-hour power-production cost of the TEG unit (EPC TEG) is consequently expressed as:

$$EPC_{TEG} = \frac{C_{TEC} + C_{pl,TEG}}{W_{TEG} * t_{op}} \quad (20)$$

The thermoelectric conversion device for the TEG unit costs CTEC. The term CTEM stands for the total cost of all TE modules (NTEG). Cpl, TEC stands for the operational and maintenance cost of the TEG unit. The average annual maintenance cost, according to the experiment's expenditures, is $46.2. Because the device and heat exchanger are processed and manufactured in a specific ratio, the heat exchange capacity of different devices is proportionate. When calculating this portion of the cost, it is similar to the ORC unit. The following are the thermoelectric conversion devices::

$$C_{TEC} = C_{BM,1} \quad (21)$$

The power-production price of the TEG unit is expressed as:

$$C_{TEM} = N_{TEG} * C_{TEG} \quad (22)$$

In the formula, C_{TEG} is the unit cost of TEG.
The perkilowatt-hours of Combined cycle system power cost (EPC_{sys}) is expressed as:

$$EPC_{sys} = \frac{C_{TEC} + C_{TEM} + C_{ORC} * C_{RF} + C_{pl}}{W_s * t_{op}} \quad (23)$$

C_{pl} is the combined operating cost of the TEG and ORC units.

Table 1. Coefficient of the ORC Unit

Coefficient	TEG Unit	Expander	Pump	Evaporator	Condenser
K_1	2.8483	3.5137	3.5793	3.2138	3.2138
K_2	0.2168	0.5888	0.3208	0.2688	0.2688
K_3	0.07961	0	0.0285	0.07961	0.07961
C_1	-0.065		0.1682	-0.06499	-0.06499
C_2	0.05025		0.3477	0.05025	0.05025
C_3	0.01474		0.4841	0.01474	0.01474
B_1	1.8		1.8	1.8	1.8
B_2	1.5		1.51	1.5	1.5
F_M	1.25		1.8	1.25	1.25
F_p		3.5			

4. Results and discussion

Bottom cycle TEG/ORC ratios are the ratios of TEG unit flue gas waste heat utilization to ORC unit flue gas waste heat utilization. (B_{CR}). Keeping the B_{CR} at 0.615, important metrics, such as the system's power output (W_{net}), system thermal efficiency (η_s), , waste heat utilization of main engine flue gas (f_g), power-production cost (C_g), and temperature drop of main engine flue gas (T_{fg}) are explored. As the P gets larger, the saturated vapor corresponding to R245fa also increases. To ensure complete vaporization of the R245fa, the temperature was raised to 283K in the TEG unit. According to the simulation analysis, by altering the jacket water and charge air volumes, the organic working fluids are increased to 295 K and 313 K at the secondary and third-stage preheaters.

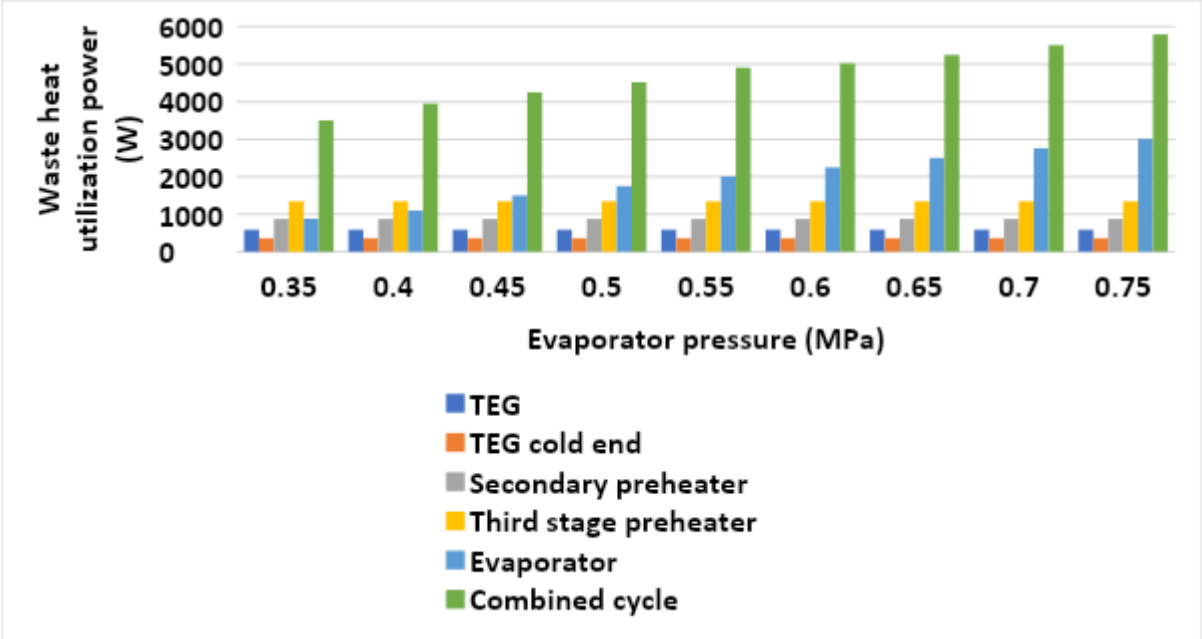

Figure 2. Comparison of utilizing waste heat power under different evaporating pressure

Figure 2 shows the waste heat utilization power analysis (W_P). As the P increases, the saturated vapor temperature also increases. If the R245fa is heated step by step to confirm it absorbs heat and vaporizes in the evaporator, the R245fa working fluid needs to absorb more heat in each stage of the preheater, and it will eventually vaporize in the evaporator. So, in the experiment, the R245fa inlet temperature kept stable in the evaporator by adjusting the volume of the jacket water and charge air. Finally, the W_P of the preheater units at all levels is kept stable. As the P gets larger, the W_P of the ORC unit increases, and the W_P of the system also increases synchronously. When the P is 0.75 MPa, the W_P of the TEG unit, the cold end, the secondary preheater, the third-stage preheater, the evaporator, and the system is 568.00 W, 360.08 W, 874.72 W, 1343.44 W, 3010.56 W, and 5796.72 W, respectively.

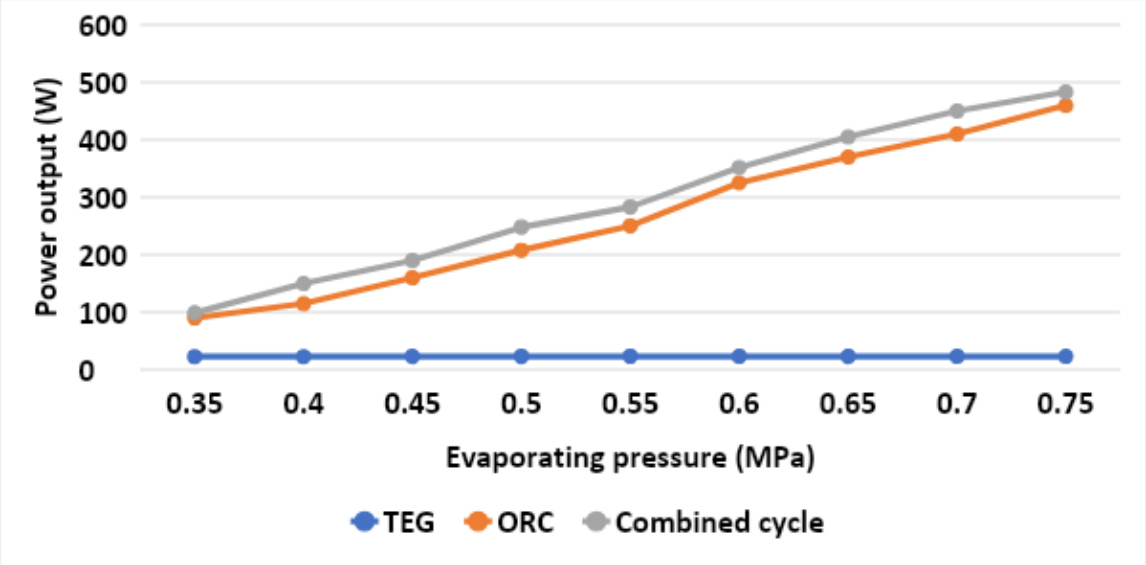

Figure 3. Power output under various evaporating pressures is compared

Figure 3 illustrates the power output (W) under different P. As the P gets larger, the W_{TEG} remains unchanged because the N_{TEG} is unchanged. With the increase of the P, the heat absorption capacity per unit time of the R245fa increases. The ability to push the expander to perform tasks additionally raises, so the W_{ORC} raises. The W_{net} include the TEG unit and ORC unit, so it increases gradually. When pressure (P) is 0.75MPa, the W_{TEG}, W_{ORC}, and the W_{net} is 23.26 W, 459.99 W, and 483.25 W, respectively.

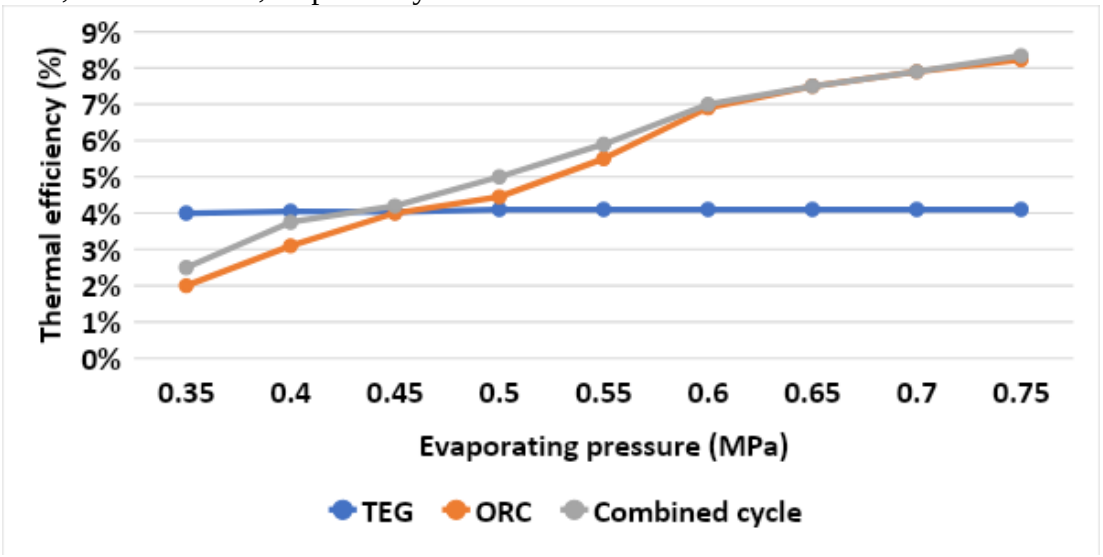

Figure 4. Comparison of thermal efficiency under different evaporation pressure

Figure 4 demonstrates the thermal efficiency (η_t) under different P. With the increase of the P, the η_1 remains almost unchanged due to the stable W_{TEG}. As the P increases, the W_{ORC}, and the W_{net} increase, so the η_1 and η_s, increase. When the P is 0.75 MPa, the η_1, η_2 and η_s is 4.10 %, 8.23 % and 8.34 %, respectively.

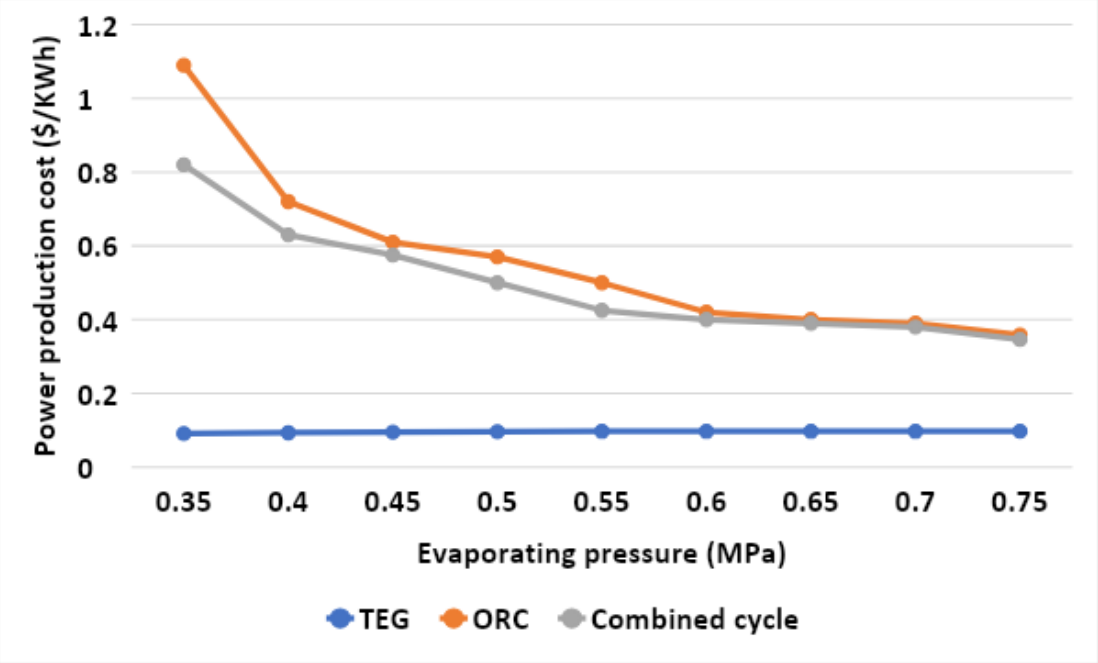

Figure 5. Costs of power production are compared under different evaporation pressure

Figure 5 shows the Cg analysis for various P. With an increase in P, the N_{TEG} remains almost unchanged. Due to the influence of environmental heat loss, the C_g of the TEG unit appears some fluctuations. The performance of the high-temperature, high-pressure R245 steam-driven expander is further improved as P increases. The C_g the ORC unit and the system decrease. It is worth noting that the system's The Cg is less than ORC unit's. The experiment confirms the viability of using a combined cycle system to recycle ship waste heat by lowering the Cg. When P = 0.75Mpa, the Cg of the TEG unit, ORC unit, and system are 0.0972 $/kWh, 0.3587 $/kWh, and 0.3461 $/kWh, respectively.

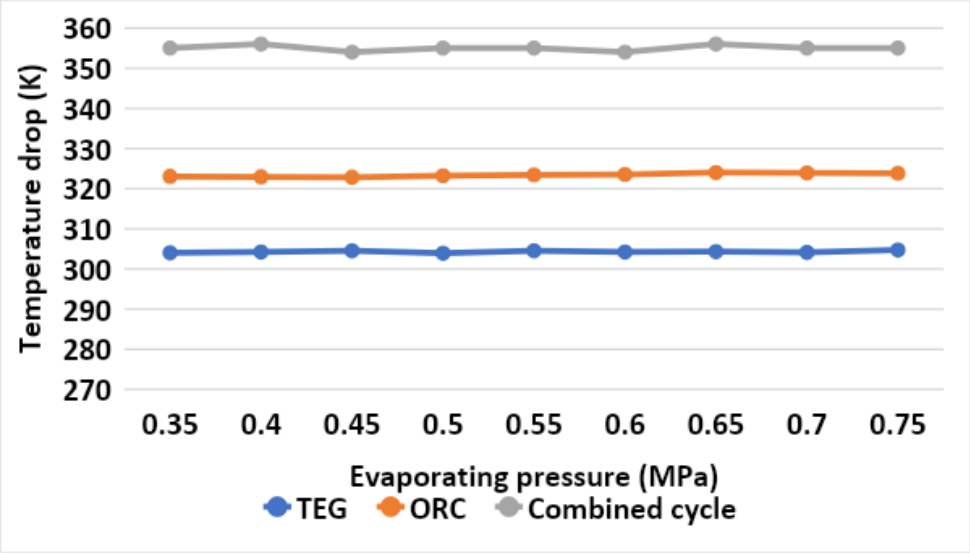

Figure 6. Temperature drops of the main engine's flue gas under various conditions

evaporating pressure

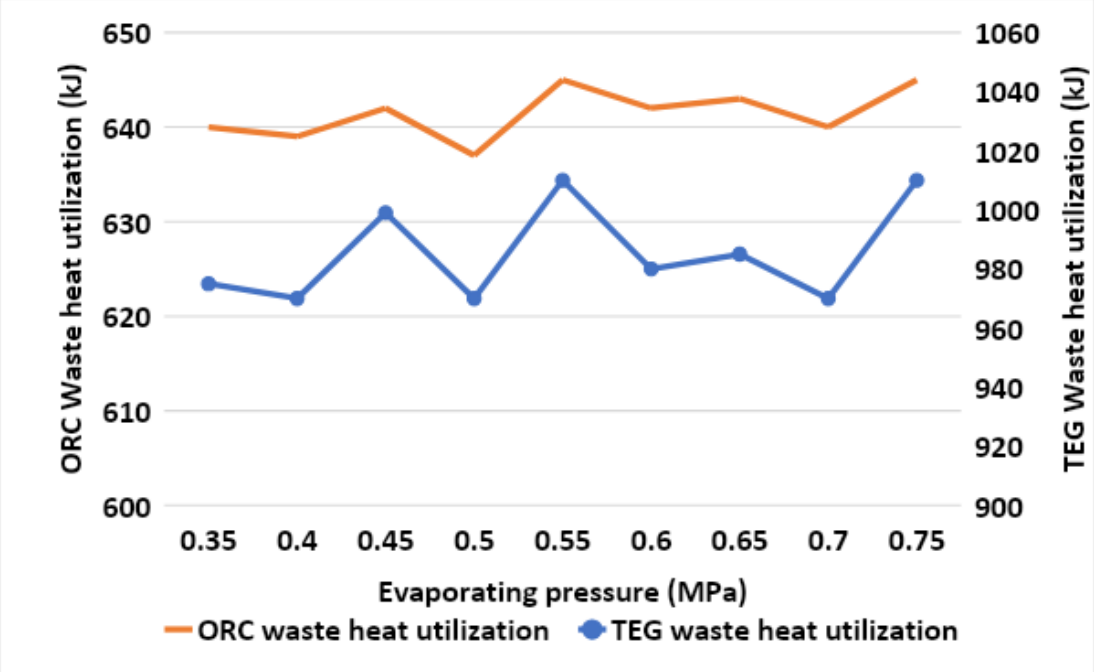

Figure 7. Waste heat utilization rate of the main engine's flue gas under various conditions

Figure 6 and Figure 7 plot the temperature drop and Rate of waste heat usage in main engine flue gas (T_{fg} and f_g) under different evaporating pressure (P). The f_g of the ORC unit is much higher than that in the TEG unit. This is consistent with the fact that the W_{ORC} is much higher than that of the W_{TEG}. As the P gets larger, the T_{fg} of the TEG unit and the ORC unit remains unchanged, so the f_g of the TEG unit and the ORC unit is unchanged. The T_{fg} of the system is composed of the above two parts and it basically remains intact, so the rate of the f_g remains unchanged. The figure also shows the f_g of the TEG unit fluctuates in a particular range, and the T_{fg} of the system is much higher than that of the TEG unit and the ORC unit. The combined cycle system takes full advantage of the f_g, reduces the emission of CO_2 to a certain extent, and decreases the pollution of the environment. When the P is 0.75Mpa, the T_{fg} of the TEG unit and the ORC unit is 304.7K and 323.8 K, respectively. The f_g of the TEG unit, the ORC unit is 1010 KJ, 645 KJ. the system rate of f_g is 62.15 %, respectively.

5. Conclusion

In this research, Under different evaporation pressures, the variation trend of the system net power output, system thermal efficiency, power-production cost, and waste heat utilization of main engine flue gas is explored using The organic working fluid is R245fa. As the evaporation pressure is not greater than 0.75 MPa, the numerical analysis maintains the mass flow rate at 0.056kg/s and the bottom cycle ratios at 0.615, With increasing evaporation pressure, the system net power output, using waste heat from the main engine's flue gas, and system thermal efficiency rise, while the power production cost lowers. Accordingly, the system's net power output is 483.25 W, thermal efficiency is 8.34%, waste heat utilization power is 5796.72 W, power production costs are 0.3464 $/kWh, and the waste heat utilization rate of the main engine's exhaust gas is 69.05% when the evaporation pressure is 0.75 Mpa.

6. References

1. Lee S, Yoo S, Park H, et al. Novel methodology for EEDI calculation considering onboard carbon capture and storage system. *International Journal of Greenhouse Gas Control* 2021; 105: 103241.
2. O, O, Kanifolskyi. TECHNICAL NOTE: EEDI (ENERGY EFFICIENCY DESIGN INDEX) FOR SMALL SHIPS OF THE TRANSITIONAL MODE. *Transactions of the Royal Institution of Naval Architects* 2014; 156: B-39-B-41.
3. Jovanovic V, Ghamaty S, and Elsner N B. Design, Fabrication and testing of quantum well thermoelectric generator. *Conference on Thermal & Thermomechanical Phenomena in Electronics Systems* 2006; 1417-1423.
4. Georgopoulou C A, Dimopoulos G G, and Kakalis N. A modular dynamic mathematical model of thermoelectric elements for marine applications. *Energy* 2016; 94(1): 13-28.
5. Wang L, and Romagnoli A. Cooling system investigation of thermoelectric generator used for marine waste heat recovery. *2nd Annual Southern Power Electronics Conference (SPEC)* 2016 1-6
6. Eddine A. N, Chalet D, Faure X, et al. Optimization and characterization of a thermoelectric generator prototype for marine engine application. *Energy* 2017; 143(1): 682-695.
7. Hoang T H, and Vinogradov S V. Research, development of the design and calculation of thermal and electrical parameters of the TEG for the ship M/V NSU Keystone. *Journal of Physics Conference* 2018; 1111(1): 012071.
8. Lion S, Taccani R, Vlaskos I, et al. Thermodynamic analysis of waste heat recovery using Organic Rankine Cycle (ORC) for a two-stroke low speed marine Diesel engine in IMO Tier II and Tier III operation. *Energy* 2019; 183(9): 48-60.
9. Ng C, Tam I, and Wu D. System modelling of organic Rankine cycle for waste energy recovery system in marine applications. *Energy Procedia* 2019; 158(2): 1955-1961.
10. Yang F, Dong X, Zhang H, et al. Performance analysis of waste heat recovery with a dual loop organic Rankine cycle (ORC) system for diesel engine under various operating conditions. *Energy Conversion and Management* 2014; 80(7): 243-255.
11. Chen T, Zhuge W, Zhang Y, et al. A novel cascade organic Rankine cycle (ORC) system for waste heat recovery of truck diesel engines. *Energy Conversion & Management* 2017; 138(8): 210-223.
12. Liu P, Shu G, Tian H, et al. Alkanes based two-stage expansion with inter heating organic Rankine cycle for multi-waste heat recovery of truck diesel engine. *Energy* 2018; 147(1): 337-350.
13. Zhu Y, Li W, Sun G, et al. Thermo-economic analysis based on objective functions of an organic Rankine cycle for waste heat recovery from marine diesel engine. *Energy* 2018; 158(9): 343-356.
14. Yang M H, and Yeh R H. Analyzing the optimization of an organic Rankine cycle system for recovering waste heat from a large marine engine containing a cooling water system. *Energy Conversion & Management* 2014; 88(24): 999-1010.
15. Hua T, Shu G, Wei H, et al. Fluids and parameters optimization for the organic Rankine cycles (ORCs) used in exhaust heat recovery of Internal Combustion Engine (ICE). *Energy* 2012; 47(1): 125–136.
16. Miller E W, Hendricks T J, and Peterson R B. Modeling energy recovery using thermoelectric conversion integrated with an organic Rankine bottoming cycle. *Journal of Electronic Materials* 2009; 38(7): 1206-1213.
17. Miller E W, Hendricks T J, Wang H, et al. Integrated dual-cycle energy recovery using thermoelectric conversion and an organic Rankine bottoming cycle. *Proceedings of the Institution of Mechanical Engineers, Part A: Journal of Power and Energy* 2011; 225: 33-43.
18. Qiu K, and Hayden A. Integrated thermoelectric and organic Rankine cycles for micro-CHP systems. *Applied Energy* 2012; 97(9): 667-672.

19. Shu G, Jian Z, Hua T, et al. Parametric and exergetic analysis of waste heat recovery system based on thermoelectric generator and organic Rankine cycle utilizing R123. *Energy* 2012; 45(1): 806-816.
20. Zhang C, Shu G, Hua T, et al. Comparative study of alternative ORC-based combined power systems to exploit high temperature waste heat. *Energy Conversion & Management* 2015; 89(1): 541-554.
21. Wang H, Hendricks T, Peterson R, et al. Experimental verification of thermally activated Power and cooling system using hybrid thermoelectric, organic Rankine cycle and vapor 210-223. compression cycle. *9th Annual International Energy Conversion Engineering Conference* 2011; 5983.
22. Johansson M T, and Söderström M. Electricity generation from low-temperature industrial excess heat-an opportunity for the steel industry. Energy efficiency 2014; 7(2): 203-215.
23. Kumar S, Roy D, and Ghosh S. Thermodynamic assessment of TEG-ORC combined cycle powered by solar energy. International Journal of Renewable Energy Technology 2017; 8(3-4): 346-359.
24. Liu C, Ye W, Li H, et al. Experimental study on cascade utilization of ship's waste heat based on TEG-ORC combined cycle. International Journal of Energy Research 2021; 45: 4184-4196.
25. Liu C, Li H, Ye W, et al. Simulation research of TEG-ORC combined cycle for cascade recovery of vessel waste heat. International Journal of Green Energy 2021; 18(11): 1173-1184.
26. Liu C, Liu J, Ye W, et al. Study on a new cascade utilize method for ship waste heat based on TEG-ORC combined cycle. Environmental Progress & Sustainable Energy 2021. https://doi.org/10.1002//ep.13661.
27. Ye W, Liu C, Liu J, et al. Research on TEG–ORC Combined Bottom Cycle for Cascade Recovery from Various Vessel Waste heat Sources. Arabian Journal for Science and Engineering 2021. https://doi.org/10.1007/s13369-021-06050-3.
28. Galindo J, Ruiz S, and Dolz V. Experimental and thermodynamic analysis of a bottoming Organic Rankine Cycle (ORC) of gasoline engine using swash-plate expander. Energy Convers Manage 2015; 103: 519–532.
29. Qiu G. Selection of working fluids for micro-CHP systems with ORC. Renew Energy 2012; 548: 565–570.
30. Yang F, Zhang H, Song S, et al. Thermoeconomic multi-objective optimization of an organic Rankine cycle for exhaust waste heat recovery of a diesel engine. Energy 2015; 93: 2208– 2228.
31. Mignard. Correlating the chemical engineering plant cost index with macro-economic indicators. Chemical Engineering Research and Design 2014; 92: 285-294.
32. Bracco R, Clemente S, Micheli D, et al. Experimental tests and modelization of a domestic-scale ORC (Organic Rankine Cycle). Energy 2013; 58: 107–116.
33. Song P, Wei M, Shi L, et al. A review of scroll expanders for organic Rankine cycle systems. *Appl Therm Eng* 2015; 75: 54–64.
34. Giuffrida A. Modelling the performance of a scroll expander for small organic Rankine cycles when changing the working fluid," *Appl Therm Eng* 2014; 70(1): 1040–1049.

Effect of Changing the Amplitude of a Sinusoidal Corrugated Absorber Plate of a Two-Pass Solar Air Heater

Mohab I. Mefreh*, Mohamed A. Alnakeeb , Mohamed A. Hassab, Wael M. El-Maghlany
Department of Mechanical Engineering, Faculty of Engineering, Alexandria University, Egypt
*Corresponding Author: es-mohabihab@alexu.edu.eg

Keywords: SAH, amplitude, CFD simulation, Thermo-hydraulic performance, Nusselt number.

Abstract. Solar air heaters (SAHs) are an extremely efficient method of turning solar radiation into thermal power for a variety of heating purposes. Due to its low thermal efficiency, multiple research efforts have formerly concentrated on enhancing the heat transfer of SAHs with a flat plate. Using ANSYS Fluent 18.2, a 3D-validated numerical model for a sinusoidal corrugated double-pass SAH was conducted to study the effect of changing the amplitude of the sinusoidal corrugated absorber on the thermo-hydraulic performance of the SAH at different air mass flow rate values ranged from 0.02 kg/s to 0.08 kg/s. These findings revealed that raising the amplitude to 30 mm improved the SAH's efficiency and Nusselt number by 48.4% and 187.44%, respectively while it increases the pressure drop across the SAH by 190.73% when compared to that of the flat plate SAH. These results also showed that increasing the air mass flow rate from 0.02 kg/s to 0.08 kg/s, increased the efficiency of the flat plate design by 61.12%. Meanwhile, this rise in air mass flow rate showed an improvement in the efficiency of the SAH with plate design parameters of 30 mm amplitude and 100 mm pitch by 23.15%. Despite the efficiency enhancement due to this rise in mass flow rate, it causes a rise in pressure drop which will increase the blower power required. The blower power at a mass flow rate of 0.08 kg/s accounts for 0.26% of the useful energy for the SAH configuration with an amplitude of 30 mm.

Nomenclature

A_p	Surface area of the absorber plate [m^2]
G_k	Production of k due to mean velocity gradients
G_t	Incident solar irradiance [W/m^2]
G_ω	Production of ω due to mean velocity gradients
$\dot{m}_a$	Air mass flow rate [kg/s]
Nu	Nusselt number
P_{blower}	Blower pumping power [W]
T_i	Air intake temperature [°C]
T_o	Air exit temperature [°C]
Y_k	Dissipation of k due to mean velocity gradients
Y_ω	Dissipation of ω due to mean velocity gradients

Greek

Γ	Effective diffusivity [m^2/s]
ΔP	Pressure drop across the SAH [Pa]
δ_{ij}	Kronecker delta
ε	Emissivity
η_{th}	Thermal efficiency
ρ	Air density [kg/m^3]
ω	Specific dissipation rate [s^{-1}]

List of abbreviations

CPDP SAH	Corrugated plate double-pass solar air heater
FSAH	Flat solar air heater
MFR	Mass flow rate
SAH	Solar air heater

TSAH Tubular solar air heater

Introduction

To fulfil the world's already increasing energy needs, fossil fuels are already being exploited. However, due to the earth's limited fossil resources, we must rely on other sources of energy to satisfy our needs. As fossil fuels deplete, sustainable and renewable energy will become increasingly crucial. One of the most abundant, environmentally friendly, and clean energy sources is solar energy. A SAH is a type of solar energy harvesting device. SAHs perform poorly due to their limited thermal conductivity, heating capacity, and convective heat transfer coefficient between both the air passing through the duct and the absorber plate. To address these concerns, the heat transfer coefficient and surface area must be raised. To enhance the overall performance of the SAH, extended surfaces, packed or porous bed absorbers, and artificial roughness in the absorber plate are used [1].
Mohamad et al. [2] examined a SAH numerically, which has a double-pass with a porous matrix. This study investigated the heat loss reduction from the collector's glass cover to boost the SAH thermal efficiency, which surpasses 75%. Manjunath et al. [3] assessed the enhancement of the SAH performance when using a sinusoidal absorber plate on SAH performance while changing the plate's aspect ratio and wavelength. An experimental investigation on three SAHs types was conducted by Gill et al. [4].Iron chips were used to design, construct, and test single, double-glazed, and packed beds for radiation absorption. For each SAH, the efficiency factor, heat removal factor, and inlet air temperature were evaluated.The optimum operating conditions and geometrical parameters for an array-based SAH with a micro-heat pipe investigated by Zhu et al. [5]. The improved temperature distribution of micro-channels reduces heat loss. The highest efficiency achieved was 66.5%. Shetty et al. [6] employed numerical techniques to examine a SAH with a rounded perforated absorber plate. Thermal efficiency was enhanced by 23.33% as compared to the typical SAH. Hassan et al. [7] reported an experimental investigation on 2 SAHs types (Flat and Tubular). For all tested mass flow rates, the results revealed that both, heat transfer and efficiency of the TSAH, are greater when compared to the FSAH. Therefore, the main objective of this research is to undertake a numerical study to assess the influence of changing the amplitude of a sinusoidal corrugated absorber plate on the flow and heat transfer characteristics of a double-pass SAH in terms of thermo-hydraulic performance.
Performance Parameters. Thermal efficiency of the SAH is obtained from [8, 9]:

- $\eta_{th} = \frac{\dot{m}_a C_p (T_o - T_i)}{G_t A_p}$. (1)

- The mechanical pumping power required is expressed by [8, 9]:

- $P_{blower} = \frac{\dot{m}_a \Delta P}{\rho}$. (2)

Numerical Analysis

- A numerical model was developed to investigate the effect of changing the amplitude of the sinusoidal absorber plate on the performance of a CPDP SAH (Thermal efficiency, Nusselt number, pressure drop, etc.).
- **Fundamental Design Elements and Geometry.** Fig. 1 depicts the geometric details of the SAH system. A wavy absorber plate and an air duct make up the SAH system. The test section chosen was the air duct. As shown in Fig. 1, the test section is 1600 mm long and has a corrugated absorber plate in the middle. In the two-pass SAH, the first pass's flow channel was addressed to be between both, the glazing glass and the absorber plate, while the second pass's flow channel was addressed to be between the bottom of the wooden frame and the absorber

plate. As a consequence, the air absorbs more energy than the air in a SAH with a single pass. The analysis was carried out for four different amplitudes of the sinusoidal corrugated absorber plate of the double-pass SAH, 0 (Double-pass SAH with a flat plate), 10, 20, and 30 mm. All cases had a pitch of 100 mm and were evaluated at four different MFRs ($\dot{m}_a$) of 0.02, 0.04, 0.06, and 0.08 kg/s.

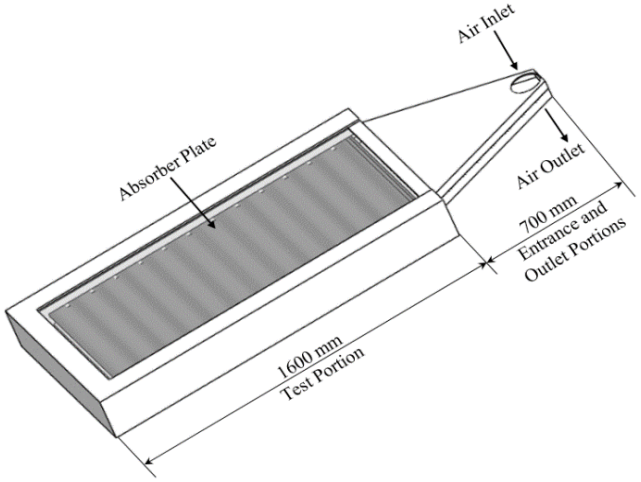

Fig. 1. Geometric details of the CPDP SAH model (All dimensions in mm).

Mesh Generation Methodology and Mesh Independence Test for the Computational Domain of the Flow. The technique utilized to generate the SAH model's meshing to achieve a balance between precision and simulation run time. A very fine mesh zone was created to effectively visualize the pattern of the airflow along the surface of the wavy absorber plate, as exposed in Fig. 2 (a). This assists in predicting the behaviour of the boundary layer and the vortices that arise near the absorber plate's surface.

Mesh independence test for different numbers of mesh elements in the range of 0.124×10^5 - 6.67×10^5 for the CPDP SAH with an amplitude and a pitch of 20 and 100 mm, respectively at a MFR ($\dot{m}_a$) of 0.04 kg/s was performed to establish the ideal mesh element size. Fig. 2 (b) illustrates the effect of changing the number of elements on the variations in exit temperature (T_o) and efficiency (η_{th}). The fluctuations in exit temperature (T_o) and efficiency (η_{th}) decreased as the number of elements rose. The number of elements employed for all undermentioned simulations is 4.8×10^5 since the fluctuations in results are negligible.

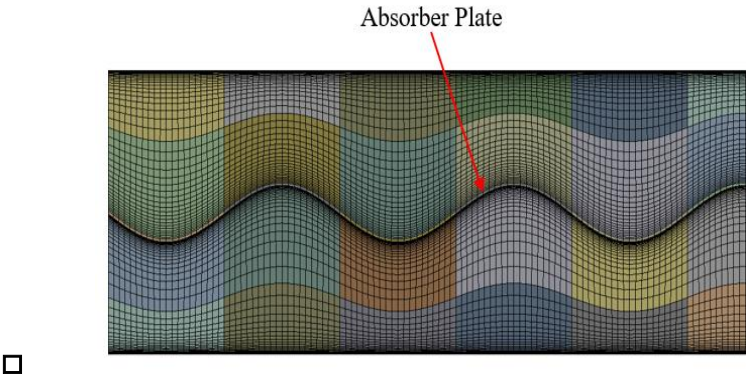

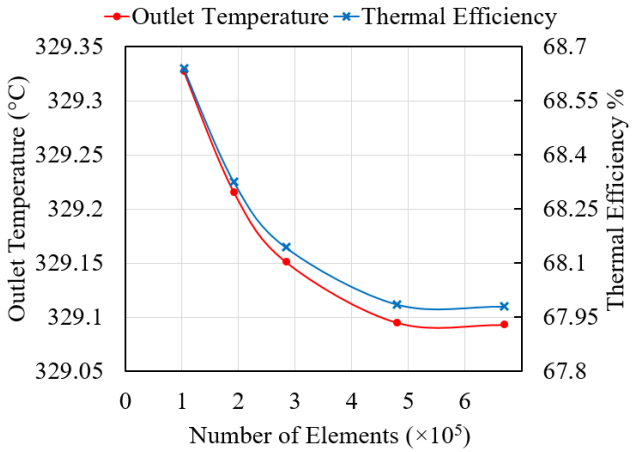

(a) (b)

Fig. 2. (a) A close-up view of a part of the plate and air-duct mesh. (b) Mesh independence test.

Boundary Conditions and Assumptions. Table 1 depicts the properties of the boundary conditions of the computational domain.

Table 1
Computational boundary conditions.

	Boundary surfaces	Boundary conditions
i.	At duct inlet	: MFR condition was specified to be 0.02, 0.04, 0.06, and 0.08 [kg/s].
ii.	At duct outlet	: Outlet atmospheric pressure condition was specified to be 101.3 [kPa].
iii.	Air-solid interface	: No-slip and impermeable wall condition.
iv.	Top surface of the glazing glass	: Uniform solar heat flux values applied from experimental readings.
v.	Bottom and side walls of the computational domain	: Adiabatic insulation (no heat loss).

For this numerical analysis following assumptions were made:

- All configurations' absorber plates have the same pitch of 100 mm.
- All the CPDP SAH configurations have the same dimensions.
- Constant solar irradiance value of 1000 W/m^2.
- Constant air inlet temperature of 27 °C.

Selection of Physics Models and Governing Equations. For numerical simulation, a pressure-based CFD solver with double precision is utilised. SIMPLE segregated solver is used for pressure-velocity coupling. The body-force weighted technique is utilised for pressure discretization, whereas the second-order upwind approach is employed for spatial discretization. The turbulent flow parameters are determined using the SST k-ω turbulence model. The solution is said to converge when the residuals in the computation domain fall below 10^{-6} for energy

equations and 10^{-5} for momentum and continuity equations. In addition to residuals, surface monitors for the air temperature at the duct exit and the temperature of the absorber plate are employed to verify convergence [3].

- The governing equations are presented by [3, 10]:
- Continuity equation:

$$\frac{\partial u}{\partial x}+\frac{\partial v}{\partial y}+\frac{\partial w}{\partial z}=0 \quad (3)$$

- Momentum equations:

$$\frac{\partial}{\partial x_i}(\rho u_i u)=-\frac{\partial p}{\partial x_i}+\frac{\partial}{\partial x_i}\left(u\left(\frac{\partial u_i}{\partial x_j}+\frac{\partial u_j}{\partial x_i}-\frac{2}{3}\delta_{ij}\frac{\partial u_l}{\partial x_l}\right)\right)-B_i-\frac{\partial}{\partial x_i}(\rho u_i' u_j') \quad (4)$$

- Equation of energy:

$$\frac{\partial T}{\partial t}+u\frac{\partial T}{\partial x}v\frac{\partial T}{\partial y}+w\frac{\partial T}{\partial z}=\alpha\left(\frac{\partial^2 T}{\partial x^2}+\frac{\partial^2 T}{\partial y^2}+\frac{\partial^2 T}{\partial z^2}\right) \quad (5)$$

- Transport equations for the shear stress transport (SST) k-ω model [3, 11]:

$$\frac{\partial}{\partial t}(\rho k)+\frac{\partial}{\partial x_i}(\rho k u_i)=\frac{\partial}{\partial x_j}\left(\Gamma_k\frac{\partial k}{\partial x_j}\right)+G_k-Y_k \quad (6)$$

$$\frac{\partial}{\partial t}(\rho \omega)+\frac{\partial}{\partial x_j}(\rho \omega u_j)=\frac{\partial}{\partial x_j}\left(\Gamma_\omega\frac{\partial \omega}{\partial x_j}\right)+G_\omega-Y_\omega+D_\omega \quad (7)$$

- **Numerical Model Validation.** The model validation was performed for the case of SAH with baffles positioned in the second half of the air channel studied by Bensaci et al. [12]. The authors conducted experimental and numerical temperature distribution along the SAH length with a mass flow rate of 0.017 kg/s. Fig. 3 showed that the present model is in good agreement with the authors' experimental and numerical results with a maximum deviation of 5.9%.

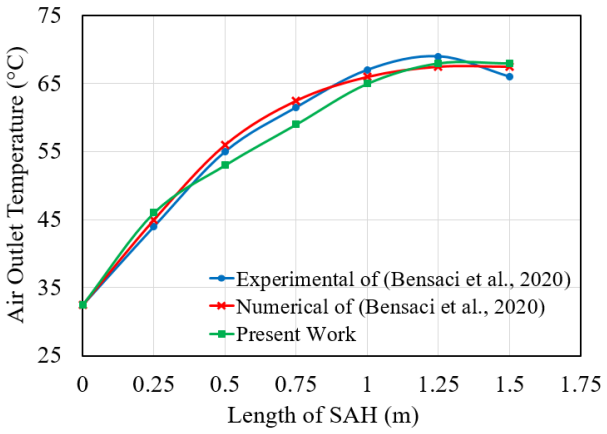

Fig. 3. Model validation.

Results and Discussion

A 3D CFD study is performed to assess the effect of changing the amplitude of the sinusoidal corrugations on the solar air heater's performance under various air mass flow rates ranging from 0.02 kg/s to 0.08 kg/s The acquired findings are compared to those of the base model to assess the performance of the sinusoidal absorber plate as a heat transfer augmentation device for solar air heaters.

Heat Transfer Characteristics. Fig. 4 illustrates the variations of the Nusselt number for various designs with a pitch of 100 mm at different air MFR. It is clear that the existence of corrugations results in greater Nusselt numbers at all MFRs regardless of the configuration employed for sine-wave corrugation. The Nusselt number is shown to grow as the amplitude of the sin-wave corrugation increases. The average Nusselt number values for the configurations with amplitudes of 10 mm, 20 mm, and 30 mm are 20.66, 34.47, and 46.02, respectively, while its value for the flat plate configuration is 16.01. It should be observed that the heat transfer area increases from the base model as a result of the presence of corrugations, with the highest rise in that area determined to be around 20% for the design with an amplitude of 30 mm when compared to the flat plate case.

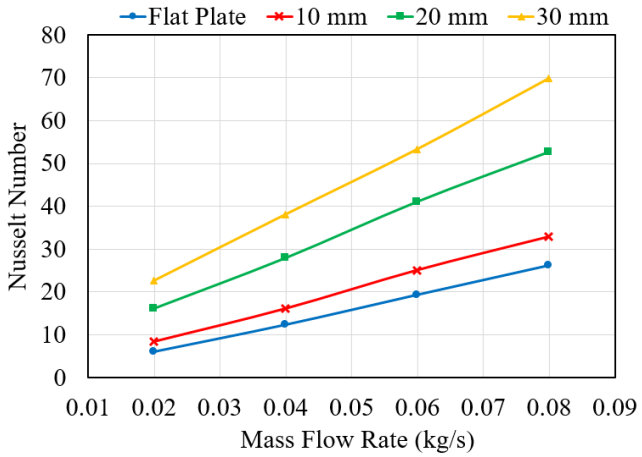

Fig. 4. Nusselt number of four configurations with different amplitudes at various air MFRs.

Efficiency. The change of the efficiency for different configurations with various amplitudes is shown in Fig. 5. Generally, the existence of wavy corrugations on the absorber plate has a considerable influence on the improvement of heat transfer, as shown by an enhancement in thermal efficiency of the CPDP SAH in Fig. 5. The reason for this is that the corrugations encourage turbulence by producing a violent perturbation in the flow of air. The average efficiencies for the configurations with amplitudes of 10 mm, 20 mm, and 30 mm are 55.32%, 62.72%, and 66.04%, respectively, with an enhancement of 24.3%, 41%, and 48.4%, when compared to the flat plate design. It is also clear that increasing the air MFR aids in thermal efficiency improvement but its positive impact diminishes at higher mass flow rates and higher amplitude values. The efficiency rises by about 61.12% for the flat plate design meanwhile it increases with a value of 41.13%, 24.24%, and 23.15% for the designs with an amplitude of 10 mm, 20 mm, and 30 mm, respectively, when increasing the air MFR from 0.2 kg/s to 0.8 kg/s.

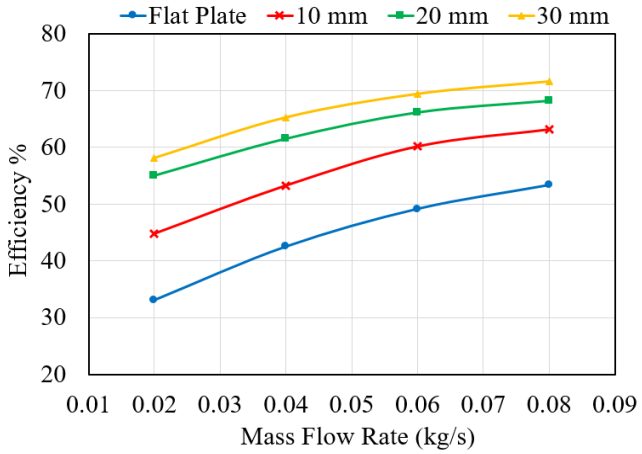

Fig. 5. Thermal efficiency of four configurations with different amplitudes at various air MFRs.

Pressure Drop. Fig. 6 depicts the pressure drop fluctuation for SAH setups with a pitch of 100 mm and varied amplitude. It should be noted that the absorber plate design with 30 mm amplitude has a considerably higher pressure drop, with an average rise of about 190.73% greater than that of the base case. The pressure drop is shown to grow as the wave amplitude increases owing to higher corrugation resistance. It is also clear that the effect of increasing the air MFR on increasing the pressure drop is significant with higher values of the sinusoidal wave's amplitude. Thus, Fig. 6 shows that the configuration of the plate with 30 mm amplitude has a pressure drop rise of approximately 27 Pa when increasing the MFR from 0.02 kg/s to 0.08 kg/s while this value is only 10 Pa for the flat plate case. This rise in pressure drop causes an increase in the blower power required to maintain the airflow across the SAH. The power of the air blower at a mass flow rate of 0.08 kg/s accounts for roughly 0.15%, 0.2%, and 0.26% of the useful energy for the configurations with 10 mm, 20 mm, and 30 mm, respectively. The flat plate case consumes 0.14% of the useful energy for blowing air through the SAH.

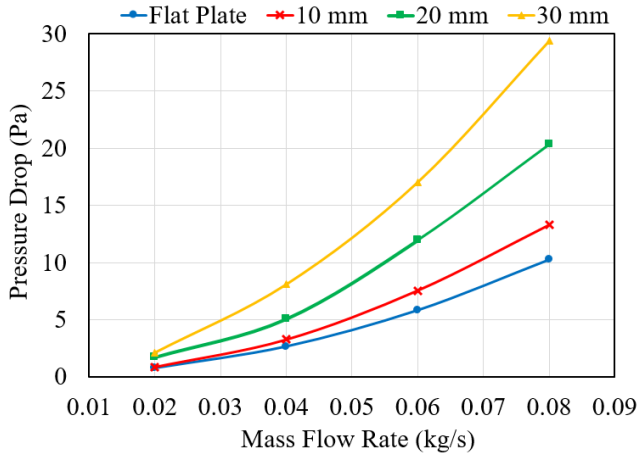

Fig. 6. Pressure drop across the SAH for four configurations with different amplitudes at various air MFRs.

Conclusion

The numerical analysis investigated the effect of changing the amplitude of the sinusoidal corrugated of a double-pass solar air heater and compare the results with the flat plate double-pass solar air heater. The evaluation focused on the following improvements in air outlet temperature, Nusselt number, and thermal efficiency:

1. Heat transfer area increased by 20% when compared to the flat plate configuration when using a corrugated plate with a 30 mm amplitude and 100 mm pitch.
2. Increasing the amplitude of the corrugations to 30 mm enhanced both efficiency and Nusselt number by 48.4% and 187.44%, respectively.

3. Raising the amplitude of the sinusoidal corrugations to 30 mm caused an increase in pressure drop across the SAH by 190.73% when compared to the flat plate design, which will cause an increase in the blower power required to maintain the airflow across the SAH.
4. The power of the air blower of the SAH with a corrugated plate with an amplitude of 30 mm at a mass flow rate of 0.08 kg/s accounts for only 0.26% of the useful energy, while it only accounts for 0.14% for the flat plate design.
5. Raising the air mass flow rate from 0.02 kg/s to 0.08 kg/s caused an enhancement in the efficiency of the 30 mm amplitude configuration by 23.15%.

References

[1] A. Saravanan, S. Parida, M. Murugan, M.S. Reddy, P.V. Elumalai, S. Kumar Dash, Thermal performance prediction of a solar air heater with a C-shape finned absorber plate using RF, LR and KNN models of Machine learning, Thermal Science and Engineering Progress 38 (2023) 101630.
[2] A.A. Mohamad, High efficiency solar air heater, Solar Energy 60(2) (1997) 71-76.
[3] M.S. Manjunath, K.V. Karanth, N.Y. Sharma, Numerical investigation on heat transfer enhancement of solar air heater using sinusoidal corrugations on absorber plate, International Journal of Mechanical Sciences 138-139 (2018) 219-228.
[4] R.S. Gill, S. Singh, P.P. Singh, Low cost solar air heater, Energy Conversion and Management 57 (2012) 131-142.
[5] T. Zhu, J. Zhang, A numerical study on performance optimization of a micro-heat pipe arrays-based solar air heater, Energy 215 (2021) 119047.
[6] S.P. Shetty, N. Madhwesh, K. Vasudeva Karanth, Numerical analysis of a solar air heater with circular perforated absorber plate, Solar Energy 215 (2021) 416-433.
[7] H. Hassan, S. Abo-Elfadl, M.F. El-Dosoky, An experimental investigation of the performance of new design of solar air heater (tubular), Renewable Energy 151 (2020) 1055-1066.
[8] R. Kumar, P. Chand, Performance enhancement of solar air heater using herringbone corrugated fins, Energy 127 (2017) 271-279.
[9] A.A. El-Sebaii, S. Aboul-Enein, M.R.I. Ramadan, S.M. Shalaby, B.M. Moharram, Investigation of thermal performance of-double pass-flat and v-corrugated plate solar air heaters, Energy 36(2) (2011) 1076-1086.
[10] A. Boulemtafes-Boukadoum, C. Abid, A. Benzaoui, 3D Numerical study of the effect of aspect ratio on mixed convection air flow in upward solar air heater, International Journal of Heat and Fluid Flow 84 (2020) 108570.
[11] M.S. Manjunath, K.V. Karanth, N.Y. Sharma, Numerical analysis of the influence of spherical turbulence generators on heat transfer enhancement of flat plate solar air heater, Energy 121 (2017) 616-630.
[12] C.-E. Bensaci, A. Moummi, F.J. Sanchez de la Flor, E.A. Rodriguez Jara, A. Rincon-Casado, A. Ruiz-Pardo, Numerical and experimental study of the heat transfer and hydraulic performance of solar air heaters with different baffle positions, Renewable Energy 155 (2020) 1231-1244.

Mohamed T. Eltantawy [1,a], Mohamed R. Shouman [2] and Mohamed M. Elgohary [1,b]
1 Department of Naval architecture and Marine Engineering, Faculty of Engineering, Alexandria University, Alexandria, Egypt

2 Marine Engineering technology Department, Arab Academy for Science, Technology and Maritime Transport (AASTMT), Alexandria, Egypt

1,a eng.altantawe@hotmail.com, 2, shouman85@aast.edu, 1,b prof.morsy@gmail.com

Keywords: Solar system; passenger ship; emission reduction; economical evaluation; Fuel saving

Abstract. Maritime transportation contributes significantly to atmospheric pollutant gases, and alternative energy systems can reduce emissions and save energy. The concept of green shipping has gained global importance, and solar energy can contribute to a ship's energy balance. This study presents a case study of installing a photovoltaic solar system on a passenger/Ro-Ro ship sailing between Safaga Port in Egypt and Yanbu Port in Saudi Arabia. The ship will accommodate 843 passengers and 227 cars, and the solar system will produce 1625 kWh/day to power the ship's hoteling system. The system will save 0.333 tons of low Sulphur fuel oil per day by the generators. Environmental impacts were assessed, indicating a reduction of 0.27 tons of SOx, 7 tons of NOx, 415 tons of CO2, and 0.18 tons of PM emissions annually. A cost analysis was conducted, showing that the installed solar system would save $326,000 per year while being environmentally friendly and promoting sustainable transportation. Overall, this study highlights the potential benefits of adopting solar power on ships and its potential to reduce emissions and contribute to a green ship.

1- Introduction

The increase in fossil fuel consumption has led to a daily increase in the amount of emission gas emitted into the atmosphere. This worldwide phenomenon has caused unexpected changes, such as climate change and global warming. Amongst all contributing sectors, the transportation sector has been identified as one of the most significant factors responsible for the rise in emission gas. According to the greenhouse gas (GHG) study conducted by the International Maritime Organization (IMO), which is the governing body in the maritime industry, maritime transportation contributes 870 million tons of CO2, equivalent to 2.7% of the total, and represents more than 80% of global cargo trade **[1]**. This percentage is predicted to rise to 5% by 2050. To minimize the emission of gases into the atmosphere and to enhance efficient ship management, the Ship Energy Efficiency Management Plan (SEEMP) and the Energy Efficiency Design Index (EEDI) were introduced. The International Convention for the Prevention of Pollution from Ships (MARPOL) Annex VI regulates the emission of pollutants, such as CO2, SOx, NOx, ozone-depleting substances, and volatile organic compounds (VOCs) **[2]**. The convention also designates Emission Control Areas (ECAs) in the seas worldwide. Control of sulfur oxide (SOx) emissions is carried out in the Baltic Sea, North Sea, North America, and the U.S. Caribbean Sea. Sulfur content in fuel is limited to 0.5% at global seas and 0.1% in ECAs. Nitrogen oxide (NOx) emissions are limited to Tier I and II in global seas, while Tier III is specified for ECAs, depending on the marine diesel engine's rpm with the technical code **[3]**. As a result of sanctions and restrictions imposed by the IMO, a more efficient management approach is adopted in maritime transportation, and the exploration of low-emission energy sources has begun. Several studies are

investigating the use of alternative energy sources and the production of energy from various fuel types, such as methanol **[4]**. While the shift towards the use of renewable and alternative energy sources on land has been underway for over a decade, the shipping industry has only recently started to embrace this transition. The shipping industry has begun to explore ways to reduce fossil fuel consumption and operate in an environmentally friendly manner **[5]**. Given the limited and depleting nature of Egypt's fuel resources, the integration of renewable energy technologies has emerged as a crucial component of national energy planning. In this regard, the implementation of a renewable energy strategy is indispensable for achieving sustainable development and protecting the environment through enhanced energy efficiency and the replacement of conventional, polluting sources with renewable alternatives **[6]**. Recent advancements in solar panel and cell design have significantly reduced the costs of solar energy, making it an attractive option for reducing fuel consumption on pleasure boats, ferries, and tourist vessels **[7]**.

Marine photovoltaic (PV) solar systems consist of multiple components, including solar panels that generate the charge, a charge controller or solar regulator that regulates the charge flow into the battery and prevents overcharging, batteries that store the energy produced by the solar panels, and an inverter that converts DC into AC power **[8]**.

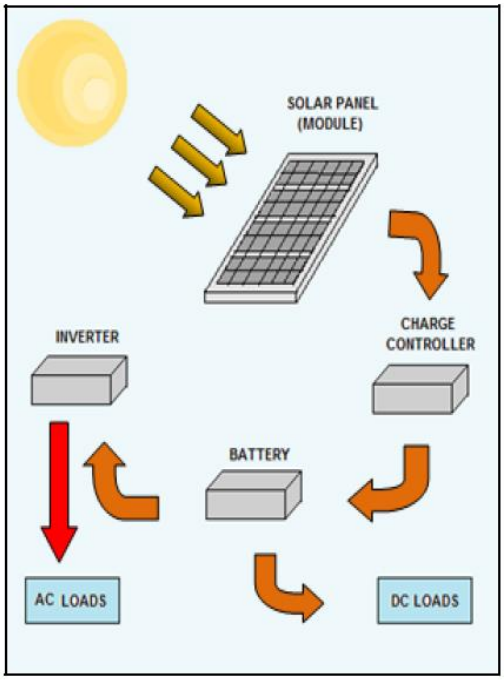

Figure 1 Solar system description

Solar cells use semiconductors to generate electrical power by converting solar radiation into DC electricity through the photovoltaic effect. PV solar cells are interlinked and encased between a transparent front and a backing material to create a PV solar panel. The operating temperature of the cells can impact the output power of a solar panel, with increased temperatures resulting in decreased output **[9]**. It is worth noting that PV modules represent approximately 60% of the total cost of a coherent system for power generation, highlighting the importance of cost reduction in modules for lowering system investments **[10]**.

2- Case Study description.

The case study for this research project examines the passenger/Ro-Ro ship named CONDOR VOYAGER, which is identified by IMO NO. 9221358. Constructed in the year 2000 by Incat Tasmania Pty Ltd, the vessel is presently owned by Condor Ferries. The ferry is capable of carrying a maximum of 843 passengers, 29 crew members, and 227 cars, with a passenger capacity of 843+29 persons (including crew). The ferry has a maximum deadweight of approximately 758 tons, and its layout is depicted in Figure 2.

Figure 2 CONDOR VOYAGER

2.1- Principal dimensions. Table 1 illustrates the principal dimensions, payload and capacities, and propulsion system of the case study vessel.

Property	Value
Length overall, m	97
Length waterline, m	90
Beam, m	26.4
Hull draft, m	3.5
Passenger capacity	843
Crew	29
Car capacity	227 cars
Car Bay size, m	4.5 * 2.35
Truck Bay size, m	3.1 meters wide by 90 lane meters
Truck deck height, m	4.35
Gross tonnage	6,581
Fuel, liters	2* 80,000
Main engine	4 × MAN 20V 28/330 STC
Gearboxes	4 × Reintjes VLJ7531
Waterjets	4 × KaMeWa 112 S3
Speed	40 knots

Table 1 CONDOR VOYAGER General Specs.

2.2- Sailing route. The ferry operates between the ports of Safaga (Egypt) and Yanbu (Saudi Arabia), which are approximately 315 nautical miles apart. A single round trip between these ports can take up to eight hours when operated at a service speed of 40 knots. Safaga was chosen for the project as it provides access to all parts of the republic, particularly Upper Egypt. Yanbu Port in Saudi Arabia was selected due to its proximity to Madinah during the hajj season. The port features seven berths (1-7) along a 1,420-meter wharf, which includes one container and one roll-on/roll-off (Ro/Ro) berth. The access channel to the port has been dredged to 14 meters below the lowest astronomical tide (LAT).

2.3- Main Engine Selection. Figure 3 presents the layout of the main engine of the CONDOR VOYAGER, while Table 2 provides the main dimensions of the engine.

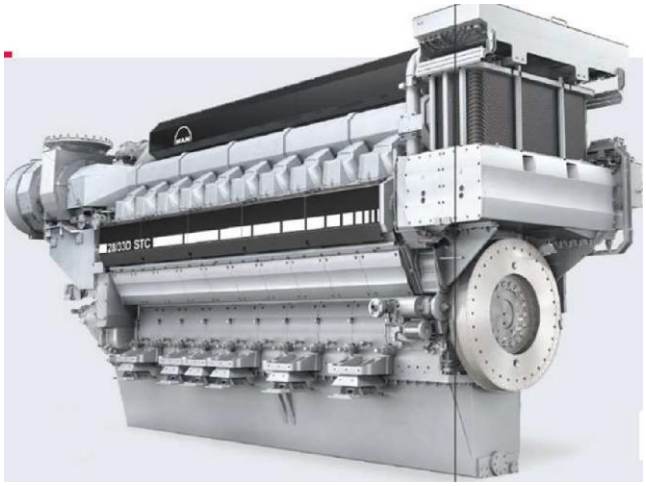

Figure 3 Layout of MAN 20V28/33D STC engine

- The vessel employs four generators to generate the required electrical power, with three generators actively operating while one remains on standby. The layout of these generators is depicted in Figure 4, while Table 2 provides an overview of the specifications for the selected generator.

Figure 4 The layout of the diesel generator.

- **Generator Set Specifications**

Specification	Value
Manufacturer	Caterpillar
Generator code	250 ekW 313 kVA
Maximum rating	250 ekW
Voltage	208 to 600 Volt
Frequency	60 Hz
Speed	1800 rpm
Duty cycle	Standby
Voltage regulation	Three phase sensing

- **Engine Specifications**

Specification	Value
Engine Model	CAT C9 In-Line 6, 4 cycle Diesel
Bore	112 mm
Stroke	149 mm
Displacement	8.8 L
Compression ratio	16.1:1

Table 2 The main specifications of generator set and engine.

3- Solar photovoltaic system onboard Passenger/Ro-Ro Ship.

The depletion of Egypt's finite fuel resources has highlighted the imperative need for the development of renewable energy technologies. In order to accurately assess the performance of a photovoltaic solar system installed on a ship, it is crucial to gather meteorological and environmental data pertaining to the ship's intended navigation route. The annual average total solar radiation across Egypt exhibits significant variations, ranging from approximately 1899 kWh/m2 along the Mediterranean coast to over 2775 kWh/m2 along the Red Sea coast. Sunshine duration follows a pattern of 8-10 hours per day from North to South, with only a few cloudy days. The distribution of direct normal irradiation in Egypt is depicted in Figure 6, a visual representation produced by the World Bank Group and funded by ESMAP. [11]

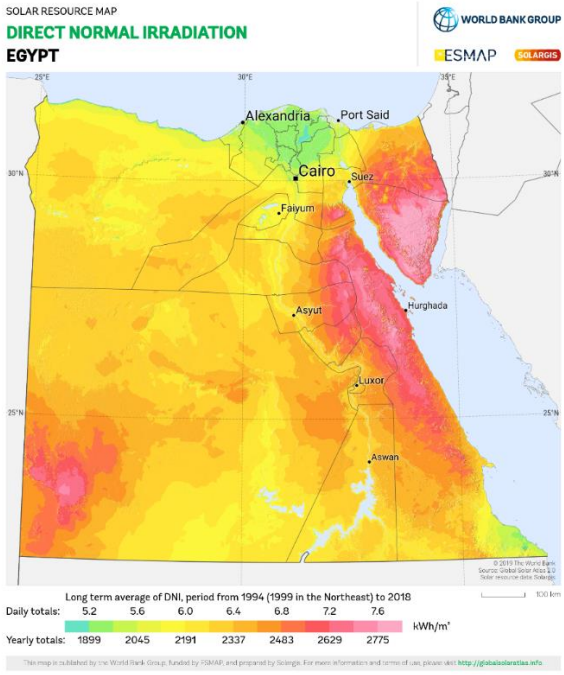

Figure 5 Direct normal irradiation

Not all-weather deck areas and bridge areas on the ferry are not fully utilized, making them suitable locations for the installation of solar panels. The feasibility of these areas for solar panel placement can be determined through an area calculation, the results of which are presented in Table 3.

Location	**Area (m²)**
Bridge deck	231.6
Upper weather deck	1461.1
Front deck	328.6
Total Area	2021

Table 3 Measured area onboard the ship

3.1- Solar Radiation Calculation. The calculation of solar radiation in the plane of the PV array is conducted using a modified version of the Klein and Theilacker algorithm [12]. This algorithm has been adapted to account for tracking surfaces, resulting in a slightly different implementation compared to the original description by Deceased and Beckman. The algorithm can be outlined as a series of three fundamental steps, as follows [13]:

1. Calculation of Hourly Global and Diffuse Irradiance on a Horizontal Surface: For each hour of an "average day" with the same daily global radiation as the monthly average, the hourly global and diffuse irradiance on a horizontal surface are computed.
2. Calculation of Hourly Global Irradiance on the Tilted (or Tracking) Surface: Hourly values of global irradiance on the tilted or tracking surface are determined for every hour of the day.
3. Summation of Hourly Tilted Values to Obtain Average Daily Irradiance in the Plane of the PV Array: The hourly tilted values are aggregated to calculate the average daily irradiance in the plane of the PV array.

The outcomes of the PV array in the Safaga city of Egypt and Yanbu in Saudi Arabia are summarized in Figure 6.

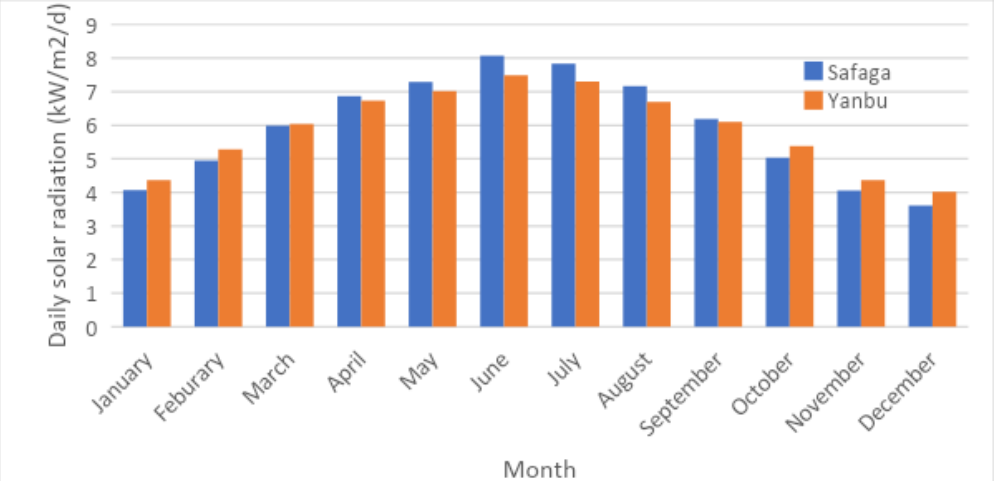

Figure 6 Daily solar radiation at different months on Safaga and Yanbu

3.2- Photovoltaic System Design. The photovoltaic solar system comprises several key components, including solar panels, a charge controller, batteries, and inverters. In this section, we will outline the design considerations for each of these components.

3.2.1- PV Solar Panel Design. The chosen PV panels are of the monocrystalline type and have been developed by Bosch Solar Energy company. Detailed specifications of the selected panels are presented in Table 4 and Figure 7.

Specification	**Value**
Manufacturer	Bosch Solar Energy
Model	mono si-c si m 60 - na44117 270 w
Capacity per unit	270 W
Frame area	1.6434 m²
Efficiency	16.42%
Length (x) * Width (y) * Height (z)	1660 * 990 * 50 mm
Cell weight	21 kg
Life span	25 years
Open Circuit voltage (Voc)	38.22 Volt
Short Circuit current (Isc)	9.33 Amps
Voltage at Pmax (Vmp)	30.85 Volt
Current at Pmax (Imp)	8.76 Amps

Table 4 Specifications of the selected PV panel

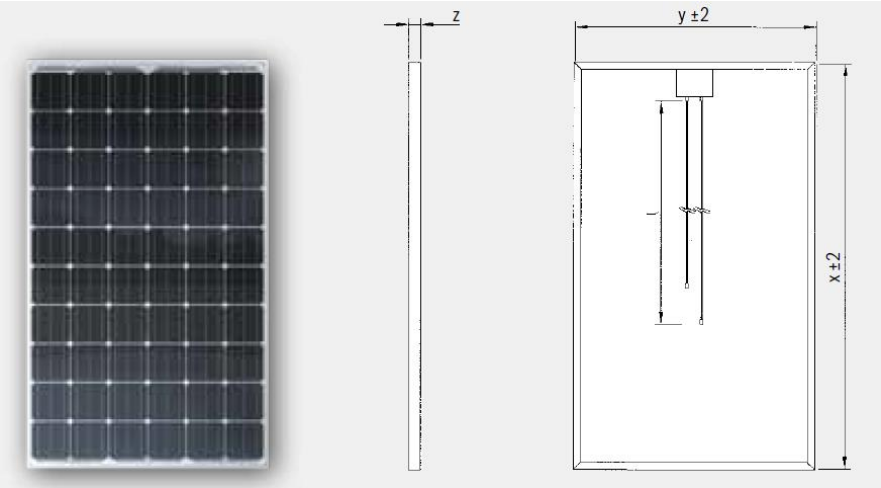

Figure 7 Basic dimensions of PV panel

The case study involved determining the required number of solar panels and their total weight for the given area. To calculate the number of panels, the available area was divided by the area of a single panel, which was determined to be 1.6434 m2. Consequently, a total of 1229 solar panels were found to be necessary to cover the available space on both the weather deck and bridge deck.
The total weight of the solar panels was determined using Equation (1):

Total weight = Number of Panels × Unit weight
(1)

Based on this calculation, the weight of the panels was determined to be 25.8 tons.

3.2.2- Charge controller's design. Charge controllers (solar regulators) are rated by the amount of current they can receive from the solar panels. Therefore, it must be capable of carrying the short circuit current of the PV solar systems. A margin of safety equal to 20% may be taken to allow for growth and the fact that the solar panels may exceed their rated output. Therefore, the total short circuit current can be calculated by using Eq. (2) [14].

$$Isc = 1.2 * I_{one\ panel} * NO_{panels}$$
(2)

where $I_{one\ panel}$ is the current of one panel which equals 9.33 and $NO_{panels}$is the number of panels that equals 1229 panels. Thus, in this case, it should be chosen to handle 13760 Amps. This result can be used to calculate the number of charge controllers. The specifications of the 60 Amps charge controller are shown in Table 5.

Specification	**Value**
Charge controller	MT6020-Pro
System Voltage	12/24/48V automatically reorganization
Max Charging Current	60 Amps
Battery Type	Liquid, GEL, AGM, Lithium
Dimensions	339 * 230 * 109 mm

Specification	Value
Max Charging Conversion Efficiency	98%
Ambient Temperature	-20 ~ +50°C
Weight	1.6 kg

Table 5 Main specifications of charge controller

Hence, a total of 230 charge controllers, each with a capacity of 60 Amps, is deemed suitable for the system. The combined weight of these charge controllers amounts to 0.368 tons.

3.2.3- Solar System Output Power. The output power of a solar system installed on a ship signifies a reduction in the electrical power generated by diesel generators on the vessel. The daily output power of the solar system (EDS) can be computed using Equation (3):

$$E_{DS} = E_P * N_P * \eta_B * \eta_{INV} \quad (3)$$

Where:
E_{DS} = Daily output power of any solar system in watt hours per day.
E_P = Output electrical power of each panel in watt hours per day.
N_P = Number of solar panels.
η_B = Battery efficiency.
η_{INV} = Inverter efficiency.

For this study, the battery efficiency (ηB) and inverter efficiency (ηINV) are assumed to be 0.85 and 0.9, respectively, based on previous research [10]. The output electrical power of each solar panel (EP) can be calculated using Equation (4) [15].

$$EP = WP * TSS * TCF \quad (4)$$

Where:
TCF = Temperature correction factor.
TSS = Average number of peak sunlight hours per day.
WP = The rated power for each solar panel in watt-hours.

To determine EP in this case, a 270-watt monocrystalline silicon PV solar panel is considered, with a sunshine duration (TSS) of 8 hours per day and a temperature correction factor (TCF) of 0.8 **[10,** [15]. Using Equation (4), this panel will produce 1.728 kWh/day. Therefore, 1229 solar panels will generate a total of 2123.7 kWh/day. By applying Equation (3), the daily output power of the designed system is calculated to be 1625 kWh/day.

3.2.4- Solar Batteries Design The design of solar batteries involves calculating the number of batteries required based on the output electrical power of all the panels. To store the output power,

a deep cycle battery with a specification of 12V 300Ah and a battery depth of discharge of 0.8 is used. Table 6 provides the specifications of the 12V 300Ah solar storage deep cycle battery.

Type	**Lead-Acid Batteries**
Size (L*W*H)	522 * 240 * 242 mm
Weight	63 kgs
Battery Lifetime	10 years

Table 6 Specifications of 12V 300Ah deep cycle battery

The number of batteries can be calculated using Equation (5):

$$NO_{batteries} = \frac{Solar\ panels\ rated\ power\ per\ day}{Battery\ rated\ per\ day\ (Voltage * Ampere\ hour\ capacity)} \quad (5)$$

Therefore, the output electrical power can be stored in 565 deep cycle batteries, with a total weight of 35.6 tons.

3.2.5- Power Inverters Design To determine the required number of inverters for a solar system, the daily output electrical power (EDS) produced by the system needs to be calculated. In this case, the amount of 1625 kWh is handled by power inverters, taking into account a battery efficiency of 0.85 and an inverter efficiency of 0.9. Considering a 20% margin of safety, it is determined that 390 power inverters with a power rating of 5000W are suitable for the system. The total weight of these inverters is 4.72 tons. Table 7 presents the specifications of a 5000W power inverter.

Type	**DC/AC inverter**
Input voltage	DC 12 volt
Output voltage	AC 220 Volt
Continuous output power	5000 watts
Peak power	10000 Watt
Output waveform	Pure sine wave
Output Frequency	50 Hz
Size (L*W*H)	544 * 199 * 146 mm
Weight	12.1 kgs

Table 7 Specifications of a 5000W power inverter

3.3- Fuel Saving To determine the amount of fuel consumed during a 7-day navigation period, data is collected from the engine logbook. In this case, the generators consumed 652 tons of low sulfur fuel oil (LSFO) throughout the year. By integrating a solar power system into the main power grid of the vessel, the load on the generators can be reduced, resulting in fuel savings. The equation (6) can be used to calculate the daily fuel savings provided by the generators.

$$F_s = SFOC\ (\frac{g}{kWh}) \times E_{DS}(kWh) \times 10^{-6}$$ **(6)**

From the engine logbook, the specific fuel oil consumption (SFOC) value is obtained as 205 g/kWh. Based on the calculations, the generators, in conjunction with the designed solar system, save approximately 0.333 tons of LSFO per day.

3.4- Environmental Evaluation The combustion of fuel can release sulfur oxides (SOx), nitrogen oxides (NOx), carbon dioxide (CO2), and particulate matter (PM). To determine the quantity of emitted gases, the emission factors for the generators given in Table 8 are utilized.

Pollutant	Emission Factor (g/kWh)
SOx	0.46
NOx	11.8
CO2	700
PM	0.3

Table 8 Emission factors of pollutants

Considering the power generated by the designed solar system and the emission factors provided in Table 8, the achieved reduction in emitted gases is illustrated in Figure 8.

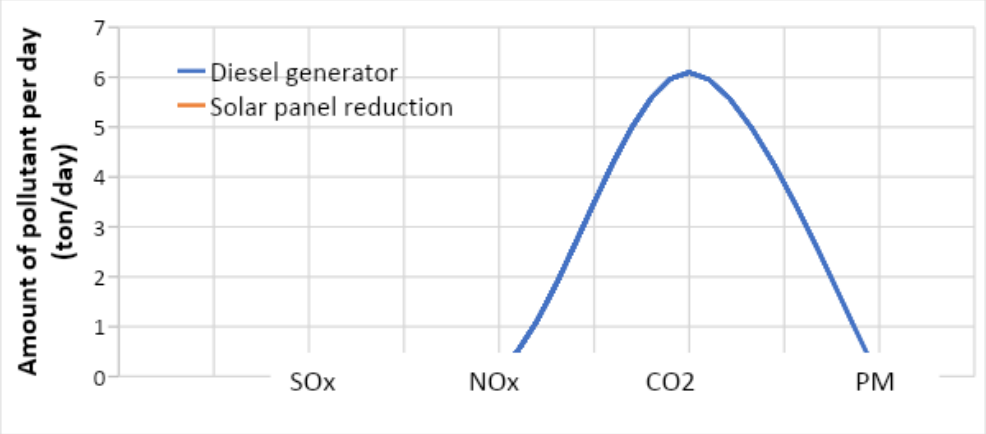

Figure 8 Pollutant amounts for diesel generator and solar panel.

The calculations reveal significant environmental benefits. By implementing the solar system on the vessel, the emissions are reduced by approximately 0.27 tons of SOx, 7 tons of NOx, 415 tons of CO2, and 0.18 tons of PM annually.

3.5- Economical Evaluation The ship is equipped with three sets of generators, each producing 250 kW, with an additional standby generator. The total annual fuel consumption of the generators, with a specific fuel consumption of 205 g/kWh, amounts to 652 tons. Using equation (7), the annual fuel cost for the three sets of generators can be calculated.

$$Annual\ fuel\ cost = Fuel\ consumption * fuel\ cost\ per\ ton \quad (7)$$

After performing the calculation, the annual fuel cost is determined to be $326,000. Therefore, incorporating the designed solar system on the ship results in fuel cost savings per year, in addition to environmental benefits such as reduced emissions, a cleaner environment, and a greener ship.

4- Conclusion

The implementation of alternative energy sources, specifically a photovoltaic (PV) system, on marine vessels has become increasingly popular due to environmental regulations and growing environmental awareness in the maritime sector. In this project, the researchers studied the integration of a PV system into the main power grid of a passenger/Ro-Ro ship. By calculating the power requirements of the ship's route using data from the World Bank, the researchers determined the contributions of the solar system. The key findings of the study are as follows:

a. The layout of the solar panel on the ship resulted in a total of 1229 solar panels. b. The proposed solar system is estimated to produce 1625 kWh/day, which is used for the ship's hoteling system. c. The calculations show that the designed solar system saves 0.333 tons of low Sulphur fuel oil per day compared to the generators. d. The study reveals significant environmental benefits. By adopting the solar system, the vessel can reduce annual emissions by 0.27 tons of SOx, 7 tons of NOx, 415 tons of CO2, and 0.18 tons of PM. e. A cost analysis demonstrates that the installed solar system can save $326,000 per year in addition to being environmentally friendly, reducing emissions, and promoting green shipping.

Based on these results, it is evident that integrating solar systems into marine vessels can lead to more efficient and environmentally friendly operations for maritime companies. Future studies are planned to design and analyze similar solar systems with tracking systems to compare their performance. The solar system not only reduces the workload on the generators but also extends their maintenance intervals and the lifespan of their components, resulting in financial benefits for maritime companies. Additionally, the adapted solar system offers the opportunity to navigate more comfortably within Emission Control Areas (ECAs) by reducing atmospheric emissions.

References

[1] E. L. A. I. R. a. A. H. S. E. A. Bouman, State-of-the-art technologies, measures, and potential for reducing GHG emissions from shipping – A review, Transportation Research Part D: Transport and Environment, 2017.

[2] M. M. E. a. M. R. S. A. G. Elkafas, Numerical analysis of economic and environmental benefits of marine fuel conversion from diesel oil to natural gas for container ships, Environmental Science and Pollution Research, 2021.

[3] A. G. E. a. M. R. Shouman, Assessment of energy efficiency and ship emissions from speed reduction measures on a medium-sized container ship, Transactions of the Royal Institution of Naval Architects, International Journal of Maritime Engineering, 2021.

[4] C. D. a. M. T. B. Zincir, Investigation of environmental, operational and economic performance of methanol partially premixed combustion at slow speed operation of a marine engine, Journal of Cleaner Production, 2019.

[5] T. L. a. H. Nam, A Study on Green Shipping in Major Countries: In the View of Shipyards, Shipping Companies, Ports, and Policies, Asian Journal of Shipping and Logistics, 2017.

[6] T. K. S. Y. a. T. H. J.-S. Park, Operation control of photovoltaic/diesel hybrid generating system considering fluctuation of solar radiation, Solar Energy Materials and Solar Cells, 2001.

[7] M. M. E. a. A. E. Z. A. G. Elkafas, Numerical study on the hydrodynamic drag force of a container ship model, Alexandria Engineering Journal, 2019.

[8] E. M. a. M. K. R. Chenni, Study of Solar Radiation in View of Photovoltaic Systems Optimization, Smart Grid and Renewable Energy, 2011.

[9] K. S. a. S. A. T. M. I. Alamsyah, Technoeconomics analysis of a photovoltaic system to provide electricity for a household in Malaysia, Proceedings of the International Symposium on Renewable Energy: Environment Protection & Energy Solution for Sustainable Development, 2003.
[10] A. E.-S. Nafeh, Design and Economic Analysis of a Stand-Alone PV System to Electrify a Remote Area Household in Egypt, The Open Renewable Energy Journal, 2009.
[11] T. W. Bank, Global Solar Atlas 2.0, Solar resource data, Bratislava: Solar resource data, 2020.
[12] J. A. D. D. a. W. A. Beckman, Solar engineering of thermal processes, Design Studies, 1982.
[13] J. E. Hay, Calculation of monthly mean solar radiation for horizontal and inclined surfaces, 1979: Solar Energy.
[14] M. Kolhe, Techno-economic optimum sizing of a stand-alone solar photovoltaic system, IEEE Transactions on Energy Conversion, 2009.
[15] M. M. &. M. a. E. E. El-Bokl, Solar energy for river Nile cruisers, Brodogradnja, 2014.

M.K. El- Saadawy[1, a], H.M.Khalil[2,b] , Y.Abuouf[3,c] and I.G.Adam[4,d]

[1] Mechanical engineering department, faculty of Engineering, Alexandria University, Egypt

[2] Mechanical engineering department, faculty of Engineering, Alexandria University, Egypt

[3] Mechanical engineering department, faculty of Engineering, Alexandria University, Egypt

[4] Mechanical engineering department, faculty of Engineering, Alexandria University, Egypt

[a]mohamed.khairy@alexu.edu.eg, [b]hekhalil@alexu.edu.eg, [c]yasser.abuouf@alex.edu.eg, [d]ihab.adam@alex.edu.eg

Keywords: Multi-phase flows, Gas-liquid flow, Slug pattern, Slug liquid holdup

Abstract. Gas-liquid flow exists in petroleum pipelines because of the nature of the gas associated with crude oil in wells. Gas-liquid flow exists in different patterns, depending on the velocity, properties, and diameter. Slug flow is one of these patterns, which is the most destructive because of its high vibrations and pressure drop behavior. Research has been published to derive a model that accurately predicts pressure drop; however, the constraints were the empirical correlations used, such as the slug liquid holdup, friction factor, and translational velocity. Slug liquid holdup is the most effective parameter because of its impact on the total pressure drop. slug liquid holdup correlation was not valid under all conditions, whereas most correlations were based on the experimental results for a low-viscosity range. Thus, applying correlations to high-viscosity liquids presents an unacceptable agreement. Therefore, this study aims to identify the most accurate correlation of viscosity, velocity, and diameter conditions, which optimizes slug liquid holdup prediction. The experimental databases used in this study include liquid viscosity > 587 CP, superficial liquid velocity > .5 m/s, and diameters 2 to 3 inches. The study shows that Gregory et al. 1978 correlation is valid for low viscosity with an average relative error of 2.64%. Al-Safran et al. 2015 show fair agreement in high-viscosity cases, whereas the average relative error is -3.28%. However, the average relative error for Gregory et al. 1978 and Al-Safran et al. 2015 correlations were -1.584% and 2.88% respectively for 3 inches of diameter.

Introduction

Two Phase flow exists in different industries such as petroleum, chemical, Nuclear, cryogenics, power plant, etc. In the petroleum industry, the two-phase flow normally occurs in pipelines coming from associated gas wells. It is usually a mixture of heavy oil and gas that is transported in both horizontal and inclined arrangements. An unexpected fluctuation in pressure is generated by the mixture along the pipeline. It considers a power loss for the pumping units.

There are different patterns of gas-liquid flow based on gas and liquid velocity, flow properties, and pipe diameter. Extensive research has been done to provide a clear flow pattern map for gas-liquid flow. It was concluded that bubble, stratified, stratified wavy, slug, plug, annular, and mist flows are all patterns of gas-liquid flow[1-11]. These studies aimed to develop a more accurate flow pattern map with precision boundary conditions.

Among the previous flow patterns, slug flow is considered the most critical. Gokcal [12, 13] studied the effect of viscosity on two-phase flow behaviors. An experiment has been done for a horizontal arrangement of 50.8-mm pipe diameter and viscosity up to 587CP. They concluded that the slug and plug flows are the most existing pattern at the viscosity range. Zahid et al. [14] studied the effect of superficial liquid velocity on slug vibration behavior. Increasing of vibration amplitudes by 64% was recorded when superficial liquid velocity increased from .65 m/s to 1.0 m/s. Mohammed et al. [15] reached the same conclusion in their result.

Slug flow consists of two sections: Slug body and liquid film (Elongated bubble). The liquid film is the section where the liquid and gas are separated. As for the slug body, it is the region that is

filled with liquid accompanied by tiny bubbles. Slug's body is filled with liquid. Tinny bubbles accumulated at the top wall by the effect of buoyancy force. Therefore, it was not filled in the total section.

Slug flow is usually characterized by several factors; slug liquid holdup, liquid film holdup, slug frequency, slug length, liquid film length, and translational velocity. Slug liquid holdup is considered one of the most important characteristics of slug flow. It can be defined as the percentage of a liquid filling the body. Therefore, it never reaches unity. Up to the authors' knowledge, no theoretical equation is available for slug liquid holdup prediction. Only empirical equations based on experimental data were developed.

Gregory et al. [16] experimentally studied slug liquid holdup in 25.8 and 51.0 mm pipe diameters, with superficial liquid velocity of less than 2.316 m/s, and oil viscosity of 6.75CP. A slug liquid holdup correlation was developed. It was a function of mixing velocity only. Marcano et al. [17] developed a correlation function of mixing velocity only while neglecting other important parameters such as fluid properties and pipe diameter. On the other hand, other research considered fluid properties, pipe diameter, and mixing velocity [18-20]. Malnes et al. [18] developed an empirical correlation including the surface tension and mixing velocity using the experimental data of Gregory et al. [16]. They illustrated that increasing surface tension cause decreasing in slug liquid holdup. Andreussi et al [19] measured slug liquid holdup for water at 50 and 90 mm. The measurements were significantly lower than Gregory et al. [16] at a mixing velocity of less than 10 m/s and a pipe diameter of 50 mm. Larger waves are created at higher velocities causing a decrease in slug liquid holdup. Nadler et al [20] noticed that oil-gas slug liquid holdup is lower than water-gas slug liquid holdup. Surface tension and liquid density effects are possible causes. In addition, the viscosity effect is limited on slug liquid holdup. Gomez et al. and Abdul-Majeed et al. [21,22] showed a different result. The liquid viscosity significantly affects slug liquid holdup. As liquid viscosity increases, slug liquid holdup increases. It was contradictory to Nadler et al. [20]. In addition, they agreed that surface tension slightly affects slug liquid holdup compared to liquid viscosity.

C. Kora et al. [23] experimentally studied high viscosity slug flow of 181 to 587 CP. A new correlation has been developed for slug liquid holdup including mixing velocity, flow properties, and pipe diameter. They indicated that viscosity has no significant effect on slug liquid holdup. It is more sensible to mixture velocity changes. Al-Safran et al. [24] and Archibong-Eso et al. [25] have different observations, they found that slug liquid holdup is sensible to the changes of liquid viscosity as mixture velocity. They observed that as viscosity increases slug liquid holdup increases.

Then, there are different slug liquid holdup correlations, each one was based on different experiment conditions. Therefore, each one was valid only for a specific range of viscosity, velocity, and pipe diameter. By the way, it will be a challenge to accurately derive a unified correlation to predict slug liquid holdup. This study aims to identify the most accurate correlation of viscosity, velocity, and pipe diameter conditions, which optimizes slug liquid holdup prediction. The experimental results used in this study include liquid viscosity less than 587 CP, superficial liquid velocity less than .5 m/s, and pipe diameters 2 to 3 inches.

Methodology

In the present analysis, several correlations are tested [16-18,21-24]. The following table summarizes the correlation used in the present analysis. Hlls, V_m, θ, Fr, $N\mu$ are slug liquid holdup, mixture velocity, inclination angle, Froude number and viscosity number respectively.

Slug liquid holdup correlations are tested against experiment data including liquid viscosity less than 587 CP, superficial liquid velocity less than .5 m/s, and pipe diameters 2 to 3 inches taken from [26] [27] results.

The analysis has been done using the operating conditions to predict slug liquid holdup for each case, then comparing it against the experiment result and evaluating a statistical parameter.

Table 1: Slug liquid holdup correlations

Author	Pipe ID (mm)	Liquid viscosity	Correlation
Gregory et al. [16]	25.8 - 51.2	6.75	$H_{lls} = \frac{1}{1+(\frac{Vm}{8.66})^{1.39}}$
Malnes et al. [18]	25.8 - 51.2	6.75	$H_{lls} = 1 - \frac{1}{[Vm+83(\frac{g\sigma}{\rho l})^{\frac{1}{4}}]}$
Marcano et al. [17]	78	1.92	$H_{lls} = \frac{1}{1.001+0.0179Vm+.001Vm^2}$
Gomez et al. [22]	51 - 203	1 – 6.5	$Hlls = e^{-(.45\theta+C\,Re)}\ \ 0 < \theta \leq 90°$ $Re = \frac{\rho l\, Vm\, D}{\mu l}, C = 2.48 * 10^{-6}$
Abdul-Majeed et al. [21]	25.8 - 200.32	1 – 6.5	$Hlls = (1.009 - CVm)A$ $C = .006 + 1.3377\ \frac{\mu g}{\mu l}$
C. Kora et al. [23]	50.4	181 : 587	$Hlls = \{1.012e^{-(.085Fr\,N\mu\cdot 2)}\ \ .15 < Fr\,N\mu\cdot 2 < 1.5\ .9473e^{-(.041Fr\,N\mu\cdot 2)}\ \ Fr\,N\mu\cdot 2 \geq 1.5\ \ 1.0\ \ Fr\,N\mu\cdot 2 \leq .15$
Al-Safran et al. [24]	50.4	181 : 587	$Hlls = .85 - .075\varphi + .057\sqrt{\varphi^2 + 2.27}$ $\varphi = Fr\,N\mu\cdot 2 - .89$

The statistical parameters are actual error Eq.1, reltaive error Eq.2, average relative error Eq.3, average actual error Eq.4 .
The analyses have been conducted using MATLAB in house code.

$$ei = \frac{Hlls(Predicted) - Hlls(Experimemtal)}{Hlls(Experimemtal)} \quad (1)$$

$$ej = Hlls(Predicted) - Hlls(Experimemtal) \quad (2)$$

$$\varepsilon 1 = \frac{1}{N}\sum_{i=1}^{N} \quad (ei) \quad (3)$$

$$\varepsilon 2 = \frac{1}{N}\sum_{i=1}^{N} \quad (ej) \quad (4)$$

The experimental conditions are categorized to the three diferent categories as the followng table:

Table 2: Experimental results categories

Viscosity	Liquid Velocity	Diameter
High (181 to 587 CP) Medium (39 to 108 CP) Low (1 to 10 CP)	Medium (.3 m/s) Low (.1 m/s)	2 inch 3 inch

Results

The following analysis shows that slug liquid holdup is significantly sensitive to mixture velocity. Whereas slug liquid holdup decreases as mixture velocity increases. As mixture velocity increases, the wave impact force in the mixing zone increases and creates a more irregular shape on the top of slug body. Then, more bubbles are joined to slug body from the liquid film zone which decreases slug liquid holdup as mentioned by Kim et al. [28] and Al-Safran et al. [24]. However, the viscosity has a slight effect on

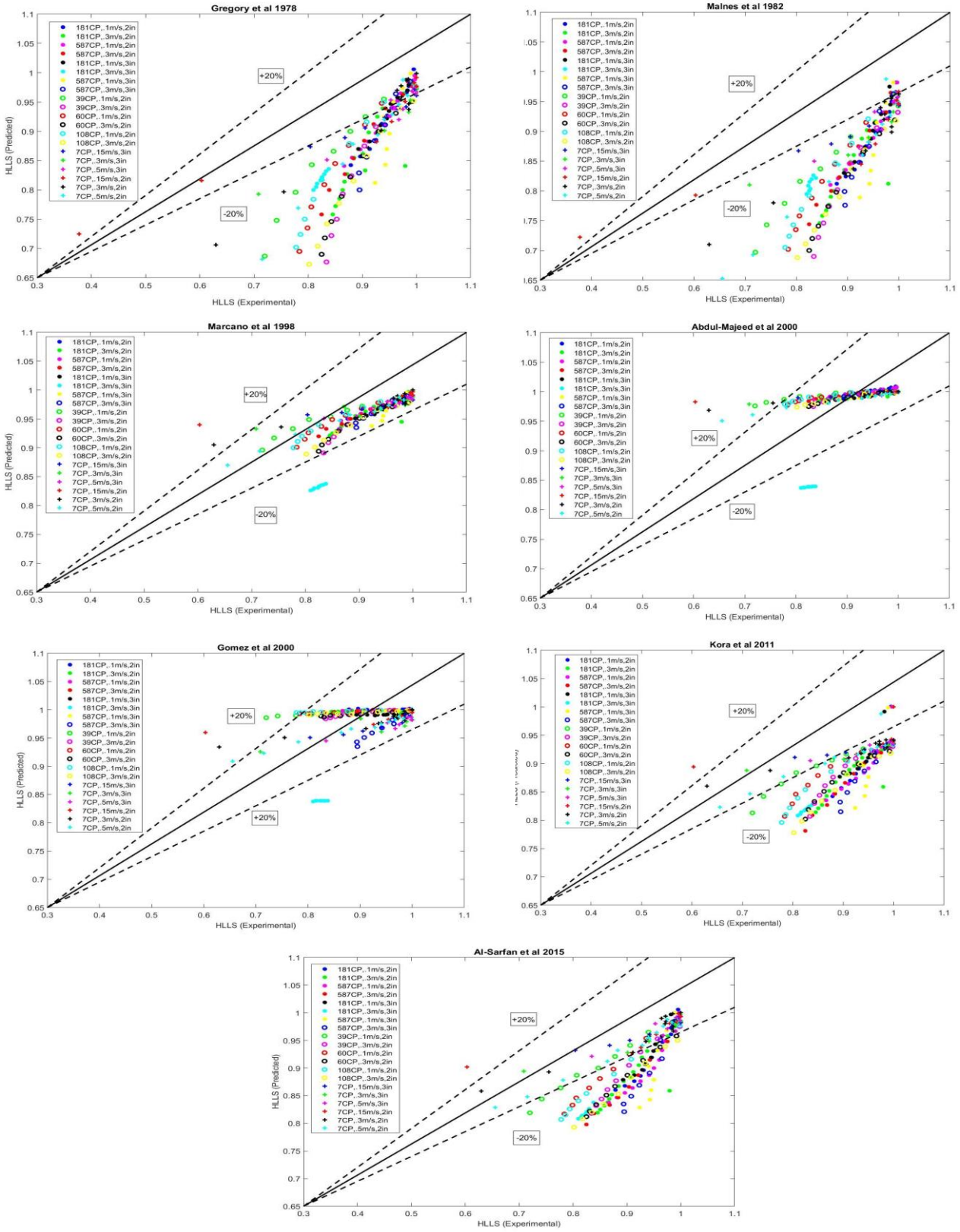

Figure.1: Slug liquid holdup correlations comparison

slug liquid holdup. In addition, the pipe diameter also has a significant effect on slug liquid holdup, and it is still a point of research.

□ The results show a different performance for all mentioned slug liquid holdup correlations as expected as shown in Fig. 1. Al-Safran et al. [24] show good agreement for 8 cases of a total of 20 cases. Whereas Al-Safran et al. [24] were valid for medium to high viscosity range, low to medium superficial liquid velocity, and 2 inches diameter.

The average relative error is -3.28%. Gregory et al. [16] were valid for low viscosity, low to high superficial liquid velocity, and 2 inches diameter with an average relative error of 2.64%. The remaining correlations have lower accuracy for all ranges. The reason could be due to the difference between its operation conditions basis and the current experimental results.In addition, the main disadvantage in all correlations is operation in 3 inches diameter including, Al-Safran et al. [24] and Gregory et al. [16]. The actual error of Al-Safran et al. [24] and Gregory et al. [16] are up to -6.901% and -6.007% respectively.

Conclusions

The study aims to identify the most accurate correlation of liquid viscosity, velocity, and pipe diameter conditions, which optimizes slug liquid holdup prediction. The experimental databases used in this study include liquid viscosity less than 587 CP, superficial liquid velocity less than .5 m/s, and pipe diameters 2 to 3 inches. The following remarks can be made based on the findings:

- Slug liquid holdup is significantly sensitive to mixture velocity. It decreases as mixture velocity increases.
- Al-Safran et al. [24] show good agreement for 8 cases of a total of 20 cases. It was valid for medium to high viscosity range, low to medium superficial liquid velocity, and 2 inches pipe diameter. The average relative error is -3.28%.
- Gregory et al. [16] were valid for low viscosity, low to high superficial liquid velocity, and 2 inches of pipe diameter. The average relative error is 2.64%.
- The remaining correlations have lower accuracy for all ranges. The reason could be due to the difference between its operation conditions basis and the current experimental results.
- The correlations in this study may require more development to increase the validity range of larger pipe diameters. The actual error of Al-Safran et al. [24] and Gregory et al. [16] are up to -6.901% and -6.007% respectively.

References

[1] Baker O (1954), Simultaneous Flow of Oil and Gas. Oil and Gas Journal, 53, pp.185.195.

[2] Mandhane J, Gregory G, Aziz K (1974) A flow pattern map for gas-liquid flow in horizontal pipes. Int J Multiphase Flow 1(4):537-553.

[3] Jones OC jr, Zuber N (1975) The interrelation between void fraction fluctuations and flow patterns in two-phase flow. Int J Multiphase Flow 2(3):273-306.

[4] Barnea D, Shoham O, Taitel Y, Dukler A (1980) Flow pattern transition for gas-liquid flow in horizontal and inclined pipes. Comparison of experimental data with theory. Int J Multiphase Flow 6(3):217-225.

[5] Lin, P. Y. & Hanratty, T. J. 1987b The effect of pipe diameter on flow patterns for air-water flow in horizontal pipes. Int. J, Multiphase Flow 13, 549-563.

[6] Spedding P, Spence D (1993) Flow regimes in two-phase gas-liquid flow. Int J Multiphase Flow 19(2):245-280.

[7] Netto JF, Fabre J, Peresson L (1999) Shape of long bubbles in horizontal slug flow. Int J Multiphase Flow 25(6-7):1129-1160.

[8] Ghajar AJ, Tang CC (2007) Heat transfer measurements, flow pattern maps, and flow visualization for non-boiling two-phase flow in a horizontal and slightly inclined pipe. Heat transfer Engineering 28(6):525-540.

[9] Vaze M, Banerjee J (2011) Experimental visualization of two-phase flow patterns and transition from stratified to slug flow. Proc Inst Mech Eng Part C J Mech Eng Sci 225(2):382-389.

[10] Kong R, Rau A, Kim S, Bajorek S, Tien K, Hoxie C (2018b) Experimental study of horizontal air-water plug-to-slug transition flow in different pipe sizes. Int J Heat Mass Transfer 123:1005-1020.

[11] C.Tan, Y. Shen, K. Smith, F. Dong, and J.Escudero, "Gas-Liquid Flow Pattern Analysis Based on Connectivity and Graph-Variate Dynamic (GVD) Connectivity of ERT", IEEE Transactions on Instrumentation and Measurement, Vol. 8, no. 5, pp. 1590-1601, 2019.

[12] Gokcal, B. (2005). Effects of High Oil Viscosity on Two-Phase Oil-Gas Flow Behavior in Horizontal Pipes. Master of Science Thesis, University of Tulsa, Tulsa, Oklahoma, USA.

[13] Gokcal, B. (2008). An Experimental and Theoretical Investigation of Slug Flow for High Oil Viscosity in Horizontal Pipes. Ph.D. Dissertation, University of Tulsa, Tulsa, Oklahoma, USA.

[14] *Expermimental investigation on the vibration incduced by slug flow in horizontal pipe ,Zahid Ibrahim Al-Hashimy and Hussain H. Al-Kayiem and R. W. Time, 2016.*

[15] Mohmmed, AO, Al-Kayiem, HH, Nasif, MS, Time, RW., 2019. Effect of slug flow frequency on the mechanical stress behavior of pipelines. International Journal of Pressure Vessels and Piping 172, 1–9.

[16] Gregory, G.A., Nicholson, M.A., Aziz, K., 1978. Correlation of the liquid volume fraction in the slug for horizontal gas-liquid slug ¯ow. Int. J. Multiphase Flow.

[17]Marcano, R., Chen, X. T., Sarica, C., and J. P. Brill. "A Study of Slug Characteristics for Two-Phase Horizontal Flow." Paper presented at the International Petroleum Conference and Exhibition of Mexico, Villahermosa, Mexico, March 1998.

[18] MALNES, D. 1982 Slug flow in vertical, horizontal and inclined pipes. Report IFE/KR/E-83/002 V. Inst. for Energy Technology, Kjeller, Norway.

[19] Andreussi P, Bendiksen K (1989) An investigation of void fraction in liquid slugs for horizontal and inclined gas–liquid fow. Int J Multiphase Flow 15(6):937–939.

[20] Nadler M, Mewes D (1995) Efects of the liquid viscosity on the phase distributions in horizontal gas–liquid slug fow. Int J Multiphase Flow 21(2):253–266.

[21] Gomez L, Shoham O, Taitel Y (2000) Prediction of slug liquid holdup: horizontal to upward vertical fow. Int J Multiphase Flow 26:517–521.

[22] Abdul-Majeed GH (2000) Liquid slug holdup in horizontal and slightly inclined two-phase slug fow. J Petrol Sci Eng 27:27–32.

[23] Kora, C., Sarica, C., Zhang, H.-Q., Al-Sarkhi, A., Al-Safran, E., 2011. Effects of high oil viscosity on slug liquid holdup in horizontal pipes, SPE 146594. In: Presented in CSUG/SPE Conference, Calgary, Canada.

[24] Al-Safran, E.M., Kora, C. & Sarica, C., 2015. Prediction of slug liquid holdup in high viscosity liquid and gas two-phase flow in horizontal pipes. Journal of Petroleum Science and Engineering, 133, pp.566–575.

[25] A. Archibong-Eso, N. Okeke, Y. Baba, A. Aliyu, L. Lao and H. Yeung, Estimating Slug Liquid Holdup in High Viscosity Oil-Gas Two-Phase F l o w , Flow Measurement and Instrumentation.

[26] Kim, T. On the Analysis of High Viscous Horizontal Slug Flow Characteristics by Changing Pipe Diameter. Master's Thesis, Seoul National University, Seoul, Korea, 2015.

[27]Kokal, S.S. An Experimental Study of Two Phase Flow in Inclined Pipes. Ph.D. Thesis, University of Calgary, Calgary, AB, Canada, 1989.

[28] Kim, T.W., Al-Safran, E., Pereyra, E., Sarica, C., 2020. Experimental study using advanced diagnostics to investigate slug aeration and bubble behavior in high liquid viscosity horizontal slug flow. J. Petrol. Sci. Eng. 107202.

Castor Biodiesel Production and its Combustion Characteristics in Diesel Engine Working With Diesel Fuel and Different Additives: A Critical Review

Mohamed Lotfy [1, a], Radwan M. El-Zoheiry [2,b], Hesham M. El-Batsh [3,c] and Ahmed I. EL-Seesy [4,d]

[1,2,3,4]Mechanical Engineering Department, Benha Faculty of Engineering, Benha University, Benha 13512, Egypt

[a]Mohamed.abdelghany@bhit.bu.edu.eg, [b]RADWAN.ABDELLATIF@bhit.bu.edu.eg, [c]helbatsh@bhit.bu.edu.eg, [d]*ahmed.elsysy@bhit.bu.edu.eg* .

Keywords: *Castor biodiesel production; physiochemical properties; Alcohol and nanoparticle additives; Combustion characteristics; Exhaust emission.*

Abstract. Fossil fuel availability has decreased and the need for alternative energy sources increased, such as biodiesel fuel. Biodiesel can be derived from both edible and non-edible oils; non-edible oils are the best option due to population growth. Castor oil biodiesel is biodegradable, non-toxic, renewable, and has low greenhouse gas emissions. transesterification pyrolysis processes can be used to produce biodiesel from castor oil. The efficient and cost-effective biodiesel production method depends on several parameters, including free fatty acid percentage in the feedstock, transesterification and pyrolysis reaction efficiency, alcohol: oil ratio, catalyst type and concentration, and several other parameters during the production process. Furthermore, blending castor oil biodiesel with diesel and some additives positively affects its physical and chemical properties. Therefore, this review article will discuss production methods, their advantages and disadvantages, the physicochemical properties of the produced castor oil biodiesel, and the performance, emission, and combustion characteristics of a diesel engine fueled by castor oil biodiesel blends with diesel.

Introduction

Conventional diesel fuel is one type of non-renewable fuel oil source, It is estimated that in 2050 the transport sector will still dominate fuel needs[1], Diesel fuel has the highest consumption compared with the other fuels as shown in Fig. 1[2], Finding alternative sources of energy is important, considering that every year the availability of fossil fuels which are always decreasing[1].

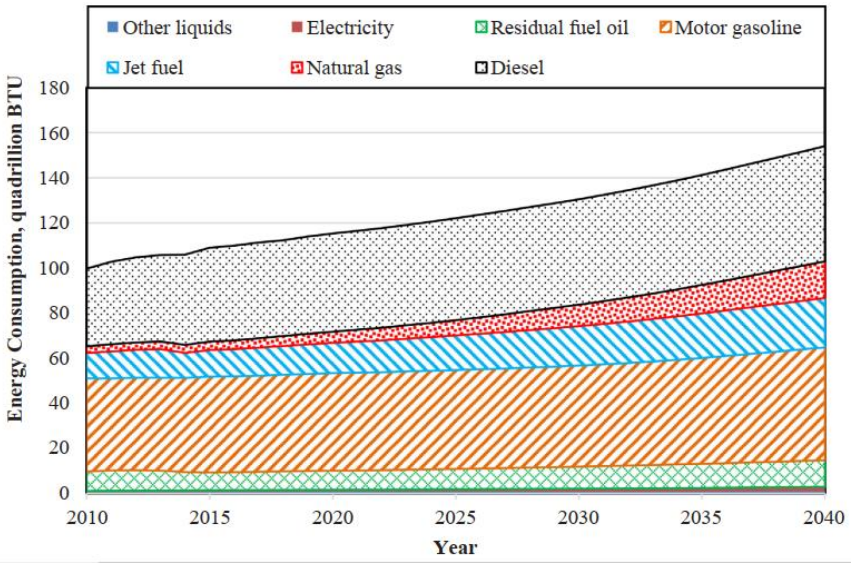

Fig 1 World energy consumption by transportation sector[2].

One of the alternative sources that can be used in diesel engines and its using is an important factor for emission control [3], biodiesel can be produced from vegetable and animal fats. Some edible and non-edible vegetable oils can be used for biodiesel production; however, due to population growth and the need for more edible oil, non-edible oils are the best option for producing biodiesel [4].

Castor oil is one of the non-edible oils that are good for producing biodiesel, The comparative advantage of it is that its growing period is much shorter than most other non-edible oils, The seeds contain between 40% and 60% oil that is rich in triglycerides, mainly ricinolein[5], castor biodiesel can be produced by many ways from which the following :

a) *Transesterification* is the most common way to produce biodiesel, it considers the conversion of one ester to another by the exchange of alkoxide groups, in which the oil is esterified with a hydric alcohol (ethanol, methanol) in the presence of a catalyst such as alkalis (sodium or potassium hydroxide), in this method raw oil is heated to boiling temperature of water and for few minutes to evaporate the water that was in oil, then oil mixed with alcohol and alkali mixture and the flip is done at certain temperature and certain time, giving fatty acid esters and glycerin as the main products, then glycerin is separated and washing the fatty acid esters to get the final product[6].
b) *Pyrolysis* consists of the thermal decomposition of oils in the presence of nitrogen gas, the fuel obtained by pyrolysis can be made cheaper than that obtained by transesterification, oil molecules are broken down into smaller molecules in an oxygen-free environment at high temperatures, This process is divided into three parts: hydrocracking, catalytic cracking, and thermal cracking, In the pyrolysis process, although the fuel properties approach diesel fuel properties and the high energy consumption is the most important disadvantage[6].

Due to transesterification biodiesel physicochemical properties, the blends, of biodiesel with diesel, that contain more than 40 % of biodiesel don't meet the ASTM standard[2]. pyrolysis biodiesel properties approach diesel fuel properties so it can be used in diesel engines with 100% pyrolysis biodiesel[7].

1. **Biodiesel production.**

Castor biodiesel can be produced from transesterification and pyrolysis. The following studies investigate materials that were used in production and their composition.

Hajlari et al [8]. they used ethanol (with a ratio of 6:1) and NaOH as catalysts with a percentage of 1 wt. % of oil, ethoxy, and oil was mixed and stirred for 30 min, at 80 °C After completing the process, the final solution was placed in the laboratory to separate.

Attia et al [2]. they produced castor biodiesel by employing methanol by volume ratio of 6:1, and KOH (typically 2% wt./wt.) dissolved in methanol (Methoxide), an ultrasonic device stirred the oil and Methoxide mix for 45 minutes, after 6 h with butting the mixture in the separating funnel, two layers were formed; bottom containing glycerol and upper containing biodiesel, the biodiesel was separated and then washed it until reaching clean water indicating removing almost all impurities, then biodiesel was heated to 110 ℃ for at least 5 min to remove all suspended water, the RSM method was used and the previous conditions were optimum for producing 85% as the yield of produced biodiesel.

Baskar and Soumiya [9]. they used the ferromagnetic zinc oxide nanocomposite as a heterogeneous catalyst (Iron (II) doped ZnO nanoparticle as nanocatalyst), Biodiesel conversion was investigated with a 12:1 ratio of methanol: oil at a temperature of 55℃ for 50 min, the catalyst concentration was 14wt%, there was a comparison between the effects of temperature, catalyst concentration, and reaction time but the previous conditions were the best.

Conceição et al [10]. they used a common way to transesterification, Methanol was added in the 20% ratio in mass, and 1% of KOH catalyst dissolved in alcohol, the mixture was

shaken at ambient temperature for 30 min, then Glycerin was removed after the decantation process, presenting a 98% yield.

- *Negm et al* [11]. they produced biodiesel castor by applying sulfonated phenyl silicate montmorillonite (Si-MMT-Ph-SO3H) as a catalyst, methanol was mixed with a catalyst (5% catalyst by weight, 1:12 oil to methanol molar ratio), and oil, the mixture at 60℃ was stirred at 800 rpm for 300 minutes. In the end, excess methanol was removed by reducing pressure, and centrifuged to separate the different phases. After centrifugation, three layers were separated: the upper layer was the obtained biodiesel; the middle layer contained the produced glycerol, and the lower layer contained the catalyst and traces of glycerol.
- *Sánchez et al* [12]. they investigated the influence of catalyst concentration, methanol: oil molar ratio, reaction temperature, and reaction time in the methyl ester content reached by castor oil transesterification, using Response Surface Methodology (RSM), the optimum conditions were 0.064 mol/L of CH3OK, 18.8:1 as methanol: oil molar ratio, 45℃ and 10 min of reaction. In these conditions, 97 wt.% methyl ester content biodiesel was achieved.
- *Sánchez et al* [13]. they applied two serial transesterification reactions, to hold back the usage of CH3OK and its concentration, to decrease the cost of biodiesel production, RSM is used to determine the optimum conditions for two steps transesterification process, variables were catalyst concentration in the first step (A), CH3OH/oil molar ratio in the first step (B), catalyst concentration in the second step (C) and CH3OH/oil molar ratio in the second step (D), the optimum conditions for the two-step process were shown in table 1.
- *Silva et al* [14]. they utilized RSM to reach the best conditions for biodiesel production, the following conditions, reaction temperature from 30 to 80 C; catalyst concentration from 0.5%wt to 1.5%wt (by weight of castor oil); ethanol: castor oil molar ratio from 6:1 to 20:1 and reaction time of 30 min, the optimum conditions gave 99%wt of ethyl ester was obtained at 30 C, with mechanic stirrer, 1 %wt. of sodium ethoxide, ethanol: castor oil molar ratio of 16:1 and at 30 min of reaction.
- *Silva et al* [15]. they also here applied RSM but used NaOH as a catalyst and ethanol as hydric alcohol, perfect circumstances for producing biodiesel were catalyst content from 0.8% wt. to 1.2% wt., with large ethanol: castor oil molar ratio, up to 19:1 at 30˚C and the reaction time was 30 min at 600 rpm.
- *Abdelfattah et al* [16]. a series of experiments were conducted to determine the influence of different catalyst-to-oil ratios at 230˚C-400˚C. These series of experiments were performed by using 1%wt of alumina (Al2O3), sodium carbonate (Na2Co3), sodium hydroxide (NaOH), potassium hydroxide (KOH), in addition to 2 cm plug of molecular sieve catalyst Zeolite (ZSM-5) combined with 1%wt of sodium hydroxide (ZSM-5 combined with NaOH), The reaction time changed between 200 and 310 min 1litter of castor oil as feed was pyrolyzed at each run, The usage of 1% by weight of NaOH as a catalyst the highest total yield of biodiesels was obtained, but such yield was reduced dramatically by using NaOH combined with ZSM-5. total yield as (CBD1, CBD2) was decreased by increasing and/or lowering the catalyst concentration. Also, the usage of 1% by weight of NaOH as a catalyst achieved the most energy saving regarding the pyrolysis process with a lower temperature range.

A	B	C	D	Predicted ester content (wt. %)	Experimental Ester content (wt. %)	Relative Error (%)
0.1 mol. L^{-1} (A=2)	3:1 (B=-2)	0.1 mol. L^{-1} (C=2)	5:1 (D=2)	101.2	97.6	3.6
0.8 mol. L^{-1}	5.2 5:1	0.8 mol. L^{-1}	4:1	96.7	96.9	-0.2

☐ (A =1)	☐ (B= 1)	☐ (C =1)	☐ (D =1)			

☐ Table 1 the optimum conditions for the two-step process of castor biodiesel production [13].

☐

2. Effect of castor biodiesel blends on the engine performance.

☐ Biodiesel properties differ from those of diesel and don't meet the ASTM standard properties, so it was refuged to blend biodiesel with diesel fuel and other additives to enhance the properties of the burned fuel Therefore, it should improve the performance and emissions of the engine, the following studies show this improvement.

☐ *Attia et al* [2]. they blended castor biodiesel with diesel to a ratio of up to 40 %, single-cylinder engine setup was used to investigate the effect of blending and the results were as follows, blending ratio (BR) of 30% was the optimum blend to give the lower brake specific fuel consumption (BSFC), with an overall increase of 8% compared to those of the neat diesel fuel, (BR) 20% gave the optimum value brake thermal efficiency (BTE), (BR) 10% gave the best emissions of carbon monoxide (CO), unburned hydrocarbons (HC), nitrogen oxides (NOx), (BR) 20% emitted the lowest carbon dioxide emissions with a reduction of more than 7.5% compared to that of the neat diesel fuel, (BR) 20% is recommended to keep high engine efficiency without environmental deterioration.

☐ *Attia et al* [6]. As previous study blends were with ratios up to 40 % (B10, B20, B30, and B40), The results were the same as previous research [2] with additional results, B10 gave comparable peak values of pressure and heat release rate, B30 produced the lowest exhaust opacity, BR 20% improved most of engine emissions flow without deteriorating its mechanical performance.

☐ *Yesilyurt* [17]. alcohols can be utilized in CI engines due to their chemical and physical characteristics that are almost near to diesel, especially higher alcohols, heptanol has higher alcohol, and biodiesel blended with diesel, a single-cylinder, a four-stroke, and the water-cooled engine was used to clarify the effect of these blends (B20, Hp20, and B20Hp20 (20% peanut oil biodiesel, 20% 1-heptanol, and 60% diesel fuel)) and the results were that all blends gave higher peak in-cylinder pressure and heat release rate than that of pure peanut oil biodiesel, peanut oil biodiesel demonstrated the lowest HC, B20Hp20 was found to be the best choice in terms of NO_X, peanut oil biodiesel emitted lowest CO emissions, all blends led to increase in the BSFC and BSEC.

☐ *Guarieiro et al* [18]. The following mixtures (v/v/v) were stable for the 90-day and were used in the emission study: diesel/ethanol(DE) – 90/10%, diesel/ ethanol/soybean biodiesel(DESB) – 80/15/5%, diesel/ethanol/castor biodiesel (DEAB)– 80/15/5%, diesel/ethanol/residual biodiesel(DERB) – 80/15/5%, diesel/ethanol/soybean oil(DESO) – 90/7/3%, and diesel/ethanol/castor oil (DEAO)– 90/7/3%[18]. adding more than ethanol (15%) to the binary mixture causes the separation of 2 phases on the first day, DEAO and DESB showed the highest reduction of NOx emissions and blends DEAB, DESB, DESO, and DEAO showed reductions of CO emissions at high loads, DEAB fuel had a lower reduction of CO2 emission rate (3%).

☐ *Rahimi1 et al* [19], castor biodiesel was used with diesel with blends ratios (B0, B5, B10, B15, and B20, blends were tested under varying engine speed conditions (1600, 1950, 2300, 2650, and 3000 rpm)[19], the effect of using these blends were as following, maximum power was detected for B0 at 2650 rpm, the specific fuel consumption (SFC) was decreased by using biodiesel blends, B10 had the minimum amount for SFC, biodiesel blends decreased CO2 and HC emissions, the concentration of CO and NOx was found to be increased when biodiesel was introduced.

☐ *Xing et al* [20]. they used a 20% volume fraction of castor oil and an 80% volume fraction of diesel fuel blended as the baseline fuel and added alcohols like ethanol and n-butanol, DC80B10E10, DC80B20, and DC60B20E20 were burned in diesel engine, BSFC was increased

by an average of 7.7%, 8.5% and 16.5% for DA80B10E10, DC80B20, and DC60B20E20 fuels respectively, NOx emissions were increased by about 30%, HC was higher for the blended fuels, CO emissions were about 22% lower than that of diesel fuel.

- *Taneja and Singh* [21], Biodiesel castor oil blended with ethanol, butanol, and diesel as the base fuel, blends used in this study were biodiesel (20%) (BD), biodiesel (20%) Ethanol (10%) (BED) and biodiesel (20%) Butanol (10%) (BbuD), there were burned in the diesel engine with two compression ratios CR16 and CR18[21], all blends exhibited lower CO emissions. BD, BED, and BbuD showed maximum CO reduction of 33.3%, 50%, and 66.67% respectively concerning pure diesel at Compression Ratios 16 and 50%, 50%, and 66.67% respectively at Compression Ratio 18, Blends exhibited higher CO2 emissions and BbuD showed the maximum increasing, NO_X emissions increased for all blends.
- *Attai et al* [22], castor biodiesel pyrolysis can be blended with diesel in volumetric ratios of 0, 10, 25, 50, 75, and 100% at different loads performed, the experiments were carried out using a single-cylinder and air-cooled diesel engine[22], Biodiesel showed the maximum increase in specific fuel consumption by 10% and the thermal efficiency was decreased by 10.5% about pure diesel, The maximum increases in NOx, CO, HC emissions, and exhaust gas temperature for CBD 100 were 22, 34, 48, and 11%, respectively related to diesel oil, maximum reductions in-cylinder pressure and net heat release rate were 5 and 13% for CBD100 about gas oil. A biodiesel percentage of 10% showed near values of performance parameters and emissions to gas oil, so, it is recommended as the optimum percentage.

Conclusion

- Castor biodiesel can be produced in many ways such as Transesterification and pyrolysis. The transesterification process is a chemical conversion process that turns one ester into another by exchanging alkoxide groups, main factors affecting the yield of the produced ester were hydric alcohol (ethanol, methanol) ratio, alkalis (sodium or potassium hydroxide) percentage, temperature of the process and stirring process conditions. The optimum conditions for the Transesterification process were methanol: oil ratio of 10:1, KOH as a catalyst with 1%wt, Mechanical stirring with a temperature of 63˚C, and the process was continuing for 3 hr. The best conditions of the thermal analysis process (pyrolysis process) 1%wt of NaOH as a catalyst, with a temperature range of 280:400˚C was applied and for 210 to 300 min,
- Biodiesel produced from transesterification can be blended to a ratio up to 40 %, and the best blend was BR20 for performance and emissions, lower and higher alcohols can be blended as well with diesel and biodiesel to enhance emissions with some slight effect in reverse on the engine performance, pyrolysis biodiesel can be blended to ratio up to 100%. A biodiesel percentage of 10% showed near values of performance parameters and emissions to diesel, so it is recommended as the optimum percentage.

References

[1] D. M. Prabowoputra, A. Sartomo, and Suyitno, “The effect of pressure and temperature on biodiesel production using castor oil,” *AIP Conf. Proc.*, vol. 2217, no. April 2020, doi: 10.1063/5.0000504.

[2] A. M. A. Attia, M. Nour, and S. A. Nada, “Study of Egyptian castor biodiesel-diesel fuel properties and diesel engine performance for a wide range of blending ratios and operating conditions for the sake of the optimal blending ratio,” *Energy Convers. Manag.*, vol. 174, pp. 364–377, Oct. 2018, doi: 10.1016/j.enconman.2018.08.016.

[3] P. Sreenivas, V. R. Mamilla, and K. C. Sekhar, “Development of Biodiesel from Castor Oil,” *Int. J. Energy Sci. IJES IJES*, vol. 1, no. 3, pp. 192–197, 2011.

[4] R. Sattanathan, “Production of Biodiesel from Castor Oil with its Performance and Emission Test,” 2013. [Online]. Available: www.ijsr.net

[5] “‘JAVADO,’ http://www.javadoplant.com/en/ricinuscommunis.html. (General Internet

site)."
[6] E. S. Aktaş, Ö. DemİR, and D. Uçar, "A review of the biodiesel sources and production methods," vol. 5, no. 1, pp. 1–10, 2020.
[7] C. S. Osorio-González, N. Gómez-Falcon, F. Sandoval-Salas, R. Saini, S. K. Brar, and A. A. Ramírez, "Production of biodiesel from castor oil: A review," *Energies*, vol. 13, no. 10, pp. 1–22, 2020, doi: 10.3390/en13102467.
[8] S. Azizzadeh Hajlari, B. Najafi, and S. Faizollahzadeh Ardabili, "Castor oil, a source for biodiesel production and its impact on the diesel engine performance," *Renew. Energy Focus*, vol. 28, no. 00, pp. 1–10, 2019, doi 10.1016/j.ref.2018.09.006.
[9] G. Baskar and S. Soumiya, "Production of biodiesel from castor oil using iron (II) doped zinc oxide nanocatalyst," *Renew. Energy*, vol. 98, pp. 101–107, 2016, doi: 10.1016/j.renene.2016.02.068.
[10] M. M. Conceição, R. A. Candeia, F. C. Silva, A. F. Bezerra, V. J. Fernandes, and A. G. Souza, "Thermoanalytical characterization of castor oil biodiesel," *Renewable and Sustainable Energy Reviews*, vol. 11, no. 5. pp. 964–975, Jun. 2007. doi: 10.1016/j.rser.2005.10.001.
[11] N. A. Negm, G. H. Sayed, F. Z. Yehia, O. I. Habib, and E. A. Mohamed, "Biodiesel production from the one-step heterogeneous catalyzed process of Castor oil and Jatropha oil using novel sulphonated phenyl silane montmorillonite catalyst," *J. Mol. Liq.*, vol. 234, pp. 157–163, 2017, doi: 10.1016/j.molliq.2017.03.043.
[12] N. Sánchez, R. Sánchez, J. M. Encinar, J. F. González, and G. Martínez, "Complete analysis of castor oil methanolysis to obtain biodiesel," *Fuel*, vol. 147, pp. 95–99, 2015, doi: 10.1016/j.fuel.2015.01.062.
[13] N. Sánchez, J. M. Encinar, S. Nogales, and J. F. González, "Biodiesel production from castor oil by two-step catalytic transesterification: Optimization of the process and economic assessment," *Catalysts*, vol. 9, no. 10, 2019, doi: 10.3390/catal9100864.
[14] N. De Lima Da Silva, Ć. B. Batistella, R. M. Filho, and M. R. W. Maciel, "Biodiesel production from castor oil: Optimization of alkaline ethanolysis," *Energy and Fuels*, vol. 23, no. 11, pp. 5636–5642, 2009, doi: 10.1021/ef900403j.
[15] N. D. L. D. Silva. M. R. MACIELr and A. R. F. CESAR BENEDITO BATISTELLA, "Optimization of Biodiesel Production From Castor Oil," 2006.
[16] M. S. H. Abdelfattah, O. S. M. Abu-Elyazeed, E. Abd El mawla, and M. A. Abdelazeem, "On biodiesels from castor raw oil using catalytic pyrolysis," *Energy*, vol. 143, pp. 950–960, 2018, doi: 10.1016/j.energy.2017.09.095.
[17] M. K. Yesilyurt, "A detailed investigation on the performance, combustion, and exhaust emission characteristics of a diesel engine running on the blend of diesel fuel, biodiesel and 1-heptanol (C7 alcohol) as a next-generation higher alcohol," *Fuel*, vol. 275, no. January, p. 117893, 2020, doi: 10.1016/j.fuel.2020.117893.
[18] L. L. N. Guarieiro, A. F. de Souza, E. A. Torres, and J. B. de Andrade, "Emission profile of 18 carbonyl compounds, CO, CO2, and NOx emitted by a diesel engine fuelled with diesel and ternary blends containing diesel, ethanol and biodiesel or vegetable oils," *Atmos. Environ.*, vol. 43, no. 17, pp. 2754–2761, 2009, doi: 10.1016/j.atmosenv.2009.02.036.
[19] A. Rahimi, B. Ghobadian, G. Najafi, F. Jaliliantabar, and R. Mamat, "Performance and emission parameters of single cylinder diesel engine using castor oil bio-diesel blended fuels," in *IOP Conference Series: Materials Science and Engineering*, Dec. 2015, vol. 100, no. 1. doi: 10.1088/1757-899X/100/1/012012.
[20] D. Qi, W. Xing, P. Luo, J. Liu, and R. Chen, "Effect of alcohols on combustion characteristics and particle size distribution of a diesel engine fueled with diesel-castor oil blended fuel," *Asia-Pacific J. Chem. Eng.*, vol. 15, no. 4, Jul. 2020, doi: 10.1002/apj.2477.
[21] S. Taneja and P. Singh, "Investigation of engine characteristics of a variable

compression ratio diesel engine using biodiesel and alcohol blends," *IOP Conf. Ser. Mater. Sci. Eng.*, vol. 1127, no. 1, p. 012001, Mar. 2021, doi: 10.1088/1757-899x/1127/1/012001.

[22] Y. A. Attai, O. S. Abu-Elyazeed, M. R. ElBeshbeshy, M. A. Ramadan, and M. S. Gad, "Diesel engine performance, emissions and combustion characteristics of castor oil blends using pyrolysis," *Adv. Mech. Eng.*, vol. 12, no. 12, 2020, doi: 10.1177/1687814020975527.

□

Utilizing Green Hydrogen as Clean Economical Thermal Energy Substitute to Conventional Fossil Fuel Combustion Boilers

Mohamed Tamer Mansour[1],[a], Amgad El-Deib1,[b] Tamer M. Mansour [2,c]

[1]Renewable Energy Engineering Dept., Zewail City of Science and Technology, Egypt

[2]Mechanical Engineering Dept., Suez Canal University, Egypt

[a] s-mohamed_tamer@zewailcity.edu.eg , [b]aeldeib@zewailcity.edu.eg, [c]tmansour@eng.suez.edu.eg

Keywords: Green Hydrogen, Simulation, Techno economic analysis, Boilers, Paper Industry.

Abstract. Substitution of conventional natural gas fired steam boilers is recently gaining interest in the industry. In this work, the implementation of this concept in paper industry with hydrogen gas or hydrogen-natural gas mixture fired boiler is studied from the economic and environmental aspect. For the convenience of this research, a preexisting paper production factory is modeled using MATLAB Simulink with actual electrical and thermal demand curves to calculate the amount of total annual energy bill in the presence of renewable energy recourses. This load is supplied partially by wind and solar renewable sources modeled with SAM and PVsyst to ensure the used hydrogen fuel substitute is green hydrogen, while the deficit in the load is made up with input from the conventional natural gas and electricity networks to fit the required output load curve of the facility. This work also looks into the values of each individual subsystem efficiency and compares it to the alternative conventional boilers and electric boilers. Through the Simulink simulation offered in this work, the economic value earned for the facility, the carbon footprint cut, and the actual system efficiency is analyzed. This offers an alternate clean and renewable source of thermal energy for the industrial sector. The work suggests a slightly moderate capital of 51M USD total CAPEX and 20 years' worth OPEX to initiate the project. The project aims to substitute the current 0.45kg/sec flowrate of methane with a more sustainable 0.174kg/sec flowrate of hydrogen and studies all related subsystems for implementation.

Introduction

The world is currently facing a critical energy transition, where renewable energy sources are playing an essential role in mitigating climate change and reducing greenhouse gas emissions. The demand for energy is increasing globally, and so is the need for cleaner and sustainable energy sources. Renewable energy is taking a rise in this aspect however a critical issue faced by renewable energy is the aspect of storage and the inability to be used as a sustainable source of

thermal energy; to which a currently presented solution is the implementation of green hydrogen. which is considered a key component of the energy transition.

Hydrogen is a clean and abundant energy carrier that has gained significant attention in recent years. It can be produced from renewable energy sources, such as wind and solar power, through the process of electrolysis. The resulting hydrogen, known as green hydrogen, has no carbon emissions and can be used as a substitute for fossil fuels in various industrial applications, including thermal energy generation.

One of the leading electrolysis methods in the current industrial cycles is Proton Exchange Membrane water electrolysis (PEM) as shown in Fig. 1-a, which is based on the reversed processes of a fuel cell. Where it was derived from fuel cell technology. It is more suitable to dynamic functioning, even under strain, than Alkaline Electrolysis (AEL) [1]. Meanwhile the implementation of PEM electrolyzer model in the analysis allows us to easily use the similar models of fuel cell [2,3]. The principle of operation of fuel cell is shown in Fig. 1-b.

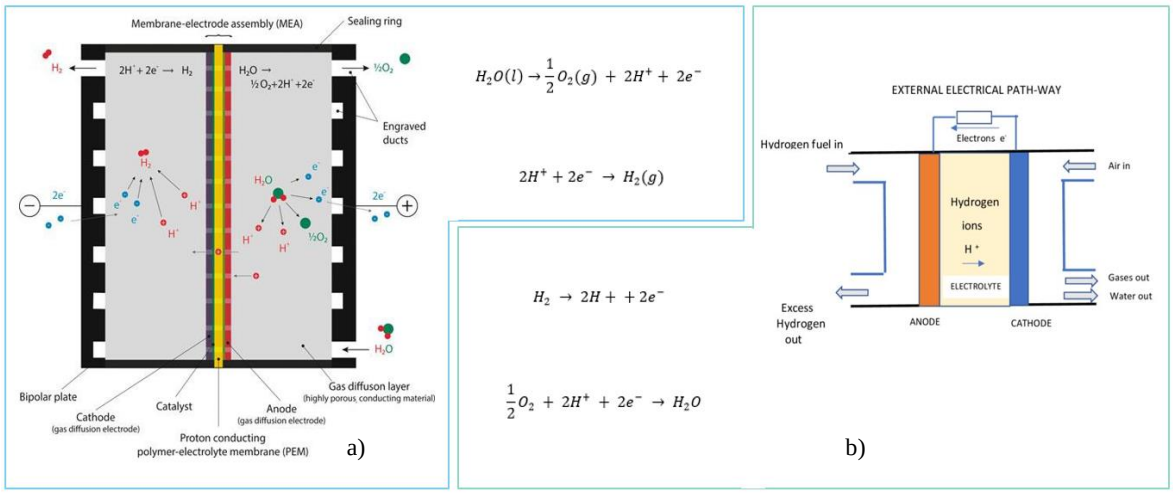

Figure 1: a) Polymer Exchange Membrane Electrolysis Working Principle b) Fuel Cell Working Principle

An industry which is highly dependent on thermal energy is the paper industry, and it is one of the largest energy consumers among the industrial sectors, the majority of its energy demand is met through the combustion of natural gas in steam boilers. The combustion of natural gas releases CO2 and other greenhouse gases, contributing to the industry's carbon footprint. Therefore, substituting natural gas with green hydrogen as a thermal energy source can significantly reduce the industry's carbon emissions and mitigate climate change.

The Aim of this paper is to present clearly whether the implementation of green hydrogen in the current industrial cycle is economically and technologically feasible or not, defining the pros and cons of hydrogen combustion boilers to conventional natural gas powered boilers technically and economically while offering suggestions and guidelines to implement this technology safely, efficiently and economically. Finally using the results identification and illustration of the implications and expected outcomes on the global industry from implementing this technology is expected while determining whether this technology is sustainable or not and presenting compelling arguments to aid in sustaining such technology.

Approach

System Definition and Assumptions. Standard ideal socio economic conditions of nations is assumed. While the region of study of this project is Egypt in the MENA region. Codes of Conduct referred to during any legal study or safety consideration is the Egyptian constitute and the global standard ISO safety regulations. Specifically, ISO 14687, ISO/TC 197, ISO/TS 19880, ISO 22734 and Law No. 203/2014, Egypt and Ministerial Decree No. 197/2021. Wind and Solar

Energy outputs are assumed constant and Stable output multiplied by their average capacity factor. System defining variables are constant throughout the simulation and the Electrolyzer, Fuel cell, and Boiler has a constant electricity to fuel conversion ratios termed Alpha and Beta throughout the simulation.

System Description and Schematics. The system compromises of a renewable energy power production section followed by energy conversion and management power electronics, the energy output of this section is used as the input to the electrolyzer and partially to the compressor used in the hydrogen tank. The entire hydrogen flowrate yield of the electrolyzer is supplied and stored in the hydrogen tank. The tank outputs two distinct flowrates to the thermal and electrical sections of the industrial facility which is used to calculated the savings made in the natural gas network and electrical grid usage. The schematic diagram for the system is shown in Fig. 2

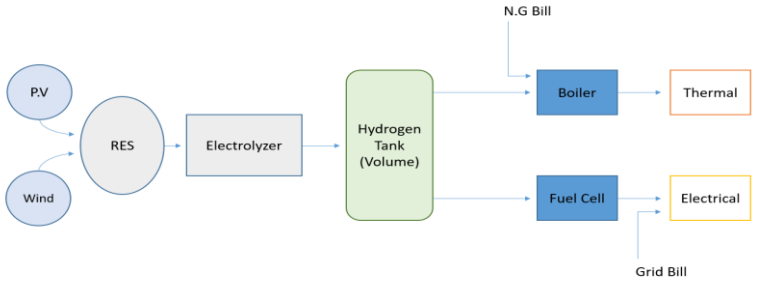

Figure 2: System Schematic

Load Specifications. The model output is strictly dependent on the current conventional thermal and electrical load, the savings are calculated through subtracting output production from the required load and multiplying the resultant with the tariffs of the natural gas network and electrical grid (Eq.1).

$$\text{Output} = \text{tariff} * (\text{Load} - \text{production}) \qquad \$ \tag{1}$$

From a collections of data sheets and trend points of an actual on going paper and pulp refinery and production facility situated in Cairo, Egypt. The electrical and thermal load curves (averaged daily) are shown in Fig. 3

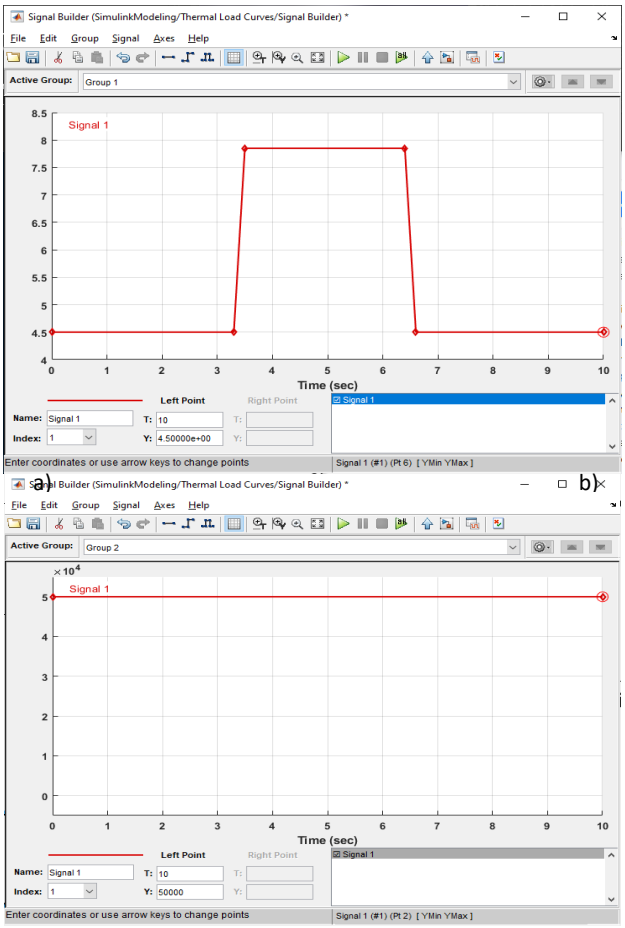

Figure 3: a) Electrical load *b) Thermal load*

Mathematical Modeling. The model design is done on MATLAB Simulink to simulate the effects each constrain and output have on the economics of the whole system, the input power is calculated using PVsyst for solar input and SAM for wind input, while the output load curves is imported as datasheets from actual working facility archive values as defined earlier. Economic analysis is manually completed using Microsoft Excel to present net cash flow diagram and the payback period as a result.

Electrolyzer Conversion Factor and Efficiency Alpha. The electrolyzer conversion factor alpha is calculated through the resultant of the rate of conversion of electrical energy to hydrogen flowrate multiplied by its efficiency. The electrolyzer conversion rate (μ)is calculated through (Eq. 3) which describes the amount of energy needed to produce a certain amount of hydrogen flow rate.

$$H_2O_{liquid} + 237.2\ kJ/mole\ (electrical) + 48.6\ kJ/mole\ (thermal) \rightarrow H_2 + \frac{1}{2}O_2 \quad (2)$$

$$\mu = \frac{Output\ Energy\ Equivelant}{Input\ Energy\ Equivelant} \quad (3)$$

Hydrogen Storage Tank Modeling. The schematic diagram for the hydrogen storage tank is shown in Fig. 4. The system governing equations are modified from the model in [5] to be suitable for the current system. The tank are presented through Eq.4 -Eq.7, while the control of the pressure tank is shown in Fig. 5.

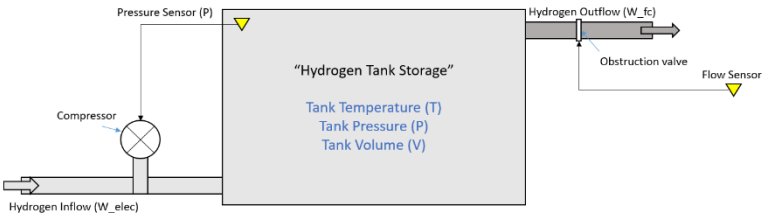

Figure 4: System Schematic for Hydrogen Storage Tank

$$P_{TP} = W_{elec} C_{pH_2} \left(\frac{T_{TP}}{\mu_{TP}}\right)\left((r)^{\frac{\gamma-1}{\gamma}} - 1\right) \quad (4)$$

$$P_{tank} = \frac{n_{H_2} R T_{tank}}{V_{tank}} \quad (5)$$

$$n_{H_2}(t) = n_0(t_0) + \int_{t_0}^{t} q_{H_2} dt \quad (6)$$

$$q_{H_2} = W_{elec} - W_{fc} \quad (7)$$

where:-

W_{elec} : Hydrogen flow rate at the compressor inlet.

C_{pH_2} : Specific heat capacity of hydrogen at constant pressure

P_{TP} : Power consumed by Compressor

μ_{TP} : Compressor operating efficiency

r : Compressor compression ration

γ : Specific heat of hydrogen under standard conditions

$n_o(t_o)$: The amount of substance inside the gas tank at time t_0

T_{TP} : Compressor inlet temperature.

P_{tank} : Pressure inside the tank.

V_{tank} : Volume of gas tank

T_{tank} : Tank gas temperature

R : Molar gas constant

n_{H_2} : Amount of substance inside gas tank

q_{H_2} : Net hydrogen feed flow rate.

W_{fc} : Hydrogen flow rate at gas tank outlet.

While the storage restrains were determinded based on the tank pressure were the tank was not allowed to have pressure less than 10% of the tank pressure (20 bar) or more than 90% of the tank pressure (180 bar) to ensure its safety and lifetime.

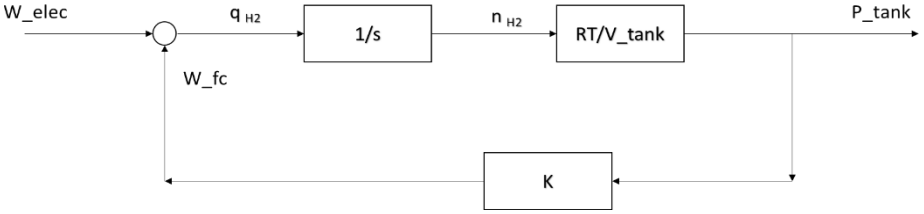

Figure 5: Block Diagram for control the hydrogen storage tank.

Fuel Cell Conversion Factor and Efficiency Beta. The fuel cell conversion factor beta is assumed to be the inverse of the Electrolyzer conversion factor alpha for simplicity.

Boiler Conversion Factor and Efficiency Theta. The boiler conversion factor theta is calculated through the resultant of the rate of conversion of hydrogen flowrate to thermal heat output multiplied by its efficiency. The boiler conversion rate is calculated through (Eq. 8) which is analogous to the model retrieved from [4] and describes the amount of hydrogen flow rate needed to produce the needed amount of heat to supply he desired steam; while the boiler efficiency is deduced through (Eq. 12).

$$f\mathrm{H}_2 + (1-f)CH_4 + \lambda(2-1.5f)(O_2 + 3.76N_2) \rightarrow \quad (1-f)CO_2 + (2-f)H_2O + 3.76\lambda(2-1.5f)N_2 + 3.76\lambda(2-1.5f)N_2 + (\lambda-1)(2-1.5f)O_2 \quad (8)$$

$$AFR = 4.76\lambda(2-1.5f) \quad (9)$$

$$\rho_{mix} = f\rho_{H_2} + (1-f)\rho_{CH_4} \quad (10)$$

$$LHV_{mix} = fLHV_{H_2} + (1-f)LHV_{CH_4} \quad (11)$$

$$Boiler\ Efficieny = \frac{Energy\ Steam - Energy\ Boiler\ Feed\ Water}{Energy\ Fuel} \quad (12)$$

where:- f represents Volumetric hydrogen percentage, λ is air–fuel equivalence ratio, AFR is the air fuel ratio, $\rho_{H2}, \rho_{CH4}, \rho_{mix}$, LHV_{H2}, LHV_{CH4} and LHV_{mix} respresnts the denisty and Lower Heating Value for Hydrogen, Methane and mixture respectively. The MATLAB-Simulink model of the whole system with its subsystem is highlighted in Fig. 6.

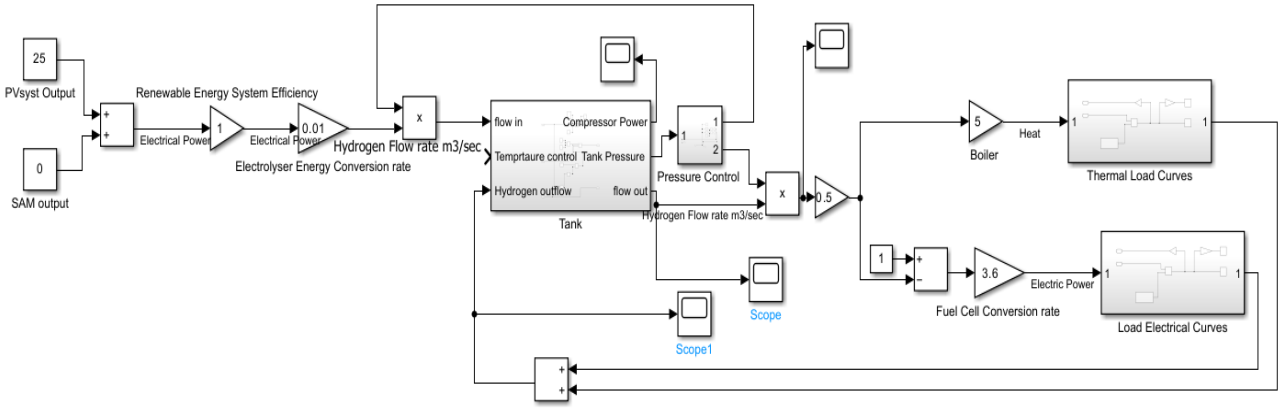

Figure 6: Simulation model for the complete system

Net Present Value (NPV). NPV is the present value of all future cash flows of a project. Calculated using the formula (Eq. 13).

$$NPV = \sum_{t=0}^{T} \frac{C_t}{(1+r)^t} \quad (13)$$

Results and Disscussion.

Simulation. All the constants and desired loads were imported into the model accourdingly. The coffetiant factors were imported as a gain block carrying the coffesient value as follows:

Alpha. The electrolyzer energy conversion coefficient Alpha; Electrical energy into hydrogen flow rate is taken to be 0.01kg/sec/kW.

Beta. While the Fuel cell energy conversion coefficient Beta; Hydrogen flow rate into Electrical energy is taken to be 3.6W/sec/kg.

Theta. Finally, the Boiler energy conversion coefficient theta; Hydrogen flow rate into thermal energy of combustion is taken to be 5kW/sec/kg.

Economic Analysis. The following values calculated for the economic analysis may be slightly inflated as the higher values of the average market prices is taken into account while calculating to present a more conservative approach to the results. Acourdingly; calculating all the CAPEX and OPEX of each unit from corrosponding datasheets for actual market products or average market price over a lifetime of 20 years of the system to deduce the total present value we would need to start this project we get that we need 1.386B EGP. The NPV diagram per year (Egypt's financial year is used starting July) we get the following visualization in Fig. 7.

Thus setting the desired payback period to the maximum theoretical allowable period which is the lifetime of the installed units, and calculating the required Net annual Cash inflow to balanceout the investment with the return we get that the facility need to produce additional products worth of net 55M EGP annually to cover the investment and operation cost without any income excluding the environmental impact and incentives gained from this project. Which for a large enterprise is a reasonable value gained.

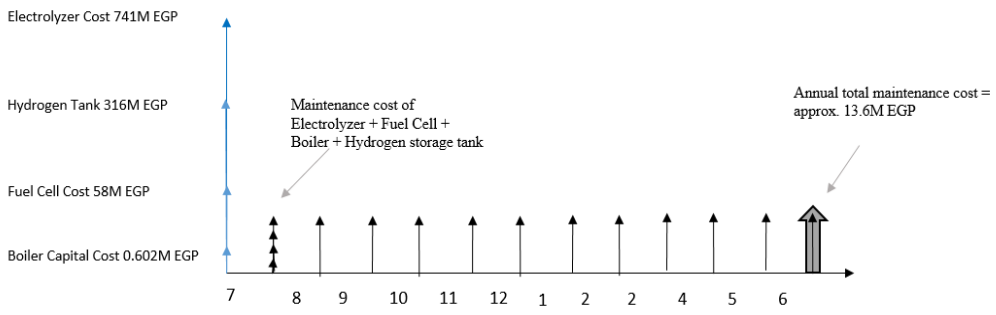

Figure 7: Net present value for the system

Conclusion and Future Work. The substitution of natural gas fired steam boilers in the paper industry with hydrogen gas or hydrogen-natural gas mixture fired boilers is a technically and economically feasible solution to reduce the industry's carbon emissions and mitigate climate change. The economic analysis showed that the capital and operating costs of the proposed

solution were higher than those of natural gas fired boilers. However, the analysis also showed that the payback period of the proposed solution was within a reasonable range, and the long-term benefits of reducing carbon emissions and mitigating climate change outweighed the initial costs.

Indepth studies regarrding optimization of the hydrogen-natural gas mixture fired boilers is advised, as well as looking up into the scale-up of the proposed solution both on the individual subsystem and on other industries (projection studies). Life cycle assessment of the proposed solution as part of an enviromental impact assesment coupled with economic analysis of the proposed solution in different regions is sought to provide general guidelines on the impliations of applying this technologu on a global scale. Finally, the consideration of integration of the proposed solution with other renewable energy sources is expected to introduce grater flexiaility and rewarding results.

Funding: No external fund is available

Authorship Contribution: Mohamed Tamer (Conceptualization, Methodology, Analysis, Writing), Amgad El-Deib (Supervision, Visualization), Tamer Mansour (Reviewing, Implementation).

References

[1] Q. Feng, X.-Z. Yuan, G. Liu, B. Wei, Z. Zhang, and H. Wang, “A review of proton exchange membrane water electrolysis on degradation mechanisms and mitigation strategies,” *J. Power Sources*, vol. 366, pp. 33–55, Oct. 2017, doi: 10.1016/j.jpowsour.2017.09.006.

[2] D. Murray-Smith, *A Review of Developments in Electrical Battery, Fuel Cell and Energy Recovery Systems for Railway Applications A Report for the Scottish Association for Public Transport*. 2019. doi: 10.13140/RG.2.2.16555.67362.

[3] “Fuel Cell Handbook (Seventh Edition)”.

[4] F. Schiro, A. Stoppato, and A. Benato, “Modelling and analyzing the impact of hydrogen enriched natural gas on domestic gas boilers in a decarbonization perspective,” Carbon Resources Conversion, vol. 3, pp. 122–129, 2020, doi: 10.1016/j.crcon.2020.08.001.

[5] J. Li, G. Li, S. Ma, Z. Liang, Y. Li, and W. Zeng, “Modeling and Simulation of Hydrogen Energy Storage System for Power-to-gas and Gas-to-power Systems,” *J. Mod. Power Syst. Clean Energy*, vol. 11, no. 3, pp. 885–895, May 2023, doi: 10.35833/MPCE.2021.000705.

Metal sulfide investigations for energy conversion and production

N. Roushdy[1]†, Mohamed S. Elnouby[2], A. A. M. Farag[3], O. El-Shazly[4], E. F. El-Wahidy[4]

[1]Electronic Materials Department, Advanced Technology and New Material Institute, City of Scientific Research and Technology Applications, New Borg El Arab City, Alexandria 21934, Egypt

[2]Composite and Nanostructured Materials Research Department, Advanced Technology and New Materials Research Institute, City of Scientific Research and Technological Applications (SRTA-City), New Borg El-Arab, Alexandria 21934, Egypt

[3]Thin Film Laboratory, Physics Department, Faculty of Education, Ain Shams University, Heliopolis 11757, Roxy, Cairo, Egypt

[4]Physics Department, Faculty of Science, Alexandria University, Alexandria, Egypta

[1]naglaa2sct@gmail.com

Keywords: Energy production, Liner sweep voltammetry, Electrochemical impedance spectroscopy, Energy storage

Abstract. Metal sulfides (MSs) nanomaterials such as CuS, FeS, and CdS are prospective materials for various applications in medicine, biology, environmental sciences, and energy production/utilization due to their light absorption, optical characteristics, high specific capacitance, and catalytic/photocatalytic capability. MSs were synthesized for energy production and storage in current research. The characterization analyses were applied for some metal sulfides such as X-ray diffraction, Scanning electron microscope and EDX. Moreover, both optical and electrochemical properties were examined. The cyclic voltammetry device was used for examined the fuel cell features by observing the characteristic peaks under various conditions. The electrochemical behavior in fuel cells detected via the linear sweep voltammetry. The selected best electrode for fuel cell was chosen by using electrochemical impedance spectroscopy (EIS) analysis.

Introduction

□ The remarkable characteristics of semiconductor nanoparticles have sparked significant interest [1]. Semiconductors offer a wide range of applications owing to their fascinating properties, including high sensitivity, a broad linear response range, rapid response and recovery behavior, exceptional selectivity, and stability [2]. Metal oxides [3] and metal sulfides [4] are

among the semiconductor materials that exhibit tremendous potential in various applications, such as sensing materials, solar cells for energy conversion, fuel cells for energy production, photocatalysts, and capacitors for energy storage. Nanomaterials composed of metal oxides and sulfides, such as TiO2, ZnO, CdS, and ZnS, have gained significant technological importance across multiple fields due to their role as sensitizers in light-induced redox processes, facilitated by their unique electronic structure [5]. Recently, metal sulfides, including ZnS, have captured the attention of researchers seeking novel materials. ZnS stands out among metal sulfides due to its abundance, non-toxic nature [6], simplicity, low cost, exceptional sensitivity, selectivity, as well as other advantageous features such as a large surface-to-volume ratio, significant Bohr exciton radius, wide band gap, high exciton binding energy, and superior refractive index. Notably, ZnS compounds possess multiple band gap values depending on their structures, with cubic ZnS having a band gap of 3.7 eV and wurtzite ZnS having a band gap of 3.4 eV. These characteristics enhance photoluminescence quantum yield, enable narrow emission, and make ZnS-based quantum dot light-emitting diodes highly exciting [6-10]. ZnS, along with other semiconductor materials, has long been utilized in electrochemical sensors due to its suitability for detecting various chemical species. The nanostructured ZnS layer in electrochemical sensors has garnered significant attention due to its ability to enhance mass transfer, provide a high surface area, increase sensitivity, and improve the signal-to-noise ratio [4]. Semiconductor materials, including environmentally friendly options like TiO2, ZnO, CdS, and ZnS, play a crucial role as heterogeneous photocatalysts, acting as sensitizers in light-induced redox processes due to their electronic structure [9]. CdS nanoparticles, known for their vibrant yellow color, find applications in ceramics, plastics, painting pigments, and enamels [11]. CdS exhibits exceptional optical, electrical, magnetic, and dielectric properties, including a direct band gap of 2.42 eV, remarkable stability, minimal absorption loss, and favorable electronic affinity. Furthermore, CdS exists in two structural phases, cubic and hexagonal, making it well-suited for optoelectronic and photoconductive applications such as photocatalysis, photoresistors, photodetectors, light-emitting diodes, solar cells, field-effect transistors, and biological sensors [12,13].

2. Experimental Methods

Metal sulfides were synthesized using a ball mill technique with a well-mixed powder of zinc and cadmium acetate (99.99%) and thiourea (≥99.0%) obtained from Sigma Aldrich. The mixture was then heated to 200°C and sintered for 2 h in a furnace [14]. A mixture of 20 mg of fabricated metal sulfide, such as cadmium and zinc sulfide (CdS), with 10 mg graphite, 10 mg PVDF, and 2 ml (DMF) solution to prepare the ink was used. To prepare electrode ink, the liquid was sonicated for 15 min at room temperature. Subsequently, the surface of the (10 × 10 mm) stainless-steel substrate was treated with a drop of the prepared ink, and the prepared electrodes were dried at 65 °C overnight [14]. The electrochemical tests were conducted using a potentiostat with a three-electrode configuration (Autolab 87070, Metrohm) [14.17] by using a platinum rod, an Ag/AgCl (3M KCl) reference electrode and the materials was the working.

Results and discussions

3.1. X-ray diffraction analysis of ZnS

The XRD spectra of the ZnS and CdS nanoparticles are examined, the XRD pattern peaks lined up with the Rhombohedral ZnS reference pattern (JCPDS No. 01-089-2162). The figure displays the XRD pattern together with the values related to the peaks. The crystalline structure results obtained here are consistent with those reported by Srinivasan and Thirumaran [15]. However, Smith [16] reported that the ZnS structure is more compatible with cubic and hexagonal structures, and it also exhibits rhombohedral structural variations due to the polytypes of one coordination scheme. The XRD patterns of the CdS nanoparticles. The large variety of unique sharp crystalline peaks that appear in each diffraction pattern attests to the polycrystalline character of the manufactured samples. These results agree with the cubic CdS system reference pattern (JCPDS No. 00-042-1411)[6, 17]. The optimal orientations of CdS were determined to be (111), (220), (311), and (400). The low intensities and broad half-peaks characterize the extra

peaks that the XRD scan may reveal. The cubic system of the CdS sample, which is nearly polycrystalline and nanocrystalline, displays exceptional crystallinity. The ZnS and CdS samples exhibit good crystallinity, which is close to the polycrystalline nature and has nanostructure properties.

In addition, the mean particle size was estimated [16,17]. The lattice microstrain of the nanocrystalline structure can be calculated from the slope of the straight line fit, and the mean crystallite size can be derived from the intercept on the vertical axis, the particle size of ZnS was to be 1.56 nm and the lattice microstrain was to be 3.7×10^{-2} [17, 18].

3.2. Morphological characteristics of the prepared metal sulfides

SEM analysis was performed on the surface morphology of the ZnS samples. As a representative example of the prepared group, ZnS material has a dense, crack-free, and generally uneven shape. The average grain sizes were determined using Picture Analyst software. Additionally, the surface exhibited considerable agglomeration made up of numerous tiny crystallites, which made the surface rougher, the grain size was approximately 110 nm, or close to the maximum percentage grain size of nanometers, appears to be where the largest percentage grain sizes are found [14].

The surface morphology of the CdS nanoparticles was studied. The images display several inhomogeneous structures that are unequally distributed and dense. Every micrograph covered the surfaces of the CdS entirely. The substance was highly dense, devoid of cracks, and commonly irregular in shape. The average grain size was determined using image analysis tools [17]. The grain size distribution through the surface of CdS was approximately 65 nm, or approximately the largest fraction of the grain size in nanometers [17]. The relative height of the surface roughness was determined to be between 40 and 50 nm [17]. The estimated average particle sizes of the samples were larger than the predicted crystallite sizes based on the X-ray diffraction examination. This is because X-rays can only see the well-ordered portions of crystallites; they cannot see the disordered grain boundaries, which take up a significant amount of space, and there is a chance that multiple crystallites can accumulate and form an aggregation of particles in the solution, even after being exposed to ultrasonic waves [19].

3.3. Structural characterization using HR-TEM

A typical transmission electron microscope (TEM) image at various magnifications for prepared samples were analyzed, precisely overlapping nearby nanoparticles with aggregation properties produces a huge film area with the required patterns. As a result, it is possible to see that the sizes of the nanoparticle distributions are practically non-uniform, and that the majority of nanoparticles essentially remain in various particles and sizes [14]. The lattice fringes in the high-magnification TEM image, illustrated in the SAED pattern indicate that the ZnS nanoparticles were well-crystallized. Moreover, the SAED pattern shows three diffraction rings that, in agreement with those inferred from XRD, correlate closely with the (0042), (1058), and (2011) crystal planes of the Rhombohedral ZnS. The EDS spectrum of zinc sulfide was represented by a peak at 2.307 keV, whereas S was represented by a peak at 2.307 keV [14].

Transmission electron microscopy (TEM) images of CdS were illustrating the crystalline features. The most conventional sizes of CdS nanoparticles are grouped together with extremely small particles in most places and in various directions. Furthermore, no surface pinholes were observed. In accordance with the XRD results, the SAED pattern displayed three diffraction rings that closely correspond to the (111), (220), (311), and (400) crystal planes of the cubic CdS [17]. The elemental composition of cadmium sulfide was investigated using energy dispersive X-ray spectroscopy (EDS). The average Cd/S ratio is good and comparable to those described in the literature [21] in terms of both atomic and weight percentages, according to the EDS results, which demonstrate that Cd and S were present in the synthesized structure. The Cd/S atomic ratios in the samples were also 1/1.102, which is quite close to the theoretical values and almost precisely fits the ideal structure [17, 22]. However, the HR-TEM images show different preferred planes that are difficult to detect. These preferred planes can be easily realized on Fourier-filtered images [17]. The lattice fringe d-spacing measurements of 0.3128 and 0.1899 nm, as well as the

related Fast Fourier Transform (FFT) images demonstrate the (111) and (220) crystal planes of cubic crystal of ZnS[14, 23]. In addition, the elemental composition was confirmed by elemental mapping using HR-TEM [17].

High-resolution transmission electron microscopy (HR-TEM) was used to determine the crystalline structure and identify the features of the CdS nanostructure can be provided (HR-TEM). HR-TEM images of the CdS nanoparticles at various magnifications [17]. The structure does not have a particular crystalline shape; however, a few crystal planes can be examined under high-resolution settings. Fourier-filtered images of the preferred planes of CdS, the lattice fringe d-spacing measurements were detected, and the corresponding Fast Fourier Transform (FFT) image was demonstrates the (111) crystal plane of cubic CdS[17, 24-25].

3.4. Photoluminescence characteristics of metal sulfides

The photoluminescence (PL) emission of ZnS nanoparticles, which may be successfully used to investigate the structural and physical characteristics of nanostructures associated with defects, is one of the most significant physical aspects of ZnS nanoparticles. The zinc sulfide PL spectrum at an excitation wavelength of 350 nm was examined [14]. The emission spectra showed a prominent peak at approximately 420 nm, fitted to 360,370,390,410,430, and 460 nm. Photoluminescence is the emission of light radiation through the absorption of photon energy that creates the electron-hole pair of ZnS [14]. It should be mentioned that the results obtained correspond to those reported in the literature[26]. Similar results were reported for the same structure by Wang et al.[27] and Ye et al. [28]. These findings can be attributed to Zn vacancies in ZnS nanoparticles, as previously reported by Juine et al. [29].

The PL spectra obtained at an excitation wavelength of 350 nm for CdS was analyzed. As already mentioned, the produced CdS exhibited a clearly blue-shifted beginning of emission in comparison to the bulk CdS particles. The quantum size effect of nanocrystalline CdS is responsible for the noticeable blue shift in these samples. The recombination of a hole in the valence band of CdS with an electron trapped in a sulfur vacancy results in a wide emission band at 390, and 430 nm, which consistent with those reported by Firooz et al.[30] and Chae et al. [31].

3.5. Electrochemical sensing of metal sulphides

The CV sensing characteristics of ZnS nanoparticles placed on a stainless steel (SS) substrate are shown in Fig. 1 (a, b) [14]. This electrode (ZnS@SS) was used to detect ethanol and contaminated water in the presence of methyl alcohol. The response of the ZnS@SS electrode biosensor to methanol was investigated in 100 mL of medium (water or ethanol) with various methanol concentrations (0.0-1000 µL). Even at relatively low methanol concentrations, the ZnS@SS electrode displayed a discernible response behavior. In the positive-going sweep, the ZnS@SS electrode exhibits an oxidation peak of (-0.25 V) for ethanol in water and (+0.25 V) for ethanol in ethanol.

The sensitivities of the ZnS nanoparticles placed on the nickel substrate are shown in Fig. 1(a) and (b). The use of this ZnS@Ni electrode allowed the detection of ethanol and contaminated water in both media. Unfortunately, in contrast to the outcomes obtained using ZnS@SS, the ZnS@Ni electrode did not exhibit a distinct alcohol sensing behavior. In contrast to the electrodes on Ni substrates, ether in water, or ethanol media, the electrodes on the SS substrate produced a distinct electrochemical sensing response for methyl [14].

Operating an electrochemical sensor requires conversion of methanol into electrical signals [27]. The straightforward settings of these sensors render them simple to use. Despite their affordability, their use is constrained by the catalytic surface degradation that occurs during the sensor operation. These sensors are built similar to DMFCs, which employ polymer electrode membranes [28]. Using fuel cells and oxidant current as additional criteria, electrochemical sensors can be further divided into two classes.

CV is a well-known method for measuring the electrochemically active surface area of a catalyst in an electrode through adsorption/desorption cycles is cyclic voltammetry. Cyclic voltammograms of the CdS electrodes in various saturated electrolytes are shown in Fig. 1(c) [17]. The scan rate was set at 100 mV/s, and the potential was modified from -1 V to +1 V. The anodic peaks for nickel material were obtained at 0.53 V and 0.25 V, respectively, for steel substance (Fig.1.(d)). A decrease in Cd behavior was shown by the cathodic peaks [17, 32-35].

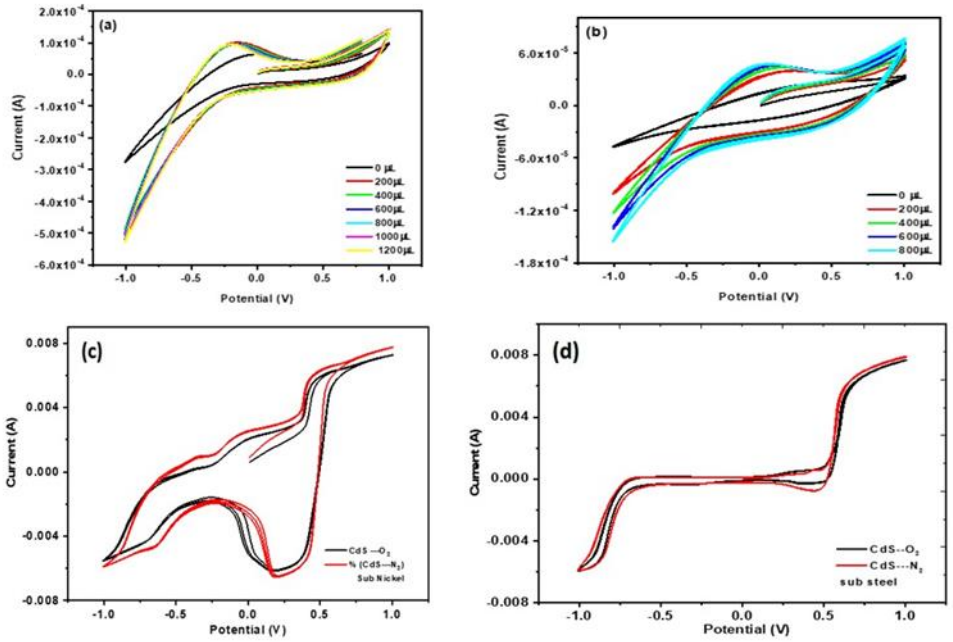

Fig. 1. Plot of sensitivity of ZnS@SS electrode toward methanol in both of (a) water and (b) ethanol, Cyclic voltammogram for different electrodes and different saturated electrolytes (c) for steel substrate and (d) for nickel substrate

4. Conclusion

Metal sulfide nanoparticles have been successfully produced and verified using several techniques. X-ray examination revealed that ZnS and CdS were polycrystalline and cubic. The average crystallite size were determined and found to be 1.56 and 2.02 nm for ZnS and cdS, respectively. ZnS and CdS emit light with powerful photoluminescence and exhibit remarkable emission spectra. The stoichiometry of ZnS and CdS was confirmed by energy-dispersive X-ray spectroscopy (EDS) using HR-TEM. Additionally, cyclic voltammetry of both ZnS and CdS revealed specific characteristics and peaks that could be used in fuel cell technology. ZnS and CdS nanoparticles with unique morphologies and stable PL emissions are essential to ensure the dependability of PL-based nanodevices and expedite their use in numerous domains. The reported ZnS and CdS nanoparticles provide exceptional performance for detecting low methanol concentrations in ethanol. Additionally, the results derived from this work could be an attractive option for applications in extensible nanodevices and electrochemical sensor fuel cells.

References

[1] K.R. Bindu, E.I. Anila, Optimized synthesis temperature and doping concentration of copper in zinc sulfide nanoparticles for green emission, Mater. Sci. Semicond. Proc. 121 (2021), 105317.

[2] P.K. Kannan, D.J. Late, H. Morgan, C.S. Rout, Synthesis, Recent developments in 2D layered inorganic nanomaterials for sensing, Nanoscale 7 (2015) 13293–13312.

[3] P.R. Somani, Synthesis, characterization and charge transport mechanism in conducting polyaniline/V2O5 composites, Sens. Stud. 42 (2001) 150–168.

□ [4] V. Guidi, B. Fabbri, A. Gaiardo, S. Gherardi, A. Giberti, C. Malagù, G. Zonta, P. Bellutti, Metal sulfides as a new class of sensing materials, Procedia Eng. 120 (2015) 138–141.
□ [5] A. Giberti, B. Fabbri, A. Gaiardo, V. Guidi, C. Malagu, Resonant photoactivation of cadmium sulfide and its effect on the surface chemical activity, Appl. Phys. Lett. 104 (2014), 222102.
□ [6] Guy A. Hembury, Victor V. Borovkov, Yoshihisa Inoue, Chirality-sensing supramolecular systems, Chem. Rev. 108 (2008) 1–73.
□ [7] P. Sakthivel, G.K.D. Prasanna Venkatesan, Kamalraj Subramaniam, P. Muthukrishnan, Structural, optical, photoluminescence and electrochemical behaviors of Mg, Mn dual-doped ZnS quantum dots, J. Mater. Sci.: Mater. Electron. 30 (2019) 11984–11993.
□ [8] P. Sakthivel, S. Muthukumaran, Investigation of Ni influence on structural and band gap tuning of Zn0.98Mn0.02S quantum dots by co-precipitation method, J. Mater. Sci.: Mater. Electron. 28 (2017) 8309–8315.
□ [9] P. Sakthivel, K. Kavi Rasu, G.K.D. Prasanna Venkatesan, Amelec Viloria, Influence of Ag+ and Mn2+ ions on structural, optical and photoluminescence features of ZnS quantum dots, Spectrochim. Acta Part A: Mol. Biomol. Spectrosc. 5 (2020), 118666.
□ [10] R. Kumar, P. Sakthivel, P. Mani, Structural, optical, electrochemical, and antibacterial features of ZnS nanoparticles: incorporation of Sn, Appl. Phys. A 125 (2019) 543.
□ [11] Devamani, R.H.P., Kiruthika, R., Mahadevi, P., Sagithapriya, S.: Synthesis and characterization of cadmium sulfide nanoparticles. Int. J. Innov. Sci. Eng. Tech. 4(2017), 2348–7968
□ [12] F.Yaying .Transition Metal Chalcogenide (Cadmium Sulfide) Nanoparticles: (Bio)synthesis, Characterization andPhotoelectrochemical Performance Duke University ProQuest Dissertations Publishing, 2019, 27545101.
□ [13] Kashuba, A.I., Andriyevsky, B., Semkiv, I.V., Ilchuk, H.A., Petrus, R.Y., Shyshkovskyi, S.V.: Calculation of the vibrational spectra of CdSe and CdS crystals with zinc blende structure. Mater. Proc. 62(2022), 5812–5818
□ [14] Mohamed S. Elnouby, O. El-Shazly, E.F. El-Wahidy, Mervet Ramadan, A.A.M. Farag, N. Roushdy, Optimized synthesis, structural and electrical enhancement of Zinc sulfide nanoparticles for electrochemical sensor applications, Optik - International Journal for Light and Electron Optics, 287(2023), 171070
□ [15] N. Srinivasan, S. Thirumaran, Synthesis of ZnS nanoparticles from pyridine adducts of zinc(II) dithiocarbamates, Comptes Rendus Chimie 17(2014), 964-970.
□ [16] F. G. Smith, Structure of zinc sulphide minerals, American Mineralogist 40 (1955) 658–675
□ [17] Mervet Ramadan, Mohamed S. Elnouby, O. El-Shazly, E. F. El-Wahidy, A. A. M. Farag, N. Roushdy, Facile fabrication, structural and electrical investigations of cadmium sulfide nanoparticles for fuel cell performance, Materials for Renewable and Sustainable Energy, 11(2022):277–286,
□ [18] V. Biju, N. Suganthan, V. Varinda, S.L. Salini, Estimation of lattice strain in nanocrystalline silver from X-ray diffraction line broadening, Mater. Sci. 43 (2008) 1175-1179.
□ [19]S.A. Saafan, S.T. Assar, B.M. Moharram, M.K. El Nimr, Comparison study of some structural and magnetic properties of nano-structured and bulk Li-Ni-Zn ferrite samplesJ. Magn. Magn. Mater. 322 (2010) 628-632
□ [20] J. Díaz-Reyes a, R.S. Castillo-Ojeda , R. Sanchez-Espíndola , M. Galvan-Arellano , O. Zaca-Moran, Structural and optical characterization of wurtzite type ZnS, Curr. Appl. Phys. 15(2015) 103-109.
□ [21]Z.M. Kakhaki, A.A.Youzbashi, P.Sangpour, N.Naderi, Y.Orooji, Influence of Cd salt concentration on the photoconductivity of CdS thin films prepared by chemical bath technique, Mater. Sci. Semicond. Proc.148(2022)106773
□ [22] J.Balavijayalakshmi, D.Sonia, Impact of iron doping on structural and optical properties of cadmium sulphide nanoparticles, Mater.Today proc. 50 (2022)117-122.

□ [23] V. Biju, N. Suganthan, V. Varinda, S.L. Salini, Estimation of lattice strain in nanocrystalline silver from X-ray diffraction line broadening, Mater. Sci. 43 (2008) 1175-1179.
□ [24]Z.M. Kakhaki, A.A.Youzbashi, P.Sangpour, N.Naderi, Y.Orooji, Influence of Cd salt concentration on the photoconductivity of CdS thin films prepared by chemical bath technique, Mater. Sci. Semicond. Proc.148(2022)106773
□ [25] J.Balavijayalakshmi, D.Sonia, Impact of iron doping on structural and optical properties of cadmium sulphide nanoparticles, Mater.Today proc. 50 (2022)117-122.
□ [26] D. Kanimozhhi, R. indirajith, Effects of L-Cysteine in Zinc Bis Thiourea Acetate (ZBTA) Crystal Lattice, J. Electron.Mater. 48 (2019) 201.
□ [27] Caifeng Wang, Bo Hu, Ligang Chen, Ni Liu, Jie Li, Preparation and characterization of ZnS nanostructures, Opt. Intern. J. Light Electron Opt. 224 (2020) 165673.
□ [28] X. C.Ye, G. Fang, L. Li, Zhang, Origin of the green photoluminescence from zinc sulfide nanobelts, Appl. Phys. Lett., 85 (2004) 3035.
□ [29] R.N. Juine, A. Das, S. Amirthapandian, Concentration controlled QDs ZnS synthesis without capping agent and its optical properties, Mater. Lett. 128 (2014)160-162.
□ [30] A. A. Firooz, A. R. Mahjoub, R. D. Ziba, Synthesis, Characterization and PL Properties of Cds Nanoparticles Confined within a Functionalized SBA-15 Mesoprous, World Academy of Science, Engineering and Technology 5 (2011) 128-130.
□ [31] Chae W-S, Ko J-H, Hwang I-W, Kim Y-R, Emission characteristics of CdS nanoparticles induced by confinement within MCM-41 nanotubes, Chem. Phys.Lett. 365(2002) 49- 56.
□ [32]Y. Liang, H. L. Li, X. Zhang, Solid state synthesis of hydrous ruthenium oxide for supercapacitors, J. Power Sources 173 (2007) 599-605.
□ [33] C.Liu, S.Alwarappan, Z.Chen, X.Kong, C.-Z Li, Membraneless enzymatic biofuel cells based on graphene nanosheets. Biosens. Bioelectron. 25 (2010)1829–1833.
□ [34] S. H. Kim, W. Han, J. Lee, Electrochemical characterization of CdSe and CdTe thin films using cyclic voltammetry, Curr. Appl.Phys. 10 (2010) S481–S483.
□ [35] K. Salaria,N. Mehta,C. Krishna, S. K.Mehta, Electrochemical detection of TNT using CdS nanoparticles via cyclic voltammetry and amperometry, Curr. Res. Green Sust. Chem. 4(2021) 100166.

Simulation of Fluid Flow and Heat Transfer for Disposal of Radioactive Waste from Fission-based Molybdenum-99 Production

NOHA SHAABANa, WALID I. ZIDANb

Nuclear and Radiological Safety Research Center,

Egyptian Atomic Energy Authority, Cairo-Egypt

anohashaaban@ymail.com, bnajzidan@gmailcom

Keywords: thermal-hydrologic processes, fluid and heat flow in porous media, saturated rock, uranium fuel, nuclear safeguards, reservoir simulation, Molybdenum production.

Abstract. In this work, a preliminary study has been proposed to analyze the ground water and surface water flow near the storage sites of low level radioactive waste, (LLRW) incorporating uranium generated from fission-based molybdneum-99 production. In order to cope with the proliferation issues, international nuclear security policy is promoting the use of low enriched uranium (LEU)' targets in order to minimize the civilian use of high enriched uranium (HEU). It is noteworthy that Mo-99 yield of the LEU target is less than 20% of the HEU target, which requires approximately five times more LEU targets to be irradiated and consequently results in increased volume of waste. The IAEA with member states has a continuous work to define specific criteria for the termination of safeguards on radioactive waste incorporating uranium in geological repositories. The proposed study explore the feasibility of using the measured environmental parameters as safeguards implementation tool for storage sites of the LLRW.

Introduction

Most of the public's concern about nuclear applications is about the hazards from radioactive waste generated. Several countries have laws prohibiting construction of nuclear installations until the waste disposal issue is settled. There have been many safety analyses of waste repository, and all of them agree that the principle hazard is that somehow the waste will be contacted with the ground water, dissolved, and carried by the ground water into wells, rivers and soil. This would cause contamination of drinking water supplies or, through pick up by plant roots and contamination of food. Rocks and soil are excellent shielding materials; while the waste remained buried.

Underground radioactive waste is traditionally enclosed in calcine or glass boxes, known to be highly resistant to thermal shock; therefore reducing the risk of immediate and complete release of the uranium. Borosilicate nonetheless degrades over time and ion exchange becomes responsible for the gradual permanent sequestration of the material in between clay layers. Often the ion exchange capacity of the clay is not high enough or not enough of it is present, allowing the uranium point source to migrate into underground water bodies. In the development of a safety case for a deep repository, national regulations governing radiological safety will be used to gauge whether requisite levels of containment appear to be achievable by a proposed disposal system. These regulations concern principally the acceptability of the radiological impact of releases of radionuclides when they reach the

biosphere, in terms of radiation doses and associated risks. Regulations will impose nuclear safeguards constraints on geological repositories containing fissile materials using institutional control arrangements, such as monitoring and records keeping.

From safeguards perspective, Nuclear Material (NM) is defined as source material or special fissile material. The safeguard regulation specifies six categories of for which reporting is required: plutonium; HEU (20% enrichment or greater); LEU (higher than natural, less than 20% enrichment); natural uranium; depleted uranium; and thorium [1]. The aim of nuclear safeguards is to detect, and therefore deter, the diversion of NM from peaceful uses to nuclear weapons. It is the means by which the international community limits the spread of nuclear weapons, through verifying that nuclear activities established for peaceful, civilian, purposes are not diverted to military use. In considering the conditions for the application of safeguards to NM contained within waste there are two key issues that need to be considered. The first of these is the actual definition of what constitutes 'waste' for the purposes of safeguards, the second being at what point safeguards can be 'terminated' on the NM associated with that waste [2]. In the latter case, it should be noted that termination does not necessarily have to involve discard to the environment, but could involve emplacement in a long- term storage facility. Following the recommendations of the 1988 advisory group. Working on the development of criteria for termination of safeguards on different waste types [3], it has been proposed that termination of safeguards could be considered on a case-by-case basis depending on the type of waste, and conditioned methods used. One view is that the waste material, being of low grade, would not be very attractive for diversion purposes and would be very difficult to use as a basis for generating significant quantities of nuclear material. When such conditioned waste is emplaced and sealed in a geological repository, a common view among waste management experts is that safeguards should be terminated at this point or before. On the other hand, it can be pointed out that there is no physical form from which NM cannot be recovered. Technological innovations might provide even easier and less costly means to recover material which safeguards had been terminated at an earlier time. At present, there is no establish consensus on these latter issues and the formal position of the international safeguards is that safeguards would have to be maintained on certain waste types even after conditioning and disposal [4]. In this study, a trial to adopt a pragmatic approach to the application of criteria for termination of safeguards and to the kind of verification activities applied for, material categorized as waste for safeguards purposes, or otherwise destined for disposal is presented.

Waste Generation from Fission-based Molybdenum-99 Production

Technetium-99m (Tc-99m) is a short-lived daughter product of the parent molybdenum-99 (Mo-99), which is mainly produced by the fission of Uranium-235. The decay scheme of Mo-99 to Tc-99m is shown in Fig.1. Tc-99m is the radioisotope most widely used as a tracer for medical diagnosis. Management of radioactive waste is an integral part of fission Mo-99 production during the planning, design, construction and operational phase.

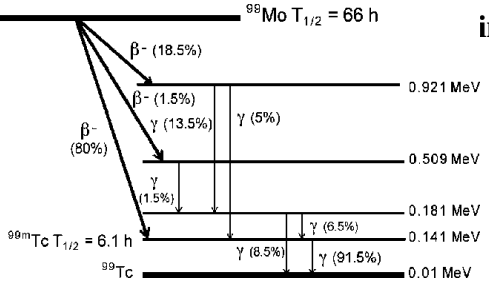

Ta **ing dissolution [5]**

Fission Product	Half Life
Xe-131m	11.93 d
Xe-133m	2.19 d
Xe-133	5.24 d
Xe-135	9.14 h
I-131	8.02 d

	Kr-85	4.48 h

Fig. 1: Decay scheme of Mo-99 and Tc-99m

The waste generated can be mainly due to: target fabrication, assembling of target, irradiation in reactor and processing of irradiated targets. A large number of radionuclides with different chemical and physical properties are formed. Irradiated targets are loaded into the hot cell where the target plates are inserted into the dissolver to separate the Mo-99 from the fission products. During the dissolution process, the produced solid, liquid and gaseous waste may be a combination of low level waste (LLW) and intermediate level waste (ILW). However no high-level waste is produced from Mo-99 as it does not contain long-lived or alpha-emitting radionuclides with activity >400 Bq/g and it does not produce heat > 2 kW/m^3 [5].

The off-gases, as indicated in Table 1, are stored in especially shielded cascades and are released into the environment after decay as required by the applicable regulations. Table 2 indicatesthe main stream of liquid waste arises from the dissolver and filtration process. In order to produce the same amount of Mo-99 from the LEU target, it must contain uranium ≥ 5 times of the uranium in the HEU target. As a result, 3 to 6 times more dissolver solution will be required. This will increase the liquid waste as well as the quantity of solid waste. The main source of solid waste in Mo-99 production process mainly consist of filtered uranium and Transuranic uranium (TRU), the ion exchange resins and absorber columns. It may consist of charcoal filters, different hot cell filters, valves, pumps, tubes, etc... Transuranic radioactive waste consists of materials containing alpha-emitting radionuclides, with half-lives greater than twenty years and atomic numbers greater than 92, in concentrations greater than 100 nano-Curies per gram of waste. It is generally consists of protective clothing, tools and equipment used in these processes. Management of radioactive waste from Mo-99 production is 26 times more Pu-239 produced from LEU targets than HEU targets with comparable to Mo-99 yield which increase the disposal cost significantly as indicated in Table 3.

Table 2: Liquid waste from a plate targets, 3000 Ci [5]

	HEU targets	**LEU targets**
^{235}U enrichment %	93	19.75
U-total, g	16.1	93.7
^{99}Mo, Ci (mg)	532(1.11)	545(1.13)
Total Mo, mg	9.8	10.0

RadioisotopesActivity (MBq/l)							
(Liter)				**ILW**	18.7	^{89}Sr	740
^{90}Sr			630				
^{137}cs			6400				
^{103}Ru			500				
^{106}Ru			46				
^{125}Sb			4.6				
LLW	12	^{103}Ru	5.040				

Groundwater Geochemistry near the Storage Sites of LLRW

This study introduces thermo-hydrologic model, TH, evaluates the coupled TH processes related to fluid flow due to impact of radioactive waste heat release on the natural hydrogeological system including thermally perturbed water and rock temperature elevations, as well as the changes in water velocity and pressure under thermal loading conditions [7]. Most geothermal reservoir simulation studies have involved fluid and heat flow equations, but had little coupling with geo- mechanical effects. Tough2 is a general purpose numerical simulator for multi-dimensional fluid and heat flow of multiphase, multicomponent fluid mixtures in porous and fractured media [8]. Through the simulation, Equation of State (EOS3) module which represent fluid mixtures and include the thermo-physical properties needed for assembling the governing mass and energy balance equations for geothermal and nuclear waste applications has been used [9]. Water flow is simulated in one- dimensional homogeneous saturated medium, the mesh grids involves 200 grid blocks consisting of 100 blocks for the waste packages and underground facility and 100 blocks for the near field rock. The geometry of the problem is indicated in Figues 2-3. Temperature-dependent fluid properties; such as fluid density, viscosity and specific enthalpy are incorporated in the formulation of the TOUGH2 code and are described in Table 4. The numerical solution is accomplished by specifying constant pressure boundary conditions, starting with constant pressures in the upstream and downstream boundary grid block with uniform initial temperature of 28 □C. The pressure distribution produces a time invariant velocity field obtained when running the problem to a steady state. From Bernoulli head measures, the piezometric head used to measure the elevation and pressures of fluids in soil is simply:

$$P\ h = hz + _ \quad (1)$$

.

Where the h_z represents the elevation with respect to an arbitrary datum, and p/□ represents the pressure head of the fluid and has units of length, □ =9.8 kN/m^3.

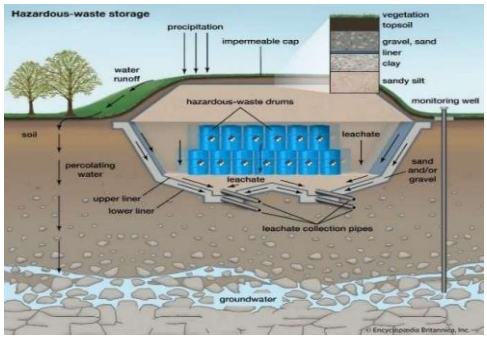

Fig.2: Schematic diagram of LLRW disposal under deep ground

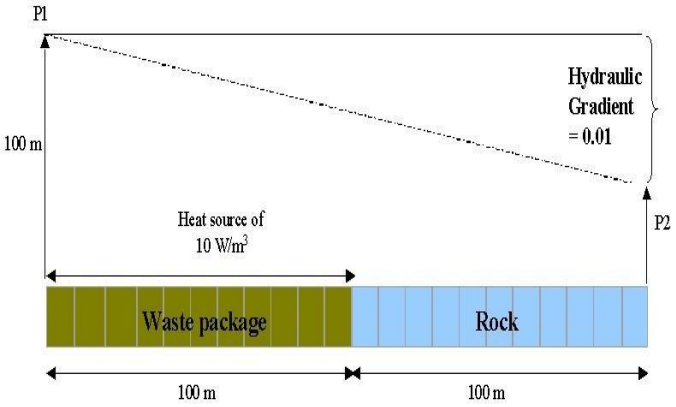

Fig. 3: Schematic diagram of fluid flow model

Fluid flows down the hydraulic gradient from point 1 to point 2, the pressure difference is calculated according to:

$$\triangle h = h1 - h2 = \frac{P1 - P2}{\gamma} \quad (2)$$

For A hydraulic gradient =0.01 and thickness, □L =200 m, Head gradient $= \frac{\triangle h}{\triangle L}$. (3)

So, $\triangle h = 2$ m, for $P2 = 1.05e5\ Pa$,

$P_1 = 1.05e5\ P_a + \triangle h \times \gamma = 1.196\ P_a$. (4)

$$Permeability = \frac{hydraulic\ conductivity \times Kinematic\ viscocity}{Gravity\ acceleration}$$

(5)

Table 4: Temperature Dependent Fluid Properties

	Sedimentary rock	Waste Package
Density of Rock kg/m^3	2350	2848
Porosity	0.2	.15
Thermal Conductivity W/m. °C	2.4	3.773
Specific Heat Kg. °C	1300	971
Permeability m^2	0.85E-6	.85E-6

The viscosity of a fluid is a measure of its resistance to gradual deformation by shear stress or tensile stress. For heat production rate of 10 W/m^3 and volume $1 \times 10 \times 10 = 100m^3$,

Energy Rate = Heat production × Volume = 1000 W.

(6) For a homogeneous porosity medium, ground water velocity, v is:

$$\frac{\text{Hydraulic conductivity} \times \text{Hydraulic gradient}}{\text{Porosity}} \quad (7)$$

Results and Discussion

A thermal–hydrologic numerical model is presented for investigating fluid flow behaviour in response to decay heat from the radioactive waste repository**.** The velocity, temperature and pressure under steady state conditions in homogeneous saturated medium with uniform ambient temperature of 28 °C are shown in 4-a, 4-c, 4-c, 4-e. The heat effect after the emplacement of a waste package generating heat of 10 W/m^3 inside the homogeneous rock was simulated as shown in Figures, 4-e, and 4-f respectively. The value of 10 W/m^3 refers to the initial thermal load that decreases with time as a result of radioactive decay.

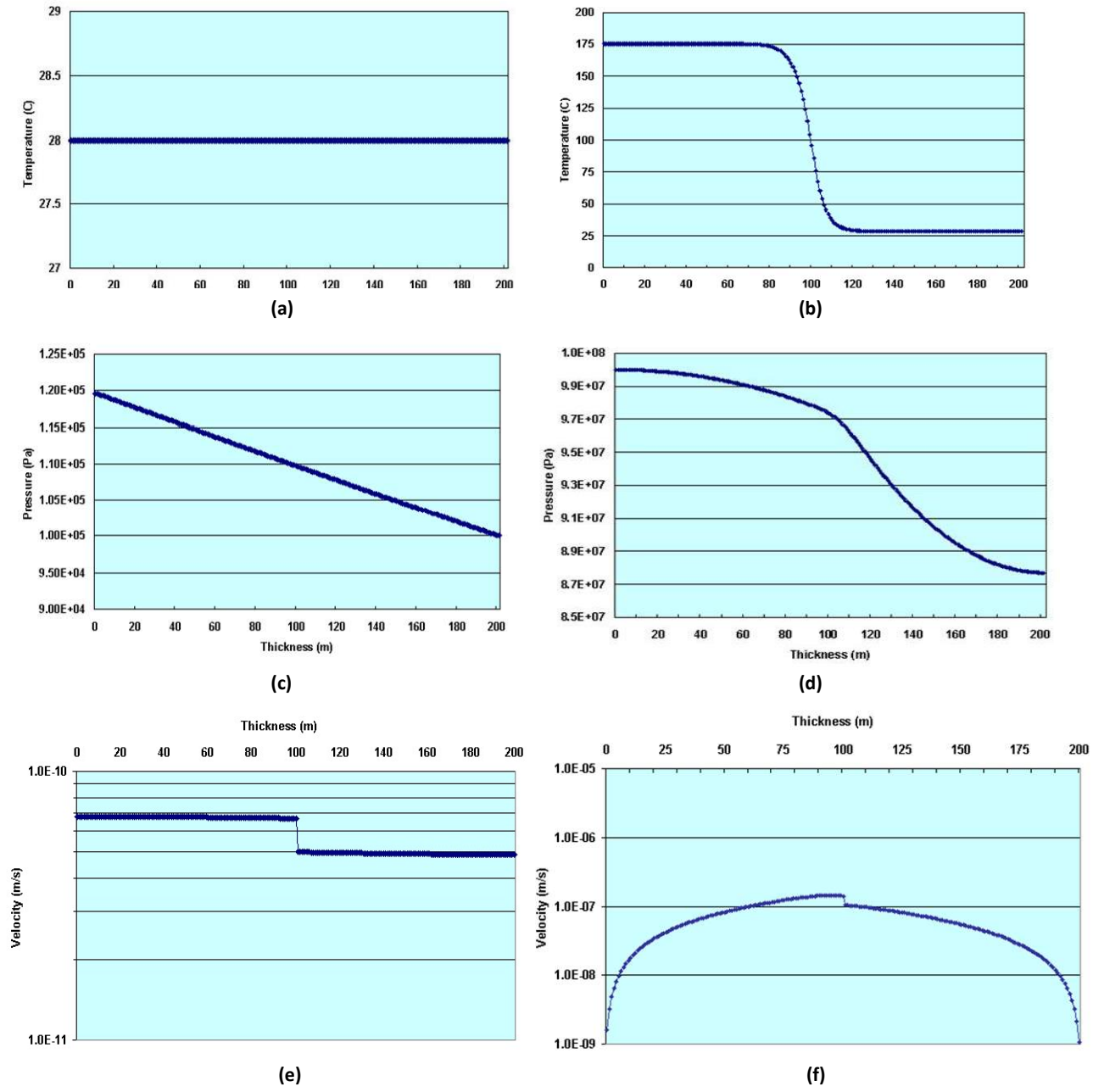

Each of them was greatly affected after emplacement of the heat source

, the emplacement of the source causes high increase in both temperature and pressure in the waste package and as a result a high increase in the velocity of the ground water with maximum value obtained at the interface between the two media. These values decrease again once the flow enter the rock medium and leave the waste package medium. Depending on this hydraulic information, a mass transport analysis could be conducted in detail. These simulations provide insights into thermally perturbed flow fields under thermal loading conditions. The need to characterize TH processes has posed a tremendous challenge for investigators, because of the large spatial and temporal scales involved in such characterization and quantitative modelling. These numerical models have played a crucial role in understanding coupled fluid and heat flow as well as in assessing how TH conditions affect various aspects of the overall waste disposal system. Since experimental studies and

field heater experiments, however necessary, are limited in terms of space and time, numerical modelling provides a powerful tool by which to investigate physical processes on the temporal and spatial scales relevant to understanding nuclear waste-repository performance in a geological formation [9-10].

Conclusion

Evaluation of the coupled fluid-flow and heat-transfer processes has proven to be essential in order to define the waste management strategy earlier at the planning stage of establishment of an LEU fission-based Mo-99 production facility. The impact on the environment should be analyzed. Monitoring the change of the environmental parameters surrounding the waste repository is needed in setting the strategy of selecting site deep underground and for establishing the suitable engineered safeguards as well as relevant regular surveillance. The present study introduces a site scale simulated model of the thermo-hydrologic behavior of fluid flow in the presence of repository waste heat which will assist the decision makers in determining the necessary steps of terminating safeguards for the disposed low level radioactive waste.

References

[1] IAEA Safety Standards for protecting people and the environment Specific Safety: Guide No. SSG-31, *Monitoring and Surveillance of Radioactive Waste Disposal Facilities*, IAEA, Vienna (2014).
https://www-pub.iaea.org/MTCD/Publications/PDF/Pub1640_web.pdf.

[2] IAEA Guidelines for states systems of Accounting for and Control of Nuclear Materials: IAEA/SG/INF/2, IAEA, Vienna (1980).

[3] *Scientific and Technical Basis for the Geological Disposal of Radioactive Wastes*: Technical Reports Series No. 413, IAEA, Vienna (2003).

[4] Gordon Linsley, Abdul Fattah: *The Interface between Nuclear Safeguards and Radioactive Waste Disposal.*
https://www.iaea.org/sites/default/files/publications/magazines/bulletin/bull36-2/36202682226.pdf.

[5] Mohamed Ul Hassan, Ho Jin Ryu: *Radioactive Waste Issues Related to Production of Fission-based 99Mo by Using Low Enriched Uranium (LEU)*, http://dx.doi.org/10.7733/jnfewt.2015.13.2.155.

[6] *Hazards of High-level Radioactive Waste – The Great Myth*, The NUCLEAR ENERGY OPTION, Chapter 11, http://www.phyast.pitt.edu/~blc/book/BOOK.html.

[7] K. Pruess by C. Oldenburg, and G. Moridis, *Tough2 User's Guide, Version 2.0*, Earth Sciences Division, Lawrance Berkeley Laboratory, University of California,Berkeley, Californi 94720, November (1999).

[8] Yu-ShuWu, Sumit Mukhopadhyay, Keni Zhang and G. S. Bodvarsson: *A mountain-scale thermal-hydrologic model for simulating fluid flow and heat transfer in unsaturated fractured rock*, Journal of Contaminant Hydrology, Volume 86, issues 1-2, 30 June (2006), Pages 128-159.

[9] A. Mushtaq, Masood Iqbal, Atta Muhammad: *Management of Radioactive Waste from Molybdenum-99 Production Using Low Enriched Uranium foil Target and Modified CINTICHEM Process*, J. Radional Nucl Chem, Volume 281 (2009), Pages 379-392.

[10] IAEA-TECDOC-1051: *Management of Radioactive Waste from* ^{9}Mo *Production*, (1998).

://www.iaea.org/publications/5348/management-of-radioactive-waste-from-99mo- production.

Numerical investigations of Darrieus turbine for tidal power applications

Ahmed. A. Abdel-Naby, Omina. M. Nawar*, Eslam. R. Lotfy

Mechanical Engineering Department, Faculty of Engineering, Alexandria University, 21544 Alexandria, Egypt

* Omnia_nawar414@hotmail.com

Keywords: Tidal energy, Hydropower, Darrieus turbine, Vertical axis water turbine, Renewable energy

Abstract

Tidal energy is one of the best solutions to reduce pollution that comes from fossil fuels. Moreover, tidal oscillation current is predictable. The maximum power generated from a tidal turbine is 61% higher than a wind turbine because of high density of water compared to air. This highlights the applicability of tidal turbines with high power density. Tidal power could be extracted via different types of turbines. Among these turbines, Darrieus turbine, a vertical axis turbine (VAT), is independent of the flow direction. Therefore, there is no need for a yawing mechanism. In this study, a 2D model of Darrieus turbine was developed using ANSYS FLUENT 17.2 to investigate the effect of operating/design parameters on the turbine's output power. The RNG k-ε turbulent model was used to solve the two transport equations. Mesh and time independence tests were done using coarse, intermediate and fine meshes and 0.01,0.005 and 0.0025 seconds respectively. Fine mesh and 0.005 seconds time step were selected to run the simulation for different parameters. The 2D CFD model was validated against experimental data from literature and a good agreement was achieved. The 3 blades Darrieus water turbine was tested at different pitch angles, blade surface roughness heights and solidities using NACA63(3)-018.

Introduction

Nowadays, technologies have been developed to harness energy from safe and clean resources to decrease greenhouse gas emissions produced from burning of fossil fuels. The ocean energy is one of the cleanest energy resources, including ocean thermal energy, wave energy and tidal energy [1]. Tidal energy represents a promising source of clean renewable energy because of its predictability. Chauhan et al. [2] discussed advantages and disadvantages of tidal energy. Besides its predictability, high density of water is an interesting advantage of harnessing energy from tides. High power could be generated even at low flow speeds due to the high density of water.

Darrieus water turbine is a vertical axis turbine that has been widely investigated for its potential in tidal power conversion. Many studies have been carried out to investigate the effect of the design parameters on its performance. Khanjanpour and Javadi [3] experimentally and numerically tested the effect of the blade surface roughness on the power losses. Patel et al. [4] carried out experiments to investigate the impact of design parameters as blade profile, solidity and number of blades on the performance of Darrieus water turbine for tidal current application. Shiono et al. [5] measured the output torque of Darrieus water turbine in water channel to determine the design parameters that have significant impact on the turbine performance. A detailed comparative overview of different rotor designs has been discussed and followed by an

examination of the turbine with different dimensions, solidities and blade shapes in Khan et al. [6]. The 2D and 3D numerical analyses of the unsteady flow through the blades of the turbine were performed using ANSYS Fluent 18.0 by Ramirez et al. [7] to define the optimal configuration for a given set of design parameters. More studies have been conducted to enhance turbine performance. Hiraki et al. [8] conducted experimental test to improve the performance of Darrieus turbine for the power generation using a tidal current. The effect of guide-vane was investigated for single Darrieus turbine and for the twin-turbine configuration. The CFD simulations were carried out to evaluate the influence of the rotor arrangement and the use of trailing edge tabs on the turbine performance by Balduzzi et al. [9]. Sahim et al. [10] experimentally studied the effect of deflector on Darrieus-Savonius water turbine performance. Numerical and experimental analyses of Darrieus water turbine in bare and shrouded configurations have been carried out by Roa et al. [11]. A 2D CFD numerical study using OpenFoam was developed to improve the efficiency of a low cut-in speed current vertical nested hybrid turbine combining Savonius and Darrieus technologies by Bouhal et al. [12].

Based on the abovementioned discussion, Darrieus water turbines hold significant potential for tidal energy utilization. Further investigations are still important to enhance the turbine efficiency against different design and operating parameters like solidity, blade surface roughness and pitch angle.

Numerical simulation and validation

Geometry

In this study, H- Darrieus water turbine was used in a parametric study to analyze the impact of the solidity, pitch angle and blade roughness on the turbine output power. Table 1 shows the parameters and dimensions of the considered turbine tested in this work which matches the one was experimentally tested by Shiono et al. [5].

Table 1. Design parametes of the tested turbine.

Diameter	**300 mm**
Height	**200 mm**
Blade shape	**NACA63(3)-018**
No. of blades	**3**
Solidity	**0.366**
Chord length	**115.2 mm**

CFD Solver and setup

The commercial software ANSYS FLUENT 17.2 was used in this study to solve the flow equations and analyze the Darrieus tidal turbine outputs. RNG K-e transient solver was used to solve the two transport equations.Table 2 represents the CFD solver setup.

Table 2. CFD solver settings.

Solver	**Ansys Fluent transient solver**
Solver type	**Pressure based**

Turbulence model	**RNG K-epsilon model**
Rotation model	**Sliding mesh model**
Time step	**0.0025,0.005 and 0.01 sec**

Mesh and time independence

A mesh sensitivity test was done using three meshes; a fine mesh, an intermediate mesh and a coarse mesh. Specifications of each mesh are listed in Table 3. An intermediate and fin meshes showed almost identical results, which have a good agreement with the experimental results. Therefore, intermediate mesh was selected to do the tidal turbine parametric study in this work. Three-time steps were evaluated-; 0.01, 0.005 and 0.0025 seconds. 0.005 and 0.0025 time steps gave approximately the same results. To save the time, 0.005 second was selected for all the simulations. Fig. 4 shows the results of mesh and time independence assessments.

Table 3. configurations of the tested meshes.

	Coarse Mesh	**Intermediate Mesh**	**Fine Mesh**
Face sizing (stationary domain)	0.025m	0.025m	**0.025m**
Face sizing (rotating domain)	0.01m	0.01m	**0.005m**
No. of Nodes	60159	67435	**77107**
No. of Elements	59501	66358	**75644**
Blades and interface refine	-	3	**3**

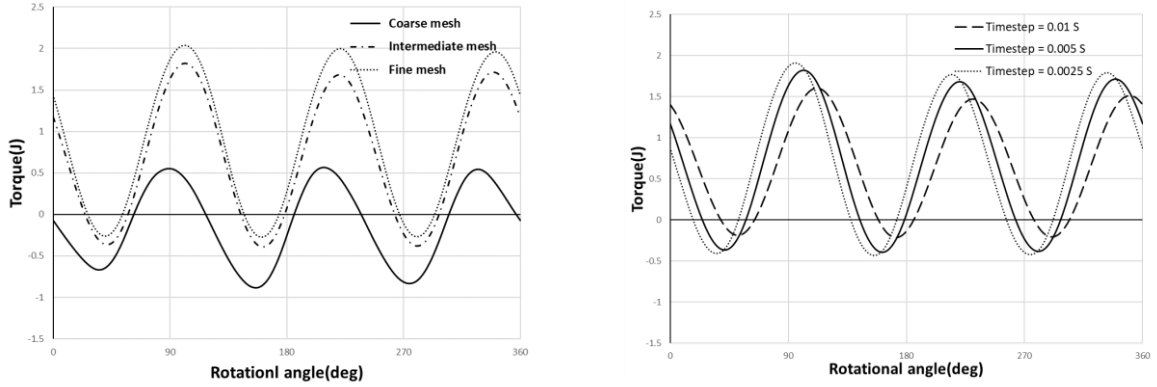

Fig. 4. (a) Mesh independence results.(b)Time independece results.

Validation of CFD numerical model

A numerical model was developed using the intermediate mesh and a time step of 0.005 sec. The validation of the numerical model was performed by comparing the torque calculated from the current work and torque measured from the experiment in Shiono et al. [5]. Current model was examined at constant flow speed 1 m/sec and solidity of 0.366 at different angular velocities. Fig. 5 represents the comparison between the numerical results and experimental results. It showed a good agreement with an average error of 7% that could be accepted especially if the experiments' uncertainty is reported.

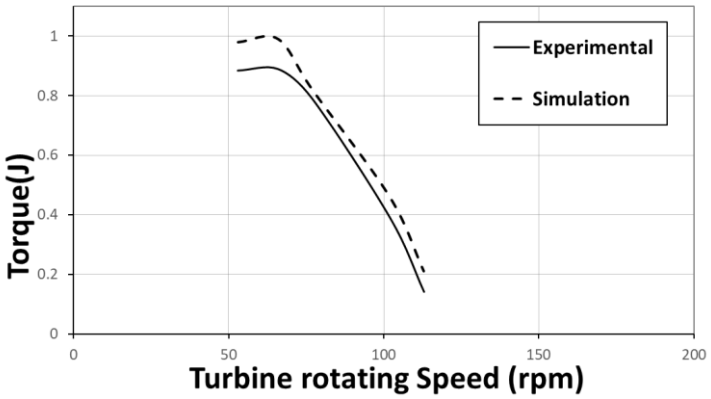

Fig. 5. Validation of the numerical setup against experimental results.

Results

In this section, the main results of the effect of solidity, blade rougness and pitch angles were reported. In this regard, different solidities of 0.244, 0.366, 0.545 and 0.733 were studied. Moreover, six different blade roughness heights and five different pitch angles were investigated.

Solidity test

In this study, the turbine solidity was modified by changing the turbine radius (r) without changing the number of blades (n = 3) and blade chord length (c = 115.2 mm). The test was conducted for four solidities of 0.244, 0.366, 0.545 and 0.733. The flow speed was kept constant at 1.5 m/sec.

Fig. 6 shows the water turbine efficiency (η) versus tip speed ratio (λ) for different solidities. It can be noticed that the peaks of the turbine efficiency for the four solidities are between tip speed ratios of 0.5 and 1.5 . The solidity of 0.366 has the maximum turbine effiecncy of 39% for a tip speed ratio of 1 . The peak of the water turbine effieciency moves towards high tip speed ratios as the solidity decreases . These results agree with Patel et al. [4] results. Patel et al. [4] showed that the maximum coefficient of power lays between solidities 0.3 and 0.4 for NACA 0018 and NACA 4415.

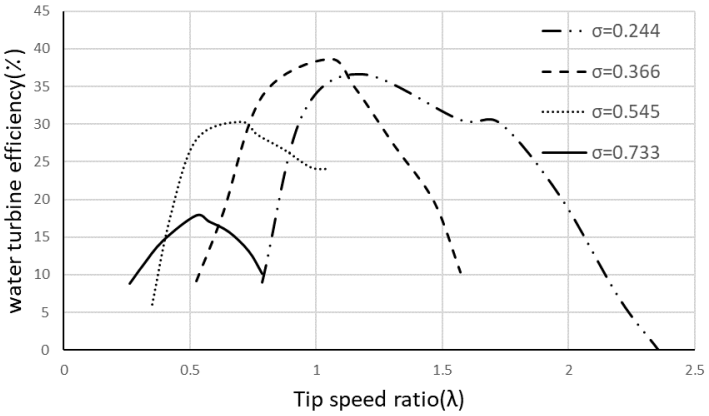

Fig. 6. Water turbine efficiency characteristics (V = 1.5m/sec).

Pitch angle test

Five pitch angles were selected to be examined; -5º,0º,5º,10º and 15º. Using a constant solidity (σ = 0.366) and constant flow speed v = 1.5 m/sec. Fig. 7 shows the different examined pitch angles. Water turbine efficiency η is represented versus the pitch angles in Fig. 8. It can be seen

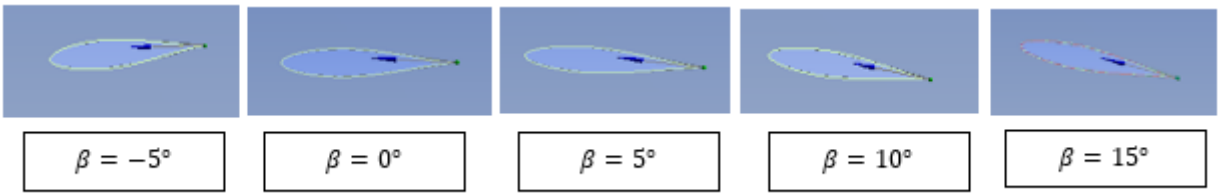

that the maximum efficiency of the water turbine is achieved at 5º pitch angle.

Fig. 7. Different pitch angles

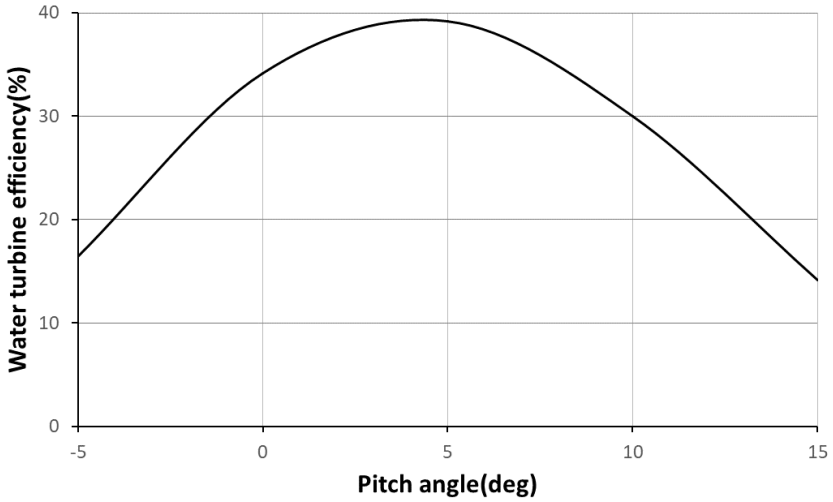

Fig. 8. Water turbine output charecterisics(σ = 0.366).

Blade roughness test

The 3 blades H-Darrieus water turbine was examined for six blade roughness heights (H_r) of 0, 50, 100, 250, 500 and 1000 µm. The blade shape was NACA63(3)-018 and a constant solidity of 0.366 was used. The flow speed was kept constant at 1.5 m/sec. Fig. 9 shows the turbine efficiency(η) versus different roughness heights/chord length ($\frac{H_r}{C}$). It could be observed that the power losses increase for the rough surfaces while the smooth blade surface generates the highest power. This observation meets the conclusions of Khanjanpour and Javadi [3].

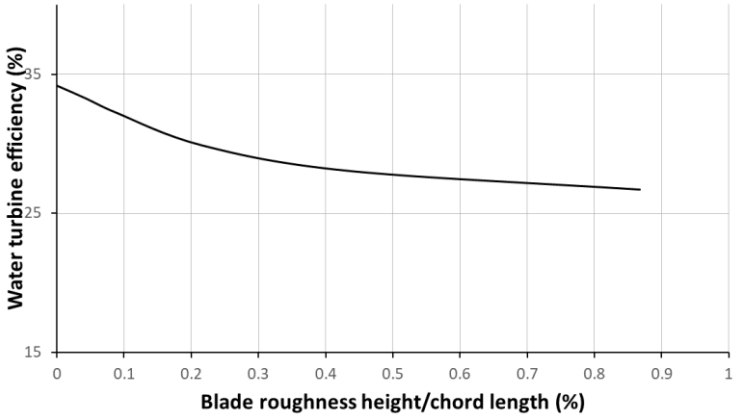

Fig.9. Water turbine output characteristics(σ=0.366)

Conclusion

In this study, a 3 blades H-Darrieus water turbine was numerically tested to analyze the effect of different design parameters on its performance. A 2D CFD model using ANSYS Fluent 17.2 was built to do the simulation. One blade profile NACA63(3)-018 was tested under four turbine solidities of σ=0.244, σ=0.366, σ=0.545 and σ=0.733. The solidity of 0.366 showed the best turbine performance at tip speed ratio of 1. Five pitch angles were examined, and the generated powers reveal that pitch angle of 5º produces the highest power. The blade surface roughness has a significant effect on the power losses.

References

1. Pelc, R. and R.M. Fujita, *Renewable energy from the ocean.* Marine Policy, 2002. **26**(6): p. 471-479.
2. Chauhan, P., P. Patel, and S. Sheth. *Tidal Stream Turbine-Introduction, current and future Tidal power stations*. in *National Conference on Innovative and Emerging Technologies SRPEC, Unjha*. 2015.
3. Khanjanpour, M.H. and A.A. Javadi, *Experimental and CFD analysis of impact of surface roughness on hydrodynamic performance of a darrieus Hydro (DH) Turbine.* Energies, 2020. **13**(4): p. 928.
4. Patel, V., T. Eldho, and S. Prabhu, *Experimental investigations on Darrieus straight blade turbine for tidal current application and parametric optimization for hydro farm arrangement.* International journal of marine energy, 2017. **17**: p. 110-135.

5. Shiono, M., K. Suzuki, and S. Kiho, *An experimental study of the characteristics of a Darrieus turbine for tidal power generation.* Electrical Engineering in Japan, 2000. **132**(3): p. 38-47.
6. Khan, M., M. Iqbal, and J. Quaicoe. *Design considerations of a straight bladed Darrieus rotor for river current turbines*. in *2006 IEEE international symposium on industrial electronics*. 2006. IEEE.
7. Ramirez, D., A. Rubio-Clemente, and E. Chica, *Design and numerical analysis of an efficient H-Darrieus vertical-axis hydrokinetic turbine.* Journal of Mechanical Engineering and Sciences, 2019. **13**(4): p. 6036-6058.
8. Hiraki, K., et al. *Guide vanes for darrieus water turbine in tidal current*. in *International Conference on Renewable Energies and Power Quality*. 2013.
9. Balduzzi, F., et al. *Some design guidelines to adapt a Darrieus vertical axis turbine for use in hydrokinetic applications*. in *E3S Web of Conferences*. 2021. EDP Sciences.
10. Sahim, K., et al., *Experimental study of Darrieus-Savonius water turbine with deflector: effect of deflector on the performance.* International Journal of Rotating Machinery, 2014. **2014**.
11. Roa, A.M., et al. *Numerical and experimental analysis of a darrieus-type cross flow water turbine in bare and shrouded configurations*. in *IOP Conference Series: Earth and Environmental Science*. 2010. IOP Publishing.
12. Bouhal, T., et al., *CFD performance enhancement of a low cut-in speed current Vertical Tidal Turbine through the nested hybridization of Savonius and Darrieus.* energy Conversion and Management, 2018. **169**: p. 266-278.

Sustainable environmental Coastal development of the surf zone of Alexandria

R.E. Mohamed[1,a], and M.M. Abd-El-Mooty[2,b]

[1]Faculty of Engineering, Alexandria University, Alexandria, Egypt

[2]Faculty of Engineering, Alexandria University, Alexandria, Egypt

[a]rania_mohamed@alexu.edu.eg

[b]mooty431@yahoo.com

Keywords: Alexandria coastline, Erosion, Sea level rise, Urban development, environmental sustainability

Abstract. Alexandria is a historical city in northern Egypt, located along the Mediterranean Sea. It is the second-largest city in Egypt and serves as an important economic and cultural hub for the country. The Alexandria coastline has faced several environmental and natural problems over the years. One of the major challenges for Alexandria's coastline is coastal erosion. The human effect and the wave erosion action caused the disappearance of most of the sand beaches along the coast. Alexandria is also exposed to the effects of climate change, particularly sea-level rise. In addition, rapid urban development along the Alexandria coastline has contributed to many of the mentioned problems. Unplanned construction, encroachment on natural habitats, and inadequate infrastructure planning have further strained the coastal environment. Sustainable coastal practices require a comprehensive approach that considers environmental sustainability, public access, and protection against erosion and other coastal hazards. These practices are crucial for preserving the Alexandria coastline's natural beauty, protecting its ecosystems, and ensuring long-term environmental sustainability. This paper outlines practices for protecting beaches in Alexandria to facilitate environmental and tourist activities. Suggestions for creating new sand beaches and a sea road are presented in this paper. Depending on the morphology of the seabed and the environmental use of the beach, the analysis and the result of the study are presented.

Introduction

The Alexandria coastline is the coastal area along the city of Alexandria, Egypt. Alexandria is on the Mediterranean Sea, and its coastline stretches along the northern part of the country. It is located on the west side of the Nile Delta between latitudes (31° 03/ N, 31° 18/ N) and longitudes (29° 40/ E, 30° 05/ E). It is built on a narrow coastal plain. Its narrowness, flatness, and a group of parallel limestone ridges also characterize Alexandria Beach. It is famous for its amazing coastline, interesting attractions, and energetic environment. It has been an important port city since ancient times, and its coastal location played a significant role in its historical and cultural development [1]. Its beaches are vulnerable to a wide variety of environmental issues induced by both natural and human activities such as beach erosion, water pollution, loss of biodiversity, and climate change impacts [2]. This paper aims to address many important aspects related to the environmental issues along the coastline of Alexandria, outline practices for protecting beaches in Alexandria to facilitate environmental and tourist activities and evaluate the current protection measures. Recommendations for enhancing the protection and conservation of the Alexandria coastline are provided. Suggestions for creating new sandy beaches and a sea road are also presented. Depending on the morphology of the seabed and the environmental use of the beach, the analysis and the result of the study are presented.

Environmental Issues Along the Alexandria Coastline

The Alexandria coastline in Egypt has faced various problems over the years. For example, it suffers from high population growth, extreme rates of erosion, seawater intrusion, salination, ecosystem pollution, and degradation, and a lack of suitable institutional management systems [3]. One of the major challenges for Alexandria's coastline is coastal erosion. The city's coastlines are exposed to erosion due to natural factors like wave action, storms, and rising sea levels. Human activities such as unregulated sand mining, construction along the shore, and the blocking of natural sediment flow exacerbate the erosion problem. This has led to the loss of beaches, damage to infrastructure, and increased vulnerability to flooding. The second problem is land subsidence. Alexandria is experiencing land subsidence. This is primarily due to the extraction of groundwater from underground aquifers, causing the land to sink. As a result, the coastline is further at risk of flooding and coastal erosion. The most dangerous challenge is also Pollution and Water Quality. The Alexandria coastline faces pollution challenges, including untreated sewage and industrial waste being discharged into the sea. This has led to water pollution and degraded water quality along the coastline, impacting marine life, ecosystems, and public health. Efforts are being made to improve wastewater treatment and reduce pollution in the area. Climate Change is a recent challenge. Alexandria is vulnerable to the effects of climate change, particularly sea-level rise. As sea levels increase, the city's coastline becomes more prone to erosion, flooding, and saltwater intrusion into freshwater resources. In addition, rapid urban development along the Alexandria coastline has contributed to many of the above-mentioned issues. Unplanned construction, encroachment on natural habitats, and inadequate infrastructure planning have further strained the coastal environment. To address these challenges, the Egyptian government and local authorities have initiated various measures such as beach nourishment projects, the construction of seawalls and breakwaters, and efforts to improve wastewater treatment facilities. Long-term strategies include coastal zone management plans, sustainable urban development practices, and raising awareness about the importance of preserving the coastline's natural resources.

The Current Protection Measures Evaluation

The eastern part of Alexandria's coastline extends from El Silcila to Abu Quir. This area's shoreline is undulating and frequently marked by rocky headlands that create embayment and pocket beaches. The length of the beaches in this area ranges from 0.3 to 1.5 kilometers. While the coast has a few small sandy beaches, it is important to remember that most of the coastline is formed from rocky outcrops with low sea cliffs and offshore shoals [1]. In this study, the coastline is divided into three zones based on morphological characteristics, and coastal protection as shown in Fig. 1.

Figure 1. Alexandria's coastline is divided into three zones depending on the coastal protection
measures and morphological features

Zone I is from El Mandara to Al Mahrousa hotel. It is characterized by narrow sandy beaches. Zone II is from Loran Beach to the Sidi Gaber area; it is characterized by hotels and clubs and is a fully protected area. Zone III is from Sidi Gaber to El Silcila, it is characterized by no beaches and some places have narrow beaches. Figure 2 shows the existing soft and hard protection structures along the eastern part of Alexandria from El Silcila to Montaza Palace.

Figure 2. The existing protection structures from El Silcila to Montaza Palace.

The executed solutions to overcome the current problems of beaches are mentioned. Al-Montazah area had problems that were overcome by building submerged breakwaters. Sea water attacks the beaches and exits to the Corniche Road in Al-Mandara and Al-Asafra area. Therefore, a submerged breakwater was constructed in this area. This existing structure is being reconsidered to work on increasing its efficiency and addressing this problem, as this barrier has partially addressed the problem, but not completely.
Miami area has a slight erosion, and therefore it needs to be fed with sand only to accommodate many visitors. Sidi Bishr and El-Mahroussa beaches are narrow and do not accommodate a large number of vacationers. Therefore, work is underway on the submerged breakwaters project (first stage), and sand nourishment to increase the width of the beach. Beaches in the Loran area (from Al-Mahrousa to San Stefano) are narrow and suffer from extreme erosion and wave

attack. Therefore, the proposal is to make submerged breakwaters, and sand nourishment work to restore the old beach to provide a sandy beach for people. San Stefano Beach is an area protected by a group of detached breakwaters and groins, where the Corniche wall is protected sufficiently and safely. The club area from Saba Pasha to Sidi Gaber is a fully protected area, where each club has done the necessary and special protection for it, but these actions need to be re-evaluated and studied, as some of these areas, such as the Engineers syndicate suffers greatly during the winter, as the water reaches the inside of the club. Although there are hard structures. Sidi Gaber area up to El Silcila includes (Cleopatra - Sporting - Ibrahimia - Camp Shizar - El Shatby), a proposal was made for it to establish three submerged breakwaters to protect about 4 kilometers from the beach. To shield the area from severe waves during the winter, these structures will be established, and the old protection blocks in front of the Corniche wall will be removed. To construct new beaches, sand will also be fed in front of the structures. Table 1 shows the suitability of the structures to the design equations and nature conditions.

Table 1. The assessment of the coastal hard structures (groins, and breakwater) at Alexandria beaches

Beach	Protection system	Groin Length (L)	Spacing (S) m	S/L	Evaluation
Groin System			**Spacing between Groins (m)**		**2<S/B<4**
El-Mandara	Groin	40	90	2.25	Effective
	Groin	100	140	1.4	Not effective
San Stefano	1 Groin	286	685	2.39	Effective
Gleem	Groin	315	235	0.75	Not effective
	Groin	215	175	0.82	Not effective
Breakwater System		**Breakwater Length (B)**	**Spacing from B.W to the Shoreline (S)**	**S/B**	**S/B<1**
Asafra	Submerged breakwaters	950	370	0.13	Not effective
		400	200	0.5	Not effective
		450	200	0.44	Not effective
Cleopatra	Breakwaters	110	120	1.09	Effective (Salient)

Alexandria Coastline Management

Managing the Alexandria coastline requires a comprehensive approach that considers environmental sustainability, public access, and protection against erosion and other coastal hazards. So, The Alexandria coastline will be divided into three zones depending on the characteristics of the shoreline. Some suggestions will be shown for Alexandria coastline management.

- Coastal Erosion and Flooding Mitigation: Invest in measures to combat coastal erosion and flooding, such as the construction of artificial reefs, submerged breakwaters, soft protection

like beach nourishment, and dune restoration. Implement coastal zone management plans that consider the impacts of climate change and prioritize adaptive strategies. For the Alexandria coastline, beach nourishment will be applied. It will be conducted periodically to replenish eroded beaches with sand. This process involves adding sediment to the beach, which helps widen the shoreline and enhance its protective function as shown in Fig. 3. For Zone I, the beaches have severe erosion, so the sand nourishment will be added to enhance the shoreline protection as shown in Fig. (3. A). Zone II is characterized by private beaches and syndicate clubs. It will be planned and implemented via private consulting, probably not linked to the beach's concerned authorities, except Gleem Beach (Fig. 3. B). It is a public beach, and the sand nourishment will be added between two groins to add new sandy beaches for recreation. Zone III will be protected by sand nourishment along the coastline from Cleopatra Beach to El-Silcila as shown in Fig. (3. C). The planned new path along the Alexandria coastline is shown in Figure (3.D). The project's goal is to build straight highways and improve traffic flow to meet the needs of urban development. The road will be 60 m wide for 12.5 km between El Montaza and El Silcila.

Figure 3. Beach nourishment projects are required along the Alexandria coastline and a new road connects Al Montaza and El Silcila

- Coastal Ecosystem Restoration: Implement programs for the restoration and protection of coastal habitats such as mangroves, seagrass beds, and coral reefs. These ecosystems act as natural buffers against storms, erosion, and sea-level rise.
- Waste Management and Pollution Control: Establish proper waste management systems to prevent plastic pollution from entering the coastal environment. Implement recycling programs, promote the use of reusable products, and introduce penalties for littering and illegal waste disposal.
- Public Awareness and Education: Conduct public awareness campaigns and educational programs to raise awareness about the value of coastal ecosystems, climate change, and sustainable practices. Engage local communities, schools, and businesses to foster a sense of ownership and encourage sustainable behaviors.
- Sustainable Coastal Development: Encourage sustainable urban planning practices that prioritize green spaces, reduce urban sprawl, and protect sensitive coastal areas. Develop and enforce regulations for responsible development, consider setbacks from the shoreline and building codes to minimize the impact of development on coastal erosion, and protect the coastal ecosystem.
- Marine Protected Areas (MPAs): Establish MPAs along the Alexandria coastline to safeguard marine biodiversity and promote sustainable fishing practices. These protected areas can help conserve fish stocks, protect vulnerable species, and allow ecosystems to recover.

- Renewable Energy Transition: Promote the development and use of renewable energy sources, such as solar and wind power, to reduce reliance on fossil fuels. Encourage the installation of offshore wind farms and solar panels on coastal buildings to harness clean energy.
- Sustainable Tourism Practices: Encourage sustainable tourism practices that minimize environmental impact. Promote responsible tourism guidelines, educate visitors about the importance of protecting the coastal ecosystem, and support eco-friendly accommodations and activities.
- Collaboration and Partnerships: Foster collaboration among government agencies, local communities, non-governmental organizations (NGOs), and private sectors to develop and implement sustainable initiatives. Encourage partnerships for funding, research, and monitoring of coastal sustainability efforts.
- Monitoring and Research: Invest in scientific research and monitoring programs to assess the health of the Alexandria coastline, identify emerging issues such as (water quality, erosion rates, and biodiversity), and measure the effectiveness of implemented solutions. This data can inform decision-making and help adapt strategies as needed.

Therefore, implementing these sustainable solutions requires long-term commitment, collaboration, and regular assessment to ensure the resilience and health of the Alexandria coastline for future generations.

Conclusion

Alexandria is located in northern Egypt, close to the Mediterranean Sea. It plays a significant role in the nation's economy and culture. Over the years, the Alexandria shoreline has experienced several environmental and ecological issues. Coastal erosion is one of the main issues facing Alexandria's shoreline. Most of the sand beaches along the coast have disappeared due to human activity and natural factors. The impacts of climate change, particularly sea level rise, also affect Alexandria. The rapid urban expansion along the Alexandria coastline has also increased many of these issues. The coastal environment is already under stress due to unplanned building, encroachment on natural habitats, and inadequate infrastructure planning. A comprehensive strategy that considers environmental sustainability, public accessibility, and protection against erosion and other coastal hazards is necessary for sustainable coastal practices. This research paper provides guidelines for safeguarding Alexandria's beaches to support recreational and tourist activity. In conclusion, the suggestion in this research is to build new sand beaches and a sea road. It is also important to note that any interventions or coastal protection measures should be based on detailed scientific studies, considering the specific characteristics of the seabed, the local environment, and the potential impacts on the overall coastal ecosystem. Engaging with environmental experts, local communities, and relevant stakeholders is essential for developing Alexandria's effective and sustainable coastal management plan.

References

[1] H. Abayazid, M. Iskander, A. Elkut, and M. Soliman: Development, Vulnerability and Resilience Capacity of Alexandria Coastal Zone: A Review. Research and Technology Development for Sustainable Water Resources Management Conference, (REDWARM), 4-6 December 2016, Cairo, Egypt.

[2] R. Mohamed, and M. Abd-El-Mooty: Coastal Environmental Issues of Climate Change Along the Nile Delta Coastline, Twenty-Third International Water Technology Conference, IWTC23, Port Said, Egypt, March 2023.

[3] M.M. Iskander, in: Sediment Transport along Alexandria Coast. M.Sc., Faculty of Engineering, Alexandria University, Egypt, 2000.

Removal of sulfides from industrial wastewater solutions by electrocoagulation

S. A. Attia†[1], M. A. El-Naggar[1], A. A. Zatout[1], E.-S. Z. El-Ashtoukhy[1] G. H. Sedahmed[1]and A. S. Fathalla[1]

[1]Chemical Engineering Department, Faculty of Engineering, Alexandria University, Alexandria, Egypt
†E-mail: shaimattia4@gmail.com

Abstract

This study focuses on the removal of sulfide ions discharged from industrial waste solutions such as leather tanning effluents, pulp and paper industries, petroleum refining effluents, petrochemical plants, and natural gas desulphurization by electrocoagulation in a new cell design. The cell consisted of an array of closely spaced woven iron screens anode enclosed between two iron screen cathodes. Variables studied were current density, solution pH, initial sulfide concentration, NaCl concentration, electrodes orientation (vertical or horizontal), number of anode screens per array, and mesh number of screens. The % removal was found to increase with increasing current density and pH. The horizontal electrode orientation was found to be more efficient than the vertical electrode orientation. A complete sulfide removal was obtained in 18 minutes using a current density of 10 mA/cm^2, pH 8, an initial concentration of sulfide 250 ppm, and a NaCl concentration of 30 g/L. Electrical energy consumption ranged from 0.27 to 48.2 kW.h/kg depending on the operating conditions. The advantages of the present technique over other techniques of sulfide removal such as the low amount of sludge, the use of clean electrons rather than chemicals, and the amenability of the process to automatic control were highlighted.

A pilot plant study is needed to confirm the present results which were obtained using a lab-scale cell.

Keywords: Electrocoagulation, Fixed-Bed Electrode, Porous Electrodes, Sulfides, Wastewater Treatment, Woven Screens.

Introduction

H2S gas is produced in large amounts from the desulphurization of fossil fuels such as natural gas, coal, and petroleum. Other sources of dissolved sulfide include leather tanning waste solutions, oil refineries wastewater, wastewater from pulp and paper mills, and sewage where SO4- -reducing bacteria reduces SO4- -pollutants to sulfide under anaerobic conditions. Sulfides are toxic, corrosive, and odorous (obnoxious odor) and therefore should be removed from air and waste solutions before the discharge of these solutions in water bodies. H2S gas produced by fossil fuel gasification plants can be removed by the well-known Claus process [1], which consists of two steps as follows:

In the first step, part of H2S gas is oxidized by O2 to SO2 according to the equation:

$$2\ H2S + 3\ O2 \rightarrow 2\ SO2 + 2H2O \quad (1)$$

In the second step H2S gas is oxidized by SO2 to S according to the equation:

$$2\ H2S + SO2 \rightarrow 3\ S + 2H2O \quad (2)$$

The disadvantage of this method is that it takes place at high temperatures (525-700◦C) which needs expensive materials of construction. To obviate the high cost of the Claus process, several authors have suggested oxidizing dissolved H2S gas (scrubbed from the gas phase by NaOH solution as Na2S) and wastewater sulfide to sulfur either chemically or electrochemically under mild operating conditions. Chemical oxidation involves treating Na2S solution by an oxidizing

agent such as O3, H2O2, Cl2, NaOCl [2]. Chemical oxidation of Na2S by air sparging in the presence of carbon powder as a catalyst has been reported by Lefers et al. [2]. Wet oxidation of Na_2S by air at 200-280◦C and a pressure of 150 bar has been studied by Carlos et al. [3]. Also oxidation of Na2S by Fenton reagent (H2O and Fe++) where the generated OH-radical resulting from the reaction between H2O2 and Fe++ oxidizes sulfide to sulfur has been reported by Rodriguez et al. [4]. Biochemical oxidation of sulfide solutions to produce sulfur has been studied by Zhang et al [5] and Syed et al. [6].

Although the chemical oxidation of Na2S is relatively fast and takes place under mild operating conditions, it suffers from some drawbacks such as the use of expensive chemicals which may add a new pollutant to the solution. To overcome this drawback, a mediated electrochemical oxidation of Na2S has been suggested [7-11], this process takes place in two steps as follows:

.Oxidation of Na2S to sulfur by an oxidizing agent such as Fe+3, Ce+4, K3Fe (CN)6, quinone, and V+5.

i.Regeneration of the oxidizing agent by anodic oxidation of the reduced form in a divided cell where H2 gas evolves at the cathode.

The advantage of this method is that it uses clean electrons in oxidizing Na2S and no chemicals are consumed, besides H2 gas which is a valuable commodity is obtained as a by-product. However, this method suffers from the drawback that the resulting sulfur is colloidal and difficult to separate.

Electrolysis of sulfide solutions in an electrolytic cell with an insoluble anode to produce H2 and sulfur was studied by different authors [12-16]. The process suffers from anode passivation by the deposited suffer which disturbs the process. Trials to solve this problem by adding an organic solvent such as toluene to the sulfide solution have met with little success [15].

Despite the wide use of electrocoagulation (E.C.) in wastewater treatment, little has been done to use this technique in treating sulfide solutions. So this work aims to remove sulfide from synthetic wastewater by E.C. using a new cell design. E.C. is usually carried out in a cell containing steel or aluminum electrodes. In the case of steel electrodes, the following reactions take place during electrolysis:

At the anode:

$$Fe \rightarrow Fe^{+2} + 2e \quad (3)$$

The dissolved Fe++ions are oxidized by dissolved O2 to Fe+++ which undergo hydrolysis to Fe(OH)3. In view of its high surface area, Fe(OH)3 adsorbs a considerable amount of pollutants such as sulfide from waste water.

At the cathode, H2 is generated according to the reaction:

$$2\,H_2O + 2\,e \rightarrow 2\,OH^- + H_2 \quad (4)$$

H2 bubbles float Fe(OH)3 floc along with the adsorbed sulfide to the solution surface where it can be skimmed.

In the present study, the performance of a new cell in removing sulfide will be examined where the cell anode is made of a fixed bed of parallel steel screens placed between two steel screen cathodes. The majority of previous studies on E.C. were conducted using the traditional parallel plate cell which suffers from the low area per unit volume and the low productivity. The present cell has a relatively high area per unit volume besides the fact that the porous structure of the bed anode allows flow induced by the rising H2 bubbles to circulate through the anode, hence the concentration polarization, cell voltage, and electrolytic energy consumption are reduced.

Experimental technique

Figs. (1.a) and (1.b) show the cell and electrical circuit used in the present study. The cell consisted of a rectangular plexiglass container of the dimensions 10 cm x10 cm for the base and 10 cm for the height. The cell anode was an array of closely spaced steel screens (3 to 5 screens)

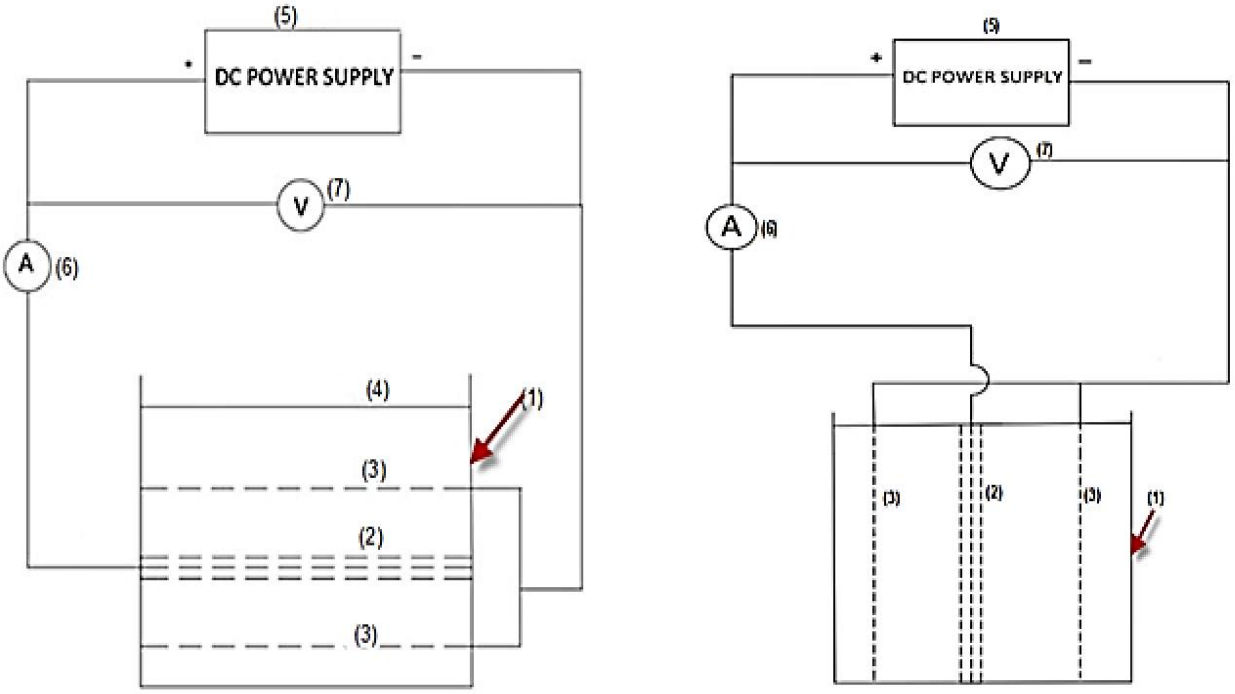

placed between two steel screen cathodes. Screens of mesh numbers 4, 6, and 10 were used in the
present study, each screen has a rectangular shape of the dimensions 10 cm x10 cm.

1. Plexiglass rectangular container, (2) Fixed bed of steel screens anode, (3) Screen cathode, (4) Electrolyte level, (5) D.C. power supply, (6) Digital ammeter, (7) Digital voltmeter.

The effect of electrode orientation (vertical or horizontal) was also studied. Electrode separation (cathode to anode distance) was fixed at 3 cm on each side of the anode in both electrode orientations. The electrical circuit consisted of a 10-volt direct current power supply with a voltage regulator, a digital ammeter connected in series with the cell, and a digital voltmeter connected in parallel with the cell to measure its voltage.

Before each run, one liter of a solution composed of Na2S and NaCl supporting electrolyte was placed in the cell. Na2S concentration ranged from 250 ppm to 1000 ppm, three different concentrations of NaCl were used, namely:10, 20, and 30 g/L, anode current density ranged from 0.5 to 10 mA/cm^2, and solutions pH ranged from 4 to 12.

During electrolysis, a sample of 5 cm^3 was taken from the cell for sulfide analysis [17]. Volumetric analysis was used to determine the residual S- - concentration by adding a known volume of standard acidified K2Cr2O7 solution where part of K2Cr2O7 is consumed in oxidizing the residual sulfide to sulfur according to the reaction:

$$K2Cr2O7+3\ Na2S+7\ H2SO4 \rightarrow K2SO4+Cr2(SO4)3+3\ Na2SO4+3\ S+7\ H2O \quad (5)$$

The rest of K2Cr2O7 was back titrated against standard ferrous ammonia sulfate using diphenylamine as an indicator. The Anode screen area was calculated in terms of the wire diameter and mesh number by the method of Armour and Canon [18]. The rate of S- -removal from the solution was expressed in terms of the % S- -removal is given by the equation:

% S--removal= C0-CCo×100 (6)

Results and discussions

Effect of different variables on the % S–removal for horizontally oriented electrodes

Fig. (2) shows that by increasing the current density (c.d.), the % S- -removal increases from 65% to 100% after 30 minutes of electrolysis. The increase in the removal efficiency with increasing c.d. is consistent with Faraday's law according to which the rate of electrochemical reaction responsible for S- -removal increases.

It is probable that S- -is removed from the solution in many ways, namely:

.The anodically dissolved Fe++ undergoes hydrolysis to Fe(OH)2 especially in neutral and alkaline solutions. The resulting Fe(OH)2 is oxidized by dissolved oxygen to Fe(OH)3 according to the reaction [19,20]:

2 Fe(OH)2+12O2+H2O→2 Fe(OH)3 (7)

S- -ions are adsorbed on the surface of Fe(OH)3 which is floated with the cathodically discharged H2bubbles to the solution surface.

ii. Some S- -are oxidized to S at the anode (e0 of S--| S=0.48V), the value of the anode potential (e) for such a reaction is given by [21]:

e=0.48+0.0592log [S- -]

(8)

where eo is the standard electrode potential, this potential which is close to Fe dissolution (eo of Fe |Fe++=0.44V) makes it possible for S- -oxidation to compete with Fe anodic dissolution. The resulting element S can be floated to the solution surface by cathodically evolved H2 bubbles.

The combination of S- -with the anodically dissolved Fe++ to form FeS precipitate which is floated to the solution surface by the cathodically evolved H2 bubbles. The possibility of FeS precipitation in neutral and alkaline solutions arises from the fact that the solubility product of FeS is 3.2×10-18[17] which can be reached easily. However, it seems that the

contribution of this mechanism to S- - removal is not significant in view of the fact FeOH3 is more stable than FeS (solubility product of the FeOH3 = 3.2×10-3817).

A considerable part of the reason why the rate of the S- -removal increases with increasing c.d. is the increase in the amount of the cathodically discharged H2 bubbles which improve the efficiency of the E.C. process via:

.As the rising bubbles swarm and the entrained solution passes through the porous anode they remove the accumulated Fe++away from the anode surface with a consequent decrease in concentration polarization and the passivation tendency of the steel anode [22, 23]. Also, the rising gas-liquid dispersion improves the mixing condition in the cell with a subsequent increase in the rate of all reactions involved in the process of S- -removal.

i.The increase in the number of H2 bubbles with increasing c.d. improves the floating ability of the bubbles to the floc of FeOH3 along with the adsorbed S- -, S, and FeS. Previous studies on the effect of c.d. on the size of H2 bubbles [24-27] have shown that the size of H2 bubbles

decrease with increasing c.d., resulting in lowering the rise velocity of the bubble which can be approximated by Stoke's law [28]:

$$6\pi \mu r Vb = 43 r3g(\rho - g) \quad (9)$$

The decrease in the rise velocity of the gas bubbles increases the gas hold up (void fraction) in the solution [29], this leads to enhancing the floating ability of H2 bubbles to the floc.

Fig. (3) shows that for a given set of conditions, the % removal of S- - decreases with increasing initial S- -concentration. This may be explained as follows:

.As the S- -concentration increases, rapid adsorption of S- -ions on the surface of Fe(OH)3 takes place with blocking the active centers available for more absorption.

i.As the S- -concentration increases, its diffusivity inside the solution and the Fe(OH)3 floc decreases because of the interionic attraction effect between S- - and surrounding positive Na+ions [30]. The interionic attraction also decreases the activity (effective concentration) of S- -with a consequent decrease in the rate of reactions involving S- -removal [30].

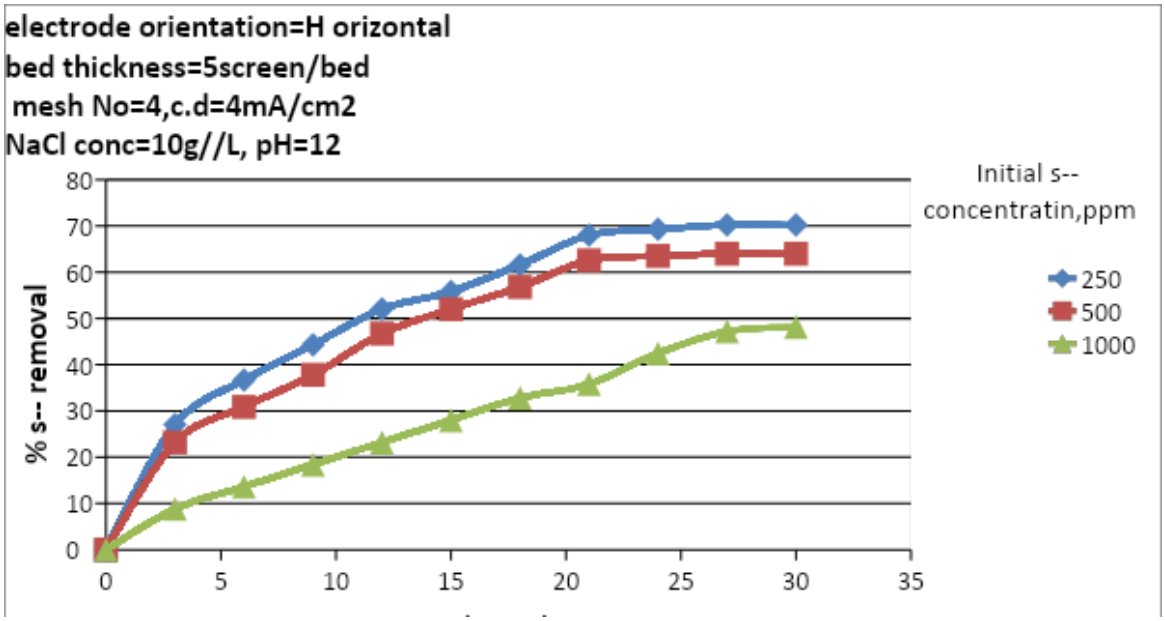

Fig. (4) shows the effect of NaCl supporting electrolyte on the % S- -removal where the data show that the % S- -removal tends to increase with increasing NaCl concentration. This may be explained by the high ability of Cl-ions to destroy passive films on the anode surface such as iron oxides and sulfur deposits [31]. It is noteworthy that increasing NaCl concentration tends to decrease the diffusivity and activity of S- -by interionic attraction [29]. However, Fig. (4) shows that the antipassive effect of Cl-out weights its negative effect concerning the decrease in S- -activity and diffusivity.

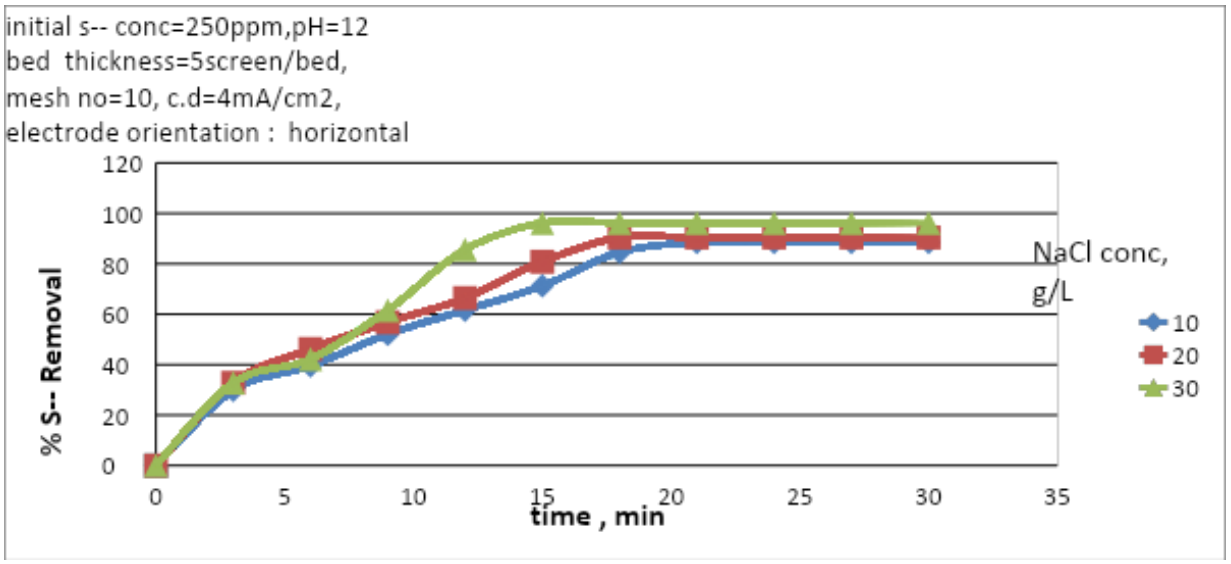

Fig. (5) shows that % S- -removal increases with increasing bed thickness (i.e., number of screens per bed), this may be attributed to the fact that increasing the bed thickness increases the number of turbulence-promoting wires. When the uprising H2 –liquid dispersion coming from the cathode passes through the bed across the wires, turbulence is generated [32] with a subsequent increase in the rate of mass transfer inside the bed. As a result, concentration polarization decreases with a consequent decrease in the anode passivation tendency besides, bed stirring by the rising gas-liquid dispersion improves the mixing conditions in the solution resulting in faster reactions and higher % S- -removal.

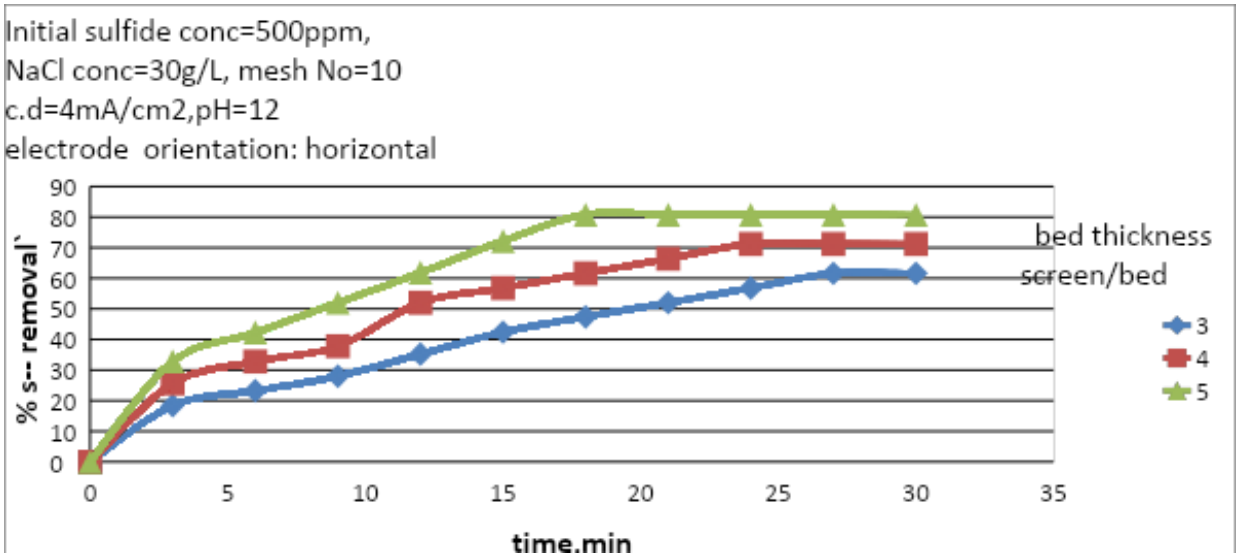

Fig. (6) shows the effect of pH on the %S- -removal where the data shows that the %S- -removal increases with increasing solution pH. Acidic solutions give low rates of %S- -removal owing to the low rate of Fe(OH)2 oxidation to Fe(OH)3 by dissolved O2. As the pH increases, the rate of oxidation increases [19,20] with a subsequent increase in the % S- -removal. Alkaline solutions favor the formation of passive film on the anode but it seems that the presence of Cl-in the solution counteract this tendency [31].

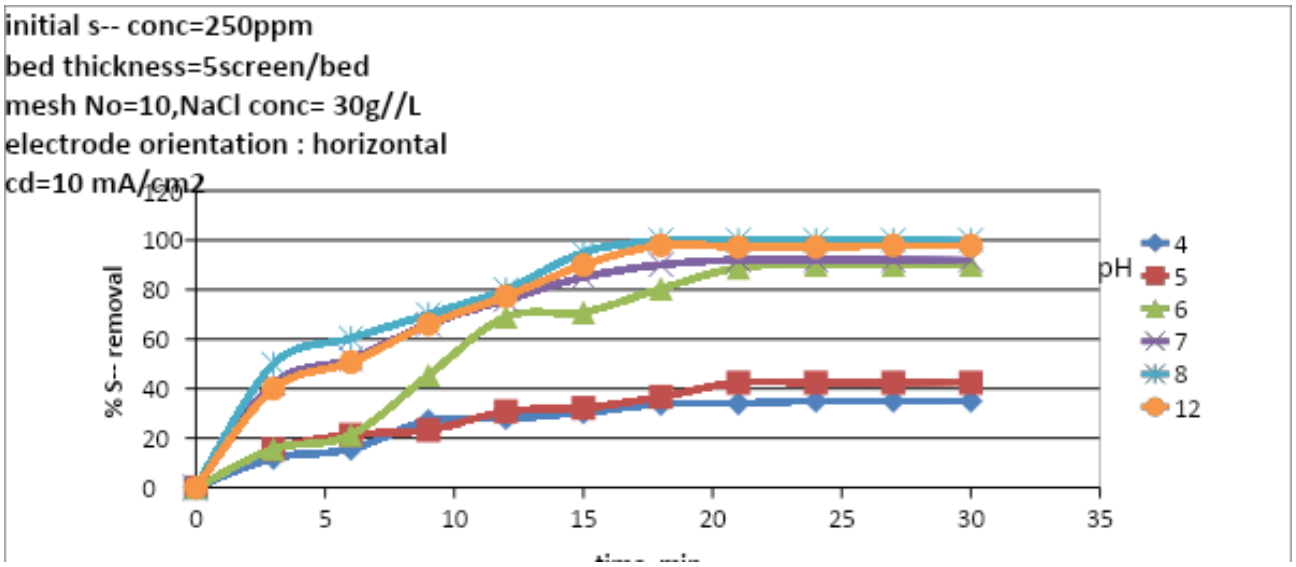

Figs. (7.a) and (7.b) show a comparison between the performance of a cell with vertically oriented electrodes and that with horizontally oriented electrodes at different current densities. For a given set of conditions, the data shows a superior performance of the cell with horizontally oriented electrodes. This may be attributed to the better mixing conditions which prevail inside the bed as the gas-liquid dispersion passes through the bed. In the case of the vertical electrodes, the stirring effect of the rising H2 bubbles influence only the gap between the cathode and anode.

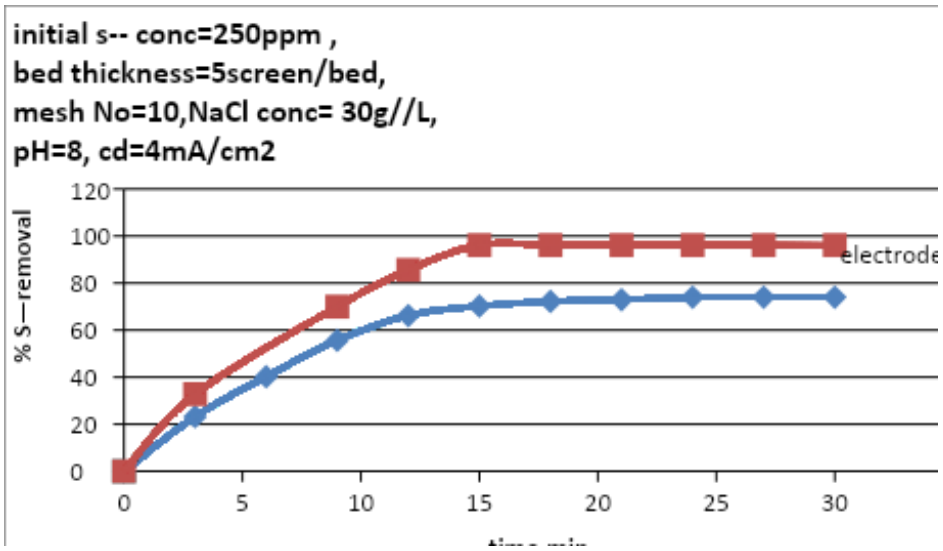

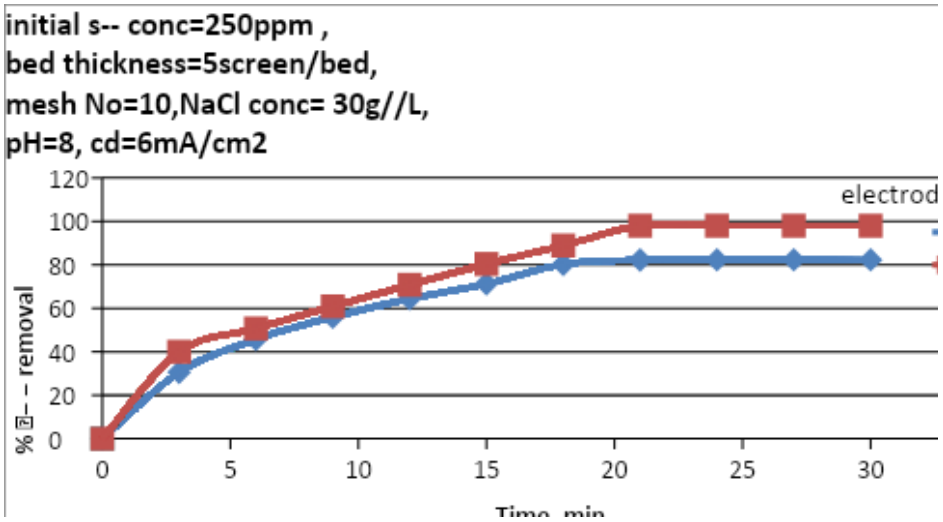

Electrical energy consumption (E.E.C,)

In assessing the economic feasibility of the present technique (E.C.) in comparison with other techniques of S- -removal from wastewater, E.E.C. which is a major cost item was calculated for horizontal and vertical cells under different current densities as shown in Table (1). E.E.C. was calculated from the equation [33]:

E.E.C. (kW. h/kg)=E× I× t×1000V Co-C (10)

Where

E (total cell voltage)=E+c+a+IR (11)

E is the equilibrium cell voltage (Volt), c is the cathodic polarization (Volt), a is the anodic polarization (Volt), I is the current (Amperes), R is the cell resistance (Ohms), t is the reaction time (hours), V is the solution volume (L), and C_o and C are the concentrations of S- - at time = 0 and at any time t, respectively.

Table (1) shows that at high current densities (> 8 mA/cm^2), the theoretical energy consumption of the horizontal cell is less than that of the vertical cell. For current densities below 8 mA/cm^2, the reverse is true. The higher energy consumption in the case of horizontal cells at relatively low current densities is attributed to the increase in cell voltage as a result of the presence of gas bubbles in the porous bed which increase the specific solution resistance according to the equation [34]:

=0(1-)-3/2 (12)

Where is the specific resistance of the gas-liquid dispersion inside the porous electrode, 0 is the specific resistance of the bubble-free solution, and is the gas holdup in the solution.

At high c.d., the beneficial effect of gas stirring on polarization and %S- -removal outweighs its deleterious effect in the case of the horizontal cells where its E.E.C. becomes less than that of the vertical cells. Table (1) shows that E.E.C. increases with increasing c.d. for horizontal and vertical cells because of the increase in polarization (c, a) and the increase in the IR drop.

Table 1 Effect of c.d. on E.E.C. for the horizontally and vertically oriented electrodes. Initial S- -concentration = 250ppm, bed thickness = 5 screens, Screens mesh Number = 10, NaCl concentration = 30 g/L, and pH = 7

		Horizontally-oriented electrodes		Vertically-oriented electrodes	
C.d. [mA/cm^2]	I [Amperes]	E [volt]	E.E.C. [kW.hkg]	E [Volt]	E.E.C. [kW.hkg]
0.5	0.29	0.7	0.803	0.214	0.27
1	0.49	0.89	1.36	0.323	0.527
2	0.99	1.29	3.45	0.374	1.029
4	1.96	1.86	9.16	0.638	3.38
6	2.99	2.27	15.97	0.931	7.23
8	3.99	2.5	22.49	3.4	39.39
10	4.99	2.7	39.28	4.1	48.2

usions

The present study leads to the following conclusions:

1. The use of horizontal and vertical screen stack as an anode in an E.C. cell is a promising electrode geometry in view of the high area per unit volume of the electrode and its high turbulence-promoting ability when subjected to the up-rising gas-liquid dispersion. Besides the high cell productivity, the cell is efficiently stirred by H2 bubbles evolved at the cathode. This obviates the need for external stirring and lowers the capital and operating costs of the process.

2. The use of vertically oriented screen electrodes is more economical than horizontally oriented screen electrodes at relatively low current densities (< 8 mA/cm^2). The use of horizontally oriented screen electrodes is more economical than vertically oriented electrodes at high current densities (> 8 mA/cm^2).
3. The %S- -removal increases with increasing c.d., pH, electrode thickness (No of screens per electrode), and NaCl concentration. However, it decreases with increasing the initial S- - concentration.
4. Energy consumption ranged from 0.803 to 39.28 kW.h/kg for cells with horizontally oriented electrodes. While for cells with vertically oriented electrodes, energy consumption ranged from 0.27 to 48.2 kW.h/kg depending mainly on the operating current density.
5. Future studies should include pilot-scale studies to confirm the present results on a large scale.

List of symbols

C_o	Initial S- -concentration (mg/L)
C	Concentration of S- - at any time t (mg/L)
E	Total cell voltage (Volt)
E	Equilibrium cell voltage (Volt)
e_o	Standard electrode potential (Volt)
e	Electrode potential (Volt)
I	Cell current (Amperes)
R	Cell resistance (Ohms)
r	H_2 bubble radius (cm)
t	Time (hours)
V_b	Rising velocity of the bubble (cm/s)
V	Solution volume (L)
g	Acceleration due to gravity (cm/s^2)

Greek symbols

	Gas holdup (-)
a	Polarization at the anode (Volt)
c	Polarization at the cathode (Volt)
	Viscosity (Poise)
	Solution density (g/cm^3)
g	Gas density (g/cm^3)
	Specific resistance of the gas-liquid dispersion (Ohms. cm)

0 Specific resistance of the bubble-free solution (Ohms. cm)

References

1. C.D. Weil and S.R . Sandler, in: *Kirk-Othmer Encyclopedia of Chemical Technology*, edited by M. Howe-Grant/ John Wiley & Sons, New York (1991)
2. J.B Lefers, W.T. Koetsier and W.P.V. Swaalj: Chem. Eng. J. Vol. 15(1978), p. 111
3. T.M.S. Carlos, C.B. Maugans, in: Wet Air Oxidation of Refinery Caustic: A Refinery Case Study; Technical Report No 427, volume 12 of NPRA Conference, San Antonio, Texas (2000)
4. N. Rodriguez, H.K. Hansen, P. Nunez and J. Guzman:J. Environ. Sci. Health A Vol. 43 (2008), p. 952
5. L. Zhang, P. De Schryver, B. Gusseme, W. Muynck, N. Boon and W. Verstraete: Water Res. Vol. 42 (2008), p.1
6. M. Sayed, G. Soreanu, P. Falletta and M. Beland: Can. Biosyst. Eng. Vol. 48 (2006), p. 2.1
7. H.Y. Hoang, R.M. Akhmadullin, F. Yu. Akhmadullina, R.K. Zakirov and A.G. Akhmadullina: Russ. J. Inorg. Chem. Vol. 63 (2018), p. 256
8. S. Mizuta, W. Kondo, K. Fujii, H. Iida, S. Isshiki, H. Noguchi,T. Kikuchi, H.sue and K. Sakai: Ind. Enf. Chem. Vol. 30 (1991), p.1601

0. K.C. Pillai, T. Raju, S.T. Chung and S. Moon: Chem. Technol. Biotechnol. Vol 84 (2009), p. 447
0. D.W. Kalina and E.T. Mass Jr: Int. J. Hydrog. Energy Vol. 10 (1985), p. 157
0. D .W. Kalina and E.T. Mass Jr: Int. J. Hydrog. Energy Vol. 10 (1985), p. 163
0. M. Murugananthan, G.Bhaskar Raju and S. Prabhakar: J. Hazard. Mater. Vol. 109 (2004), p. 37
0. B.G. Atteya, F.M. Al-Kharafi, R.M. Abdallah and A.S. Al- Azab: J. Appl. Electrochem. Vol. 35 (2005), p. 297
0. Y.S. Shih and J.L. Lee: J. Chin. Chem. Eng. Vol. 16 (1985), p. 297
0. Y.S. Shih, S.L. Kuo and C.W. Cheng: J. Chin. Chem. Eng. Vol. 20 (1989), p. 366
0. J.P. Fornes and J.M. Bisang: Electrochem. Acta Vol. 243 (2017), p. 90
0. V. Alexeyev: *Quantitative Analysis* (Mir publisher, Moscow 1979)
0. J.C. Armour and J.N. Canon: AIChE J. Vol. 14 (1968), p. 415
0. H.A.M. Casillas, D.L. Cocke, J.A.G. Gomes, P. Morkovsky, J.R. Parga and E. Peterson: Sep. Purif. Technol. Vol. 56 (2007), p. 204
0. O. Sahu, B. Mazumdar and P.K. Chaudhari: Envron Sci. Pollut. Res. Vol. 21 (2014), p. 2397
0. T.F. Fuller and J.N. Harb: *Electrochemical Engineering* (John Wiley & Sons, New York 2018)
0. M.G. Fouad and G.H. Sedahmed: Electrochem. Acta Vol. 20 (1975), p. 615
0. F.A. Katkout, A.A. Zatout, H.A. Farag and G.H Sedahmed: Can. J. Chem. Eng. Vol. 66 (1988), p. 497
0. N.K. Khosla, S. Venkatachalam and P. Somasundaran: J. Appl. Electrochem. Vol. 21 (1991), p. 986

0. N. Adhoum and L. Monser: Chem. Eng. Process. Vol. 43 (2004), p. 1281
0. P.P. Das, M. Sharma and M.K. Purkait: Sep. Purif. Technol. Vol. 292 (2022), p. 121058
0. K. Kikuchi, S. Nagata, Y. Tanaka, Y. Saihara and Z. Ogumi: J. Electroanal. Chem. Vol. 600 (2007), p. 303
0. A.A. Kulkarni and J.B. Joshi: Ind. Eng. Chem. Res. Vol 44 (2005), p. 5873
[29] Y.T. Shah, B.G. Kelkar, S.P. Godhole and W.D. Deckwer: AIChE J. Vol. 28 (1982), p. 353
[30] E.L. Cussler: *Diffusion: Mass Transfer in Fluid Systems* (Cambridge University Press Cambridge 2004)
0. N. Sato and G. Okamato, in*: Electrochemical Materials Science*, edited by J.O. Bockris, B.E. Conway, E. Yeager and R.E. White, volume 4, Comprehensive Treatise of Electrochemistry, Springer, Boston (1981)
0. E.M. Laws and J.L. Livesey: Ann. Rev. Fluid Mech. Vol. 10 (1978), p. 247
0. F. Walsh: A First Course in Electrochemical Engineering (The Electrochemical Consultancy, Hants 1993)
0. H. Vogt, in: *Comprehensive Treatize of Electrochemistry*, edited by E. Yeager, J.O. Bockris, B.E. Conway, and S. Sarangapani, volume 6, Comprehensive Treatise of Electrochemistry, Springer, Boston (1983)

ZIF 8@graphene hybrid preparation and characterization nano-hybrid material

S.E. Tantawy[1], R.I. Saman[1], A.M. Soultan[1], A.N. Soliman[1], A.A. Shahien[1], D.M. Moustafa[1], M.F. ElKady[1,2]

[1]Egypt-Japan University of Science and Technology, Alexandria, Egypt
[2]City of Scientific Research and Technological Applications, Alexandria, Egypt
E-mail: salma.essam-eldin@ejust.edu.eg ,retag.ismail@ejust.edu.eg , ahmed.soultan@ejust.edu.eg , abdulla.soliman@ejust.edu.eg , ahmed.shahien@ejust.edu.eg , dina.mamdouh@ejust.edu.eg , marwa.elkady@ejust.edu.eg

Keywords: *ZIF-8, graphene, characterization, nano-hybrid, separation techniques*

Abstract. Development of ZIF-8 metal organic framework material onto graphene nano-platelets was successfully prepared to fabricate novel nano-hybrid material. The distribution of ZIF-8 crystals at the fabricated nano-hybrid was confirmed using electron scanning microscope the average particle size of the prepared nano composite was determined as 80 nm. XRD pattern of fabricated ZIF-8@graphene nano-platelets elucidate the interaction between both the MOF and graphene. Furthermore, the interaction between graphene nano-platelets and synthesis MOF was confirmed using FTIR. The synthetized nano hybrid material showed superior surface area of

978 m^2/g that indicates the ability of synthetized composite as promising material for various separation technique such as adsorption application.

Introduction

Metal Organic Frameworks (MOFs) are a new class of hybrid materials that consists of organic ligand and inorganic metals. They have very useful advantages such as high porosity and specific surface area. MOFs can be created using different inorganic metals and organic ligands, and their designable structure can be altered to fit specific applications, this makes a very wide ranges of MOFs that are applied in several applications [1]. MOFs are typically created in a one-pot reaction by self-assembly of metal ions and organic ligands, with solvothermal processes being the most common method with solvents like dimethyl formamide, diethyl formamide, and water being the most widely used. [2]

ZIFs, a subclass of MOFs, have isomorphic zeolite topologies and a coordinative MOF composition. They combine the benefits of both zeolites and MOFs, with higher thermal and moisture stability and larger cavities. ZIF-8, a well-researched ZIF [3], has a high separation factor for mixtures of hydrogen and carbon dioxide, and is suitable for separating parts of biofuels, specifically water and ethanol [4]. ZIFs also serve as chemical sensors due to their tunable absorbance characteristics, making them desirable materials for biosensor matrices.[5]

Graphene, a two-dimensional hexagonal honeycomb material made of single-atom-thick, sp^2 hybridized carbon atoms, exhibits great surface area, exceptional chemical, thermal, and mechanical stability. It serves as structural templates for the initiation, adsorption, and expansion of various nanocomposites, such as metal nanoparticles and metal organic frameworks [6]. Composites made of Go/graphene and MOFs have recently attracted more study attention, with graphene templates being a novel method for adding hierarchical porosity to MOFs for effective gas adsorption. Therefore, during this work ZIF-8 was formed on the suafce of the graphene nanoplaletes to synthesis a nano-hybrid composite that will be used for different separations processes.

Experimental

Materials. Zinc nitrate hexahydrate ($Zn(NO_3)_2 \cdot 6H_2O$) and 2-Methylimidazole ($C_4H_6N_2$) were used as precursors for ZIF-8 synthesis. Methanol was used as a solvent for the reactants and the reaction medium. Ethanol and distilled water were used for the washing of the prepared ZIF-8 crystals and the nano-hybrid composite powder. Lastly, graphene nano-platelets were used as a substrate to form ZIF-8 crystals on its surface to prepare the nano-hybrid composite.

ZIF-8 preparation. ZIF-8 was prepared by the protocol followed by Kebria et al. [1]. 0.734 g of zinc nitrate hexahydrate and 0.8106 g of 2-methylimidazole were dissolved separately in 50 mL of methanol. The two solutions were mixed and stirred for 1 hour at 500 rpm at room temperature. The solution was left overnight to settle. The formed ZIF-8 crystals were collected by centrifugation at 8000 rpm for 1 hour. The collected ZIF-8 crystals were washed twice with ethanol to get rid of any unreacted precursors. Then, washing twice with distilled water was done to remove ethanol from the ZIF-8 pores. Finally, ZIF-8 crystals were dried in an oven at 60°C to obtain solvent-free ZIF-8 crystals.

ZIF-8 @ graphene preparation. ZIF-8 was prepared on graphene nano-platelets surface. To prepare the nanocomposite of ZIF-8 @ graphene with ratio 1:1 of ZIF-8 to graphene, an equal amount of the yield of plain ZIF-8 powder (about 0.2 g) from graphene nano-platelets was added to 50 mL of methanol. The graphene nano-platelets in methanol solution were left in

the sonication bath for one hour to ensure the homogeneity of the suspension. The limiting reactant, which is the zinc nitrate hexahydrate, is dissolved in the prepared suspension. Same procedures of ZIF-8 preparation were followed.

Characterization. The prepared ZIF-8 crystals and the nano-hybrid ZIF-8 @ graphene composite were characterized and examined by using X-ray Diffraction (XRD), Fourier Transform Infrared (FTIR), Scanning Electron Microscope (SEM). XRD gives information about their crystallographic structure, chemical composition, and physical properties. X-ray Diffraction patterns of the prepared nanomaterials were recorded at 2θ of 5–80° with a step of 12°/min (Cu-Kα , λ = 1.5406 Å). Fourier Transform Infrared (FTIR) spectra of ZIF-8 and the nano-hybrid composite were carried out by FTIR spectrometer with wavelength of 500–4000 cm^{-1} to identify the organic bonds that exist in the molecules of the prepared materials. Lastly, the morphologies and average particle size of the prepared materials were analyzed by scanning electron microscopy (SEM). Also, SEM is used to confirm the crystallinity of the prepared samples.

Results and discussion

The powder X-ray diffraction patterns of the pure ZIF-8 and the ZIF-8 @ graphene nanoplatelets composite are shown in Fig. 1. For the pure ZIF-8, only crystalline pattern with sharp diffraction and high intensity peaks is indicated at 2θ = 7.25, 12.62, 17.916, 26.55, 10.29, which matches with the ZIF-8 prepared by Saliba and his co-workers [8]. Interestingly, there is no significant change in the XRD pattern compared to ZIF-8, which indicates that graphene nanoplateles is well dispersed in the ZIF-8. However, the sharp peaks of the composite becam less intense as the graphene is semicrystalline, therefore, the degree of crytsalinity of the composite is less than the pure ZIF-8. The XRD pattern of graphene has a wide and broad peak around 2θ = 26° which indicates semi crystalline nature of the graphene [9].

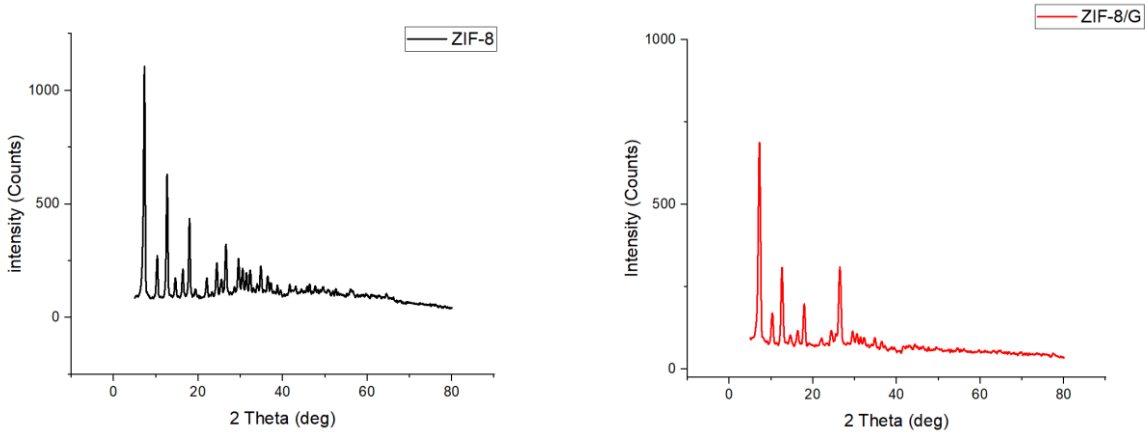

Fig. 1 XRD patterns of different synthesized samples (a) ZIF-8 (b) ZIF-8 @graphene nanoplatelets

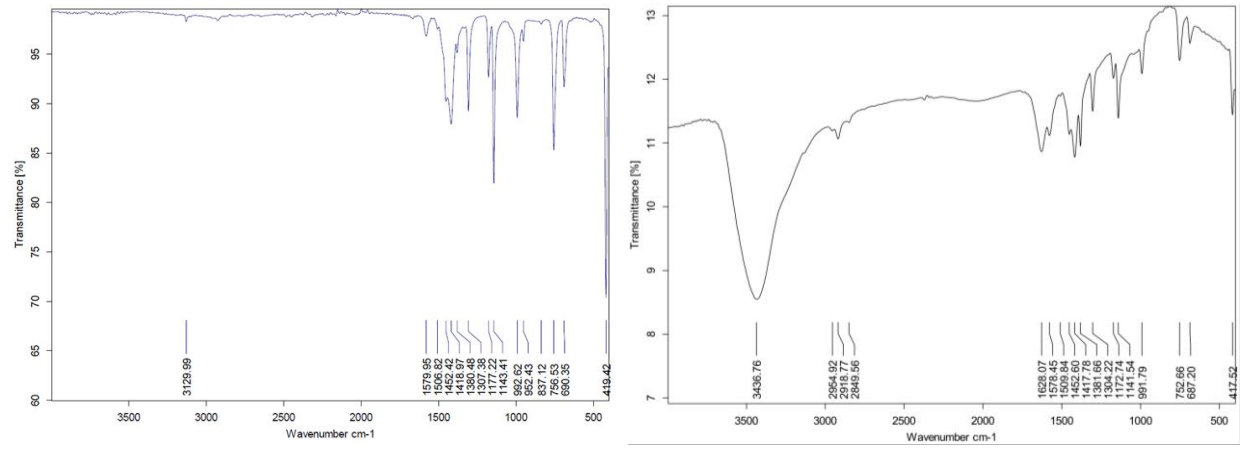

(a) (b)

Fig. 2 FTIR spectra of different synthesized samples (a) ZIF-8 (b) ZIF-8 @graphene nanoplatelets

FTIR spectra of the prepared ZIF-8 is shown Fig. 2 (a). The FT-IR band of ZIF-8 is in good agreement with those of previously reported ZIF-8. The peak at about 1579.95 cm^{-1} can be assigned as the C=N stretch mode, whereas the bands at 1452 and1418 cm^{-1} are associated with the entire ring stretching [11, 12]. The bands in the spectral region of 1000-1350 cm^{-1} are for the C-N stretch vibration and the band at 419 cm^{-1} is attributed to Zn-N stretch [13].

In the second sample where graphene nanoplatelets are used as substrate on which ZIF-8 is formed, FTIR spectra is shown in fig 2 (b). The peaks at the range of 400 to 1700 cm^{-1} were consistent with that of the zif-8 sample at fig. 2(a) at the range of 1700 cm^{-1} to 4000 cm^{-1} there were formation on new bonds as O-H stretching at 3436 cm^{-1}, C-H stretching at 2918 cm^{-1}[14]. The formation of these new bonds indicates good interaction between graphene nanoplatelets and ZIF-8.

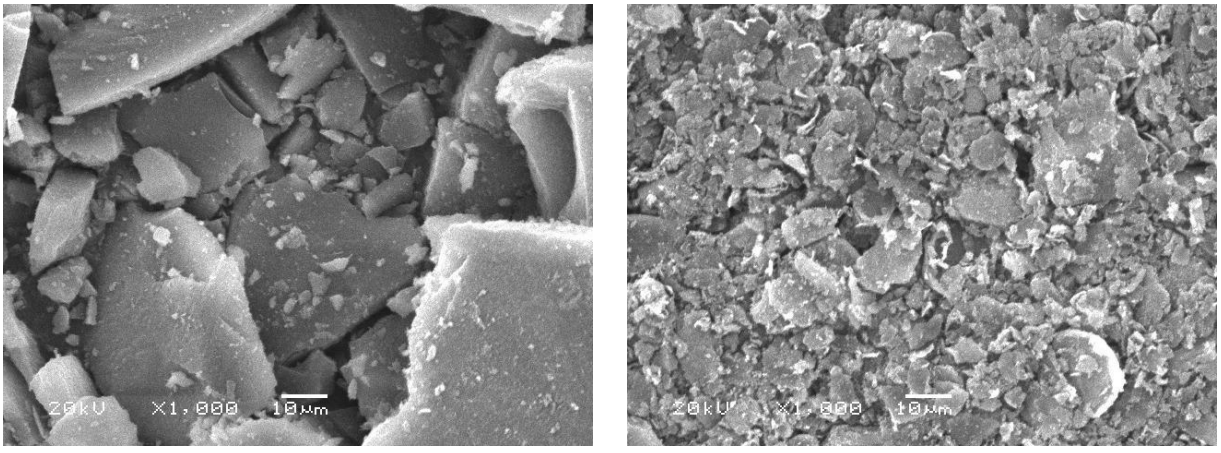

(a) (b)

Fig. 3 SEM images of different synthesized samples (a) ZIF-8 (b) ZIF-8 @graphene nanoplatelets

ZIF-8 and and ZIF-8@graphene nanoplatelets composite were successfully synthesized in this work. ZIF-8 was synthesized following the procedures reported by Kebria et al. [7]. The morphologies of ZIF-8, and the ZIF-8@ graphene nanoplatelets composite are shown in SEM images in fig (3). The sharp edges of the ZIF-8 particles indicate a very high degree of

crystallinity as shown in fig 3 (a). The average particle size is in the range of 400 nm. However, crystallinity is decreased in the case of preparation at the graphene nanoplatelets due to its semi-crystalline nature as shown in fig 3 (b). The average particles size is higher than the pure ZIF-8 as the ZIF-8 is supported onto the graphene nanoplatelets surface. The average particle size is about 900 nm.

Conclusion

In the present work, ZIF-8 @ graphene nanoplatelets composite was prepared by simple synthesis technique at room temperature. Pure ZIF-8 was first synthesized from Hmim and Zinc nitrate hexahydrate in methanol, then ZIF-8 crystals were subsequently direct growth on the surface of graphene nanoplatelets. XRD results provided evidence for the formation of ZIF-8 and the composite with a crystalline structure. SEM images confirmed the crystallinity of the prepared samples. FTIR analysis provided evidence for the formation of bonds between the ZIF-8 and the graphene nanoplatelets which confirm good interactions between them. We expect the synthesis methodology proposed in this work can open new opportunities to grow various composites with zeolitic imidazolate framework@ different nano-carbon materials, and the ZIF-8@ graphene nanoplatelets composite can potentially be applied in many applications such as separations processes.

References

[1] Gongke Li, Ling Xia, Jianwei Dong, Yanlong Chen, Yanxia Li, 10 - Metal-organic frameworks, Editor(s): Colin F. Poole, In Handbooks in Separation Science, Solid-Phase Extraction, Elsevier, 2020,Pages 285-309, ISBN 9780128169063,https://doi.org/10.1016/B978-0-12-816906-3.00010-8
.(https://www.sciencedirect.com/science/article/pii/B9780128169063000108)

[2] Raptopoulou CP. Metal-Organic Frameworks: Synthetic Methods and Potential Applications. Materials (Basel). 2021 Jan 9;14(2):310. doi: 10.3390/ma14020310. PMID: 33435267; PMCID: PMC7826725.

[3] zou, D., liu, D., & zhang, J. (2018, November 22). *From zeolitic imidazolate framework-8 to metal ... - wiley online library*. Wiley Online Library. https://onlinelibrary.wiley.com/doi/10.1002/eem2.12018

[4] Zhang, K., Nalaparaju, A., Chen, Y., & Jiang, J. (2014, March 28). *Biofuel purification in zeolitic imidazolate frameworks: The significant role of functional groups*. Physical Chemistry Chemical Physics. https://pubs.rsc.org/en/content/articlelanding/2014/CP/C4CP00739E#!divAbstract

[5] Chen, B., Yang, Z., Zhu, Y., & Xia, Y. (2014, July 17). *Zeolitic imidazolate framework materials: Recent progress in synthesis and applications*. Journal of Materials Chemistry A. https://pubs.rsc.org/en/content/articlelanding/2014/TA/C4TA02984D

[6] Kim, D., Kim, D. W., Hong, W. G., & Coskun, A. (2016, April 19). *Graphene/zif-8 composites with tunable hierarchical porosity and electrical conductivity*. Journal of Materials Chemistry A. https://pubs.rsc.org/en/content/articl landing/2016/ta/c6ta0189

[7] Kebria, M. R., Rahimpour, A., Bakeri, G., & Abedini, R. (2019). Experimental and theoretical investigation of thin zif-8/Chitosan coated layer on air gap membrane distillation performance of PVDF membrane. Desalination, 450, 21–32. https://doi.org/10.1016/j.desal.2018.10.023

[8] Saliba, D.; Ammar, M.; Rammal, M.; Al-Ghoul, M.; Hmadeh, M. Crystal growth of ZIF-8, ZIF-67, and their mixed-metal derivatives. *J. Am. Chem. Soc.* **2018**, *140*, 1812–1823.
[9] Johra, F. T., Lee, J.-W., & Jung, W.-G. (2014). Facile and safe graphene preparation on solution based platform. Journal of Industrial and Engineering Chemistry, 20(5), 2883–2887. https://doi.org/10.1016/j.jiec.2013.11.022
[10] Jibrael, R. I., & Mohammed, M. K. A. (2016). Production of graphene powder by electrochemical exfoliation of graphite electrodes immersed in aqueous solution. *Optik*, *127*(16), 6384–6389. https://doi.org/10.1016/j.ijleo.2016.04.101
[11] Don, Ta & Nguyen, Hong & Trinh, Bai & Le, Quynh & Ta, Hung & Nguyen, Ha. (2018). Preparation of Nano-ZIF-8 in Methanol with High Yield. The Canadian Journal of Chemical Engineering. 96. 10.1002/cjce.23155.
[12] Abd Rahim, Atiqah & Yusuf, Siti & Majid, S. & Osman, Zurina. (2022). One-step co-precipitated β-Ni (OH)2 at different ratios of Ni/2-methylimidazole and its energy storage behaviour. Journal of Applied Electrochemistry. 52. 1-14. 10.1007/s10800-021-01627-0.
[13] Zeng, X., Chen, R. Y., Yang, X. B., Li, J. T., & Luo, X. T. (2016). Synthesis and characterization of zeolitic imidazolate framework-8@sodalite composite particles. Materials Science Forum, 852, 1250–1255. https://doi.org/10.4028/www.scientific.net/msf.852.1250
[14] Li, H.; Cheng, Y.; Li, J.; Li, T.; Zhu, J.; Deng, W.; Zhu, J.; He, D. Preparation and Adsorption Performance Study of Graphene Quantum Dots@ZIF-8 Composites for Highly Efficient Removal of Volatile Organic Compounds. Nanomaterials 2022, 12, 4008. https://doi.org/10.3390/nano12224008

Numerical investigation of the effect of different configurations on the resistance of twin-hull ships

T.M. Ahmed [1, a], A.M. Abdelrahman [2,b], Y.M. Ahmed [3,c] and A.A. Banawan [4,c]

[1]Dept. of Naval Architecture & Marine Engineering, Alexandria University, Egypt

[2]RSC for Marine Design and Research, Khartoum, Sudan

[3] Dept. of Naval Architecture & Marine Engineering, Alexandria University, Egypt

[4] Dept. of Naval Architecture & Marine Engineering, Alexandria University, Egypt

[a]tmahmed@alexu.edu.eg, [b]A.abdelrahman@rsc-naval.com, [c]yasserahmed@alexu.edu.eg, [d]adel.banawan@alexu.edu.eg

Keywords: *CFD, Catamarans, Separation–length ratio, Non-parallel demi-hulls.*

Abstract. Catamarans and other multi-hull configurations have better performance with regards to; speed, resistance, manoeuvrability and, transverse stability when compared to mono-hull configurations. In this study, a CFD simulation of the flow about a displacement catamaran model is conducted over a range of forward speeds by solving the Reynold's Average Navier-Stokes equation (RANSE). The Shear Stress Transport (SST) turbulence model is selected to capture the turbulence in the flow and, the volume of fluid (VOF) method is adopted to capture the free surface flow about the catamaran. In this study, the total resistance of the twin-hull vessel is calculated at low, medium and, high Froude numbers, of the operating range of the catamaran, using three different mesh sizes; a Coarse, a Medium and, a Fine mesh. This is followed by a mesh convergence study to obain numerical uncertainty. Validation of results is achieved by comparison with experimental data available in the literature. The aim of the study is to investigate the effect of separation-length ratio and non-parallel configuration of the demi-hulls on the total resistance and wave pattern generated by the catamaran. Subsequently, the Response Surface Method for optimization is applied at a particular Froude number and over a selected range of separation-length ratio and non-parallel configuration to provide minimum total resistance. Obtained results are satisfactory with a reduction in the optimized total resistance as compared to that of the original catamaran.

Introduction

The resistance behavior of twin-hulled ships, in general, is similar to that of mono-hulled ships where, the two main components are viscous resistance and wave-making resistance. In a way, the nature of the total resistance on catamarans is more complicated and involved than that on conventional single-hull ships due to the interference phenomena between the two demi-hulls. Twin-hull vessels experience a large viscous resistance component due to the large-wetted surface area of the two demi-hulls. This is obvious at low Froude numbers where, the skin friction resistance is predominant. In contrast and at high Froude numbers, catamarans demonstrate less wave-making resistance compared to corresponding mono-hulls. In addition, interaction between the two demi-hulls could have an either favorable or an adverse effect on the total resistance. The interaction between the two demi-hulls is composed of two main components, namely the interference between the two wave systems generated by each demi-hull and deformations of the fluid flow around each demi-hull due to existence of the other [1, 2].

Various design parameters that affect the resistance quality of catamarans have been investigated by numerous researchers over the years [1, 3-7]. It has been shown that one of the most important influencing parameters is the separation-length ratio (demi-hulls spacing). Variations of this parameter have a direct effect on the interaction behaviour between the two demi-hulls with a resultant effect of increasing or decreasing the total resistance [2].

In this paper, a numerical investigation is carried out using the CFD finite volume analysis code (ANSYS CFX) to study the effect of the demi-hulls spacing on the total resistance of a selected catamaran, over a range of Froude numbers. A new arrangement of the catamaran's demi-hulls is introduced in this study (non-parallel configuration), which is a non-conventional configuration for twin-hull vessels. The total resistance is obtained at different Froude numbers and non-parallel angles. Finally, a suitable optimization method is applied to determine the optimum separation-length ratio Sc/L and non-parallel angle (α).

Hull Model Data

The numerical results presented in this paper are validated by experimental data obtained by Ir. Riaan van't veer [8] in the towing tank of the Delft University of Technology. The tank is of dimensions L × B × D = 145 × 4.2 × 2.6 (m).The model used in the experiments is the Delft 372 catamaran model with the main particulars and lines plan as shown in Table 1 and Fig. 1, respectively.

Table 1 Main particulars of the Delft 372 catamaran model (Ir. Riaan van't veer 1998).

Main particular	Symbol	Unit	Value
Overall length	Loa	m	3.11
Loaded Length	L	m	3
Catamaran beam	B	m	0.94
Demi-hull beam	b	m	0.24
Draft	T	m	0.15
Separation between demi-hulls centerline	Sc	m	0.7
Displacement	Δ	kg	87.07
Longitudinal center of gravity (from aft)	LCG	m	1.41
Block coefficient	Cb	-	0.403
Separation to Length ratio	Sc/L	-	0.233

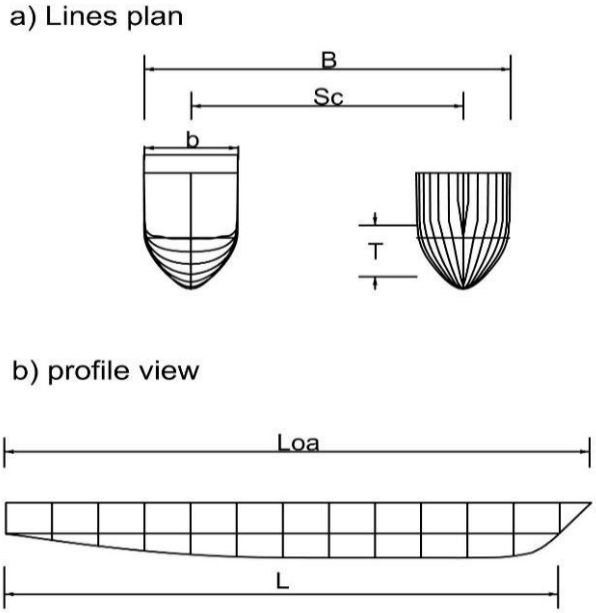

Fig. 1 Lines plan of the Delft 372 catamaran model.

Computational and Analysis Methods

The numerical code used in this study is the ANSYS CFX software [9] which is a well-known general-purpose computational fluid dynamics code with robust capabilities in solving the

Reynolds-Average Navier–Stokes (RANS) equations then, converting them back into algebraic equations by employing the Finite Volume discretization Method (FVM). To capture the free surface wave profile generated by the catamaran, the Volume of Fluid method (VOF) is selected in the CFD solver. The shear Stress Transport (SST) turbulence model is adopted in the current study for its high numerical stability and suitability for complex flows as has been recommended by numerous researchers [10, 11 & 12].

In the results presented here within, CFD simulations are—first—conducted over a whole range of Froude numbers (0.3 to 0.748) for validation purposes. Subsequently, only three Froude numbers (0.348, 0.549, and 0.748) are selected for the optimization study over a range of separation-length ratios varying from Sc/L = 0.15 to 0.7 and over a range of angles of ($\alpha°= -8°$to 8°) representing nonparallel demi-hulls configurations, as illustrated in Fig. 2. The negative sign (−) —in Fig. 2—indicates that the separation distance, between the two demi-hulls, at the bow of the catamaran is less than that at the stern and vice versa. The separation distance is measured at the longitudinal center of gravity (LCG).

Subsequently, an optimization method (the Response Surface method) is applied to the obtained results to determine an optimum configuration that provides the best resistance qualities of the catamaran, i.e. minimum total resistance.

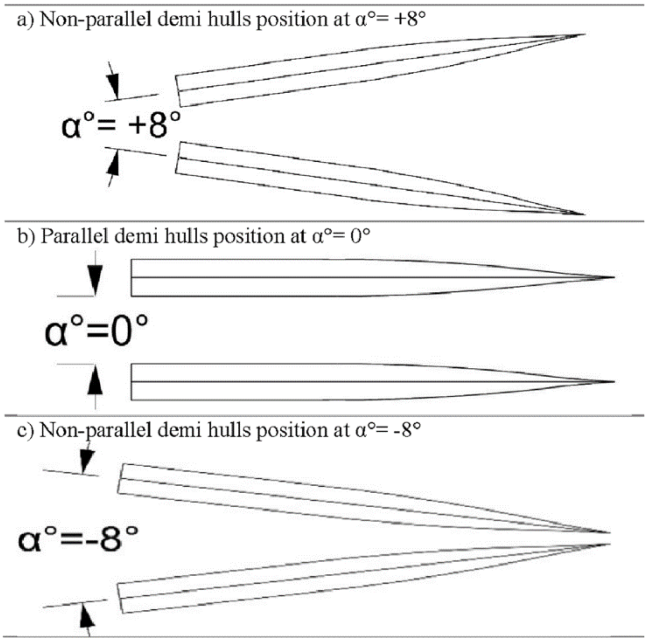

Fig. 2 Three different positions of the catamaran demi hulls. a) Non-parallel demi hulls position at α°= +8°. b) Parallel demi hulls position at α°= 0°. c) Non-parallel demi hulls position at α°= -8°.

Total Resistance Calculations:

The catamaran's total resistance may be calculated using the following equation:

$$Ct=1+\beta kCf+\tau CW \quad (1)$$

Where, Ct is the catamaran's total resistance coefficient, C_f is the ITTC'57 friction resistance coefficient, Cw is the wave making resistance coefficient, $(1+\beta k)$ is the catamaran's viscous form

factor, β is the viscous resistance interference factor and τ is the wave resistance interference factor.

The first term in equation (1) represents the catamaran's viscous resistance coefficient (Cv) while, the second term represents the catamaran's wave making resistance coefficient. The ITTC'57 friction resistance coefficient may be calculated using the following formula:

$$Cf=0.075(Re-2)\ 2 \quad (2)$$

Where, Re is the Reynolds number.

The catamaran's viscous form factor may be determined using the following equation [6]:

$$1+\beta k=3.03(L\nabla\ 13)-0.4+0.016(ScL)-0.65 \quad (3)$$

Where, ∇ is the immersed volume of the hull.

The friction resistance can be calculated from the C_f coefficient using the following equation.

$$Rf=0.5\rho SV2Cf \quad (4)$$

and the viscous resistance can be calculated by

$$Rv=0.5\rho SV2Cv \quad (5)$$

Where, Rf is the catamaran's friction resistance, Rv is the catamaran's viscous resistance, ρ is the water density, S is the catamaran's wetted surface area and, V is the ship velocity.

Mesh generation strategy

The grid type that has been used in the simulations is an unstructured tetrahedral cells type of mesh distributed over the entire domain with a focus on certain regions to properly capture important flow characteristics. First, a fine mesh is generated on the hull surface with small size elements assigned to the hull-block domain with mesh elements densely distributed along the free surface zone. Second, the background domain is specified with larger in size elements. Special attention is paid to the free surface zone by using prism layers around it with small elements size to help the solver accurately predict the generated wave pattern. The total layers' thickness is made large enough to cover the entire height of the waves generated by the hull.

Optimization

In order to determine the optimum values of the design parameters under investigation, an optimization study is applied to the obtained results. At a particular Froude number, two design parameters were chosen to be the independent variables (input variables) of the study namely the separation–length ratio (Sc/L) and the demi-hulls configuration, angle (α). The total resistance of the catamaran was chosen as a response variable (output variable). The optimization method opted for in this study is the—well-known— Response Surface Method (RSM) where a response surface is generated based on a sequence of designed experiments to obtain an optimal response. This was deemed to be a suitable method since only two decision variables and one response

variable were involved in the study, as shown in Fig. 3. In total, 9 simulations of 9 tests are carried out and summarized in the following Table 2.

Figure 3 indicates that there is an optimum value for the non-parallel angle α° for each separation–length ratio Sc/L. As for Sc/L, the response surface consolidates the previously drawn conclusions that the total resistance decreases as the separation–length ratio increases. From that, the upper limit of the separation–length ratio is limited to Sc/L = 0.3 to generate the response surface since optimization will always pick the upper limit of Sc/L to be the optimum. As a start to the optimization process, a starting point must be specified to determine the region of the design space to be explored. The original configuration parameters of the delft 372 catamaran model are chosen in this case, Sc/L = 0.233, α = 0°.

Table 2 Test conditions for optimization.

Froude numbers (Fr)	0.549
Sc/L	0.15, 0.233, 0.3
Non-parallel angle (α°)	-8°, 0°, +8°

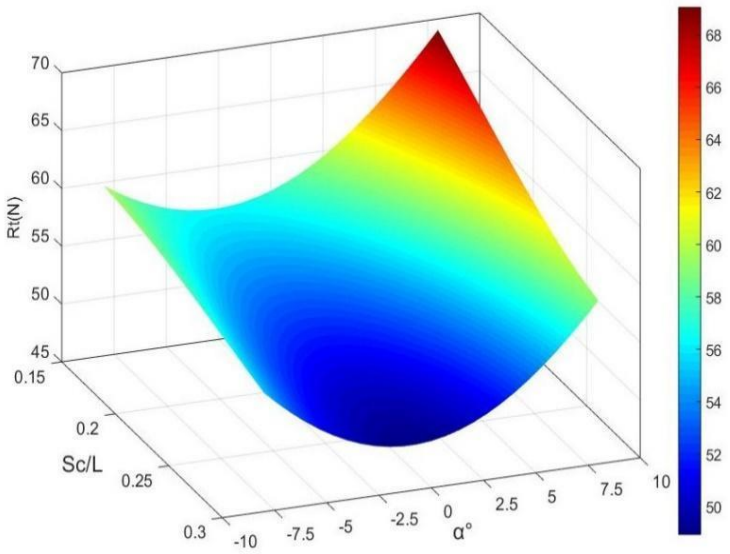

Fig. 3 The generated response surface for total resistance (output variable) as a function of Sc/L and non-parallel angle α°at Fr=0.549.

Conclusions

In this study, a detailed numerical investigation of the generated flow about the Delft 372 displacement catamaran model is performed over a range of speeds using CFD simulations. An optimization study is conducted on the effect of the separation-length ratio and the non-parallel demi-hulls configuration on the total resistance and generated wave pattern.

Investigating the dependency of the catamaran's total resistance on the demi-hulls separation-length ratio has revealed that; a smaller separation-length ratio generates the highest total resistance whereas, the largest separation-length ratio generates a lower total resistance. This is due to a more intensive wave interaction and negative viscous interference between the two demi

hulls at lower separation-length ratios which leads to an increase in the total resistance, in general, and in the wave making resistance component in particular. Moreover, investigations have revealed that the influence of varying the separation-length ratio at lower Froude numbers is insignificant compared to its influence at higher Froude numbers. This all, very well agrees with what has been documented in the literature on the resistance of catamarans.

Optimization of the obtained results has shown that; there is an optimum value for α° that provides minimum resistance for each separation-length ratio and Froude number. The applied optimization method always nominated the chosen upper limit of the separation-length ratio (Sc/L=0.3) as an optimum. While, in general, the total resistance tends to decrease by increasing Sc/L, however, beyond a Sc/L value of approximately 0.4, the influence of increasing the spacing on the total resistance tends to drop sharply. At higher values of Sc/L, the influence of the spacing is almost non-existent and each demi-hull behaves individually as a mono-hull. Determining the spacing between demi-hulls is governed by various aspects other than resistance. For instance, structural loads -due to very wide beams- are a major consideration. In the current study and at the chosen upper limit of Sc/L=0.3 and Fr=0.549, the optimum non-parallel angle was found to be equal to α°= -0.988°. The non-parallel configuration at this particular optimum angle generated a total resistance that is less by 5.5% compared to that experienced by the original Delft catamaran model.

References

1. S. Zaghi, R. Broglia, A. di Mascio, Experimental and numerical investigations on fast catamarans interference effects. J. Hydrodyn. **22**, 528–533 (2010). https:// doi. org/10.1016/S1001-6058(09)60250-X.
2. E.V. Lewis, *Principles of naval architecture, second revision* (Society of Naval Architects and Marine Engineers, New Jersey, 1988).
3. R. Broglia, S. Zaghi, A. Di Mascio, Numerical simulation of interference effects for a high-speed catamaran.
J. Mar. Sci. Technol. **16**, 254–269 (2011). https://doi. org/10.1007/ s00773- 011- 0132-3.
4. M. Haase, K. Zurcher, G. Davidson, J.R. Binns, G. Thomas, N. Bose, Novel CFD-based full-scale resistance
prediction for large medium-speed catamarans. Ocean Eng. **111**, 198–208 (2016). https://doi.org/10.1016/J.
OCEAN ENG. 2015. 10. 018.
5. M. Insel, A.F. Molland, An investigation into the resistance components of high speed displacement catamarans. R. Inst. Nav. Archit. **134**, 1–20 (1992).
6. M. Iqbal, A. Trimulyono, Optimization of catamaran demihull form in early stages of the design process.
Kapal **11**, 126–131 (2014). https:// doi. org/ 10. 12777/ kpl. 11.3. 126- 131.
7. G. Zaraphonitis, D. Spanos, A. Papanikolaou, Numerical and Experimental Study on the Wave Resistance
of Fast Displacement Asymmetric Catamarans, in: *International Euro Conference on High-Performance*
Marine Vehicles. (2001).
8. R.V. Veer, Experimental results of motions, hydrodynamic coefficients and wave loads on the 372 catamaran model, Report 1129, TU Delft. (1998).
9. *ANSYS CFX-solver theory guide* (2016).
10. M.A. Yengejeh, M.M. Amiri, H. Mehdigholi, M.S. Seif, O.Yaakob, Numerical study on interference

effects and wetted area pattern of asymmetric planing catamarans. Proc. Inst. Mech Eng. Part M J. Eng.
Marit. Environ. **230**, 417–433 (2014). https:// doi.org/ 10. 1177/ 14750 90215 586638.
11. H. Wang, R. Zhu, L. Zha, M. Gu, Experimental and numerical investigation on the resistance characteristics of a high-speed planing catamaran in calm water. Ocean Eng. **258**, 111837 (2022). https://
doi. org/ 10. 1016/J. OCEAN ENG. 2022. 111837.
12. D. Frisk, L. Tegehall, *Prediction of high-speed planing hull resistance and running attitude. A numerical*
study using computational fluid dynamics (Chalmers University of Technology, Goteborg, 2015).

Synthesis and characterization of NiO nanoparticles for potential application in enhanced oil recovery

WISDOM KWAME KEWU[1, a], AHMED HASSAN ELSHAZLY[2, b], ABDELRAHMAN ZKRIA[3, c], HIROSHI NARAGINO[4, d], and USAMA NOUR ELDEMERDASH[5, e]

[1]Egypt-Japan University of Science and Technology, Alexandria, Egypt

[2]Egypt-Japan University of Science and Technology, Alexandria, Egypt

[3]Kyushu University, Fukuoka, Japan

[4]Kyushu University, Fukuoka, Japan

[5]Egypt-Japan University of Science and Technology, Alexandria, Egypt

[a]wisdom.kewu@ejust.edu.eg, [b]abdelrahman@ejust.kyushu-u.ac.jp, [d]naragino.hiroshi.443@m.kyushu-u.ac.jp, [e]usama.nour@ejust.edu.eg

Keywords: Nanoparticles, nickel oxide, sol-gel technique/method, characterization techniques, and enhanced oil recovery (EOR)

Abstract

Nanoparticles have been considered a significant cutting-edge technology that has been investigated and employed to increase petroleum crude oil extraction due to their unique characteristics such as tiny size, high surface area-to-volume ratio, and increased mechanical strength and stability. The tiny size of nanoparticles can alter the pores and openings of reservoirs in an advantageous manner which is not possible by conventional methods. In this research, nickel oxide (NiO) nanoparticles are synthesized and characterized to analyze their properties for

potential application in enhanced oil recovery (EOR). The metal oxide nanoparticles were synthesized using the sol-gel technique. The sol-gel approach is simple and aids in easy control of the particles' morphology. In enhanced oil recovery (EOR) application, the size of the synthesized nanoparticles is critical. Various characterization techniques were carried out including using scanning electron microscopy (SEM), X-ray diffraction (XRD), and Fourier-transform infrared resonance (FTIR) to investigate NiO nanoparticles. Results from SEM revealed a uniform particle size distribution whereas FTIR and XRD confirmed the nickel and oxygen elements present. The results suggest that the prepared metal oxide is a good candidate for application in enhanced oil recovery due to it small size.

Introduction

Nanotechnology is a cutting-edge application that has a significant impact in so many fields such as petroleum extraction, electrical devices and sensors, biomedical engineering, agriculture, and wastewater treatment [1]–[5]. Nanoparticles have excellent properties and characteristics which have provided tremendous modification and advantages to processes and technological outputs. In view of that, a lot of research has been and is being conducted to formulate nanoparticles using different synthesis procedures, different raw materials, and different analysis techniques to investigate nanoparticles. Nanoparticles possess a high surface area to volume ratio, good mechanical and chemical stability, smaller size, and excellent shapes which offers them an advantageous property to be used in several fields [6]–[12].

NiO nanoparticles come in a green powder form with a cubic crystal lattice structure[13]. Although NiO nanoparticles are toxic, it has unique properties such as excellent stability which can be employed in areas such as petroleum extraction due to high temperature and pressure of oil reservoirs. The choice of synthesis of NiO is very important because it influences the properties of the nanoparticles formed. El-Kemary et al synthesized NiO oxide nanoparticles using the thermal decomposition method to investigate the mode of interaction between the NiO nanoparticles and glucose[13]. Yadav et al utilized a hydrothermal synthesis route to produce NiO. Yadav et al investigated the refractive index of the prepared NiO nanoparticles and the results proved that the material is an excellent candidate for use in solar applications[14]. Sahila et al initiated a green synthesis route by using allium cepa bulb extract as an additive to synthesize NiO nanoparticles [15]. Sahila et al investigated the dielectric property of NiO and proved its potential application in capacitors. In this work, the sol-gel technique was used to synthesize nickel oxide nanoparticles. The sol-gel technique was selected because it offers better control of material morphology, smaller particle size, and shape as well as the process being simple. Nickel nitrate hexahydrate was dissolved in an appropriate solvent and an ammonia solution was added. The gel formed was calcined at 450˚C to form high purity nickel oxide. Various characterization techniques which include FTIR, XRD, and SEM were performed to investigate the NiO produced.

Experimental Procedure

Reagents

Nickel nitrate hexahydrate (98% purity) and triton X 100 were purchased from Loba Chemie Pvt. Ltd. Polyethylene glycol ($HO(C_2H_4O)_nH$) of MW: 35000-4000 was purchased from Research-Lab Fine Chem Industries. 2-Propanol was purchased from Merck and ammonia solution of S.G: 0.88 (35% ammonium hydroxide) was purchased from Fisher Scientific UK.

Synthesis of NiO nanoparticles

NiO nanoparticles were synthesized using the sol-gel technique[16]. In this method, 10g of $(Ni(NO_3)_2 \cdot 6H_2O$ was dissolved in 50ml of 2-Propanol solvent. The mixture was placed on a magnetic stirrer and stirred for about 45 minutes at 500 rpm. 0.3g of polyethylene glycol was weighed and dissolved into the mixture. It was left to stir for 24hrs for complete dissolution. Ammonia solution was added to the mixture dropwise while monitoring the pH using a pH meter. A Dropwise addition of ammonia solution was stopped when the pH of the solution reached 11. The temperature of the mixture was gradually raised to 80˚C. After 1hr of stirring small amount of triton X 100 was added. The mixture was allowed to stir for about 18hrs. The mixture was taken off the heating mantle and stirrer and allowed to cool naturally. The mixture was decanted into a different beaker and the precipitate was obtained. Distilled water was added to the precipitate and shaken vigorously to form a suspension. The suspended solution was centrifuged at 7000 rpm for five minutes. The centrifugation process was repeated thrice for a complete washing of the precipitate. The precipitate was dried in a dryer for 3hrs at 70˚C. After, it was taken out and allowed to cool. Precipitate was transferred into a crucible and calcined at 450˚C to obtain black NiO.

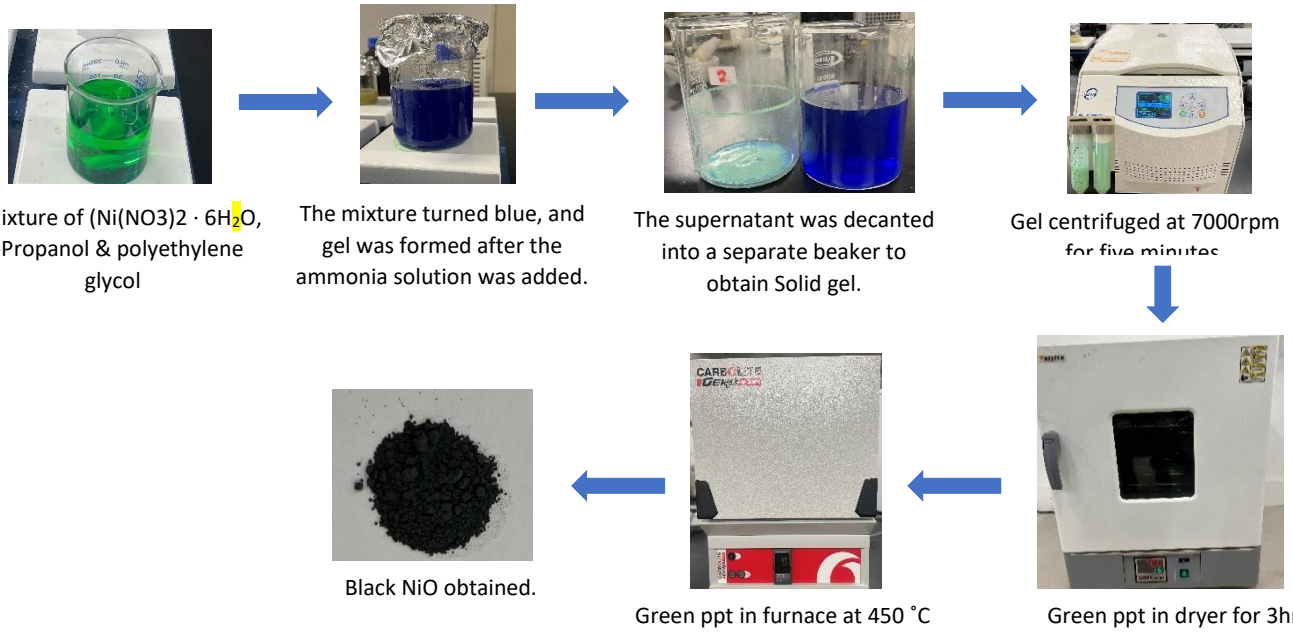

Fig 1 Showing the procedure for the synthesis of NiO nanoparticles

Results and Discussion

Structural Analysis

XRD Analysis

NiO nanoparticles was passed through X-ray diffraction spectrophotometer with measurement condition: (target = Cu, voltage = 40.0 kV and current = 30.0 mA) to analyse the crystallinity of the NiO nanoparticles. Fig.2a illustrates that the NiO nanoparticles possess high crystallinity with well-defined and sharp peaks at 2 theta (37.1˚, 43.1˚, 62.7˚, 75.4˚, 79.3 ˚) which corresponds to JCPDS card number 47-1049. The diffraction pattern is indexed at the planes of (111), (200), (220), (311) and (222) which is similar to bunsenite NiO structure [15]. The diffraction illustrated no abnormal and odd peaks which confirms the presence of high purity NiO. The crystallite size of the nanoparticles was calculated according to Scherrer formula [17].

$$D = \frac{k\lambda}{\beta cos\theta} \quad (1)$$

Where k = 0.9 which is the Scherrer constant, λ = 0.15406 nm which is the wavelenght of the incidented x-ray, β stands for full width at half maximum (FWHM) converted in radian of highest peak and θ = the diffraction angle with the highest peak. The average crystallite size was calculated to be 15 nm which makes it promising for use in enhaced oil recovery due to its small size.

FTIR Analysis

FTIR analysis is used to determine the existence of functional groups in a compound. As illustrated from fig.2b There is an absorbance peak at 590 cm^{-1} which depicts the presence of NiO due the stretching of Ni-O bonds. Generally, metal oxides exhibit absorbance peaks below

800 cm^{-1}[18]. The sharp absorbance peaks at 3410 cm^{-1} and 1620 cm^{-1} signifies the presence of O-H and N-H bonds respectively.

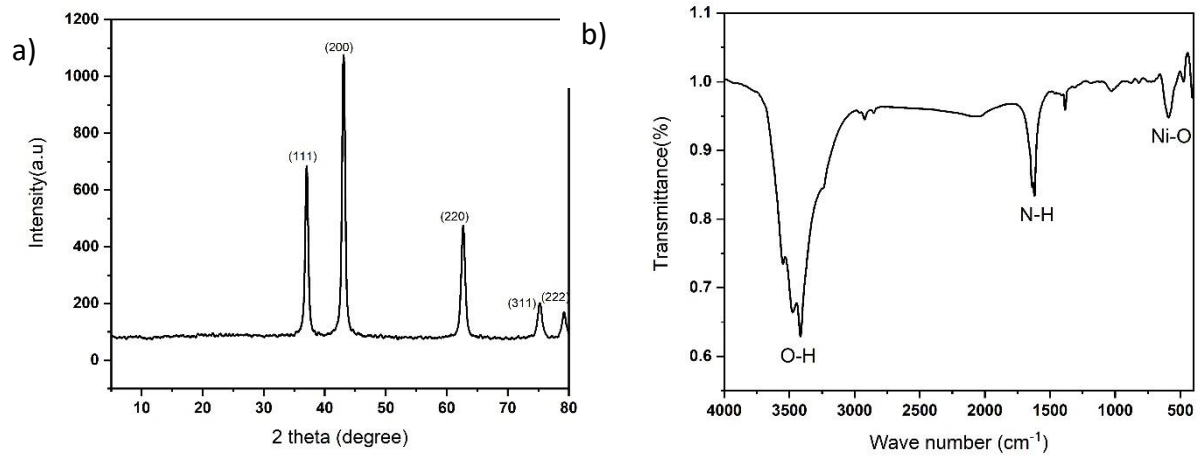

Fig 2 Showing the various characterization results. a) XRD graph, b) FTIR graph, c) & d) SEM images at 3400X and 2400X respectively

Morphological Analysis

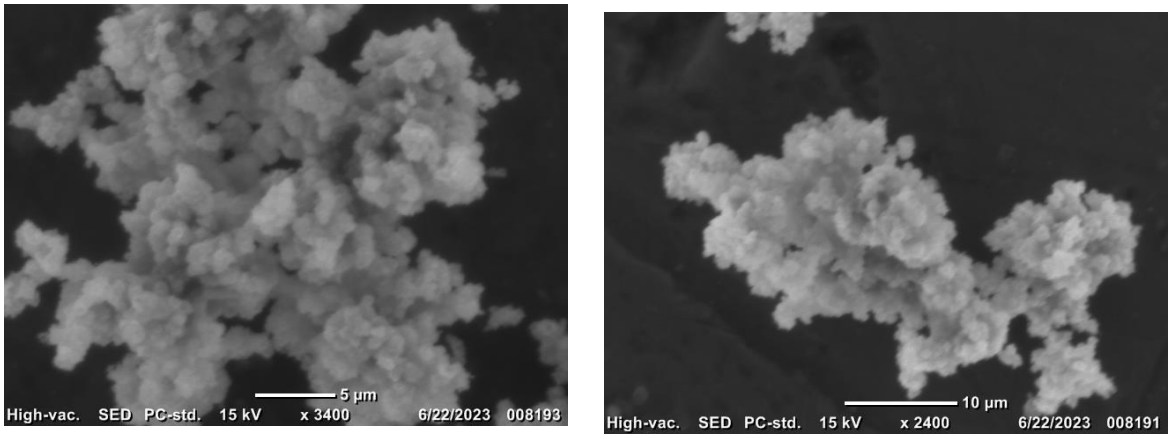

From fig.2c-d, it shows the suface morpholgy of the synthesized NiO nanoparticles in a microstructure dimension. The NiO particles are bonded to one another in a form of agglomeration which may be due to the ferromagnetic property of NiO. The naonoparticles appears to be spherical in shape which is excellent for application in enhanced oil recovery.

Conclusion

Nickel oxide nanoparticles were successfully synthesized through the sol-gel method after calcination at 450˚C. Characterization techniques including XRD and FTIR confirmed the existence of NiO due to the formation of diffraction peaks and the formation of chemical bonds conforming to nickel and oxygen. SEM analysis revealed the morphology of NiO nanoparticles

having a sperical shape and an average particle size of 15nm using the scherrer equation. Therefore, the synthesized NiO nanoparticles have the potential to be explored in the area of enhanced oil recovery.

References

[1] T. Behl *et al.*, "The dichotomy of nanotechnology as the cutting edge of agriculture: Nano-farming as an asset versus nanotoxicity," *Chemosphere*, vol. 288, 2022, doi: 10.1016/j.chemosphere.2021.132533.

[2] K. Sinha, J. Ghosh, and P. C. Sil, "New pesticides: a cutting-edge view of contributions from nanotechnology for the development of sustainable agricultural pest control," in *New Pesticides and Soil Sensors*, 2017. doi: 10.1016/b978-0-12-804299-1.00003-5.

[3] M. R. Wiesner and J. Bottero, *Environmental Nanotechnology: Applications and Impacts of Nanomaterials*, vol. 13, no. 5. 2007.

[4] V. Mohan, "'Graphene-Based Nanotechnologies for Energy and Environmental Applications,'" *Johnson Matthey Technol. Rev.*, 2020, doi: 10.1595/205651320x15904919310284.

[5] M. A. Raza, Z. Kanwal, A. Rauf, A. N. Sabri, S. Riaz, and S. Naseem, "Size- and shape-dependent antibacterial studies of silver nanoparticles synthesized by wet chemical routes," *Nanomaterials*, vol. 6, no. 4, 2016, doi: 10.3390/nano6040074.

[6] M. Amiri, M. Salavati-Niasari, and A. Akbari, "Magnetic nanocarriers: Evolution of spinel ferrites for medical applications," *Advances in Colloid and Interface Science*, vol. 265. 2019. doi: 10.1016/j.cis.2019.01.003.

[7] M. Amanullah and A. M. Al-Tahini, "Nano-technology- its significance in smart fluid development for oil and gas field application," in *Society of Petroleum Engineers - SPE Saudi Arabia Section Technical Symposium 2009*, 2009. doi: 10.2118/126102-ms.

[8] A. M. Ealias and M. P. Saravanakumar, "A review on the classification, characterisation, synthesis of nanoparticles and their application," in *IOP Conference Series: Materials Science and Engineering*, 2017. doi: 10.1088/1757-899X/263/3/032019.

[9] Z. Lu and Y. Yin, "Colloidal nanoparticle clusters: Functional materials by design," *Chem. Soc. Rev.*, vol. 41, no. 21, 2012, doi: 10.1039/c2cs35197h.

[10] R. Fuhrer, E. K. Athanassiou, N. A. Luechinger, and W. J. Stark, "Crosslinking metal nanoparticles into the polymer backbone of hydrogels enables preparation of soft, magnetic field-driven actuators with muscle-like flexibility," *Small*, vol. 5, no. 3, 2009, doi: 10.1002/smll.200801091.

[11] S. Shahrokhian, L. Naderi, and R. Mohammadi, "High-Performance Fiber-Shaped

Flexible Asymmetric Microsupercapacitor Based on Ni(OH)2 Nanoparticles-Decorated Porous Dendritic Ni-Cu Film/Cu Wire and Reduced Graphene Oxide/Carbon Fiber Electrodes," *ACS Sustain. Chem. Eng.*, vol. 6, no. 11, 2018, doi: 10.1021/acssuschemeng.8b03196.

[12] S. U. S. Choi, S. Li, and J. A. Eastman, "Measuring thermal conductivity of fluids containing oxide nanoparticles," *J. Heat Transfer*, vol. 121, no. 2, 1999, doi: 10.1115/1.2825978.

[13] M. El-Kemary, N. Nagy, and I. El-Mehasseb, "Nickel oxide nanoparticles: Synthesis and spectral studies of interactions with glucose," *Mater. Sci. Semicond. Process.*, vol. 16, no. 6, 2013, doi: 10.1016/j.mssp.2013.05.018.

[14] D. Deep Yadav, R. Jha, S. Singh, and A. Kumar, "Synthesis and characterisation of Nickel oxide nanoparticles using CTAB as capping agent," *Mater. Today Proc.*, vol. 73, 2023, doi: 10.1016/j.matpr.2022.11.012.

[15] S. Sahila, N. Prabhu, G. G. Simiyon, and L. S. Jayakumari, "A novel green and eco-friendly synthesis of nickel oxide nanoparticles by auto combustion technique using allium cepa bulb extract and their dielectric behaviour," *Chem. Data Collect.*, vol. 38, 2022, doi: 10.1016/j.cdc.2022.100837.

[16] N. Nadia, M. Zorkipli, N. Haida, M. Kaus, and A. Azmin, "Synthesis of NiO Nanoparticles through Sol-gel Method," *Procedia Chem.*, vol. 19, pp. 626–631, 2016, doi: 10.1016/j.proche.2016.03.062.

[17] R. Bhardwaj, R. Jha, M. Bhushan, and R. Sharma, "Electrochemical studies of synthesized nickel sulphide nano-particles," in *Materials Today: Proceedings*, 2021. doi: 10.1016/j.matpr.2021.07.138.

[18] N. Venkatalakshmi, H. Jyothi Kini, and H. S. Bhojya Naik, "Green-synthesized Nickel oxide nanoparticles: Magnetic and biomedical applications," *Inorg. Chem. Commun.*, vol. 151, 2023, doi: 10.1016/j.inoche.2023.110490.

Evaluation of tomato irrigation treatments sustainability: a principal component analysis

Yasmen Heiba[1,2,a], Mahmoud Nasr[1,3,b], Manabu Fujii[4,c], Abdallah E. Mohamed[5,d] and Mona G. Ibrahim[1,6,e]

[1]Environmental Engineering Department, Egypt-Japan University of Science and Technology (E-JUST), Alexandria, Egypt

[2]Civil Engineering Department, Shoubra Faculty of Engineering, Benha University, Cairo 11629, Egypt

[3]Sanitary Engineering Department, Faculty of Engineering, Alexandria University, P.O. Box 21544, Alexandria 21526, Egypt

[4]Civil and Environmental Engineering Department, Tokyo Institute of Technology, Meguro-Ku, Tokyo 152-8552, Japan

[5]Land and Water Technologies Department, Arid Lands Cultivation Research Institute, City of Scientific Research and Technological Applications (SRTA-City), New Borg El-Arab, Alexandria 21934, Egypt

[6]Environmental Health Department, High Institute of Public Health, Alexandria University, Alexandria 21544, Egypt

yasmen.heiba@ejust.edu.eg, mahmoud.nasr@ejust.edu.eg, fujii.m.ah@m.titech.ac.jp, abdallahelsayed44@yahoo.com, mona.gamal@ejust.edu.eg

Keywords: nano-fertilizer, IWUE, NUE, nitrate leaching, the net return, SDGs

Abstract. Irrigation and fertilization are critical practices for improving tomato irrigation treatments' sustainability. This study evaluated irrigation treatments' performance based on four environmental and two economic indicators. A pot-scale experimental study was performed using drip and furrow irrigation (DI; FI) and two fertilization types, chemical- and nano-fertilizer (C, N). The Principal Component Analysis (PCA) was used to evaluate the performance of the four irrigation treatments using the comprehensive score. The results showed that DI treatments had better tomato yield, IWUE, and lower nitrate leaching than the FI treatments due to applying water and fertilizer directly to the active rooting zone. The nano-treatments showed higher NUE, net return, and lower N_2O emissions than the chemical. This high performance of nano-treatments could be attributed to (i) an easy penetration of nutrients of nano-scale into the plant tissue and (ii) high adsorption capacity, which fixes the NH_4^+ followed by minimizing N_2O emissions. The PCA findings revealed that DN had the highest comprehensive score (12.1) among all the irrigation treatments. The utilization of nano-fertilizer in conjunction with drip irrigation has the potential to be a viable approach to enhance tomato yield, reduce environmental pollution (N_2O emission and nitrate leaching), and increase economic benefits from tomato production in arid regions. Accordingly, the study's findings were linked to various environmental, social, and economic sustainable development goals (SDGs).

Introduction

Tomato (*Lycopersicon esculentum L.)* is the second worldwide consumed vegetable as it represents an essential source of vitamins C and A in our diet and a good source of minerals. Several countries rely on tomato-related industries to boost their economies. Assessing tomato irrigation strategies is crucial for increasing crop yield and profitability. However, irrigation and fertilization conservation is essential to prevent the deterioration of the surrounding environment from N loss in the soil matrix and water bodies. Therefore, developing irrigation strategies to minimize environmental pollution without compromising yield and profit is essential. In addition,

this irrigation strategy has the potential to sustain various environmental, social, and economic advantages.

Furrow irrigation is the most widely used method globally due to insufficient financial and technical knowledge. Nonetheless, this irrigation technique presents several drawbacks, such as water loss and nitrogen leaching [1]. Farmers tend to apply more fertilizers to the soil to compensate for the nutrient loss, which results in several issues, such as soil degradation, increasing nitrogen leaching, and economic losses. Therefore, drip irrigation may solve these problems by efficiently applying irrigation and nutrients to the root zone [2]. Also, nano-fertilizers offer a potential alternative to chemical ones because of their small particle size, which controls the release of nutrients at the target sites rather than through interactions with soil, water, air, and microorganisms, thus reducing the risk of environmental degradation [3]. However, choosing the most sustainable irrigation system necessitates considering economic feasibility, ecological integrity, and social acceptability. The 2030 Sustainable Development Goals (SDGs) agenda may delineate the interplay between environmental and socioeconomic factors.

Consequently, the present study aims to (i) evaluate four irrigation treatments based on environmental and economic dimensions of sustainability, (ii) select the best irrigation treatment based on comprehensive performance evaluation using PCA, and (iii) establish a correlation between research outcomes and possible SDGs.

Materials and Methods

Tomato plants were grown from November 2021 to April 2022 at the Arid Lands Cultivation Research Institute (ALCRI) farm, City of Scientific Research and Technological Applications, Borg Al-Arab City, Alexandria, Egypt. Tomato seedlings were transplanted into pots containing 10 kg of sandy loam soil.

Experimental Design. Two irrigation methods, namely drip (DI) and furrow irrigation (FI), and two fertilizer types, chemical (C) and nano-fertilizer (N) were used. Specifically, four irrigation treatments, FC, FN, DC, and DN, were studied. The experimental design employed in this study was a randomized block design, where each treatment was allocated to three pots with three replicates [4].

Irrigation Treatments Design. The irrigation techniques were implemented to correspond with the potting circumstances and simulate the actual conditions of their application (Fig. 1) [4]. All irrigation treatments received an equal amount of water of 752 mm [5]. The nano-fertilizer utilized in the study was Hyper feed motawazen 19:19:19 N:P:K, procured from Bio NanoTech for fertilizer development in Egypt, and was applied at the recommended dose (10 kg/fed). According to the Ministry of Agriculture and Land Reclamation of Egypt, 120 kg N/fed of conventional 19:19:19 NPK fertilizer was applied.

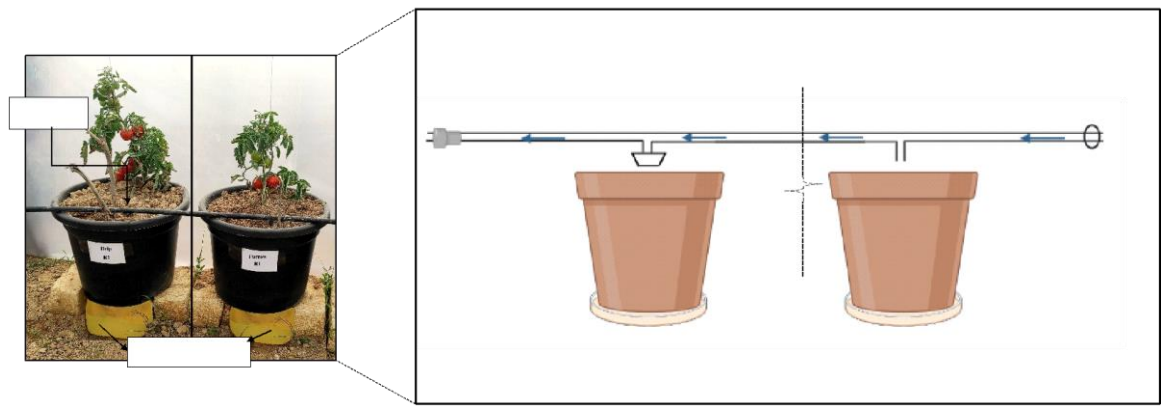

Fig. 1 Experiment layout

Measurement of Parameters. The yield (kg) was measured using an electronic weighing scale at the harvesting stage. The IWUE (kg/m^3) and NUE (kg/kg) were calculated using Eqs. 1 and 2.

$$IWUE = \frac{Y}{I}. \quad (1)$$

$$NUE = \frac{Y}{N}. \quad (2)$$

Where I and N represent the quantity of irrigation water (m^3) and N fertilizer (kg) applied, respectively, and Y denotes the total yield of tomato (kg).

Nitrate leaching from each pot was collected daily for three consecutive days after each watering event and stored in centrifuge tubes at -20°C [2] and analyzed by utilizing a UV-visible spectrophotometer (Hitachi U-3900, Japan) following [6]. The N_2O emitted from fertilizer application was estimated using the Intergovernmental Panel on Climate Change (IPCC) methodology [7]. The Net return was calculated following [4] and [8].

Statistical Analysis. The PCA was performed for the six indicators to evaluate the comprehensive performance of the irrigation treatments, following Yang et al. [9].

Results

Table 1 shows the impact of irrigation treatments on the six sustainability indicators. The results indicated that DI showed higher IWUE, NUE, and yield than FI treatments. These results were due to the irrigation water and nutrients supplied to the tomato plant's active rooting zone. These results were confirmed by Li et al. [1], drip fertigation improved IWUE by 62% and NUE by 44.5%, while increasing tomato yield by approximately 11% compared to conventional techniques. The NO_3 leaching under nano-treatments was lower than those for chemical treatments by more than 11% due to its smaller size, assisting in nutrient dispersion and solubility in the soil. Applying nano-nitrogen chelate resulted in a 35.7% reduction in N leaching than urea fertilizer [3], enhancing plant absorption of nutrients. Nitrate leaching under FI was six times higher than DI. The lower nitrate leaching under DI irrigation is attributed to delivering irrigation water more often and in smaller amounts, according to LV et al. [10]. The N_2O emission from chemical treatments was approximately 12 times higher than from nano-treatments. Compared with chemical fertilizer, a higher adsorption capacity of nano-fertilizer tends to reduce N_2O emissions through the fixation of the NH_4^+ in soil, thereby minimizing the nitrification/de-

nitrification cycle [11]. This result was confirmed by Kundu et al. [12], who found that using urea coated with 2% nano zinc oxide reduced approximately 45% in N_2O emissions compared to the conventional urea fertilizer. The tomato yield from nano-treatments was higher than chemical treatments by about 33% and 17% under FI and DI, respectively (Table 1). This result can be attributed to the rapid uptake of nano-fertilizers by stomatal tissues [13]. The increased net return generated by nano treatments could be validated by applying small quantities of fertilizer in conjunction with a rise in crop yield. Therefore, substituting chemical fertilizers with nano-fertilizers is a potentially promising approach for mitigating expenses, augmenting net income, and circumventing the negative consequences of chemical supplementation, such as N_2O emissions and N leaching.

Table 1 Impact of irrigation treatments on IWUE, NUE, Yield, Net return, Nitrate leaching, and N_2O emission

Treatment	FC	FN	DC	DN
IWUE [kg/m^3]	32.08	42.7	51.01	59.59
NUE [kg/kg]	202.7	3234	322.3	4519
Yield [kg]	6.95	9.24	11.05	12.91
Net return [$]	2.54	4.51	4.94	6.56
Nitrate leaching [mg/l]	18.2	16.1	2.92	2.51
N_2O emission [kg]	0.006	0.001	0.006	0.001

PCA for Comprehensive Performance Evaluation. PC_1 and PC_2 were extracted due to explaining 99.71% of the total variance. The loading plots (Fig. 2a) showed that the PC_1 was positively associated with IWUE, NUE, Yield, and Net return and negatively influenced by nitrate leaching. The PC_2 was negatively affected by N_2O emissions. The PCA scores of tomatoes under irrigation regimes (Fig. 2b) show the correlation between the irrigation treatments and the two principal components (PC_1 and PC_2). The DN treatment was aligned with the positive direction of PC_1 axis, indicating superior yield, IWUE, and Net return than the other treatments, as previously reported in Table 1. The NUE was located in the upper right-hand quarter of the graph alone, illustrating the ability of nano-fertilizer to deliver nutrients efficiently to the plant. The N_2O emission was situated in the lower-hand corner of the plot, indicating the potential of nano-fertilizer to reduce the N_2O emissions. Moreover, Fig. 2c shows the ranking of the irrigation treatments according to the comprehensive score of PCA, which directly demonstrates the priority of different irrigation treatments. The DN treatment was ranked first, followed by FN, DC, and FC treatment.

Fig. 2 Loading plots for the six indicators (a) and scores of PCA (b) on PC_1 and PC_2, and the comprehensive score and ranking (c) for the results of tomato plants grown under irrigation regimes (FC, FN, DC, and DN)

SDGs Associated with Sustainable Irrigation Treatment. The application of DN treatment would support the achievement of several SDGs.

Environmental. The implementation of DN has the potential to mitigate nitrate leaching, thereby reducing the risk of biodiversity loss and soil degradation [14]. This approach aligns with the objectives of SDG14 "Life below water" and SDG15 "Life on land". Also, it would have a positive effect on the water quality conditions, thereby contributing to SDG6 "Clean water and sanitation". Mitigating N_2O emissions under DN can help to address the issue of air quality degradation, which is in line with SDG13 "Climate Action".

Economic. The increased crop yield, NUE, and IWUE under DN would increase tomato cultivation's profitability, contributing to SDG8 "economic development and growth". Furthermore, the efficient utilization of natural resources in tomato cultivation contributes to the achievement of SDG12" Responsible consumption and production".

Social. The cultivation of tomatoes serves as a means of fulfilling both market and household demands, thereby contributing to the achievement of SDG1 "Eradicate poverty". Further, it can meet SDG2 "Zero hunger" by increasing the agricultural revenues of small-scale farmers. Enhancing resource utilization efficiency under DN can lead to increased profitability in cultivating tomatoes, which directly benefits producers and contributes to reducing poverty in rural areas, which aligns with SDG1. Mitigating the degradation of air quality and enhancing waste management efficiencies by reducing N_2O emissions would facilitate the attainment of SDG11 "Sustainable cities and communities". Reducing nitrate leaching could have a favorable effect on the quality of water, thereby enhancing the achievement of SDG6 "Clean water and sanitation". Reducing waste generation (N_2O emission and nitrate leaching) would mitigate the negative effects of pollution on human health, achieving SDG3 " Good health and well-being".

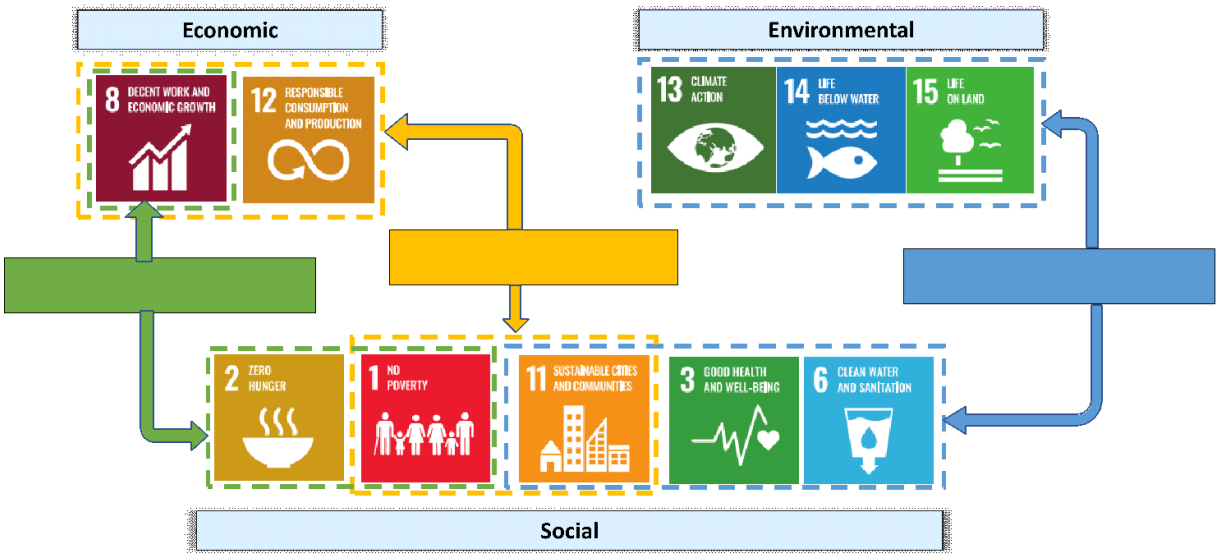

Fig. 3 Interactions between DN treatment attributes and SDGs

Conclusion

The findings of this study illustrated that the DN treatment has the potential to serve as a viable and sustainable irrigation approach. This can be attributed to its ability to conserve natural resources, reduce pollution, and enhance economic profitability. According to the PCA results, the DN treatment exhibited the highest overall score (12.1), whereas the FN, DC, and FC treatments demonstrated comparatively lower scores. Moreover, the utilization of DN is closely linked to the environmental, social, and economic pillars of sustainable development. The study outputs were found to be closely associated with ten Sustainable Development Goals (SDGs).

References

[1] H. Li, X. Mei, J. Wang, F. Huang, W. Hao and B. Li, "Drip fertigation significantly increased crop yield, water productivity and nitrogen use efficiency with respect to traditional irrigation and fertilization practices: a meta-analysis in China," Agricultural Water Management, vol. 244, p. 106534, 2021.

[2] H. Lv, S. Lin, Y. Wang, X. Lian, Y. Zhao, Y. Li, J. Du, Z. Wang, J. Wang and K. Butterbach-Bahl, "Drip fertigation significantly reduces nitrogen leaching in solar greenhouse vegetable production system," Environmental Pollution, vol. 245, pp. 694-701, 2019.

[3] H. Zareabyaneh and M. Bayatvarkeshi, "Effects of slow-release fertilizers on nitrate leaching, its distribution in soil profile, N-use efficiency, and yield in potato crop," Environmental Earth Sciences, vol. 74, no. 7, pp. 3385-3393, 2015.

[4] Y. N. M. F. M. Heiba, A. Mohamed and M. Ibrahim, "Improving irrigation schemes using sustainable development goals (SDGs)-related indicators: a case study of tomato production in pot-scale experimentation," Environ Dev Sustain, pp. https://doi.org/10.1007/s10668-023-03357-z, 2023.

[5] M. Gabr, "Management of irrigation requirements using FAO-CROPWAT 8.0 model: A case study of Egypt," Modeling Earth Systems and Environment, pp. 1-16, 2021.

[6] A. Eaton, L. Clesceri and A. Greenberg, Standard Methods for the Examination of Water and Wastewater, twentyfirst ed., Washington: American Public Health Association/American Water Works Association, 2005.

[7] IPCC, "Chapter 11: N2O emissions from managed soils, and CO2 emissions from lime and urea application," in 2006 IPCC guidelines for national greenhouse gas inventories, vol. 4, H. Eggleston, L. Buendia, K. Miwa, T. Ngara and K. Tanabe, Eds., Japan, Institute for Global Environmental Strategies (IGES), 2006.

[8] Y. Li, Y. Sun, S. Liao, G. Zou, T. Zhao, Y. Chen, J. Yang and L. Zhang, "Effects of two slow-release nitrogen fertilizers and irrigation on yield, quality, and water-fertilizer productivity of greenhouse tomato," Agricultural Water Management, vol. 186, pp. 139-146, 2017.

[9] X. Yang, P. Zhang, Z. Wei, J. Liu, X. Hu and F. Liu, "Effects of CO2 fertilization on tomato fruit quality under reduced irrigation," Agricultural Water Management, vol. 230, p. 105985, 2020.

[10] H. Lv, W. Zhou, J. Dong, S. He, F. Chen, M. Bi, Q. Wang, J. Li and B. Liang, "Irrigation amount dominates soil mineral nitrogen leaching in plastic shed vegetable production systems," Agriculture, Ecosystems and Environment, vol. 317, p. 107474, 2021.

[11] Y.-N. Liu, Y.-C. Li, Z.-P. Peng, Y.-Q. WANG, S.-Y. MA, L.-P. GUO, E.-D. Lin and X. Han, "Effects of different nitrogen fertilizer management practices on wheat yields and N2O emissions from wheat fields in North China," Journal of Integrative Agriculture, vol. 14, no. 6, pp. 1184-1191, 2015.

[12] S. Kundu, T. Adhikari, Mohanty, R. M. S.R., M. Vassanda Coumar, J. Saha and A. Patra, "Reduction in nitrous oxide emission from nano zinc oxide and nano rock phosphate coated urea," Agrochimica, vol. 60, no. 2, pp. 59-70, 2016.

[13] M. Abd El-Azeim, M. Sherif, M. Hussien, I. Tantawy and S. Bashandy, "Impacts of nano-And non-nanofertilizers on potato quality and productivity," Acta Ecologica Sinica, vol. 40, no. 5, pp. 388-397, 2020.

[14] Z. Fan, S. Lin, X. Zhang, Z. Jiang, K. Yang, D. Jian, Y. Chen, J. Li, Q. Chen and J. Wang, "Conventional flooding irrigation causes an overuse of nitrogen fertilizer and low nitrogen use efficiency in intensively used solar greenhouse vegetable production," Agricultural Water Management, vol. 144, pp. 11-19, 2014.

Simulation Study to investigate the effect of Anode Material and Thickness on the Thermal Properties of Lithium-Ion Batteries

A. El-Tayeb[*,1], Jackleen S. Same[*,1], Esam H. Abdelhameed[1], Adel Z. El-Dein[1,2], Ibrahim Moukhtar[1]

[1]Electric Engineering Department, Faculty of Energy Engineering, Aswan University, Aswan, Egypt.
[2]Faculty of Technological Industry and Energy, Thebes Technological University, Thebes, Luxor, Egypt.
[*]E-mail: Ahmed_al_tayeb@aswu.edu.eg;

Keywords: Lithium-ion batteries' energy capacity will rise from 330 GWh in 2021 to 550 GWh in 2022, an increase of roughly 65%, primarily because of the rising demand for energy storage on a global scale. Understanding the temperature behavior of Li-ion batteries is therefore critical to meet this demand and to maximize performance, safety, and durability. With the help of a simulation program based on finite element analysis, this work aims to investigate the thermal performance of Li-ion batteries by altering the anode's composition and thickness as well as introducing Matel nanoparticles. Based on the (FEM) method. The simulation's findings indicate that electrode thickness and material play a significant role in improving the thermal performance of Li-ion batteries. The five components were lithium metal (Li), lithium titanium oxide (LTO), silicon (LixSi), hard carbon, and graphite. Lithium metal and LTO have a longer service life because to their high thermal stability and excellent heat dissipation. Hard carbon is perfect for batteries with high energy densities since it also has exceptional thermal stability. However, due to silicon and graphite's poor thermal conductivity, there may be more hot spots, unequal heat dissipation, and shorter cycle durations. The next step was to investigate the thickness of graphite. The modeling findings show that the thickest anode may cause a higher volume change during cycling, putting mechanical stress. The thinner anode hence provides more thermal stability than the thicker anode.

Introduction:

The anode material's features and composition play a significant effect in the battery's overall performance. The anode material's shape and intrinsic characteristics have a big impact on the capacity and performance of the battery. As novel LIB materials, numerous high-performance anode materials have been studied. Chemicals based on silicon, substances based on carbon, transition metal compounds of the conversion type, and alloy materials are a few examples. Over the past few years, numerous advancements in the study of materials for lithium-ion batteries have caused changes and development in the thermal and physical properties of materials [1-2]. Early in the 20th century, the first thin-film anodes were created, greatly reducing the anode's thickness and enhancing battery performance. [3]. with the advent of novel materials like silicon, graphene, and others in recent years, the field of anode development has advanced further. These materials offer greater performance and a longer battery life than traditional anode materials due to their increased energy density [4-5]. Researchers can find strategies to enhance the performance and safety of lithium-ion batteries by examining their thermal behavior [6]. Negative electrode (anode), positive electrode (cathode), electrolyte, separator, or dielectric of the lithium-ion type. The anode, cathode, and electrolyte materials utilized affect how well lithium batteries work [7]. Thermal behavior, which manifests when temperatures are evenly distributed and displays the heat flow rate throughout the battery, is notably evident while the battery is being charged and discharged. Battery size is notably enlarged by the high temperature,

which causes thermal escape to reduce efficiency and eventually cause a fire or explosion [8–9]. The main goal of the paper is to increase battery performance by altering the anode's thickness and composition, as well as by selecting the best nanoparticles (NP) for use in the research to lower battery temperature and increase battery efficiency.

1. Material and Method

1.1 Finite Element Method (FEM)

The finite element method (FEM) is a computational technique for simulating and analyzing the behavior of objects by applying various loads and pressures under various environmental and environmental variables. As seen in Figure 1, the FEM method also entails breaking down complex structural components into smaller, simpler, and easier components that can be quickly evaluated and simulated [10-13].

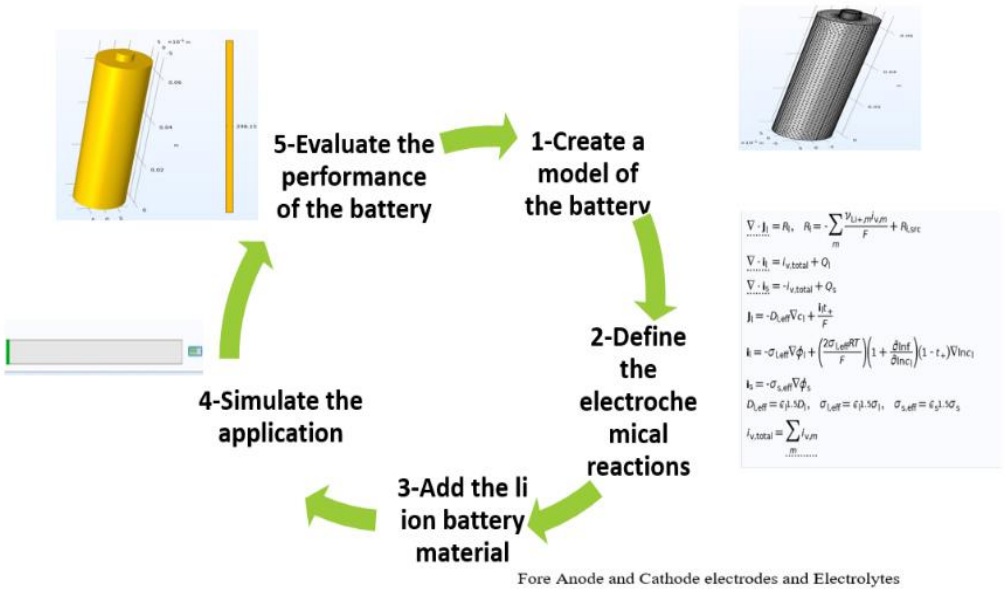

Figure 1. Steps of Simulation Work.

Involving materials science, FEM can be used to study the behaviour of materials in general under conditions in different surroundings as this technique allows researchers to predict the thermal properties of materials and design materials with specific properties to meet different engineering applications [14-16]. One of the advantages of this technology is the ability to simulate complex structures and predict their behaviour, whether thermal, chemical, or physical under different loads and conditions, as well as the advantage of acceptable cost, which allows the possibility of improving structures and materials, which reduces the need for costly physical tests. Overall, the FEM simulation study is a powerful tool in material science and engineering that enables researchers to understand the thermal behaviour of battery with properties to meet various engineering applications [17-20].

1.2 thermal model

In order to create a heat source in the active battery material using simulation software based on FEM, a 2D axisymmetric thermal model is connected to a lumped battery model. The positive electrode (cathode) of the traditional lithium-ion cell is constructed of NCA, and the electrolyte is a lithium salt in an organic solvent (LiPF6). These three components make up the LIB . There are three domains in the model: Domain of active battery material, mandrel, and cylindrical battery connector are listed in that order. a 7.5 C alternating charge/discharge current with a 600 s duration, a 1500 s relaxation period, and a square wave function with a 20 W/(m2.K) heat transfer coefficient at a 298.15 K external temperature. In Figure 3, the results of the simulation and the operating profile from the battery's cell voltage, load current, and temperature are displayed along with the cell potential and load cycle current.

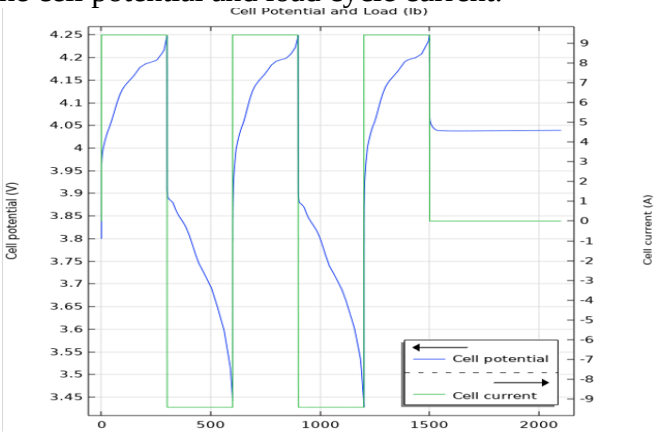

(a)

Figure 2. Cell potential and the load cycle current,

The average temperatures of the battery throughout the simulation, the difference in heating rate between charge and discharge, and it is the temperature difference between the ambient temperature and the temperature of the battery are caused by the difference in entropy change for the charge and discharge reactions (set by the dEeq/dT parameter).

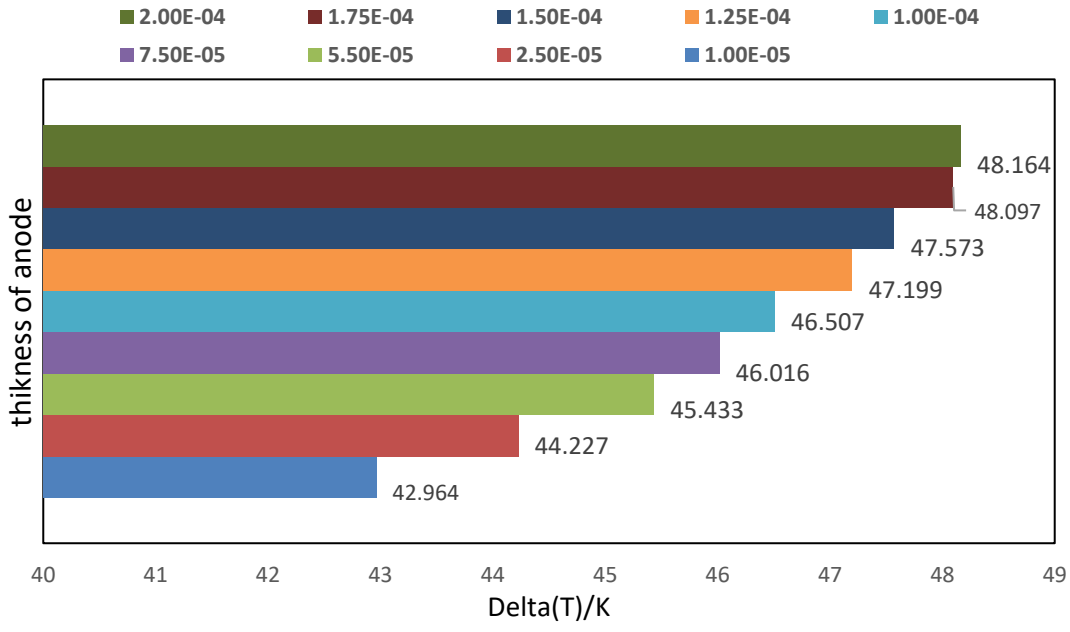

Figure 3. change the thickness of anode.

2. Different thickness

The temperature of a Li-ion battery during charging and discharging may be impacted by the thickness of the anode. Figure 3, thermal behaviour can change depending on whether the anode is thicker or thinner [21-23]. If the temperature rises above the safe operating range during the charging and discharging processes, this may result in safety problems like thermal escape, electrolysis, and a shorter battery life cycle. The negative effects of increased thickness include increased internal resistance and longer diffusion paths of lithium ions. Also reverse to thin out the anode, albeit this could result in decreased capacity and energy density [24-27].

3. Different anode material's

The anode electrode is installed using a variety of materials, which are LixC6, LixSi, carbon steel, LTO, lithium metal, and silicon. Research has shown that each of these materials has benefits and drawbacks that can affect the battery's performance and temperature [28-31 as depicted in Figure 4.

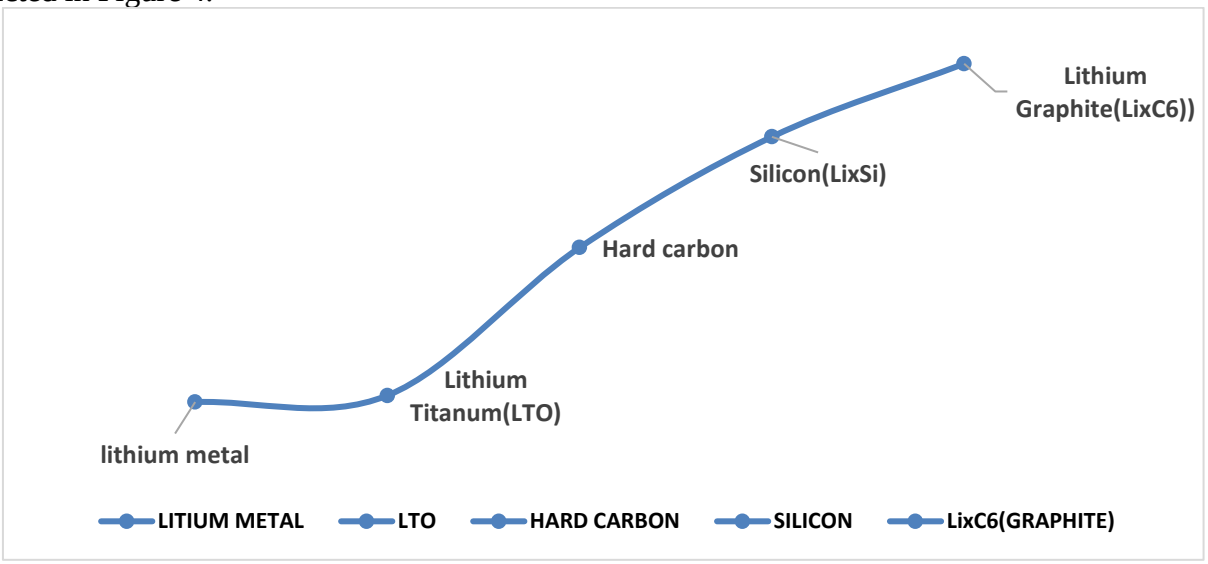

Figure (4). An overview of anode materials & Effect of variation of material's anode for temperature.

Figure 4 displays the outcome of anode material variation with temperature; as the image makes clear Although lithium graphite (LiC6), a frequently used anode material in industrial Li-ion batteries, experiences the battery's maximum temperature during charging and discharging. After hard carbon and before this lithium titanium, silicon comes in second place for temperature rise, followed by lithium metal in third place. In general, the Li-ion battery's temperature can be considerably impacted by the anode material selection. The battery may operate at a greater temperature as a result of materials including LiC6, LixSi, hard carbon, and silicon that produce more heat when charging and discharging. This could hasten the battery's aging process and reduce its performance over time. The battery can run at a lower temperature and last longer by using materials that pose a lower danger of producing heat, such as LTO.

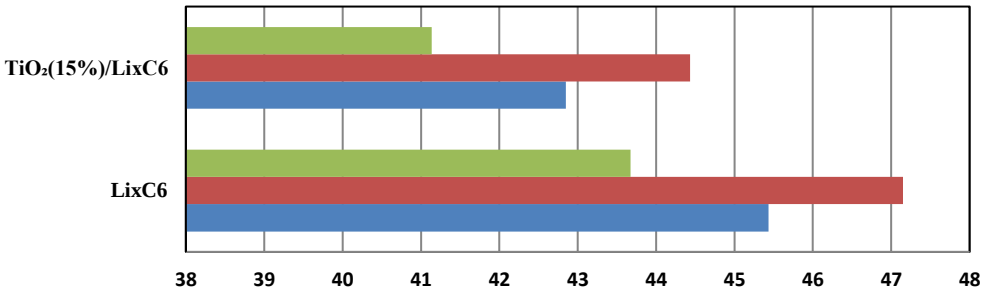

	LixC6	TiO_2(15%)/LixC6
Min temperature	43.674	41.138
Max temperature	47.152	44.435
Mean temperature	45.433	42.849

Delta(T)/K

Figure 5. Compare the temperature of battery between before and after adding NP/ TiO_2 (15%), Anode thickness $100e^{-7}$m

4. Effect of adding nano particulars to anode material and overall Lithium Battery Optimization.

In commercial Li-ion batteries, lithium graphite (LiC6) is frequently utilized as the anode material due to its low cost and wide availability. LiC6 is created by introducing lithium ions into graphite, a cheap and plentiful material, and is primarily used because, as was previously noted, it records the battery's greatest temperature. Therefore, increasing the temperature requires adding nanomaterials and altering the anode electrode's thickness. According to a previous study, the anode electrode thickness in this study was reduced from 55 e-6 m to 100 e-7 m, and NP-TiO2 with a volume fraction of 15% was added. TiO2 is a popular material used in the anode electrode of lithium-ion batteries because of its excellent properties, including high stability, safety, and low cost. Since they can perform even better than bulk TiO2, nano sized TiO2 particles have received a lot of attention as an anode material in recent years. We can state that these results are suitable for reducing battery temperature because they lower the temperature of the battery during operation as shown in Figure 6 Note the temperature differential decrease of 2.6 K.

Conclusion

Anode material play essential role in in battery temperature distribution which make reduce in temperature of battery by decrease in anode thickness. Internal resistance, which can reduce the heat generated during charging and discharging. This, in turn, can help the battery stay cooler during operation. Adding nano-particle materials to anode electrode with certain thermal and physical properties such as thermal conductivity, density, and heat capacity in different volume fraction, which improve the temperature of the battery. Overall optimization for battery until it reaches a better improvement, which is by using anode material Lithium graphite (LiC_6), it achieves the highest operating time temperature, which is improved by changing the thickness of the anode to $100e^{-7}$ m and using TiO_2 by volume fraction 15%.

5. Acknowledgment

The authors appreciatively recognize the Egyptian Science and Technology Development Fund (STDF) for subsidizing this work among the STDF project with ID no. 43247.

6. References

[1] Jonathan Wood, "The top advances in materials science", Materials Today, volume 11, Number1-2, JAN-FEB 2008.
[2] W. B. Gu and C. Y. Wang, "Electrochemical–Thermal Characterization and Thermal Modeling for Batteries", the Electrochemical Society, volume 147, Number8, 10 February 2017
[3] Taesoo D. Leea, "A review of thin film solar cell technologies and challenges", Renewable and Sustainable Energy Reviews, Volume 70, Numbers 1286-1297, 3 December 2016.
[4] Chengzhi Zhang and et al., "Challenges and Recent Progress on Silicon-Based Anode Materials for Next-Generation Lithium-Ion Batteries", Materials & Design, Volume 195, 2020,
[5] J. M. Tarascon and M. Armand, "Issues and challenges facing rechargeable lithium batteries", Nature, volume 414, numbers 359 -367, 2001.
[6] Nourhan Mohamed and Nageh K. Allam, "Recent advances in the design of cathode materials for Li-ion batteries", Nature RSC Adv, volume 10, ,numbers 37,2020 jun 8.
[7] Luca Giammichele and et al., "Thermal behaviors assessment and electrical characterization of a cylindrical Lithium-ion battery using infrared thermography" Applied Thermal Engineering, Volume. 205, Number1359-4311, July, 2021.
[8]Jianqiang Kang and et al. "How electrode thicknesses influence performance of cylindrical lithium-ion batteries", Energy, Volume 186, February 2019.
[9] Tai-Ran Hsu, "Introduction to Finite Element Methods", Applied Engineering Analysis, August 20, 2021, ISBN 9781119071204.
[10] K.G. Johnson, "A study into the use of the process failure mode and effects analysis (PFMEA) in the automotive industry in the UK", Materials Processing Technology, 139, 348–356 , 2003.
[11] Dragan Marinkovic , Manfred Zehn," Survey of Finite Element Method-Based Real-Time Simulations" , Applied Engineering Analysis ,10 July 2019
[12] Jai-Woh Kim and Anil V. Virkar, "The Effect of Anode Thickness on the Performance of Anode-Supported Solid Oxide Fuel Cells", the Electrochemical Society, Volume. 19, 830, 1999.
[13] Zhao, Rui and et al., "The effects of electrode thickness on the electrochemical and thermal characteristics of lithium ion battery," Applied Energy, volume 139(C), numbers 220-229. , 2015 .
[14] Petros Selinis , Filippos Farmakis . " A Review on the Anode and Cathode Materials for Lithium-Ion Batteries with Improved Subzero Temperature Performance," Electrochem. Soc, volume 169,numbers 010526, 19 January 2022.
[15] Sid Megahed, Bruno Scrosati , "Lithium-ion rechargeable ",power-sources, ,volume 10,numbers 79-104 September 1994,.
[16] G. Nagasubramanian," Electrical characteristics of 18650 Li-ion cells at low temperatures", Electrochemistry ,volume 31, pages 99–104 ,2001.
[17] Byungchan Han," Structures and Formation Energies of LixC6 (x=1-3) and its Homologues for Lithium Rechargeable Batteries" , Bulletin of the Korean Chemical Society · June 2011

[18] Jakob Asenbauer, Tobias Eisenmann, Matthias Kuenzel, Arefeh Kazzazi, Zhen Chen and Dominic Bresser ," The success story of graphite as a lithium-ion anode material – fundamentals, remaining challenges, and recent developments including silicon (oxide) composites" , Sustainable Energy & Fuels,Nov 2020
[19] Xiuyun Zhao and Vesa-Pekka," Challenges and prospects of nanosized silicon anodes in lithium-ion batteries", Nanotechnology, Lehto 2021 , 32 042002
[20] Wen-Feng Ren , Yao Zhou , Jun-Tao Li , Ling Huang , Shi-Gang Sun ," Si anode for next-generation lithium-ion battery",Journal Pre-proof, 16 September 2019.
[21] Shuai Maa, , Modi Jianga, , Peng Taoa , Chengyi Songa , Jianbo Wua , Jun Wangb , Tao Denga , Wen Shanga," Temperature effect and thermal impact in lithium-ion batteries: A review", A123 Systems Research Center, 200 West Street, Waltham, MA 02451, USA.
[22]Xianfeng Huang a, Guangxing Yang b, Shuang Li a, Hongjuan Wang b, Yonghai Cao b, Feng Peng c, Ho Yu," Noble-metal-based high-entropy-alloy nanoparticles for electrocatalysis", Journal of Energy Chemistry,Volume 68, May 2022, Pages 721-751
[25] Wang, H., Liu, Y., Li, Y. et al,"Lithium Metal Anode Materials Design: Interphase and Host", Electrochem. Energ. Rev. 2, 509–517 (2019).
[26] Renheng Wangb, Weisheng Cuib, fulu Chua, feixiang Wu," Lithium metal anodes: Present and future", Journal of Energy Chemistry, 2020.
[29] Thomas, Y. Grohens, N. Ninan,"Nanotechnology Applications for Tissue Engineering", Elsevier Inc, ISBN: 978-0-323-32889-0 ,2015.
[30] Raphael Wegmann, Volker Döge," Optimized operation of hybrid battery systems for electric vehicles using deterministic and stochastic dynamic programming", Journal of Energy Storage, 11 September 2017.
[31] O.K. Benson, C.B. Christensen, R.W. Burrows, Y.D. Shinton, "New Phase Change Thermal Energy Storage Materials for Buildings", International Conference on Energy Storage for Building Heating and Cooling Toronto, Canada, 1985.

Design and Simulation of a Thermally Controlled Wind Tunnel

M. H. Abdel-Moniem†, E. R. Lotfy
Mechanical Engineering Department, Faculty of Engineering, Alexandria University, Alexandria, 21544 Alexandria, Egypt
†*E-mail: es-MohamedHatem2024@alexu.edu.eg*

Keywords: Convective boundary layer, Richardson number, Thermal stability, Turbulent boundary layer, Wind tunnel

Abstract

Wind tunnel experiments can benefit the efficient utilisation of wind energy in many aspects, such as the testing of new products, the validation of numerical models, and the exploration of underlying mechanisms of urban ventilation. However, thermal stability changes the properties of the turbulent boundary layer, and in turn affects the behaviour and results of atmospheric flow simulation. To better understand the effect of thermal stability on the wind flow, a thermally controlled wind tunnel was designed and simulated. The numerical experiments targeted simulating a convective boundary layer. The convective boundary layer was generated by heating up the test section floor up to 73 degrees Celsius, while the inlet air conditions were set to a temperature of 25 degrees Celsius and a free stream velocity of 2.5 m/s. The proposed wind tunnel dimensions and flow conditions were intended to generate a 60-cm thick convective boundary layer with a bulk Richardson number of -0.1. The simulations were conducted by ANSYS fluent simulation package. The results revealed the thermal and dynamic characteristics of the convective boundary layer under the prescribed conditions. The study provides an avenue for building thermally controlled wind tunnels that can be employed in simulating realistic atmospheric flows over civil and mechanical structures.

1. Introduction

The wind tunnel plays a vital role in the field of fluid dynamics as an essential tool of studying the complex behaviour of aerodynamic flows. In particular, wind tunnel modelling provides numerous advantages for wind energy applications, such as the evaluation of new products, validation of different numerical models, and exploration of urban ventilation mechanisms. To ensure accurate and reliable results, it is crucial to maintain precise control over the wind tunnel's environmental conditions, including temperature. Thermal stability has a significant impact on the behaviour of atmospheric flow simulations, as it impacts the properties of the turbulent boundary layer.

Wind tunnels equipped with convective boundary layers are special types of tunnels that are designed to replicate the effects of natural wind and atmospheric conditions on aerodynamic prototypes. To simulate the real-world conditions encountered in the atmosphere, the convective boundary layer is formed through the utilization of heating elements. These elements generate a vertical temperature gradient, which in turn induces an airflow that mimics the desired neutral conditions in the atmosphere. The design and operation of wind tunnels with a convective boundary layer pose unique challenges. The wind tunnel's test section must be carefully designed to mimic the thermal gradients, turbulence, and velocity profiles encountered in real-world conditions. Furthermore, accurate measurement techniques are essential for quantifying flow properties within the convective boundary layer, such as temperature, velocity, and turbulence characteristics.

Many studies have been proposed to develop innovative designs and extensive examinations for wind tunnels. [1] provide comprehensive examination of low-temperature materials that experience sublimation when subjected to continuous blow-down hypersonic wind tunnel conditions. [2] investigates the characteristics of the non-uniformity and turbulence behaviour of mean velocity within the test-section of a wind tunnel specifically designed for civil and aeronautical purposes. [3] conducted research on a steady-flow wind tunnel to examine the impact of thermal stratification on flow within the atmospheric boundary layer. [4] have performed an experimental study to examine

the impact of turbulence generation and velocity fluctuations caused by pressure waves in a large low-speed wind tunnel. [5] analyse the impact of progressive heating on fluid flow and temperature distribution by evaluating the velocity and thermal characteristics inside the test section using numerical and experimental methods.

[6] introduce a numerical approach to simulate flow conditions in a closed-loop wind tunnel. They have created a full-scale computational fluid dynamics (CFD) model of the real wind tunnel and employ a combination of structured and unstructured grids to generate a computational domain. Later, [7] have conducted extensive research focusing on the evaluation of flow quality within the test section of a wind tunnel. The study aimed to provide a comprehensive understanding of the three-dimensional flow characteristics by developing six distinct indices to assess various aspects of flow quality. [8] have performed a computational fluid dynamics (CFD) examination to analyse the flow characteristics in essential sections of a closed-loop wind tunnel. The main focus was to optimize the wind tunnel design, aiming to decrease its overall cost and size while ensuring the capability to maintain a high-quality flow within the test section.

The importance of thermally controlled wind tunnels in simulating atmospheric flow around mechanical and civil structures is doubtless. This research investigated the characteristics of a convective boundary layer generated by a wind tunnel. The results are intended to guide the design and operation of atmospheric flow wind tunnels.

2. Experiment setup

2.1 Geometry

The considered wind tunnel design was inspired by the thermally controlled wind tunnel in [9]. TheClick or tap here to enter text.tunnel has a total length of 37 meters. The contraction section is 10 meters long and has an inlet cross-sectional area of 4.5 by 4.5 meters. The contraction area ratio is 6.6. The main test section length is designed to generate a 0.6-meter turbulent boundary layer, the test section is designed to be 16 meters long with a cross-sectional area of 1.7 by 1.7 meters. The diffuser section has a total length of 11 meters, an expansion area ratio of 5.5, and an outlet cross-sectional area of 4 by 4 meter (refer to Fig.1). For more information on this wind tunnel configuration and its operations, please refer to [11] and [12].

Fig.1(Geometry of the wind tunnel)

2.2 Boundary Conditions

To achieve a mean velocity of 2.5 m/s inside the test section, the inlet velocity was calculated to be 0.36 m/s using the continuity equation. The diffuser outlet pressure was set to zero gauge, allowing the air to exhaust into the atmosphere. In order to create the necessary convective boundary layer, the air was supplied to the tunnel at 27° C, and the test section floor was heated to a temperature of 73° C.

2.3 Grid Dependence Analysis

Three meshes, namely, 1.5, 3 and 6 million cells, were tested to validate the grid-independence of the results. The comparison was based on the axial pressure distribution along the tunnel. The analysis

revealed that the pressure distribution in the last two simulations was almost identical. Therefore, the mesh with 3 million cells was considered for further investigations.

2.4 Monitoring lines Along the Test Section

To obtain the variations in velocity and temperature profiles along the test section, we employed eleven monitoring lines that were not equally distributed along the test section. The distribution of these monitoring lines is presented in Table 1. Monitoring lines were strategically placed to gather data at specific locations along the test section, enabling us to analyse and compare the flow and temperature characteristics at different points within the system.

Line 1	2	3	4	5	6	7	8	9	10	11
X = 0 m	3 m	5 m	7 m	9 m	11 m	13 m	13.5 m	14 m	14.5 m	15 m

Table 1(locations of the monitoring lines)

2.4 Mathematical Model

The continuity, momentum and energy equations were solved for each cell in the domain iteratively to reach the steady state solution. Furthermore, the turbulence was modelled via the k-epsilon model. Several studies have used the k-epsilon model to simulate the airflow inside thermally controlled wind tunnels and to predict the variation of the velocity profile inside the test section. For example, in a study by [13], the k-epsilon model was used to simulate the airflow inside a thermally controlled wind tunnel with a rectangular test section. The simulation predicted that the velocity profile inside the test section was not uniform, with the velocity being higher in the centre of the test section and lower near the walls. In another study by [14], the k-epsilon model was used to simulate the airflow inside a thermally controlled wind tunnel with a circular test section. The simulation predicted that the velocity profile inside the test section was more uniform than in a wind tunnel with a rectangular test section. In order to predict the variation of the velocity profile along the test section, computational fluid dynamics (CFD) simulations have been utilized. The numerical simulations can identify areas where the velocity profile is not uniform and can predict the variation of the velocity profile along the test section. Several studies have used these techniques to predict the velocity profile along the test section of thermally controlled wind tunnels.

3. Results and Discussion

3.1 Velocity simulation

As shown in Fig. 2 and Fig. 6, the velocity profile is flat at the centre of the test section and steep near the walls. The type of flow being simulated also affects the velocity profile along the test section, resulting in a varied Reynolds Number at each monitoring line, as shown in Fig. 4. The impact of the variation in the velocity profile can have a significant effect on the accuracy of the measurements taken in the wind tunnel. Inaccurate velocity measurements can lead to inaccurate drag and lift measurements, which can have serious consequences in the design of aircraft and other aerodynamic systems. Unlike the neutral wind tunnels, the velocity profile in the diffuser section is not symmetric in the upper and lower halves. This is attributed to the vertical temperature gradient in the thermally controlled wind tunnel. This produces separation eddies in the lower half of the tunnel towards its exit.

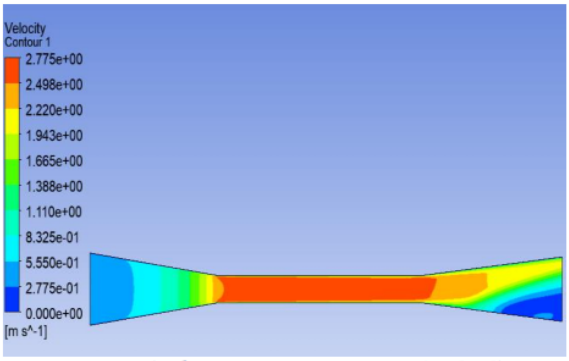

Fig. 2 (velocity contour from ANSYS)

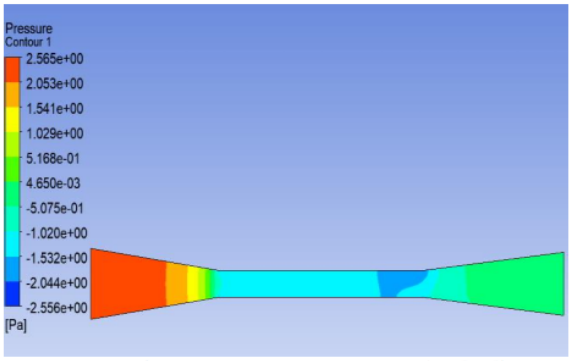

Fig.3 (pressure contour from ANSYS)

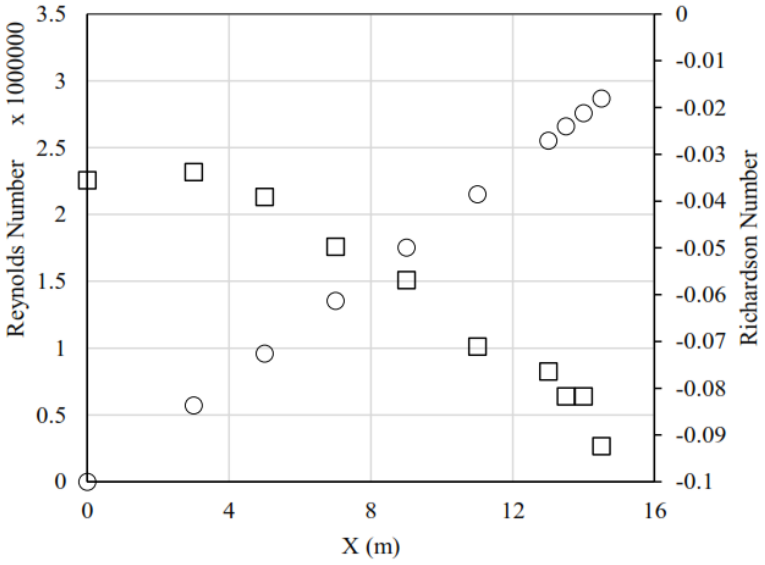

Fig.4 (variation of Reynolds Number and Richardson Number along the test section)

3.2 Stability of the flow

The bulk Richardson number calculated from Eq.1 is a dimensionless parameter that is used to describe the stability of the atmosphere or the flow within the wind tunnel. A negative bulk Richardson number as shown in fig.4 indicates an unstable flow, which can have significant implications for the behaviour of the flow.

$$Rib = \frac{\delta\, g\, \Delta\theta}{\Theta\, U_0^2} \qquad (1)$$

Where Δθ is the temperature difference between the freestream flow and the surface

In a thermally controlled wind tunnel, the temperature of the air flow can be controlled to simulate different atmospheric conditions. When the temperature gradient is steep or the difference in temperature is large, the buoyancy forces can become stronger than the shear forces, leading to an unstable flow. A negative bulk Richardson number can indicate this instability, which can lead to the onset of turbulence and the transition from laminar to turbulent flow. This can have important implications for the accuracy of experimental results and the design of aerodynamic systems.

To address the issue of an unstable flow in a thermally controlled wind tunnel, designers and engineers can modify the temperature control system or the design of the wind tunnel. One approach

is to create a more stable temperature gradient by adjusting the temperature of the upper and lower parts of the test section or changing the design of the temperature control system to create a more gradual temperature gradient. Additionally, modifying the design of the wind tunnel itself, such as increasing the length or width of the test section or adding flow straighteners, can help reduce turbulence caused by flow separation.

3.3 Pressure variation

During simulations inside the test section of a thermally controlled wind tunnel, changes in pressure as shown in Fig. 3 can occur due to a variety of factors, such as changes in the temperature as shown in of the air flow as shown in Fig.5, the presence of objects in the test section, or the use of different experimental setups. These changes in pressure can have significant implications for the accuracy and reliability of the simulation results. Though the pressure gradient is null along the test section, the thermal stratification drives streamwise and vertical pressure gradients towards the end of the test section which can impact the results gathered at this area.

One of the primary effects of changes in pressure during simulations inside the test section of a thermally controlled wind tunnel is a change in the velocity of the air flow. Another effect of changes in pressure during simulations inside the test section of a thermally controlled wind tunnel is a change in the flow regime.

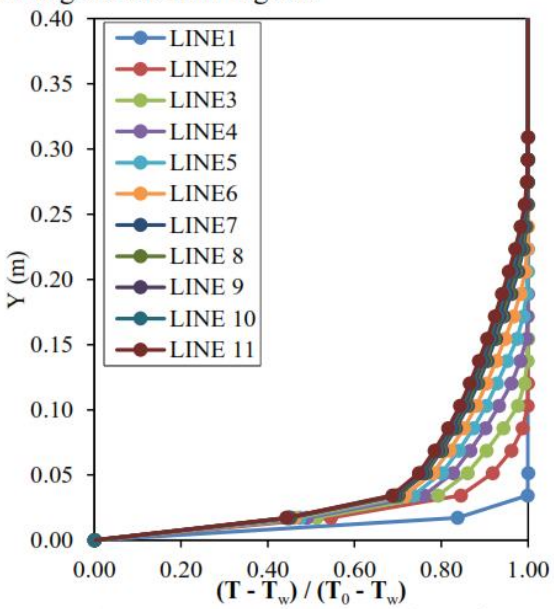

Fig.5 (variation of temperature along the test section)

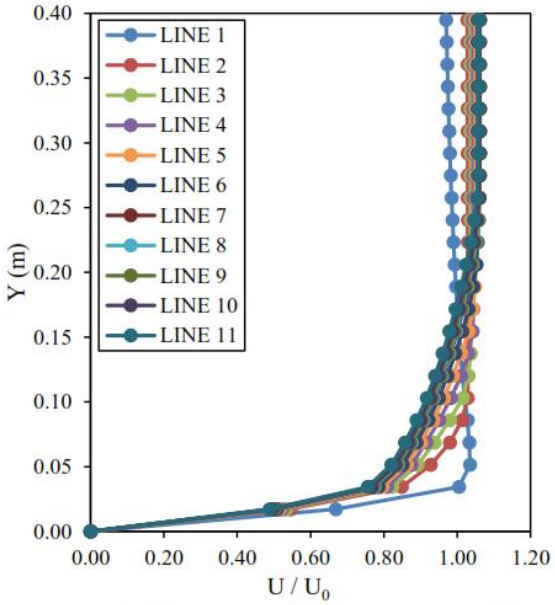

Fig.6 (velocity profile variation at each monitoring line)

4. Conclusion

This work considered the design and simulation of a thermally controlled wind tunnel with specific dimensions to cater to diverse testing requirements such as achieving a maximum velocity of 2.5 m/s, generating a turbulent boundary layer of 0.26-m thickness suitable for testing multiple models, including wind turbines, and obtaining a Bulk Richardson Number of -0.1. The wind tunnel's test section design and simulation were based on a square cross-section, measuring 1.7 meters in width, 1.7 meters in height, and 16 meters in length. To ensure the design was optimized for accurate testing, we used ANSYS CFD software to simulate the aerodynamics of the flow in the wind tunnel. The present work agreed with the results in the. Overall, the thermally controlled wind tunnel's design and simulation represent a valuable tool for researchers and engineers looking to test and optimize various objects. With careful consideration of factors such as dimensions, speed range, thermal control, and turbulence level, the wind tunnel provides an accurate and reliable testing environment.

5. References

[1] A. F. Charwat, *Exploratory Studies on the Sublimation of Slender Camphor and Naphthalene Models in a Supersonic Wind-Tunnel*. Advanced Research Project Agency , 1968.

[2] G. Diana, S. De Ponte, M. Falco, and A. Zasso, "A New Large Wind Tunnel for Civil-Environmental and Aeronautical Applications," *Journal of Wind Engineering and Industrial Aerodynamics*, vol. 74, pp. 553–565, 1998.

[3] Y. Ohya, M. Tatsuno, Y. Nakamura, and H. Ueda, "A thermally stratified wind tunnel for environmental flow studies," *Atmos Environ*, vol. 30, no. 16, pp. 2881–2887, 1996, doi: https://doi.org/10.1016/1352-2310(95)00256-1.

[4] M. D. Manshadi, K. Ghorbanian, and M. R. Soltani, "Experimental study on correlation between turbulence and sound in a subsonic wind tunnel," *Acta Mechanica Sinica*, vol. 26, no. 4, pp. 531–539, 2010, doi: 10.1007/s10409-010-0362-3.

[5] J. K. Calautit, H. N. Chaudhry, B. R. Hughes, and L. F. Sim, "A validated design methodology for a closed-loop subsonic wind tunnel," *Journal of Wind Engineering and Industrial Aerodynamics*, vol. 125, pp. 180–194, 2014.

[6] P. Moonen, B. Blocken, S. Roels, and J. Carmeliet, "Numerical modeling of the flow conditions in a closed-circuit low-speed wind tunnel," *Journal of Wind Engineering and Industrial Aerodynamics*, vol. 94, pp. 699–723, Jul. 2006, doi: 10.1016/j.jweia.2006.02.001.

[7] B. Moonen, J. Blocken, Carmeliet, P. Moonen, B. Blocken, and J. Carmeliet, "Indicators for the evaluation of wind tunnel test section flow quality and application to a numerical closed-circuit wind tunnel," *International Journal of Wind Engineering and Industrial Aerodynamics*, vol. 9502, pp. 1289–1314027, Jul. 2007, doi: 10.1016/j.jweia.2007.02.027.

[8] R. Gordon and M. Imbabi, "CFD Simulation and Experimental Validation of a New Closed Circuit Wind/Water Tunnel Design," *Journal of Fluids Engineering-transactions of The Asme - J FLUID ENG*, vol. 120, Jul. 1998, doi: 10.1115/1.2820650.

[9] M. Bastankhah and F. Porté-Agel, "Experimental and theoretical study of wind turbine wakes in yawed conditions," *J Fluid Mech*, vol. 806, pp. 506–541, Jul. 2016, doi: 10.1017/jfm.2016.595.

[10] M. Bastankhah and F. Porte-Agel, "Wind tunnel study of the wind turbine interaction with a boundary-layer flow: Upwind region, turbine performance, and wake region," *Physics of Fluids*, vol. 29, no. 6, Jun. 2017, doi: 10.1063/1.4984078.

[11] M. Carper and F. Porté-Agel, "Subfilter-scale Fluxes over a Surface Roughness Transition. Part I: Measured Fluxes and Energy Transfer Rates," *Boundary Layer Meteorol*, vol. 126, pp. 157–179, Jul. 2008, doi: 10.1007/s10546-007-9228-z.

[12] L. P. Chamorro and F. Porté-Agel, "Effects of Thermal Stability and Incoming Boundary-Layer Flow Characteristics on Wind-Turbine Wakes: A Wind-Tunnel Study," *Boundary Layer Meteorol*, vol. 136, no. 3, pp. 515–533, 2010, doi: 10.1007/s10546-010-9512-1.

[13] G. Liu, L. Ren, and Y. Gao, "Numerical study on flow characteristics of a thermally controlled wind tunnel.," *J Aerosp Eng*, pp. 353–362, 2013.

[14] X. Huang, Z. Li, and X. Zhang, "Numerical simulation and experimental verification of a circular section thermally controlled wind tunnel," *Aerosp Sci Technol*, pp. 393–401, 2019.